LARGE METEORITE IMPACTS
AND
PLANETARY EVOLUTION IV

Vredefort Dome, South Africa

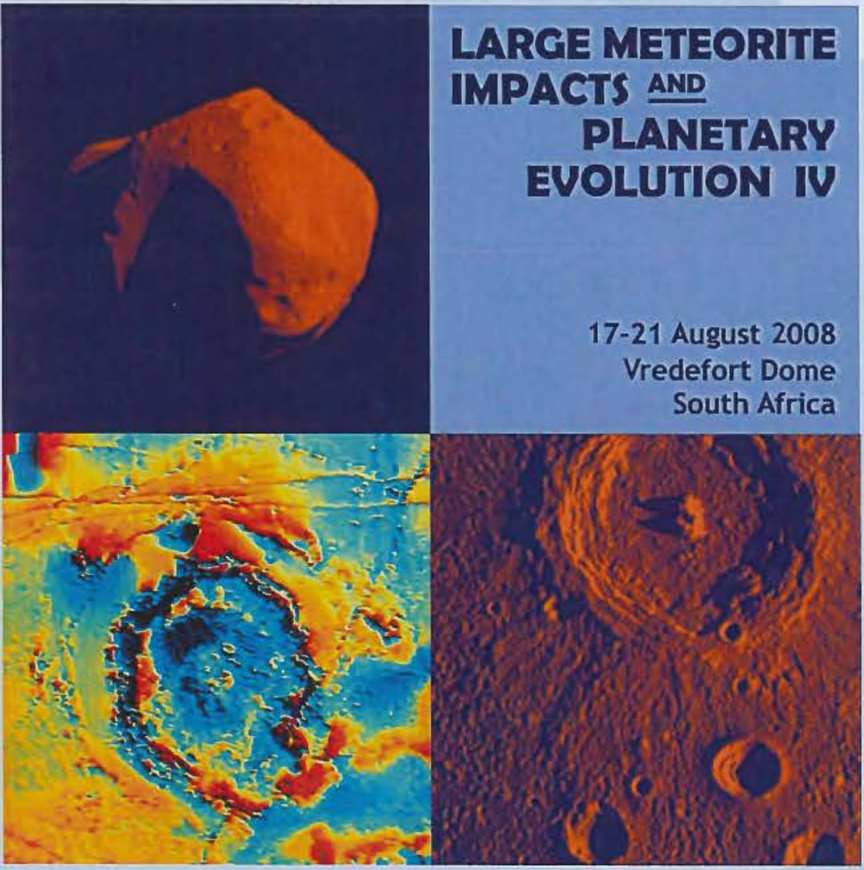

CONFERENCE PROGRAM
&
ABSTRACT VOLUME

LARGE METEORITE IMPACTS AND PLANETARY EVOLUTION IV

August 17–21, 2008 • Vredefort Dome, South Africa

HOSTED BY

University of the Witwatersrand, Johannesburg, South Africa

SPONSORED BY

Lunar and Planetary Institute
National Aeronautics and Space Administration
Barringer Family Fund
Council for Geoscience, South Africa
Department of Agriculture, Conservation and Environment, North West Province
Department of Tourism, Environmental and Economic Affairs, Free State Province
Fezile Dabi District Municipality
Geological Society of South Africa
Geological Society of America
KWV Wineries
National Research Foundation of South Africa
School of Geosciences, University of the Witwatersrand
South African Airways
South African Mint

CONVENERS

Roger Gibson, *University of the Witwatersrand, Johannesburg*
Uwe Reimold, *Museum für Naturkunde, Humboldt University, Berlin*

ORGANIZING COMMITTEE

Charles Cockell, *The Open University*
Christian Koeberl, *University of Vienna*
Jo Morgan, *Imperial College, London*
James Mungall, *University of Toronto*
Elisabetta Pierazzo, *Planetary Science Institute, Tucson*
Ulrich Riller, *McMaster University, Canada*

Conference logo design by Dona Jalufka (Vienna)

Lunar and Planetary Institute 3600 Bay Area Boulevard Houston TX 77058-1113
LPI Contribution No. 1423

Compiled in 2008 by
LUNAR AND PLANETARY INSTITUTE

The Lunar and Planetary Institute is operated by the Universities Space Research Association under a cooperative agreement with the Science Mission Directorate of the National Aeronautics and Space Administration.

Abstracts in this volume may be cited as

Author A. B. (2008) Title of abstract. In *Large Meteorite Impacts and Planetary Evolution IV,* p. XX. LPI Contribution No. 1423, Lunar and Planetary Institute, Houston.

This volume is distributed by

ORDER DEPARTMENT
Lunar and Planetary Institute
3600 Bay Area Boulevard
Houston TX 77058-1113, USA
Phone: 281-486-2172
Fax: 281-486-2186
E-mail: order@lpi.usra.edu

Mail orders requestors will be invoiced for the cost of shipping and handling.

ISSN No. 0161-5297

PREFACE

This volume contains abstracts that have been accepted for presentation at the Conference on Large Meteorite Impacts and Planetary Evolution IV, August 17–21, 2008, Vredefort Dome, South Africa.

Administration and publications support for this meeting were provided by the staff of the Publications and Program Services Department at the Lunar and Planetary Institute.

FOREWORD

The essentially quintennial Large Meteorite Impacts conferences (Sudbury 1992, Sudbury 1997, Nördlingen 2003, Vredefort 2008) provide regular occasions where researchers of all aspects of impact cratering – from planetary remote sensing to terrestrial field studies, the mineralogical, geochemical, and geochronological analysis of impactites, shock experimentation, and numerical modelling of impact processes – can assemble to discuss new developments in the discipline. Traditionally, the three large terrestrial impact structures - Chicxulub, Sudbury and Vredefort - have featured prominently in these conferences, which is why it gives us great pleasure to welcome delegates to the Vredefort Dome for LMI IV. This event represents a return, after 21 years, to the site of the international *Cryptoexplosion and Catastrophes in the Geological Record Workshop* of July 1987, which triggered extensive multidisciplinary analysis of the geology and geophysics of the Vredefort Dome and which, ultimately, provided the impetus for new research endeavours that led to confirmation of the dome and some of its enigmatic features as the products of an impact event 2 billion years ago. This scientific analysis of the Vredefort Dome and its impact-related features over the past 20 years has been a major contributing factor to raising public awareness of the geology of the area. As a consequence, in July 2005, a portion of the Vredefort Dome was declared a World Heritage Site by UNESCO because of Vredefort's special geological status as the largest, oldest and most deeply-eroded known impact structure on earth. When combined with its special scenic and natural beauty, its long record of human habitation since the early Stone Age and its close links to the spectacular Witwatersrand gold deposits, the Vredefort Dome has the potential to become a popular international tourist attraction centered on its geological heritage.

The Large Meteorite Impacts and Planetary Evolution IV conference provides an opportunity to present to delegates, through the conference program and field trips, recent research results on the spectacular geological features of the Vredefort impact structure as well as to highlight the growing partnership between scientific researchers, the people of the Vredefort Dome and local, provincial and national levels of government that seeks to harness the geological heritage of the region for the upliftment of its people.

Twenty-one years after the *Cryptoexplosions Workshop* it is no longer likely that a vote among geoscientists regarding an impact model for the Vredefort Dome would be split as it was in 1987. Nonetheless, research in the dome is far from complete and the dome remains a laboratory for numerous local and international research teams. Judging by the varied and innovative research described in this Abstract Volume, there is no doubt that this conference will prove to be fertile ground for discussion of all spheres of current impact research and that it will sow the seeds of new research initiatives on Vredefort and other impact structures.

This event would not have been possible without the generous support of the sponsors who are listed on the previous page. A special word of thanks is due to the staff of the Publications and Program Services Department at the Lunar and Planetary Institute for the compilation of this Abstracts Volume and CD-Rom.

To all delegates, may your participation be both scientifically rewarding and personally relaxing. Thank you for your support.

Roger Gibson
Wolf Uwe Reimold
(for the LMI IV Organizing Committee)

TRAVEL AWARDEES

Tomoko Adachi	USA
Carl Anhaeusser	South Africa
Natasha Artemieva	Russia
Katerina Bartosova	Austria
Katherine Bron	Australia
Dirk Elbeshausen	Germany
Tiiu Elbra	Finland
Ludovic Ferrière	Austria
Mikhael Gerasimov	Russia
Jennifer Glidewell	USA
Steven Goderis	Belgium
Axel Hoffman	South Africa
Maria Khirfan	Jordan
Cristiano Lana	South Africa
Karin Louzada	USA
Rogerio Machado	Brazil
Roy McG. Miller	Namibia
Michael Poelchau	Germany
Steve Prevec	South Africa
Nele Muttik	Estonia
Jayanta Pati	India
Frank Schönian	Germany
Eric Tegtmeier	USA
Sean Wright	USA

MEETING CALENDAR

Sunday, August 17, 2008

2:00 p.m.	World Heritage Site	Minting of Vredefort Dome World Heritage Site Coin
5:30 p.m.	Parys Country Club	Welcome Reception Coaches will transport delegates leaving the Sunwa Lodge at 5:15 p.m. and returning at 8:30 p.m.

Monday, August 18, 2008

7:45 a.m.	Fisheagle Room	Registration Desk Opens
8:20 a.m.	Hippo Room	Opening Remarks
8:30 a.m.	Hippo Room	Symposium — Large Impact Structures
2:00 p.m.	Hippo Room	Nomenclature Debate
2:45 p.m.	Hippo Room	Terrestrial Cratering I
3:30 p.m.	Hippo Room	Special Contribution
3:45 p.m.	Fisheagle Room	Poster Session
7:45 p.m.	Hippo Room	Invited Evening Lecture by R. M. Miller

Tuesday, August 19, 2008

8:30 a.m.	Hippo Room	Terrestrial Cratering II (continued)
10:45 a.m.	Hippo Room	Extraterrestrial Cratering
2:00 p.m.	Hippo Room	Symposium: Drilling of Impact Structures I
4:00 p.m.	Hippo Room	Geoparks/World Heritage in Impact Structures
6:30 p.m.	Sunwa Restaurant	Dinner
7:30 p.m.	Sunwa Restaurant	Wine Tasting

Wednesday, August 20, 2008

8:30 a.m.	Hippo Room	Drilling of Impact Structures II
10:45 a.m.	Hippo Room	Symposium: Modeling Impact Cratering — Code Improvements and Outcomes
2:00 p.m.	Hippo Room	Symposium: Structural Geology of Impact Craters: From Macro to Micro
6:30 p.m.	Vredefort Interpretation Centre	Presentation of Donations for Vredefort Interpretation Centre and Reception

Thursday, August 21, 2008

8:30 a.m.	Hippo Room	Impact Ejecta
12:00 p.m.	Hippo Room	Open Debate

CONTENTS

* *Denotes speaker*

Monday, August 18, 2008
WELCOME
8:20 a.m. Hippo Room

8:20 a.m. Gibson R. L.
Welcome and Introductory Remarks

SYMPOSIUM — LARGE IMPACT STRUCTURES

Chairs: **Ulrich Riller**
Stephen Prevec

8:30 a.m. Warner M. R. * Morgan J. V. Grieve R. A. F. Barton P. J. Christeson G. L. Gulick S. P. S. Surendra A. T. **[KEYNOTE]**
Does Chicxulub Possess a Differentiated Melt Sheet? **[#3026]**
Seismic reflection, velocity and drill core data at Chicxulub, are compared to velocity and observational data at Sudbury, in order to examine the possibility that Chicxulub possesses a differentiated melt sheet.

9:00 a.m. Newsom H. E. * Nelson M. J. Spilde M. N.
Yaxcopoil-1 Impact Melt Bearing Breccias: The Controversy Over Multiple Composition Melts and the Role of Hydrothermal Alteration **[#3079]**
The chemistry and mineralogy of the Yaxcopoil-1 breccias are not consistent with formation from a single melt composition altered by hydrothermal processes, but require both silicate and dolomitic melts coupled with the infiltration of seawater.

9:15 a.m. Milkereit B. * Artemieva N. Ugalde H.
Geophysical Signature of the Footwall of Large Meteorite Impact Craters **[#3024]**
Through the integration of remote sensing, geophysics, exploration drilling and numerical modeling, we investigate strain distribution in the footwall, the cooling history of the footwall and heterogeneities as seen by seismic and remote sensing data.

9:30 a.m. Prevec S. A. * Kuhn B. K. Büttner S. H.
Tectosilicate Oikocrysts in Impact Melt-hosted Mafic Xenoliths, Contact Sublayer of the Sudbury Igneous Complex, Canada **[#3009]**
A mafic xenolith hosted by basal contact sublayer of the Sudbury impact melt has been found to contain a range of unusual tectosilicate mineral textures, including anhedral oikocrysts of sanidine, suggesting incipient remelting.

9:45 a.m. Hecht L. * Wittek A. Riller U. Mohr T. Schmitt R. T. Grieve R. A. F.
Differentiation and Emplacement of the Worthington Offset Dike of the Sudbury Impact Structure, Ontario **[#3058]**
Based on petrological data and thermal models of the cooling history of the Sudbury Igneous Complex, the two-stage emplacement of the Worthington Offset Dike occurred likely thousands to about ten thousand years after impact.

10:00 a.m. Andreoli M. A. G. * Maier W. D. McDonald I. Barnes S.-J. Roelofse F. Cloete M. C. Okujeni C. Hart R. J.
Siderophile Minerals in the Melt Sheet of the Morokweng Impact Crater, South Africa: Similarities and Differences with the Sudbury Deposits **[#3049]**
The melt sheet of the Morokweng impact crater hosts a variety of Ni, PGE-rich sulphides as impactor-derived condensates. Dykes in the basement carry impactor-derived magmatic segregations of pyrite-pentlandite-pyrrhotite and chalcopyrite.

10:15 a.m. Galdeano A. Andreoli M. A. G. Hart R. J. *
Magnetic Imaging of the Vredefort Dome: Implications for the Size and Geometry of the Vredefort Crater **[#3051]**
Models predicting the size of the Vredefort Crater vary considerably due to the fact that so little of the original crater is exposed. In this study we combine geological observation with magnetic and gravity imaging to visualize the original crater.

10:30 a.m. BREAK

11:00 a.m. Kletetschka G. * Adachi T.
Magnetic Detection of Large Magnetic Fields that Occurred During the Vredefort Impact, Implications for Mars Magnetic Anomalies **[#3094]**
Novel method allows finding microscopic volumes that were magnetized with contrasting magnetic efficiency. Data suggest a presence of large cm-scale magnetic fields during the impact.

11:15 a.m. Crasselt C. * Reimold W. U.
Impact Related Pseudotachylitic Breccias in the Schurwedraai and Baviaan-Krantz Alkali Granite Complex in the Collar of the Vredefort Dome **[#3018]**
Pseudotachylitic breccias in alkali granite of the NW Vredefort Dome were analysed structurally and petrographically. Contrary to Archean Gneiss of the central Dome, the alkali granite lacks structural and compositional heterogeneities.

11:30 a.m. Mohr-Westheide T. * Reimold W. U. Riller U. Gibson R. L.
Pseudotachylitic Breccia and Microfracture Networks in Archean Gneiss of the Central Uplift of the Vredefort Dome, South Africa **[#3021]**
Detailed microstructural investigations of pseudotachylitic breccias and two systems of microfractures, supplemented by field data, has resulted in improved understanding of emplacement of melt into Archean gneiss of the Vredefort Dome.

11:45 a.m. Lieger D. * Riller U. Reimold W. U. Gibson R. L.
Formation of Fragment Rich Pseudotachylite Zones During Central Uplift Formation in the Vredefort Impact Structure, South Africa **[#3020]**
Field-based structural analysis of the Vredefort Dome focused on mapping of pre-impact planar mineral fabrics and structural properties of fragment-rich pseudotachylite zones, such as geometry, orientation, brecciation intensity of the zones.

12:00 p.m. Riller U. * Lieger D.
Geological Evidence for Acoustic Fluidization in Large Impact Structures **[#3025]**
Structural observations from Sudbury and Vredefort suggest that fragment-rich pseudotachylite zones may well be important agents of acoustic fluidization.

12:15 p.m. Jahn A. * Riller U. Reimold W. U.
Three-Dimensional Modeling of Ground-Truth Data — A New Approach for Understanding the Significance of Prominent Discontinuities During Formation of the Vredefort Central Uplift, South Africa **[#3040]**
The sedimentary rocks and faults of the Vredefort Central Uplift have been constructed in a 3D model. This model is based on ground-truth data and geophysical data. It provides new insights into the deep structure of the Vredefort Dome and its formation.

12:30 p.m. Gibson R. L. * Ogilvie P.
The Hottest Rocks in the Vredefort Dome, South Africa — Extending the Links Between Impact-induced and "Normal" Metamorphism **[#3108]**
Impact structures are sites of extreme pressure and temperature fluctuations related to the interaction and decay of the shock wave with the target rocks through which it passes.

12:45 p.m. Elston W. E. *
Proposed Bushveld Scenario: Impact, Mantle Upwelling, Meltdown, Collapse **[#3015]**
The 2.06 Ga Bushveld impact triggered mantle upwelling and lithosphere melts, creating world's largest igneous complex. Its history is recorded in repeated overflows from a superheated meltpool, accumulated in an outer ring (pseudovolcanic Rooiberg Group).

1:00 p.m. LUNCH

Monday, August 18, 2008
NOMENCLATURE DEBATE
2:00 p.m. Hippo Room

Chair: **Jared Morrow**

2:00 p.m. Reimold W. U. * Horton J. W. Jr. Schmitt R. T.
Debate About Impactite Nomenclature — Recent Problems **[#3033]**
Several recent issues with impactite nomenclature are discussed against the proposed Nomenclature of the IUGS Subcommission on Metamorphic Geology. A debate of this issues is to be held.

2:10 p.m. Open Discussion

Monday, August 18, 2008
TERRESTRIAL CRATERING I
2:45 p.m. Hippo Room

Chairs: **Roger Gibson**
Jared Morrow

2:45 p.m. Crósta A. P. *
Basaltic Impact Structures of the Paraná Basin, Brazil **[#3014]**
The impact record of the Paraná Basin comprises three structures formed on Cretaceous basalts. This paper presents the characteristics of these structures and their importance as the only medium-sized complex structures formed over basalt.

3:00 p.m. Pati J. K. * Reimold W. U. Koeberl C. Singh H. K. Pati P.
Dhala — A New, Complex, Paleoproterozoic Impact Structure in Central India **[#3041]**
The Dhala structure (N25°17'59.7" and E78°8'3.1") is a newly discovered impact structure of paleoproterozoic age in central India and occurs on a granitoid basement with a currently estimated diameter of 11 km contains nearly all evidences of shock metamorphism.

3:15 p.m. Salameh E. * Khoury H. Reimold W. U. Schneider W. Kenkmann T.
First Large Meteorite Impact Structure Discovered in the Middle East:
Jebel Waqf As Suwwan, Jordan **[#3106]**
A 5.5 km diameter, complex, circular structure was discovered in the central eastern region of the Kindom of Jordan.

Monday, August 18, 2008
SPECIAL CONTRIBUTION
3:30 p.m. Hippo Room

3:30 p.m. Kato M. * Takizawa Y. Sasaki S.
The Kaguya (SELENE) Mission: Present Status and Lunar Science **[#3115]**
Lunar orbiter Kaguya (SELENE) was successfully launched from TNSC on September 14, 2007.

Monday, August 18, 2008
POSTER SESSION
3:45 p.m. Fisheagle Room

Baker T. Phillips M. E.
Remote Sensing of the Morokweng Impact Structure, South Africa **[#3064]**
Landsat Thematic Mapper/Enhanced Thematic Mapper data have been studied to look for arcuate, impact-related structures. Probable arcuate structures and arcuate drainage patterns were seen on the processed and enhanced imgery.

Andreoli M. A. G. Hart R. J. Cooper G. R. J. Webb S. J.
The Morokweng Impact Crater, South Africa: A Complex, Multiring Structure with a ~130 km Radius External Ring and Asymmetric Radial Sectors **[#3048]**
The poster summarizes the main features of the Morokweng Crater on the basis of up-to-date geophysical imagery and borehole data. The authors conclude that Morokweng is a multiring crater with a final rim of ~190 km and an external ring of ~260 km.

Mielke Ch. Riller U. Reimold W. U.
Assessing Different Remote Sensing Techniques for Geological Mapping in Complex Impact Structures, an Example from the Central Rand Group in the Vredefort Impact Structure **[#3116]**
Remote sensing is a powerful tool for mapping large-scale geological structures such as the Vredefort impact structure.

Asabi O. Phillips M. E.
3D-GIS and Remote Sensing for Modelling the Size and Extents of the Gardnos Impact Structure, Norway **[#3065]**
Integration of field survey data, 3D-GIS data, stereo air photos and satellite remote sensing was used to model and map the structure and morphology at Gardnos. Results appear to be in correlation with recent ground-based studies.

Phillips M. E. Townsend C. Bartels K.
Remote Sensing and GIS Analyses for Determining Size, Morphology and Lithological Mapping of the Vredefort Impact Structure, South Africa **[#3061]**
Satellite remote sensing data with 3D GIS data were used for three interrelated project analyses of the Vredefort structure, over the period 1999–2005. Many different and previously unrecognised features and lithologies were mapped.

Townsend C. L. Phillips M. E.
Morphological Investigation of Vredefort Using Remote Sensing, GIS and 3D Modelling **[#3084]**
An interactive, 3D Digital Elevation Model (DEM) was created of the Vredefort impact structure at a spatial resolution of 30 metres.

Wittmann A. Fernandes V. A. Renne P. R. Schmitt R. T. Reimold W. U. Hecht L. Povenmire H.
Preliminary Age of Impact Melts from the Chesapeake Bay Impact Structure **[#3093]**
First preliminary Ar-Ar ages for melt rocks of the Chesapeake Bay impact structures are between 44.8 and 48.1 Ma. The difference to the ages of ~35–36 Ma that were based on ejecta and biostratigraphic correlations may be due to inherited Ar.

Marcus R. A. Stewart S. T. Barranco J. A. Hernquist L. Sasselov D.
SPH Simulations of Planetary-Scale Impacts **[#3075]**
We discuss applications of a new smoothed particle hydrodynamics code designed for simulations of planetary-scale impacts.

Pugacheva S. G. Shevchenko V. V. Chikmachev V. I.
Structure and Morphology of the Multiring Lunar Basins **[#3029]**
The morphological features of the multiring lunar basins are considered. The common characteristics of the multiring basins were researched. The South Pole-Aitken Basin (SPA) represents a compositionally and topographically unique lunar formation.

Lambert P. Trumel H.
Physical Modeling: Multi-Scale Approach and its Applicability to Large Meteorite Impacts **[#3035]**
Shifting from phenomenological to physical modeling implies downscale characterization of mechanisms, transcoding into a mathematical form and upscaling. The aim is to show that such an approach developed in the defense community can be applied to large impact cratering.

de Niem D. Kührt E. Motschmann U.
Condensate Composition from Asteroid Impacts **[#3054]**
A model of formation of condensate from vaporizing asteroidal impactis presented. Applications: 1) Spinels in the Chicxulub impact; 2) Chondrules in Bencubbin-like meteorites.

Milam K. A.
Petrogenesis of Central Peak Formation on Mars **[#3089]**
Deformation fabrics displaying similar to and displaying the same cross-cutting relationships as those identified in terrestrial complex craters have been identified on Mars using high-resolution imagery from the MOC and HiRISE imaging systems.

Stewart S. T. Senft L. E.
Advances in Modeling Collisions on Icy Bodies **[#3085]**
We present recent advances in the quality of the equation of state and consititutive models for H2O and discuss the implications for collisional processes on icy bodies.

Giuli G. Eeckhout S. G. Pratesi G. Koeberl C. Cicconi M. R. Paris E.
Variations in Fe Oxidation State Between Dark and Light Layers of Muong Nong-type Tektites **[#3047]**
The Fe oxidation state along a profile across dark and light layers of a Australasian Muong Nong tektite sample has been studied by Fe K-edge XANES. The dark layer results to be slightly but reproducibly more oxidized respect to the light layers.

Vetvicka I. Frank J. Drtina J.
Morphological Differences Between Irghizites and Splash-Form Glasses from Lonar Crater — Evidence of Different Conditions of Origin of Those Glasses **[#3088]**
Most of splash-form glasses from Lonar have a dull rough surface, because after the impact they were flying in cloud of ash and dust, while irghizites are smooth and lustrous, because they were flying for some time out of the cloud of ash and dust.

Buchner E. Deinerth N. J. Schmieder M.
A Possible Upper Eocene-Oligocene Impact Spherule Layer in the North Alpine Foreland Basin, Upper Bavaria, Germany? **[#3104]**
Layers of distal impact ejecta have been reported from various sites on Earth through geologic time.

Meyer C. Artemieva N. Stöffler D. Reimold W. U. Wünnemann K.
Possible Mechanisms of Suevite Deposition in the Ries Crater, Germany: Analysis of Otting Drill Core **[#3066]**
In this presented work we to revisited the suevite problem of the Ries cCater, Germany, in an interdisciplinary study by combining geological and petrograhic observations from Otting drill core with numerical models of crater and ejecta plume formation/deposition.

Schönian F. Stöffler D. Kenkmann T.
On the Distribution of Impact Melt and Basement Clasts in the Chicxulub Ejecta Blanket **[#3100]**
The distribution of melt particles and basement clasts within the Chicxulub ejecta blanket suggests that vapor plume material overrun the ejecta curtain, was deposited first and subsequently eroded and incorporated by the secondary ejecta flow.

King D. T. Jr. Petruny L. W. Harris R. S. Glidewell J. Johnson R. C.
Comparison of Marine-Crater Stratigraphy: Chesapeake Bay and Wetumpka **[#3110]**
Chesapeake Bay Crater, Virginia, is a late Eocene impact structure, which is completely buried beneath the Atlantic Coastal Plain.

Schmieder M. Buchner E.
Paleoenvironmental Charts for Terrestrial Impact Structures — A Simple Tool to Test Impact Ages and Marine/Continental Impact Conditions **[#3028]**
We present paleoenvironmental charts as a tool to refine poor and/or equivocal impact ages and to discriminate between marine and continental impact events on Earth.

Khirfan M. Kenkmann T. Salameh E. Omary Y. Reimold W. U.
Remote Sensing and Structural Analysis of Jabal Waqf As Suwwan Meteorite Impact **[#3109]**
A large meteorite impact structure has recently been discovered in the Middle East, in Jordan at Jabal Waqf As Suwwan.

Raiskila S. Elbra T. Öhman T. Pesonen L. J.
Petrophysical and Palaeomagnetic Studies of the Keurusselkä Impact Structure, Central Finland **[#3056]**
The sampling at Keurusselkä impact structure started in 2007. Samples were collected from shatter cone outcrops and along a profile. Petrophysical and palaeomagnetic measurements were measured at the Solid Earth Geophysics Laboratory in University of Helsinki.

Kenkmann T. Artemieva N. A. Wünnemann K. Poelchau H. Elbeshausen D. Nunez del Prado H.
The Remarkable Meteorite Impact Event on September 15, 2007, Carancas, Peru: What Did We Learn? **[#3063]**
The Carancas event showed that metre-sized stony meteorites can survive atmospheric passage under specific circumstances. We present results of a detailed crater survey, reconstruct crater formation, and derive conditions during atmospheric traverse.

Tegtmeier E. L. Newsom H. E. Elston W. E. McElvain T. H.
Breccias and Geological Setting of the Santa Fe, New Mexico USA Impact Structure **[#3090]**
Primary evidence for the new Santa Fe impact structure consists of spectacular shatter cones. In addition, breccia pods that form conspicuous walls in the region may have been emplaced from above into zones of subcrater dilation.

Adachi T. Kletetschka G.
A New Method of Testing the Heterogeneity of the Impact Origin, Shatter Cones of Newly Discovered Impact Site, Santa Fe, New Mexico, USA **[#3092]**
The magnetic signatures of the two shatter cones showed the heterogeneous orientations and intensity of natural remanent magnetizations that may attribute to the impact event.

Elbeshausen D. Wünnemann K.
Asymmetries in Complex Craters due to Oblique Meteorite Impacts? **[#3080]**
We conducted several 3D-hydrocode simulations to discover how an oblique impact affects complex crater formation. We focus on the evolution of central peaks and the quest for asymmetries in the target as possible indicators for the impact angle or direction.

Yokoyama E. Trindade R. I. F. Lana C. C. Marangoni Y. R. Tohver E.
Magnetic Fabrics of Araguainha Impact Structure (Central Brazil): Impact Products and Collapse History in the Central Peak-Ring **[#3086]**
Petrographic and AMS studies in impact-related materials inside the central peak ring allow recognition of four lithofacies that record different magnetic fabrics.

Ferrière L. Morrow J. R. Amgaa T. Koeberl C.
Systematic Comparison of Universal Stage-indexed Planar Deformation Features in Quartz: Implications for Statistical Significance and Representation of Results **[#3010]**
Universal stage analysis is a standard technique used for determining the crystallographic orientations of planar deformation features in quartz. The quality, precision, repeatability, and representativeness of the measurements have been tested.

Coney L. Reimold W. U. Hancox P. J. Mader D. Koeberl C. McDonald I. Struck U.
Vajda V. Kamo S. L.
The Permian-Triassic Boundary, Karoo Basin, South Africa: Geochemical Insight into this Mass Extinction Event **[#3032]**
The P-T mass extinction has been documented as the largest Phanerozoic mass extinction. Geochemical and mineralogical results from terrestrial sections in the Karoo Basin, South Africa will be presented.

Tredoux M.
PGE Enrichment at the KTB: Is it a Sign of Cause or a Sign of Effect? **[#3074]**
Investigation of the geochemistry of the KTB has brought to light data that are not easily reconciled with a primary fall-out layer. It is suggested that the Deccan traps provided a better source.

Elston W. E.
Proposed Bushveld Scenario: Impact, Mantle Upwelling, Meltdown, Collapse **[#3015]**
The 2.06 Ga Bushveld impact triggered mantle upwelling and lithosphere melts, creating world's largest igneous complex. Its history is recorded in repeated overflows from a superheated meltpool, accumulated in an outer ring (pseudovolcanic Rooiberg Group).

Schenk P. M. McKinnon W. B.
A Gallery of Multiring Basins on Europa, Ganymede, and Callisto **[#3107]**
The largest craters on Earth, the other terrestrial planets, and major icy satellites (of Jupiter) possess one or more exterior rings.

Monday, August 18, 2008
INVITED EVENING LECTURE
7:45 p.m. Hippo Room

7:45 p.m. Miller R. McG. *

The Roter Kamm Meteorite Impact Crater and its Ejecta Apron in the Southern Namib Desert of Southwestern Namibia **[#3008]**

Mappable features in the rim and ejecta apron of the 3.7 Ma Roter Kamm Crater suggest that the impact projectile was travelling in a northwesterly direction.

Tuesday, August 19, 2008
TERRESTRIAL CRATERING II (continued)
8:30 a.m. Hippo Room

Chairs: **Roger Gibson**
Jared Morrow

8:30 a.m. Baegi M. *
Carbonatites Versus Meteorite Impact Origin of Two Circular Structures Outcrop at Eastern Al-Awaynat Area, SE Libya **[#3036]**
Two major circular structures of 3 km in diametres each, located about 120 km southwest of Jabal Arkeno were identified by airborne geophysical survey in 1973, and designated as R33 and R34A.

8:45 a.m. Di Martino M. * Cigolini C. Orti L.
Non-Impact Origin of the Arkenu Craters (Libya) **[#3012]**
Our study suggests the Arkenu craters (S-E Libya) are not of impact origin, but have been formed by the intrusion of a paired nearly cylindrical subvolcanic stocks (coupled with ring dike injection) accompanied by hydrothermal degassing.

9:00 a.m. Anhaeusser C. R. * Stettler E. Cooper G. R. J. Gibson R. L.
Setlagole Megabreccia, South Africa: Clues to a Possible Mesoarchaean Impact Event and Aeromagnetic Recognition of a c.30 km Concentric Multiple Ring Structure **[#3053]**
A spectacular Archaean megabreccia in the granite-greenstone terrane of the North West Province South Africa led to the recognition of a new, possible Mesoarchaean-age, impact site exceeded in size only by the Vredefort and Morokweng structures.

9:15 a.m. Muttik N. * Kirsimäe K. Osinski G. R. Somelar P. Vennemann T. W.
Alteration of Surfical Suevites at the Ries Crater, Germany: Mineralogical and Stable Isotope Evidences **[#3003]**
The origin of secondary phases in surfical suevites has been interpreted as resulting from post-impact hydrothermal processes. We show that the alteration has occurred due to weathering processes other than impact induced hydrothermal alteration.

9:30 a.m. Buchner E. * Kenkmann T.
Upheaval Dome, Utah, USA: Impact Origin Confirmed **[#3005]**
We have documented shocked quartz grains of the Upheaval Dome structure, Utah, USA, with multiple sets of thin planar deformation features that provides definite evidence for the impact origin of Upheaval Dome.

9:45 a.m. Lambert P. *
Impact Deposits at Rochechouart-Chassenon **[#3034]**
Excavation and readjustment did not mix nor homogenise proximal ejecta at Rochechouart-Chassenon large impact crater. The structure is much less eroded than previously thought and actual deposits which include airborne ash, are representative of the initial crater fill.

10:00 a.m. Dypvik H. * Kalleson E.
Marine Impacts — Mechanisms of Early Post-Impact Crater Sedimentation **[#3004]**
In marine craters comparable post-impact sedimentary successions have been found; developing from avalanches, screes, slides and slumps, through mass flows before ending with density currents and fine-grained sedimentation from suspension.

10:15 a.m. BREAK

Tuesday, August 19, 2008
EXTRATERRESTRIAL CRATERING
10:45 a.m. Hippo Room

Chairs: **Nadine Barlow**
Bill McKinnon

10:45 a.m. Marinova M. M. * Aharonson O. Asphaug E.
Crustal Consequences of Planetary-Scale Impacts **[#3097]**
Planetary-scale impacts on early Mars are investigated, for a wide parameter space. The conclusions focus on melt production, crustal excavation and redistribution, antipodal disruption, escaping and orbiting material, and angular momentum transfer.

11:00 a.m. Öhman T. * Aittola M. Kostama V.-P. Korteniemi J. Raitala J.
The Control of Target Structure on the Crater Morphology on the MoonMars, and Venus — Evidence and Implications **[#3046]**
Polygonal impact craters may form by thrusting along pre-existing fault planes. They are preferentially formed in the size range of small to mid-sized complex craters, and may perhaps indicate the presence of basin-induced conjugate shear fractures.

11:15 a.m. Fuller M. *
The Paleomagnetic Record of Large Meteorite Impacts and Lunar Magnetism **[#3023]**
Large meteorite impact related shock appears to play a major role in lunar magnetism. This work uses ground truth from terrestrial impacts and basic rock magnetism techniques to investigate the role of this impact related shock in lunar magnetism.

11:30 a.m. Hirata N. * Haruyama J. Ohtake M. Matsunaga T. Yokota Y. Morota T. Honda C. Ogawa Y. Torii M. Sugihara T. Miyamoto H. Demura H. Asada N.
Amount and Distribution of Impact Melt of Large Lunar Craters: Views from LISM/Kaguya **[#3060]**
The LISM on Kaguya provide high-resolution and multi-spectral mapping data of the Moon. The purpose of this study is to make morphological analyses of those craters with the data from LISM.

11:45 a.m. Demura H. * Haruyama J. Ohtake M. Matsunaga T. Yokota Y. Morota T. Honda C. Ogawa Y. Torii M. Hirata N. Asada N. Sugihara T. Saiki K.
Photogeological Mapping of Orientale Basin on the Moon, LISM/Kaguya (SELENE) **[#3069]**
This presentation is a quick report of photogeological mapping of the Orientale Basin on the Moon, LISM/Kaguya (SELENE).

12:00 p.m. Louzada K. L. * Stewart S. T.
The Effect of Planet Curvature on the Shock Pressure Field Around Martian Impact Basins **[#3101]**
We performed a simplified ray path numerical calculation to investigate the effects of curvature on the depth of the interference zone and the pressure field around large impact basins.

12:15 p.m. Barlow N. G. * Alzate N.
Central Pit Craters on Mars and Ganymede: Characteristics, Distributions, and Implications for Formation Models **[#3071]**
Central pit craters on Mars and Ganymede display both similarities and differences. Comparing central pit craters on these two bodies gives us a better understanding of the environmental conditions producing these features and better constrains pit formation models.

12:30 p.m. McKinnon W. B. * Schenk P. M. **[KEYNOTE]**
Multiring Basins on Icy Satellites: A Post-Galileo View **[#3103]**
Icy satellites offer a valuable laboratory to explore multiring basin formation, as icy lithospheres can be quite thin and ring systems quite extensive. Structures on Europa are emphasized, and compared with their much larger cousins on Callisto.

1:00 p.m. LUNCH

Tuesday, August 19, 2008
SYMPOSIUM: DRILLING OF IMPACT STRUCTURES I
2:00 p.m. Hippo Room

Chairs: **Christian Koeberl**
J. Wright Horton

2:00 p.m. Koeberl C. * **[KEYNOTE]**
What can be Learned from Drilling into Impact Craters: A Review of Recent Projects **[#3083]**
Discover of some features, as well as study of the subsurface of impact structures, involves drilling. Recent efforts at Chicxulub, Bosumtwi, and Chesapeake Bay are described.

2:30 p.m. Horton J. W. Jr. * Kunk M. J. Belkin H. E. Aleinikoff J. N. Jackson J. C. Chou I.-M.
Investigations of Impactites and Crystalline Target Rocks in the ICDP-USGS Eyreville-B Core, Chesapeake Bay Impact Structure **[#3102]**
Studies of deep drill cores from the Chesapeake Bay impact structure provide insights into marine cratering processes.

2:45 p.m. Powars D. S. * Catchings R. D. Gohn G. S. Horton J. W. Jr Edwards L. E. Daniels D. L.
Geophysics and Deep Coreholes Reveal Anatomy and Complex Infilling of the Central Crater, Chesapeake Bay Impact Structure, U.S.A **[#3087]**
Seismic and corehole studies within the Chesapeake Bay impact structure reveal that target asymmetry significantly affected the complex infilling of the crater.

3:00 p.m. Elbra T. * Kontny A. Pesonen L. J.
Rock Magnetic Investigations of Impactites from Deep Drill Cores of Bosumtwi and Chesapeake Bay Impact Structures **[#3042]**
We present and compare our rock magnetic investigations of the deep drill core samples from Bosumtwi and Chesapeake Bay impact structures. Results show that pyrrhotite and magnetite are carrying magnetic properties of impactites in both structures.

3:15 p.m. Horton J. W. Jr. * Gibson R. L. Reimold W. U. Wittmann A. Gohn G. S. Edwards L. E.
Geologic Column for the ICDP-USGS Eyreville-B Core, Chesapeake Bay Impact Structure: Impactites and Crystalline Rocks, 1,095–1,766 m **[#3091]**
The ICDP-USGS Eyreville drill cores in the Chesapeake Bay impact structure provide one of the most complete geologic sections ever obtained from an impact structure. Geologic columns are presented for the deepest sections.

3:30 p.m. Bartosova K. * Koeberl C. Reimold W. U.
Stratigraphy of the Impactite Section (1397–1551 m) from the Eyreville Drillcore, Chesapeake Bay Impact Structure, USA **[#3013]**
Petrographic analyses of impactites from the Eyreville drill core, Chesapeake Bay impact structure. Suevites from the impactite section (1397–1451 m) were divided into six subunits according to their clast and melt content and characteristics.

3:45 p.m. BREAK

Tuesday, August 19, 2008
GEOPARKS/WORLD HERITAGE IN IMPACT STRUCTURES
4:15 p.m. Hippo Room

Chair: **Uwe Reimold**

4:15 p.m. Gibson R. L. * Blom M.
Geotourism Potential of the Vredefort Dome, South Africa - Challenges, Opportunities, Progess and Recommendations **[#3112]**
The Vredefort Dome is a 90-km-wide geological entity located ~120 km southwest of Johannesburg, South Africa, that represents the eroded central uplift of the world's oldest and possible largest known meteorite impact structure.

4:30 p.m. Stöffler D. Pösges G. * Barfeld R.
Development of Geotourism in the National Geopark Ries, Southern Germany **[#3070]**
The Geopark Ries devoted to the Ries impact crater is currently under development. The Geopark covers an area of 1800 km^2 comprising a total of 53 communities. The Ries has been certified as a national geopark in May 2006.

4:45 p.m. Barnardo D. J. *
The Role of the Geological Society of South Africa in Promoting the Establishment of Africa's First Geopark at the Tswaing Meteorite Impact Crater **[#3111]**
The Geological Society of South Africa (GSSA) has a Conservation and Tourism Committee as part of its activities.

Wednesday, August 20, 2008
DRILLING OF IMPACT STRUCTURES II
8:30 a.m. Hippo Room

Chairs: **Christian Koeberl**
J. Wright Horton

8:30 a.m. Jolly L. C. * Gibson R. L. Reimold W. U. Horton J. W. Jr.
Clast Characteristics in the Suevitic and Lithic Breccias from the ICDP-USGS Eyreville B Drillcore, Chesapeake Bay Impact Structure, Virginia, USA **[#3052]**
This abstract provides detailed petrographic descriptions of the mineral, lithic and melt clasts that are present in the 154 m suevitic and lithic breccia recovered from the Eyreville B drillcore.

8:45 a.m. Wittmann A. * Reimold W. U.
The Volume of Impact Melt in the Chesapeake Bay Crater **[#3039]**
Quantitative analyses of a drill core through the Chesapeake Bay Crater confirm a max. amount of ~10 km^3 of melt inside the crater. This suggests dispersal of 95 % of potentially produced melt due to release of volatiles from the marine target.

9:00 a.m. Glidewell J. * Harris R. S. King D. T. Jr. Petruny L. W.
Shock Feature Analysis of Selected Samples from the Eyreville Core: Chesapeake Bay Impact Structure, Virginia, USA **[#3095]**
Further analysis of the Chesapeake Bay impact structure Eyreville A and B cores reveals evidence of at least low levels of shock in each major stratigraphic interval of the core section.

9:15 a.m. Goderis S. * Vanhaecke F. Hertogen J. Claeys Ph.
Platinum Group Element (PGE) Ratios in the Cored Impactites of the Eyreville Drill Site of the Chesapeake Bay Impact Structure **[#3031]**
An attempt is made to characterize the chemical nature of the Chesapeake Bay projectile using platinum group elements in combination with nickel and chromium. The results for six selected samples of the Eyreville drill site are reported.

9:30 a.m. Malinconico M. L. * Sanford W. S. Horton J. W. Jr.
Post-Impact Thermal History of the Chesapeake Bay Impact Structure, Based on Downhole Vitrinite Reflectance, ICDP-USGS Eyreville Deep Cores and Other Cores **[#3068]**
Vitrinite reflectance data and heatflow modeling indicate post-impact heating in the Chesapeake Bay impact structure is due primarily to compaction-driven advective flow from suevitic and deeper brines with minor conductive heating from the suevites.

9:45 a.m. Coney L. * Reimold W. U. Gibson R. L. Koeberl C. Czaja P. Born K.
The Bosumtwi Impact Structure, Ghana: Comparison Between Within-Crater and Out-of-Crater Suevites with Particular Focus on Melt Particle Compositions **[#3043]**
Geochemical data for the various suevites (and their melt particles) from the Bosumtwi structure, Ghana, are reported in order to refine a model for the cratering event.

10:00 a.m. Pohl J. Poschlod K. Reimold W. U. * Crasselt C.
Ries Crater, Germany: The Enkingen Magnetic Anomaly and Associated Drill Core SUBO 18 **[#3030]**
A new 100 m drill hole in a local magnetic anomaly area located in the southern inner ring of the Ries crater yielded 80 m of suevite and, surprisingly, massive impact melt rocks. The petrology and magnetic properties of the core are discussed.

10:15 a.m. BREAK

Wednesday, August 20, 2008
SYMPOSIUM:
MODELING IMPACT CRATERING — CODE IMPROVEMENTS AND OUTCOMES
10:45 a.m. Hippo Room

Chairs: **Elisabetta Pierazzo**
Joanna Morgan

10:45 a.m. Melosh H. J. * **[KEYNOTE]**
Equation of State and Material Strength for Impact Cratering Simulations **[#3113]**
Numerical simulations of impact events rest on three major pillars: Newtonian mechanics, thermodynamics, and the contimuum mechanics of material strength.

11:15 a.m. Pierazzo E. * Artemieva N. Asphaug E. Baldwin E. C. Cazamias J. Coker R. Collins G. S. Crawford D. A. Davison T. Elbeshausen D. Holsapple K. A. Housen K. R. Korycansky D. G. Wünnemann K.
The Impact Hydrocode Benchmark and Validation Project **[#3022]**
When properly benchmarked and validated against observations computer models offer a powerful tool for understanding the mechanics of impact crater formation. We present results from a project to benchmark and validate shock physics codes.

11:30 a.m. Wünnemann K. * Collins G. S. Elbeshausen D.
Limitations of Point-Source Analogy for Meteorite Impact and Implications to Crater-scaling **[#3076]**
We use hydrocode modeling to study scaling laws and the applicability of the point-source analogy. We conducted numerous of numerical experiments for oblique and vertical impacts of crater formation over a large parameter range and present the available database.

11:45 a.m. Collins G. S. * Kenkmann T. Wünnemann K. Wittmann A. Reimold W. U. Melosh H. J.
A Model for the Formation of the Chesapeake Bay Impact Crater as Revealed by Drilling and Numerical Simulation **[#3059]**
The combination of numerical simulation results and petrographic analysis of drill core from the recent ICDP-USGS drilling project provides new insight into the formation of the Chesapeake Bay impact crater.

12:00 p.m. Senft L. E. Stewart S. T. *
Frictional Melt Formation Around Large Craters **[#3077]**
Frictional melts (pseudotachylites) are observed around many large impact craters and may play a role in aiding crater collapse. Here we use numerical modeling to predict where frictional melts should form and compare results to field observations.

12:15 p.m. Artemieva N. *
Impact Ejecta Modeling: Main Principles and a few Examples **[#3082]**
We shortly discuss numerical methods to solve two-phase hydrodynamics (gas loaded by solid/molten particles) and present the results for directed volcanic blast, the Ries and the Chicxulub impact craters.

12:30 p.m. Pierazzo E. * Sassi F.
Short-Term Effects of Impact-related Heating of the Upper Atmosphere **[#3081]**
We use WACCM to look at the effects of a strong heating of the upper atmosphere from a KT-size impact event. The heating produces an immediate LW radiation to the surface, while effects on atmospheric chemistry extend well beyond the heating.

1:00 p.m. LUNCH

Wednesday, August 20, 2008
SYMPOSIUM:
STRUCTURAL GEOLOGY OF IMPACT CRATERS: FROM MACRO TO MICRO
2:00 p.m. Hippo Room

Chairs: **Thomas Kenkmann**
Gareth Collins

2:00 p.m. Kenkmann T. * Poelchau M. H. **[KEYNOTE]**
The Structural Inventory of Oblique Impact Craters **[#3057]**
The bilateral symmetric stacking of imbricate thrusts in the central uplifts of some complex craters accommodates shortening in thrust direction. It reflects a migration of the uplifting crater floor down range and is a tool to infer impact vectors.

2:30 p.m. Elbeshausen D. * Wünnemann K.
Complex Crater Formation Driven by Oblique Meteorite Impacts **[#3078]**
Several 3D-hydrocode simulations were performed to study the formation of complex craters driven by oblique impacts. We focus on the temporal evolution of the crater shape, especially the central peak, and the origin of crater asymmetries caused by the impact angle.

2:45 p.m. Lana C. *
Structural Evolution of an Asymmetric Central Uplift; Effects of Target Heterogeneities or Oblique Impact? **[#3045]**
The Araguainha central uplift is a prominent asymmetric feature in central Brazil. In this study, I investigate the structural evolution of this asymmetric feature and make inferences of a possible oblique impact, with a northerly downrange direction.

3:00 p.m. Milam K. A. * Deane B.
Deformation/Modification Sequence in Target Rocks of Complex Craters <20 km Diameter: Implications for Impact Crater Identification **[#3096]**
Deformation fabrics occur in predictable cross-cutting relationships in floors and central uplifts of complex craters. The resulting petrogenetic sequence may provide another method for confirming additional complex craters on Earth and other planets.

3:15 p.m. Poelchau M. H. * Kenkmann T. Kring D. A.
Structural Aspects of Meteor Crater and Their Effect on Cratering **[#3073]**
Bedding and GPS data were collected in the rim of Meteor Crater, Arizona. Based on field observations, a model was developed describing the formation of "thrust wedges". A second model is presented that the effect of joint sets on the crater shape.

3:30 p.m. Kearsley A. T. * Burchell M. J. Abell R. Cole M. J.
Use of X-Ray Computer Tomographic Imagery in Location of Target Fractures and Projectile Fragments Around Laboratory Hypervelocity Impact Craters **[#3050]**
The three dimensional shape of fractures with embedded projectile fragments can be interpreted from high resolution X-ray CT reconstructions of polymer targets impacted by steel and copper projectiles in laboratory hypervelocity impact experiments.

3:45 p.m. BREAK

4:15 p.m. Morrow J. R. * Koeberl C. Reimold W. U.
Microscopic Shock-Alteration Features in Shatter Cones from the Santa Fe Impact Structure, New Mexico, USA **[#3037]**
Microscopic shock-alteration features, including planar microstructures in quartz and probable melt veneers, are documented near the surface of shatter cones from the Santa Fe impact structure, New Mexico, USA.

4:30 p.m. Ferrière L. * Koeberl C. Reimold W. U. Libowitzky E. Greshake A.
Ballen Quartz and Cristobalite in Impact Breccias: Types, Occurrence, and Possible Origin **[#3011]**
Ballen silica occurs in 28 impact structures. Five types of alpha-cristobalite and alpha-quartz ballen have been described and coesite have been characterized for the first time within alpha-cristobalite ballen from the Bosumtwi crater.

4:45 p.m. Machado R. A. * Lana C. Filho C. R. S. Stevens G.
Optical and Scanning Electron Microprobe Study of Shock Veins from the Araguainha Central Uplift, Central Brazil; Evidence for Selective Melting of Rock Forming Minerals and Immiscible Phases in the Impact Melts **[#3062]**
In this study we present result of a detailed optical and scanning elctron microprobe analysis of shock veins from the Araguainha impact structure. The results are used to discuss the generation and crystallization of impact melts.

5:00 p.m. Gerasimov M. V. * Dikov Yu. P. Yakovlev O. I.
Impact-Induced Vaporization of Magnesiosilicates: Domination of Enstatitic Cluster **[#3027]**
Experiments on impact-induced vaporization of magnesiosilicates shows that formation of chemical composition and structure of condensates is driven by volatilization of "enstatite" clusters.

Thursday, August 21, 2008
IMPACT EJECTA
8:30 a.m. Hippo Room

Chairs: **Joanna Morgan**
Axel Hofmann

8:30 a.m. Hofmann A. * Reimold W. U. Koeberl C. **[KEYNOTE]**
A Review of Impact Spherule Layers in the Barberton Greenstone Belt **[#3105]**
In the Barberton greenstone belt, four specific spherule horizons, named S1 to S4, have been proposed as being of inpact origin.

9:00 a.m. Morgan J. V. * Artemieva N. **[KEYNOTE]**
Chicxulub Distal Ejecta: Modeling Versus Observations **[#3016]**
We investigate the formation of the K-P layer through numerical modeling. A subset of our models replicate the observational data reasonably well, and suggest that non-ballistic ejection is required for shocked minerals to reach distal sites.

9:30 a.m. de Niem D. *
Models of an Ejecta Curtain **[#3055]**
I develop an analytical model for the density distribution in an evolvingejecta curtain. This will be compared to two-fluid (dust + gas) simulations.

9:45 a.m. Goldin T. J. * Melosh H. J.
Thermal Radiation from Atmospheric Reentry of Chicxulub Ejecta **[#3114]**
The discorty of soot within the K/T boundary sequence led to the hypothesis that thermal radiation from the atmospheric reentry of hypervelocity impact ejecta was sufficient to ignite flobal wildfires.

10:00 a.m. BREAK

10:30 a.m. Schmieder M. * Buchner E.
Can Impact Ejecta Survive Fluvial Reworking? **[#3006]**
In contrast to impact ejecta reworked by marine and glacial processes, fluvial reworking is sparsely mentioned in the literature. This is the first report of impact ejecta that show evidence for multiple fluvial reworking.

10:45 a.m. Addison W. D. * Brumpton G. R. Fralick P. W. Kissin S. A.
Sudbury Impact Ejecta Features in Base Surge Debrisites North of Lake Superior, Ontario, Canada **[#3007]**
Ejecta-bearing debrisites from the 1850 Ma Sudbury impact are described from eight base surge deposits north of Lake Superior. Despite being deposited on stromatolites, evidence suggests that the study area was sub-aerial before, during and after the base surges.

11:00 a.m. Wright S. *
Ejecta Facies at Lonar Crater, India: Inventory of Expected Impactites, Thermal Infrared Spectroscopy, and Implications for Mars **[#3099]**
The structure of the Lonar Crater, India ejecta blanket is described along with SEM data and spectroscopy on impactites from a range of shock pressures.

11:15 a.m. Bron K. *
Accretionary Lapilli from the Tookoonooka Impact Event, Australia **[#3072]**
The Tookoonooka subsurface impact structure (Queensland, Australia) is located in the lower K, sedimentary Eromanga Basin succession. An ejecta layer identified in drillcore hosts unusual clasts that have been interpreted as accretionary lapilli.

11:30 a.m. Warme J. E. * Morrow J. R. Pinto J. A.
Processes and Products of the Marine Alamo Impact Event, Central Great Basin, Western USA **[#3038]**
A wide variety of impact processes and resulting products are summarized in the context of genetic depositional realms proposed for the marine, Late Devonian Alamo Impact Event, central Great Basin, western USA.

11:45 a.m. Giuli G. * Eeckhout S. G. Cicconi M. R. Koeberl C. Glass B. P. Pratesi G. Paris E.
North-American Microtektites are More Oxidized Compared to Tektites **[#3044]**
We studied a group of North-American (NA) microtektites from five DSDP sites by Fe K-edge XANES in order to obtain information on the Fe oxidation state. Fe^{3+}/Fe_{tot} ratios vary from 0 to 45% for NA microtektites, whereas is almost 0 in NA tektites.

Thursday, August 21, 2008
OPEN DEBATE
12:00 p.m. Hippo Room

Chair: **Kai Wünnemann**

12:00 p.m. Open Discussion

1:00 p.m. LUNCH

A NEW METHOD OF TESTING THE HETEROGENEITY OF THE IMPACT ORIGIN, SHATTER CONES OF NEWLY DISCOVERED IMPACT SITE, SANTA FE NEW MEXICO, USA.

T. Adachi[1, 2] and G. Kletetschka[1, 2, 3], [1] Department of Physics, Catholic University of America, 200 Hannan Hall, Washington DC, USA (Tomoko.Adachi-1@nasa.gov), [2] NASA Goddard Space Flight Center, Code 691, Greenbelt, MD, USA (gkletetschka@nasa.gov), [3] Institute of Geology, Academy of Sciences of the Czech Republic, Prague, Czech Republic).

Abstract: A meter scale shatter cone structures were found in the Sangre De Cristo Mountains near Santa Fe, New Mexico. The possible impact deformed rocks are consist of Proterozoic biotite schist and granite. Well pronounced shatter cone structures are pervasive throughout the outcrops. The impact origin can be tested a line of magnetic analysis and a new method of magnetic scanning for 2-dimentional imaging. Along with magnetic signature analysis, the magnetization orientation may be a proxy indicator for an impact origin.

Previous study on a suite of rocks from Sierra Madera, Texas showed the impact pressure controlled magnetization orientations. We characterized the magnetic signatures of two distinct physical characteristics of shock fractured rocks, A: small scale, and B: large scale shatter cones. The magnetic signatures of the two shatter cones showed the heterogeneous orientations and intensity of natural remanent magnetizations that may attribute to the impact event (Figure 1 & 2).

Along with the conventional magnetic analysis, a new method of magnetic scanning gives us another line of proxy indicator for impact origin.

Introduction: The Sierra Madera Impact crater is located in Pecos county, Texas, USA. It is a complex impact crater with an intensely folded and faulted central uplift [1][2]. It had been initially described by [3] and [4]. The shock pressure was estimated as ~40 (central uplift) GPa by [5]. Huson et al. [6] estimated 8 to 30 GPa using X-ray powder diffraction (XRD) analysis of shatter cones. Sharpness of the peaks in the XRD pattern indicate crystallinity, and asymmetric broadening in the XRD patterns indicates spatial inhomogeneity due to shock effects [7].

We performed magnetic analyses for two localities of Sierra Madera impact deformed rocks that have different physical characteristics of shock deformation. The magnetic signatures of the two locations, sites A and B showed the distinct magnetic signatures. Shatter cone at site A has a fine-scale (few to ~10 mm) distributed array of complete shatter cones with sharp apex. Natural remanent magnetization (NRM) of site A shatter cone is distributed within the plane that is perpendicular to the apexes of the cones. Shatter cone at site B shows no apparent cone shape or apex, instead, a relatively larger scale and multiple striated joint set (MSJS) and sinusoidal continuous peak. NRM of site B shatter cone is clustered along the apexes. The difference in magnetization direction is a likely indicator of the shock pressure where parallel to apex indicates pressures larger than 10 GPa and perpendicular to apex indicate pressures less than 10 GPa. Intensities of NRM and saturation isothermal remanent magnetization (SIRM) contrast and fluctuate within a shatter cone as well as in between two sites. We observed a random orientation of magnetic vector directions and amplitudes changing over small scales, leading to the absence of coherent macro-scale signature.

Impact magnetization and demagnetization: Hypervelocity impact produces an amount of energy that deforms, fractures, and melts the target rocks. Hargraves and Perkins [8] used magnetic techniques to study rocks affected by shock induced high strain rate deformation. The noted effects of impacts were: changes in NRM directions, remagnetization, and reduction in bulk susceptibility. An important finding was that the impact effect on NRM was detectable. Shock remanent magnetization (SRM) collectively includes various effects that must be identified: demagnetization and/or remagnetization which may involve changes in magnetic remanence directions. The mechanism of shock induced magnetic effects (SRM) in shatter cones has not been satisfactory explained. [9] suggested the relatively late formation of shatter cone structures in the Vredefort impact crater during the impact compression. [10] suggested the high remanent magnetism over the Vredefort impact structures is due to elongated, micron-size single-domain magnetite that formed along PDFs under extreme P-T conditions. In their studies magnetizations of shatter cones were not considered.

Method: The magnetic characterization was designed to observe small-scale (centimeters) heterogeneity in magnetism possibly recorded at an impact event. The Sierra Madera shatter cone samples were prepared to preserve orientations and spatial configurations. Shatter cone subsamples were cut out into cubes from A: 1.2 to B: 1.5 cm^3 in order to preserve the spatial orientation of each other respect to the parent sample, and the orientations of the apex axis. The orientations of the apex axis were kept to be parallel to the z-axis of the magnetometer with the errors ranging ±5 degrees. The sub-samples of A were cut out and labeled as: A1, A2, A3, through A10, and eight out of ten of them were used for analysis. A1 and A2 were basal (below apex, no striations), and A3 through A10 were with apex structures with striations, and re-crystalized surfaces. The sub-samples of B were cut out and labeled as B1, B2, B3 though B10. B1 through B7 are basal (below apex and no striations), and B8, B9a, and B10 has multiple striated joint set.

With the orientation maintained throughout the analysis, natural remanent magnetization (NRM), alternating field demagnetization (AF-demag), and saturation magnetization (SIRM) were performed.

Results: *Small scale shatter cone A:* Fig. 3 shows that the fluctuation of NRM (solid squares) values has bimodal distribution, where samples A1, A2, A4, A6, and A10 are 1 to 2 x 10^{-7} Am^2/kg, while A3, A5, and A7 are 6 to 7 x 10^{-7} Am^2/kg. SIRM (open squares) values are narrowly distributed within 3 to 5 x 10^{-5} Am^2/kg.

Large scale shatter cone B: Fig. 3 shows a relatively uniform distribution of NRM (0.5 to 0.9 x 10^{-6} Am^2/kg) (solid squares) except B9a and B10 (ridgeline apex) show slightly higher values (1 to 2 x 10^{-6} Am^2/kg). Whereas the SIRM (open squares) shows bimodal distribution where B4 and B6 have order of magnitude lower SIRM (1.17 x 10^{-5} Am^2/kg and 1.60 x 10^{-5} Am^2/kg), respectively, compared with 1 to 4 x 10^{-4} Am^2/kg for the rest of the B-samples.

The NRM values of B are similar to the higher NRM values of A (A3, A5, A7). These fluctuations are reflected in the REM (magnetic efficiency) values (solid triangles). The overall efficiency (averaged REM values of all the sub-samples) is ~0.005, which is lower than suggested terrestrial NRM values of 0.01 [11] [12] However, the efficiency of B4 (0.06) and B6 (0.05) is much higher than the rest of the samples or common terrestrial values.

The vector orientations as declination (x-axis) versus inclination (y-axis) were plotted in Fig. 1 for A, and Fig. 2 for B, to depict the vector behaviors. The NRM fluctuations of shatter cone A shows that most of the vectors except A4 and A6 are oriented perpendicular to the shatter cone axes that is normal to the base. The NRM directions in shatter cone B clusters in about 70° inclination, and parallel to shatter cone axis as in Fig. 4.

Application: We test the result of the heterogeneity of the magnetic signatures of the Sierra Madera shatter cones by using 2-D magnetic scanning method to depict the orientation and intensity of the magnetizations of Sierra Madera shatter cone, and apply for the newly discovered impact site, Santa Fe possible impact site to test the origin of the shatter cone rocks.

References: [1] Wilshire et al. (1971) *GSA Bulletin*, v.82, p1009-&. [2] Wilshire et al (1972) *USGS Prof. Paper*, v.599-H, p.1-49. [3] Boon and Albritton, Jr. (1936) *Field and Laboratory*, v.5, p.1-9. [4] Eggleton and Shoemaker (1961) *USGS Prof. Paper*, v.424-D. [5] Goldin et al. (2005) *LPSC XXXVI*, 1071. [6] Huson et al. (2006) LPSC. [7] Ashworth and Schneider (1985) *Physics and Chemistry of Minerals*, v.11, p.241-249. [8] Hargraves and Perkins (1969) *JGR*, v.74, p.2576-2589. [9] Nicolaysen and Reimold (1999) *JGR-Solid Earth*, v.104, p.4911-4930. [10] Hart et al. (2000) *Geology*, v.23, p.277-280. [11] Kletetschka et al. (2003a) *Meteoritics & Planetary Science*, *v.*38, p.1-last. [12] Kletetschka et al. (2003b) *The Leading Edge*.

Figure 1:

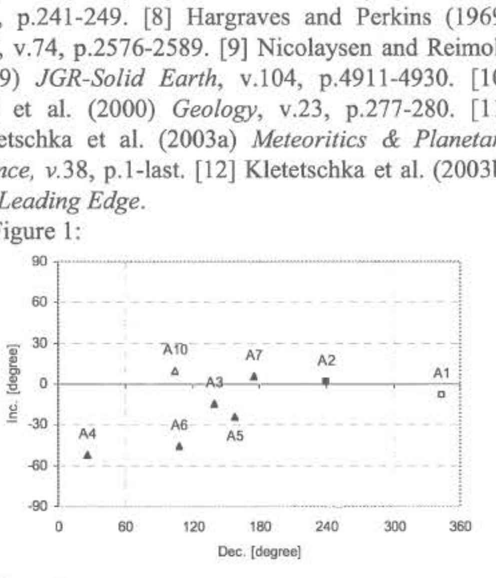

Figure 2:

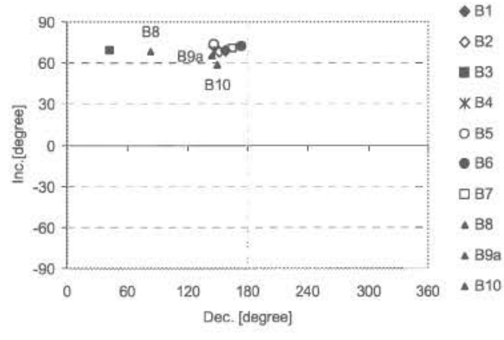

Figure 3:

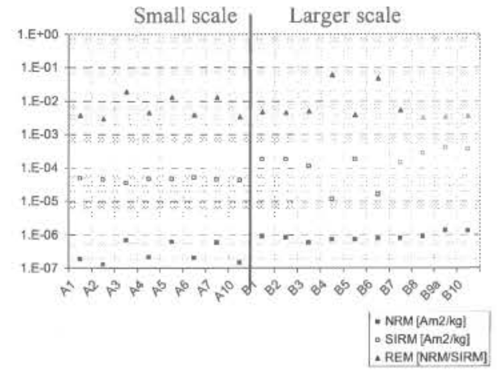

SUDBURY IMPACT EJECTA FEATURES IN BASE SURGE DEBRISITES NORTH OF LAKE SUPERIOR, ONTARIO, CANADA.

W. D. Addison, G. R. Brumpton, P. W. Fralick, and S. A. Kissin, Department of Geology, Lakehead University, 955 Oliver Road, Thunder Bay, P7B 5E1, Canada. E-mail: baddison@tbaytel.net.

Introduction: Eight new sub-aerially exposed debrisites containing ejecta from the 1850 Ma [1] Sudbury impact event have been found in and near the City of Thunder Bay, north of Lake Superior, Ontario (Fig. 1). These exposures are interpreted as base surge deposits whose features differ significantly from previously described ejecta units in drill cores. Ejecta features in the debrisites include PDFs and planar fractures in quartz grains, vesicular devitrified glass clasts, unshocked angular and sub-rounded quartz and feldspar grains, accretionary lapilli and possible microtektites.

The Debrisites: Two sites show in situ fractured Gunflint chert-carbonate at the base of the debrisite indicative of earthquake activity prior to debrisite deposition. All sites show clasts of shattered Gunflint chert-carbonate in the debrisite ranging from submillimeter shards to blocks over a metre in size. The debrisite also contains large quantities of microcrystalline carbonate that we interpret as a pre-impact, subaerial lagoon floor sediment. Thus, powerful activity stripped the sediment down to bedrock, incorporating it and a shallow layer of earthquake-shattered Upper Gunflint chert-carbonate into the debrisite, heavily diluting the ejecta.

The debrisites range from ~ 0.3 m to ~3.5-4 m in thickness and lie on chert-carbonates, which are part of a marine regressive assemblage at the top of the Gunflint Formation. Only one site exposes the transition from debrisite to overlying Rove Formation shale. Glacial erosion has truncated the vertical extent of the other seven sites. Most of the debrisites rest on in situ microbialites or stromatolites, suggesting, at the least, a moist depositional environment if not a peritidal environment.

Base Surge: A variety of features suggest the debrisite was deposited sub-aerially:

1. The ocean regression assemblage indicates a trend toward sub-aerial exposure.
2. Most importantly, four debrisite sites show an iron-rich alteration profile (a possible paleosol) 0.5-1.5 m below the debrisite.
3. Devitrified vesicular glass is very common at the base of the debrisite, some of it so vesicular that its density may have approached that of water. If it was deposited in water, it should be stratified in the debrisite with the least vesicular clasts near the base of the debrisite with the more vesicular clasts higher in the stratigraphic column. This is not the case.
4. Some vesicular clasts have ovoid vesicles with their long axes aligned parallel to each other, suggesting that the clasts were deposited while still warm enough to be deformed by the weight of overlying debris. Had water been present, it would have quickly quenched the still warm glass, preventing its deformation.

In the absence of water, base surges and/or air fall are the remaining options for deposition of the debrisite. An air fall deposit should show obvious upward fining, and it should not contain large Gunflint clasts. The debrisite does not fine upwards, and it does contain many Gunflint clasts, some over a metre in size. Thus, we conclude that the debrisites are base surge deposits laid down on a sub-aerial Gunflint surface.

Post-depositional History: Previous geochronology work with drill core material has shown that ~ 15 My passed from when the 1850 Ma debrisite was deposited until dated zircons just 6 m higher in Rove Formation tuff were deposited [2]. Such a minor amount of sediment for ~ 15 my strongly suggests a depositional hiatus and a period of sub-aerial exposure before the ocean again transgressed the area depositing the organic-rich mud and volcanic ash layers of the Rove Formation. Several features within the debrisite support this idea.

At the only site where the top of the debrisite is present, a period of sub-aerial exposure appears to have led to weathering, leaching, erosion and removal of an unknown quantity of debrisite. These processes likely moved or removed the late stage fine air fall material that would have settled onto the base surge debrisite making it unlikely that spherules and a fireball layer will be found near Thunder Bay. The leaching led to the formation of an iron-rich (primarily pyrite) alteration profile similar to that seen below the debrisite at four locations. The physical and chemical features of blocky calcite cement in the debrisite indicate its formation in the freshwater phreatic zone [3].

Post-depositional anastomosing chert and agate ridges stand out from the more easily weathered debrisite at some sites. Comparable microscopic anastomosing chert is seen in thin sections. We interpret the anastomosing chert as a precipitate from sub-aerial leachate produced higher in the debrisite.

In some cases silica or silicates have replaced ejecta features; however, carbonate replacement is far more common. Replacement complicates the interpretation of ejecta features by destroying detail within the features or by destroying the entire feature. For example, it is impossible to determine if carbonate replaced features, which show the size and shape of microtektites, including syneresis cracks, are in fact microtektites because the key textural and color features have been destroyed. Recrystallization of the replacement carbonate has further compounded the problem.

The debrisite is overlain by a carbonate-rich ocean transgressive assemblage ~ 0.7 m thick which shows millimeter-sized mudstone rip-ups, centimeter-sized carbonate rip-ups and cross bedding features, further supporting the period of sub-aerial exposure. There is an abrupt transition from the transgressive assemblage to the Rove Formation shale which, in turn, has been intruded by a Logan diabase sill. Heat from the sill may explain why carbonate replacement and recrystallization is so pervasive and why it has been so destructive of ejecta features at this site compared to other sites.

Conclusion: A variety of features support the hypothesis that the study area was sub-aerial before, during and after base surges deposited the debrisites, containing a multifaceted mixture of ejecta and non-ejecta features, which allow interpretation of a rich, complex history. These debrisites may well be useful Earthly analogues for those studying Martian impacts, especially in terms of accretionary lapilli [4] and, perhaps, chemical alteration profiles.

References: [1] Krogh T. E. et al. 1984. pp. 431-446 *in* The Geology and Ore Deposits of the Sudbury Structure. Ontario Geol. Survey., Spec. Vol. 1. [2] Addison W. D. et al. 2005. Geology 33: 193-196. [3] Fralick P. W. and Burton J. Goldschmidt 2008: abstract 1342. [4] Knauth L. P. et al. 2005. Nature 438: 1123-1128.

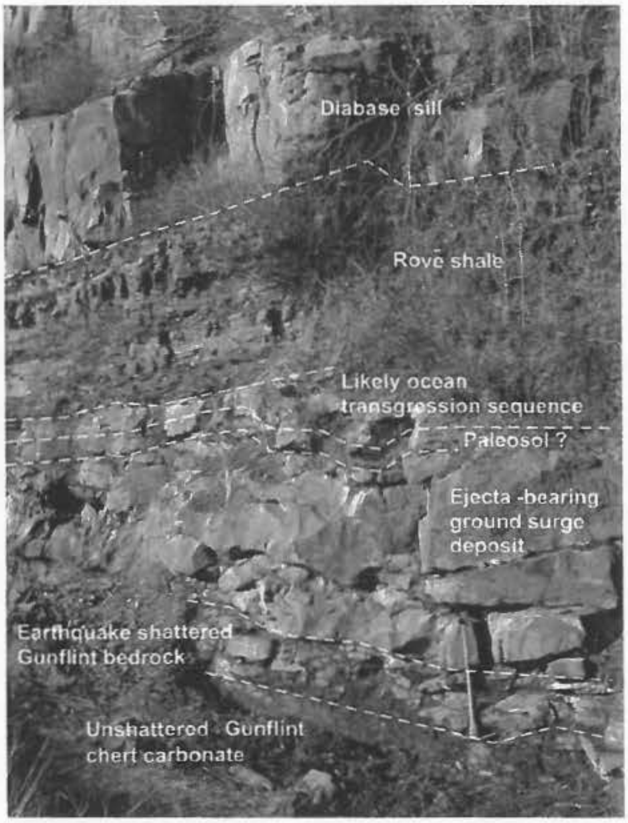

Figure 1. The Highway 11-17, Terry Fox Lookout site is the only one of the eight sites showing a complete stratigraphic section. This photo extends from unfractured Upper Gunflint Formation chert-carbonates → earthquake shattered, slickensided Gunflint chert-carbonate clasts (~ 0.5 m) → ejecta-bearing base surge debrisites (~ 2.2 m) → an iron-rich alteration profile (possible paleosol, 0.3-0.5 m) → marine transgressive assemblage (~ 0.7 m) → Rove Formation shale. An iron-rich alteration profile, ~ 1.5 m below the debrisite in the Gunflint, lies to the right out of the photo. The study area was sub-aerially exposed between the two alteration profiles, a period ≥ 15 My.

THE MOROKWENG IMPACT CRATER, SOUTH AFRICA: A COMPLEX, MULTIRING STRUCTURE WITH A ~130 KM RADIUS EXTERNAL RING AND ASYMMETRIC RADIAL SECTORS. M. A. G. Andreoli[1, 2], R. J. Hart[3], G. R. J. Cooper[2], S. J. Webb[2], [1]Necsa, P. O. Box 582, Pretoria 0001, South Africa, marco@necsa.co.za, [2]University of the Witwatersrand, P. O. Box 3, Wits 2050, South Africa, [3]iThemba Labs, South Africa, P. Bag 3, Wits 2050, South Africa.

Introduction: The ~144 Ma Morokweng impact crater, largely buried beneath shallow Late Cretaceous to Cenozoic Kalahari sediments (Fig. 1-A, [1, 2]), comprises a ~30 km wide and ≥ 870 m deep, magnetically anomalous melt sheet surrounded by a magnetically quiet aureole (D ~ 70 km [1, 3, 4, 5]). The melt sheet is vertically differentiated and contains pristine to partly recrystallized LL-chondrite clasts and disseminated, siderophile-elements rich sulphides in a variety of settings [2, 4, 5, 6]. However, the one aspect that requires clarification is the final rim size, as previous estimates range from ~70 km [7, 8] to ~240 km [3] even up to ~ 320 km [1, 9, 10]. In this abstract we reassess this issue, and provide a new insight for the apparently poor circular symmetry of the crater.

Methods: Due to the virtual absence of outcrops in the core of the crater, its size and structure were assessed by carefully integrating petrographic observations of the available boreholes (Fig. 1a), with images of the national gravity (Fig. 1b) and airborne magnetic fields. We also reinterpret a mosaic of geological maps published by the South African Council for Geoscience.

Results: The careful analysis of the above data sets shows that the Morokweng crater comprises both concentric rings, arcs and radial features (faults, dykes; Figs. 1a, 1b) that cover a significant part of the northwestern sector of the Kaapvaal Craton. A description of these features is presented as follows:

Ring structures. All boreholes drilled within a radius of ~14 km from the centre (Ring I, Fig. 1a; Ring A, Fig. 1b) intersect impact melt rocks, whereas only three boreholes within a radius of ~33 km (Ring II, Fig. 1a; Ring B, Fig 1b) intersect melt rock, shocked breccia and/or suevite [2]). Borehole logs, satellite imagery, surface samples and data from a Vibroseis seismic profile provide evidence that Ring III (radius ~40 km) marks the outer limit of shock metamorphism, major structural disruption and brecciation of the cover rocks. Polymict, suevitic impact breccia and brecciated dolomite were recorded in boreholes HKH-1 and NEV-1 respectively (Fig. 1a, [11]). The ~ 70 km radius Ring IV (Ring C, Fig. 1b) is defined in the SE quadrant of the structure by the arc-shaped contact between Archaean granite and its supracrustal Cover. The extension of this arc in the other quadrants coincides with a high concentration of water boreholes [11], suggesting that Ring IV marks, at least in places, an impact-related fault/breccia zone. Indeed, a Vibroseis seismic profile [12] reveals a post–Permian fault where it intersects Ring IV. PDFs-bearing quartz is largely absent within this ring, having been reported only near Heuningvlei, close to Ring III [9]. Finally, the incomplete

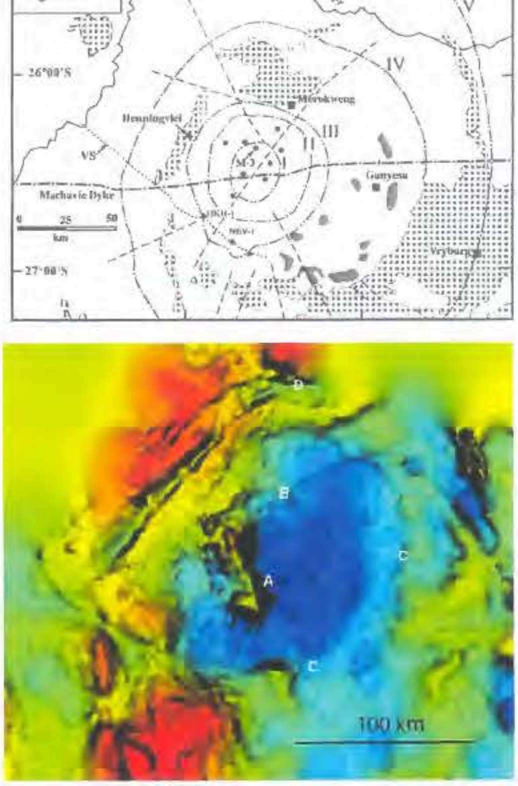

Figure 1. The Morokweng impact crater: a [top]) Generalized geology modified after [5] showing the major structural features - Rings I to V. Archaean granite (dark stippled); supracrustal rocks (light stippled); Kalahari Cenozoic Cover (blank); observed and interpreted faults (broken lines); location of boreholes (stars). VS is the trace of Vibroseis seismic profile [12]; b [bottom]) Edge-enhanced image of the Bouguer gravity of the Morokweng area (gravity data supplied by the Council for Geoscience).

Ring V (R ~ 130 km) is mapped out in the airborne magnetic images [3, 11] and is caused by outcrops of highly magnetic BIFs in the Late Archaean Kraaipan Group.

Radial features. A close examination of Fig. 1a reveals the presence of several radial faults that dissect the Morokweng structure into at least 4 distinct sectors exposing different stratigraphic levels. The Eastern, or Ganyesa Sector is the more deeply eroded as it exposes a large, ~ 100° arc of poorly exposed granite known as the Ganyesa dome [2]. The overlying early Palaeoproterozoic strata (mainly quartzite and dolomite) dip gently in a southeasterly direction towards a broad synform. The synform runs through the town of Vryburg (Fig. 1a) and is broadly concentric to the Morokweng structure (radius ~130 km). The Western, or Heuningvlei Sector consists of younger Palaeoproterozoic BIFs and is the most asymmetric when compared to the Ganyesa Sector. The Northern, or Morokweng Sector and the Southern Sector represent intermediate levels of erosion (Fig. 1a). The most important radial fault extends in a SSE direction up to a distance of ~200 km from the center of the structure and is accompanied by a ~100 km long dolerite dyke (Fig. 1a).

Discussion: Until recently, little consideration has been given to the formal definition of terms such as crater diameter and multiring structure [13]. In the case of the Morokweng crater, the problem of attributing accurate morphometric values is more complex because of the thick Kalahari cover.

Transient crater. No firm evidence for this feature has been found. However, it appears that cover rocks (Palaeoproterozoic quartzite, dolomite and BIFs) have ben obliterated over a radius of at least 66 km (Ring II). This is a minimum value for the transient cavity, if allowance is made for erosion in the past ~144 Ma.

Central Uplift. In typical meteorite impact craters this feature approximately coincides with the ~10 GPa isobar that marks the incipient development of shock metamorphism and PDFs in many rock-forming minerals [14]. In the case of Morokweng, the radial distance from the centre of PDFs/shocked carbonate occurrences is ~40 km (Fig. 1a). These findings point to a central uplift diameter of 80 km. This inference is consistent with the occurrence in borehole HKH-1 of a polymict, suevite breccia dyke, a rock only found at the margin of central uplifts [15].

Final rim. Various formulas have been proposed to calculate the diameter of the crater rim from the size of the central uplift. Using the formula proposed by [16], the crater rim diameter could be as large as ~190±10 km, a value close to that of Ring IV in Fig. 1a, and D in Fig. 1b.

External ring. Given the ~190 km diameter for the final rim, Ring V (Fig. 1a) is assumed to represent the external ring of a multiring structure [13] having a diameter of ~260 km.

Conclusions. The Morokweng impact crater stands out in all available geophysical and geological datasets of South Africa as a remarkable set of concentric rings with diameters ranging from ~30 km to ~260 km. Shock deformation features mark the extent of a large central uplift with a diameter of ~ 80 km, and a crater final rim of ~190±10 km. In spite of the uncertainties, these morphometric parameters rank Morokweng among the largest terrestrial craters [13]. Our interpretation is consistent with the exceptional thickness of the Morokweng melt sheet, and the discovery that the latter rests on mafic pyroxene gneisses [5] probably representing uplifted middle crust.

In addition, the disarmonic response of the crust to the impact, resulting in an asymmetric crown of 4 main radial sectors is highly unusual and unexplained, yet reminiscent of the Bethlehem structure in the Hidden Quadrant of the Vredefort impact structure [17].

References: [1] Hart R. J. et al. (1997) *EPSL, 147*, 25–35. [2] Andreoli M. A. G. et al. (1999) *Geol. Soc. Am. Spec. Pap. 339*, 91–108. [3] Andreoli M. A. G. et al. (2008) *LPS XXXIX*, Abstract #1236. [4] McDonald I. et al. (2001) GCA, 65, 299-309. [5] Hart R. J. et al. (2002) *EPSL, 198*, 49–62; [6] Meier W. et al. (2006) *Nature, 441*, 203–206. [7] Reimold W. U. et al. (2002) *EPSL, 201*, 221–232. [8] Henkel H. et al. (2002), *J. Applied Geophys., 49*, 129–147. [9] Corner B. et al. (1997) *EPSL, 146*, 351–364. [10] Reimold W. U. et al. (1999) *Geol. Soc. Am. Spec. Pap. 339*, 61–90. [11] Andreoli M. A. G. et al. (2007) *Proceed. 10th SAGA Conference*, 4 pp. [12] Tinker J. et al. (2002) *South African J. Geol., 105*, 107–134. [13] Turtle E. P. et al. (2005) *Geol. Soc. Am. Spec. Pap. 384*, 1–24. [14] Grieve R. A. F. and Pilkington M. (1996) *AGSO J. Geol. Geophys, 16*, 399-420. [15] Dressler B. O. and Reimold W. U. (2004) *Earth-Science Rev., 67*, 1–160. [16] Therriault A. M. et al. (1997). *Meteoritic and Planetary Sci., 32*, 71–78. [17] Galdeano A. et al. (2008) this volume.

SIDEROPHILE MINERALS IN THE MELT SHEET OF THE MOROKWENG IMPACT CRATER, SOUTH AFRICA: SIMILARITIES AND DIFFERENCES WITH THE SUDBURY DEPOSITS.

M. A. G. Andreoli[1, 2], W. D. Maier[3], I. McDonald[4], S. – J. Barnes[5], F. Roelofse[6], M. C. Cloete[6], C. Okujeni7, and R. J. Hart[8], [1]Necsa, P. O. Box 582, Pretoria 0001, South Africa, marco@necsa.co.za, [2]University of the Witwatersrand, P. O. Box 3, Wits 2050, South Africa, [3]University of Western Australia, Crawley, WA6009, Australia 3, [4]Cardiff University, Cardiff CF10 3YE, U.K., [5]Universite' du Quebec, Chicoutimi G7H 2B1, Canada, [6]Council for Geoscience, P.O. Box 112, Pretoria 0001, South Africa, [7]University of the Western Cape, P. Bag X17, Bellville, 7535, South Africa, [8]iThemba Labs, South Africa, P. Bag 3, Wits 2050, South Africa.

Introduction: The ~144 Ma Morokweng impact crater, buried beneath Cenozoic Kalahari sediments [1, 2], coincides with multiple concentric rings (radii up to 130 Km) in the airborne magnetic and Bouguer gravity images of the Kaapvaal craton [3, 4]. Its voluminous melt sheet (diameter: ~30 km, maximum thickness > 900 m) is exceptionally enriched in PGE and displays a patent, vertical differentiation from more siliceous near the top to more mafic (quartz) norite 500 m below [1, 2, 5, 6]. Crystallization of the impact melt was protracted and complex, as shown in borehole WF 05 by a dyke of a more mafic impact melt intruding a more siliceous pyroxene granophyre [1]. The melt in borehole M3 is instead unique because it hosts scattered, cm to dm-scale inclusions of pristine to partly recrystallized LL chondrite [7]. The melt also hosts numerous inclusions of nickel-PGM rich sulphides and oxides, particularly between 300 to 350 m in borehole M3 [2, 5, 6, 8]. Given these features, and the observation that a significant percentage of impact structures is host to economic mineral deposits [9], we assess here the possibility that Morokweng may host Sudbury type deposits.

Methods: Due to the regional Kalahari sand cover, our knowledge of the Morokweng melt sheet is derived from gravity and airborne magnetic data [3, 10, 11], soil (sand) geochemistry [12, 13], diamond and percussion drilling [1, 2, 6, 14]. The borehole cores were carefully logged, sampled at regular intervals [2, 5] and characterized by mineralogical and geochemical techniques.

Results: Most boreholes drilled in the melt sheet were found to intersected a gamut of minerals rich in siderophile elements (here referred to as "siderophile minerals") within these four main stratigraphic settings:

Disseminated siderophile minerals in quartz norite. These are the more common type, and in M3 (between 350-365 m), the minerals are spatially associated to swarms of small inclusions of (pre-impact) deeply altered, serpentinized ultramafics [6] and of (impact melt) melanorite/hyperstenite. Millerite (NiS) and trevorite (a Ni-magnetite) are almost ubiquitously present as a pair, in complex aggregates ~0.1-3.0 cm across and in variable proportions [6] . Associated to this pair we also found minor to trace amounts of bornite, chalcopyrite, chalcocite, selenides, and possibly talnachyte [$Cu_9(Fe, Ni)_8O_{16}$; [2, 8] see below). Other siderophile minerals observed in in borehole WF 05 bunsenite (almost pure NiO), liebenbergite (the Ni olivine end member), willemseite (a Ni-rich serpentine), and ilmenite with_NiO ~11.0 wt%. Platinum-group elements (PGE) associated to the siderophile minerals include both native minerals (platinum), and complex, poorly characterized siderophile – chalcophile element (Fe, Ni, Cu, Se, S, Br, Mo, Pb, etc.) aggregates where Pt varies between ~0.4 wt.% and ~14 wt.% [2, 8].

Siderophile minerals in vein. In WF 05, at a depth of 270 m, a flute-shaped, subvertical vein (>6 cm x ~3 cm wide) was found in quartz norite that consisted almost entrely of pegmatoidal millerite+trevorite in subequal proportions, in addition to small amounts of chalcopyrite and graphite [2]. An INAA analysis of this vein yielded Fe 18.4.wt%, Ni: 27 wt%, Co: 0.45 wt%, Cu: ~1% wt%, Ir: 7.5 ppm, Pt: 2.7 ppm, Pd: 23 ppm [2]. Absolute PGEs values in the vein are 10x chondrite, and the Pt/Pd ratios ratios depart from chondritic inter-element ratios [2].

Siderophile minerals in meteorite inclusion. Main opaque phases in the ~30 cm LL-chondrite boulder intersected by M3 at a depth of ca. 750 m are pyrrhotite, pentlandite and minor chalcopyrite [7] displaying embayed outlines suggestive of late crystallizate textures. Metallic phases are absent, and the only PGM noted are minute (1-2 m long) grains/platelets of Pt- and Rh arsenides (PtAs, RhAs) [15].

Sulphides in footwall dyke. In M3, a subvertical, vein of impact melt (depth: 1000 m; length: ~1 m) that intrudes mafic pyroxene gneiss displays euhedral ortho- and clinopyroxe and pools of interstitial pyrite ($FeS_{1.9-2.0}$) in a glass matrix of (Na>>K) syenitic to tonalitic composition. Minor consituents of the vein include pyrrhotite, pentlandite, and chalcopyrite.

Discussion: The data presented provide clear evidence that siderophile-chalcophile minerals, inluding sulphides, are widely distributed in the Morokweng melt sheet. This inference is supported by a) a broad sulphur anomaly (500 to ~1200 ppm SO_4) in groundwater from the area underlain by the melt sheet (Necsa , unpblished data). Similarly, soils from the same area yield localized siderophile elements (Ni, Pd) anomalies [12, 13]. On the basis of the available data, the sulphide occurrences in the Morokweng boreholes may be divided into: High-, Intermediate- and Low-Temperature Assemblages.

The High-T Assemblage is represented by the sulphides in the meteorite and in the footwall dyke, as these are the only minerals in our investigation that are truly magmatic sulphides. Textural observations suggest that these phases are not primary, but are probably secondary after a transient monosulphide solid solution (MSS) that existed when the clast was thermally re-equilibrated with the host impact melt. The stability field in the footwall dyke is constrained by the 710 °C, upper stability limit of pyrite [16] and by the quenched character of melt sheets in general. The Medium-T Assemblage is represented by the pair millerite+trevorite. This assemblage has never been describede before in magmatic Ni deposits including Sudbury. The presence of millerite, a Ni sulphide common in metamorphic, hydrothermal environments, suggests that the pair might represents a low temperature condensate rich in Ni,-Fe,-Cu, C- and PGE. The Low-T Assemblage is represented by the pyrite-chlorite-coated subvertical joints that were predominantly intersected below a depth of 600 m. This hydrothermal assemblage (not listed above) has yet to be investigated.

The siderophile-rich minerals described above provide direct evidence for heterogeneous sulphur distribution in the melt sheet, whereby the very rare crystals of liebenbergite (in WF 05) may perhaps record (transient?) *sulphur-depleted* domains, The millerite-trevorite-C(?) assemblage could testify instead to the *sulphur-undersaturated* nature of the known melt sheet, but only if we knew the thermodynamic conditions for the simultaneous crystrallization of the said pair. However it formed, the condensate was apparently capable of migrating, even if only on a limited scale (cm / dm?) and to collect in small veins. In M3, the broad association of the PGMs-rich trevorite-millerite pairs and mafic-ultramafic nodules seems to favour the latter as the primary source of the metals-rich condensates. What the nodules represent is debatable, as some resemble meteorite fragments [7], while others best compare to orthopyroxene cumulates (coarse melanorite – hypersthenite). Finally, the sulphides (pyrite-pyrrhotite-pentlandite-chalcopyrite) in the impact melt dyke (M3; depth: 1000 m) implie derivation from a *sulphur-oversaturated* melt compartment quite separated from the previously described S-understurated compartments.

The mineral potential of Morokweng: The data presented place Morokweng as a potential candidate to impact-related Ni, PGE (Cu, Co) mineral deposits like those of Sudbury [17]. Indeed, the preserved thickness/volume of the melt sheet [6], its complex crystallization history [2], the clear evidence for vertical differentiation [5, 6], and the widespread occurrence of economically significant minerals even in footwall dykes, all reinforce the Sudbury analogue. However, unlike Sudbury, the crustal contribution to the PGEs budget of the Morokweng melt sheet appears minimal [5, 6, 17]. Likewise, the quartz-norite of the Morokweng boreholes differs from its Sudbury equivalent because it lacks the diagnostic magmatic sulphides (pyrrhotite, pentlandite, chalcopyrite) of the latter [16].

In conclusion, the potential for economically mineable deposits at Morokweng [18] appears linked to the probability to find large volumes of millerite-trevorite condensates. Alternatively, we may speculate that Sudbury-type magmatic sulphides could have fractionated from one or more compartments of sulphur-oversaturated melts like that which fed the pyrite-pentlandite-pyrrhotite-chalcopyrite-bearing dyke described above.

References: [1] Hart R. J. et al. (1997) *EPSL, 147*, 25–35. [2] Andreoli M. A. G. et al. (1999) *Geol. Soc. Am. Spec. Pap., 339*, 91–108. [3] Andreoli M. A. G. et al. (2007) *Proceed. 10th SAGA Conference*, 4 pp. [4]. Andreoli M. A. G. et al. (2008) *LPS XXXIX*, Abstract #1236. [5] McDonald I. et al. (2001) *GCA, 65*, 299-309. [6] Hart R. J. et al. (2002) *EPSL, 198*, 49–62; [7] Maier W. D. et al. (2006) *Nature, 441*, 203–206. [8] Dutta R. K. et al. (2001) *Nuclear Instruments and methods in Physics Research B, 181*, 551-556. [9] Grieve R. A. F. (2005) *Geol. Soc. London Spec. Publ., 248*, 1-29. [10] Henkel H. and Reimold W. U. (2002) *J. Applied Geophys., 49*, 129–147. [11] Corner B. et al. (1997) *EPSL, 146*, 351–364. [12] Xu J. (2006) *M. Sc. Thesis (unpublished), Univ. Western Cape*, 82 pp. [13] Yang J. (2006) *M. Sc. Thesis (unpublished), Univ. Western Cape*, 72 pp. [14] Reimold W. U. et al. (2002) *EPSL, 201*, 221–232. [15] Barnes S. –J. et al. in preparation. [16} Arnold R. G. (1962) *Econ. Geol., 57*, 72-90. [17] Zieg M. J. and Marsh B. D. (2005) *GSA Bulletin, 117*, 1427-1450. [18] Maier, W. D. et al. (2003) *Applied Earth Sci. (Trans. Inst. Min. Metall. B), 112 (2)*, 150-152 (abstract).

SETLAGOLE MEGABRECCIA, SOUTH AFRICA: CLUES TO A POSSIBLE MESOARCHAEAN IMPACT EVENT AND AEROMAGNETIC RECOGNITION OF A *C.* 30 KM CONCENTRIC MULTIPLE RING STRUCTURE. C.R. Anhaeusser[1], E. Stettler[2], G.R. J. Cooper[3], and R.L. Gibson[4], [1]Economic Geology Research Institute, School of Geosciences, University of the Witwatersrand, Johannesburg, Private Bag 3, Wits 2050, South Africa, e-mail: carl.anhaeusser@wits.ac.za [2]Thani Dubai Mining Ltd., P.O.Box 88188 Dubai, UAE, e-mail: estettler@thani.ae [3]Department of Geophysics, School of Geosciences, University of the Witwatersrand, Johannesburg, Private Bag 3, Wits 2050, South Africa, e-mail: gordon.cooper@wits.ac.za [4]Impact Cratering Research Group, School of Geosciences, University of the Witwatersarnd, Johannesburg, Private Bag 3, Wits 2050, South Africa, e-mail: roger.gibson@wits.ac.za

Introduction: The Kraaipan Archaean granite-greenstone terrane of the North West Province, South Africa has revealed a spectacular megabreccia (Fig. 1) which crops out in a river bed near Setlagole village in the west-central region of the Kaapvaal Craton some 300 km west of Johannesburg [1], [2]. Kalahari sand and calcrete covers much of the Archaean basement in this area where only sporadic exposures of banded iron-formation and amphibolite occur as xenoliths in a variety of massive and gneissic granitoid rocks ranging in age from about 3160 to 2790 Ma [3], [4]. The megabreccia, exposed in the Setlagole river approximately midway between Mafikeng and Vryburg, was first noted by A.L. du Toit [5], who described the breccia as marking a major thrust fault. This interpretation could not be verified and instead it is now speculated that it may be of meteorite impact origin.

Field Observations: The megabreccia is exposed in two meanders of the Setlagole river, roughly 2 km apart. Despite poor exposure, the region south of the megabreccia consists of granitic terrane, which can be followed intermittently for over 18 km to the village of Madibogo. No further breccia was recorded, but the granitic rocks are fractured, jointed and mylonitised, and in places show highly altered fracture fillings. The Setlagole megabreccia consists of countless rock fragments with angular and rounded shapes of various sizes in a dark, fine-grained matrix containing small to microscopic fragments and particles of predominantly granitic material. The lithic fragments in the megabreccia consist predominantly of granite and gneiss with rare clasts of banded iron formation, amphibolite, chert and calc-silicate rocks, all of which occur in the vicinity. The largest granitic fragment measured 6.5m x 3.5m in size. A crude gently-dipping layering is seen locally within more sandy, clast-poorer, regions. A single granite clast containing pseudotachylite in a brittle-ductile shear zone was found. Flattened irregular dark grey masses up to decimeters in length are locally deformed around the clasts. These were tentatively described as altered melt clasts, but the low-grade metamorphism has obscured any original features, and they may be metamorphosed argillaceous clasts.

Microscopic Observations: The breccia matrix comprises decussate to radiating fine-grained chlorite masses that enclose highly angular mineral clasts (predominantly quartz, plagioclase and K-feldspar, with biotite, amphibole, epidote and zircon) that are derived from the same medium- to high-grade granite-greenstone source as the lithic clasts. Analysis of 62 thin sections has failed to provide conclusive evidence of shock metamorphism – quartz grains contain a variety of undulose and mosaic extinction features, deformation bands, subgrains and fluid inclusion trails whereas feldspars show twinning and undulose extinction. No planar features were found in zircon, but epidote contains sets of planar fractures. Alteration of the feldspars is variable. Biotite grains are commonly bent, rather than kinked, and variably chloritised. The chloritisation indicates that the megabreccia experienced a lower greenschist metamorphism, which has obscured the original nature of the matrix.

Geophysical Evidence: High density aeromagnetic data from the Council for Geoscience of the region south of the Setlagole outcrops, available on 200m line spacing flown in the late 1980s, shows a fairly faint magnetic signature, but a 7 km central core can be clearly identified, together with curved semi-concentric magnetic lineaments. Filtering techniques involving fractional derivative and circular-shaded relief algorithms have been applied to enhance the magnetic signatures (Fig. 2). The surrounding collar is not symmetrical around the core, but exhibits semi-concentric magnetic lineaments. The exact dimensions of the structure have yet to be determined, but the outer perimeter of the collar is more than 20 km in diameter and appears as an oblate ring of strong magnetic anomalies. Preliminary estimates suggest a structure of between 25-30 km diameter.

Age Relationships: No direct age dating of the megabreccia or the circular structure have yet been attempted. Indirect lines of evidence suggest the structure may be of Mesoarchaean age. Firstly, the megabreccia comprises rock fragments derived from the

Archaean Kraaipan granite-greenstone basement on which it lies. Although Ventersdorp (*c.* 2700 Ma) [6] and Transvaal (2642-2224 Ma) [7] Supergroup rocks occur in the region, there are no fragments of these rocks in the megabreccia, suggesting that these formations had not yet been deposited at the time of impact. Secondly, the megabreccia experienced a low-grade metamorphic event not recorded in the Ventersdorp and Transvaal successions, but which is not as high as the upper amphibolite facies metamorphism seen in the greenstone fragments. Thirdly, geophysical evidence suggests that the Setlagole ring structure is cut by at least three dyke events, which show up clearly on the aeromagnetic images. Some of the dykes, which are not exposed in the Setlagole area, may be feeders to the Ventersdorp volcanic succession, while the youngest set, probably of Karoo (*c.*180 Ma) age, appears to have been disrupted by the 145 Ma Morokweng impact structure located 135 km to the west [8],[9],[10]. An east-west-trending dyke (Machavie dyke [8]), which cuts through the centre of the Morokweng structure, is representative of the youngest dyke event in the North West Province and is possibly of Cretaceous age (*c.* 142-65 Ma).

Conclusions: An impressive megabreccia near Setlagole pointed the way to the discovery of a sizeable ring structure, which we speculate could represent remnants of a meteorite impact structure. The age of the structure remains uncertain, but is, at the very least, older than the 145 Ma Morokweng impact structure and the 180 Ma Karoo-aged magmatic dyke event. Support for a much older age for the structure lies in the fact that the NNE-SSW-trending dykes that cut across it (Fig. 2) and the Kaapvaal Craton appear to be terminated by the *c.* 2060 Ma Bushveld Complex in the east, and by the *c.* 1890-1928 Ma Olifantshoek Supergroup rocks to the west. If this is correct these dykes may be at least pre-Bushveld in age. However, the possibility exists, on the basis of the nature of the megabreccia and its subsequent metamorphism, that the structure may have formed even earlier, in pre-Transvaal or pre-Ventersdorp times. This suggests the structure may post-date the granitoid rocks of the 2790-3160 Ma Mesoarchaean to Neoarchaean basement complex. The precise diameter of the structure is also unknown, but recent suggestions that the Morokweng impact crater may be up to 240 km in diameter [10] may imply that the outer effects of this structure overlap with those of the Setlagole structure. The origin of the megabreccia remains enigmatic. If linked to the ring structure, its location beyond the limits of the latter would suggest some form of debris flow.

References: [1] Anhaeusser C.R. (2007) *GSSA Geobulletin, 50 (2),* 7-9. [2] Anhaeusser C.R. et al. (2007) *GSSA Geoforum Abstract* , 63-64. [3] Poujol et al. (2002) *J. Afr. Earth Sci., 35(2),* 147-161. [4] Robb L.J. et al. (2006) in: *The Geology of South Africa, Geol Soc. S. Afr.,* 57-94. [5] Du Toit A.L. (1906) *Ann. Rep. Geol. Comm. Cape of Good Hope (1905),* 205-258. [6] Armstrong R.A. et al. (1991) *Precambr. Res. 53,* 243-266. [7] Eriksson et al. (2006) in: *The Geology of South Africa, Geol Soc. S. Afr.,* 237-260. [8] Corner et al. (1997) *EPSL 146,* 351-364. [9] Hart et al. (1997) *EPSL 147,* 25-35. [10] Andreoli et al. (2008) *GSSA Geobulletin, 51(1),* 12-15.

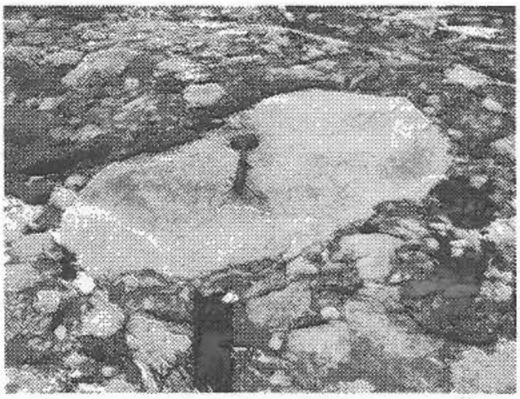

Fig.1 Setlagole megabreccia showing a large block (3.6m x 1.5 m) of gneissic granite in a mass of rock fragments and finer-grained chloritized matrix.

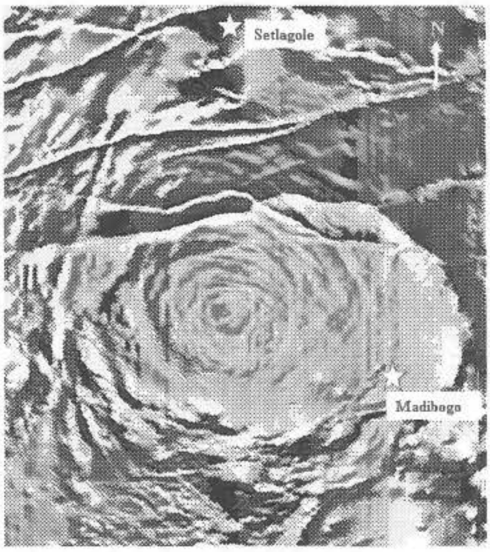

Fig. 2 Aeromagnetic image (filtered) of the Setlagole impact structure showing a central uplift, concentric rings and a variety of cross-cutting, pre-impact structure, mafic dykes. The distance between Setlagole and Madibogo is 18 km.

IMPACT EJECTA MODELING: MAIN PRINCIPLES AND A FEW EXAMPLES.

N. Artemieva[1],[1]Institute for Dynamics of Geospheres, RAS, Moscow, [2]Planetary Science Institute, Tucson, Arizona, artemeva@psi.edu, shuvalov@idg.chph.ras.ru.

Introduction: Most part of impact ejecta is deposited ballistically at some distance from a crater, defined by ejection velocity V and ejection angle α: $d=v^2\sin\alpha/g$. In case of giant impacts, planetary curvature should be taken into account [1]. Combined with ejecta scaling [2], these relations allow to define ejecta thickness as a function of distance. Ejecta from large craters are deposited at velocity high enough to mobilize substrate material and to thicken ejecta deposits [3]. Ballistic approximation is valid for airless bodies (if impact vaporization is not vast) or for proximal ejecta of large impact craters, where ejecta mass per unit area is substantially greater than the mass of involved vapor/atmosphere (M-ratio). Deposition of distal ejecta, in which ejecta mass is negligible compared to the atmosphere, may be also treated in a simplified manner, i.e. as 1) passive motion of ejected particles within an impact plume and 2) later, as sedimentation of particles in undisturbed atmosphere (equilibrium between gravity and drag). In all intermediate M-ratio values, impact ejecta move like a surge, i.e. dilute suspension current in which particles are carried in turbulent flows under the influence of gravity. Surges are well-known for near-surface explosive tests, described in detail for volcanic explosions (Plinian column collapse, phreato-magmatic eruption, lateral blast), and found in ejecta from the Chicxulub [4] and the Ries [5]. Important aspects of surge transport include its ability to deposit ejecta over a larger area than that typical of continuous ballistic ejecta and to create multiple ejecta layers.

Numerical models. Surges should be modeled in the frame of two-phase hydrodynamics, i.e. interaction between solid/molten particles and atmospheric gas/impact vapor should be taken into account. There are two techniques of solving equations for dust particle motion in a gas flow. The first one describes solid/molten particles as a liquid with specific properties, i.e. finite-difference equations are the same as in standard hydrodynamics [6-7]. This approach is quite simple, but has some limitations such as low resolution, strong numerical diffusion, and impossibility to describe particles of different size within one computational cell. The latter disadvantage is overcome in [8], but the price is the much greater number of equations to be solved and, hence, more arrays to be stored.

Another approach is based on solving equations of motion for representative particles [9]. Each of these markers describes the motion of a large number of real particles with similar sizes, velocities, and trajectories. Equation of motion (gravity, viscosity, and drag) is solved for every marker and then exchange of momentum, heat and energy with surrounding vapor-air mixture is taken into account. This approach is used in the SOVA code [10] and allows to vary particle sizes within a broad range (from a few m to a few microns). Implicit procedure of velocity update allows a larger time step. The substantial advantage of the model is its three-dimensional geometry, allowing modeling of asymmetric deposits of oblique impact ejecta. Turbulent diffusion is taken into account in a simplified manner [6].

Fragments size-frequency distribution (SFD) may be of crucial importance: while large fragments move ballistically, the smallest ones are passively involved in gas motion. Ejected material is usually transformed into particles under tension. The initial particle velocity is given by the hydrodynamic velocity, but the object's initial position within the cell is randomly defined. The SFD of solid fragments in high velocity impacts has been studied experimentally [2,11], numerically [12,13], and has been derived from the lunar and terrestrial crater observations [14,15]. Standard cumulative SFD ($N\sim D^{-b}$) is a consequence of the entire process, i.e., it represents the sum of individual ejection events taking place through time and space. Various approaches may be used to implement fragment size in a dynamic model: in Grady-Kipp model the average fragment size is defined by strain rate [12]; alternatively, average ejection velocity [16] or maximum shock compression [17] may be used. All methods may be verified through comparison with known data.

Volcanic direct blast. Numerical modeling of pyroclastic flows, checked against recent observations and young deposits, may be then a useful instrument for reconstruction of terrestrial craters' ejecta, which are mostly eroded or buried; and for impact ejecta study on other planets (first of all – on Mars), where remote sensing data are still the only source of our knowledge. In volcanology typical velocities are usually below 300 m/s, temperatures may be as low as 300 K (wet surge) and not higher than 1000 K (dry surge), solid/gas mass ratio ranges between 5-50, particle size rarely exceeds several cm, while the mass fraction of fine micron-sized particles is usually poorly defined.

Fig. 1 shows modeled direct blast at Bezymianny volcano (Kamchatka, Russia) in 1956.

Crater ejecta. Impact ejecta parameters vary in a substantially wider range: distal ejecta velocities reach several km/s, km-sized fragments are typical for large craters, gas content may be high enough for cratering in volatile rich (or water-covered) target or in the presence of a dense atmosphere.

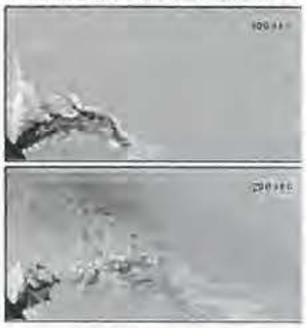

Fig.1 Directed blast at Bezymianny volcano (1956). Eejected material in atmosphere for tephra/gas ratio at the vent of 20. Modeled deposited area extends to 20-30 km from the vent and has a width of 10-15 km in a reasonable agreement with geological observations.

Moldavites from the Ries crater. The Ries impact site is characterized by a thick sedimentary layer, from which a large amount of vapor (e.g., CO_2) is shock-released. This vapor contributes to the ejected particles acceleration, or at least, to the sustainment of their motion. The initial ejection velocities of material are rather high, up to 10 km/s, which are close to the velocity of the expanding gas. As a result, the particles are not subject to high dynamic pressures (Fig. 2) that otherwise would disrupt them into fine mist immediately after ejection. The temperature of the entraining gas is rather high, so the particles do not cool quickly during the flight, allowing enough time to have them aerodynamically shaped (typical for tektites), and to lose volatiles [18,19]. Tektites are distributed up to 400-500 km away from the impact, in a fan of ~75° symmetrically distributed with respect to the downrange direction.

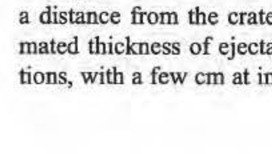

Fig.2 Trajectory of tektites in Earth's atmosphere. Molten cm-sized particles move within an impact plume without drag and are deposited by fallout hundreds km away from parent crater.

Chicxulub distal ejecta. We model the Chicxulub crater formation and use ballistic continuation to define ejecta thickness and composition as a function of a distance from the crater. The total amount and estimated thickness of ejecta is comparable with observations, with a few cm at intermediate distances of 1800-2500 km (e.g. in North America), and a few mm thick worldwide (at distances > 4000 km). However, ejecta thickness decreases with distance in contradiction with observations (2-3 mm world-wide). We also do not have any basement material in distal ejecta, as ejection velocity from a depth of 3 km is lower than 3.5 km/s. To find better correlation with observations, we suggest additional re-distribution of ejecta by floating of impact debris above the atmosphere [20,21].

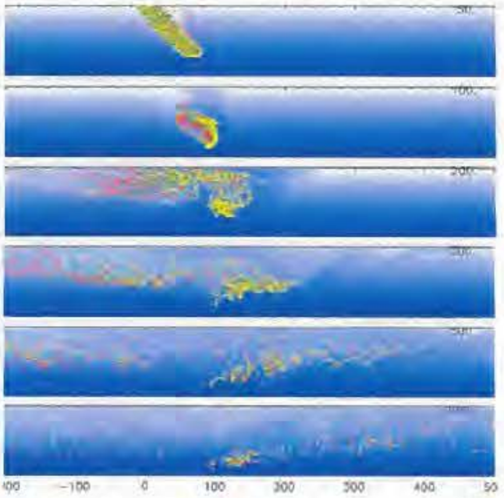

Fig.3 Chicxulub ejecta. Shock waves in atmosphere and dispersion of re-entry ejecta. Atmosphere thickness (Y-axis) is 100 km, numbers along the X-axis show distance from the re-entry point in km. Y-scale shows 100 km of the Earth's atmosphere. Numbers in the upper right corner of each snapshots – time in seconds.

References: [1] Dobrovolskis A. (1981) *Icarus 47,* 203–219. [2] Cintala M.J., et al. (1999) *M&PS. 34,* 605–623. [3] Oberbeck V.R. (1975) *Rev. Geophys. Space Phys. 13,* 337-362. [4] Dressler et al. (2004) *M&PS 39,* 857-878. [5] Hörz F. et al. (1983) *Rev Geophys.Space Phys. 21,* 1667-1725. [6] Valentine G.A. and Wohletz K.H. (1989) *JGR 94,* 1867-1887, [7] Dobran F. and Neri A. (1993) *JGR 98,* 4231-4259. [8] Neri A. et al. (2003) JGR 108, doi:10.1029/2001JB000508. [9] Boothroyd R.G. (1971) *Flowing gas-solids suspension,* Chapman and Hall Ltd, London. [10] Shuvalov V.V. (1999) *Shock waves 9,* 381-390. [11] Nakamura A. and Fujiwara A. (1991) *Icarus 92,* 132–146. [12] Grady D.E. and Kipp M.E. (1980) *Int. J. Rock Mech. Min. Sci. Geomech. Abstr.* 17, 147–157. [13] Melosh H.J. et al. (1992) *JGR 97,* 14735–14759. [14] Gault, D.E. et al. (1963) *NASA TND-1767.* [15] Vickery A.M. (1986) *Icarus 67,* 224–236. [16] Melosh H.J. (1984) *Icarus 59,* 234–260. [17] Shuvalov V.V. (2002) *LPSC-33,* abstr.#1259. [18] Stöffler et al. (2002) *M&PS 37,* 1893-1908. [19] Melosh H.J. and Artemieva N.A. (2004) *LPSC-35,* abstr. #1723. [20] Colgate S.A. and Petschek A.G. (1985) *LA-UR-84-3911.* [21] Artemieva N. and Morgan J. (2008) LPSC-39, abstr. # 1581.

3D-GIS AND REMOTE SENSING FOR MODELLING THE SIZE AND EXTENTS OF THE GARDNOS IMPACT STRUCTURE, NORWAY

Asabi, O.[1], Phillips M.E.[1,2] [1]Centre for GIS & Remote Sensing, School of Science, University of Greenwich, Chatham Maritime, U.K. [2]Planetary Science Research Group, Environmental Science Department, University of Lancaster, Lancaster, U.K. (email: m.phillips@gre.ac.uk)

Introduction: The Gardnos Structure is ~600 Ma with a diameter ~5km [1], in Hallingdal, Norway (Fig.1). The structure was only properly recognized in 1991 as being of impact origin [1] and had been mapped from the ground, but no Remote Sensing, 3D-GIS or regional-scale modelling had been done [2].

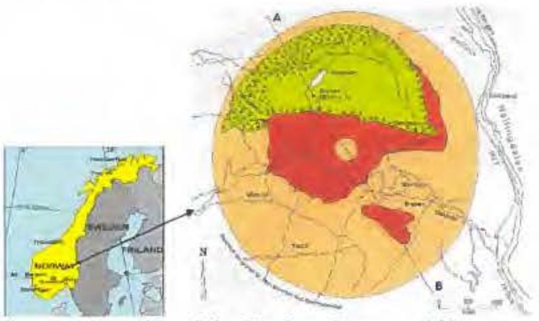

Figure 1. Location of the Gardnos Structure [4].

Methodology & Results: Initial field surveys in 2003-2004 using orthophotos to produce a Digital Elevation Model from stereo air photos [2] showed promise (Fig.2). The DEM, in conjunction with age and deformation of the structure applied to complex crater morphologies, suggested that the simplistic circular shape and size of the original map (Fig.1) could be revised and better defined by Remote Sensing.

Figure 2. Orthophoto on DEM looking N from above and just W of the central peak. Branden Lake top right; N extent of Gardnos Breccia top left (red dashed line).

The second stage of the work involved construction of a larger DEM from 20m contours (Fig.3) which helped to further reveal structural morphology, faulting, and the deformed crater signature [3]. On the DEM, lineaments that could be residual/trace-radial faults can be seen to the NW, N and NE. A number of post-Caledonian faults to the W cut across the structure.

Figure 3. Hill-shaded DEM. Red point is centre of the structure; Hallingdal (valley) to the north and east.

Extents of the structure were fitted to the DEM (Fig.4) and the geological map was added (Fig. 5) [3].

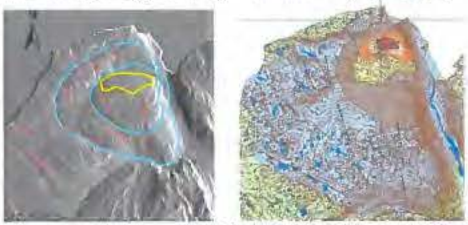

Figures 4 (left) and 5 (right). 3D with geological maps.

Conclusion: A 3D geological map [3] confirmed ground-based mapping by other workers [4]. Integration of geological, image and 3D data can help reveal overall structure. Work remains to be done and is in progress, to determine the exact shape and extents.

References: [1] Dons, J.A. & Naterstad, J. 1992. Meteoritics, 27, 215. [2] Phillips, M.E. 2003. Field and Lab Report, Dept. of Geography, University of Bergen, Norway. [3] Asabi, O. 2007. Unpublished BSc Thesis, University of Greenwich, UK. [4] Kalleson *et al.* 2005. Field Report, Lunar and Planetary Institute.

Acknowledgements: Digital contour data: Kjell Helge Sjøstrøm, Department of Geography, University of Bergen, Norway; Air photos, maps, field tours: Tom Jahren, Hallingdal Geologipark, Nesbyen, Norway.

Carbonatites Versus Meteorite Impact Origin Of Two Circular Structures Outcrop At Eastern Al-Awaynat Area, SE Libya

Dr M.Baegi
Libyan Remote Sensing Centre
Libya

Two major circular structures of 3 km in diametres each, located about 120 Km southwest of Jabal Arkeno were identified by airborne geophysical survey in 1973, and designated as R33 and R34A. Hunting, in 1974 was the first to report the presence of a carbonatitic body associated with the radiometric and magnetic high. Such association has invoked interest in these structures. Detailed investigation by C.R.G 1980, reported presence of distinctive abundance of apatite, magnetites, rare earth elements, nobium, uranium ,thorium and zirconium and document their carbonatitic origin. More recently, an alternative impact origin of these structures has been introduced by a Japanese group on the basis of radar images interpretation, supported by field work data and reported presence of Planer Deformation Foliations (PDF), shatter cones, breccia and named them respectively as Arkeno 1 and Arkeno 2.

Such controversy bring the present author to review and discuss all the existing data combined with more recent field work such as presence of numerous gas tubes, zoned complexes of alkaline igneous rocks, kaolinized syanites, bleaching zones, magnetite minerals which produces the positive magnetic anomalies at the central parts of the plugs, and presence of many volcanic plugs as well as small carbonatite plugs in the surrounding area that are following a tectonic trend, in NE direction. Therefore, the author strongly in support of the former interpretation as carbonatites plugs and exclude impact origin at the present.

REMOTE SENSING OF THE MOROKWENG IMPACT STRUCTURE, SOUTH AFRICA

Baker, T.[1], Phillips M.E.[1,2] [1]Centre for GIS & Remote Sensing, School of Science, University of Greenwich, Chatham Maritime, U.K. [2]Planetary Science Research Group, Environmental Science Department, University of Lancaster, Lancaster, U.K. (email: m.phillips@gre.ac.uk)

Introduction:
Morokweng is a ~144 Ma impact structure largely buried beneath Kalahari sediments [1] (Fig.1).

Figure 1. Location of the Morokweng Structure [1]

Other workers had suggested from geophysical methods that the structure could be very large [1], or <80km [2]. In this study, Landsat TM and ETM+ images were used in False Colour Composites (FCC) (Fig.2) from Landsat ETM+ from May 2001. All image bands were inspected visually and statistically both for defects and the extraction and enhancement of predominant structures. The images were then atmospherically and geometrically corrected, balanced, sharpened, filtered and converted to Principal Components. Best results were produced when using the thermal (far) infrared band (10.4-12.5μm) in conjunction with one mid infrared band (2.08-2.35μm) and the visible blue band (0.45-0.52μm) [4]. Despite the lower spatial resolution of the thermal band (TM, 120m; ETM+, 60m) compared to the reflective bands (TM, 30m; ETM+, 30m, 15m), it is often overlooked, but can reveal geological and morphological structures that are thermally emitting. Features hard to see in visible and near/mid infrared were revealed, such as banded ironstone formations (BIFs). Previously unrecognised arcuate features were also seen ~100km from the centre, north of Vryburg [4] (Fig.3) and have recently been confirmed by other work [5]. Additionally, arcuate drainage and possible palaeo-drainage features can be seen on the processed imagery. These features, if genuine and not image artifacts, may provide further evidence to origin as a multi-ring structure with an original diameter of at least 200km, as proposed by other workers [5].

Figure 2. Landsat ETM+, FCC RGB 671 of the realm of the Morokweng Structure, May 2001. GLCF [3]

Figure 3. Subscene of the RGB 671 image: orange outline = BIFs. Following, all inferred: dashed blue lines = arcuate (palaeo) drainage; dashed white lines = arcuate features; diamond = antiforms; cross = synform.

Due to extensive burial, impact-related features, such as rings, can be difficult to see on standard public domain imagery using standard displays of RGB. Therefore a detailed image processing project was undertaken to produce the best possible image of Morokweng, in order to investigate surface expressions of buried and exposed morphologies [4].

Methods & Results: Two scenes were used; the first was Landsat TM from April 1990 [4] and recently

References: [1] Andreoli, M.A.G. *et al.* 1999. Meteoritics & Planetary Science, vol. 34, A9. [2] Reimold, W.U. *et al.* 2002. Earth & Planetary Science Letters, 201, 221-232. [3] GLCF, University of Maryland, USA. [4] Baker, T. 2001. BSc Thesis, University of Greenwich, UK. [5] Andreoli, M.A.G. *et al.* 2007. SAGA Biennial Technical Meeting & Exhibition.

CENTRAL PIT CRATERS ON MARS AND GANYMEDE: CHARACTERISTICS, DISTRIBUTIONS, AND IMPLICATIONS FOR FORMATION MODELS. N. G. Barlow and N. Alzate, Dept. Physics and Astronomy, Northern Arizona University, Flagstaff, AZ 86011-6010. Nadine.Barlow@nau.edu; na84@nau.edu.

Introduction: Central pit craters display a central depression either directly on the crater floor (in place of a central peak) or atop a central rise/peak. They are common on Mars, Ganymede, and Callisto but have not been identified on volatile-poor bodies such as the Moon and Mercury. Their presence on bodies with ice-rich crusts suggests that target volatiles are necessary for central pit formation. Several formation models have been proposed for central pits: release of impact-generated gases during crater formation [1], excavation into subsurface liquid layers [2], collapse of central peak [3], and coalescence of pits formed by impact melt-target ice interactions [4]. Analysis of the sizes, distributions, and general characteristics of central pit craters on Ganymede and Mars can provide constraints on these formation models [e.g., 5,6].

Martian Central Pit Craters: Martian central pits are classified as floor pits (pit occurs directly on crater floor) and summit pits (pit occurs on central peak or other central rise). Floor pits are further subdivided into symmetric or asymmetric pits, depending on pit shape. Using Viking, MOC, and THEMIS imagery, we have identified 1522 central pit craters, although our analysis is continuing. Half of all central pit craters are symmetric floor pit (SY) craters while 41% are summit pit (sP) craters and 9% are asymmetric floor pit (AP) craters. While pit craters are seen on all terrains within the ±70° latitude range, strong concentrations are seen in the Xanthe, Margaritifer, and Arabia Terrae regions. No strong regional variations in distribution are seen between floor and summit pit craters. There is similarly no difference in occurrence of floor pits versus summit pits as a function of crater size—pit craters have diameters between 5 and 60 km (frequency peak near 13 km), suggesting excavation depths between ~1 km and 4.5 km based on standard depth-diameter relationships [7]. Central pit craters display a wide range of preservational states, from 2.0 (degraded) to 7.0 (pristine) [8, 9], indicating that the conditions favoring central pit formation have existed for most of the planet's history including up to the present. Those central pit craters fresh enough to display an ejecta blanket are typically associated with a multiple-layer ejecta morphology rather than single layer or double layer.

Comparison of the pit diameter (D_p) to the crater diameter (D_c) reveals that floor pits tend to be larger compared to their parent crater than summit pits. SY craters have D_p/D_c ranging between 0.07 and 0.28 with a median of 0.15. Summit pit D_p/D_c ranges between 0.05 and 0.19 with a median of 0.11.

On Ganymede, most central pits are superposed on an updomed crater floor. This updoming is believed to result from relaxation of the ice-rich crust after crater formation. We have used MOLA topography to investigate whether martian floor pits are similarly located on updomed floors. Based on analysis of 485 floor pit craters in the northern hemisphere of Mars, we find no indication of floor updoming [10]. This suggests that high crustal ice concentrations, such as seen on Ganymede and Callisto, are not necessary to produce central pits. The ~20% crustal ice concentration estimated from martian layered ejecta blanket studies [11, 12] is consistent with the lack of crater floor updoming.

Ganymede Central Pit Craters: We have identified 432 central pit craters on Ganymede using Galileo and Voyager imagery. Ganymede central pit craters range from 5 to ~100 km in diameter (frequency peak ~40 km), suggesting excavation depths of ~1 km to 8 km. The diameter of the frequency peak is almost 3 times greater than the corresponding diameter for martian central pit craters. Since Mars' gravitational acceleration is 2.6 times greater than that of Ganymede, the difference in crater size is likely due to the difference in gravity between the two bodies.

Our study reveals that craters in the 5 to ~100 km diameter range can show either a central pit or a central peak. This is contrary to Voyager results which reported no central peak craters in the diameter range where central pits were seen [3, 13]. However, Ganymede central pits occur as floor pits on updomed crater floors. No examples of pits atop central peaks, comparable to the martian summit pits, have been identified on Ganymede.

Ganymede central pit craters have D_p/D_c values ranging from 0.11 to 0.38 with a median value of 0.19. The median value is larger than that of either the floor pits or summit pits on Mars indicating that central pits on Ganymede are larger relative to their parent crater than central pits on Mars.

Comparison: Comparison of our current results for central pit craters on Mars and Ganymede reveal both similarities and differences between the two bodies:

- Central pits are common over all terrains on both bodies. No statistically significant latitudinal variation is seen on either body although some regional concentrations are suggested for Mars.

- Central pit craters can be small (~5 km diameter) up to large (~60 km on Mars, ~100 km on Ganymede). The diameter at which the frequency of central pits peaks is about 3 times larger on Ganymede than on Mars, probably due to the 2.6x difference in gravity between the two bodies.
- Central pit craters display a large range in preservational state on both Mars and Ganymede, suggesting that the conditions favoring central pit formation have existed over most if not all of the history of these two bodies. Fresh central pit craters on Mars tend to be associated with the multiple layer ejecta morphology.
- Central pits tend to be larger relative to their parent crater on Ganymede than on Mars. The difference in median D_p/D_c is less than 2.6 so gravity alone does not explain the difference. The higher ice concentration in the target on Ganymede or possibly higher impact velocities of the crater-forming projectiles could be responsible.
- Central pit craters on Ganymede are floor pits while those on Mars are both floor pits and summit pits. The greater strength of the target material may explain the occurrence of summit pits on Mars.
- Central pit craters on Ganymede typically occur on a updomed crater floor. Floors of floor pit craters on Mars do not show this updoming. Updomed floors on Ganymede are believed to result from rebound of the ice-rich target material [13]. The lack of updoming of the martian central pit crater floors indicates a much smaller concentration of ice is present. This indicates that central pits can form in targets with a large range in ice concentration (from ~20% to 100%).
- Central peak craters are seen in the same diameter range as central pit craters on both bodies.

Implications for Pit Formation Models: By comparing the distributions and characteristics of central pits on Mars and Ganymede, we get a better understanding of the range of environmental conditions producing these features and can better constrain the various formation models proposed for these features.

We can reject the model that central pits form by the collapse of central peaks in weak target material [3]. The presence of summit pits on Mars and the occurrence of central peaks within the same diameter range and regions as central pit craters argues against this mechanism.

The model proposing layered targets with liquid layers at depth [2, 5] may have some support. The Xanthe, Margaritifer, and Arabia Terrae regions of Mars, where an abundance of central pit craters is seen, also display other geologic features (i.e., outflow channels, chaotic terrain) indicative of subsurface water and Arabia Terra has been proposed to be the site of a long-term subsurface aquifer [14]. The association of fresh central pit craters with multiple layer ejecta morphologies is consistent with subsurface liquid layers since multiple layer ejecta have been proposed to result from excavation into liquid water reservoirs [15, 16]. Ganymede is expected to have harbored subsurface liquid layers/oceans throughout its history. The greatest problem with this model is the fact that central pit craters are seen practically everywhere on both Mars and Ganymede. This would suggest that subsurface liquid water layers exist within the upper 5 km on Mars and the upper 8 km on Ganymede everywhere on these bodies.

Vaporization of subsurface volatiles during crater formation [1], supported by high temperature gradients under the transient cavity in numerical simulations [17], remains a viable mechanism for central pit formation. More investigation of coalescence of impact melt-generated pits on craters floors as a mechanism of central pit formation [4] is needed as additional HiRISE imagery becomes available.

Acknowledgements: This work has been supported by NASA MFRP Award #NNG05GM14G, OPRP Award #NNG05G116G, and MDAP Award #NNX08AL11G

References: [1]Wood C. A et al. (1978), *Proc. 9th LPSC*, 3691-3709. [2] Croft S. K. (1983), *Proc. 14th LPSC, JGR, 88*, B71-B89. [3] Greeley R. et al. (1982), *Satellites of Jupiter*, UAz Press, 340-378. [4] Tornabene L. L. et al. (2007), *7th Intern. Conf. on Mars*, Abstract #3288. [5] Bray V. J. et al. (2005), *LPS XXXVI*, Abstract #1889. [6] Bray V. J. et al. (2006), *LPS XXXVII*, Abstract #1175. [7] Garvin J. B. et al. (2003), *6th Intern. Conf. on Mars*, Abstract #3277. [8] Barlow N. G. (2004), *GRL, 31*, doi: 10.1029/2003GL019075. [9] Barlow N. G. (2007), *LPS XXXVIII*, Abstract #1242. [10] Kagy H. M. and N. G. Barlow (2008), *LPS XXXIX*, Abstract #1166. [11] Woronow A. (1981), *Icarus, 45*, 320-30. [12] Stewart S. T. et al. (2001), *LPS XXXII*, Abstract #2092. [13] Schenk P. M. (1993), *JGR, 98*, 7475-7498. [14] Dohm J. M. et al. (2007), *Icarus, 190*, 74-92. [15] Barlow N. G. and T. L. Bradley (1990), *Icarus, 87*, 156-179. [16] Barlow N. G. and C. B. Perez (2003), *JGR, 108*, doi: 10.1029/2002JE002036. [17] Pierazzo E. et al. (2005), *Large Meteorite Impacts III*, 443-457.

THE ROLE OF THE GEOLOGICAL SOCIETY OF SOUTH AFRICA IN PROMOTING THE ESTABLISHMENT OF AFRICA'S FIRST GEOPARK AT THE TSWAING METEORITE IMPACT CRATER.

D. J. Barnardo, Council for Geoscience, Private Bag X112, PRETORIA, 0001, South Africa; barnardo@geoscience.org.za .

Introduction: The Geological Society of South Africa (GSSA) has a Conservation and Tourism Committee as part of its activities. This Committee has several activities and projects going and meets about once every three months to discuss the progress of these.

One of the most ambitious of these projects is a cooperative effort, with the Council for Geoscience (CGS), which performs duties as the Geological Survey of South Africa, to establish a Geosites database for South Africa. This site is up and running and available on the Internet at http://196.33.85.17/geosites/. It is also possible for contributors to register new Geosites on the system via the Internet. The site is growing steadily and currently contains about 90 descriptions of Geosites in South Africa. A sophisticated query and output system forms part of the site and allows a list of all or selected records in the database to be selected and output obtained in either PDF or html format. It is maintained by the CGS.

On 22 June 2007, the Conservation Committee organized a workshop, also in collaboration with the CGS, to discuss the possibility to establish formal UNESCO-recognized International Geoparks in South Africa. The keynote speaker was a well-known staff member from English Nature, Dr Colin Prosser. He visited several possible Geoparks in South Africa and eventually identified the Tswaing Meteorite Impact Crater as the prime candidate in South Africa for a first Geopark. Not only will it be the first in South Africa, but, in fact, the first in Africa.

About Tswaing: The Tswaing Meteorite Impact Crater is one of the youngest identified impact craters on Earth, being approximately 220 000 years old ([1]-[3]). It is situated about 50 km north-west of Pretoria, in a densely-populated area, with very good access routes and a well-established infrastructure. It is one of the best preserved and most accessible small impact craters on Earth and contains a central crater lake as an added draw card.

The site was originally viewed as a volcanic caldera [4], but was later proved to be of meteorite impact origin [1]. It is situated in the central, acid phase granites of the Bushveld Complex that form part of the Nebo Granite Suite [2]. This constitutes one of the added attractions of this site – the famous Busveld Igneous Complex can be one of the added draw cards for Tswaing visitors. The site is situated on a 2 000 hectare farm and is already recognized as a protected area, making the establishment of a Tswaing Geopark more attractive.

The site is managed as a museum by the Northern Flagship Institute (NFI), which manages several museums in the Gauteng region. A new Museum building was erected on the site about two years ago, but financial problems are prohibiting the installation of a modern impact museum, as is planned. A system of hiking trails already exists at Tswaing and accommodation in the form of bungalows allows a group of about 60 persons to be housed. A kitchen for visitors and adequate bathroom facilities are available. These are specifically aimed at accommodating school and youth groups, but adults are also welcome.

Several species of game were introduced to the site a number of years ago and the area has a rich bird population and diversified and interesting vegetation. The cultural and historical significance of Tswaing is also an advantage, since water from the crater lake has been, and still is, used for medicinal purposes by the local peoples, adding archaeological significance to the site. Salt and especially soda ash was extracted from the crater during the first half of the previous century and an agricultural research station was in operation on the farm during the 1970's. All these factors add to the attractiveness of the site and to the motivation for the establishment of a Geopark at Tswaing.

Obstacles to establishing a Geopark: Since Tswaing is already managed by a recognized organization, the establishment of a Geopark at the site should be so much easier. The only added requirement is to submit a motivation in the official format as required by the UNESCO management body and to establish a management plan for the site. However, because of the financial difficulties mentioned, the latter proves to be a real obstacle. The NFI Management Board has already approved the efforts to establish a Geopark at Tswaing. This is a first, important step on the way towards establishing a geosite. Now the only issue is to compile the motivation and complete the management plan.

Another problem specific to South Africa, is to find an authority to take ownership of the South African Geosites. This is needed, since some organization needs to oversee the proper management of such sites in South Africa.

An additional cause of concern is that no equivalent body to, for instance, English Nature exists in

South Africa to drive the establishment of Geosites. The only formal body currently in existence is the Conservation Committee of the GSSA. However, the members of this Committee are volunteers and, as such, have their own permanent jobs and all the work needed to drive the aims of the Committee must be done in their private time.

Suggestions to further the cause: The first and most important consideration is to establish funding for the project. As usual, this constitutes the major obstacle to the success of the project. Secondly, the NFI should prioritize the project and complete and implement the management plan for the site. In the third instance, adequate funds should be made available to enable the appointment of a suitable and dedicated contractor to drive the documentation of the site and compile a suitable motivation to UNESCO to allow the formal acceptance of Tswaing as the first African Geopark.

References: [1] Reimold, W.U. et al. (1991) *LPS XXII*, pp. 1117-1118. [2] Reimold et al. (1999) *Tswaing Meteorite Crater: An introduction to the natural and cultural history of the Tswaing region including a description of the hiking trail,* Popular Geoscience Series 1, Council for Geoscience. [3] Partridge, T.C. et al. (1999) *Memoir 85*, Council for Geoscience, Pretoria. [4] Wagner, P.A. (1922) *Memoir 20*, Geological Survey of South Africa.

STRATIGRAPHY OF THE IMPACTITE SECTION (1397-1551 m) FROM THE EYREVILLE DRILLCORE, CHESAPEAKE BAY IMPACT STRUCTURE, USA.

K. Bartosova[1], C. Koeberl[1], and W. U. Reimold[2], [1]Department of Lithospheric Research, University of Vienna, Althanstrasse 14, A-1090 Vienna, Austria. E-mail: katerina.bartosova@univie.ac.at. [2]Museum of Natural History (Mineralogy), Humboldt University, Invalidenstrasse 43, D-10099 Berlin, Germany.

Introduction: The Chesapeake Bay impact structure, 35 Myr old and 85 km in diameter, is one of the largest and best preserved impact structures on Earth [1]. The structure was drilled in the central part at Eyreville in 2005-2006 during an ICDP-USGS drilling project. Three drill cores (Eyreville A, B, and C), intersecting the impact structure to a total depth of 1766 m, were recovered within the central zone of the structure in the deep crater moat. The crater fill comprises post-impact sediments, sediment clast breccias and sedimentary megablocks (the so-called Exmore breccia beds, interpreted as resurge breccias), a large granitic and a small amphibolitic megablock, gravelly sand, suevites and lithic impact breccias (SLIB; 1397-1551 m; [2]), and granites/pegmatites and mica schists [1]. In the upper part (above ~1474 m) of the section of SLIB the suevite is mostly melt rich and contains two intervals (5.5 and 1 m thick) of impact melt rock [3]. In the deeper parts of the section (below 1474 m) mostly suevitic polymict impact breccia alternates with large blocks of cataclastic gneiss [2].

Samples: Petrographic and geochemical analyses of 43 impactite samples were performed. The samples comprise 30 samples of suevite, three samples of impact melt rock, one polymict lithic breccia, three conglomerate clasts, and six samples of cataclastic gneiss/schist.

Suevites and impact melt rocks: The suevite has a grayish, fine-grained clastic matrix and consists of a variety of rock and mineral clasts, melt particles, as well as secondary minerals (e.g., phyllosilicates). The impact melt rocks contain melt matrix mostly recrystallized to feldspar/pyroxene microlites. Lithic fragments comprise sedimentary, metamorphic, and igneous lithologies; their relative proportions vary significantly through the SLIB section. Mineral clasts include quartz, K-feldspar, plagioclase, muscovite, biotite, opaque (mostly pyrite) and other accessory minerals. Quartz grains in suevite show planar fractures and planar deformation features. Toasted appearance of quartz is very common and ballen quartz occurs in melt-rich intervals. Melt fragments are most abundant near the top of the SLIB section (up to 34 vol% in the interval 1399-1422 m) and around 1450 m (up to 77 vol%). In these intervals also some impact melt rocks occur. The millimeter- to centimeter-sized melt particles are mostly altered, commonly contain small undigested clasts and show flow structures. Several major types of melt particles have been distinguished on the basis of color, micro-texture, and chemical composition: 1) clear, brownish, or greenish, unaltered glass, commonly with flow texture (dark and light colored schlieren); 2) brown melt, entirely altered to fine-grained phyllosilicate minerals, commonly with undigested clasts; 3) recrystallized silica melt; 4) melt with intersertal texture, with feldspar and/or pyroxene microlites; 5) dark brown melt (of shale precursor).

Stratigraphy of the SLIB section: Horton et al. [2] have divided the SLIB section into subunits according to lithological differences. We focused on the suevites and divided them into subunits according to clast (abundance, size, type) and melt (abundance, type) content and characteristics (Fig. 1).

Subunit 1 (U1, 1397.2 - 1430 m) is the most homogeneous subunit. Clasts are smaller in size and the proportion of matrix is larger than in the other subunits. Sedimentary clasts (e.g., siltstone, sandstone, conglomerate) prevail, but schist clasts are also present. Large melt particles (up to 5 cm) occur. Suevite is melt-rich and contains an interval (1402.2-1407.5 m) of impact melt rock, where melt with intersertal structure (type 4) is abundant. Occurrence of unaltered glass (type 1), commonly with shard-like structure, is typical for this subunit and much more limited in lower subunits.

Subunit 2 (U2, 1430 – 1448.4 m): Clast-rich suevite, with clasts mostly from crystalline basement lithologies (gneiss, schist, and granite). Rare sedimentary clasts (e.g., siltstone, shale, and conglomerate) occur. Melt particles (mostly type 2) are rare (<3 vol%).

Subunit 3 (U3, 1448.4 – 1457 m) consists of melt-rich suevite and contains a thin interval of impact melt rock (1450.2 - 1451.2 m). Many clasts are difficult to resolve due to partial melting. There are abundant sedimentary clasts (e.g., siltstones, mudstones, sandstone, graywacke) and some crystalline clasts (e.g., schist and granite). At about 1455 m depth there are abundant larger clasts, >10 cm in size (shale, conglomerate, schist). Melt particles of types 3 and 5 are the most common ones in this subunit.

Subunit 4 (U4, 1457 – 1474.1 m): Suevite in subunit 4 contains abundant melt particles, but the proportion of melt is lower and the proportion of matrix is higher than in U3. There are various types of lithic clasts (e.g., siltstone, sandstone, conglomerate, schist) commonly larger than ~10 cm. Sedimentary clasts prevail. Only melt particles of type 2 occur in this subunit.

Subunit 5 (U5, 1474.1 – 1486.1 m) is similar to subunit 2. The proportion of melt is very low (less than 2 vol%, on average). The suevite is porous and clast-rich; crystalline clasts (i.e., schist/gneiss) prevail. Only altered melt particles (type 2) occur.

Subunit 6 (U6, 1486.1 – 1551.2 m): The lowermost subunit is very heterogeneous. Suevite alternates with large blocks of cataclastic gneiss/schist. Sedimentary clasts (e.g., siltstone, shale, sandstone, conglomerate) are generally more abundant than crystalline clasts (schist/gneiss and granite), but some crystalline clast rich parts occur (e.g., 1510.8 - 1512.0 m). Melt particles are relatively abundant in upper parts of the subunit (e.g., ~12 vol% in samples from about 1505 m), but is low (<3 vol%) in the lowermost parts. Melt particles are strongly altered; some samples contain abundant smectite.

Conclusions: The relative abundance of melt particles varies significantly through the suevitic section; melt is most enriched near the top, where the suevite is intercalated with impact melt rock. Five different types of melt particles have been distinguished. Six different subunits of suevite have been recognized based mostly on the abundance and characteristics of lithic clasts and melt particles. There are melt-rich parts (U1 and U3); sedimentary clasts are dominant in most subunits (especially 1, also 3, 4, and 6). There are two melt-poor sections with predominantly crystalline clasts (U2 and U5). The lower parts (U5 and U6), which contain large blocks of cataclastic gneiss, probably represent ground-surge material, as has been suggested by [3]. The shard-like melt particles from U1 of the suevitic unit solidified before incorporation into the breccia and represent fall-back material. Due to the position of the core in the central moat near the central uplift, the stratigraphy could have been disturbed by slumping of material from the central uplift. This could be the case for subunit U2. Similarly, in the nearby STP testhole, it has been suggested that the gneiss blocks were mixed into the fallback suevite, possibly during central-uplift rise and collapse [4].

References: [1] Gohn G. S. et al. (2006) *EOS* 87, 349 & 355. [2] Horton J. W. et al. (2008) *this meeting* [3] Wittmann et al. (2008) *LPS XXXIX* Abstract #2435. [4] Horton et al. (2005) *LPS XXXVI* Abstract #2003.

Acknowledgment: Thanks to L. Ferriere (U Vienna), J.W. Horton (USGS Reston), A. Wittmann (LPI Houston), and S. Gier (U Vienna) for discussion. Supported by the Austrian Science Foundation FWF, grant P18862-N10 (to C.K.).

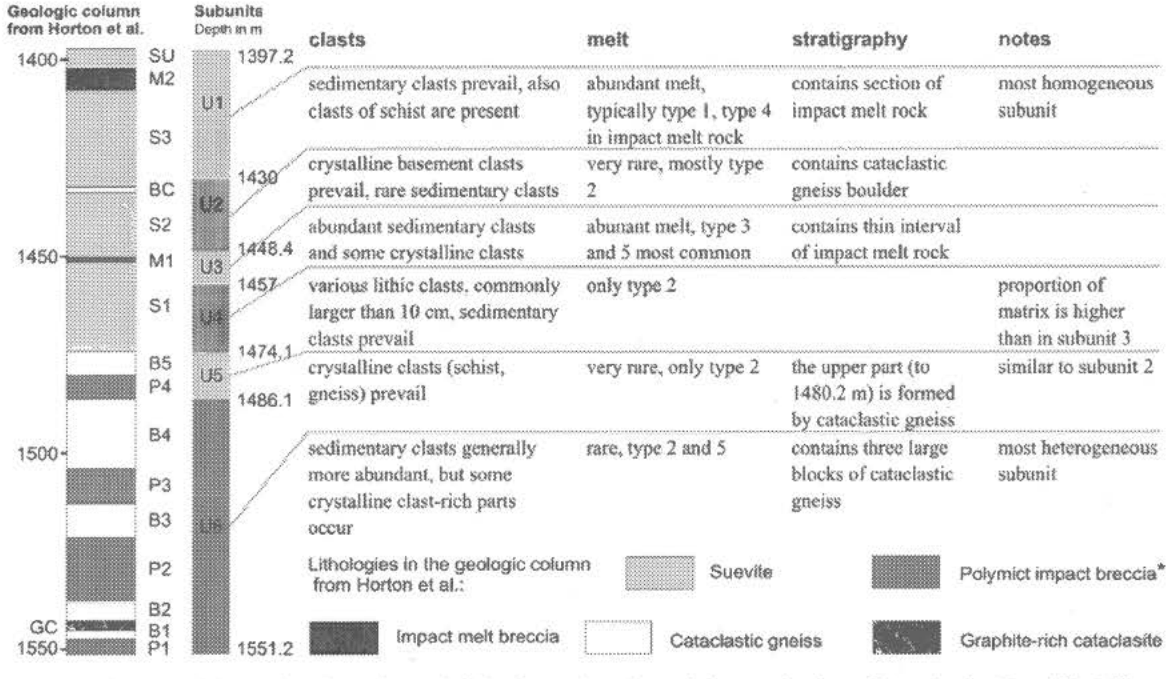

clasts	melt	stratigraphy	notes
sedimentary clasts prevail, also clasts of schist are present	abundant melt, typically type 1, type 4 in impact melt rock	contains section of impact melt rock	most homogeneous subunit
crystalline basement clasts prevail, rare sedimentary clasts	very rare, mostly type 2	contains cataclastic gneiss boulder	
abundant sedimentary clasts and some crystalline clasts	abunant melt, type 3 and 5 most common	contains thin interval of impact melt rock	
various lithic clasts, commonly larger than 10 cm, sedimentary clasts prevail	only type 2		proportion of matrix is higher than in subunit 3
crystalline clasts (schist, gneiss) prevail	very rare, only type 2	the upper part (to 1480.2 m) is formed by cataclastic gneiss	similar to subunit 2
sedimentary clasts generally more abundant, but some crystalline clast-rich parts occur	rare, type 2 and 5	contains three large blocks of cataclastic gneiss	most heterogeneous subunit

Fig. 1: Stratigraphy of the section of suevites and lithic impact breccias and characterization of the subunits, Eyreville drill core, Chesapeake Bay impact structure. Left column - Horton et al. [2], * polymict impact breccia comprises suevite and minor polymict lithic impact breccia; right column - our subunits.

ACCRETIONARY LAPILLI FROM THE TOOKOONOOKA IMPACT EVENT, AUSTRALIA.

K. Bron, Australian School of Petroleum, University of Adelaide, Adelaide, SA 5005, Australia – tbron@asp.adelaide.edu.au

Introduction: The lower Cretaceous Tookoonooka proven impact structure (27°07'S, 142°50'E) is a subsurface structure of the Eromanga Basin in Queensland, Australia. A Tookoonooka ejecta layer has now been identified in drillcore in the extensive sedimentary basin succession, [1]. The investigation of probable accretionary lapilli associated with the ejecta layer is discussed here.

Background - Accretionary Lapilli: Accretionary lapilli have been recognized in association with a number of impact events worldwide, including the Ries [2], Alamo [3], Popigai [4], Azuara [5], and Chicxulub [6,7,8] among others. Typical characteristics of impact-produced accretionary lapilli include internal concentric zonation, rims and nuclei, inclusions of rock fragments or grains (which may exhibit shock features), a fining outward texture, elemental anomalies suggesting a meteoritic input, and an original spherical to sub-spherical shape.

For clarification, this discussion will use the same terminology as [3], i.e. "crust" for the outer rim or shell, "mantle" for the main body of the lapilli comprising accreted particles, and "nucleus" where an inner core is present.

Observations and Discussion: Within the ejecta layer are unusual, light brown-tan clay-rich clasts. The apparent diameters of these clasts in core sample are commonly less than 1.5 cm, but may be up to 6 cm. Clast shapes are ellipsoidal, spherical, elongate, and irregular, and are consistently rounded (no angular or broken examples of these clasts have been observed). Clasts exhibit concentric zonation, a very fine-grained outer crust (possibly altered from a devitrified texture), and a relatively coarser-grained mantle with inclusions of quartz and partially-altered feldspar. Rare lithic nuclei are present. The clasts have been observed in a number of stratigraphic drillcores in the basin. Within 4 crater radii (proximal to the impact site), they may occur in clast-supported breccia layers which are interpreted to contain primary ejecta. More distal occurrences are reworked within tsunami deposits, often 'floating' within planar-bedded sandstone or in matrix-supported conglomerates.

Petrographic observations reveal that inclusions within the mantle of the clasts are complex. Minor feldspar (predominantly plagioclase, with some K-feldspar; both heavily altered) and quartz (some of which have a euhedral crystal shape) are enveloped in colourless, crystalline carbonate overgrowths. In some cases, pyritic overgrowths are also present. These complex mantle grains are set in a largely massive, brownish sideritic matrix exhibiting poikilotopic fabric under cross-polars. The carbonate and pyrite phases (and likely the euhedral quartz) are interpreted to be the result of post-depositional diagenesis; it is clear that these clasts have experienced extensive alteration although the primary zonation is still subtly apparent below the diagenetic overprint in many.

Conclusion: The clasts described are unusual within the context of the predominantly siliciclastic sedimentary basin. They exhibit many of the characteristics of previously described impact lapilli, [e.g. 2-8], even though they are pervasively altered and much of their original texture has been lost. These clasts are interpreted to be accretionary lapilli derived from the Tookoonooka impact event. Their presence provides evidence of impact provenance for the ejecta layer.

Ongoing work which will be presented includes geochemical studies and microscopic investigation of the primary crystal inclusions within the mantle of the lapilli for shock metamorphic features.

References: [1] Bron K., in prep. [2] Graup G. (1981) *EPSL, 55,* 407–418. [3] Warme J. et al. (2002) *GSA SP 356,* 489-504. [4] Masaitis V. (2003) *Impact Mark. in the Strat. Rec., Springer,* 137-162. [5] http://www.impact-structures.com/Archiv/archiv.html [6] Ocampo A. et al. (1996) *GSA SP 307,* 75-88. [7] Pope K.O. et al. (1999) *EPSL, 170,* 351–364. [8] Montanari A. (1990) *J. Sed. Petrol., 61,* 315–339.

UPHEAVAL DOME, UTAH, USA: IMPACT ORIGIN CONFIRMED. E. Buchner[1] and T. Kenkmann[2], [1]Institut für Planetologie, Universität Stuttgart, Herdweg 51, 70174 Stuttgart, Germany, e-mail: elmar.buchner@geologie.uni-stuttgart.de, [2]Museum für Naturkunde-Mineralogie, Humboldt-Universität zu Berlin, 10115 Berlin, Germany, e-mai: Thomas.Kenkmann@MUSEUM.HU-Berlin.de.

Introduction: Upheaval Dome is a unique circular structure on the Colorado Plateau in SE Utah whose origin has been controversially discussed for decades [1]. The "Sphinx of Geology" has been interpreted as a crypto volcanic feature, a salt diapir, a pinched-off salt diapir, and as an eroded impact crater. While recent structural mapping, modeling, and analyses of deformation mechanisms strongly support an impact origin, e.g., [2], [3], ultimate proof, namely the documentation of unambiguous shock features, has yet to be successfully provided.

Samples and methods: Our microstructural study focuses on rock samples collected from bedrocks of the Early Jurassic Kayenta Formation during a field campaign in September 2005. The samples were taken from bedrocks in the "Intermittent Creek" (Fig. 1) about 1.3 km northeast of the proposed crater center and 450 m southwest of the ring syncline axis. Here, we document a localized shock metamorphic overprint of quartz grains in sandstone samples making use of optical, scanning, and transmission electron microscopy (TEM).

Fig. 1: Investigated rocks at the sample location about 1.3 km NE of the center of the crater. Sandstones of the Early Jurassic Kayenta Formation are partly brecciated and display narrow-spaced networks of meso-to-microscale faults.

Results and conclusions: We have documented quartz grains of the Upheaval Dome structure, Utah, USA, with multiple sets of thin planar lamellae, which we identify as decorated planar deformation features (PDFs). TEM analysis revealed that the lamellae are dislocation bands with extremely high dislocation densities that contain numerous fluid inclusions precipitated on the dislocations (Fig. 2). The original amorphous material of the lamellae was devitrified by thermal annealing. The documentation of PDFs provides the definite evidence for the impact origin of Upheaval Dome [4]. The documented PDF lamellae suggest shock pressures of ~10 GPa and probably more at 1.3 km distance from the crater center. This order of pressure magnitude is in conflict with significant lower pressures previously estimated. Possible explanations for elevated shock pressures are (a) local pressure excursions formed by shock-induced collapse of pore space, (b) impedance mismatches between feldspar and quartz, and (c) oblique impact trajectories.

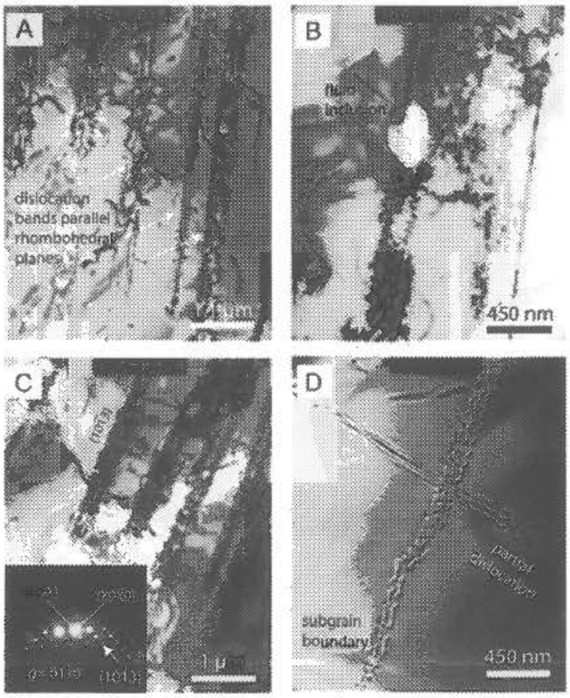

Fig. 2: Bright field TEM micrographs of quartz grains studied [4]; A: Rhombohedral lamellae are straight and parallel, and have varying thickness. The defect density is extremely high within the lamellae; B, C: the dislocation bands contain numerous bubbles and fluid inclusions <400 nm in diameter; D: Partial dislocation and low angle sub grain boundary.

References: [1] Koeberl C. et al. (1999) *Meteoritics & Planet. Sci., 34,* 861-868. [2] Kenkmann T. (2003) *Earth Plant. Sci. Lett., 214,* 43 58. [3] Okubo C. H. and Schultz R. A. (2007) *Earth Planet. Sci. Lett., 256,* 169-181. [4] Buchner E. and Kenkmann T. (2008) *Geology, 36,* 227-230.

A POSSIBLE UPPER EOCENE-OLIGOCENE IMPACT SPHERULE LAYER IN THE NORTH ALPINE FORELAND BASIN, UPPER BAVARIA, GERMANY?

[1]E. Buchner, N. J. Deinerth, and M. Schmieder, Institut für Planetologie, Universität Stuttgart, Herdweg 51, D-70174 Stuttgart, Germany, [1]elmar.buchner@geologie.uni-stuttgart.de.

Introduction: Layers of distal impact ejecta have been reported from various sites on Earth through geologic time [1]. Two ejecta layers are known from Late Eocene-Oligocene sections: first, the so-called clinopyroxene microkrystite layer that is derived from the ~100 km and 35.7 ± 0.2 Ma Popigai crater, Russia; second, the slightly younger North American mircotektite layer linked to the ~90 km and 35.5 ± 0.3 Ma Chesapeake Bay crater, Virginia, USA [1-3]. No spherule layers associated with the smaller impact structures of Lake Mistastin (Labrador, Canada; 28 km and 36.4 ± 4 Ma) and Lake Wanapitei (Ontario, Canada; 8 km and 37.2 ± 1.2 Ma) have been described. Apart from the Massignano stratotype section for the Eocene/Oligocene boundary, Marche, Italy, which is known to contain altered spherules of the clinopyroxene (Popigai) layer [4], no Eocene-Oligocene impact ejecta are known in Europe. Here we report a possible spherule layer in uppermost Eocene to Oligocene sediments of the North Alpine Foreland Basin of Upper Bavaria (Southern Germany).

Samples, Geological Setting, and Methods: Samples were obtained from two Upper Eocene to Oligocene sedimentary sections: first, a natural outcrop of parautochthonous, medium-grained marine sandstones at the Katzenlochgraben near the village of Hammer (within a sedimentary suite regionally known as the "Katzenlochschichten" [5]); second, from the top of red algae-bearig biohermal limestones (regionally known as the "Lithothamnienkalke" [6]) that outcrop in the active cement quarry at Rohrdorf operated by the Rohrdorfer Zement^{TM} enterprise. Both sample locations are ~40 km apart (Fig. 1). Preliminary petrographic and geochemical studies were carried out using optical microscopy (magnifiers and polarization microscopes) and SEM-EDX (energy dispersive X-ray analysis).

Fig. 1: Sample locations at Hammer and Rohrdorf in the North Alpine Foreland Basin (southern Upper Bavaria, Germany).

Petrography and Geochemistry: Black 'clayey' spheres of submetallic luster are abundant on (but limited to) one bedding plane of the Katzenlochgraben sandstones and the Lithothamnienkalke, respectively. Most of the spheres occur as individuals up to ~0.5 mm in diameter (Fig. 2); agglomerates of two or more spheres also exist (Fig. 3). The majority of the spheres is hollow or filled by secondary phases. The geochemical composition of the spheres is of mixed silicatic (and probably partially sulphidic) character, with a strongly variable distribution of Si, distinct EDX peaks for Mg, Al, K, Ca, Fe, S, and slight enrichment in Cl, P, Ti, Mn, and Ni (Table 1).

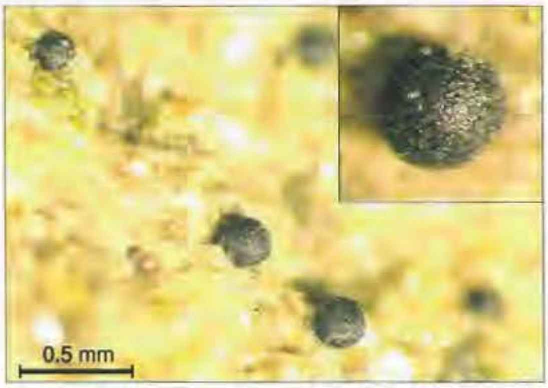

Fig. 2: Individual spheres on sandstone from the Katzenlochgraben near Hammer (same scale for inset).

	#1	#2	#3	#4	#5
Na_2O	0.00	0.00	0.00	0.35	0.14
MgO	4.94	2.40	2.87	3.68	2.89
Al_2O_3	19.92	17.02	20.10	19.52	21.79
SiO_2	34.08	53.72	42.25	46.55	49.91
P_2O_5	0.35	0.16	0.31	0.37	0.87
SO_3	6.08	2.01	1.91	2.66	2.74
Cl_2O	0.76	1.14	0.33	1.22	0.37
K_2O	3.20	3.50	3.74	3.70	4.54
CaO	16.80	5.47	7.70	8.01	5.24
TiO_2	0.88	2.77	0.48	0.59	0.96
MnO	0.54	0.87	0.54	0.63	1.86
FeO	11.62	10.34	19.59	12.83	8.14
NiO	0.82	0.61	0.17	0.00	0.56
Total*	100.00				

Table 1: Preliminary geochemical composition of the Katzenlochgraben spheres (EDX data without volatiles; measured at 15 kV).

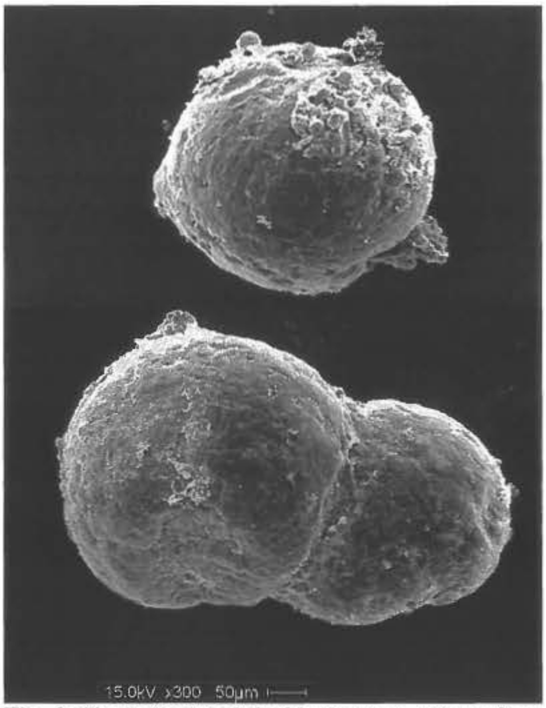

Fig. 3: Single (top) and double (bottom) spheres from the Upper Eocene-Oligocene section at the Rohrdorf quarry (SEM-secondary electron image).

Discussion and Results: The Hammer-Rohrdorf spheres occur locally within Upper Eocene to Oligocene sediments of the Katzenlochgraben and the Rohrdorf quarry sections; we did not detect the spheres in other sedimentary units. As many of the spheres are hollow (partially filled with secondary phases), an origin as small concretions or ooids can be ruled out. A strong variability in size, shape, and type of agglomeration also suggests that the spheres were not generated by organisms. The geochemical composition precludes that the spheres are reworked and rounded grains of authigenic glauconite linked to microfossils as earlier described by [6]; we also observed glauconite in the Katzenlochgraben sandstones and the Lithothamnienkalke, but these grains differ from the spheres in composition, shape, and colour. Taking the above facts into account, we propose that the spheres might represent altered and/or reworked impact spherules probably linked to one of the Late Eocene-Oligocene impact events. The hollow clayey character of the spheres, however, indicates strong alteration (compare [7-9]) and, accordingly, geochemical values different from their original composition.

The search for unmelted impact ejecta material, such as shocked quartz grains, did not yield reliable signs for an impact origin of the Hammer-Rohrdorf sphere layer but is currently continued. So far, we detected only quartz with one set of straight deformation lamellae that appear distinct from abundant Boehm lamellae in optical microscopy. Thus, convincing evidence for shock metamorphism still needs to to be presented. However, besides the spheres, irregularly shaped particles of devitrified-spherulitic feldspar glass occur in the Katzenlochgraben sandstones. It remains unclear whether these glass particles are of volcanic, tectonic-frictional, or possible impact origin.

Further petrographic work and geochemical analyses will be needed to harden evidence for an impact origin of the Hammer-Rohrdorf spheres. Moreover, C- and O-isotopic studies of the Upper Eocene-Oligocene sediments at the Rohrdorf quarry, as well as a refined biostratigraphic characterization of these sediments will be necessary to link the spheres with one of the Eocene-Oligocene large impact events and to establish (or discredit) the first occurrence of Upper Eocene-Oligocene distal impact ejecta in Central Europe.

Acknowledgements – we are grateful to Holger Maurer (Rohrdorfer Zement) and Robert Darga (Naturkunde- und Mammut-Museum Siegsdorf) for their support.

References: [1] Simonson B. M. and Glass B. P. (2004) *Annu. Rev. Earth Planet. Sci., 32,* 329-361. [2] Glass B. P. (2002) *Chem. Erde, 62,* 173-196. [3] Whitehead J. et al. (2000) *Earth Planet. Sci. Lett., 181,* 473-487. [4] Montanari A. and Koeberl C. (2000) Impact stratigraphy – The Italian Record. Springer, Berlin, Germany, 377 pp. [5] Hagn H. (1978) *Mitt. Bayer. Staatsslg. Paläont. hist. Geol., 18,* 167-235. [6] Maier W. (1957) *ZDGG, 109,* 448-451. [7] Walkden G. M. et al. (2002) *Science, 298,* 2185-2188. [8] Bohor B. F. and Glass B. P. (1995) *Meteoritics, 30,* 182-198. [9] Smit J. (1999) *Annu. Rev. Earth Planet. Sci., 27,* 75-113.

A MODEL FOR THE FORMATION OF THE CHESAPEAKE BAY IMPACT CRATER AS REVEALED BY DRILLING AND NUMERICAL SIMULATION.

Gareth S. Collins[1], Thomas Kenkmann[2], Kai Wünnemann[2], A. Wittmann[3], W. U. Reimold[2], H. J. Melosh[4]. [1]Impacts and Astromaterials Research Centre, Dept. Earth Science and Engineering, Imperial College London, London, SW7 2AZ, UK (g.collins@imperial.ac.uk); [2]Museum für Naturkunde, Humboldt-Universität Berlin, D-10115, Berlin, Germany; [3]Lunar and Planetary Institute, 3600 Bay Area Blvd, Houston, TX 77058, USA; [4]Lunar and Planetary Lab, University of Arizona, Tucson, AZ 85721, USA.

Introduction: The Chesapeake Bay crater, Virginia, is the largest known impact structure in the United States [1]. It is well-preserved beneath ~500-m of post-impact sediments and has been investigated by seismic studies, as well as by several drill cores [e.g., 2-7]. Seismic data interpretation revealed that the basement structure of the crater an "inverted sombrero" morphology, with a deep inner basin (~40-km diameter) surrounded by a shallower brim (80-90 km diameter) [1-7]. The surface morphology of the crater, however, is almost entirely flat due to the presence of an unusually thick (several hundred meters) synimpact crater fill deposit, the Exmore breccia [1-7]. The structural and morphologic form of the Chesapeake Bay crater is similar to that of other marine craters on Earth, but is quite unconventional when compared with similar-sized subaerial craters on Earth.

Recent numerical simulations of the Chesapeake Bay impact using the iSALE hydrocode, which included a large contrast in material strength between the weak sedimentary and strong crystalline units, reproduced the unusual structural form of the Chesapeake Bay crater and many of the structural features interpreted from the seismic data [8]. According to this model of a 3.2-km diameter impactor colliding vertically at 17.8 km/s with a two-layer (water-saturated sediment over crystalline basement) target:

i. A deep basin in the crystalline basement is formed near the crater center that contains inwardly collapsed (resurge) sediments and is bounded by a ring of uplifted basement.
ii. Outside of this, the model predicts a shallower outer basin where deformation is confined to the sedimentary layer.
iii. The unusually thick impact breccia/resurge deposit that fills the entire crater is a direct consequence of the extremely weak sedimentary unit at the time of impact.

Petrographic analyses of drill core from the recent ICDP-USGS drilling project provide new constraints on the inner crater stratigraphy (Fig. 1) with which to test this model [e.g., 9-12]. Here, we compare a new 3-layer model of the Chesapeake Bay impact (Fig. 2), similar to [8], with ground truth data from the new drill core. In addition, we use the combination of drill core analysis and results from numerical simulation to provide new insight into the duration of different stages of the Chesapeake Bay and other marine target impacts.

Overview of ICDP-USGS-drilling results: The principal stratigraphy as revealed in the combined Eyreville cores (Fig. 1) is documented in [9-12]. It consists, from top to bottom, of 444 m post-impact sediments resting on 652 m of resurge deposits, the so-called Exmore beds [9]. Underneath this unit is a single, coherent 275 m granite block, which, in turn, overlies 22 meters of smaller sedimentary and granite blocks. Beneath this is 157 m of lithic impact breccia, suevites, and impact melt rocks [10, 11]. The lowermost sequence in the drill core comprises 215 m of basement-derived lithologies (Fig. 2) [10, 11]. Significantly, a shock metamorphic overprint is lacking in both the 275-m granite boulder and the lowermost basement blocks [12].

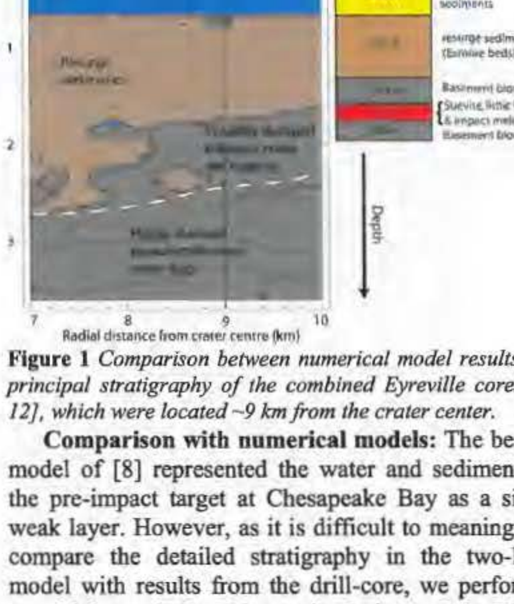

Figure 1 *Comparison between numerical model results and principal stratigraphy of the combined Eyreville cores [9-12], which were located ~9 km from the crater center.*

Comparison with numerical models: The best-fit model of [8] represented the water and sediments in the pre-impact target at Chesapeake Bay as a single weak layer. However, as it is difficult to meaningfully compare the detailed stratigraphy in the two-layer model with results from the drill-core, we performed new high-resolution 3-layer simulations of the Chesapeake Bay impact that show the same good agreement with geophysical interpretation and also enable better comparison between final modeled crater stratigraphy and the results of drilling. Figure 2 shows a radial cross-section through the final crater in our new numerical simulation of the Chesapeake Bay impact. The model is identical to that of [8] apart from separating the upper target layer into a 500-m water layer above a 1-km thick weak sediment layer. The impact velocity was also reduced from 17.8 km/s to 16 km/s.

The Eyreville drill site is situated at a radial distance of approximately 9 km from the crater center (marked on Fig. 2) [12]. The large-scale stratigraphy observed in the model is shown in Fig. 1 for comparison with the drill core observations. Comparison between the model and borehole suggests the following:

i. At 9-km radial distance, the numerical model shows a 1-kilometer thick sequence of heavily deformed sediments (see lack of tracer lines in Fig. 1&2). The recovered Exmore beds (652 m) in the drill core are thinner than this; however, the 275 m thick granite block and the underlying unit (22 m) of smaller sedimentary and amphibolite blocks are also part of this sequence, which has an aggregate thickness of 950 m.

ii. Below the heavily deformed sediments in the model is a ~600-m thick zone of deformed, predominantly basement material that collapsed (and was pushed) inward from the transient crater rim during resurge. This zone contains material exposed to a wide range of shock states. The corresponding unit(s) in the drill core may be the suevite-like unit and, perhaps, the basement blocks beneath. In the model, the highly-shocked, parautochthonous crater floor is located at a depth of 2.5 km (dashed white line); if this is correct, it implies that the drill core did not reach the crater floor.

iii. Modeling predicts that the sediment-laden resurge (Exmore beds) flowed back into the crater at speeds on the order of 100 m/s, and filled the inner basin in a matter of minutes after the impact. According to simple physical analysis [12], fluid flow on this scale and at this speed would be sufficient to "pluck" or drag a boulder up to several hundred meters in size from the transient crater rim area and carry it into the crater. This offers a potential explanation for the presence of a 275-m wide granite block, which shows no evidence of shock metamorphism, near the base of the resurge sequence in the drill core.

Insight into Chesapeake Bay crater formation: The combined results of numerical models and observations from the ICDP-USGS drill core provide insight into the timing and order of marine cratering processes during the Chesapeake Bay impact [12]:

i. The sequence of polymict lithic breccia, suevite and impact melt rock (1393-1550 m) must have been deposited prior to the arrival of, or concurrent with, the 950 m thick resurge and avalanche-delivered beds and blocks within 6-8 min after impact.

ii. This short period for transportation and deposition of impactites suggests that the majority of the impactites of the Eyreville core never left the transient crater and were emplaced by ground (re)surging. This is in accordance with observations of the impact breccia fabrics. However, the uppermost part of the suevite section contains a pronounced component of airborne material from the collapsing ejecta plume.

iii. Limited amounts of shock deformed debris and melt fragments also occur throughout the Exmore beds. A shard-enriched interval in the upper Exmore beds indicates that late ejecta plume deposits were incorporated and dispersed into the later resurge. Modeling indicates that the major resurge flow was concluded some 12 to 15 min after impact. This also marks a late stage of deposition from the ejecta plume.

References: [1] Poag, C.W. et al., (1994) *Geology*, 22:691-694. [2] Poag, C.W. (1996) *MAPS*, 31:218-226. [3] Powers and Bruce (1999) *USGS Professional Paper* 1612, 82 p. [4] Poag et al., (1999) *GSA Special Paper* 339: 149-164. [5] Poag et al., (2004) *The Chesapeake Bay crater—Geology and geophysics of a late Eocene submarine impact crater*, Springer, Heidelburg, 522 p. [6] Catchings, R.D. et al (2008) *JGR*, doi:10.1029/2007JB005421, in press. [7] Horton, J.W. et al (2005) *USGS Professional Paper 1688*. [8] Collins and Wünnemann (2005) *Geology*, 33(12): 925-928. [9] Gohn, G.S. et al. (submitted) *GSA Special Paper*. [10] Horton, J.W. et al. (submitted) *GSA Special Paper*. [11] Reimold, W.U. et al. (submitted) *GSA Special Paper*. [12] Kenkmann, T. et al. (submitted) *GSA Special Paper*.

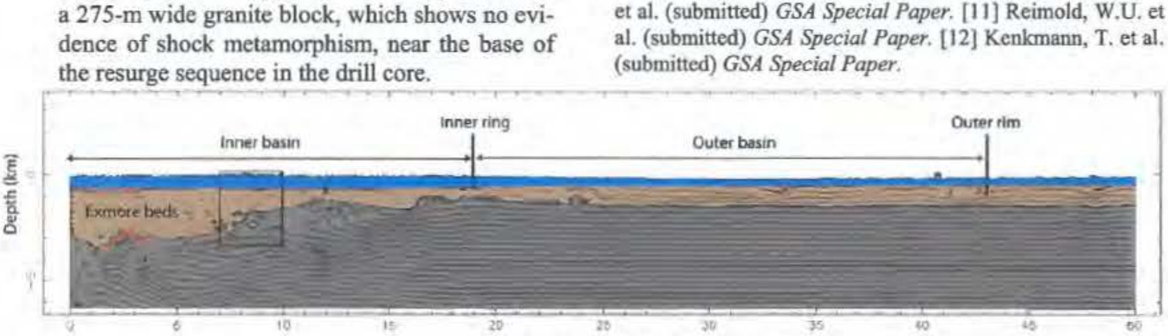

Figure 2 *Radial cross-section through final simulated Chesapeake Bay crater. Large-scale crater structure is consistent with seismic data interpretation. Rectangle corresponds to section of model in Fig. 1; the Eyerville drill core was located ~9 km from the crater center. Target deformation is illustrated by Lagrangian tracer lines. Tracers are only connected to form lines if their separation is less than twice their original separation; hence, regions of high deformation have few or no lines.*

THE BOSUMTWI IMPACT STRUCTURE, GHANA: COMPARISON BETWEEN WITHIN-CRATER AND OUT-OF-CRATER SUEVITES, WITH PARTICULAR FOCUS ON MELT PARTICLE COMPOSITIONS.

L. Coney[1], W.U. Reimold[2], R.L. Gibson[1], C. Koeberl[3], P. Czaja[2] and K. Born[2]. [1]Impact Cratering Research Group, School of Geosciences, University of the Witwatersrand, Private Bag 3, P.O. WITS, Johannesburg, 2050, South Africa (louise.coney@gmail.com), [2]Museum for Natural History (Mineralogy), Humboldt-University, Invalidenstrasse 43, D-10115 Berlin, Germany, [3]Department of Lithospheric Research, University of Vienna, Althanstrasse 14, A-1090 Vienna, Austria.

Introduction: The Bosumtwi impact structure, Ghana [1-2] is one of only a few craters at which suevites - both within and outside the crater - as well as distal ejecta (the Ivory Coast tektite strewn field [1, 3-4]) occur. The crater was excavated 1.07 Ma ago [3] in lower greenschist-facies rocks of the 2.1-2.2 Ga Birimian Supergroup [5-7]. It is filled almost entirely by Lake Bosumtwi, which is ~8 km in diameter and up to 80 m deep [2]. The impact crater was the subject of an interdisciplinary drilling program undertaken by the International Continental Scientific Drilling Progam (ICDP) in late 2004, which led to the recovery of two hard-rock cores from the central part of the crater structure, through the impact breccia fill and underlying crater basement [2]. The results of detailed lithostratigraphic, petrographic, geochemical and geophysical analysis of both cores were reported in a special issue of Meteoritics and Planetary Science (vol. 42, nos. 4/5) in 2007.

This study: The present study is focused on rocks from core LB-07A, which intersected the moat surrounding the central uplift [8-9]. In early 2007, a field visit to Ghana to collect samples of the suevites from the exterior to the north and south of the crater was undertaken. The suevite samples were examined using optical and scanning electron microscopy (SEM). Additionally, XRF was used to determine bulk major element compositions and ICP-MS was used to determine bulk trace element compositions of selected samples. Electron microprobe analysis was performed on melt particles to determine their major element compositions.

Petrographic differences: The suevites from within the crater are substantially different from the out-of-crater suevites. The within-crater suevites are derived from dominantly metasedimentary precursors: particularly metagreywacke and shale, with a previously unidentified small carbonate component [8]. Only a minor (<0.1 vol%) granitoid component is present. This is supported by studies on the suevites from core LB-08A [10], where no granitoid component was found, but carbonate is present as a discrete clastic phase in the suevites. In contrast, the out-of-crater suevites contain large volumes (up to 18 vol%) of granite clasts, and crystalline clasts as large as 25 cm have been recorded in the suevites from north of the crater (<1 cm diameter in the within-crater suevites). Hardly any clastic calcite was identified in the out-of-crater suevites.

Even more striking is the contrast in melt particle volumes. In the within-crater suevites, a maximum of 18 vol% melt was recorded in one sample only, whereas the average abundance is only 5.4 vol%. In contrast, in the out-of-crater suevites, a maximum of 60 vol% melt is noted in selected samples, and an average of 37 vol% (for comparison, 20 vol% was measured by [11]) was calculated for suevites from north of the crater and 18 vol% for suevites from outside the crater to the south. Melt particles are larger (up to 40 cm size) than those within the crater (< 1 cm). Additionally, relatively more quartz grains contain shock metamorphic features, and contain more PDF sets per host grain (6.7 rel% of all quartz grains contain ≥ 2 PDF sets), on average, than those from the within-crater suevites (0.9 rel% of all quartz grains contain ≥ 2 PDF sets). In out-of-crater suevites, diaplectic quartz glass is common, and ballen quartz is also noted; the former is rare in within-crater suevite and the latter was not noted in either core from within the crater at all [8, 10]. Thus, substantial differences exist between the out-of-crater and within-crater suevites.

In contrast to work performed by [12] on the Ries suevites, SEM has revealed that the groundmass of the suevites is not formed by a melt phase; instead it consists of the common clastic phases (metagreywacke, shale, quartz, feldspars) in addition to a limited (<10 vol%) component of partially altered melt particles. These locally seem to form aggregates of apparently welded-together particles.

Geochemical differences: The within-crater and out-of-crater suevites have major and trace element differences directly related to the differences in the lithological compositions of their precursors. The within-crater suevites are relatively depleted in Al_2O_3 and enriched in CaO in comparison to the out-of-crater suevites, as a direct consequence of the differing granitoid and calcite proportions.

Trace element abundances are very similar in the impactites from both cores – enrichment in Cr, Ni and As are noted owing to significant amounts of sulphides in the samples from the crater interior and in the out-of-crater suevites. Other trace element abundances are also directly comparable. In terms of rare earth elements (REE), some differences between the suevites from south and north of the crater are apparent. The suevites from south of the crater display small Ce anomalies (not observed in the suevites from within the crater and from north of the crater). This is explained by the larger proportion of organic (C-rich) material that is present within a distinct graphitic shale component, and which could not be dissolved during the ICP-MS sample preparation. This material will preferentially absorb all REE except Ce, thus leaving a higher proportion of Ce in the residue that is analyzed [13]. However, the normalized overall abundances [14] of the REEs for the suevites from south of the crater are very similar to those from the north and within the crater.

Melt particle compositions. A number of melt particles were analysed from different stratigraphic positions in core LB-07A and from the out-of-crater suevites. The melt particles of the within-crater suevites are variably roundish or angular in shape and belong to a strongly different size class of the out-of-crater suevites. The melt particles in the out-of-crater suevites contain flow structures, and are aerodynamically shaped, indicating that they were airborne. Their size and shape differences imply that they were emplaced from different parts of the ejecta cloud. The melt particles from the out-of-crater suevites are more altered than those from within the crater. Element mapping of melt particles from outside the crater revealed that the individual melt particles themselves are somewhat heterogeneous with regards to their major element composition. The melt particles either have compositions of individual minerals or are composed of mixtures of minerals. The within-crater melt particles are comparatively more enriched in FeO and MgO than those from north of the crater, but similar to the melt particles from the suevites from south of the crater. This could represent comparatively more shale being incorporated in the high Fe, Mg melt particles (supported petrographically by relative enrichment in shale clasts in these two sets of impact-produced breccias). The melt particles from both north and south of the crater are more enriched in Na_2O in comparison to those from within the crater – consistent with their higher granitoid clast content. Additionally, the Al_2O_3 contents are slightly higher in the out-of-crater melt particles. Most intriguing, however, is the observation that the CaO content in the melt particles of the out-of-crater suevites is higher than in the particles from within the crater: this may be a consequence of the previously unidentified carbonate component being preferentially incorporated into the melt phases of the out-of-crater suevites.

Interpretation: A model for the formation of the crater needs to take into account the differences in lithic clast and melt particle sizes and compositions; and the different relative shock states of the clasts in the suevites. The traditional model of Stöffler (1977) [15] distinguished between "ground-surged suevite" deposited as the lower part of the suevite inside the crater and "fallback/fallout suevite" shed by the rising and collapsing ejecta plume. More work is currently underway refining a model that will satisfy all the parameters of the Bosumtwi suevites, and results will be presented at the conference.

Acknowledgments: Drilling at Bosumtwi was supported by the ICDP, the U.S. NSF-Earth System History Program under grant no. ATM-0402010, Austrian FWF (project P17194-N10), the Austrian Academy of Sciences, and by the Canadian NSERC. Drilling operations were performed by DOSECC. This work is funded through a National Research Foundation (NRF) of South Africa grant (to W.U.R. and R.L.G.), a Scarce-Skills Bursary from the NRF (to L.C.), a Jim and Gladys Taylor Trust award (to L.C.), and an Austrian FWF grant (project P17194-N10 to C.K.).

References: [1] Koeberl C. and Reimold W.U. (2005) *Jahrbuch der Geologischen Bundesanstalt, 145,* 31-70. [2] Koeberl C. et al. (2007) *Meteoritics & Planet. Sci., 42,* 483-511. [3] Koeberl C. et al. (1997) *Geochim. Cosmochim. Acta, 61,* 1745-1772. [4] Glass B.P. et al. (1991) *Earth and Planet. Sci. Lett., 107,* 182-196. [5] Wright J.B. et al. (1985) *Geology and mineral resources of West Africa,* 38-45. [6] Leube A. et al. (1990) *Precambr. Res., 46,* 136-165. [7] Watkins A.P. et al. (1993) *J. Afr. Earth Sci., 17,* 457-478. [8] Coney L. et al. (2007a) *Meteoritics & Planet. Sci., 42,* 569-589. [9] Coney L. et al. (2007b) *Meteoritics & Planet. Sci., 42,* 667-688. [10] Ferrière L. et al. (2007a) *Meteoritics & Planet. Sci., 42,* 611-633. [11] Boamah D. and Koeberl C. (2006) *Meteoritics & Planet. Sci., 41,* 1761-1774. [12] Osinkski G.R. et al. (2004) *Meteoritics & Planet. Sci., 39,* 1655-1683. [13] Leleyter et al. (*in press*). *Int. J. Environ. Anal. Chem.* [14] Taylor S.R. and McLennan S.M. (1985). *The Continental Crust: Its Composition and Evolution, Blackwell Scientific,* 312 pp. [15] Stöffler D. (1977) *Geol. Bavarica, 75,* 443-458.

THE PERMIAN-TRIASSIC BOUNDARY, KAROO BASIN, SOUTH AFRICA: GEOCHEMICAL INSIGHT INTO THIS MASS EXTINCTION EVENT. L. Coney[1], W.U. Reimold[2], P.J. Hancox[1], D. Mader[3], C. Koeberl[3], I. McDonald[4], U. Struck[2], V. Vajda[5] and S.L. Kamo[6], [1]School of Geosciences, University of the Witwatersrand, Private Bag 3, P.O. WITS, Johannesburg, South Africa (louise.coney@gmail.com), [2]Museum for Natural History (Mineralogy), Humboldt-University, Invalidenstrasse 43, D-10115, Berlin, Germany, [3]Dept of Geological Sciences, University of Vienna, Althanstrasse 14, A-1090, Vienna, Austria; [4]School of Earth, Ocean and Planetary Sciences, Cardiff University, Park Place, Cardiff, CF10 3YE, U.K., [5]Dept of Geology, GeoBiosphere Science Centre, Lund University, Sölvegatan 12, SE-223 62, Lund, Sweden, [6]Jack Satterly Geochronology Laboratory, Dept of Geology, University of Toronto, 22 Russell Street, M5S 3B1, Toronto, Canada.

Introduction: The Permian-Triassic (P-Tr) mass extinction has been documented as the largest of the mass extinctions that took place in the Phanerozoic [1-2]. The cause of the extinction event has been the subject of much debate: theories proposed range from asteroid/comet impact [3-6] to volcanism [7-9], methane clathrate dissociation events [1; 10-11], oceanic anoxia [12-14], and combinations of these processes [15-19]. The Karoo Basin of South Africa contains a number of palaeontologically well-constrained terrestrial sections (particularly in the south and east of the Basin; [20]). Until recently, research on the P-Tr sections in the Karoo Basin was mostly of a palaeontological and sedimentological nature: the present study [21] has focused on fully characterising a number of sections geochemically and mineralogically.

Study Area: Two sections from the southern Karoo Basin (Commando Drift Dam and Wapadsberg, Eastern Cape Province, South Africa) have been evaluated geochemically and mineralogically. The Commando Drift Dam section has been constrained palaeomagnetically by a previous study [22]. The palaeomagnetic boundary (reversed to normal signatures) occurs approximately 5.3 m above the palaeontologically defined boundary [22]. Additionally, sedimentological and geochemical evaluation of a third section in the eastern Karoo Basin, Injusiti (Kwazulu-Natal Province, South Africa), has taken place. The sections comprise mostly mudstones, together with siltstones and sandstones. Carbonate nodular horizons have been noted in the southern Karoo sections. Each section is marked by an "event bed" at the stratigraphic position of the respective palaeontological boundary; this event bed comprises a centimeter to metre thick, laminated mudstone layer. All sections are characterized by a change in colour of the mudstones from green-grey to red-brown at the palaeontologically-defined boundary.

Geochemistry: No substantial changes related to the major and trace element geochemistry have been found in any section, and any changes relate either to the lithological changes (i.e., silica-rich rocks vs. carbonate nodular horizons) or to weathering effects. Iron content increases concomitantly with the colour change from green-grey to red-brown across the palaeontologically-defined boundary, and at the Commando Drift Dam section, a second maximum is attained at the palaeomagnetically defined boundary. The increase has been caused by post-deposition oxidation of Fe^{2+} to Fe^{3+}, potentially caused by climatic warming, aridification or the influx of a post-depositional fluid; the last possibility may be rejected as there is the presence of red-beds at the boundary worldwide, which implies at least a regional, rather than local cause.

The Injusiti section shows similar geochemical characteristics to the southern Karoo sections, although there is a lack of carbonate nodular horizons. Additionally, there is relative enrichment in Na_2O and depletion in K_2O contents (by a few wt%) across the palaeontologically-defined boundary in this section. This is not observed in the southern Karoo sections, and is thought to represent local lithological variation.

Trace element variation largely reflects associated major element changes. Rare earth element concentrations do not change across the respective palaeontologically-defined boundaries in the two sections.

Plantinum Group Element (PGE) results. The Commando Drift Dam section was evaluated for variation in PGE content in order to ascertain whether a possible enrichment due to meteorite impact had taken place: all analysed samples from above, at and below the palaeontologically constrained boundary had similar PGE contents, reflective of the background PGE contents found in clay-rich sediments. This is in agreement with other geochemical studies of P-Tr sections [23]. Additionally, no evidence for impact-generated microdeformation features were found, which agreed with the negative – with respect to impact - chemical results.

Carbon isotope results. The Commando Drift Dam section was measured for bulk and carbon isotope results. Samples from the Injusiti section were measured for their organic carbon signature. The bulk carbon isotope values revealed negative excursions (relative to background values) at both the palaeontological and palaeomagnetic boundaries. Both sections have comparable results for their organic carbon content, which is also similar to those reported from previous studies of P-Tr sections in the Karoo Basin [10, 24]. The cause of the carbon isotope excursions is, as yet, unclear, but it can be mooted that the negative excrusions were caused by a variety of contributions, including the Siberian Flood Basalts in addition to methane from other sources (e.g. coal beds [19] or the collapse of primary ocean productivity [25]). The contribution of massive methane clathrate dissociation is rejected, as this would have caused larger than observed carbon isotope excurision.

Palynology: Low diversity flora (composed of bryophytes, lycophytes and gymnosperms) have been reported from the Commando Drift Dam section. These forms are interpreted as traces of the surviving plants enduring the major extinction pulse. At. and above the level of the palaeomagnetic boundary only fungal spores are present, which is similar to patterns observed for the Cretaceous-Palaeogene boundary [26-27].

Timing of the mass extinction in the Karoo Basin: U-Pb age dating was performed on zircon crystals extracted from the event bed. The timing of the vertebrate extinctions in the Karoo Basin has so far not been determined, but one of the crystals analysed here yielded an age of 252.5 Ma. This age is in good agreement with the accepted age of the boundary [28-30], and provides a maximum constraint on the age of the event bed.

Conclusions: The combined geochemical and mineralogical study of rocks covering mass extinction events can provide valuable information elucidating (or rather refining) the causes of such a mass extinction. This study has shown that extinction caused by meteorite impact is seemingly not viable for the P-Tr mass extinction and that rather a complicated chain reaction of greenhouse gas emission leading to the mass extinction of fauna and flora took place.

Acknowledgements: This work was funded by: the Palaeo-Anthropology Scientific Trust, Johannesburg; the National Research Foundation of South Africa; the Geological Society of South Africa; the Barringer Family Fund for Meteorite Impact Research; the Swedish Research Council. Analytical work in Vienna was supported by the Austrian FWF, project P17194-N10 (to CK). Bernd Bodiselitsch (formerly University of Vienna, Austria) is thanked for assistance with some of the carbon isotope analysis.

References: [1] Erwin D.H. (1994) *Nature, 367,* 231-236. [2] Erwin D.H. et al. (2002) *GSA Spec. Paper, 356,* 363-383. [3] Retllack G.J. et al. (1998) *Geology, 26,* 979-982. [4] Kaiho K. et al. (2001) *Geology, 29,* 815-818. [5] Becker L. et al. (2001) *Science, 291,* 1530-1533. [6] Becker L. et al. (2004) *Science, 304,* 1469-1476. [7] Renne P.R. et al. (1995) *Science, 269,* 1413-1416. [8] Reichow M.K. et al. (2002) *Science, 296,* 1846-1849. [9] Kamo S.L. et al. (2006) *Geochim. Cosmochim. Acta, 70, Suppl. 1,* A303. [10] De Wit M.J. et al. (2002) *J. Geol., 110,* 227-240. [11] Retallack G.J. et al. (2003) *GSA Bull., 115,* 1133-1152. [12] Wignall P.B. and Twitchett R.J. (1996) *Science, 272,* 1155-1158. [13] Isozaki Y. (1997) *Science, 276,* 235-238. [14] Weidlich O. et al. (2003) *Geology, 31,* 961-964. [15] Erwin D.H. (1996) *Evolutionary Paleobiology, Univ. Chicago Press,* 398-418. [16] Ward P.D. et al. (2000) *Science, 289,* 1740-1743. [17] Benton M.J. and Twitchett R.J. (2003) *Trends Ecol. Evol., 18,* 358-365. [18] Maruoka T. et al. (2003) *Meteoritics & Planet. Sci., 38,* 1255-1262. [19] Retallack G.J. et al. (2006) *GSA Bull., 118,* 1398-1411. [20] Smith R.M.H. and Botha J. (2005) *C. R. Paleovol., 4,* 555-568. [21] Coney L. et al. (2007). *Palaeoworld, 16,* 67-104. [22] De Kock M.O. and Kirschvink J.L. (2004) *Gondwana Res., 7,* 175-183. [23] Koeberl C. et al. (2004) *Geology, 32,* 1053-1056. [24] MacLeod K.G. et al. (2000) *Geology, 28,* 227-230. [25] Rampino M.R. and Caldeira K. (2005) *Terra Nova, 17,* 554-559. [26] Vajda V. et al. (2001) *Science, 294,* 1700-1702. [27] Vadja V. and McLoughlin S. (2004) *Science, 303,* 1489. [28] Gradstein F.M. et al. (2004) *A Geologic Time Scale 2004. Cambridge University Press, Cambridge,* 500 pp. [29] Mundil R. et al. (2004) *Science, 305,* 1760-1763. [30] Bowring S.A. et al. (1998) *Science, 280,* 1039-1045.

IMPACT RELATED PSEUDOTACHYLITIC BRECCIAS IN THE SCHURWEDRAAI AND BAVIAAN-KRANTZ ALKALI GRANITE COMPLEX IN THE COLLAR OF THE VREDEFORT DOME.

Claudia Crasselt and Wolf Uwe Reimold, Museum of Natural History (Mineralogy), Humboldt University, Invalidenstrasse 43, 10115 Berlin, Germany; claudia.crasselt@museum.HU-Berlin.de.

Introduction: The formation of impact related pseudotachylitic breccias and their occurrence in large impact structures is still a matter of debate. As part of a working group [1, 2] that investigates the formation of impact related pseudotachylitic breccia bodies in the Archean Gneiss of the central uplift of the Vredefort impact structure (South Africa), the aim of this project is to contribute to the understanding of the genesis of such pseudotachylitic bodies in a different host lithology, namely the Schurwedraai and Baviaan-Krantz Alkali Granite complex in the northwestern collar of the Vredefort Dome [Fig.1] [3]. This alkali granite complex is one of five ultramafic-mafic and felsic intrusions in the Late Archean to Paleoproterozoic subvertical to overturned supracrustal collar rocks of the Vredefort Dome. The pluton intruded into the lower Witwatersrand Supergroup at ~ 2.05 Ga ago [4]. Pre-impact lithological heterogeneities are absent in the complex and pre-impact textural and structural features are scarce in contrast to the Archean granitic gneiss of the core and the metasedimentary collar strata. For the pre-impact metamorphism a temperature of 300-400℃ is estimated [5].

Results: *(a) Field observations:* The alkali granite is mainly whitish to reddish, homogeneous, and massive, with hypideomorphic minerals, and mostly of medium to fine grain size. It consists of quartz, K-feldspar, albite, potassic amphibole, potassic pyroxene, and minor biotite. Veins of aplitic and pegmatitic nepheline syenite, quartz, K-feldsdspar with hornblende and aegerine are common. No distinct foliation was found. At some locations shatter cones are present. Pseudotachylitic breccia occurrence are widespread [Fig.2]. These breccias occur typically as single veins or dykes from a few millimeters to about 1.5 m wide, or as networks up to 6 m wide; maximum extensions are delimited by the patchy outcrop conditions to about 20 m. Occasionally, they can also form irregular pods. Most of the pseudotachylitic breccia veins seem to be oriented perpendicular to the genarally subhorizontal outcrop surfaces. However, this is certainly a cutting effect, because on many vein margins in outcrop it is observed that these veins mostly dip at angles of 65 to 35 degree. Most contacts to host rock are sharp. Clasts in pseudotachylitic veins > 2 cm in wide are common. They are mainly composed of alkali granite; only at three localities "exotic" clasts of quartz or quartzite were observed. It may be possible that they represent relicts of older engulfed quartz veins or are xenoliths from the surrounding Witwatersrand quartzites. Most clasts are rounded. Some longitudinal axes of elongated clasts are oriented in strike direction of the vein, and in some rare cases clasts are located at just one side of the vein. At three localities en echelon patterns of pseudotachylitic breccia veins are observed. Flow banding in veins is common [Fig.3]. At some contacts of veins to host rock quench zones are apparent. The pseudotachylitic breccia veins crosscut the pegmatitic and aplitic veins and sometimes even displace them for distances up to 10 m.

(b) Macroscopic structural analysis: The apparent strike orientations of over 500 pseudotachylitic breccia veins were measured. The data scatter but imply a preferred NE-SW to ENE-WSW trend. Locally strike orientations of larger pseudotachylitic networks could be estimated; they show prominent directional trends at NW-SE and ENE-WSW. This indicates that larger pseudotachylitic breccia zones seemingly follow a concentric and radial pattern with respect to the center of the Vredefort Dome. In some localities dilation was observed with a mean N-S dilation vector orienttation. The structural analysis also indicates that veins < 1 m in width strike mainly ENE-WSW and NW-SE direction, but veins > 1 m in width mainly in NW-SE direction. Individual veins in networks also mainly strike ENE-WSW and NW-SE. Fractures cutting pseudotachylitic breccias mostly strike N-S and ESE-WNW. As yet, it is not clear whether their origin can be related to the modification phase of the impact event, or whether they are of significantly later post-impact age.

(c) Petrography: First microscopic analysis shows that the matrix of the pseudotachylitic veins is devitrified and composed of quartz, feldspar and amphibole. More detailed SEM and electron mircoprobe studies are required to determine the feldspar and amphibole compositions. Clasts in pseudotachylitic breccia are made up of quartz, K-feldspar and plagioclase, with feldspar grains more extensively melted and showing stronger recrystallization than quartz grains. First micro-

scopic analysis also indicates that where the contact between host rock and a pseudotachylitic breccia vein is not sharp, the host rock is thermally affected and shows heterogeneous recrystallization near the contact. The rounding of clasts seems to be related to thermal abrasion. The matrices of marginal quench zones appear compositionally similar to the matrices of vein interiors. Clasts within these margins are relatively more strongly recrystallized. Some alkali granite grains and some quartz and feldspar clasts show shock effects. Strongly fractured and mechanically twinned amphibole is noted. In a few quartz and feldspar grains PDFs, mostly one set but occasionally two sets, are observed [Fig.4]. Most PDFs are decorated; planar fluid inclusion trails in quartz and feldspar are commonly observed. These observations indicate a regional shock pressure of about 10 GPa and local attainment of shock pressures of 15-20 GPa [6], calibrated for cold targets, whereas the pre-impact temperature of the alkali granite under investigation were 300-400 °C.

Outlook: Further petrographic analysis is in progress, and so is chemical analysis of pseudotachylitic breccia vein and host rock pairs. The macroscopic structural analysis will be complemented with microstructural studies. These results will be presented at the conference.

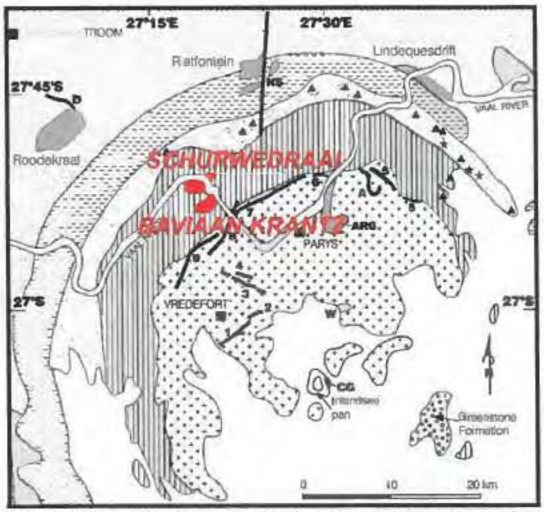

Fig.1: Simplified geological map of the Vredefort Dome with location of the Schurwedraai and Baviaan-Krantz Alkali Granite complex in the northwestern part of the collar (modified after[7]).

Fig.2: Pseudotachylitic breccia network with rounded clasts of alkali granite. Pen for scale, ~ 15 cm long.

Fig.3: Flow banding in ~ 15 cm wide pseudotachylitic breccia vein.

Fig.4: Two sets of PDFs in feldspar grain. Cross polarized light, width of view field 0.52 mm.

References: [1] Mohr-Westheide et al., this vol. [2] Lieger et al., this vol. [3] Gibson & Reimold (2008), Gb LMI IV Conf. [4] Graham et al. (2005), JAES 43, 537-548. [5] Gibson et al. (1995), Geol.J. 30, 319-331. [6] Stöffler & Grieve (2007), R.A.F. [7] Reimold et al. (2006), GC 66, 1-35.

BASALTIC IMPACT STRUCTURES OF THE PARANÁ BASIN, BRAZIL. A. P. Crósta[1], [1]Institute of Geosciences, University of Campinas, Campinas, SP, Brazil (alvaro@ge.unicamp.br).

Introduction: The Paraná Basin in southern Brazil contains one of the largest continental flood basalt provinces of the world. The volcanic rocks related to this event correspond to the Serra Geral Formation, with the main activity dated 133-132 Ma. This stratigraphic unit exhibits a large volume of volcanic rocks, comprising mostly basalts of tholeiitic composition, with some sequences of acidic compostion (rhyodacites) in the southern portion of the basin.

The impact record of the Paraná Basin includes the Araguainha Dome (d=40km), aged 145 Ma, plus three other impact structures located in the southern portion of the Basin. These three structures are Vargeão Dome (d=12km), Vista Alegre (d=9.5km) and Cerro do Jarau (d=13km), all of them formed on basalts of the Serra Geral Fm. (Figure 1).

Basaltic craters are common in terrestrial planets such as Mars and Venus, as well as in the Moon and a number of smaller planetary bodies. On Earth, basalts are not extensively found on continents and, therefore, the cratering record over this rock type is quite limited. Until recently, the only known impact structure on continental flood basalts was Lonar crater, in the Deccan Traps in India [1]. However, Lonar is a small (d=1.8km) and simple crater and the access to its interior and to the rocks exhibiting impact features is limited, due to the fact that is filled with lake water.

This papers describes the basaltic impact structures of the Paraná Basin and their importance as the only medium-sized complex structures formed over this type of volcanic rocks known on Earth. In addition, it stresses their potential role as analogues for impact cratering studies on basaltic terrains, an important issue for modeling crater formation on terrestrial planets and moons.

Vargeão Dome: This complex structure has its center in 26°49'S/52°10'W, with a diameter of 12 km and a 3 km wide central uplift. It has is a multi-ring internal structure due to annular faulting (Figure 2). A number of blocks of Jurassic-Triassic sandstones of the Botucatu/Pirambóia formations, bounded by faulting, are exposed at the central uplift of the structure. Deformation features recognized in the rocks of the interior of the structure include monomict and polymict breccias of basalt/diabase and sandstones, shatter cones in basalt and sandstone, pseudo-tachyllite veins, and shock lamemallae (PDFs) in quartz and feldspar in sandstone [2] [3]. Most of the breccias in Vargeão appear to be para-authoctonous, exposed by erosion.

Vista Alegre: The structure is located at 25°57´S/52°42´W, with a diameter of 9.5km, only 100 km away from Vargeão Dome (Figure 3). Vista Alegre was only recently reported as an impact structure [4], and depicts an almost perfectly round morphology and steep internal borders. Impact breccias have limited exposure within this structure, due to extensive soil overburden. However, the few existing outcrops reveal the existence of layers of allochtonous polymictic breccia underneath the top soils, bearing clasts of basalt, diabase and sandstone, as well as fragments of shatter cones. Microscopic analysis of the breccias shows the occurrence of shock lamellae (PDFs) in quartz and the presence of melted material. The central uplift has no topographic expression and its existence is inferred from the occurrences of sandstones of the Botucatu/Pirambóia formations in the central portion, uplifted several hundred meters from their original stratigraphic position.

Cerro Jarau: The structure has its center in 30°12´S/56°32´W and a diameter of approximately 13km (Figure 4). It has been considered for some time as a possible impact impact site [2][5]. Only recently evidence of its impact origin became available [6]. It is a complex structure, with a 5km central uplift formed on deformed sandstones of the Botucatu Fm, which were uplifted from their original position several hundred meters below their present level. Evidences of the impact origin comprise the formation of breccias in basalts and sandstones, and shock lamellae in quartz and feldspar (PFs and PDFs). The borders of the structure have apparently been entirely removed by erosion.

Concluding remarks: The three basaltic impact structures of the Paraná Basin have been formed on the same stratigraphic unit, the Cretaceous Serra Geral Fm, and are relatively well exposed on the present continental surface. Although there are no isotopic ages available, the fact that they show different levels of erosion and degrees of preservation suggests their formation in different times, and are not related to a multiple-impact event, as suggested previously [2]. The exposure of impact-related rocks and deformation features at various scales in these three structures, combined with ease of access to their interiors, represent a unique opportunity for analogue studies of cratering processes in terrestrial planets.

References:

[1] Osae, S. et al. (2005) *MAPS, 40,* 1473–1492. [2] Hachiro J. & Coutinho J.M.V. (1993) *3° Simp. Geol.*

Sudeste, Brazilian Geol. Soc., 276-281. [3] Crósta, A.P. et al. (2005), *Geol. & Palaeontol. Sites of Brazil*, http://www.unb.br/ig/sigep/sitio114/sitio114english.pdf [4] Crósta, A.P. et al. (2004) *MAPS, 39-Suppl, p. A28.* [5] Romano, R. & Crósta, A.P. (2004) *LPS XXXV*, Abstract #1546. [6] Crósta et al. (2008) *MAPS (submitted).*

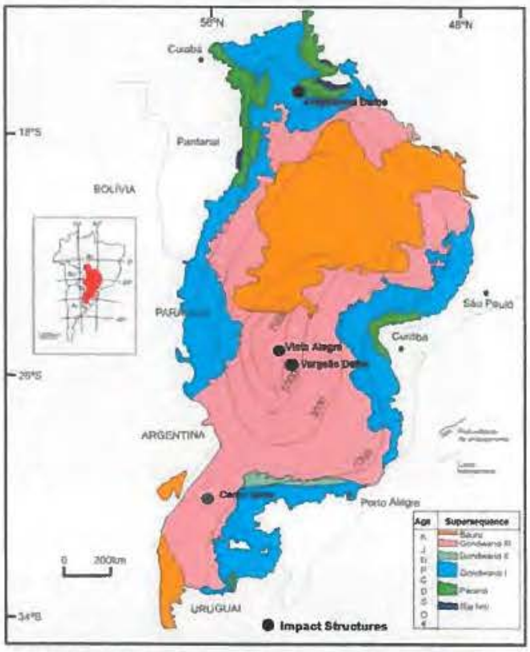

Figure 1. Impact structures of the Paraná Basin, Brazil.

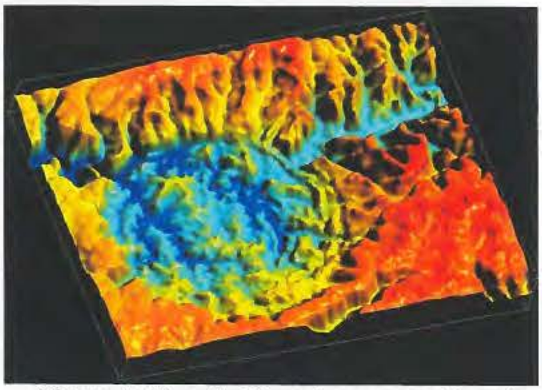

Figure 2. Vargeão Dome in a perspective view using Shuttle Radar Topographic Mission (SRTM) digital elevation model.

Figure 3. Vista Alegre in a perspective view using Landasat ETM+ image draped over Shuttle Radar Topographic Mission (SRTM) digital elevation model.

Figure 4. Cerro Jarau in a perspective view using Landasat ETM+ image draped over Shuttle Radar Topographic Mission (SRTM) digital elevation model

MODELS OF AN EJECTA CURTAIN

Detlef de Niem[1], [1]DLR Institute of Planetary Research, Rutherford Str.2, D-12489 Berlin, Germany (detlef.deniem@dlr.de)

Introduction

Much effort in experiments and theory has gone into the study of the motion of sometimes vaporized, molten and solid matter during the formation of hypervelocity impact craters [1]. Except for large impact basins, the majority of ejecta is in the form of solid debris. The most obvious feature outside the growing cavity is the formation of an ejecta curtain [1]. Whereas inside the forming crater the flow has been studied using so-called hydrocodes, [2, 3], these techniques are not well suited to describe the phenomenon of dusty ejecta flow nor is the computational region large enough in space and time, so more simple methods have to be used [7]. The limit of applicability of the analytical solution is eventually reached when the drag between solid debris and gas leads to two-fluid interactions which necessarily have to be treated numerically [8].

Model

Following Cintala et al. [5], the solution of Newton's equation for the trajectory in cylindrical coordinates is

$$r = r_0 + v_{ej} t \cos\beta, \qquad (1)$$

$$z = v_{ej} t \sin\beta - \frac{g}{2} t^2, \qquad (2)$$

where the surface is at $z = 0$, the launch angle is β, the ejection velocity $v_{ej} = v_{ej}(r_0)$ and g the surface gravity [5]. Eliminating time, the equation of the trajectory is

$$\frac{z}{L}\cos^2\beta - \frac{r - r_0}{L}\sin\beta\cos\beta + \\ + \frac{gL}{2v_{ej}^2}\left(\frac{r - r_0}{L}\right)^2 = 0, \qquad (3)$$

where L can be identified with final radius of the transient cavity e.g. Cintala et al. [5] did not evaluate the density inside the ejecta curtain, to derive it write the last equation as $\Omega(r, z, r_0) = 0$ and regard the complete differential

$$\frac{\cos\beta}{Lv_{ej}}(v_r dz - v_z dr) + \left(\frac{\partial\Omega}{\partial r_0}\right)_{r,z} dr_0 = 0. \qquad (4)$$

Now multiply equ.(4) by $r\ Lv_{ej}/\cos\beta$ and apply the exterior derivative d a second time, so

$$d(rv_r dz - rv_z dr) + d\left[\frac{rLv_{ej}}{\cos\beta}\left(\frac{\partial\Omega}{\partial r_0}\right) dr_0\right] = 0. \qquad (5)$$

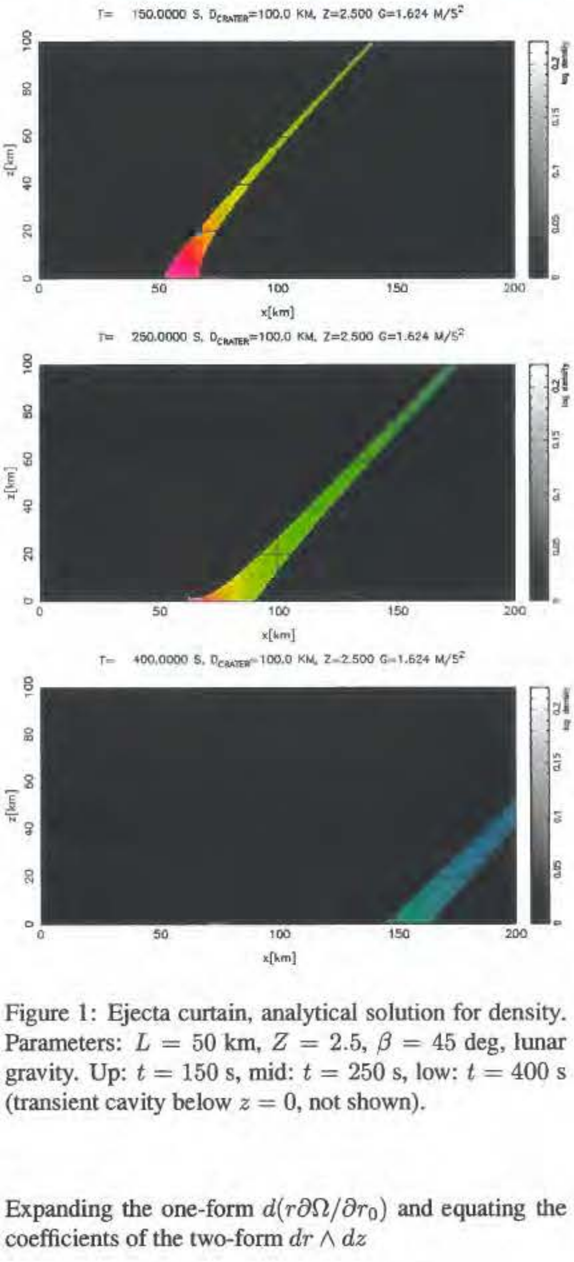

Figure 1: Ejecta curtain, analytical solution for density. Parameters: $L = 50$ km, $Z = 2.5$, $\beta = 45$ deg, lunar gravity. Up: $t = 150$ s, mid: $t = 250$ s, low: $t = 400$ s (transient cavity below $z = 0$, not shown).

Expanding the one-form $d(r\partial\Omega/\partial r_0)$ and equating the coefficients of the two-form $dr \wedge dz$

$$\frac{1}{r}\frac{\partial(rv_r)}{\partial r} + \frac{\partial v_z}{\partial z} = \left(r\frac{\partial\Omega}{\partial r_0}\right)_{r,z}^{-1} \times \\ \times\left\{v_r\frac{\partial}{\partial r}\left(r\frac{\partial\Omega}{\partial r_0}\right)_{r,z} + v_z\frac{\partial}{\partial z}\left(r\frac{\partial\Omega}{\partial r_0}\right)_{r,z}\right\}, \qquad (6)$$

where it has been used that β and v_{ej} are functions of r_0 only. This shows that the function $J := (r\partial\Omega/\partial r_0)^{-1}$ satisfies the continuity equation in the stationary velocity field (v_r, v_z). The solution is not unique: it may be multiplied by an arbitrary function of ground-zero distance[1] $f(r_0)$. To draw the velocity field and density at an arbitrary point in space one has to know the particular r_0 of the trajectory passing through that point. This can be found easily from the trajectory equation (3), with the help of Newton's method, using the partial derivative $(\partial\Omega/\partial r_0)$. The solution obtained so far is stationary, but the domain of existence is bounded by a leading and trailing front or isochrone. The time of flight $t_{of}(r_0)$ is known at any point in space, so the condition is that at 'observation time' t the leading isochrone passed but the not the trailing isochrone. The latter is described by the same solution of Newton's equation of motion (1,2), with the replacement $t \to t - t_0$ where the t_0 is the local excavation time depending on r_0. The time it takes to flow along a streamline until it emerges at the free surface at distance r_0 from ground zero is $t_0 = r_0/(Z+1)/(v_{ej}\cos\beta)$ in the Z model [6], see also equ.(5.5.12) of [1]. Particles on the leading isochrone start at some $t_s(r_0)$ when the shock wave has passed, this may be not be neglected for very large craters where one has to replace $t \to t - t_s$ in eqns.(1,2). As illustration the ejecta curtain developement is shown in fig.1 for a lunar crater of 100 km diameter (of the transient cavity).

I will also show how to include drag in the presence of a planetary atmosphere. Then a characteristic parameter is the ratio of drag to gravitational force

$$\Pi_D = \frac{C_D A \rho_g v_{ej}^2}{2mg} = \frac{3 C_D L \rho_g}{4 r_s \rho_s (Z+1)^2 C^2 \cos^2\beta_0} \left(\frac{L}{r_0}\right)^{2Z}, \tag{7}$$

where ρ_g is the atmospheric density, C_D the drag coefficient, r_s and ρ_s denote the density and radius of solid ejecta, assuming particles as spherical and a Stokes drag regime. The second identity resulting form scaling laws [4], or in the Z model [7] shows that for gravity scaling g drops out and the flow becomes self-similar. Densities for different particle sizes r_s have to be overlain. A procedure analogous to that above can be applied to obtain the evolution of the density, then Ω in equ.(6) is given by $\Omega = v_z(\partial r/\partial r_0)_u - v_r(\partial z/\partial r_0)_u$ where u is a function of β, and $v(u)$ can be found explicitely.

Consequences

A semi-analytical model of the density in an evolving ejecta curtain has been developed. Some form of drag force can be modeled, although only in a homogeneous atmosphere. An analytical solution for the ejecta curtain easily allows to derive other interesting quantities like the thickness of ejecta layers and allows comparison with a fully numerical treatment. The case of a spatially varying gravity field $g \propto r^{-2}$ is solvable as well.

There are caveats of such a 'test-particle' picture: it may underestimate ballistic range. If two-fluid or 'swarm' phenomena develop, the hydrodynamic state of gas near to the dust concentrations is modified, creating a boundary layer, possibly allowing solid ejecta to penetrate towards larger distances, despite of a dense atmosphere. Frictional energy and heat transfer will occur, and dusty ejecta act as a heat reservoir. This can only be studied with numerical simulations using a similar approach as in [8]; the analytical solution obtained here is helpful as a test case. In a two-fluid picture there are implications for the depth of penetration of meteorite debris into the atmosphere. Similiar effects have been hypothesized for the unusual Peruvian Carancas meteorite structure recently [9].

References

[1] H. J. Melosh 1989. *Impact cratering: A geologic process*, (Oxford University Press, New York, Clarendon Press, Oxford)

[2] Pierazzo, E., Vickery, A. M., Melosh, H. J., 1997. *Icarus* **127**, 408-423.

[3] Pierazzo, E., Kring, D. A., Melosh, H. J., 1998. *J. Geophys. Res.* **103**, 28607-28626.

[4] R. M. Schmidt, K. A. Holsapple 1982. *Geol. Soc. Am. Spec. Pap.* **190**, 93-162.

[5] M. J. Cintala, L. Berthoud, and F. Hörz 1999. *Meteoritics & Planetary Science* **34**, 605-623.

[6] D. E. Maxwell 1973. In *Impact and explosion cratering* (D. J. Roddy, R. O. Pepin, and R. B. Merril, eds.), Pergamon, N. Y., 1003-1008.

[7] J. E. Richardson, H. J. Melosh, C. M. Lisse, and B. Carcich 2007. *Icarus* **190**, 357-390.

[8] M. Pelanti, R. LeVeque 2006. *SIAM J. Sci. Comput.* **28** **No 4**, 1335-1360.

[9] P. H. Schultz, R. S. Harris, G. Tancredi, and J. Ishitsuka 2008. *Lunar Planet. Sci. Conf.* **XXXIX**, abstract, 2409.pdf

---

[1] such a function is an integral of motion

CONDENSATE COMPOSITION FROM ASTEROID IMPACTS

Detlef de Niem[1], Ekkehart Kührt[1], Uwe Motschmann[1,2], [1]DLR Institute of Planetary Research, Rutherford Str.2, D-12489 Berlin, Germany (detlef.deniem@dlr.de) and [2]Institute of Theoretical Physics, Technical University of Braunschweig, Mendelssohnstrasse 3, D-38106 Braunschweig, Germany

Introduction: Impacts of meteorites, asteroids and comets on the earth are sometimes capable of causing vaporization of most of the impactor and a comparable or larger volume of target rocks [10]; the average impact velocity of near earth objects (NEOs) is ~ 20 km s^{-1} [14]. The Cretateous-Paleogene (K-P) boundary thought to be due to impact of an extraterrestrial body, is globally characterised by a layer containing spinel-bearing spherules [5], associated with the maximum iridium anomaly [13]. The chondritic meteorites Gujba and Hammadah al Hamra (HH237), belonging to the group of Bencubbin-like meteorites [3, 11], have been hypothesized to result from collisions of proto-planets in the early solar system [4]. Formation ages are ~ 5 Myr younger than those of calcium-aluminium-rich inclusions (CAI's) [4].

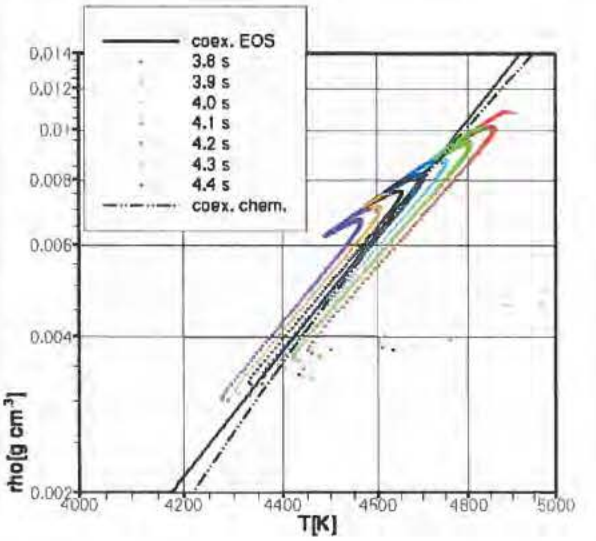

Figure 1: Example hydrodynamic run for K-P-sized impact. Impactor modelled as chondritic object, see text, bulk properties of dunite, 50 % porosity, at 22 kms^{-1}. Symbols: (T, ρ) values in computational cells at different times after impact, from a spherically symmetric simulation [9]. Curves: coexistence curve (Maxwell construction from EoS, thick line, and from chemical equilibrium solver, dash-dotted line). Region above the coexistence curve corresponds to saturated vapour.

Comparing primary condensate and K-P spinels: Previous calculations of chemical equilibrium in impact-generated vapour [2] related to the K-P boundary have been confined to $T < 2400$ K and used a (P, T) path extracted from hydrocode calculations. Our new equation of state [9] is a semi-analytical development, incorporationg chemical equilibrium in the gas phase and using an interpolation formula for the free energy [7]. Gaseous species (183 formed by 26 elements) are from a model of condensation in the solar nebula [12]. Atmospheric air is a distinct material in hydrodynamics. This disregards the role of interfacial instabilities for mixing with target material. For a K-P-sized event, the hydrodynamic expansion of an impact-generated plume is simulated in simplified spherical geometry, the hydrodynamic algorithm is a variant of [8]. The thermodynamic history of computational cells is shown in Fig.1. As a post-processing step we perform chemical equilibrium calculations with condensed phases using an implementation of SOLGASMIX [15] currently allowing three mixture phases. Endmembers of liquid solution model(s) are a condensible subset of 26 elements and liquid CaO, FeO, FeS, MgO, TiN, VN, ZrN, NiS, TiO, VO, NiS_2, SiO_2, TiO_2, ZrO_2, Al_2O_3, Cr_2O_3, $MgSiO_3$, $MgTiO_3$, Ni_3S_2, Ti_2O_3, V_2O_3, K_2SiO_3, Na_2SiO_3, $MgAl_2O_4$, Mg_2SiO_4, V_2O_5, $MgTi_2O_5$, Ti_3O_5, Ti_4O_7, $MgFe_2O_4$ and $FeAl_2O_4$. Initial abundances of the vapor plume are from [6]. There is some evidence for a carbonaceous chondritic Chicxulub impactor [1], so the oxygen abundance (atomic) is lowered by a factor of two, relative to CI and hydrogen is reduced to simulate a dry asteroid. Data of electron-microprobe analyses of spinels from K-P spherules [5] are displayed together with that of the high-temperature condensate from chemical equilibrium calculations corresponding to a typical release path, see Fig.2. The overall composition of primary high-temperature condensate is roughly compatible with the data from the Pacific K-P spinels for such elements as Fe, Ni, Fe, Al, Cr, Ti. The Ca and Si will form separate minerals or be incorporated into silicate later.

Young chondrules in Gujba and Bencubbin: In separate model runs of the chemical equilibrium program, the question if 'young chondrules' can be formed in a collision of large planetesimals is investigated. The composition of the (so-called) dark matrix material and that of metal globules in Gujba and Bencubbin ([11], their table 3) is compared with that of model condensates, see Fig.3.

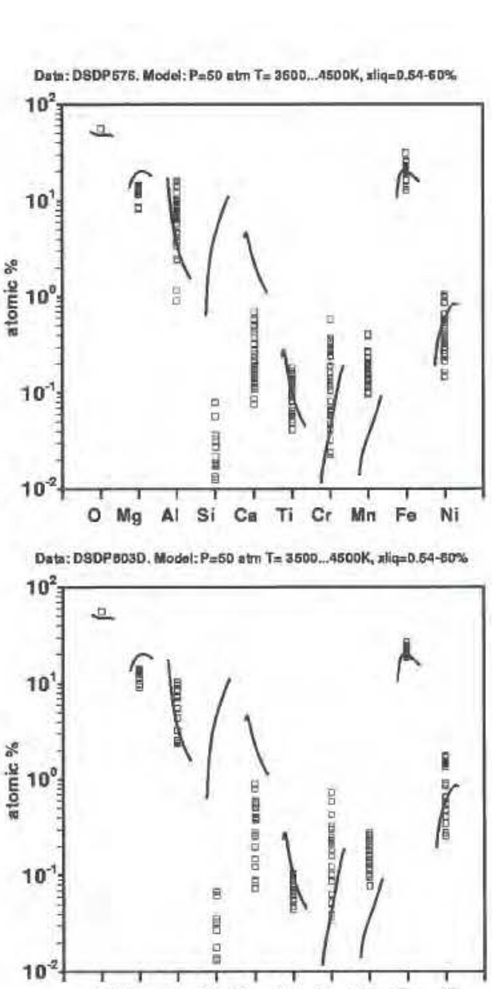

Figure 2: Abundance of elements in K-P spinels analysed by [5] as compared to condensation model results. Open black squares: data for Pacific K-P spinels DSDP576 (upper part), DSDP803D (lower part). Curves: To indicate compositional change with liquid fraction, model values displaced into the x-direction in proportion to liquid fraction.

Uncertainties arise due to the treatment of solution properties of volatiles like S above their liquid-vapour critical temperature. At about 3000 K, depending on pressure, an immiscible metallic phase appears, the overall atomic of which well compares to that of metallic globules.

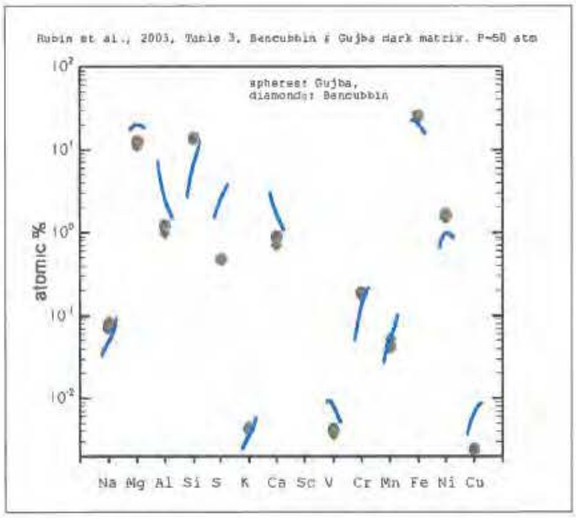

Figure 3: Abundance of elements in Gubjba and Bencubbin, dark matrix material, from Rubin et al. [11], their table 3, compared to condensation model. Blue curve: model condensation path.

References

[1] Bottke, W. F., Vokrouhlický, D., Nesvorny, D., 2007. *Nature* **449**, 48-53.

[2] Ebel, D. S., Grossman, L., 2005. *Geology* **33**, 293-296.

[3] Greshake, A., Krot, A. N., Meibom, A., Weisberg, M. K., Zolensky, M. E., Keil, K., 2002. *Meteor. Planet. Sci.* **37**, 281-293.

[4] Krot, A. N., Amelin. Y., Cassen, P., Meibom, A., 2005. *Nature* **436**, 989-922.

[5] Kyte, F. T., Bostwick, J. A., 1995. *Earth and Planet. Sci. Lett.* **132**, 113-127.

[6] Lodders, K., 2003. *Astrophys. J.* **591**, 1220-1247.

[7] Melosh, H. J., 2007. *Meteorit. Planet. Sci* **42 (12)**, 2079-2098.

[8] de Niem, D., Kührt, E., Motschmann, U., 2007. *Computer Phys. Comm.* **176**,170-190.

[9] de Niem, D., Kührt, E., Motschmann, U., 2007. *Icarus* **(in press)**

[10] Pierazzo, E., Vickery, A. M., Melosh, H. J., 1997. *Icarus* **127**, 408-423.

[11] Rubin, A. E., Kallemeyn, G. W., Wasson, J. T., Clayton, R. N., Mayeda, T. K., Grady, M., Verchovsky, A. B., Eugster, O., Lorenzetti, S., 2003. *Geochimica et Cosmochimica Acta* **67**, **No. 17**, 3283-3298.

[12] Sharp, C. M., Huebner, W. F., 1990. *Astrophys. J. Suppl.* **72**, 417-431.

[13] Smit, J., 1999. *Ann. Rev. Planet. Sci.* **27**, 75-113.

[14] Stuart, J. S., Binzel, R. P., 2004. *Icarus* **170**, 295-311.

[15] Weber, C. F., 1998. *J. Comput. Phys.* **145**, 655-670.

PHOTOGEOLOGICAL MAPPING OF ORIENTALE BASIN ON THE MOON, LISM/KAGUYA (SELENE).

H. Demura[1], J. Haruyama[2], M. Ohtake[2], T. Matsunaga[3], Y. Yokota[2], T. Morota[2], C. Honda[2], Y. Ogawa[3], M. Torii[2], N. Hirata[1], N. Asada[1], T. Sugihara[4], and K. Saiki[5], [1]University of Aizu, Aizu-Wakamatsu City, Fukushima 965-8580, JAPAN, [2]Inst. of Space and Astronautical Science, Japan Aerospace Exploration Agency, [3]Natl. Inst. for Environmental Studies, [4]Center for Deep Earth Exploration, Japan Agency for Marine-Science and Technology, [5]Osaka Univ. Corresponding author's e-mail address: demura@u-aizu.ac.jp.

Introduction: The Orientale Basin on the Moon is one of the most famous large impact structures. This remains some questions; the size and shape of the crater of excavation and the origin of multiple rings [1]. Its appearance is obviously found on a photogeologic mapping [2], and its diameters of plural ring features are 320, 480, 620, 930, 1300, and 1900 km [3]. Although some might be made of central uplifts or massive slumps, the true crater size has not been fixed yet. It is hard to say which model is plausible for its origin; the mega-terrace model, the nested model, and the ring tectonic theory [e.g. 4]. We need further understanding in the modification stage of cratering and close-up views of the Orientale for collecting obvious evidence. Detailed geometry of faults, slumps, and some emplacement modes would bring restriction of the process of modification stage.

LISM/Kaguya (SELENE): Japanese lunar explorer, Kaguya (SELENE) orbited around the Moon and obtained global photographs by LISM (Lunar Imager / Spectro-Meter) [5-7]. This imager system brings high resolution images and spectrum, which are panchromatic images for reading surface texture (10m/pixel), digital terrain model for quantitative geomorphological discussion, multiband images from visible to near-infrared wavelength for finding mineral and rock composition, the degree of space weathering, etc. Although we have a chance to cover the Orientale Basin soon, present coverage of the site is two strips of digital terrain model and a part of the east side of the basin for multiband images. This presentation would be a quick report of LISM/Kaguya for photogeologic mapping of the Orientale Basin. Of course, additional information derived from gravity modeling [8] and global shape [9] will support our interpretations.

Planned procedures of photogeological analysis: The first step is confirmation of geologic units [2]. This photogeological map with classifications was processed on the basis of medium resolution photographs (0.1 - 0.5 km/pixel) of Lunar Orbiter missions and USSR Zond 8. High resolution images of LISM/Kaguya will refresh the view. Next step is to know emplacement of Orientale Group formations; "Iorm" Massif facies, "Iork" Knobby facies, "Iohi" Inner facies, "Ioht" Transverse facies, "Ioho" Outer facies, and "Iohs" Secondary crater facies. Their boundaries along cliffs or terraces should be surveyed based on detailed surface texture. Third step is to classify some photogeologic units which have been remained undivided because of insufficient pictures, such as Terra Material which is gently rolling terrain with numerous craters and indistinct depressions.

Crater chronology also plays a vital role for these mappings. Panchromatic high resolution images with the digital terrain model give a size distribution of sub-km craters. Obtained stratigraphy based on its relative age and geometrical emplacement in the Orientale Basin will bring insight to modification stage for large impacts.

References: [1] Spudis, P. D. (1993) *The Geology of Multi-Ring Impact Basins,* Cambridge Univ. Press. [2] Scott D. H. et al. (1977) *I-1034: Geologic Map of the West Side of the Moon.* [3] Wilhelms D. E. (1973) *JGR, 78,* 4084–4095. [4] Melosh H. J. (1988) *Impact Cratering: A Geologic Process,* Oxford Univ. Press. [5] Haruyama J. et al. (2008) *Earth Planets and Space, 60,* 243-255. [6] Ohtake M. et al. (2008) *Advances in Space Research,* in press. [7] Matsunaga, T. et al. (2001) *Proc. SPIE,* 4151, 32-39. [8] Namiki N. et al. (2008) *LPS XXXIX,* Abstract #1596. [9] Araki H. et al. (2008) *LPS XXXIX,* Abstract #1510.

NON-IMPACT ORIGIN OF THE ARKENU CRATERS (LIBYA). M. Di Martino[1], C. Cigolini[2], L. Orti[3], [1]INAF-Osservatorio Astronomico di Torino, 10025 Pino Torinese, Italy, dimartino@oato.inaf.it, [2]Dipartimento di Scienze Mineralogiche e Petrologiche, Università di Torino, via Valperga Caluso 35, 10125 Torino, Italy, corrado.cigolini@unito.it, [3]Dipartimento di Scienze della Terra, Università di Firenze, via La Pira 4, 50121 Firenze, Italy; letiziaorti@libero.it.

Introduction: A double circular structure, located in S-E Libya about 250 km south of Kufra oasis, was recognized as a double impact crater (the Arkenu craters) by [1], first in satellite imagery and then in the fieldwork, and was thus included in the terrestrial impact crater list. The Arkenu craters consist of an N-E (Arkenu 1) and a S-W structure (Arkenu 2), 10.3 km and 6.8 km in diameter, respectively, whose centers are located about 10 km apart. The interpretation of Arkenu structures as impact-related is based on the observation of shatter cones and impact breccias with planar fractures in quartz grains. We visited the area on November 2007 and we carried out a preliminary geological and structural survey. Our field, petrographic and textural observations do not support the idea that the Arkenu "impact craters" have been originated by the collision of two cosmic bodies. In fact, we did not observe PDF in the collected quartz grains and, in addition, the so called "shatter cones" (brought by Paillou and co-workers as an evidence of an impact event) have been likely produced by the erosion of sandstones (see [2]): all of them, in fact, are oriented in the same direction of the dominant winds (we prefer to name these structures as "pseudo-shatter cones").

Geological Survey: The rocks outcropping in the craters' area are a variety of Paleozoic sandstones and subordinated siltstones. Sandstones on the top of the sequence that also outcrop within the craters, are coarser and carry abundant concretions of diagenetic hematite (millimeters to tens of centimeters in size). These sandstones are well preserved within the Arkenu 2. Conversely, within Arkenu 1 the floor consists essentially of disaggregated portions of these rocks coexisting with massive magnetite deposits. In this case, field evidence and mineral distribution (diagenetic hematite recrystallized as magnetite), suggests digestion of the above sandstones by a subvolcanic intrusive body (now partially outcropping within the crater area). The intrusion is characterized by a mafic precursor, followed by granite locally preserved in the northern sector of the crater. It is suggested that the mafic precursor contributed to the melting of the original sandstone sequence and was then followed by the injection of a granitic magma within the subvolcanic region.

Discussion: We, therefore, suggest the craters forming episode is the result of intrusion of a paired, nearly cylindrical subvolcanic stocks (coupled with ring dike injection in the surroundings) accompanied by hydrothermal degassing. This process was then followed by local structural adjustments, likely due to thermal contraction of the whole edifices along circular fractures. This produced moderate folding and subsidence of the "crater sectors" (currently delimited by the crater rims) as well as the origin of the outer circular structures. Erosion did its cycle and finally revealed the architecture we are now observing.

The present work is part of a more wide study of several circular structures of eastern Sahara and the first results have been recently published [2]. In that contribution we presented our observations on the non-impact origin of the circular structures in the Gilf Kebir area (S-W Egypt), previously identified as an impact crater field [3,4].

References: [1] Paillou Ph., Rosenqvist A., Malezieux J.-M., Reynard B., Farr T. & Heggy E. (2003). Discovery of a double impact crater in Libya: the astrobleme of Arkenu. *Comptes Rendus Geoscience* 335:1059-1069. [2] Orti L., Di Martino M., Morelli M., Cigolini C., Pandeli E., Buzzigoli A., Matassoni L. & Serra R. (2008) *Meteoritics & Plan. Sci.* (in press). [3] Paillou Ph., El-Barkooky A., Barakat A., Malezieux J.-M., Reynard B., Dejax J. & Heggy E. (2004) *Comptes Rendus Geoscience* 336:1491-1500. [4] Paillou Ph., Reynard B., Malezieux J.-M., Dejax J., Heggy E., Rochette P., Reimold W.U., Michel P., Baratoux D., Razin Ph. & Colin J.-P. (2006) *J. African Earth Sci.* 46:281-299.

MARINE IMPACTS – MECHANISMS OF EARLY POST-IMPACT CRATER SEDIMENTATION.

H.Dypvik [1] and E. Kalleson [2], [1] Department of Geosciences, University of Oslo, P.O.Box 1047, Blindern, NO 0316 Oslo, Norway – henning.dypvik@geo.uio.no [2] Elin Kalleson, Natural History Museum, P.O.Box 1172, NO 0318 Oslo, University of Oslo, Norway - elin.kalleson@nhm.uio.no.

Introduction: Marine impacts are found in sparse numbers on the Earth. Of the 174 impact crater known so far, only 27 are of proven marine origin. This is a relatively small number taking into consideration that about 70 % of the Earth is covered by water, [1],[2]. The poor representation is partly due to attenuation of impact energy by deep water columns, leaving the relatively shallow platforms or continental margins as most promising search areas for impact craters along the sea floor. Preservation of marine impact structures can be limited, as most ocean floors are dynamic features of relatively young age. Furthermore the fast infill and burial by sediments in these environments will mask and protect the structures, and discoveries rely on advanced subsurface information like seismic or drill holes.

Recognition and understanding of the sedimentary successions and the related depositional crater infill processes could be of importance for the e.g. recognition of new impact structures. This sedimentological information, in addition, may result in better understanding of crater formation and possible crater exploitation.

Discussion: In marine craters comparable sedimentary successions have been found deposited on autochthonous breccias and allochthonous suevites. The early post-impact depositional conditions (post-suevites) seem to be related in the marine craters studied; developing from avalanches, screes, slides and slumps, through sequences of mass flows before ending with density currents and fine-grained sedimentation from suspension. Data from several structures have been studied, and in this presentation examples from the Chesapeake Bay, [3], Mjølnir, [4], [5] and Gardnos, [6] impact structures will be presented. These craters represent very different conditions e.g. various target rock type, water depth and different impactor sizes. They also differ in age of formation and present state of preservation. The Chesapeake Bay Crater is 90 km in diameter and was formed in late Eocene, the 40 km in diameter Mjølnir Crater was formed at the Jurassic/Cretaceous boundary, while the 6 km in diameter Gardnos Crater probably is of Late Precambrian age. In the Mjølnir case the bolide impacted into about 400 m of water and a sedimentary succession of more that 8 km, while in the Gardnos case Precambrian gneisses just covered with a few tens? of meter of water and some hundred meters of marine claystones were impacted. Target-wise the Chesapeake Bay Crater probably represents a situation somewhere in-between. These differences can explain some of the thickness and compositional variations in the post-impact successions found, while the overall sedimentary processes active seem to have been comparable in the craters studied.

Conclusion: A common sequence of sedimentary processes has been recognized in the marine impact structures studied. The main early post-impact successions reflect the shallow marine conditions and sedimentary processes controlled by the size of the impact along with water depth, basinal geometry and qualities of target lithologies. Succeeding the fall-back impactite and suevite sedimentation , tectonic movements related to crater modification and instability of the steep crater walls and central high, result in deposition of various coarse grained breccias. Avalanches, screes, slides and slumps will dominate. Sea water flushing back, resurging into the crater may deposit thick successions within a very short time-span. At this stage slumping, mass- and density flows will be important. Once stabilized and refilled with water, sedimentation processes in the crater may return to close to pre-impact conditions and suspension dominated sedimentation. At least two major differences of depositional significance can be recognized;

1) the new and often steeper topography of the crater basin and

2) the presence of newly generated debris from the impact as an easily available sediment source.

These changes in depositional conditions may favor episodic high-energy processes like turbidity currents and mass flows with influx of coarser-grained sediments to the crater basin.

References: [1] Dypvik, H. and Jansa, L. (2003) Sedi-ment. Geol.,161, 309-337. [2] Dypvik, H. et al., (2004) Impact Series, Springer [3] Gohn, G. et al., in prep. [4] Dypvik,H. et al., (2005) Sediment. Geol.,168, 227-247. [5] Dypvik et al. (2006) Norwegian Journal of Geology, 84, 143-167. [6] Kalleson et al. (2008), GSA SPE 437, in press.

ASYMMETRIES IN COMPLEX CRATERS DUE TO OBLIQUE METEORITE IMPACTS?

D. Elbeshausen and K. Wünnemann, Museum for Natural History Berlin, Department of Research, Invalidenstr. 43, D-10099 Berlin, Germany (dirk.elbeshausen@museum.hu-berlin.de)

Introduction: Field studies at terrestrial craters, laboratory experiments of crater formation and numerical modeling significantly contributed to our current understanding of the formation of simple and complex crater structures. However, most of this knowledge is based on vertical impact scenarios and the effect of an oblique angle of incidence is often believed to be negligible. Despite the fact that almost all craters are more or less circular in shape it is still a matter of debate whether oblique impacts cause structural asymmetries or not (e.g. [1,2]) and it is basically unknown how far the formation of a crater resulting from a vertical impact resembles crater formation for the much more common case of an oblique impact angle. At vertical impacts the excavation flow differs in vertical (depth) and radial (diameter) direction. For instance, when crater growth has ceased already in vertical direction the radial excavation of the cavity may still continue (e.g. [3]). In case of an oblique impact we have to distinguish additionally between crater growth in up- and downrange direction. This is primarily due to the fact that an oblique impact angle causes an unbalanced material flow in up- and downrange direction with a gradual transition in between [4]. Therefore it is feasible that structural asymmetries exists that may indicate the direction of impact. Hydrocode modeling of oblique impacts [4,5] supports this assumption. However, identifying clear structural indications for the direction of impact at terrestrial craters, on planetary surfaces and in impact experiments is ambiguous and controversial discussed in the literature (see e.g. [6-11]). The only clear indication for the direction of impact is the distribution of ejecta; however, ejecta deposits are only poorly preserved. Erosion may have also removed structural indications in the uppermost section of a crater. For terrestrial craters pre-impact target heterogeneities and, for smaller craters, target topography may also affect crater excavation and could explain crater asymmetries.

We are conducting a systematic parameter study which aims at distinguishing how an oblique impact angle affects (complex) crater formation. In particular we focus on the formation of central peaks and the quest for asymmetries in the target as possible indicators for the impact angle or direction.

Methods and model setup: We are performing three-dimensional (3D) numerical-simulations with iSALE-3D [12], a highly efficient hydrocode optimized for studying late stage crater formation. For the very first beginning of this study we start with simulating a single-layer scenario and using the same material (granite) for both target and projectile. We used earth gravity (g=9.81m/s^2) and kept velocity constant at U=6.5 km/s. To investigate crater formation for different-sized craters we varied projectile radii in a range from [125m…1.5km]. We used Tillotson EOS [13] for granite and assumed a Mohr-Coulomb strength model (where shear strength Y is proportional to pressure P, $Y = Y_{coh} + f \cdot P$) with no cohesion (Y_{coh}=0.). Since we did not consider Acoustic Fluidization [14] so far we chose lower friction coefficients f in a range between 0. and 0.7 for compensation.

Preliminary results: Fig. 1 and Fig. 2 illustrate the shape of the crater for impacts at angles between 90° (vertical) and 30° as cross sections (Fig.1) and in plane view (Fig.2). Snapshots are taken at the time when the central peak reaches its maximum height. Our models show that (1) the height of the central peak decreases with the impact angle (2) the position of the central peak is offset downrange for lower impact angles (3) the time of central peak formation decreases with the impact angle in a sinusoidal manner (4) crater size decreases with the impact angle proportional to the sinus of the impact angle α. Furthermore, our results suggest that for impacts with α<30-60° (a) no overturning of the uppermost part of the layer in uprange direction occurs, (b) the central peak begins to collapse in uprange direction (c) a "forbidden zone" of ejecta deposits in uprange direction emerges.

Future prospects: Here we present preliminary results of a more detailed parameter study that is still in progress. The goal is to quantify the observations listed above (1-4 and a-c) and shown in Fig.1 and Fig.2. Additionally, we want to investigate (a) whether the collapse of the central peak introduces further asymmetries to the crater (b) crater formation for highly oblique impacts (10°<α<30° (c) the relative thickness, radial extent and position of the ejecta layers and/or crater rim as a function of azimuth. Since structural indications for an oblique impact angle in the uppermost strata of the crater is often lost due to erosion, we will also look at deep-seated deformations in the target, in particular below the central peak. Our preliminary results show an unusual tracer distribution beneath the central structure that differs from comparable 2D-simulations for vertical impacts. We suspect that this is an effect of resolution. We are going to study this observation in more detail in order to identify whether it is a numerical artifact or has some real physical meaning that can be correlated with the crater formation.

Acknowledgements: Our work was funded by DFG-Wu 355/5-1

References: [1] Collins, G. S. et al. (2008) *Earth Planet. Sci. Lett. (in press)*. [2] Gulick, R. A. F. et al. (2008) *Nature Geo-*

science (in press). [3] Turtle E. P. et al (2005) *Geol. Soc. Am. Spec. Paper 384*, 1-24. [4] Elbeshausen, D. and Wünnemann, K. (2008) *LMI IV* (this volume). [5] Shuvalov V.V. (2003) *LMI III*, Abstract #4130. [6] Wallis D. et al. (2005) *Mon. Not. R. Astron. Soc. 359*, 1137-1149. [7] Schultz P. H., Anderson J. L. B. (1996) *Geol. Soc. Am. Spec. Paper 203*, 397-417. [8] Poelchau M. H. et al. (2007) *LPS XXXVIII*, Abstract #1698. [9] Scherler D. et al. (2006) *Earth Planet. Sci. Lett. 248*, 28-38. [10] Herrick R. R., Forsberg-Taylor N. K. (2003) *Meteor. Planet. Sci. 38* (11) 1551-1578. [11] Ekholm A. G., Melosh H. J. (2001) *Geophys. Res. Letters 28* (4), 623-626. [12] Elbeshausen D. et al. (2007) *LPS XXXVIII*, Abstract #1952. [13] Tillotson J. H. (1962) *Report GA-3216*, General Atomic, San Diego, CA. [14] Collins, G. S. and Melosh, H. J. (2003) *J. Geophys. Res. 108 (10)*, 1-14.

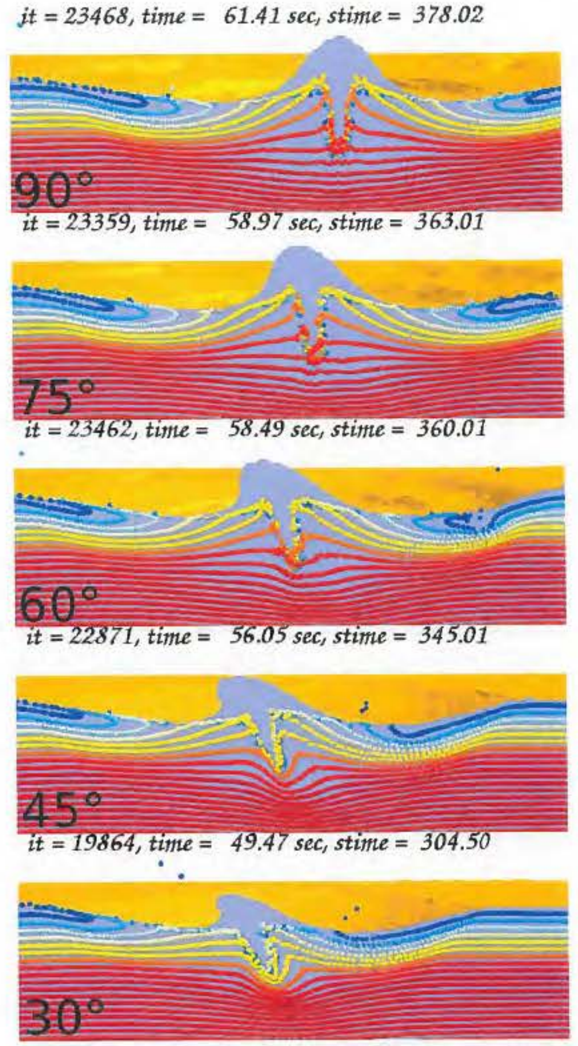

Fig. 1 Snapshots of craters caused at different impact angles at the time when the central peak reaches its maximum extent. Massless tracers are colored by their initial depth.

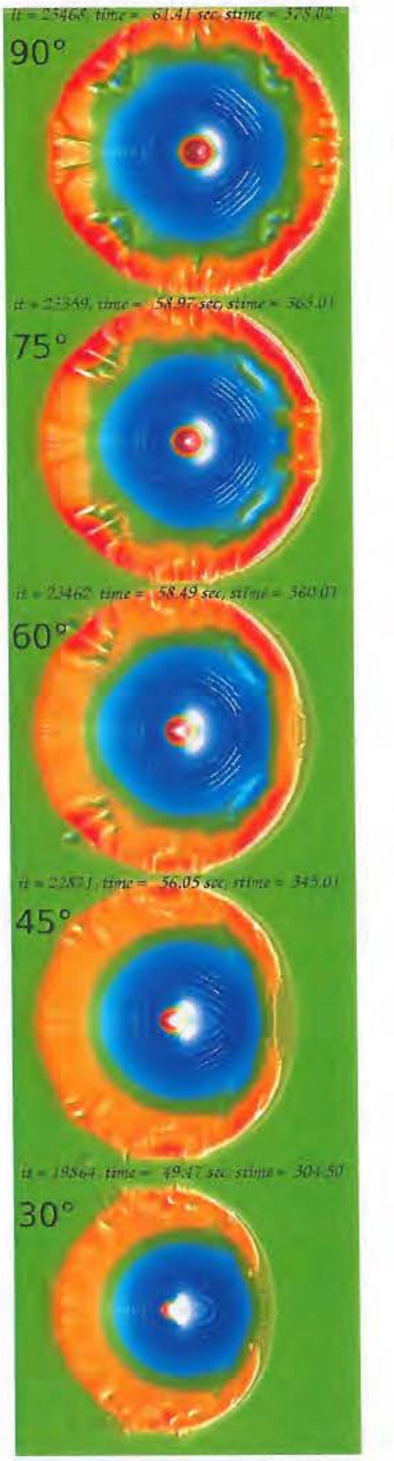

Fig. 2 Top view of the craters presented in Fig. 1. Surface is colored by its height.

COMPLEX CRATER FORMATION DRIVEN BY OBLIQUE METEORITE IMPACTS

D. Elbeshausen and K. Wünnemann, Museum for Natural History Berlin, Department of Research, Invalidenstr. 43, D-10099 Berlin, Germany (dirk.elbeshausen@museum.hu-berlin.de)

Introduction: Although nearly all impacts occur at an oblique angle of incidence [1] the vast majority of impact structures that can be observed on planetary surfaces are more or less circular in shape. However, the asymmetric distribution of proximal (and distal) ejecta (e.g. [2]) if preserved, provides evidence for and oblique impact angle and information about the direction of impact.

It is well known that the angle of impact affects crater efficiency [3,4,5], the propagation of shock waves [6] the generation and distribution of impact melt [7] and may also influence the expansion of the ejecta plume. Crater shape, however, seems to be unaffected by the angle of impact. This may be unintuitive, but is conform with the assumption that an impact can be considered as a point-source [8]) analogous to an explosion. Nevertheless, detailed morphological and morphometric data from field studies and remote sensing revealed that minor deviations exist. There have been several (e.g. [9-15]) attempts to link structural crater asymmetry to the impact angle or direction. However, in particular at terrestrial craters this linkage is ambiguous since deviations from circular symmetry may be also due to asymmetric and heterogeneous target conditions [16, 17].

In this study we investigate the different stages of crater formation for oblique impacts by numerical modeling. We aim to quantify the relationship and origin of structural asymmetries due to impact angle. We focus on the temporal evolution of crater shape with respect to deviations from circular shape and the formation of the central peak. We expect the central part of the crater the most likely location for potential asymmetries.

Methods and model setup: We performed several 3D simulations of crater formation for oblique impacts with our newly developed hydrocode iSALE-3D [3]. For simplicity we used granite for both projectile and target material and computed the thermodynamic material response to shock compression by the Tillotson equation of state [18]. In our models the dynamic material strength Y is proportional to pressure P, according to the Mohr-Coulomb strength model: $Y = Y_{coh} + f \cdot P$ with the cohesion $Y_{coh}=0.$ and a friction coefficient f. We varied the friction coefficient f between 0.0 and 0.7, the projectile radius between 125m and 1500m and the impact angle from 30° to 90° in steps of 15°. All other parameters were kept constant (impact velocity U=6.5 km/s, gravity g=9.81m/s^2).

Results: Fig. 2 shows a series of snapshots of crater formation for the impact of a 1km-sized projectile at 6.5km/s and an impact angle of 30° (measured from target surface).

Very early crater excavation: Fig. 2a shows a very early stage of crater formation immediately after the end of the so-called *contact and compression stage* (e.g. [19]). The kinetic energy of the projectile is completely transferred into the target and shock waves propagate away from the point of impact [7]. In the beginning of the sequence of crater formation a cavity is formed by the penetration of the projectile pushing material out of its way. A momentum parallel to the direction of impact is transferred to the target material. Therefore, an oblique angle of impact results in an elliptical crater shape, initially (Fig. 2a, right).

Excavation stage: In the course of time crater formation is due to shockwave-induced excavation. The generated shockwaves propagate in all directions away from point of impact. After release from shock pressure some energy in terms of particle velocity remains to the material and sets a material flow in motion resulting in the excavation of the crater. The excavation flow becomes more symmetric further away from point of impact causing an increasingly more circular cavity shape when looking at crater evolution in plane view (Fig1a-c, right column).

The excavation stage is finished when the shockwave-induced upward and outward directed material flow ceases. The resulting crater is well-known as the transient crater. However, the exact moment in time when excavation process halts is difficult to determine since the end of excavation is reached at different times at different locations in the crater. Therefore, the transient crater has to be looked at a virtual construct as it never really exists in the course of crater formation. This is especially true in case of oblique impacts where crater growth in up- and downrange direction distinctly differs. For this study we use the time when material starts fluxing back towards the crater centre to determine the end of excavation. For vertical impacts this corresponds approximately to the time when the cavity has reached its maximum extent. In case of small craters, where lithostatic pressures are small compared to material strength the final crater is similar to the transient cavity. At larger impacts, on the other hand, gravitational forces exceed material strength and the whole cavity becomes instable.

Modification stage: The crater floor first collapses where excavation has stopped and the gravity forces exceed material strength. This is usually the deepest point of the transient cavity. Where strength is exceeded the crater floor starts to rise forming a central peak structure. Initially the material flow is directed upwards (Fig. 2b). However, short time later an inward directed flow of matter from uprange towards the crater centre superimposes (Fig. 2c). This leads to a downrange movement of the central peak, since at this time material flux at the opposite site is still directed outwards. Fig. 2d shows a snapshot of the moment, when the inward directed material flow from downrange is already in progress. This causes some sort of distortion of the central peak, since this flow interferes with fluxes from other directions. Depending on the differences in the time when the inward directed fluxes occur the subsequent collapse of the central peak (Fig. 2 e, f) may even lead to an overturning of the strata in the central peak structure for very weak material.

Even though these asymmetries may not be obvious in the topography of the resulting crater the underlying structure should show clear indications according to our model example. Moreover, there occurs a characteristic low density zone, asymmetric in shape (see density plot in Fig. 2e,f), in all our models that may also indicate structural asymmetries buried beneath the crater centre due to an oblique angle of impact.

Quantification of observations: The degree of asymmetries in the crater shape and structure below the central peak depend on (i) the angle and velocity of impact, (ii) the time shift between the beginning of the inward-directed material flux from downrange and uprange, (iii) the amount, (iv) the velocity and direction, and (v) the duration of the material flux. Note that (ii)-(v) also depend on material properties such as friction.

Fig. 1 shows our first attempt in quantifying the observations discussed above. We found that with a decreasing impact angle the formation time of the transient crater in downrange direction increases, while it is decreasing for uprange direction. The lower the impact angle, the larger is the difference in the formation time between downrange and uprange and, thus, more complex and asymmetric structures are expected.

Acknowledgements: Our work was funded by DFG-Wu 355/5-1

References: [1] Shoemaker E. M. (1962) In Kopal, Z. (Ed.) *Physics and Astronomy of the Moon*, Academic Press, San Diego, 283-359 [2] Yamamoto, S. (2002) *Icarus 158*, 87-97. [3] Elbeshausen D. et al. (2007) *LPS XXXVIII*, Abstract #1952. [4] Elbeshausen D. et al. (2008) *LPS XXXIX*, Abstract #1795. [5] Gault D. E. and Wedekind J. A. (1978) *Proc. LPS IX*, 3843-3875. [6] Pierazzo E., Melosh H. J. (2000) *Meteor. Planet. Sci. 35*, 117-130. [7] Pierazzo E., Melosh H. J. (2000) *Icarus 145*, 252-261. [8] Holsapple K. A., Schmidt R. M. (1987) *J. Geophys. Res. 92*, 6350-6376. [9] Wallis D. et al. (2005) *Mon. Not. R. Astron. Soc. 359*, 1137-1149. [10] Schultz P. H., Anderson J. L. B. (1996) *Geol. Soc. Am. Spec. Paper 203*, 397-417. [11] Poelchau M. H. et al. (2007) *LPS XXXVIII*, Abstract #1698. [12] Scherler D. et al. (2006) *Earth Planet. Sci. Letters 248*, 28-38. [13] Herrick R. R., Forsberg-Taylor N. K. (2003) *Meteor. Planet. Sci. 38 (11)* 1551-1578. [14] Shuvalov V.V. (2003) *LMI III*, Abstract #4130. [15] Ekholm A. G., Melosh H. J. (2001) *Geophys. Res. Letters 28 (4)*, 623-626. [16] Collins, G. S. et al. (2008) *Earth Planet. Sci. Lett. (in press)*. [17] Gulick, R. A. F. et al. (2008) *Nature Geoscience (in press)*. [18] Tillotson J. H. (1962) *Report GA-3216*, General Atomic, San Diego, CA. [19] Melosh, H. J. (1989) *Impact Cratering, Oxford Univ. Press.*

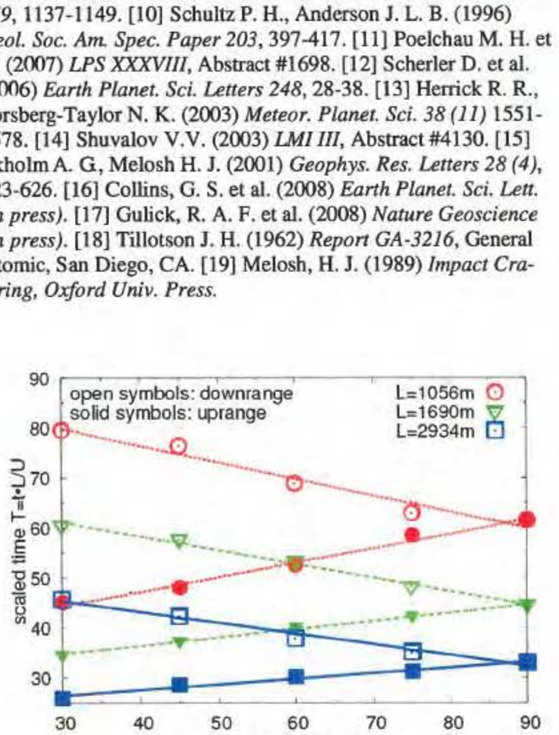

Fig. 1 Formation time of the transient crater, depending on the impact angle and projectile size. Solid symbols mark the formation time in downrange, open symbols in uprange. Impact velocity and gravity were kept constant at g=9.81m/s^2, U=6.5km/s.

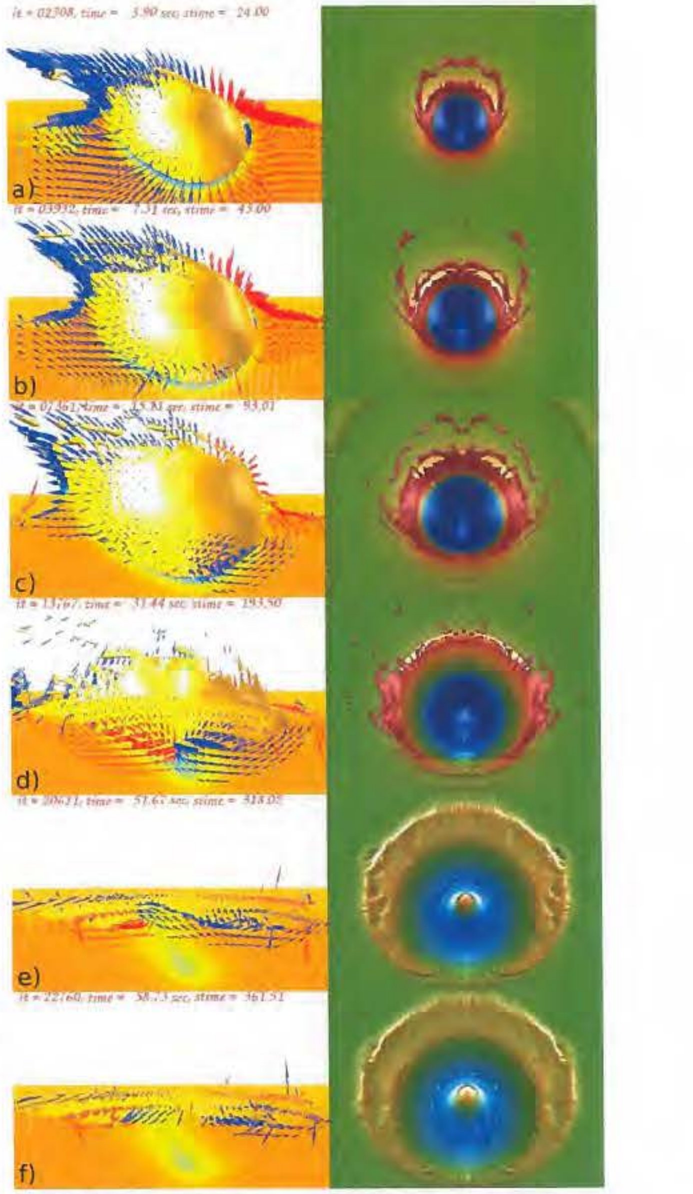

Fig. 2 Snapshots of central peak formation. Impact of a 1km-sized granitic projectile with an impact velocity of 6.5km/s. Impact angle is 30°. Left column: Cross section through the symmetry plane depicts material density, material flux is indicated by arrows which are scaled with absolute velocity and coloured by the radial velocity component (blue: flux downrange, red: flux uprange). Impact direction is from right to left. Right column: Plane view of the crater. Topography is colored by height. Impact direction from bottom to top.

ROCK MAGNETIC INVESTIGATIONS OF IMPACTITES FROM DEEP DRILL CORES OF BOSUMTWI AND CHESAPEAKE BAY IMPACT STRUCTURES.

T. Elbra[1], A. Kontny[2] and L. J. Pesonen[1], [1]Department of Physics, P.O.Box 64, 00014 University of Helsinki, Finland, tiiu.elbra@helsinki.fi; [2] Institute of Geology, Hertzstraße 16, 76187 Karlsruhe University, Germany.

Introduction: The meteorite impact processes are fundamental mechanisms which have shaped the surface of the Earth and the bodies of our solar system. Currently the total of 174 impact structures are confirmed [1] on Earth, however, many of them are not exposed and cannot be directly studied. Thus it has become clear that the scientific deep drilling is essential to provide ground truth data of the subsurface properties of the impact structures and therefore give constrains for understanding the geological processes shaping the Earth.

Recently, the drillings have been extended to penetrate huge meteorite impact structures such as: Chicxulub (Mexico), Bosumtwi (Ghana) and Chesapeake (USA). Here we present and compare the results from rock magnetic investigations of the Bosumtwi and the Chesapeake Bay impact structures.

Results: The magnetic susceptibility indicates the dominance of paramagnetic minerals ($<400*10^{-6}$SI) and a very small, inhomogeneously distributed ferrimagnetic component in impactites from the Bosumtwi [2, 3] structure. In the Chesapeake Bay case, the results show a large variation of magnetic susceptibility. Lithic breccias in lower part of the section are characterized by low magnetic susceptibility ($<300*10^{-6}$SI). The upper part, however, consists of magnetically stronger (susceptibility up to 6000 10^{-6}SI) melt-rich suevites.

According to our rock magnetic investigations (including thermal behavior of magnetic susceptibility and magnetic hysteresis experiments), mainly pyrrhotite (Fig.1) but in some cases also magnetite, two main magnetic minerals creating crustal magnetic anomalies, are suggested as carriers of natural remanent magnetization [2-5] of impactites and impact modified rocks in both structures. The magnetic mineral pyrrhotite occurs in Chesapeake as single-domain size. Although the pyrrhotite from Bosumtwi shows a large grain size variations, the numerous shock-induced nanostructures are assumed to behave also as single-domain grains.

Magnetic minerals show a significant oxidation in the suevite and the lithic breccia unit of the Chesapeake Bay impact structure, indicating a strong degree of alteration. The observations have shown that Fe-oxides in the upper part of impactite unit show also strong resorption features and a porous texture, which indicate melting. In the polymict impact breccia from the Bosumtwi drilling [3], the twin lamellae of pyrrhotite show strong brittle to brittle-ductile deformation features. These and other results will be discussed.

References:

[1] http://www.unb.ca/passc/ImpactDatabase/

[2] Elbra, T., et al. (2007) *Meteoritics & Planet. Sci., 42*, Nr 4/5, 829–838.

[3] Kontny, A., et al. (2007). *Meteoritics & Planet. Sci., 42*, Nr 4/5, 811–827.

[4] Elbra, T. and Pesonen (2007). *Eos Trans. AGU, 88(52)*, Fall Meet. Suppl., Abstract U23A-0858.

[5] Kontny, A., et al. (2007) *GSA Abstracts with Programs, 39*, No. 6.

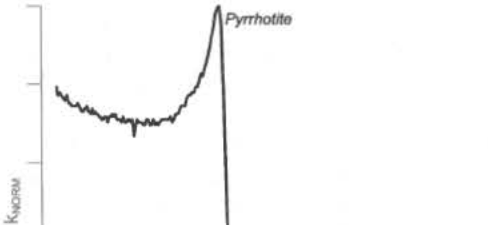

Figure 1. Normalized susceptibility as function of temperature of impactites from Bosumtwi and Chesapeake Bay deep drill cores.

PROPOSED BUSHVELD SCENARIO: IMPACT, MANTLE UPWELLING, MELTDOWN, COLLAPSE

W. E. Elston, Department of Earth and Planetary Sciences, MSC03 2040, University of New Mexico, Albuquerque, NM 87131-0001, USA, welston@unm.edu.

Unique Bushveld Rocks: The unique Bushveld is the largest continental igneous complex and in a class by itself among proposed terrestrial impact structures. Each component (~85% endogenic) is the largest known of its kind ($V_t=10^6 km^3$): mafic cumulates (Rustenburg Layered Suite), A-type Lebowa Granite Suite, multi-origin Rashoop Granophyre, and the Rooiberg Group of unique high-T pseudovolcanic meltrocks with major sedimentary components [1], commonly misinterpreted as *felsite* or "classical example" of rhyolite [2]. Rooiberg rocks share some characteristics with the Onaping Fm. (Sudbury) but rarely preserve shock features in an environment dominated by heat. They span the entire history of the Bushveld Complex [3] and record its proposed stages: impact, mantle upwelling (or *plume* [3]) with melting in mantle and crust, quiescence interrupted by catastrophic caldera-like collapse, and the beginning of a >100 m.y. period of adjustment.

Impact: A catastrophe at ~2.06 Ga, interpreted as a cluster of quasi-simultaneous impacts, abruptly ended epicontinental sedimentation (Pretoria Group, Transvaal Supergroup). A multiring [4] four-lobed transient crater (or overlapping crater cluster) was modified by collapse of its central uplift(s) and peak ring. The Rooiberg Group began to accumulate in the first outer ring (eventual depth 4-5 km [2]) from repeated overflows of a superheated Sudbury-type meltpool [5].

Evidence for Crater Collapse: Segments of the collapsed central uplift and peak ring are exposed in paired *inliers* of Pretoria Group rocks (diam. tens of km) inside the western and eastern lobes [6]. A prominent Pretoria Group unit, 500-m Magaliesberg Quartzite, is absent. In each pair, brecciated, faulted, but otherwise mildly deformed post-Magaliesberg units are overlain by undeformed basal Rooiberg meltrocks and juxtaposed by a strike-slip fault against intensely deformed pre-Magaliesberg units. The deformed units are attenuated, metamorphosed to pyroxene hornfels facies, and highly contorted [6]. Such deformation of Pretoria-age rocks is unknown in the RSA beyond the Bushveld.

Interpretation: Mildly deformed inliers are segments of the collapsed peak ring; deformed inliers parts of the collapsed central uplift. In the juxtaposing fault of the eastern pair, quartzite slabs from the undeformed inlier, up to hundreds of m long, were engulfed by basal Rooiberg debris flows of recrystallized-to-melted sediments. The source of the sediments was the "missing" Magaliesberg Formation, detached from the collapsing central uplift. Impact timing is bracketed between Pretoria sedimentation and Rooiberg coming-to-rest.

Mantle Upwelling, Lithosphere Melting: Impacts triggered an upwelling of the upper mantle [7]. Decompression partial melting created the Rustenburg Layered Suite, induced crustal melting the Lebowa Granite Suite. Rising through inward-dipping fractures [8] into the first outer ring,. successive mafic and granitic melts spread below Rooiberg accumulations, as km-thick sills. In most places, evidence for impact in basal Rooiberg zones was obliterated by contact metamorphism and metasomatism [9]. Rustenburg cumulate zones, traceable over hundreds of kilometers on the Bushveld perimeter, imply extraordinary quiescence. Meanwhile, explosive overflows from the meltpool into the outer ring continued, triggered by influxes of water.

Models suggest that "an impact big enough to lift hot mantle rocks close to the surface" with "a final crater 400-500 km" is "possible, but...highly improbable...in the last 3.3 b.y years of terrestrial... history" [10]. It is proposed that the *improbable* happened.

Caldera-Like Collapse: Generation of Lebowa Granite by crustal melting resulted in instability (e.g., crustal diapirs, also known as "cold fingers in a hot magma" [11]). It culminated in catastrophic caldera-like collapse, creating the present lobate Bushveld basin. Paleomagnetic evidence [12] shows Rustenburg sills to have been horizontal until at least the emplacement of the upper zones. They acquired their present basinward dip when collapse enlarged the Bushveld basin beyond the limit of the outer ring. Much reduced be erosion, it still covers 67,349 km^2. By comparison, Sudbury, also a remnant, covers only 1,341 km^2 [13]. The resulting Bushveld structure is compatible with a *dipping sheets* geophysical model [14], modified by replacing some Lebowa Granite in the center with the geophysically indistinguishable Rooiberg meltpool. In this model, unlike the classic *lopolith*, Rustenburg sills do not extend into the center of the Bushveld basin.

Evidence for Caldera-Like Collapse: A succession of tuff breccia, megabreccia (with clasts up to tens of meters), and ash-fall tuff (Union Tin "shale") in the upper part of the Rooiberg Group preserves evidence for caldera-like collapse. It resembles collapse breccias of large ignimbrite calderas [15] in all but vastly greater scale. As a marker around the Bushveld periphery [16], it shows the Rooiberg Group to be a single stratigraphic package. Rhyolite provinces of similar $10^5 km^3$ volume resolve into ignimbrite sheets radiating from numerous calderas. Remarkably, no Rooiberg source is known, other than a meltpool largely obscured by invading granite. Only a segment of its massive red granophyric upper zone (cf., Sudbury) survived, at *the* Rooiberg (the atypical Rooiberg Group type locality).

The same granite invasions obliterated all *in situ* evidence for impact. In the meltpool, they triggered further Rooiberg eruptions and generated a type of Rashoop Granophyre by reaction between granite magma and hot melt [17]. Late Rooiberg flows equilibrated with granophyre and granite [3]. Physically and chemically, they superficially resemble rhyolite.

Aftermath: The last Rooiberg flows intertongue with sedimentary crater fill (Loskop Formation [18]); deformation reached the Waterberg Supergroup [19].

The Extrusive Bushveld: It has frequently been ignored that the Bushveld Complex is *extrusive*. Its members intrude each other, with low-density Rooiberg rocks as roof, but there is "no continuous sedimentary roof at all" [20]. Confusion arose from a misguided ruling that "the Rooiberg is not part of the Bushveld Complex" [21)] and its mistaken assignment to the Transvaal Supergroup [2]. Subsidence of the first outer ring, concomitant with central upwelling [22], allowed >10 km of magma to accumulate *on the surface*, without collapse.

Rooiberg Evidence: Exposures of all four Rooiberg formations (Dullstroom, Damwaal, Kwaggasnek, Schrikkloof) are confined to the southeastern Bushveld [16]. The scoured and locally polished Pretoria-Rooiberg contact was preserved from later intrusions in only in only three places: the two undeformed inliers (not reached by dipping sheets) and distal paleochannels at the base of the type-Dullstroom Formation, a 1,200-m sliver of basal Rooiberg *beneath* the eastern Rustenburg limb [16]. Critical exposures of impact ejecta (as distinguished from later overflows) are confined to a 200-m basal Dullstroom Fm. section in the same three locations. They consist of inflated debris avalanches of recrystallized cm-to-m quartzite clasts in a variable matrix of average crust and siliciclastic sediments, in every stage toward *superheated* melting and quenching, with residues of sedimentary quartz but no phenocrysts (*Basal Rhyolite* [16]). Quartz paramorphs after three high-T SiO_2 polymorphs ("tridymite" [23]), unknown in volcanic rocks, are typical; the lowest-temperature form (swallow-tailed needles) is known from partially melted basal Onaping breccia [24]. Though not yet systematically sampled, these basal zones have yielded examples of medium-level shock (cataclasis, mosaicism, deformation twins in quartz).

The remainder of the Dullstroom Formation is a heterogeneous succession of mainly mafic rocks. At the base of the Damwal Fm., a glassy rock with quench needles, enriched in Fe, Ti, and P appears. The remainder of the Damwal Formation consists of siliceous rocks of highly complex petrography. Interlayered high-energy siliciclastic sedimentary deposits (unsorted matrix-supported exotic clasts [25]) record cold water influxes into the meltpool, causing explosive eruptions.

The mafic-siliceous succession with high Fe-Ti-P interface mimics the Sudbury meltpool [5]. Textures suggestive of Sudbury-style immiscible superheated emulsion droplets [5] include spherules. A 1-m "cool" *Rosetta Stone* bed (in a 3,500-m section) revealed diaplectic quartz, maskelynite in plagioclase, kink bands, and features that remain unexplained.

Over much of the Bushveld. granite intrudes the basal Kwaggaskop Fm. [16]; it is unknown whether Dullstroom and Damwal exist in the subsurface. Kwaggaskop and Schrikkloof Fms. resemble conventional rhyolite; the collapse megabreccia is at their contact. Interbedded sediments have local origin.

Regional and Global Implications: Space permits only brief hints: From field evidence, both Bushveld and Vredefort impacts preceded Rustenburg magmatism. A multiple Bushveld-Vredefort impact disturbed paleomagnetic orientations and isotopic systems, remobilized Wits gold, and left anomalous lithosphere to this day. There is evidence for a global $\delta^{13}C$ excursion and a significant increase in atmospheric oxygen, with biological and sedimentological implications [31].

Acknowledgments: This study would have been impossible without generous (if skeptical) field guides (David Twist, Jochen Schweitzer, Frik Hartzer) and field assistants (E. G. Deal, M. Caress, J. M. de Moor, T. Manyeruke), and support by the University of Pretoria (Professors von Gruenewaldt, De Waal, Eriksson). My sincere thanks to them all!

References: [1] Coetzee, G. L. (1970*) Geol. Soc. S. Africa Spec. Pub. 1,* 312-325. [2] Eales, H. V. (2001) *Pop. Geoscience Ser. 2,* Council for Geoscience. [3] Schweitzer *et al.* (1997) *J. African Earth Sci.* 24, 95-104 [4] Rhodes, R. C. (1975) *Geology* 3, 549-554. [5] Zieg, M. J. & Marsh, B. D. (2005) *Geol. Soc. America Bull.* 117, 1427-1450. [6] Hartzer, F. J. (2000) *Geol. Surv. S. Africa Mem.* 88. [7] Jones, A. P. *et al.* (2003) *E&PSL* 202, 551-561. [8] Sharpe, M. R. *et al.* (1981) *Geol. Soc. S. Africa Trans.* 84, 139-244. [9] von Gruenewaldt, G. (1972) *Geol. Soc. S. Africa Trans.* 75, 121-134. [10] Ivanov, B. A. & Melosh, H. J. (2003) *Geology* 31, 869-872. [11] Gerya, T. V. *et al.* (2003) *Geology* 31, 753-756. [12] Hattingh, P. J. (1998) *Southern African Geophys. Rev.* 2, 75-77. [13] Hunter, D. R. (1975*) Bushveld Map*, Econ. Geol. Res. Unit, Univ. Witwatersrand. [14] Meyer, R. and de Beer, J, H. (1987) *Nature* 325, 610-612. [15] Lipman, P. W. (1976) *Geol. Soc. America Bull.* 87, 1397-1410. [16] Schweitzer, J. K. *et al.* (1995) *S. African J. Geology* 98, 245-255. [17] De Bruiyn, H. (1975) *Geol. Soc. S. Africa Trans.* 78, 185-190. [18] Martini, J. E. J., 1998, *J. African Earth Sci.* 27, 193-222. [19] de Bruiyn, H. (1971-72) *Annals Geol. Survey* 9, 91-94. [20] Daly, R. A. & Molengraaff, G. A. F. (1924) *J. Geology* 32, 1-25. [21] South African Committee for Stratigraphy (1980), *Geol Surv. Handbook* 8. [22] Marsh, B. D. (1982) *Am. J. Sci* .282, 908-955. [23] von Gruenewaldt, G. (1968) *Geol .Soc S. Africa Trans.* 71, 153-176. [24] Stevenson, J. S. *(1963) Canadian. Mineralogist.* 7, 413-419. [25] Eriksson *et al.* 1994, *J. Sedimentary Research* 64, 836-846. [26] Melezhik, V. A. *et al.* (2005) *Geology Today* 15, no. 11, 4-11.

BALLEN QUARTZ AND CRISTOBALITE IN IMPACT BRECCIAS: TYPES, OCCURRENCE, AND POSSIBLE ORIGIN.

L. Ferrière[1], C. Koeberl[1], W. U. Reimold[2], E. Libowitzky[3], and A. Greshake[2], [1]Department of Lithospheric Research, University of Vienna, Althanstrasse 14, A-1090 Vienna, Austria (ludovic.ferriere@univie.ac.at; christian.koeberl@univie.ac.at). [2]Museum of Natural History (Mineralogy), Humboldt-University, Invalidenstrasse 43, D-10115 Berlin, Germany (uwe.reimold@museum.hu-berlin.de; ansgar.greshake@museum.hu-berlin.de). [3]Institute of Mineralogy and Crystallography, University of Vienna, Althanstrasse 14, A-1090 Vienna, Austria (eugen.libowitzky@univie.ac.at).

Introduction and Summary: So-called "ballen quartz" was first described in 1890, in impact melt rock from the Mien impact structure [1]. "Ballen quartz" has since been reported from about one in seven of the known terrestrial impact structures [2]. The first detailed study of these features was reported by [3], who concluded that the ballen texture represented pseudomorphs after cristobalite that had replaced lechatelierite initially formed by shock-induced thermal transformation of quartz. Then Bischoff and Stoeffler [4] found that ballen represent recrystallized diaplectic quartz glass that had undergone the transition to cristobalite and then to α-quartz. Three types of "ballen quartz" were recognized by [4], based on optical characteristics: ballen with optically homogeneous extinction, ballen with different crystallographic orientations, and ballen with intraballen-recrystallization. Recently, optical and electron microscopic observations, as well as Raman spectroscopy (Fig. 1) and transmission electron microscopy (TEM) investigations, have indicated that five types of ballen silica can be distinguished [2]: α-cristobalite ballen with homogeneous extinction (type I); α-quartz ballen with homogeneous extinction (type II), with heterogeneous extinction (type III), and with intraballen recrystallization (type IV); and chert-like recrystallized ballen α-quartz (type V). In addition, ballen with a "toasted appearance", similar to what has been described for shocked quartz grains (e.g., [5]), were reported from Popigai [6], from Wanapitei [7], and from Dhala [8] craters.

Ballen, with either α-quartz or α-cristobalite structure, occur as independent clasts or enclosed in diaplectic quartz glass or lechatelierite inclusions (Fig. 2), mostly in impact melt rock and, more rarely, in suevite [2]. Ballen are more or less spheroidal in shape or in some cases elongate (ovoid), and range in size from about 10 to 220 µm [2]. Furthermore, for the first time, coesite was identified by [2] in the form of tiny inclusions exclusively within ballen cristobalite (type I) from the Bosumtwi crater (Fig. 1).

Regarding the formation of ballen, we have recently [2] suggested that two genetic processes are possible: (a) an impact-triggered solid-solid transition from α-quartz to diaplectic quartz glass, followed by the formation at high temperature of ballen of β-cristobalite and/or β-quartz, and finally back-transformation to α-cristobalite and/or α-quartz; and (b) a solid-liquid transition from quartz to lechatelierite followed by nucleation and crystal growth at high temperature.

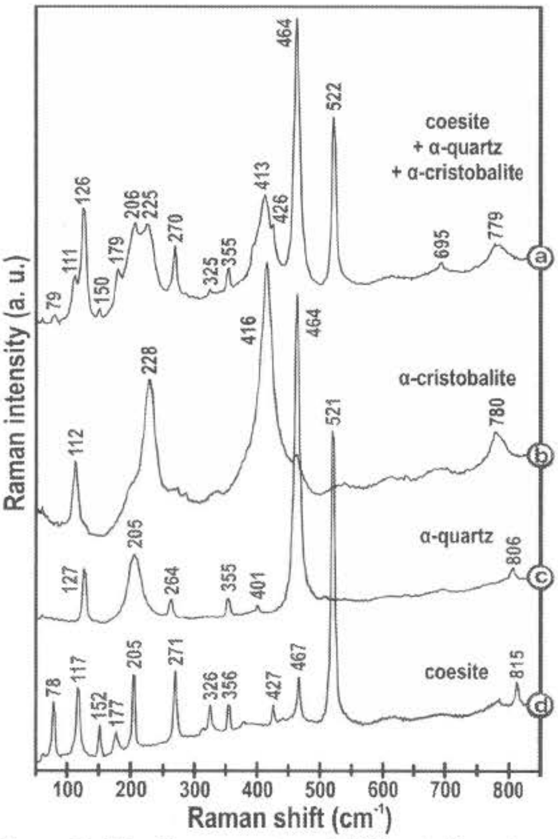

Figure 1. MicroRaman spectra of different silica phases characteristic or associated with ballen silica. a) Minute intra-ballen inclusion; b) α-cristobalite ballen (type I); c) α-quartz (ballen of types II-V); d) Aggregate of coesite for reference (sample LB-44B from the Bosumtwi crater).

According to [2], the different types of ballen silica are interpreted to be the result of retrogression/back-transformation of β-cristobalite and/or β-quartz to α-cristobalite and/or to α-quartz with time. Furthermore, because ballen silica has been so far only observed in impactites, these features have been added to the list of impact-diagnostic criteria [2].

New Observations and Discussion: In addition to the 28 impact structures listed by [2] in which ballen silica have been described, we have recently observed ballen in impact melt rock from the Logoisk (ballen of types I, II, and III) and Puchezh-Katunki (ballen of types III, IV, and V) craters.

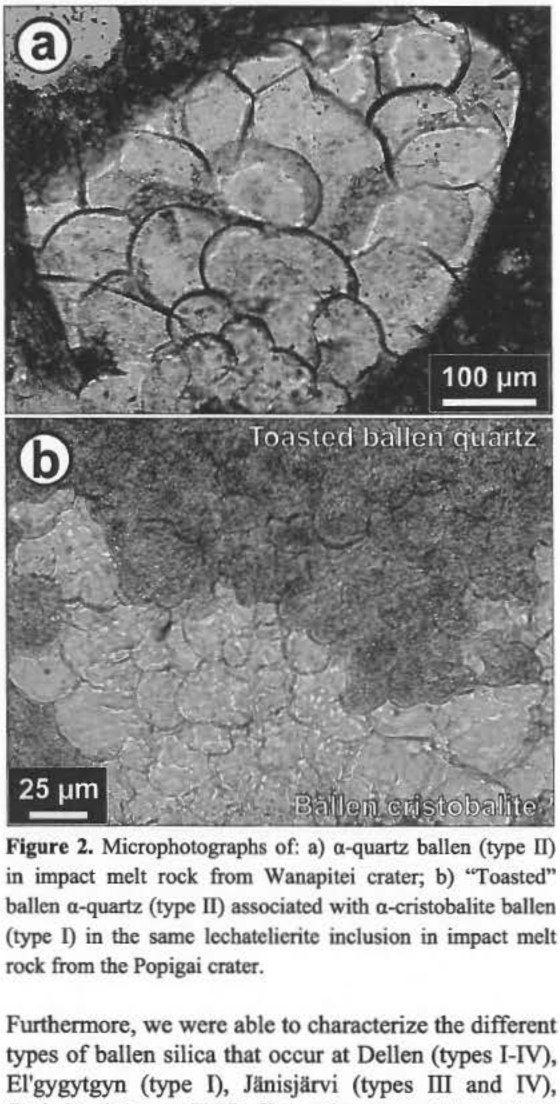

Figure 2. Microphotographs of: a) α-quartz ballen (type II) in impact melt rock from Wanapitei crater; b) "Toasted" ballen α-quartz (type II) associated with α-cristobalite ballen (type I) in the same lechatelierite inclusion in impact melt rock from the Popigai crater.

Furthermore, we were able to characterize the different types of ballen silica that occur at Dellen (types I-IV), El'gygytgyn (type I), Jänisjärvi (types III and IV), Sääksjärvi (types II-V), Ternovka (types III and IV), and Wanapitei (types I-V) craters. Surprisingly, no coesite inclusions were observed within α-cristobalite ballen from these structures. However, interestingly, cristobalite ballen (type I) were observed together with ballen quartz (types II and III), associated in the same inclusions, in impact melt rocks from Wanapitei and from Popigai crater. Additionally, some of the ballen quartz from Popigai has "toasted" appearance (ballen cristobalite associated within the same inclusions are not "toasted"; Fig. 2). "Toasted" ballen quartz was also observed for the first time in impactites from the Rochechouart, Sääksjärvi, and Ternovka craters. However, based on our Raman spectroscopy investigations, these "toasted" ballen show only the typical α-quartz signature. Consequently, the origin for this "toasting" is still somewhat mysterious (further analyses are ongoing).

In addition, we were able to investigate ballen of α-cristobalite and α-quartz structure occurring within the same silica inclusion using TEM. As already recognized by [2], α-cristobalite ballen are composed of numerous tiny individual crystals with sizes up to ~2 μm. And we show that, similarly, α-quartz ballen are composed of numerous tiny crystals of α-quartz.

Conclusions: Our observations of: a) α-cristobalite ballen occurring together with α-quartz ballen in the same inclusion, b) similar micro-texture under the TEM for α-cristobalite and α-quartz ballen, and c) the occurrence of α-cristobalite ballen only in the "youngest" impact structures, confirm that α-quartz ballen are the result of back-transformation of β-quartz and/or α-cristobalite with time, as suggested by [2-4]. We should also consider that if α-cristobalite ballen were rapidly quenched, the conversion of α-cristobalite to α-quartz would have been inhibited. Furthermore, α-cristobalite ballen from Bosumtwi, with coesite occurring as tiny intraballen inclusions, is so far unique, as we were not able to detect coesite in α-cristobalite ballen from any other impact structure. It is likely that with time, coesite inclusions in materials from much older structures could have been transformed back to α-quartz; note the Bosumtwi structure is, at 1.07 Ma age, by far the youngest impact structure investigated by us.

Acknowledgments: This work is supported by the Austrian Science Foundation (FWF), grant P18862-N10, the Austrian Academy of Sciences, and a grant by SYNTHESYS. Dieter Stöffler is gratefully acknowledged for allowing investigation of thin sections from his impactite collection. Thanks to Roald Tagle for providing thin sections from Popigai.

References: [1] Holst N. O. (1890) *Sveriges Geologiska Undersökning*. Serie C, No 110. Stockholm. [2] Ferrière L. et al. (2008) (in revision). [3] Carstens H. (1975) *Contrib. Mineral. and Petrol., 50,* 145-155. [4] Bischoff A. and Stöffler D. (1984) *J. Geophys. Res., 89,* B645-B656. [5] Short N. M. and Gold D. P. (1996) *Geol. Soc. Am. Spec. Paper 302,* 245-265. [6] Whitehead J. et al. (2002) *Meteoritics & Planet. Sci., 37,* 623-647. [7] Dressler B. O. et al. (1997) *Meteoritics & Planet. Sci.*, 32, 249-258. [8] Pati J. K. et al. (2008) *Meteoritics & Planet. Sci.* (in press).

SYSTEMATIC COMPARISON OF UNIVERSAL STAGE-INDEXED PLANAR DEFORMATION FEATURES IN QUARTZ: IMPLICATIONS FOR STATISTICAL SIGNIFICANCE AND REPRESENTATION OF RESULTS. L. Ferrière[1], J. R. Morrow[2], T. Amgaa[1], and C. Koeberl[1], [1]Department of Lithospheric Research, University of Vienna, Althanstrasse 14, A-1090 Vienna, Austria (ludovic.ferriere@univie.ac.at; christian.koeberl@univie.ac.at). [2]Department of Geological Sciences, San Diego State University, 5500 Campanile Drive, San Diego, California 92182-1020, USA (jmorrow@geology.sdsu.edu).

Introduction and Methods: Universal stage (U-stage) analysis is a standard technique used for determining the crystallographic orientations of planar deformation features (PDFs) in quartz. Detection of these features and the values of their orientations in quartz are crucial evidence for the impact origin of geological structures. However, the quality, precision, repeatability, and representativeness of the measurements (in terms of personal and laboratory bias) for a given sample have not been thoroughly tested. For these reasons, two shocked quartz-bearing thin sections (metagreywacke clast in breccia from Bosumtwi crater [BOS-3] and gneiss from Manson crater [M8-427.7]) were independently analyzed by each of three operators (two experienced and one inexperienced) using a four-axis U-stage. Investigations on a third thin section (sandstone from Gosses Bluff crater) are still in progress.

We determined the crystallographic orientations of a maximum number of measurable PDFs (excluding planar fractures [PFs]) contained within ~50-100 quartz grains present in each thin section, following standard measurement techniques [e.g., 1-4]. Each operator subsequently plotted the PDF plane orientations manually on a stereonet [e.g., 1-4], and then indexed the planes to Miller indices (hkil) for quartz as described in [2]. However, a new version of the stereographic projection template for quartz was drawn and used (Fig. 1), including four additional typical PDF orientations ($\{22\bar{4}1\}$, $\{31\bar{4}1\}$, t$\{40\bar{4}1\}$, and k$\{51\bar{6}0\}$) that were not included on the previous, commonly used template [1-4]. The analyses were "blind", in that each operator selected grains without prior knowledge of the specific grains measured by the other two workers. To allow a detailed statistical study, each operator reported the values of polar angles between the quartz c-axis and poles to the planes of PDFs, as well as the assigned specific Miller indices for each set measured, in a standardized, formatted Excel spreadsheet.

Results and Discussion: Results obtained by the different operators on the distribution of the frequency percent indexed PDF orientations are reported in Figure 2. Surprisingly, no major difference occurs from operator to operator; the average standard deviation on the orientation measurements between the three operators is only 1.2%, with a maximum standard deviation of 4.1% for the ω$\{10\bar{1}3\}$-equivalent crystallographic orientation in sample M8-427.7 (Fig. 2). Regarding the relative proportion of unindexed planes, it is evident that observer ability had an influence, as only about 7-8 rel% of the planes measured by the two experienced operators were unindexed, whereas the inexperienced operator reported 12-15 rel% unindexed planes (Fig. 2).

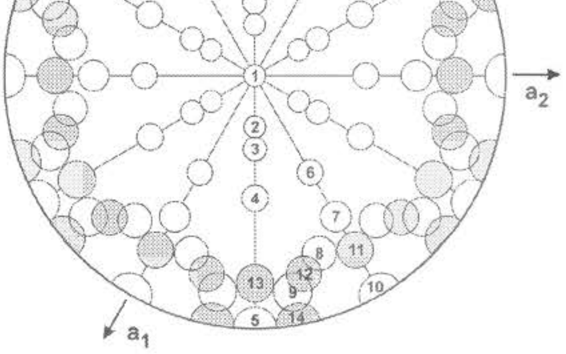

Plane	Angle to c-axis	Plane	Angle to c-axis	Plane	Angle to c-axis
1 (0001)	0.00°	**6 $\{11\bar{2}2\}$**	47.73°	**11 $\{22\bar{4}1\}$**	77.20°
2 $\{10\bar{1}3\}$	22.95°	**7 $\{11\bar{2}1\}$**	65.56°	**12 $\{31\bar{4}1\}$**	77.91°
3 $\{10\bar{1}2\}$	32.42°	**8 $\{21\bar{3}1\}$**	73.71°	**13 $\{40\bar{4}1\}$**	78.87°
4 $\{10\bar{1}1\}$	51.79°	**9 $\{51\bar{6}1\}$**	82.07°	**14 $\{51\bar{6}0\}$**	90.00°
5 $\{10\bar{1}0\}$	90.00°	**10 $\{11\bar{2}0\}$**	90.00°		

Figure 1. Standard stereographic projection of quartz with the c-axis in the center. Each circle (5° radius) marks the position of the PDF orientations in quartz. Modified from [2]; four additional PDF orientations (Planes 11-14) are indicated (grey circles).

For the same thin section, the number of PDF sets per grain (denoted D) varies from operator to operator (Fig. 2). However, the variation does not seem to be directly influenced by the observer experience. The total number of grains measured can influence D in the case of non-homogeneously shocked rock (further analyses are ongoing); an unintentional "selection" of the more heavily shocked grains can be another explanation. Nevertheless, it appears that D value variability between the three operators for each sample does not exceed ~20%. We are currently working on a chart that will allow the evaluation of the reliability and precision of U-stage measurements as a function of the number of grains and planes investigated, etc.

Recommendations: Using the revised indexing template (Fig. 1), which includes the positions of additional typical PDFs, the abundance of unindexed planes may be reduced by up to 5 rel%, especially in samples with common high-index planes. Use of such a revised template, however, requires a sufficient number of PDF sets per grain (at least 2 sets) to confidently plot both the polar and azimuth position of the high-index plane poles [cf. 2-4]. Further, it is critical that published PDF orientation histograms clearly define what frequency measurement is used (i.e., relative or absolute frequency [cf. 1-2]), whether or not unindexed PDF sets are included in the frequency calculations, and the numbers of grains and sets analyzed. This information is essential for comparing datasets from different studies or from different workers examining the same samples (cf. Fig. 2).

Acknowledgments: This work is supported by the Austrian Science Foundation (FWF), grant P18862-N10, and the Austrian Academy of Sciences. Bevan French is gratefully acknowledged for his ongoing assistance with this project.

References: [1] Engelhardt W. v. and Bertsch W. (1969) *Contrib. Mineral. and Petrol., 20,* 203-234. [2] Stöffler D. and Langenhorst F. (1994) *Meteoritics & Planet. Sci., 29,* 155-181. [3] Grieve R. A. F. et al. (1996) *Meteoritics & Planet. Sci., 31,* 6-35. [4] Langenhorst F. (2002) *Bulletin of the Czech Geological Survey 77(4),* 265-282.

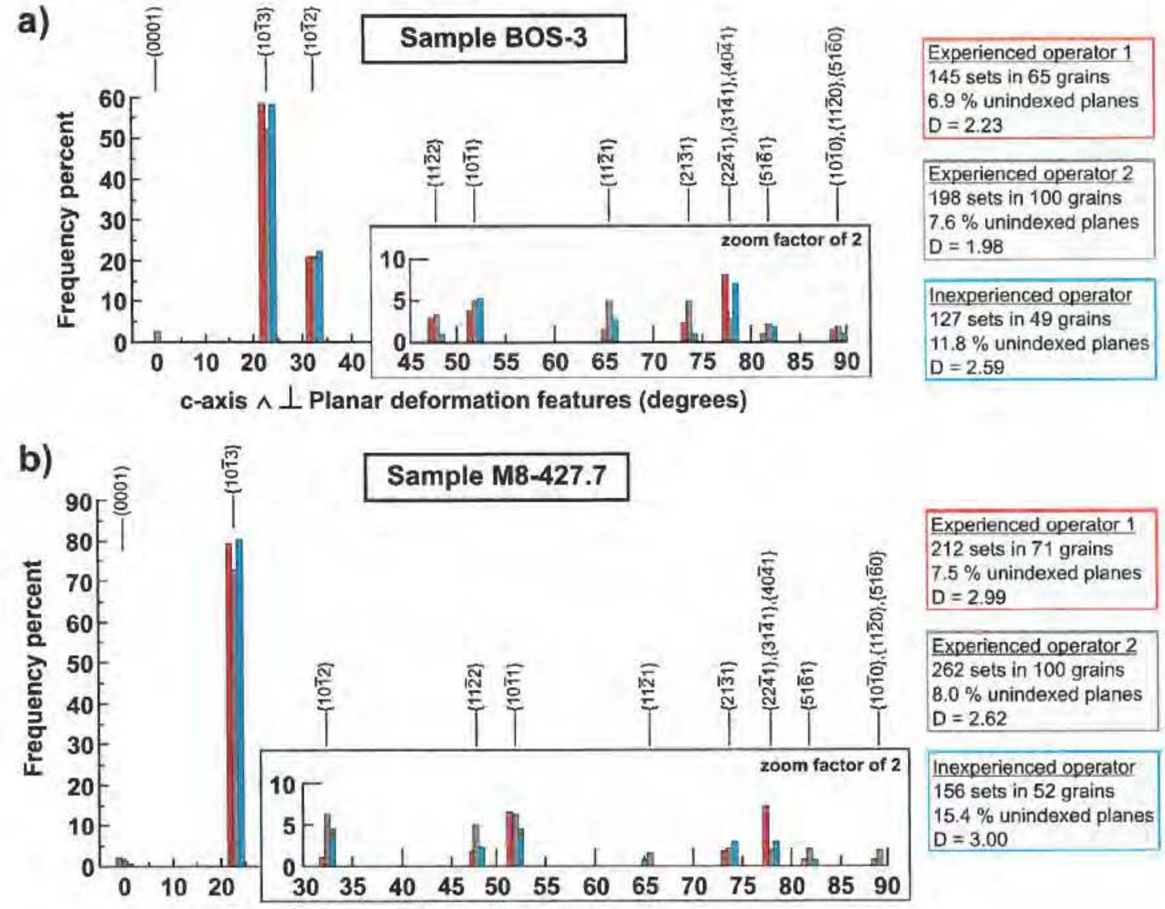

Figure 2. Histograms of the absolute frequency percent of indexed PDFs (recalculated to 100% without unindexed PDF orientations) in quartz grains from (a) BOS-3 and (b) M8-427.7, as determined by the three operators, two experienced and one inexperienced. Recalculation without unindexed PDF orientations, which vary between operators, was performed to allow consistent comparison of the datasets. The number of PDF sets per grain (denoted D) varies as well from operator to operator.

THE PALEOMAGNETIC RECORD OF LARGE METEORITE IMPACTS AND LUNAR MAGNETISM.

M. Fuller University of Hawaii

Models of lunar magnetism need to explain (a) strong Natural Remanent Magnetization (NRM) in some of the returned Apollo samples with ages from about 3.95Ae to 3.75Ae, (b) magnetic anomalies antipodal to the young basins of a similar age, (c) the absence of major magnetic anomalies over these same basins, (d) the presence of central anomalies over some Nectarian and PreNectarian basins, and finally (5) strong fields with scale lengths of homogeneity of the order of kms, or less, found over the Cayley Formations and similar material. Given the evident role of large impact basins on the moon in lunar magnetism, ground truth from large meteorite impacts are important. Here, we concentrate on the interpretation of the magnetism of the Apollo samples.

Observations (a) and (d) have frequently been taken to require the presence of a lunar dynamo. The samples all came from the regolith, so that their original orientation, when they might have acquired their NRM is not known. Emphasis then turned to the possibility of finding the intensity of the ancient fields in which the samples were magnetized. This has proved difficult because the necessary heating required in the classical paleointensity determinations produced irreversible changes, thereby for the most part invalidating the methods (1). Results from various methods, which did not involve heating, suggested that there was a strong field era, as we noted above. There was little evidence available for earlier times. There was a wide range of intensity values during the possible high field era. However, recent results (2) have now suggested that the possible high field era may have begun earlier and showed an even greater variability in intensity values. If there had been a lunar dynamo during this possible high field era, why are there so few samples that carry an unequivocal strong NRM appropriate for TRM (Thermal Remanent Magnetization) in the proposed dynamo fields? It is also an uncomfortable coincidence that the dynamo appears to cease to give strong fields close to the end of the time of heavy bombardment.

Given these difficulties with the interpretation of TRM acquired in a lunar dynamo field, it is worth reexamining other possible explanations of lunar magnetism. The obvious candidate is impact related shock magnetization, which already appears to provide an explanation for the magnetization of 62235, a key sample with strong magnetization. This sample passed standard criteria for satisfactory paleointensity yielding a value for the field comparable with the geomagnetic field. Yet examination of the alternating field demagnetization of this sample reveals that much of its magnetization is demagnetized by 40mT. Moreover, the demagnetization characteristics are similar to those from experimentally shocked basalts and suggest that the magnetization is probably SRM (Shock Remanent Magnetization). Similar results from samples known to be strongly shocked have prompted a reexamination of the level of shock experienced by lunar samples and the expected magnetic effects of these levels.

Although the magnetic record of the Apollo samples rather than crustal magnetization is the main emphasis of this work, it is clear that some variant of Hood's model accounts for the antipodal anomalies of the young basins (3) while the observations at Vredefort (4) and other terrestrial impact craters may relate to the anomalies over central peaks and uplifted ring structures in older major basins on the moon.

The key question that remains is whether magnetism acquired in impact related shock still requires a dynamo field source, or whether fields generated in the impact events can account for the paleomagnetic record.

References. (1) Lawrence, K.P. and Johnson. C.L., LPSC XXXIX, 1381, (2008) (2) Garrick-Bethell, I, and Weiss,B.P., LPSC XXXIX, 2521 (2008) (3) Hood, L.L. and Huang, Z., J. Geophys, Res. Lett., 96, 9837-9846, (1991) (4) Carporzen, L., Gilder, S.A., and Hart, R.A., Nature, 435, 198-201, (2005)

MAGNETIC IMAGING OF THE VREDEFORT DOME: IMPLICATIONS FOR THE SIZE AND GEOMETRY OF THE VREDEFORT CRATER.

A. Galdeano[1], M. A. G. Andreoli[2,3], R. J. Hart[4] [1]Institute de Physique du Globe, Equipe de Géomagnétisme, 75252 Paris Cedex 05 France. [2]Necsa, P. O. Box 582, Pretoria 0001, South Africa, [3] School of Geosciences, University of the Witwatersrand, P. O. Box 3, Wits 2050, South Africa, [4]iThemba Labs P. Bag 11 Wits 2050 Johannesburg, South Africa. Hart@tlabs.ac.za.

Introduction: Models which predict the original size of the Vredefort impact crater vary considerably between 200 and 300 km [e.g. 1,2,3,4]. This is largely due to the fact that so little of the original crater is visible to view to constrain modelling procedures. Most of the 2.0 Ga Vredefort crater has been eroded away and all that remains are the remanents of the central uplift, that is, the Vredefort dome [2]. This problem is further exacerbated by the fact that the southeast half of the dome is largely hidden from view by younger sediments (Fig 1b), which makes it difficult to fully visualize the structure and size of the dome in its entirety. In this study we combine geological observation with magnetic and gravity imaging across the dome and beyond in an attempt to visualize what the Vredefort crater may have looked like shortly after the ~2.0 Ga impact event.

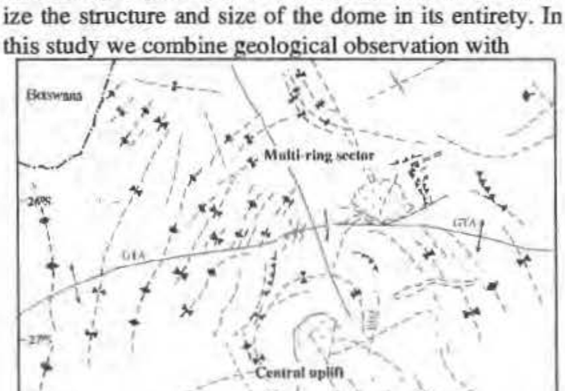

Figure 1. a) Geologic map of the Vredefort crater showing the central uplift, the multiring sector in the north and the hidden sector in the south. b) Geological map of the Vredefort dome and a northwest-southeast section across it. Vertical scale exaggerated. c) Inverted 3- D perspective image of the airborne magnetic image across the Vredefort dome. The outer negative anomaly (shown as positive peaks in blue) corresponds to the iron-rich shales of the Witwatersrand basin.

The Vredefort impact crater in a sketch: The eroded remnant of the grand Vredefort crater is subdivided in three broad, clearly distinct geological domains (Fig. 1a): the Central Uplift, the (north-western) Multiring Sector, and the (south-eastern) Hidden Quadrant. Current literature on the Vredefort impact crater is heavily biased on the Central Uplift. Conversely, much less has been written of the Multiring Sector where the position of the final rim is still uncertain, and virtually nothing on Vredefort-related features in the Hidden Sector.

The Central Uplift: Our modelling of the Central uplift of the Vredefort crater is largely based on the crust-on edge-model and the key observation that depleted upper mantle rocks are exposed near the centre of the crater. The model simply states that the northern half of the dome (Fig. 1b) consists of a 36 km wide arc of near vertical Mesoarchean and Neoarchean stratified rocks: a traverse across this sequence essentially corresponds to a traverse through the earths crust, culminating in depleted upper mantle near the centre of the dome [see 5,6, as well as counter arguments by 7].

The southeastern half of the Vredefort dome. The problem faced by all workers on Vredefort is that most of the southeast part of the dome is hidden from view by younger sediments (Fig. 1b). The few observations that we can make, all suggest that the lithology metamorphic grade and structure of the southeast side of the dome are very different from what is observed in the crustal section exposed in the north-west and most workers [8,9] believe that the northwest and southeast segments of the dome must be separated by a fault or shear zone. A km wide northeast trending zone of intense shearing at the locality Broodkop (see Fig.1a) provides the evidence for shearing. Previous workers [8,9] speculate that the shear zone may be part of an Achaean fault (circa 3.1 Ga) that has been rotated into its current sub-vertical orientation during central peak formation. However, to date, no definitive radiometric dating has been done on the Broodkop shear zone. Most of the arguments put forward by previous workers hinge around observations that are thought to suggest that the shearing observed at Broodkop has not affected the collar strata of the Witwatersrand supergroup. In contrast, our enhanced magnetic imaging suggest that the shearing in the south-east can be extended into the collar strata and has effected the entire Southeast sector of the dome, indicating collapse of the central uplift, shortly after the 2.0 Ga impact event.

Magnetic imaging. A 3-D perspective of the magnetic fields across the dome (Fig. 1c) clearly shows that the northwest and southeast sides of the dome are very different. Most notably, the prominent magnetic anomalies that are caused by ferruginous shales in the stratified rim in the northwest are largely missing in the southeast. It is also clear that the eastern and western limbs of the anomalies associated with the amphibolites-granulite transition are truncated across the centre of the dome (Fig. 1c), which strongly suggests the presence of a northeast trending structural discontinuity at this locality. An extension of this line into the eastern and western limbs of the stratified rocks also shows that the magnetic shales are significantly rotated and truncated both on the eastern and western sides of the dome (Fig. 1c). The few geological observations that have been made on the isolated outcrops that are found along the southeast flanks of the dome show that the attitude of the stratified rocks are chaotic having both overturned and normal dips [9].

The Multiring Sector. With this name we refer to the broad arc that encompasses the whole of the Witwatersrand basin in a series of concentric anticlines and synclines with the centre on the Vredefort structure (see Fig. 1a). This model has often been quoted as the basis to assign a diameter of up to ~350 km to the impact crater [1, 10]. More recent modelling of the Vredefort crater points to a rim-to-rim diameter of ~120-200 km [3]. On this basis the fold axes at radial distances >160 ± 40 km would be considered 'external rings', hence diagnostic of a true multiring impact crater [3]. More recently, however, slates and phyllites of the Transvaal Supergroup on the northern and western side of the Johannesburg dome yielded $^{40}Ar/^{39}Ar$ ages of ~2150.Ma and ~2043 Ma [1,12,13]. These ages coincide, within error, with the SHRIMP U-Pb ages of monazite and xenotime yielded by rocks and gold-bearing reefs within the Witwatersrand basin [14]. Significantly, no evidence of resetting was found by [11, 14] of resetting at 2023 Ma, the age of Vredefort [15]. The new ages for post-Transvaal deformation and metamorphism in the Witwatersrand Basin [14] and its hinterland [11] have an important bearing with regard to the Vredefort structure. Firstly, the data cast doubt on the hypothesis that the Vredefort impact caused the localized (small-scale), but region-wide remobilization of autigenic gold [16]. Secondly the new ages imply that the target of the Vredefort impactor was not represented by subhorizontal Transvaal Supergroup strata [17] but of rocks already deformed by the intracratonic "Transvaalide thrust and fold" belt [11].

The Hidden Sector: Practically all recent maps of the Vredefort structure show no geological structures past the edge of the Wits Basin southeast of Vredefort, in a an area where the basement is covered by a substantial Karoo cover. However, a robust linear element extending from Vredefort to the SSE is clearly visible in the regional Bouguer gravity image, This radial features, previously referred to as the Vredefort axis [18] was the object of detailed investigations by a number of mining companies, especially close to the town of Bethlehem. A combination of geophysical forward modeling, drilling and Vibroseis seismic profiles conducted over that area clearly reveal what has been referred to, in unpublished company reports, as the "Bethlehem structure". The latter consists of a very complex swarm of horst (suboutcrop granite), grabens (suboutcrops of Wits basin) and tangential thrusts fanning out from the core of Vredefort, past Bethlehem, up to a radial distance of ~170 km from the crater centre (see Fig. 1a). The Bethlehem Structure is difficult to explain with the current knowledge of how large craters form. However, the Bethlehem structure suggests impact–related deformation was still very robust at a distance of 170 km from the centre.

Acknowledgments: the authors are very grateful to the management of Gold Fields Ltd. for access to unpublished data.

References: [1] Therriault A. M. et al. (1997) *Meteoritics & Planetary Sci., 32*, 71-77. [2] Henkel H. and Reimold W. U. (2002) *J. Appl. Geophys. 51*, 43-62. [3] Turtle E. P. et al. (2005) *Geol. Soc. Amer. Spec. Paper 384*, 1 -24. [4] Ivanov B. A. (2005) *Solar Syt. Res. 39*, 381-409. [5] Hart R. J. et al. (1990). *Chemical Geology, 83*, 233-248. [6] Tredoux M. et al. (1999) *Geology, 27*, 923-926. [7] Gibson R. L. et al. (2005) *S. Afr. J. Geol. 108*, 309-313. [8] Hart R. J. et al. (2004) *S. Afr. J. Geol. 107*, 83-94. [9] Lana C. et al. (2006) S. Afr. J. Geol. 109, 265-278. [10] McCarthy T. S. et al. (1990) *S. Afr. J. Geol. , 93*, 1-4. [11] Alexandre P. et al. (2006) *S. Afr. J. Geol., 109*, 393-410. [12] Reimold W. U. et al. (2007) *S. Afr. J. Geol., 110*, 157-159. [13] Alexandre P. et al. (2007) *S. Afr. J. Geol., 110, 160-162*. [14] Rasmussen B. et al. (2007) *Geology, 35*, 931-934. [15] Kamo S. L. et al. (1996) *EPSL, 144*, 369-399. [16] Hayward C. L. et al. (2005) *Geol. Soc. London Spec. Publ., 248*, 31-58. [17] Lana C. et al. (2003) *Meteoritics Planet. Sci. 38*, 1093-1107. [18] Corner B. et al. (1986) *Geol. Soc. S. Afr., Proceedings Geocongress '86*, 27-30.

IMPACT-INDUCED VAPORIZATION OF MAGNESIOSILICATES: DOMINATION OF ENSTATITIC CLUSTER.

M.V.Gerasimov[1], Yu.P.Dikov[1,2], O.I.Yakovlev[1,3]. Russian Academy of Sci.: [1]Space Research Inst., Profsoyuznaya st., 84/32, Moscow, 117997, mgerasim@mx.iki.rssi.ru; [2]Inst. of Ore Deposits, Petrography, Mineralogy and Geochemistry; [3]Vernadsky Inst. of Geochem. and Analytical Chemistry; Moscow, Russia.

Introduction: Ultramafic and mafic minerals are the main components which could represent the material of large impacting meteorites. There is still a question about possible transformation of magnesiosilicates during high-temperature impact-induced processing, which form distal ejecta. Some early experimental works [1,2,3,4] stated congruent evaporation of forsterite giving no changes in the mineral composition. Sata et al. [5] argued for a certain disproportionation of Mg and Si between melt and vapor for forsterite and enstatite. Most of experiments on evaporation are performed at vacuum chamber pressures and temperatures not exceeding ~2500 K. Such conditions are not compatible with that of impact-generated dense vapor plumes with temperatures about 4000-5000 K. The goal of our experiments was to investigate behavior of Mg and Si during vaporization of ultramafic and mafic rocks and minerals at conditions typical for hypervelocity impact vaporization.

Experiment: Experiments were performed using two stage light-gas-gun (LGG) and laser pulse (LP) simulation techniques [6]. Expansion of the vapor cloud in LGG experiments was into ~10 mbar air and in case of LP experiments into 1 bar He gas. Condensates were collected on Ni and Cu foils which were placed into the path of the vapor plume expansion. Analyses of initial samples and of condensed films were performed using X-ray photoelectron spectroscopy (XPS) technique. Condensed films were etched layer by layer (with an exposition equivalent to removal of ~20 nm of solid silicate) by a beam of argon ions and for every layer XPS analysis was performed providing sequential chemical analysis of the cross-section of the film. XPS analyses gave both elemental chemical composition of the condensate and the distribution of elements between different bonding states.

LGG experiments were performed with olivinite and serpentinite targets (Cu projectile v_{imp} ~6 km/s). LP experiments were done with olivine, serpentine, pyroxene, enstatite, peridotite, and meteorites: Tsarev (L5), Etter (L5), Allende (CV3), and Indarch (EH4).

Experimental results: a) *Chemical composition.* Chemical bulk composition of starting samples and related condensates are presented in Fig. 1. Compositions of condensates are regularly shifted towards higher concentration of silicon and depletion in magnesium and iron. It is worth to note that in two cases (LP experiments with pyroxene and enstatite chondrite Indarch) the increase of Si/Mg ratio was insufficient.

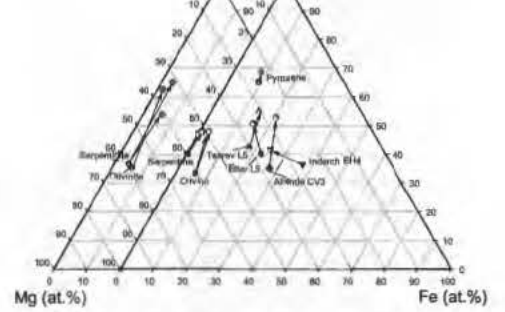

Fig. 1. Mg-Fe-Si ternary diagrams for chemical bulk compositions of starting samples (dark symbols) and their condensates (transformation is indicated by arrows). Left diagram is related to LGG experiments and right one to LP experiments.

It was also interesting to find that Mg/Si ratio for olivine, serpentine and enstatite through the thickness of the condensed films was about unity (see Fig.2).

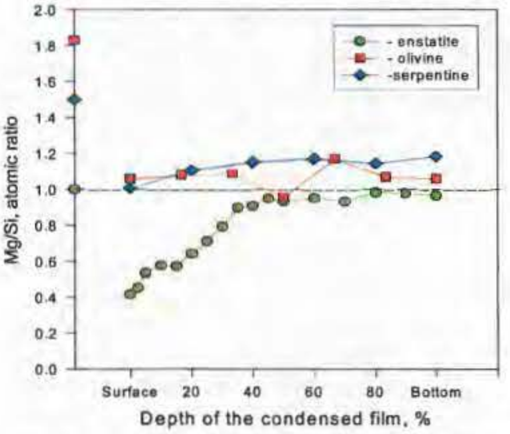

Fig. 2. Mg/Si profiles through the thickness of the condensed films which were produced during LP experiments with olivine, serpentine and enstatite. Symbols on the ordinate indicate Mg/Si ratios in starting samples.

Recalculated composition of olivine condensate corresponded to En 93-95. That indicates the shift of composition of condensate during evaporation of olivine toward enstatite but no reasonable changes for enstatite.

b) *Chemical structure*. There is a uniformity of chemical structure of condensed materials which is characterized by dominant chain polymerization of silicon-oxygen tetrahedrons with sufficient portion of framework and some portion of isolated structures (see Fig. 3). Condensed films also contain some quantities of reduced forms of elements (Si^{+2}, Si^{0}, Fe^{0}, Mg^{0}) as a result of redox processed inside a vapor cloud [7]. Condensates from LP experiment with olivine and from LGG experiment with olivinite have good structural coincidence. It is remarkable that both olivine and olivinite condensates are characterized by the absence of isolated silicon-oxygen tetrahedrons but polymerization of tetrahedrons in chain and framework structures. Here we have a total loss of initial olivine structure and its transformation towards pyroxene type structure. Mg is redistributed between chain polymerization and traces of reduced and pure oxide forms.

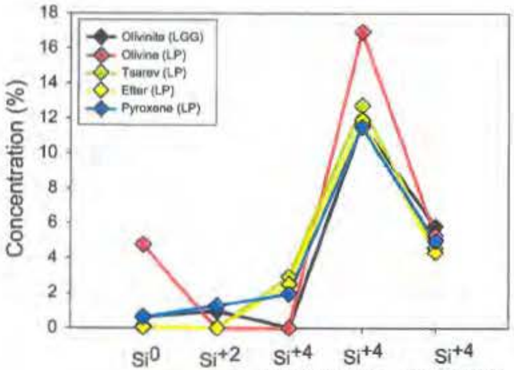

Fig. 3. Proportions between different polymerization types of Si in bulk condensates which were produced in LGG experiment with olivinite and LP experiment with olivine, pyroxene, and meteorites Tsarev and Etter.

In case of experiments with serpentine and serpentinite their condensates had mostly layered structure. About 1/3 of magnesium here was present in the form of $Mg(OH)_2$. This effect was due to the interaction of plume components with water vapor inside the vapor cloud [8] which provided ~14 wt. % of water chemically bound to condensate.

Discussion: Produced condensates show compositional uniformity for Mg/Si ratio and chain polymerization. This effect works for ultramafic and mafic minerals providing in one case deep difference between starting samples and their condensates (e.g. olivine, serpentine) but week change for other (e.g. pyroxene, enstatite).

Near critical point vaporization of complex systems is characterized by volatilization of molecular clusters [6] which can become a dominant part of the vapor. Cited effect provides strong evidence for volatilization of Mg and Si from high-temperature melts as molecular clusters which have Mg/Si ratio about 1, or "enstatite" cluster. The effect is more evident for simple minerals while for complex samples it is obscured by multiple vapor components.

Thermodynamic evaluation was done using "Magma" code [9] which uses empirical model of ideal mixing of complex components in the silicate melt. Such an approach considers silicate melt as an ideal mixture of complex oxides and silicate pseudocomponents (clusters). The concentration of such pseudocomponents is proportional to their stability in the melt. Extrapolation of thermodynamic data to temperatures up to 5000 K shows that at temperatures over ~2500 K melts looses the domination of "olivine" clusters and "enstatite" clusters become dominant. Calculations shows that "enstatite" component is dominant in high-temperature melts (>2500 K). SiO_2 has noticeable activity which provides framework features (see Fig. 3) in condensates. "Olivine" component rapidly decreases with growing temperature and gives low input of isolated features in condensates. MgO component is abundant in melts but shows volatility less than that of "enstatite" cluster providing enrichment of melt residua in Mg.

Volatility of elements in the form of molecular clusters is the effect of very high temperatures which are typical for impacts. Disproportion of elements between plum and residual melt in impacts is more an effect of cluster formation rather than their behavior according to the row of elements individual volatility.

Acknowledgment: This work was supported by RFBR grant 07-05-01054.

References: [1] B.O.Mysen, J.Kushiro (1988) *American Mineralogist*, v. 73, p. 1-19. [2] H.Nagahara et al. (1988) *Nature*, v. 331, p. 516-517. [3] A.Hashimoto (1990) *Nature*, v. 347, p. 53-55. [4] J.D.Kubicki, E.M.Stolper (1993) *LPSC XXIV*, p. 829-830. [5] T.Sata et al. (1978) *Rev. Houtes. Refract., Fr.*, v. 15, p.237-248. [6] Gerasimov M.V., et al. (1998) *Earth, Moon, and Planets*, vol. 80, Nos. 1-3, pp.209-259. [7] O. I. Yakovlev, et al. (2006) *Geochemistry International*, vol. 44, No 9, pp. 847-854. [8] Gerasimov M.V., et al. (2002) *Deep-Sea Research Part II: Topical Studies in Oceanography*, vol. 49, No 6, pp. 995-1009. [9] B.Fegley,Jr, A.G.W.Cameron. *Earth and Plenet. Sci. Lett.*, 82, 1987, p. 207.

GEOTOURISM POTENTIAL OF THE VREDEFORT DOME, SOUTH AFRICA – CHALLENGES, OPPORTUNITIES, PROGRESS AND RECOMMENDATIONS.

R.L. Gibson[1] and M. Blom[2], [1]Impact Cratering Research Group, School of Geosciences, University of the Witwatersrand, P/Bag 3, P O WITS, Johannesburg 2050, South Africa, roger.gibson@wits.ac.za; [2]Fezile Dabi District Municipality, Box 10, Sasolburg 1947, South Africa.

Introduction: The Vredefort Dome is a 90-km-wide geological entity located ~120 km southwest of Johannesburg, South Africa, that represents the eroded central uplift of the world's oldest (2023 ± 4 Ma) and possibly largest known meteorite impact structure. It is a site of unprecedented geological significance not only because of the impact-related effects visible in its rocks, but also because it is one of only a handful of areas around the world that exposes a near-continuous, >25 km deep, crustal section.

The topographic expression of the dome is restricted to its northern and western sectors (the remainder being covered by younger sedimentary strata), with the most prominent feature being a crescent of steep ridges and valleys cut by the Vaal River. The combination of the spectacular rugged scenery and the Vaal River has created a well-established tourism industry that is primarily focussed on recreational and adventure tourism and the business market. By contrast, geotourism linked to the spectacular geological features is relatively minor, being restricted to a few information displays in resorts and *ad hoc* tours run by local enthusiasts and academics. In 2005, a 30000 ha portion of the dome (approximately one-quarter of the exposed area of the dome) was inscribed as a World Heritage Site (VDWHS) on the strength of the dome's internatonal geological significance.

Challenges: The most significant challenges to the development of the geotourism potential of the Vredefort Dome relate to its immense size and the deep levels of erosion, and to the land ownership profile in the dome. In the first instance, the large size presents an interpretive challenge as visitors cannot drive or walk up to a single viewpoint from which they can see the entire structure, such as is possible, for instance, at Tswaing crater. Second, large distances may need to be travelled between different geosites, which makes it difficult for the visitor to maintain perspective. The deep levels of erosion also create confusion about the size of the feature – the crescent of hills defining the Vredefort Mountainland is commonly confused with the crater rim because visitors are looking for a classic bowl-shaped crater. Whereas previously the Vredefort Dome was often mistaken as the Vredefort crater, additional confusion has arisen recently among visitors who equate the WHS area with the Vredefort crater. The deep levels of erosion, which have completely removed the crater topography and most of the tell-tale breccias and impact deposits, also mean that any explanation of the geological significance of particular features requires lengthy explanation if first-time visitors are to build an understanding of the Vredefort impact event. Logistically, the fact that 89% of the land in the WHS is privately owned, with many absentee owners, creates a challenge for access to key sites, as well as issues such as accident liability.

Progress: Following the WHS inscription in 2005, provincial and district and local municipal structures have embarked on several projects aimed at enhancing the geotourism potential of the VDWHS and the larger dome region, including a 3-year roads programme aimed at upgrading much of the 145 km of gravel road in the WHS. A Strategic Environmental Assessment (2006) and an Integrated Management Plan (2007) were completed for the North West and Free State Province governments, respectively. These assessments have considered the VDWHS holistically, examining other resources (archaeological, cultural, biodiversity) and other challenges to development and management of the natural resources, including pollution, access, communication and socio-economic and legal aspects. The Free State government has sponsored additional projects aimed at addressing some of the challenges presented by the geology of the dome. These include the distribution of information pamphlets and accompanying posters outlining the geological features that are freely available to visitors and locals (in English, Afrikaans and Sesotho), and a summary brochure outlining the main conclusions of the 2000-page Integrated Management Plan, as well as posters for public display. A geological guidebook and audiovisual presentation are also planned. The Fezile Dabi District Municipality has built a Visitor and Geological Interpretation Centre outside Vredefort town that, once completed in 2009, will address the challenges of explaining to visitors the problems of scale and erosion depth that characterise the Vredefort impact structure as well as showcasing other geological features of the dome. This centre will also provide a hub for the development of local crafts industries, thereby allowing economic upliftment through small enterprise development, and should become a key tourism site in its own right.

Recommendations: Several key initiatives have already been set in motion to address the dissemination of information concerning the geological heritage resources of the Vredefort Dome. One of the acknowledgements of the IMP is that the selection of only a small portion of the dome as a WHS (for historical as well as logistical reasons) presents new management challenges, and the possibility of creating a UNESCO Geopark covering the rest of the dome and several key geosites presently outside of the VDWHS must receive serious consideration. Geotourism also needs to be managed within the context of the other attractions of the area. Specifically, the dome area contains a wide range of habitats that have promoted a broad floral biodiversity, and the re-introduction of large game animals by the tourism sector is strengthening the faunal biodiversity once more. Additionally, the area contains a highly diverse archaeological and cultural-historical heritage, ranging from Stone Age San-Bushman petroglyphs and tool-making sites to extensive Iron Age settlement ruins, traces of the earliest European settler dwellings, an historic goldfield and several key sites related to the Anglo-Boer War of 1899-1900. In contrast to the geology, these resources have received little attention from researchers and require immediate attention so that suitable heritage sites may be identified for tourism purposes.

The private ownership of much of the land raises issues of access to key geosites. The Management Authority will need to assess a variety of measures, including purchase of land and facilitation of access (re-aligning fences, stiles, gates); however, an alternative that may need to be considered is the creation of roadside stops that allow easy access to visitors and that can be arranged in a story format, with visitors progressing from one stop to the next in a specific order. If placed strategically between proper outcrop geosites, these 'artificial' sites can allow visitors to learn about the geological aspects of the dome at the same time as enjoying scenic views and information about cultural and heritage resources. Consideration should also be given to enhancing the value of specific sites of cultural and biodiversity significance by emphasizing nearby geological features. Owners of tourist establishments should also be encouraged to enhance hiking, riding and biking trails for their guests with geological information.

Much of the value of enhanced geotourism in the Vredefort Dome to the local population will lie in the tourism support industries (accommodation, catering). Given its close proximity to Johannesburg and the excellent road links, the challenge is to get visitors to view the Vredefort Dome as an overnight destination, rather than just a day-visit site. The creation of an interest in the geological resources, together with the opportunity to explore cultural and biodiversity resources and engage in a range to adventure activities can, if properly packaged, achieve this goal. With the necessary visitor numbers, additional job creation linked directly to the tourist experience (properly trained museum and field guides and educational officers) will create additional benefits.

Aside from the local and international tourism market, the Vredefort Dome is ideally placed to align itself as a first-choice destination for field school educational activities serving the highly populace Gauteng region. At present, such activities involve a combination of adventure activities (hiking, rafting, abseiling) with ecological awareness activities. By presenting a combination of geological and cultural heritage-based learning activities in addition to this standard format, a more holistic educational programme can be presented that will set it apart from its competition.

Conclusions: The Vredefort Dome is an area of superlative geology, rare scenic beauty, rich biodiversity and cultural heritage that is located close to South Africa's major international gateway and largest population centre. Development and effective management of its geological and other heritage resources as a tourism and educational resource has the potential to uplift an economically-depressed region and act as a flag-bearer for the development of other geological heritage resources in South Africa. A joint marketing initiative with the other principal tourist attractions of the Gauteng region (Cradle of Humankind, Origins Centre, Apartheid Museum) will strengthen its international profile.

THE HOTTEST ROCKS IN THE VREDEFORT DOME, SOUTH AFRICA – EXTENDING THE LINKS BETWEEN IMPACT-INDUCED AND "NORMAL" METAMORPHISM.

R.L. Gibson and P. Ogilvie, Impact Cratering Research Group, School of Geosciences, University of the Witwatersrand, P/Bag 3, P O WITS, Johannesburg 2050, South Africa; roger.gibson@wits.ac.za.

Introduction: Impact structures are sites of extreme pressure and temperature fluctuations related to the interaction and decay of the shock wave with the target rocks through which it passes. Temperatures closest to the point of impact are invariably sufficiently high to fuse target rock to produce a range of melt-rocks that are preserved either as glasses or supercooled crystalline impact-melt bodies. Further from the point of impact, intact target rocks display a variety of shock metamorphic features that range, with increasing radial distance, from mineral melts and shock glasses to high-pressure polymorphs, intragrain deformation effects (planar deformation features, planar fractures) and, ultimately, rock-scale fracturing. This pattern reflects the decrease in shock pressure and, consequently, shock-induced heating, in the impact structure.

In most impact structures, the volume of rock affected by elevated shock-induced temperatures is both small and restricted to the upper few kilometres of the planetary crust. As a consequence, the thermal anomaly caused by the impact is comparatively short-lived, and features such as shock glasses may be preserved essentially undisturbed as the thermal anomaly that accompanied their formation is rapidly dissipated by conduction and hydrothermal fluid circulation. It is unsurprising, then, that shock metamorphism is largely ignored by mainstream metamorphic petrologists as violating the fundamental tendency of "normal" metamorphic rocks towards chemical equilibrium.

In the 90-km-wide Vredefort Dome, however, the combination of a giant impact event and deep levels of subsequent erosion presents a unique window into shock metamorphosed rocks that were buried by between 8 and 11 km following the impact and that, consequently, cooled from shock-metamorphic temperatutes over time-scales that begin to approach those seen in contact-metamorphic aureoles.

Geological Setting: The Vredefort Dome, located 120 km southwest of Johannesburg, South Africa, forms the eroded central uplift of the originally much larger, 2023 ± 4 Ma, Vredefort impact structure [1,2]. The most recent field-based estimates of the size of the Vredefort crater range from 250 to 300 km, however, numerical modeling studies by [3] and [4] suggest a diameter of 170-180 km. Greater agreement exists on the amount of structural uplift, with rocks originally buried at ~25-27 km depth before the impact now exposed in the central parts of the dome [4,5]. The dome comprises a central, 40 km wide core of upper amphibolite to granulite facies Mesoarchean granite-greenstone gneisses that is surrounded by a 20-25 km wide collar of Mesoarchean to Paleoproterozoic supracrustal rocks [2]. Impact-melt rock is found in several vertical, kilometres-long dykes and the rocks contain abundant voluminous pseudotachylitic breccias, the origin of which remains debated. Shatter cones, decorated PDFs in quartz and rare coesite and stishovite associated with shock melt veins provide additional evidence of the impact event (see review in [2]).

Shock metamorphism in the Vredefort Dome: Initial studies of PDF orientations in quartz (e.g., [6]) noted an apparent lack of increase in the shock pressure towards the center of the dome, and [7] suggested that the absence of any definitive shock evidence in other major rock-forming minerals in the central parts of the dome was problematic. However, [8] subsequently determined that the absence of shock glasses relates to the slow rates of cooling of the shocked rocks. They documented a range of mineral textures that they inferred to be the product of annealing of diaplectic feldspar glasses and feldspar, biotite and amphibole mineral melts, as well as whole-rock melts that resemble the pseudotachylitic breccias seen at greater radial distances in the dome. From this they conservatively deduced shock pressures in excess of 30 GPa. Cation-exchange thermometry suggested post-shock temperatures in excess of 700 °C and possibly as high as 900 °C [5,9]; however, considerable uncertainty accompanied these estimates as a result of the well-known problem of retrograde re-equilibration at high temperatures. Complicating matters further was the uncertainty regarding the degree to which chemical equilibrium was likely to have been attained in these rocks.

This study: Detailed analysis has been performed on the rocks lying within ~8 km of the center of the Vredefort Dome to determine their post-impact thermal history. These rocks straddle the lower limit of shock glass formation in feldspar, which has been experimentally constrained by [10] for similar rocks as occurring at 25-30 GPa. Within 5 km of the center, the unusual glassy, indurated appearance of the rocks ("Inlandsee granofels") signifies almost complete recrystallization of the coarse (1-20 mm) Archean gneiss feldspar grains into extremely fine-grained (10-50 micron) aggregates, inferred to be pseudomorphs after shock glass and, locally, melt [8,11]. Recrystallization appears to have been largely static, however, the granofelses contain some evidence of plastic deformation of the original Archean foliations.

Garnets in metapelitic units within the greenstone granulites are surrounded by complex coronas of cordierite+orthopyroxene±plagioclase±biotite±spinel. These coronas are considerably finer-grained and more complex than garnet coronas in regional metamorphic belts, consistent with faster cooling from high temperatures. Detailed compositional mapping and diffusion modeling have confirmed that the Vredefort coronas reflect highly variable reaction affinities that indicate arrested reactions. Applying non-equilibrium thermobarometry to these textures has quantified the post-shock temperatures and established a strong lateral thermal gradient, ranging from ~740 °C at 8 km from the center of the dome to 890-920 °C at 5 km; however, THERMOCALC [12] phase-equilibria modeling suggests that these temperatures also reflect retrograde cation exchange and that original temperatures may have exceeded 900 °C throughout the section. The latter is in good agreement with THERMOCALC phase-equilibria modeling of highly aluminous cordierite+K-feldspar+spinel±corundum±rutile±sillimanite metapelitic assemblages from ~4 km from the center of the dome that suggests temperatures in excess of 1000 °C. Conventional cation-exchange thermometry for these rocks ([5]) also does not constrain the peak temperatures.

Discussion: The geothermometric results obtained from the central parts of the Vredefort Dome are in very close agreement with the numerical modeling predictions of [4], and indicate an overlap with the metamorphic conditions encountered only very rarely in contact-metamorphosed xenoliths in mafic-ultramafic igneous complexes. In fact, modeling predicts temperatures as high as 1300 °C [4], which are unattainable in contact metamorphic rocks, but may have assisted plastic deformation of the granofelses during central uplift formation. According to [4], these temperatures should have persisted for several hundred thousand years. The exceptional lateral thermal gradient of ~60 °C/km recorded in the central parts of the Vredefort Dome also indicates that the primary contributer to the post-shock temperature must have been the increase in the shock pressure conditions towards the center of the dome. This is despite the fact that both structural mapping [13] and the numerical modeling [4] indicate that the central parts of the dome show little rotation of the crust. This lateral gradient rules out the heating being caused by an overlying impact melt sheet. Finally, given that the pre-impact crustal geotherm could not have exceeded 20 °C/km [14], and using the depth estimates of 25-27 km obtained by [4], these figures can be used to obtain an estimate of the amount of shock heating that must have occurred. Temperatures in excess of 1000 °C suggest a shock heating component of between ~500 and ~650 °. Comparison with the data of [15] suggests that peak shock pressures must have lain between 40 and 45 GPa over the inner 5 km from the center of the Dome, revising the previous estimates upwards and agreeing well with the numerical modeling predictions [4].

References: [1] Kamo et. al (1996) *EPSL, 144,* 369-388. [2] Gibson R.L. and Reimold W.U. (2001) *Memoir Council for Geoscience, 92,* 111p. [3] Turtle E.P. et al. (2003) *MAPS, 38,* 293-303. [4] Ivanov, B. (2005) *Solar Sys. Res., 39,* 381-409. [5] Gibson R.L. (2002) *JMG, 20,* 57-70. [6] Grieve R.F. et al. (1990) *Tectonophys., 171,* 185-200. [7] Reimold W.U. (1990) *SAJG, 93,* 645-663. [8] Gibson R.L. and Reimold W.U. (2005) *GSA Spec. Paper, 384,* 329-349. [9] Gibson R.L. et al. (1998) *Geology, 26,* 787-790. [10] Ogilvie P. et al. (2007) *LPS XXXVII,* Abstract #1551. [11] Gibson R.L. et al. (2002) *Geology, 30,* 475-478. [12] Holland T.J.B. and Powell R. (1998) *JMG, 16,* 309-343. [13] Lana C. et al. (2003) *MAPS, 38,* 1093-1107. [14] Gibson, R.L. and Jones, M.Q.W. 2002. *Basin Res., 14,* 169-181. [15] Stoffler D. (1984) *J. Non-crystalline Solids, 67,* 465-502.

NORTH-AMERICAN MICROTEKTITES ARE MORE OXIDIZED COMPARED TO TEKTITES.

Gabriele Giuli[1*], Sigrid Griet Eeckhout[2], Maria Rita Cicconi[1], Christian Koeberl[3], Bill P. Glass[4], Giovanni Pratesi[5], and Eleonora Paris[1]. [1]Dip. Scienze della Terra, Università di Camerino, Italy; gabriele.giuli@unicam.it. [2]European Synchrotron Radiation Facility (ESRF), Grenoble, France. [3]Dept. of Lithospheric Research, University of Vienna, Austria. [4] Dept. Geology, University of Delaware, Newark, USA. [5]Dip. Scienze della Terra, Università di Firenze, Italy

Introduction: Despite the availability of geochemical studies on microtektites, very few studies exist of the Fe coordination number and oxidation state in such materials. As microtektites constitute a large fraction of the mass of the glass produced by a tektite-generating impact event, such studies are of great importance for a more complete understanding of impact-generated glasses and, in particular, to try to reconstruct the oxygen fugacity conditions prevailing during impact melt formation.

Previous data showed a set of microtektites from the North American strewn field to be consistently more oxidized with respect to microtektites from the other strewn fields [1]. This case is unique among tektites and microtektites and, if confirmed, may provide further constrains for a better understanding of microtektites generation processes. In order to confirm previous data, we studied a larger set of microtektites from the same strewn field from other four DSDP cores collected at different distances from the source crater and spanning a wider compositional range. For comparison, also four bediasites and two georgiaites have been studied, as well as a tektite fragment from the DSDP612 site.

Experimental: The XANES data have been collected at the ID26 beamline of the ESRF storage ring (Grenoble, F) using a Si (311) monochromator and with a beam size at the sample of 55 x 120 μm.

XANES spectra have been collected in fluorescence mode over a 270 eV energy interval across the Fe K-edge (7112 eV) with a 0.1 eV energy step and 45 ms counting time. Average of about 20 scans for each sample allowed to obtain very good signal to noise ratios despite the low beam size. The energy reproducibility has been estimated to be 0.05 eV or better.

Background subtracted pre-edge peaks have been fitted with sums of two to three pseudoVoigts components according to the procedure described in [2].

Results: XANES spectra of few samples are shown in Fig. 1. The spectra display only few wide features, as is expected for amorphous material. The inset shows the background subtracted pre-edge peaks along with the pseudoVoigt components used for extracting centroid energy and integrated intensity. Clear differences can be detected in the shape of these pre-edge peaks related to the amount of trivalent Fe present. Comparison with pre-edge peak data (integrated intensity and centroid energy) of Fe model compounds with known oxidation state and coordination number can provide information on Fe oxidation state and coordination environment in the studied glasses.

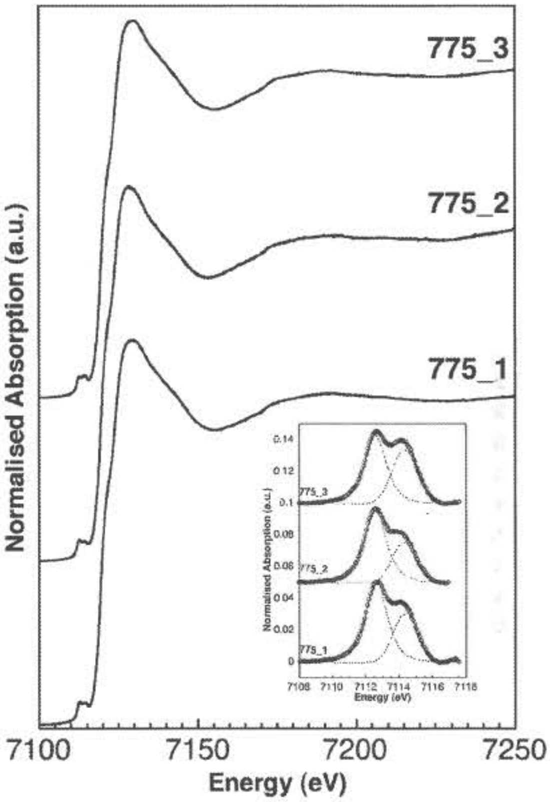

Fig. 1: example of Fe K-edge XANES spectra North American microtektites.

Figure 2 shows the pre-edge peak data of all the samples studied. The origin of the X axis refers to the edge energy of metallic Fe. Shadowed ellipses show the fields for Fe model compounds (numbers in square brackets refer to the coordination numbers), whereas the open ellipse encloses values found for a range of tektites from all four known strewn fields.

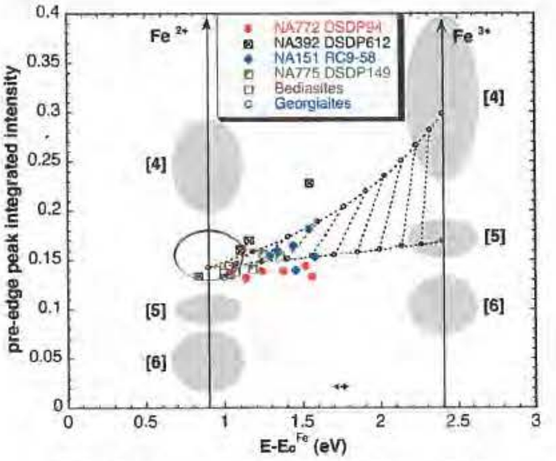

Fig. 2: Pre-edge peak integrated intensity vs. centroid energy. 0 refers to the edge energy of metallic Fe.

Data for the analyzed bediasites and georgiaites plot within the open ellipse, as expected. Thus, for these samples, Fe is essentially divalent and in a mixture of [4] and [5] coordinated sites. On the other hand, data for the North-American microtektites plot well outside this range, extending up to 0.6 eV at higher energy with respect to divalent Fe model compounds.

Mixing lines can be calculated between possible end-members in order to quantify $Fe^{2+}/(Fe^{2+}+Fe^{3+})$ ratios. Most data plot along a trend, falling between two mixing lines joining a point calculated as the mean of a group of the tektites studied so far (consisting of 4- and 5- coordinated Fe^{2+}) to $^{[4]}Fe^{3+}$ and $^{[5]}Fe^{3+}$, respectively. Thus, the XANES spectra can be interpreted as a mixture of $^{[4]}Fe^{2+}$, $^{[5]}Fe^{2+}$, $^{[4]}Fe^{3+}$ and $^{[5]}Fe^{3+}$. There is no evidence for six-fold coordinated Fe; however, its presence in small amounts cannot be excluded from XANES data alone.

$Fe^{3+}/(Fe^{2+}+Fe^{3+})$ ratio of the studied North American microtektites range from 0 to 45 (±5) %.

Discussion: No obvious correlation has been found between Fe oxidation state and chemical composition of the studied microtektites. In particular, no inverse relationship has been found with Na depletion, which might have been expected in case of oxidation due to sea-water alteration; no any other correlation has been found that would suggest alteration in a marine environment.

Thus, we believe that the oxidation states determined are a signature of the formation process of these microtektites, and not the product of subsequent alteration. Such a wide range in Fe oxidation state is unique within microtektites: microtektites from the Ivory Coast and Australasian strewn fields contain almost purely divalent Fe, as do tektites from the same strewn fields[1, 2].

The marked difference in the $Fe^{3+}/(Fe^{2+}+Fe^{3+})$ ratio of tektites and microtektites from the North American strewn field raises the question whether or not microtektites should simply be considered as microscopic analogous of tektites.

Although no clear explanation can be provided, we note a similarity with impact glass spherules from the K/T boundary, which showed a similar trend in pre-edge peak data extending up to 100% trivalent Fe [3,4]. Remarkably, both impacts were of considerable size and occurred in a shallow marine environment. As the variation in Fe oxidation state of K/T impact glass spherules may be explained by oxidation of the impact melt droplets within a CO_2- and/or H_2O-rich plume, we suggest that a similar mechanism may have worked in the case of North American microtektites. However, no chemical correlation has been found with Fe oxidation state to support this suggestion so far.

References:

[1] Giuli G. et al. (2007) Meteoritics and Planetary Sciences, 42, A56. [2] Giuli G. et al. (2002) *Geochimica et Cosmochimica Acta*, 66, 4347-4353. [3] Giuli G. et al. (2005) *Meteoritics and Planetary Science*, 40, 1575-1580. [4] Giuli G. et al (2008). *Meteoritics and Planetary Science*, 43, (in press).

VARIATIONS IN FE OXIDATION STATE BETWEEN DARK AND LIGHT LAYERS OF MUONG NONG-TYPE TEKTITES.

Gabriele Giuli[1*], Sigrid Griet Eeckhout[2], Giovanni Pratesi[3], Christian Koeberl[4], Maria Rita Cicconi[1], and Eleonora Paris[1]. [1]Dip. Scienze della Terra, Università di Camerino, Italy; gabriele.giuli@unicam.it. [2]European Synchrotron Radiation Facility (ESRF), Grenoble, France. [3]Dip. Scienze della Terra, Università di Firenze, Italy; [4]Dept. of Lithospheric Research, University of Vienna, Austria.

Introduction: Muong Nong tektites differ in appearance from common splash form tektites by being larger, having irregular blocky shape, and a layered structure. Usually, dark layers are less abundant and, in thin section, they seem embedded in a light colored matrix. Systematic chemical and physical variations are observable between dark and light coloured layers. In particular, light layers display a relatively higher Al and Fe content and a lower Si content with respect to dark layers. Moreover, the light layers have a higher refractive index (see [1] and references therein for a more complete description of Muong Nong type tektites from the Australasian tektite strewn field) .

Previous unpublished XANES data have been collected on powder samples obtained by hand-picking separation of dark and light layers of three different Muong-Nong samples. These data showed small but detectable differences in the Fe oxidation between dark layers and light layers, the former being slightly but reproducibly more oxidized.

A new set of data has been acquired with an X-ray micro-beam on a thin section of a Muong Nong indochinite sample across the boundary between a dark layer and the light matrix in order to confirm wether or not there are systematic variations of the Fe oxidation state across Muong Nong layers.

Experimental: The XANES data have been collected at the ID26 beamline of the ESRF storage ring (Grenoble, F) using a Si (311) monochromator and with a beam size at the sample of 55 x 120 μm.

XANES spectra have been collected in fluorescence mode over a 270 eV energy interval across the Fe K-edge (7112 eV) with a 0.1 eV energy step and 45 ms counting time. An average of about 20 scans for each sample allowed to obtain very good signal to noise ratios despite the small beam size. The energy reproducibility has been estimated to be 0.05 eV or better.

Background subtracted pre-edge peaks have been fitted with sums of two to three pseudoVoigts components according to the procedure described in [2].

Results: Experimental XANES spectra are very similar in shape to those of tektites already published. However, small and reproducible changes occur in the pre-edge peak involving the centroid energy: the pre-edge peak of the spectra collected within the dark layer is reproducibly 0.2 eV at higher energy than those of the spectra collected within the light matrix. This difference in energy position is four times the estimated energy reproducibility and, therefore, is significant.

By comparison with pre-edge peak data of Fe model compounds, we estimate the $Fe^{3+}/(Fe^{2+}+Fe^{3+})$ ratios in the light matrix and dark layer of the studied sample to be 5 % and 15 % (±5) respectively.

References:

[1] Koeberl, C. (1992) *Geochimica et Cosmochimica Acta*, 56, 1033-1064. [2] Giuli G. et al. (2002) *Geochimica et Cosmochimica Acta*, 66, 4347-4353.

SHOCK FEATURE ANALYSIS OF SELECTED SAMPLES FROM THE EYREVILLE CORE: CHESAPEAKE BAY IMPACT STRUCTURE, VIRGINIA, USA.

J. Glidewell[1], R. S. Harris[2,3], D. T. King, Jr.[4], and L. W. Petruny[5], [1]Jackson School of Geosciences, University of Texas, Austin, TX 78712 USA [glidewell@mail.utexas.edu], [2]Dept. of Geological Sciences, Brown University, Providence, RI 02912 USA [robert_harris@brown.edu], [3]Dept. of Geology, University of Georgia, Athens, GA 30602 USA, [4]Dept. of Geology, Auburn University, Auburn, AL 36849 USA [kingdat@auburn.edu], [5]Astra-Terra Research, Auburn, AL 36831-3323 USA [lpetruny@att.net].

The Chesapeake Bay impact structure (CBIS) is an 85 km-diameter buried crater centered near Cape Charles, Delmarva Peninsula, Virginia. The CBIS is a well-preserved feature and core samples from the mile-long Eyreville drill core provide a remarkable opportunity for analysis of shock metamorphism. Several likely shock-related features of selected samples from the ICDP/USGS CBIS Deep Drilling Project Eyreville core have been analyzed from throughout the impact-structure filling sequence.

Our work is built upon results from [1, 2, 3], further measurements of planar microstructures on a petrographic microscope fitted with a U-stage, and additional supplemental analyses.

Shock metamorphic effects: Effects of what may be at least low levels of shock deformation are noted in each section of the stratigraphic column of the Eyreville core as outlined by [3, 4, 5, 6].

The upper portion of the granite section (Assemblage 4 defined by [6]) displays what could be evidence of minor shock deformation. This evidence includes grains of potassium feldspar with vesiculated cores as well as albite, which displays alternated twin alteration likely due to asymmetric isotropization.

Lower suevites contain relatively large quartzose clasts with abundant PDFs dominated by {10-13} with subordinate {21-31} and {51-61} orientations. Judging from the volume of melt, the suevite section (Assemblage 2 in [6]) likely experienced shock from 13 GPa for KP 42 (4779.25-4779.40 ft or 1456.72-1456.76 m) and up to more than 35 GPa, in the cases of melt-dominated samples [7].

The schist/pegmatite and lower granite section (Assemblage 1 noted by [6]) contains kink-bands in muscovite, planar fractures and possible incipient PDFs in quartz, and fine, mechanical micro-twins in microcline. Sample KP 49 (5464.30-5464.75 ft or 1665.43-1665.56 m) consists of pieces of sheared clasts of granite possibly sourced from granites at the base of Assemblage 1 (5795.10-5795.25 ft or 1766.17-1766.21 m) entrained in flow-banded material as well as common microfaulting (Fig. 1). These features are suggestive of a shear zone.

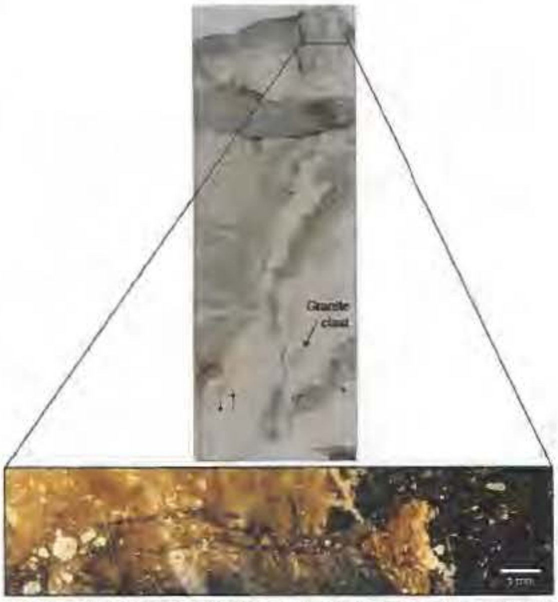

Fig. 1. Sample KP 49 displays features such as micro-faulting and flow-banding likely associated with shearing. Inset image highlights a breccia dike.

Quartz grains display a wide range of shock effects throughout the drill core. PDF orientations have been extensively measured to estimate the pressures experienced in the various sections.

References: [1] Glidewell J. et al. (2007) *GSA Abstracts with Programs, 39(6),* 452. [2] Glidewell J. et al. (2008) *LPS XXXIX*, Abstract #2438. [3] Glidewell J. (2008) Unpubl. M.S. thesis, Auburn University. [4] Gohn G. S. et al. (2006) *EOS, 87,* 349, 355. [5] Powars D. S. et al. (2007) *GSA Abstracts with Programs, 39(6),* 314. [6] Horton J. W. et al. (2007) *GSA Abstracts with Programs, 39(6),* 314. [7] Kieffer S. W. (1971) *Journal of Geophysical Research 76,* 5449-5473.

PLATINUM GROUP ELEMENT (PGE) RATIOS IN THE CORED IMPACTITES OF THE EYREVILLE DRILL SITE OF THE CHESAPEAKE BAY IMPACT STRUCTURE.

S. Goderis[1,2], F. Vanhaecke[2], J. Hertogen[3], Ph. Claeys[1], [1]Vrije Universiteit Brussel, Pleinlaan 2, B-1050 Brussels, Belgium, [2]Universiteit Gent, Krijgslaan 281 - S12, B-9000 Ghent, Belgium, [3]Universiteit Leuven (KULeuven), Celestijnenlaan 200E, PB 2408, B-3001 Leuven-Heverlee, Belgium (Steven.Goderis@vub.ac.be).

Introduction: The late Eocene epoch is characterized by both a 2.5 Ma long period of increased presence of extraterrestrial ^{3}He, first detected in the marine carbonates of the Massignano section, Italy [1], and the formation of possibly 5 or more impact structures (Popigai, Chesapeake Bay, Wanapitei, Haughton, and Mistastin). One scenario attributes the high impact rate and enhanced flux of interplanetary dust particles to the arrival of long-period comets in the inner solar system caused by a perturbation of the Oort cloud [1]. Determination of platinum group element (PGE) concentrations is one of the methods (next to Os and Cr isotopic analysis) capable of identifying sometimes minute (~0.2 wt.%) amounts of extraterrestrial projectile material in impactites. A comparison of the specific inter-elemental ratios measured in impact-melt with the same ratios in the different types of meteorites (e.g., chondrites), enables reliable projectile identification [2, 3, 4]. By using this method, both the Popigai [2] and Wanapitei [5] impactors proved to be L-type ordinary chondrites. The presence of two impact structures formed by the same type of projectile supports an asteroid shower on Earth after a major collision in the asteroid belt [6]. The aim of this study is to identify the projectile component in the 2005-2006 ICDP-USGS Deep Drilling Project cores using determination of the PGE together with nickel (Ni) and chromium (Cr).

Samples: Sixteen samples, macroscopically resembling impact melt-like material, were selected from the Eyreville core material [7]. Major and trace elements were determined with respectively ICP-OES and ICP-MS after acid-digestion, to ensure representativeness. The 6 samples with the highest siderophile element concentrations (based on Ni and Cr concentrations) were prepared for PGE analysis using ICP-MS after preconcentration with NiS fire assay, based on the procedure described in [2] and [8]. Sample intakes reach ~50 g. Determined detection limits are 0.01 ng/g Ir, 0.09 ng/g Ru, 0.03 ng/g Pt, 0.03 ng/g Rh, 0.20 ng/g Pd and 0.23 ng/g Au. The identification of the projectile component is carried out following the procedure described in [2].

Results: The results of the analyses of the Chesapeake Bay impactites revealed that major and trace element compositions are moderately heterogeneous. The Ni content varies from ~2 to 112 ppm between samples, while Co and Cr fluctuate from ~1 to 61 ppm and ~12 to 277 ppm, respectively. No clear link between stratigraphic interval and siderophile concentrations is revealed.

Discussion and conclusion: The determination of the PGE in six selected samples of the Eyreville drill site (sampled intervals: 524.09-524.18 m, 1382.10-1382.20 m, 1404.27-1404.36 m, 1418.72-1418.81 m, 1448.90-1448.99 m and 1607.93-1608.02 m) could allow the identification of the projectile responsible for the formation of the Chesapeake Bay impact structure. Projectile proportions of ~0.1-0.2% were quantified in a previous study [9] based on PGE concentrations and Os isotopic ratios in impact-melt rocks from an 823 m deep scientific test hole over the central uplift at Cape Charles, Virginia. According to this study, a meteoritic contamination alone cannot reproduce the observed PGE abundances in the impact-melt rocks, suggesting a high indigenous, but so far not yet sampled, target rock component. Possible fractionation during syn- or post-impact events and/or an unknown or undistinguishable (in comparison to the crustal values) projectile type could also not be excluded [9].

In this study, we therefore hope to constrain the chemical nature of the Chesapeake Bay projectile.

References: [1] Farley K. A. et al. (1998) *Science, 280,* 1250-1253; [2] Tagle R. and Claeys Ph. (2005) *Geochim. Cosmochim. Ac., 69,* 2877-2889; [3] McDonald I. et al. (2001) *Geochim. Cosmochim. Ac., 65,* 299-309; [4] Goderis S. et al. (2007) *Meteoritics & Planet. Sci., 42,* 731-741; [5] Tagle R. et al. (2006) *LPS XXXVII,* Abstract #1428; [6] Tagle R. and Claeys Ph. (2004) *Science, 305,* 492; [7] Gohn et al. (2006) *LPS XXXVII,* Abstract #1713; [8] Plessen H.-G. and Erzinger J. (1998) *Geostandard. Newslett., 22,* 187-194; [9] Lee S. R. et al. (2006) *Meteoritics & Planet. Sci., 41,* 819-833.

THERMAL RADIATION FROM ATMOSPHERIC REENTRY OF CHICXULUB EJECTA.

T. J. Goldin[1] and H. J. Melosh[2], [1]Department of Geosciences, University of Arizona, Tucson, Arizona USA 85721 (tgoldin@email.arizona.edu), [2]Lunar and Planetary Lab, University of Arizona, Tucson, Arizona USA 85721 (jmelosh@lpl.arizona.edu).

Introduction: The discovery of soot within the K/T boundary sequence [1] led to the hypothesis that thermal radiation from the atmospheric reentry of hypervelocity impact ejecta was sufficient to ignite global wildfires. Survival patterns of terrestrial organisms at the K/Pg boundary are also consistent with a thermal radiation pulse contributing to the biological catastrophe following Chicxulub [2]. Calculations of the expected thermal radiation at the ground support this claim [3, 4]. Here we present modeling work which includes a more accurate treatment of thermal radiation than previously considered. Using the KFIX-LPL code we are able to model the atmospheric reentry of distal Chicxulub ejecta and calculate the transmission of thermal radiation, both throughout the atmosphere and through time.

Numerical Modeling: We model the interactions between distal Chicxulub ejecta spherules and the atmosphere using the two-dimensional, two-phase fluid flow code KFIX-LPL, which has been modified from KFIX [5] to suit the problem of ejecta atmospheric reentry and subsequent sedimentation through the atmosphere onto the Earth's surface. Because most of the high speed deceleration of spherules occurs in the upper atmosphere where the concentration of air molecules is small, we have incorporated drag coefficient and heat transfer functions [6] into KFIX-LPL which are accurate within the required range of free molecular to normal Stoke's flow. In addition we have implemented a full treatment of thermal radiation, which includes the effects of optical opacity. This allows us to examine what effects opacity of the spherules themselves has on the transfer of thermal radiation to the ground.

The initial mesh approximates a 150-km-high slice of the Earth's atmosphere into the top of which 250-μm spherules are injected. The spherules are modeled as a simple incompressible fluid with the properties of basaltic glass and enter our model atmosphere at 8 km/s with a flux based on previous calculations of atmospheric reentry of Chicxulub ejecta [3] and the spherule mass density observed on the ground of 0.5 g/cm^2 [7].

The spherules fall through the thin upper atmosphere, compressing the air as they decelerate. At 70 km in altitude, the spherules accumulate in a band of particles which becomes denser with time. Despite having lost their initial high velocities, the spherules continue to settle downwards at their fall velocities and begin to deposit on the ground after a few hours.

Thermal Radiation: The deceleration of spherules from hypervelocities implies the conversion of a large quantity of kinetic energy. Some of this energy heats the spherules (~1000 K) and some of this energy heats the upper atmosphere (~3000 K), but both phases are kept relatively cool due to efficient loss of heat via thermal radiation. Our models calculate the flux of thermal radiation throughout the mesh assuming the lower boundary (ground) is absorptive but fixed in temperature (273 K) and the upper boundary is 100 % transmission, meaning that any radiation reaching the top of the mesh will escape (into space). We model the maximum flux of thermal radiation at the ground to be ~7 kW/m^2, coincident with the time of peak flux of spherules reentering the atmosphere. However, the thermal radiation flux at the ground rapidly decreases and is less than the normal solar constant (1.4 kW/m^2) after 25 minutes. The reason the high fluxes are not sustained is due to the increasingly opaque layer of settling spherules, which increasingly blocks the transmission of thermal radiation from the decelerating spherules in the upper atmospherer above. Hence, the spherules themselves limit the magnitude and duration of thermal radiation at the ground.

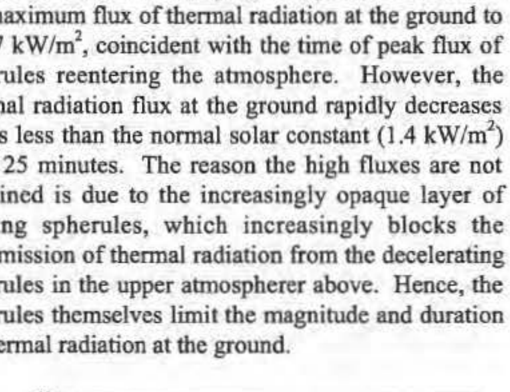

Figure 1. Vertical flux of thermal radiation as a function of time at the bottom of the mesh (red) and the top of the mesh (blue), which represent the ground and space respectively. Negative fluxes are towards the ground.

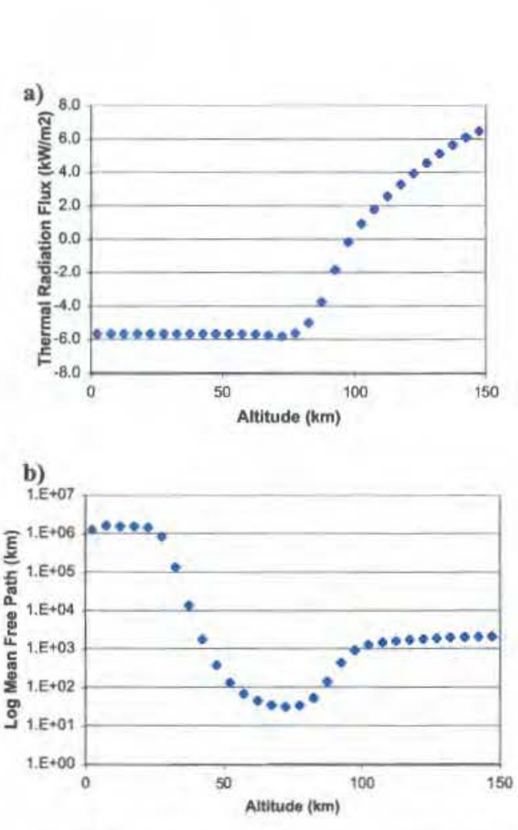

Figure 2. (a) Flux of thermal radiation as a function of altitude at the time of peak spherule reentry (600 s). Negative fluxes are towards the ground. (b) Optical mean free path as a function of altitude, also at 600 s. Shorter mean free paths indicates a higher opacity (or higher concentration of spherules at that altitude).

Discussion: Our KFIX-LPL models calculate a half-hour long pulse of high thermal radiation at the ground, peaking at ~7 kW/m^2. This is less than previous calculations [3, 4] of >10 kW/m^2 sustained over an hour or more. Previous calculations, however, did not include the effects of spherule opacity. Our model shows that, although a pulse of thermal radiation exceeding the solar norm is maintained for over an hour in the upper atmosphere where there are few spherules, the settling cloud of ejecta has sufficient opacity to limit transmission of thermal radiation to the ground. Absorption by the air will further reduce the thermal radiation reaching the ground and future models including an accurate treatment of air opacity will add further constraints.

7 kW/m^2 is analogous to an oven set on "broil" and there are mechanisms by which the thermal radiation experienced on the Earth's surface may be even more severe. A non-uniform distribution of spherule reentry may produce gaps in the opaque spherule layer through which the downward thermal radiation may be concentrated. Our current model also only considers the 250-μm spherules, not the unknown quantity of fine dust particles which are thought to have also been injected into the upper atmosphere from the expanding impact plume. An opaque cloud of dust in the upper atmosphere would act to reflect some of the space-bound thermal radiation downwards.

References: [1] Wolbach W. S. et al. (1988) *Nature*, 334:665-669. [2] Robertson D. S. et al (2004) *GSA Bulletin*, 116:760-768. [3] Melosh H. J. et al (1990) *Nature*, 343:251-253. [4] Toon O. B. et al. (1997) *Rev. Geophys*., 35:41-78. [5] Rivard W. C. & Torrey M. D. (1977) *Los Alamos National Laboratory Report* LA-NUREG-6623. [6] Melosh H. J. & Goldin T. J. (2008) *LPSC XXXIX*, Abstract #2457. [7] Smit J. (1999) *Annu. Rev. Earth. Planet. Sci.*, 27, 75-113.

DIFFERENTIATION AND EMPLACEMENT OF THE WORTHINGTON OFFSET DIKE OF THE SUDBURY IMPACT STRUCTURE, ONTARIO. L. Hecht[1], A. Wittek[1], U. Riller[2], T. Mohr[1], R.T. Schmitt[1], R.A.F. Grieve[3], [1]Museum für Naturkunde, Humboldt-Universität zu Berlin, 10099 Berlin, Germany, [2]School of Geography and Earth Sciences, McMaster University, Hamilton, Ontario, Canada L8S 4K1, [3]Earth Sciences Sector, Natural Resources Canada, Ottawa, Canada K1A 0E4.

Introduction: The Offset Dikes of the 1.85 Ga Sudbury Igneous Complex (SIC) constitute a key topic in understanding the chemical evolution of the impact melt, its mineralization, and the interplay between melt migration and impact-induced deformation. The origin of the melt rocks in Offset Dikes as well as mode and timing of their emplacement, are still a matter of debate [1,2,3,4,5]. In order to test existing hypotheses of dike origin and emplacement and to discern the effects of post-impact deformation on primary mineral fabrics, structural, petrological, and geochemical investigations on the Worthington dike were acquired.

Results: *Petrology and geochemistry.* Like many other Offset Dikes, the Worthington is composed of an early emplaced texturally rather homogeneous quartz-diorite (QD) phase at the dike margin, and an inclusion- and sulfide-rich quartz-diorite (IQD) phase emplaced later and mostly in the centre of the dike [4]. Both dike rocks are mainly composed of plagioclase, amphibole±biotite, quartz, and K-feldspar. Actinolite, epidote, secondary plagioclase, and chlrorite represent secondary metamorphic assemblages. Zircon is often strongly fractured, pulled apart and displays marginal embayments that point to dissolution or resorption. These zircons are interpreted as grains inherited from host rocks during assimilation by the impact melt before emplacement of the dike magmas. There are some chemical differences between the QD and IQD samples. Contents in MgO and Cr are lower and SiO_2 is slightly higher in IQD than in QD. Moreover, the IQD samples have higher average concentrations of the lithophile high field strength elements (HFSE) including the rare earth elements (REE), Zr, Hf, Th, U, Y, Nb and Ta. This indicates that the QD is either less fractionated or relatively enriched in a more mafic component (e.g., high in Mg, Cr, Fe, and low in Si, HFSE), compared to the IQD. No indication for in situ magmatic fractionation between QD and IQD have been identified.

Structural geology. Orientation analysis of elliptical host rock fragments was conducted on a total of five dike segments. The strike of the long axis trajectories corresponds well to the strike of inclined metamorphic foliation surfaces measured at the dike margins in quartz diorite and host rocks. Moreover, the metamorphic foliation in the dike strikes generally E-W, i.e., at high angles to its margins, suggesting that alignment of fragments was accomplished by ductile deformation. Collectively, the micro-structural and mineralogical characteristics indicate that mineral fabrics developed under greenschist-facies metamorphic conditions.

Conclusions: The chemical heterogeneity within and between QD and IQD is mainly attributed to variable assimilation of host rocks at the base of the SIC, prior to emplacement of the melt into the dike. Minor chemical modification at the dike margins is likely due to assimilation of partial melts and/or subsolidus alteration and mass transfer of mobile elements during post-impact regional metamorphism. Constraints on sulfide segregation and petrological data suggest that the parental magma of the Worthington Dike formed at temperatures above the liquidus of the SIC (>1200°C) but well below the temperature of zircon decomposition (1690°C, [6]), and most likely close to the temperature of sulfide segregation (ca. 1450°C, [7]). Based on thermal modeling of cooling rates of the SIC (e.g., [8,9]), the two-stage emplacement of the Worthington Dike occurred likely thousands to about ten thousand years after impact (Fig. 1). Structural analysis indicates that an alignment of minerals and host rock fragments within the Worthington Dike was caused by ductile deformation under greenschist-facies metamorphic conditions rather than flow during melt emplacement. It is concluded that the Worthington Offset Dike resulted from crater floor fracturing, possibly driven by late-stage isostatic readjustment of crust underlying the impact structure.

References: [1] Grant R.W. and Bite A. 1984, OGS Spec. Publ. 1, 275-300. [2] Wood C.R. and Spray J.G. 1998, Meteoritics & Planet. Sci., 33: 337-347. [3] Therriault et al. 2002, Econ. Geol., 97, 1521-1540. [4] Lightfoot P.C. and Farrow C.E.G. 2002, Econ. Geol., 97, 1419-1446. [5] Wichmann R.W. and Schulz P.H. 1993, Meteoritics & Planet. Sci., 28, 222-231. [6] Finch, R.J. and Hanchar, J.M. 2003, Rev. Mineral. Geochem, 53, 1-25. [7] Keays R. R. and Lightfoot P.C. 2004, Mineral. Petrol., 82, 217-258. [8] Ivanov B. A. and Deutsch A. 1999, GSA Spec. Paper, 339, 389-398. [9] Prevec S.A. and Cawthorn R.G. 2002. JGR 107(B8), 2176, doi: 10.1029/2001JB000525.

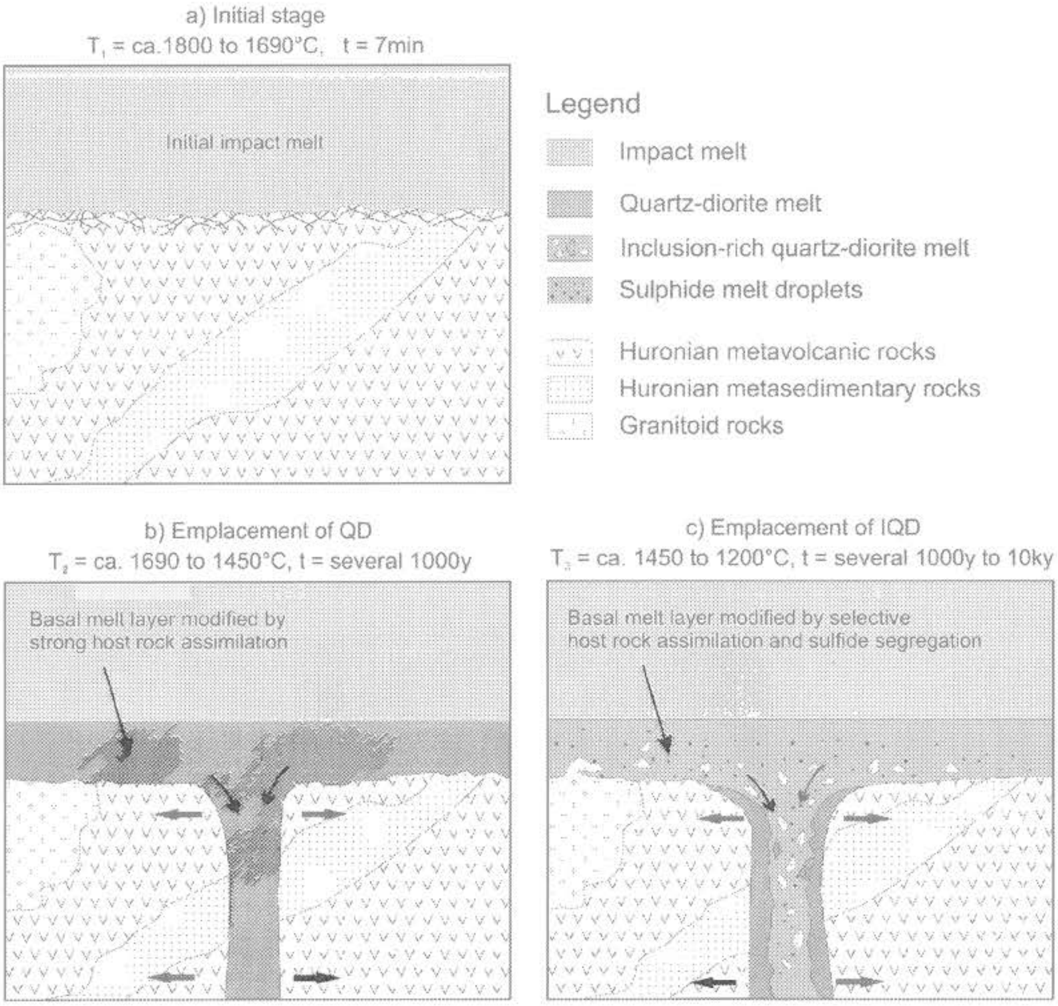

Figure 1: Model showing the two-stage emplacement of the Worthington Offset Dike below the impact melt sheet of the Sudbury Impact Structure. The continuously evolving impact melt sheet is divided into three pre-liquidus temperature intervals (T1 to T3). (a) Initial stage at the beginning of first temperature interval. (b) The emplacement of the inclusion-free quartz-diorite likely occurred towards the end of the second temperature interval after some host rock assimilation but before the onset of sulfide segregation (>1450°C). (c) The emplacement of the inclusion-rich quartz-diorite occurred within the third temperature interval after the onset of sulfide segregation and after some selective host rock assimilation. The elapsed time after impact (t) estimated from geophysical modeling is given for each stage or interval.

AMOUNT AND DISTRIBUTION OF IMPACT MELT OF LARGE LUNAR CRATERS: VIEWS FROM LISM/KAGUYA. N. Hirata[1], J. Haruyama[2], M. Ohtake[2], T. Matsunaga[3], Y. Yokota[2], T. Morota[2], C. Honda[2], Y. Ogawa[3], M. Torii[2], T. Sugihara[4], H. Miyamoto[5], H. Demura[1], and N. Asada[1], [1]The University of Aizu, Ikki-machi, Aizu-Wakamatsu, Fukushima, 965-8580, JAPAN, [2]The Institute of Space and Astronautical Science, Japan Aerospace Exploration Agency, [3]National Institute for Environmental Studies, [4]Center for Deep Earth exploration, Japan Agency for Marine-Science and Technology, [5]The University Museum, The University of Tokyo. Corresponding author's e-mail address: naru@u-aizu.ac.jp

Introduction: Various features outside/inside of craters give important clues to reconstruct and understand impact cratering. Large and fresh lunar craters are best targets for such investigations, because only space weathering and limited degradations by small impacts are major processes that disturb original structures of ejecta units. Lunar Imager/Spectrometer (LISM), which onboard the Kaguya (SELENE) lunar explorer, will provide high-resolution and multi-spectral mapping data of the Moon [1-3]. Combination of high-resolution images, digital terrain models, multiband images, and spectral profiles is a complete set for geologic mapping of a crater and its surroundings. The purpose of this study is to make morphological analyses of those craters with the data from LISM and to reveal details of impact cratering processes. In this report, we concentrate on the amount and distribution of impact melt of lunar craters.

Impact Melt: Impact melt is a product of high temperature condition at the contact and compression stage of impact cratering. An amount of impact melt gives clues to a scale of an impact, the impactor size and the impact velocity. Field researches on terrestrial craters give constraints on model estimations of the amounts of impact melt [4], because thick melt sheets are preserved within terrestrial craters. Since erosive processes are limited on the lunar surface, impact melts of lunar craters remain not only as melt sheets within a cavity but also as small melt deposits within or around a cavity, and as glassy materials. As impact melt glasses spread around a rim of a crater, they are observed as dark rings in Clementine UVVIS images. We have already demonstrated that the total amount of impact melt could be estimated from multi-spectral images [5]. Images from LISM will give better constraints than previous studies. Extent of melt deposits, which have not been considered in the previous study, can be investigated with high-resolution images. Extent of a dark ring will be clearer in high-resolution images, and glass contents of dark ring materials will be able to estimate with spectroscopic data.

After its production, melted materials are transported with other ejecta during cratering process. Thus, final distribution of impact melt deposits around a crater reflects individual characteristics of its formation process. One important factor is an obliqueness of the impact. Distributions of dark rings are obviously affected by impact obliqueness [5]. It is suggested that the distribution of the melt ponds around the crater Tycho are controlled by the oblique impact [6].

Results on Jackson (D = 71 km): We pick up several target craters of our study [7]. Jackson is one of those targets that LISM images are currently available. It is a typical fresh crater on the lunar farside. Jackson has a bright ray system with a large forbidden zone in the NW sector and two minor ones in both S and SE sectors. This appearance suggests that Jackson was formed by an oblique impact of the NW-SE direction.

Impact melt ponds. The ponds on the ejecta blanket show a heterogeneous distribution, whereas the ponds on the terrace zone do not. There are few small ponds in the uprange (NW-N-NNE) sector. The ponds in the downrange (SE) sector and the side (S-SW) sector are large, and their number density is also high. The ponds in the side range (S-SW) seem to be larger than those in the downrange.

Impact melt sheet. Crater floor is mostly filled with a large sheet of impact melt. The uprange half of the floor is characterized with numerous blocky hummocks, ribbon-like pattern weaves and a networked cracks, and the rest half is more smooth. There is a good correlation between the scale of melt deposits (melt ponds and melt sheets) and their surface texture: smaller ones are more smoother.

References: [1] Haruyama J. et al. (2008) *Earth Planets and Space*, 60, 243-255,. [2] Ohtake M. et al. (2008) *Advances in Space Research,* in press. [3] Matsunaga, T. et al. (2001) *Proc. SPIE*, 4151, 32-39. [4] Cintala M., J., and Grieve R., A. F. (1998) *MAPS, 33,* 889-912. [5] Hirata N. et al. (1999) *LPS XXX*, Abstract #1350. [6] Morris A. et al. (2000) *LPS XXXI*, Abstract #1828. [7] Hirata N. et al. (2008) *LPS XXXIX*, Abstract #1588.

A REVIEW OF IMPACT SPHERULE LAYERS IN THE BARBERTON GREENSTONE BELT. A. Hofmann[1], W.U. Reimold[2], and C. Koeberl[3], [1]School of Geological Sciences, University of KwaZulu-Natal, 4000 Durban, South Africa (hofmann@ukzn.ac.za); [2]Museum für Naturkunde, Humboldt University, Berlin, Germany; [3]Department of Geological Sciences (Geochemistry), University of Vienna, Althanstr. 14, A-1090 Vienna, Austria.

In the Barberton greenstone belt, four specific spherule horizons, named S1 to S4, have been proposed as being of impact origin [1, 2]. Zircon dating yielded ages of 3.47 to 3.24 Ga for these strata, with the S1 horizon seemingly having a coeval counterpart in the Pilbara craton [3]. Spherules in the Barberton belt are interpreted to have formed by condensation of global clouds of impact-generated rock vapor and to represent distal impact deposits far from the original crater sites [1, 2]. Debate has taken place as to whether or not there is sufficient and unambiguous evidence for all spherule-bearing horizons to be considered of impact origin [4, 5, 6, 7]. Mostly the debate involves stratigraphic, petrological and geochemical arguments.

Apart from the S1–S4 spherule horizons, a number of other layers with spheroidal particles of volcanic origin, such as accretionary lapilli, have been identified in the Barberton stratigraphy [8]. A careful study of these layers is necessary, because accretionary lapilli have been observed as an integral part of some impact ejecta [e.g., 9].

Because of widespread silica metasomatism in the Barberton greenstone belt, unequivocal distinction between spherical particles of volcanic or impact origin may not always be easy. Although chromium isotope analyses clearly indicate an extraterrestrial component in some of the spherule layers [10, 11], many problems concerning mainly their geochemical characteristics still remain unanswered.

However, a better understanding of the Barberton spherule layers is significant for a better understanding of early Earth evolution. Impacts by large extraterrestrial objects are undoubtedly capable of causing major changes in Earth's atmosphere, hydrosphere, biosphere, and lithosphere [12]. On the other hand, ancient impact ejecta may also help in elucidating secular variations in the evolution of the Earth [13]. In this contribution we present a critical review of the current knowledge about the Barberton spherule layers, and highlight a number of problems with the proposition of frequent and large meteorite impacts during mid-Archean times. Field data indicate that some of the four previously proposed impact spherule layers may be laterally correlative units that may have formed from the same impact event. Petrographic work reveals the presence of volcaniclastic particles associated with some spherule layers, whereas other layers not regarded as impact deposits contain clasts commonly observed in the spherule beds. Major and trace element compositions of spherule layers reflect the composition of the immediate host rocks. The existing PGE and chromium isotope data are difficult to reconcile with the current knowledge of the composition of meteoritic debris. A thorough discussion of these problems is necessary, before meaningful estimates of Archean impact flux and bolide diameters can be attempted.

References: [1] Lowe, D. R. et al., 1989. Science 245, 959-962. [2] Lowe, D. R. et al., 2003. Astrobiology 3, 7-47. [3] Byerly, G. R. et al., 2002. Science 297, 1325-1327. [4] Koeberl, C. et al., 1993. Earth Planet. Sci. Lett., 119, 441-452. [5] Koeberl, C. & Reimold, W. U., 1995. Precambrian Res., 74, 1-33. [6] Reimold, W. U. et al., 2000. In: Impacts and the Early Earth, Springer, Berlin-Heidelberg, pp.117-180. [7] Hofmann, A. et al., 2006. Geol. Soc. Amer. Spec. Pap. 405, 33-56. [8] Heinrichs, T., 1984. Precambrian Res. 24, 237-283. [9] Addison, W. D. et al., 2005. Geology, 33, 193-196. [10] Shukolyukov, A. et al., 2000. In: Impacts and the Early Earth, Springer, Berlin-Heidelberg, pp. 99-116. [11] Kyte, F. T. et al., 2003. Geology, 31, 283-286. [12] Sleep, N. H., and Zahnle, K. J., 1998. J. Geophys. Res., 103, 28529-28544. [13] Simonson, B. M., and Harnik, P., 2000. Geology, 28, 975-978.

GEOLOGIC COLUMN FOR THE ICDP-USGS EYREVILLE-B CORE, CHESAPEAKE BAY IMPACT STRUCTURE: IMPACTITES AND CRYSTALLINE ROCKS, 1,095-1,766 M.

J. W. Horton Jr.[1], R. L. Gibson[2], W. U. Reimold[3], A. Wittmann[4], G. S. Gohn[1], and L. E. Edwards[1], [1]U. S. Geological Survey, 926A National Center, Reston, VA 20192 USA, whorton@usgs.gov, [2]School of Geosciences, Univ. of Witwatersrand, Johannesburg, South Africa, [3]Museum for Natural History (Mineralogy), Humboldt-University in Berlin, Invalidenstrasse 43, 10115 Berlin, Germany, [4]Lunar and Planetary Institute, 3600 Bay Area Blvd., Houston, TX 77058-1113, USA.

Geologic column: The ICDP-USGS Eyreville drill cores, in the Chesapeake Bay impact structure, USA, provide one of the most complete geologic sections ever obtained from an impact structure [1]. Figs. 1-4 show geologic columns for the deepest sections. A 275-m allochthonous granite body (1,371–1,096 m depth), beneath thick crater-fill sediments, includes gneissic biotite granite, fine- and medium-to-coarse-grained biotite granites, and red altered granite near the base. This granite overlies 26 m (1,397–1,371 m) of gravelly quartz sand that contains an amphibolite block and boulders of cataclasite and suevite. Below the sand, a sequence of suevites and lithic impact breccias (1,551–1,397 m) includes a lower section of polymict impact breccias with boulders and blocks (up to 17 m) of cataclastic gneiss, and an upper section (above 1,474 m) of suevites and clast-rich impact melt rocks. The deepest sequence (1,766–1,551 m) consists of basement-derived mica schists (commonly containing graphite and fibrolitic sillimanite), granite pegmatite that grades into coarse granite, and a zone (1,655–1,641 m) of mylonitic rocks. This basement-derived sequence is variably overprinted by cataclastic fabrics and locally cut by dikes of polymict impact breccia, including suevite.

Table 1. Composite geologic section for Eyreville cores [2,3]; shaded units discussed herein.

Depth in meters	*Geologic sequence*
0 - 443.9	Post-impact sediments
443.9 – 1,095.7	Sediment-clast breccia and sediment megablocks (ocean resurge and avalanche deposits)
1,095.7 - 1,371.1	Granite (allochthonous)
1,371.1 - 1,397.2	Gravelly sand and lithic blocks
1,397.2 – 1,474.1	Suevites and impact melt rocks
1,474.1 - 1,551.2	Polymict impact breccias and cataclastic gneiss blocks
1,551.2 - 1,766.2	Schist and granite/pegmatite with impact breccia dikes and veins

References: [1] Gohn G. S. et al. (2006) *EOS*, 87(35), 349, 355. [2] Horton J.W. Jr. et al. (2007) *GSA Abstracts*, 39(6), 314. [3] Powars D. S. et al. (2007) *GSA Abstracts*, 39(6), 314.

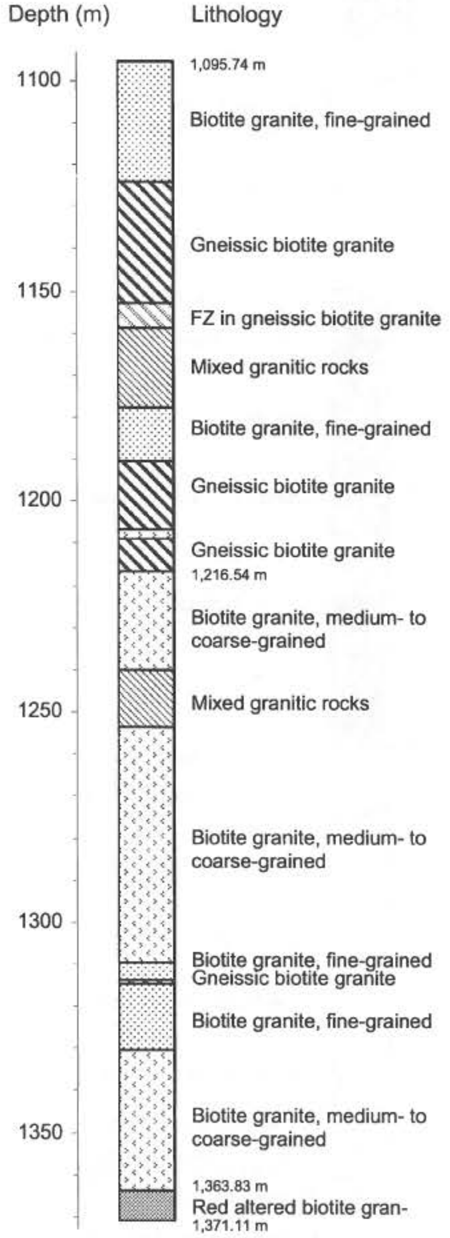

Figure 1. Granite (1,371–1,096 m); FZ=fracture zone.

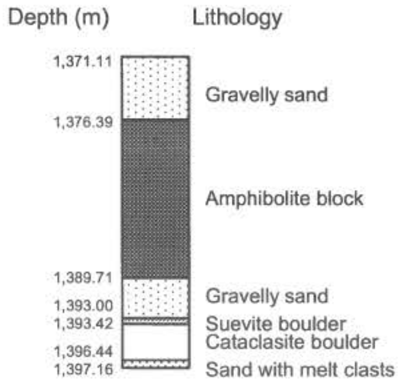

Figure 2. Sand and lithic blocks (1,397–1,371 m).

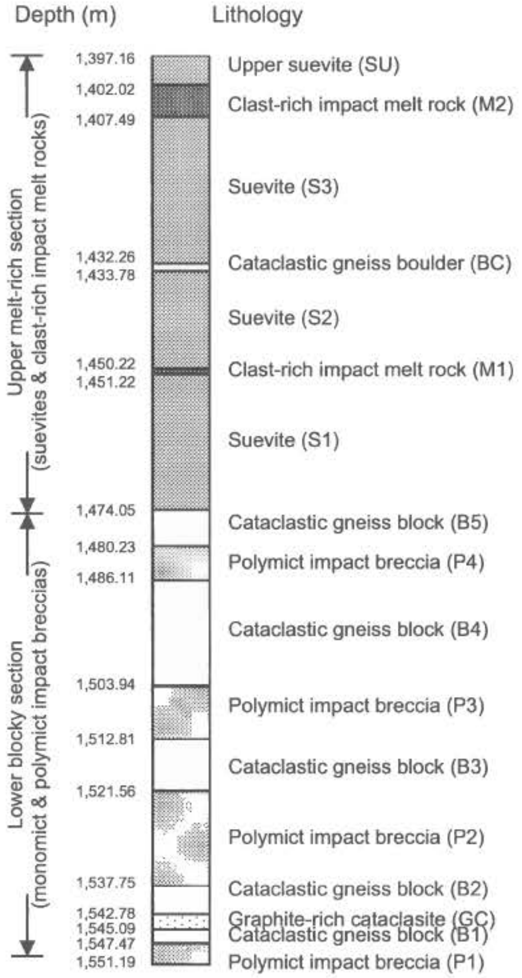

Figure 3. Suevites and lithic impact breccias (1,551–1,397 m), including informal designations for polymict impact breccias (P1-P4), blocks (B1-B5), suevites (S1-S3, SU), melt rocks (M1, M2), and a boulder (BC).

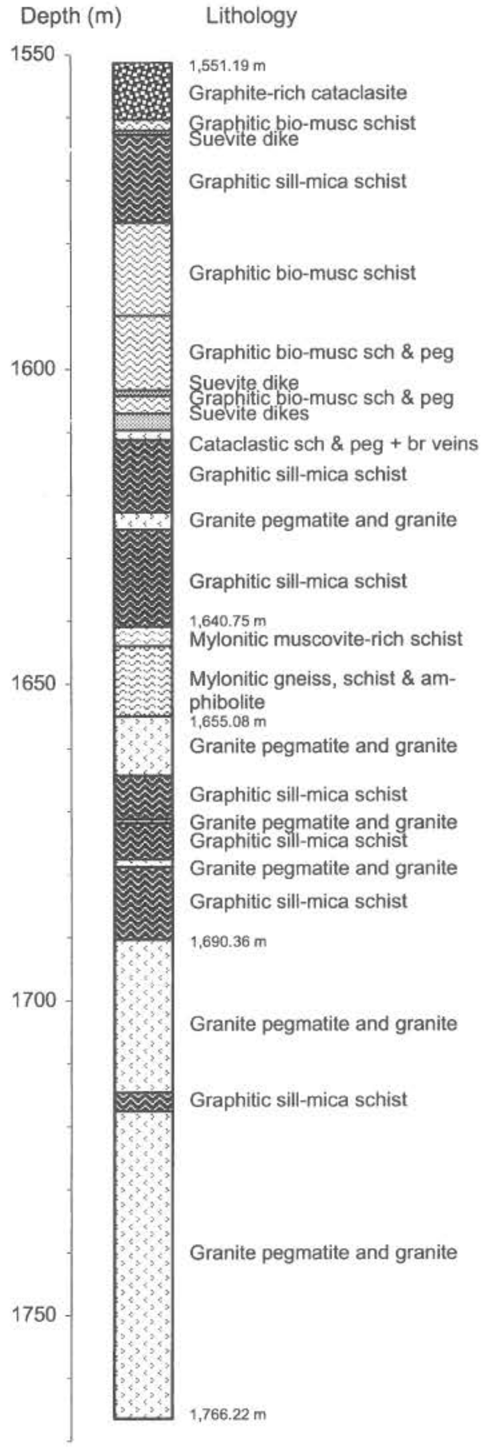

Figure 4. Schist, pegmatite and granite with impact breccia dikes (1,766–1,551 m); bio=biotite, musc=muscovite, sill=sillimanite, sch=schist, peg=pegmatite, br=breccia.

INVESTIGATIONS OF IMPACTITES AND CRYSTALLINE TARGET ROCKS IN THE ICDP-USGS EYREVILLE-B CORE, CHESAPEAKE BAY IMPACT STRUCTURE.

J. W. Horton Jr.[1], M. J. Kunk[1], H. E. Belkin[1], J. N. Aleinikoff[2], J. C. Jackson[1], and I-M. Chou[1], [1]U. S. Geological Survey, 926A National Center, Reston, VA 20192 USA, whorton@usgs.gov, [2]U. S. Geological Survey, MS 963, DFC, Denver, CO 80225 USA.

Introduction: The ICDP-USGS Eyreville coreholes in the Chesapeake Bay impact structure (CBIS) were drilled during 2005-2006 on the Delmarva Peninsula, 7 km northeast of the town of Cape Charles, Virginia, USA [1]. The drilling penetrated the moat of the central crater that surrounds the central uplift as delineated by seismic and gravity surveys [2,3]. This study focuses on impactites and crystalline target rocks in the deepest core, Eyreville-B, from 1,766.2 to 1,095.7 m depth (shaded in Table 1). The geologic sequences include, in ascending order: 215 m of basement-derived schist, pegmatite, and coarse granite with veins and dikes of impact breccia; 154 m of suevites and lithic impact breccias; 26 m of quartz sand with lithic boulders and blocks; and a 275 m allochthonous granite body. These are overlain by 652 m of sedimentary breccias and sediment megablocks, and 444 m of post-impact sediments.

Table 1. Composite geologic section for Eyreville cores A, B, and C [4,5]; shaded units discussed herein.

Depth in meters	*Geologic sequence*
0 - 443.9	Post-impact sediments
443.9 - 618.2	Diamicton with clasts in muddy glauconite-quartz sand matrix (ocean-resurge sediments)
618.2 - 866.7	Nonmarine sediment blocks injected by quartz-glauconite sand
866.7 - 1,095.7	Nonmarine sediment blocks (sediment-avalanche deposits)
1,095.7 - 1,371.1	Granite (allochthonous)
1,371.1 - 1,397.2	Gravelly sand & lithic blocks (basal avalanche deposit?)
1,397.2 1,474.1	Suevites and clast-rich impact melt rocks
1,474.1 - 1,551.2	Polymict impact breccias and cataclastic gneiss blocks
1,551.2- 1,766.2	Schist and granite/pegmatite with impact breccia veins and dikes

Schist, pegmatite, and granite with impact breccia dikes (1,766–1,551 m depth): The deepest sequence consists of basement-derived mica schists, and granite pegmatite that grades into coarse granite. The schists commonly contain graphite and knots of fibrolitic sillimanite. A zone (1,655-1,641 m) of variably mylonitic muscovite-rich schist, gneiss, and amphibolite contains disseminated calcite, minor epidosite, and rare tourmalinite [4]. Ductile structures are inherited from the pre-impact basement. Brittle cataclastic deformation is much more pervasive than that observed outside the structure, and drilling did not reach undisturbed rock. The rocks locally are cut by dikes of breccia, including suevite, which decrease in size and abundance with depth [4,6]. Shock-metamorphic features are rare except in association with breccia dikes. ^{40}Ar/^{39}Ar plateau ages of two muscovites from the pegmatite indicate cooling through the ~350°C isotherm at ~244 Ma [6] without disturbance by the ~35.5 Ma impact.

Suevites and lithic impact breccias (1,551–1,397 m depth): The suevites and lithic impact breccias include a lower section of polymict impact breccias and blocks (up to 17 m) of cataclastic gneiss, and an upper section (above 1,474 m) of suevites and clast-rich impact melt rocks. Lithic clasts in the sequence include variably cataclastic greenschist-facies rocks, metaplutonic rocks, and sub-greenschist-facies sedimentary rocks previously unknown in the target.

Impact-melt clasts in the suevite include anhydrous to hydrous glasses that are commonly flow laminated, partly devitrified, and variably altered. Meniscus-like textures between glasses of different composition indicate immiscible silicate melts at quench. Coexisting sulfide melts now appear as small Fe+S ± Ni spheres. Tiny crystals of the oxide minerals chrome spinel, baddeleyite, and corundum in silicate glass indicate high-temperature crystallization under conditions of silica undersaturation. X-ray diffraction (XRD) indicates that melt glass is partly altered to well-crystallized Fe-rich smectite.

Shocked quartz is common in the suevite and lithic blocks within it. Two sets of planar deformation features (PDFs) are common, and three are visible in some grains. Ballen quartz [6], is observed locally in melt clasts and melt-rich domains. Raman spectra of selected grains from the melt-rich suevite show that some consist of coesite + quartz. Coesite from the CBIS was first reported in samples from this core [6], and studies are in progress to understand its distribution with depth and lithology.

Examination of suevites and clast-rich impact melt rocks by optical and electron-beam scanning microscopy, cathodoluminescence, electron microprobe analysis, and Raman micro-spectroscopy confirms the presence of zircon ($ZrSiO_4$); its shocked equivalent, reidite; and baddeleyite (ZrO_2). Zircon textures include: (1) seemingly un-shocked, euhedral to subhedral crystals; (2) fractured to highly fractured but unaltered crystals; (3) altered crystals with decomposition zones; severely altered crystals with decomposition zones containing baddeleyite; (4) and severely altered crystals partially transformed to reidite and also with decomposition zones containing baddeleyite.

Sand and lithic blocks (1,397–1,371 m depth): The sequence of suevites and lithic impact breccias is overlain by the gravelly quartz sand that contains a block of amphibolite, a cataclasite boulder, a probable rip-up clast of suevite, and smaller lithic clasts. The lowest gravelly quartz sand contains altered melt clasts [4]; it is also slightly darker and more lithified, suggesting a hydrothermal overprint within meters of the underlying suevite. Individual detrital microcline grains from the sand have $^{40}Ar/^{39}Ar$ laser fusion ages of ~328-218 Ma. Age spectra from three size fractions of the microcline have climbing spectra with ages ranging from 267-252 Ma and show no clear indication of the time of impact, so maximum temperatures in the sand during and after the ~35.5 Ma impact must have been <~150°C.

Granite (1,371–1,096 m depth): The 275 m granite body overlies the sand and must be allochthonous. It is free of intervening material that would require more than one slab but is locally faulted and fractured. The rocks are not shocked, and cataclastic fabrics are lacking except locally. The main rock types are gneissic biotite granite, medium- to coarse-grained biotite granite, fine-grained biotite granite, and a red altered granite near the base [4]. The gneissic biotite granite has a SHRIMP U-Pb zircon age of 615 ± 7 Ma [6], which is similar to Neoproterozoic granites from drill cores in the western part of the CBIS. The massive, medium- to coarse-grained biotite granite has a SHRIMP U-Pb zircon age of 254 ± 3 Ma (Permian)[6] and must be from a late Alleghanian pluton. The granite is overlain by gravelly sand derived from the Lower Cretaceous Potomac Formation.

Discussion: The Eyreville drilling recovered a remarkable variety of basement-derived Proterozoic and Paleozoic rocks, including multiply-deformed, upper-amphibolite-facies schist (and pegmatite) in the deep, basement-derived sequence, greenschist-facies metamorphic rocks and sub-greenschist-facies sedimentary rocks as clasts in the sequence of suevites and lithic impact breccias, an amphibolite block in sand above the suevites, and Neoproterozoic to Permian granites. This structural partitioning of basement-derived rocks is attributed mostly to the late, modification stage of crater formation. In addition to the impact effects, these rocks provide important information about the deeply buried and rarely sampled eastern part of the Appalachian orogen beneath the Atlantic Coastal Plain.

Clast lithologies suggest that the suevites and lithic impact breccias formed mostly from basement-derived material that never left the crater. The vertical distributions suggest a lithic block-rich ground surge near the base with more melt-rich deposition from the collapsing ejecta plume in the upper part. Modeling [7] allows only about 7 minutes for deposition of the 154 m sequence of suevites and lithic impact breccias before it was covered by crater-fill sediments at the corehole location 9 km from the center.

The granite slab above the sand and suevite must be allochthonous, and its source is constrained by a general lack of shock metamorphism. A likely source is part of the transient crater rim that collapsed and slid into the moat, with underlying sand providing a low friction substrate. This is consistent with modeling [7] that shows the radius of the central crater expanding 6 km by inward collapse.

Syn- and post-impact heating below the suevite was <~350°C based on the undisturbed $^{40}Ar/^{39}Ar$ plateau age spectra of muscovites. Temperatures in sand above the suevite were <~150°C, based on undisturbed $^{40}Ar/^{39}Ar$ laser-fusion ages of detrital microcline. Ongoing studies will further constrain the thermal histories.

Acknowledgements: The International Continental Scientific Drilling Program, the U.S. Geological Survey, and the National Aeronautics and Space Administration Science Mission Directorate provided funding for the drilling project. The U.S. National Science Foundation provided supplementary funding for the drill-site operations. DOSECC, Inc. conducted the administrative and operational management of the deep drilling project. We thank the Buyrn family for use of their land as a drilling site, and the scientific and technical staff of the CBIS Drilling Project for their many contributions.

References: [1] Gohn G. S. et al. (2005) *EOS*, 87(35), 349, 355. [2] Shah A. K. et al. (2005) *Geology*, 33, 417-420. [3] Catchings R. D. et al. (2007) *EOS*, 88(52), Fall Meet. Suppl., Abstract U21E-06. [4] Horton J.W. Jr. et al. (2007) *GSA Abstracts*, 39(6), 314. [5] Powars D. S. et al. (2007) *GSA Abstracts*, 39(6), 314. [6] Horton J.W. Jr. et al. (2007) *GSA Abstracts*, 39(6), 451. [7] Collins G. S. and Wünnemann K. (2005) *Geology, 33*, 925-928.

THREE-DIMENSIONAL MODELING OF GROUND-TRUTH DATA - A NEW APPROACH FOR UNDERSTANDING THE SIGNIFICANCE OF PROMINENT DISCONTINUITIES DURING FORMATION OF THE VREDEFORT CENTRAL UPLIFT, SOUTH AFRICA.

A. Jahn[1], U. Riller[2] and W. U. Reimold[1]: [1]Museum for Natural History (Mineralogy), Humboldt University, Invalidenstrasse 43, D-10115 Berlin, Germany (Andreas.Jahn@museum.hu-berlin.de), [2]McMaster University, 1280 Main Street West, Hamilton, ON, L8S 4K1, Canada.

Introduction: In order to investigate the subsurface structure of the Vredefort dome, the central uplift of the 2.02 Ga Vredefort impact structure, structural, petrological and geophysical work [1, 2, 3], as well as numerical modeling [4], have been conducted. Based on these studies and new ground data, we constructed a 3D structural model for the upper parts of the central uplift. In particular, we present a new interpretation o a fault system in the northern collar that has been proposed to be a pre-impact half-graben [5]. Our modeling results are more consistent with an impact-induced suite of normal and reverse faults in this area.

The Vredefort Dome is the eroded remnant of the collapsed central uplift structure [1]. The inner core of the Dome is approximately 40 km in diameter and consists mainly of Archean (> 3.1 Ga) granitoids and minor mafic intrusions. It is surrounded by the collar, an assembly of steeply dipping and overturned sedimentary and volcanic strata of Paleoproterozoic (3.07 - 2.1 Ga) age. To the north and west, the collar rocks are well exposed and form a series of concentric, morphologically prominent quartzite ridges, and valleys along less resistant shale horizons, wrapping around the crystalline core. To the east and the south, the central uplift is largely covered by the Phanerozoic Karoo Supergroup and Quaternary deposits.

Methods: In a field campaign in 2007 we collected structural data, mostly in the northwestern collar region, and created a detailed map of bedding plane orientations and faults identifiable in outcrop. Combining surface structural data with seismic data and information from drill holes we used the software *ArcGIS* and *GOCAD* to construct a 3D model of the respective collar strata. For the visualization of the rock orientations we chose prominent lithological interfaces within the Archean sediments (West Rand and Central Rand Group) as marker surfaces. We also included a number of major faults known from previous field studies [6] and geophysical imaging. In order to test the plausibility of our results, we compared them to those of predicted by numerical models [3].

The construction of a 3D multi-surface model characterized by impact-induced faults allowed us to identify coherent rock domains and their possible displacement during collapse of the central uplift. The model is limited by the exposure of pre-impact rocks and, therefore, to the northwestern quadrant of the central uplift.

Results: The dips of inclined to steeply dipping, overturned sedimentary strata in the collar region increase from < 60° to 70-90° at a depth of 2 to 3 km (Fig.1). Hence, the current erosion surface is situated within the hinge zone between the steeply dipping strata and the overturned parts in the roof of the collapsed central uplift [4]. This observation agrees with erosion of 6 to 8 km. The dip of bedding planes also varies with the individual domains defined by faults. Generally, the bedding planes display maximal rotations in the northwest, but this may be blurred by differential rotation between adjacent domains (Fig.2).

On the km-scale, a significant number of faults is exposed in the collar. Most of them are either concentric or radial faults with respect to the centre of the Vredefort Dome. Concentric faults strike parallel to the outcrop lines of strata, but intersect the strata. Thus, thicknesses of strata are reduced by movements on concentric faults. Radial faults, however, are more curved at surface, listric in geometry and displace concentric faults

Conclusions: Our field structural analysis revealed the existence of a set of faults with variable orientations and truncation relationships. The observed fault geometry does not support the hypothesis of a simple pre-impact normal fault system that led to the formation of a half-graben.

Rather, the geometry and geometric relationship of bedding and fault surfaces point to impact-induced deformation. The shape and orientation of the faults with respect to orientation of bedding planes excludes an origin of the faults in their current orientation. Concentric faults formed likely by reverse sense of slip toward the crater centre and appear to be younger than the collapse of the central uplift. By contrast concentric faults are displaced by radial ones, which were tilted later. Consequently, the concentric faults must have formed during an early stage of crater modification.

Back rotation of the collar strata to their pre-impact orientation leads us to the following kinematic model of faulting during central uplift formation.

Back rotation of the concentric faults by the same rotation magnitude as bedding planes, suggests an origin of these faults as normal faults. Thus, concentric faults are likely relics of discontinuities accomplishing terracing of the rim of the transient cavity. The geometry of concentric faults was subsequently modified by radial faults which formed as reverse or thrust faults. Overall, the fault kinematics point to a constrictional rock flow, which is compatible with the formation of the central uplift by crater-inward mass flow. As a consequence of convergent rock flow toward the crater centre, the strata and faults were uplifted and rotated as well as displaced outwards with respect to the crater centre. This kinematic model does not require pre-impact normal faulting to account for the observed fault geometry and seems crudely to account also for other sectors of the collar.

References: [1] Reimold W.U. and Gibson R.L. (2006) *Chemie der Erde, 66,* 1–35. [2] Lana C., Gibson R. L. (2006) *S. Afr. J. of Geol., 109,* 265-278. [3] Henkel H. and Reimold W.U. (2002) *J. of Applied Geophys.,* 43–62. [4] Ivanov B. (2005) *Solar System Research, 39,* 381-409. [5] Brink M.C.et al. (1997) Tectonophysics, 270, 83-114. [6] A.A. Bisshoff and J.J. Mayer (1999), *Council for Geoscience, Pretoria,* Geol. Map 1:50.000.

Figure 1: Three-dimensional model of the complex fault pattern. Displayed are the top (yellow) and base (orange) of the Central Rand Group that is cut by concentric and radial faults (transparent green). The vertical extent of this section of the model is 3km below the surface.

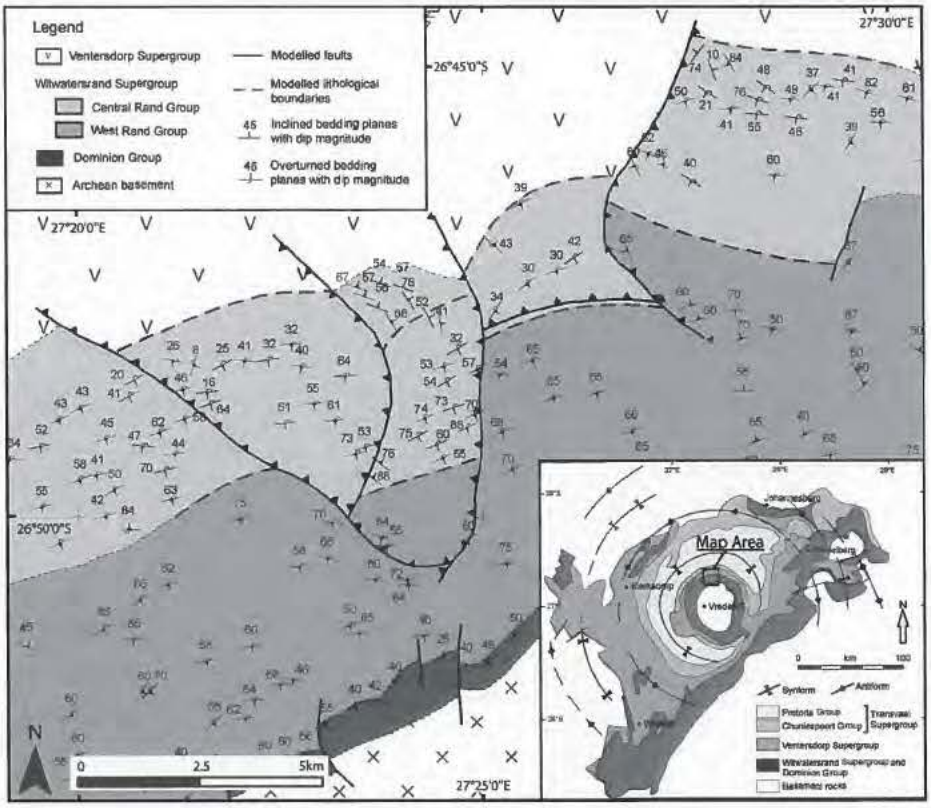

Figure 2:. Maps of the study area. (A) Detailed structural map of the Witwatersrand Supergroup in the northern collar. The dashed lines indicate the extent of the bedding planes in the model, the full lines show the modeled faults. (B) Inset shows the extent of the map area within the Witwatersrand Basin region.

CLAST CHARACTERISTICS IN THE SUEVITIC AND LITHIC BRECCIAS FROM THE ICDP-USGS EYREVILLE B DRILLCORE, CHESAPEAKE BAY IMPACT STRUCTURE, VIRGINIA, USA. L.C. Jolly[1], R.L. Gibson[1], W.U. Reimold[2], J.W. Horton Jr.[3]. [1]Impact Cratering Research Group, School of Geosciences, University of the Witwatersrand, Private Bag 3, PO WITS, Johannesburg 2050, South Africa, lcjolly@yahoo.com. [2]Museum of Natural History (Mineralogy), Humboldt University, Invalidenstrasse 43, Berlin, D-10115, Germany. [3]U.S Geological Survey, MS 926A, 12201 Sunrise Valley Drive, Reston, VA 20192 USA.

Introduction: The Chesapeake Bay impact structure is a late Eocene complex crater that formed in a predominantly siliciclastic, continental shelf environment on the Atlantic margin of Virginia, United States [1]. This buried structure is the seventh largest and one of the best preserved on Earth [1]. In 2005-2006, three coreholes (A, B, C) were drilled as part of the ICDP-USGS drilling project. The Eyreville B core, which reached a depth of 1766.2 m, was drilled in the annular moat within the collapsed transient cavity and comprises post-impact sediments, sediment-clast breccia and lithic blocks, a large granitic and smaller amphibolitic megablock, gravelly sand, a thick sequence of suevitic and lithic breccias that also contain cataclastic gneiss blocks, and a basal section comprising granites/pegmatites and mica schists [2]. The 154 m thick suevitic and lithic breccia sequence that was recovered from depths of 1397.16 to 1551.19 m is the subject of this study, which involved macroscopic and hand-lens description of clasts in the core and more detailed analysis of thin sections from 70 samples. Only the lithic and mineral clasts are considered in the present study; the melt clasts are the subject of separate investigations (e.g., [5]). In total, some 1400 clasts over the entire breccia sequence were examined and precise shape and size data collected.

Results: The breccias comprise an upper, melt-rich, portion and a lower portion that is dominated by polymict and monomict lithic breccias [1, 5] and that contains less matrix material. Clasts of cataclased quartzofeldspathic gneiss up to several metres across are found in the lower section. Preliminary analysis of the >4 cm clast population (i.e., clasts larger than the nominal 4.7 cm core diameter) indicates a preponderance of lithologies seen in the underlying crystalline basement section (granitoid, mica schist, and rare mafic and felsic orthogneiss) and that the proportion of the large clasts increases with depth. Overall, approximately 60% of the large clasts are derived from the medium- to high-grade crystalline rocks. The remainder of the large clasts are made up predominantly of 30% sedimentary rock (arkosic grit) and 10% phyllite. In contrast to the large clasts, the clast population below 4 cm diameter is dominated by 57% fine-grained sedimentary rocks (shale and silty claystone), with 25% comprising igneous components (granitoid and quartz pegmatoid) and 17% metamorphic components (mica schist and mafic orthogneiss).

Mineral clasts: In this study, mineral fragments above 0.5 mm have been classified as clasts. The population of mineral clasts throughout the impactite section is a highly heterogeneous mixture of quartz, K-feldspar, plagioclase, muscovite, biotite, opaques (pyrite), and other, accessory, minerals (epidote, chlorite, zircon and garnet). Preliminary analysis suggests that approximately 60% of the entire clast population (mineral, lithic, and melt clasts) is made up of mineral clasts. Variation of the volume percentages for the main mineral clasts along the core interval are: quartz (25 to 50 rel%), K-feldspar and plagioclase (20 to 30 rel%), and micas (15 to 20 rel%), all increasing with depth. The grain size and internal features of the mineral clasts (e.g., types of internal strain, recrystallization and alteration) indicate primary derivation from the crystalline metamorphic-granitoid sequence. The average minimum and maximum grain sizes in length, measured for the clasts were 0.8 and 2.4 mm, respectively. Initial results show that, in general, the mineral clast size increases with depth. Clast shapes vary from angular (quartz and feldspars) to rounded (opaques) to platy/elongate (micas). Point counting analysis is in progress to better constrain the mineral fragment population.

Lithic clasts: Initial results indicate that the lithic clasts make up approximately 25% of the total fragment population (<4 cm clasts). The lithic clasts comprise igneous (quartz pegmatoid and granitoid), sedimentary (shale, grit, sandstone, siltstone, silty claystone, and claystone) and metamorphic (phyllite, mica schist and felsic and mafic orthogneiss) lithologies. Analysis of the variation of the relative percentage of the clast types with depth shows that granitoid (11 to 5%), mica schist (1.4 to 0.3%), mafic orthogneiss (1.6 to 0.25%), and silty claystone (10 to 4%) decrease with depth, whereas quartz pegmatoid (5 to 6%), mica schist (2 to 3%), phyllite (0.7 to 1%), shale (10 to 14%), sandstone (0.2 to 0.3%), and grit (1.1 to 1.5%) increase in abundance with depth. The igneous, metamorphic and sedimentary lithologies have average clast sizes of 1.23 cm, 1.2 cm and 0.8 cm, respectively. The sedimentary components, which constitute 63% of the total lithic clast population in the <4 cm size fraction, come from sedimentary rocks of undetermined age, with shale comprising 42% of the population, whereas the metamorphic (12%) and igneous (25%) components are from the crystalline basement.

Discussion and Conclusion: The clast population in general does not show a uniform mixture of lithologies: the larger clasts are derived more from the crystalline basement whereas the smaller clasts are derived predominantly from a hitherto unidentified sedimentary sequence. This dichotomy may reflect impact-induced fracturing behaviour linked to rock type, with the more massive and coarser-grained igneous and metamorphic rocks producing larger clasts. Precursor rock character may also explain the variation in clast shape, with the larger clasts being rounded (length-to-breadth ratio of 1.2), whereas the smaller, sedimentary and phyllite clasts are more elongated with a ratio of 2. Preliminary petrographic analysis of mineral and lithic clasts, and analysis of clast sizes and shapes, suggest that most of the smaller clasts were derived from fine- to medium-grained sedimentary rocks (sandstone, shale and arkose) and greenschist-facies rocks that have yet to be intersected beneath the crater, whereas the remaining clasts were derived from medium- to coarse-grained, metamorphic and igneous basement rocks (mica schist and granite) [3, 4]. This suggests a heterogeneous target structure, possibly in part related to amalgamation of disparate Appalachian terranes, but also requiring an unmetamorphosed, consolidated, post-Appalachian sedimentary succession. Observations of the mineral and lithic clasts show that the volume of the sedimentary component decreases with depth, whereas the igneous and metamorphic components increase in volume with depth. This may reflect an increasingly autochthonous character of the breccias with respect to the underlying crater basement.

Acknowledgements: Funding for the drilling came from the ICDP, the USGS, and the NASA Science Mission Directorate. DOSECC managed the drilling operations, and Major Drilling America did the core drilling. Funding for this project (MSc, L.C. Jolly) is from the National Research Foundation (NRF) of South Africa.

References: [1] Horton, J.W. Jr., et al. (2005) *USGS Professional Paper # 1688.* [2] Gohn G.S. et al. (2006) *Scientific Drilling 3, 34-37.* [3] Townsend, G.N. et al. (2007) *GSA Abstracts, 39(6), 314.* [4] Horton et al. (2005) *in* Horton J. W. Jr. et al. eds., *USGS Prof. Paper 1688-B,* B1–B29.
[5] Bartosova et al. (2008) this conference.

THE KAGUYA(SELENE) MISSION: PRESENT STATUS AND LUNAR SCIENCE.

M. Kato, Y. Takizawa, S. Sasaki, and Kaguya team, Japan Aerospace Exploration Agency (Yoshinodai 3-1-1, Sagamihara, Kanagawa 2298510, Japan. E-mail: kato@planeta.sci.isas.jaxa.jp)

Introduction: Lunar orbiter Kaguya(SELENE) has been successfully launched from TNSC on September 14, 2007. On October 4 the Kaguya has been inserted into large elliptical orbit circulating the Moon after passing the phasing orbit rounding the Earth with 2.5 times. After lowering the apolune altitudes the Kaguya has reached the nominal orbit with 100 km circular and polar on October 18. On the way to the orbit two subsatellites Okina and Ouna have been released into the elliptical orbits of 100 km perilune, and 2400 km and 800 km apolune, respectively. After the checkout of bus system the extension of four sounder antennas with 15 m length and the 12 m mast for magnetometer, and deployment of plasma imager were successfully carried out to start checkout of science instruments.

Nominal observation term for ten months has been started on December 21, 2007 after performance test for about 1.5 months. Seven lunar days of observation are already passing till now, and science data of each instrument are being acquired to study lunar science.

Science Instruments and Goals: 14 science instruments including high definition TV cameras are onboard the spacecrafts for science data collection and public outreach. Science instruments and experiments have been shown in Table 1 [1]. Global mapping of elemental abundance on the lunar surface are made by XRS and GRS using advantages to each instrument. Global mapping of major elements by XRS has never been tried till now, although only 10% of the lunar surface has been analyzed in the Apollo XRSs [2]. Global mineralogical distributions are being mapped by MI and SP measuring reflectance two- and one-dimensionally of the lunar surface, respectively. Topographic measurements to study the surface evolution of the Moon are participated by three instruments of TC, LRS, and LALT. Stereo images of the TC by two linear CCDs are being employed for global map of digital elevation. The LALT is a conventional altimeter using Nd:YAG laser. The LRS sounds lunar surface and subsurface within about 5 km to study lunar topography and tectonic activity of subsurface. The LRS equips function receiving radio waves to 30 MHz to detect natural waves emitted from Jupiter, Sun and others in electromagnetically quiet environment of lunar farside. VRAD and RSAT are onboard Okina, Ouna, and Kaguya to determine precise gravity field of the whole Moon. Two radio sources emit three S-band and an X-band radio waves to determine the satellites positions with accuracy of 10 cm by differential VLBI technique between subsatellites and ground VLBI stations referencing with the signals of pulsars. In order to track main orbiter flown on farside the RSAT is used to relay S-band signals. 4-way Doppler technique between main orbiter and a ground station via Okina are determining the gravity field of the farside. This is first experiment never performed till now.

LMAG, CPS, PACE, RS, and UPI are employed to observe the environments of the Moon and the Earth. The LMAG is used to measure magnetic field distribution or local remnant magnetization on the Moon with accuracy of 0.5 nT. In order to measure with reliable accuracy the magnetometers are attached on the top of extendable mast of 12 m length so distant to alleviate effects of electromagnetic disturbance from spacecraft. Primary purpose of CPS is to measure charged particles such as protons of cosmic-ray origin. This instrument can also detect alpha-ray from the lunar faults which presumably originated by tectonic activity. The PACE is investigating sorts, energy, and incident angles of environment particles of ions, electrons, and neutral atoms using mass spectrometers of time-of-flight type. The RS team tries to confirm tenuous ionosphere of the Moon, detection of which was reported by Soviet lunar orbiter Luna 19. The S-band and X-band radio waves passing through the limb of the Moon emitted from VRAD2 on Ouna are received on ground stations to detect which any variation exist in frequency of waves. The UPI instrument is an imager to observe plasma phenomena of terrestrial upper atmosphere such as aurora from lunar orbit.

HDTV cameras are onboard for public outreach and stunning movies of "Earthrise", lunar surface etc. have already been broadcasted.

Table1. Science instruments and experiments

XRS	X-ray spectrometer
GRS	Gamma-ray spectrometer
MI	Multi-band imager
SP	Spectral profiler
TC	Terrain camera
LRS	Lunar radar sounder
LALT	Laser altimeter
RSAT	Relay satellites transponder
VRAD	Differential VLBI radio source
LMAG	Lunar magnetometer
CPS	Charged particle spectrometer
PACE	Plasma energy, angle, composision and experiment
RS	Radio Science
UPI	Upper-atmosphere and plasma imager
HDTV	High definition TV camera system

Detectors of these instruments are allocated on the panels of Kaguya spacecraft as shown in Fig. 1. The figure shows the schematic diagram of Kaguya on transfer orbit to the Moon before release of subsatellites. Most of instruments are fixed on the +Z panel which directs to the Moon to observe the lunar surface. Detectors observing the Sun and space are put on the –Z panel.

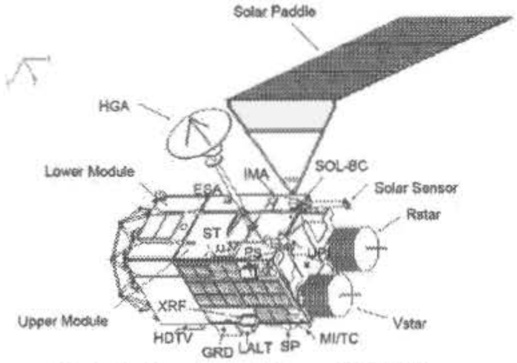

Fig.1. Configuration of Kagya (SELENE)

Science Targets: All instruments have highest-level quality in their specification which expect to get highest-level data for lunar science. First level of science can be achieved by integrating data obtained complementarily by plural instruments in a same category of useful characteristics.

Lunar chemical constituents: Second level of lunar sciences are studied integrating each category of science data. Lunar chemical constituent is a first priority target in studying origin of the Moon and Chemical distribution of the inner area of primordial solar system.Two categories of data, elemental abundance of lunar surface by XRS and GRS, and mineral composition by MI and SP define the rock types and their distribution on the lunar surface. Information of subsurface constituents in lunar crust can be acquired by investigating central peaks of craters formed by rebound of impact shock in crater formation, which are observed larger than 15 km in diameter on the Moon. Large basins such as South Pole Atkins in diameter of 2500 km are scooped to 12 km depth and expose interior materials of lower crust or extrude upper mantle of the Moon. These remote-sensing data reveal about 15 % volume of chemical constituent of the Moon.

Gravity field measurement deduces knowledge on polar moment of inertia of the Moon, to estimate the size of lunar core. Gravity data by Lunar Prospector estimates the iron core radius of 220 to 450 km[3]. Science results of Kaguya mission can not definitely estimate the whole abundance of the Moon, because the mission has never had any instruments of in-situ measurement of lunar interior. However, it is possible to improve intensively the knowledge on chemical constituent of the Moon by assuming mantle material constituent by Apollo seismological investigation.

Lunar interior structure: As mentioned in previous subsection, size of lunar core allows to be estimated using polar moment of inertia deducing from gravity field measurement. Shallow interior and subsurface structures can be investigated directly by LRS. Sounding by 5 MHz radio wave reveals subsurface layer structure such as density and/or material discontinuity up to about 5 km depth. Gravimetry data by RSAT and VRAD, and topographic ones by LALT will be used to estimate thickness of crust of whole Moon. Crust in basin area and mares in nearside is thin, and highland in farside is overlaid on thick crust. Kaguya mission definitely improve certainty of crustal thickness.

Dichotomy of nearside and farside: The dichotomy in the Moon is recognized in topography and rock distribution between nearside and farside. Large mares are occupied 60 % of lunar nearside. Large altitude difference more than 16 km is formed in farside. The dichotomy is investigated by geological study of material distribution and crustal thickness.

Differentiation in magma ocean: If the origin of the Moon is formation of "magma ocean", many evidences must be retained on the lunar surface. Rock distribution must be identified as an evidence of differentiation of magma ocean. Formation of South Pole Atkins basin and large mares by flooded magma in nearside are main geological events after occurrence of magma ocean 4.6 billion years ago. Therefore, geological recovery or reburying of the basin and mares is necessary to reproduce magma ocean age. Detailed investigation on geology by Kaguya makes clear the origin of magama ocean. Magma ocean model has large advantage in giant impact origin for lunar formation. Short duration of accretion to the Moon after the giant impact allows to heat up the surface of the Moon enough realize magma.

Origin of lunar magnetic field: Apollo rock sample contains magnetic minerals assuming magnetization in weak but definite magnetic field. In early time the Moon may have definite magnetic field such in the Earth. LMAG Kaguya mission is searching weak magnetic remnant less than 10^{-5} Tesla collaborating with electron reflectometer.

Origin and evolution of the Moon: Ultimate targets in lunar science are "Origin and Evolution of the Moon". Second level of science targets as mentioned in previous section may direct to the final target. Kaguya mission is expected to get new insight in lunar science. In-situ observation using lander system must be executed to study structure and material distribution of the lunar interior.

References:[1] Kato et al., Adv. Space Res., 42, 294-300, 2008. [2] Adler et al., Proc. LSC. 4th, 2783-2791, 1973, [3] Konopoliv et al., SCIENCE, 281, 1476-1480, 1998.

USE OF X-RAY COMPUTER TOMOGRAPHIC IMAGERY IN LOCATION OF TARGET FRACTURES AND PROJECTILE FRAGMENTS AROUND LABORATORY HYPERVELOCITY IMPACT CRATERS.

A. T. Kearsley[1], M. J. Burchell[2], R. Abell[1] and M. J. Cole[2]. [1]IARC, Department of Mineralogy, Natural History Museum, London, SW7 5BD, UK, (antk@nhm.ac.uk), [2]School of Physical Science, University of Kent, Canterbury, CT2 7NH, UK,

Introduction: Fracture development is an important process in hypervelocity impact cratering on brittle targets of every scale from micrometers to 100s of kilometers. Careful mapping and orientation of structures visible at the surface may allow interpretation of cratering mechanisms e.g. [1], especially those related to formation and late stage modification of much larger craters. However, large scale structural trend information available from down-well sensing or cores from deep-drilling is unfortunately limited, and fine-scale interpretation of seismic data returned from beneath highly fragmented crater infill is very difficult.

Analysis of melt at impact craters may reveal the type of bolide [2], although discovery of (modified) cm scale solid chondritic fragments [3] in melt of high meteoritic content at the Morokweng crater [4], and the complex behaviour of iron projectiles in laboratory impacts [5] highlight limitations in current understanding of projectile processing during impact. Signatures of bolide components have also been found in fractures containing breccia and impact melt e.g. [6-8], usually as distinctive minor- and trace-element and extraterrestrial isotope signatures within bulk rock, rather than as discrete impactor fragments. Projectile residue occurs in fractures around sub-mm craters formed by micrometeoroid impact on brittle surfaces of spacecraft in low Earth orbit, and also in experimental mm scale impacts of metal onto rock [9].

Mechanisms of impact-driven fracturing have been studied by a number of authors, e.g. [10] who used tensile and fracture strengths determined in laboratory experiments to model fracturing at Barringer Crater [6]. Direct, true-scale comparisons between numerical simulations and experimental impacts can include realistic brittle fracturing, and it is therefore worthwhile to document target subsurface structure in detail. Cut sections have been used to show fractures in a number of studies e.g. [5, 10]. In this paper we show the results of testing high-resolution X-ray Computed micro-Tomographic imaging (micro-CT) [11] in locating three dimensional sub-surface fractures and impactor residue in laboratory impacts at cm scale.

Experimental methods: Targets for preliminary study were cast blocks of transparent silicone polymer, density ~2.3 gcm^{-3}, in which optical imagery could verify CT reconstructions. Projectiles were spheres of Cu (1 mm) and stainless steel (2 mm), fired at ~5 kms^{-1} in the two-stage light gas gun at the University of Kent. Impacted targets were photographed, and imaged in the X-Tek HMX-ST CT system at the Natural History Museum. A range of electron gun accelerating voltages were used (typically 180 kV), onto tungsten which generated 50-70 keV X-rays, filtered through a 1 mm Cu foil to reduce X-ray background. The Perkin-Elmer detector captured images at 720 rotation points, each accumulated for 1 second. Tomographic reconstructions with fine voxel size (40 µm) were then computed for specific subsets of transmission intensity, representing solid polymer, open fractures and projectile remnants.

Subsurface Fracturing: Targets showed extensive damage, with spallation of the surface in roughly triangular shards, bounded by subvertical radial fractures and low angle basal fractures. The melt-lined pit, marking the location of the transient crater, was lost by extensive spallation due to relatively deep penetration resulting from strong density contrast between projectile and target. Nevertheless, melt-pit dimensions can be inferred as ~1 mm diameter. Below the surface, both optical and CT images reveal a complex suite of intersecting fractures (Figures 1, 2 and 3).

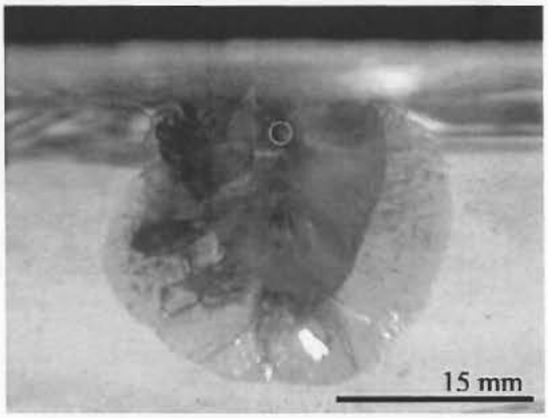

Figure 1. Side view optical image of structure below surface of block, created by impact of 1 mm Cu sphere from above. Approximate position of spalled crater melt pit shown in red. Note the extensive inclined sub-radial fractures, and fragments of reflective Cu projectile, to ~18 mm depth and ~12.5 mm radius.

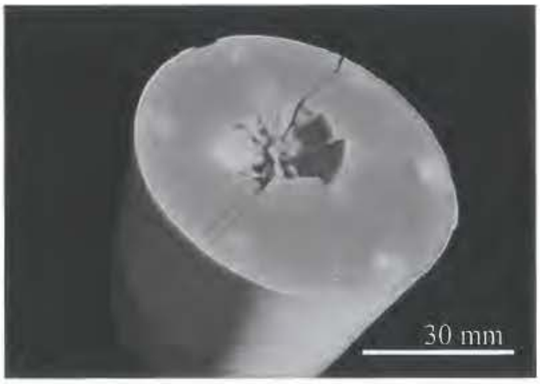

Figure 2. CT reconstruction of target surface viewed from above/oblique. Stainless steel projectile, 2mm diameter, shot G160606#1. Note extensive spall detachment of segments bounded by radial fractures.

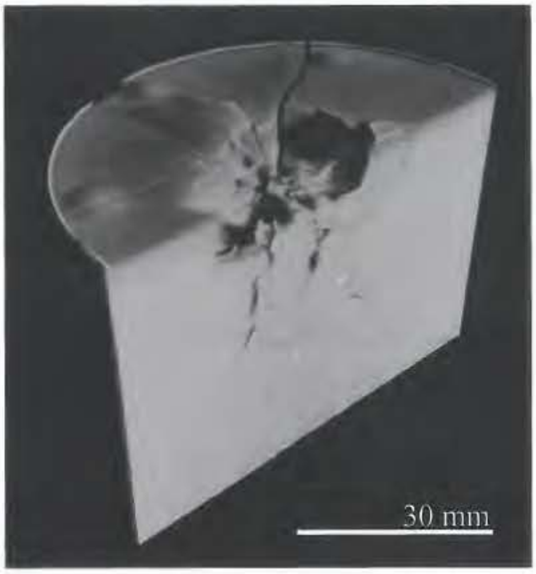

Figure 3. Cutaway vertical section in CT reconstruction, showing fracture system extending to >> 10 times melt pit dimensions, shot G160606#1.

Projectile fragment distribution.: Irregular shrapnel, up to mm size, were found scattered along the full extent of the fracture systems (Figure 4).

Discussion: X-ray micro-CT clearly shows great potential for visualization of fracturing and projectile debris location. Our first target samples have proven ideal for testing CT technique on material of similar density to many rocks, but we do not yet have an adequate equation of state for the polymer to enable numerical modeling of impact fracture development.

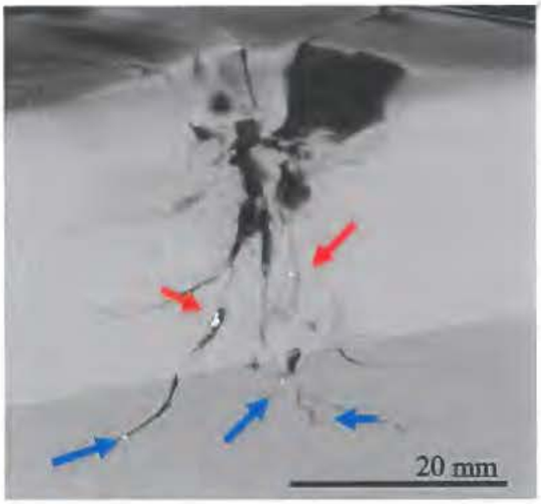

Figure 4. CT cutaway, showing steel projectile fragments (bright) in the fracture system below impact structure, shot G160606#1. Red arrows denote location of fragments in vertical section, blue horizontal.

We are currently examining an impacted block target of a porous sandstone, which shows a well-defined (albeit irregular) melt pit, and a surrounding zone of shallow conchoidal spallation, with melt-lined surfaces that display abundant droplets of impactor metal composition. We shall use micro-CT to determine the extent of sub-surface fracturing and deposition of projectile-derived residue in this sample. Our next experiment will impact a meteoritic kamacite grain onto a target of laminated mylonitic garnet gneiss, from which we aim to document both projectile emplacement and compositional fractionation in ejecta.

Acknowledgements: We wish to thank the staff of X-Tek for their assistance in the acquisition and processing of our CT reconstructions.

References: [1] Kenkmann T et al. (2005) *GSA Spec. Paper, 384,* 85-115. [2] Koeberl C (2002) *Min. Mag., 66,* 745-768. [3] Maier W D et al. (2006) *Nature, 441,* 203-206. [4] Koeberl C and Reimold W U (2003) *Geochim. et Cosmochim. Acta, 67,* 1837–1862. [5] Kenkmann T et al. (2007) *LPS XXXVIII,* Abstract #1831. [6] Kring D A (2007) *Guidebook to the Geology of Barringer Meteorite Crater, Arizona (a.k.a. Meteor Crater). LPI Cont. 1355.* [7] El Goresy A and Chao E C T (1976). *EPSL, 31,* 330-340. [8] Koeberl C et al. (1996) *Geology, 24,* 913-916. [9] Kearsley A T et al. (2004) *Meteoritics and Planetary Sci., 39,* 247-265. [10] Ai H-A and Ahrens T J (2004) *Meteoritics and Planetary Sci., 39,* 233-246. [11] Koeberl C et al. (2002) *JGR, 107,* 1-9.

THE STRUCTURAL INVENTORY OF OBLIQUE IMPACT CRATERS: T. Kenkmann[1] and M. H. Poelchau[1], [1]Museum für Naturkunde, Mineralogie, Humboldt-Universität Berlin, thomas.kenkmann@museum.hu-berlin.de

Introduction: Gilbert [1] and Shoemaker [2] derived the probability for oblique impacts. Statistically, 50% of all collisions of asteroids or comets occur at angles of less than 45°, and about 7% at angles less than 15°. While the highest probability exists for an angle of incidence of 45°, vertical and horizontal collisions are extremely unlikely. Thus, nearly all impacts are somehow oblique. Here we use the term "oblique" for craters formed at angles between 35° and 15° from the horizontal, and as "highly oblique" or "acute-angled" impacts below 15° incidence.

Based on the existing analogy of explosion and impact cratering that assumes a point-like source of energy, craters should bear no hints to the impact vector. However, experimental analysis [3; 4], remote sensing [5], field studies [6], and recent 3D numerical simulation [7; 8] show that for oblique and highly oblique impacts it is possible to decipher impact incidences. Several methods were proposed to reconstruct azimuth and angle of impacts. These techniques are based on (i) the uneven distribution of ejecta around impact craters, e.g. [3; 5], (ii) asymmetries in crater morphology, e.g. [3; 9] (iii) the uneven distribution of shock metamorphic overprint of target rocks [10], and (iv) asymmetries in the subsurface structure of the crater [6; 9]. In this contribution we mainly focus on the criterion (iv).

(i) Method (i) is a generally accepted and experimentally proven technique [3; 4] that is sensitive if the impact angle is oblique. In such cases a preferential concentration of ejecta occurs down range and a "forbidden" ejecta zone develops up range. This zone further expands with decreasing angle. At highly oblique angles, "butterfly" ejecta blankets form, where the majority of ejecta is distributed cross range. Ricochet can occur at grazing angles when a significant fraction of the projectile rebounds from its initial point of contact on the target surface and continues down range. In all cases the ejecta pattern shows a bilateral symmetry along the trajectory axis. The uneven ejecta blanket is certainly the best suited criterion to infer oblique impact trajectories. However, as ejecta blankets are rarely preserved on Earth, (ii-iv) have to be considered.

(ii) The crater outline is insensitive to the impact trajectory and remains circular with the exception of highly oblique impacts. Schultz and Anderson [9] proposed an enhanced rim/wall collapse in the up range direction, an up range offset of the central uplift, combined with a down range breaching, and a large central uplift diameter relative to crater diameter for oblique complex craters. However, Ekholm and Melosh [11] who studied Venusian craters concluded that these are statistically unwarranted criteria for assessing an oblique impact.

(iii) Experimental and numerical studies have shown that the distribution of peak shock pressures within the target is asymmetrical in the case of oblique impacts with a concentration down range [10; 12]. However, to our knowledge no systematic field study has been carried out until now that documented the shock metamorphic overprint sector-wise and related the derived pressure magnitudes to an oblique impactor trajectory.

(iv) Field studies at Upheaval Dome, UT, USA [6; 13] in 2002, at Spider, WA, Australia, and Matt Wilson, NT, Australia in 2006 and 2007 [14], as well as revisiting the structural analysis of Gosses Bluff, WA, Australia by [15] revealed that bilaterally symmetrical arrangements of structural features exist in the subsurface of these impact craters which indicate a preferred motion and deformation along the axis of symmetry. In the following section we briefly summarize some structural aspects of these craters:

Upheaval Dome, UT, USA, 5,2 km diameter at present level of erosion: The central uplift shows a systematic departure from a pure radial symmetric flow. Enhanced shortening roughly in the NW–SE direction is most evident in the core of the central uplift, where a set of imbricated slices displays dominantly top to the SE thrusting. The thrusts are bent and have a concave, down range-facing outline. The center is subdivided into two halves by a large NW-SE-trending reverse fault which continues as a syncline up range and an anticline down range. Further outward and upward the structural asymmetry is preserved in dominant radial faults and an elliptical bedding outline but disappears at the edge of the central uplift, i.e. the ring syncline. If we define the extent of the central uplift as the radius of the ring syncline R_s, the ratio of R_s to the present crater radius R is ~0.7.

Spider, WA, Australia, proposed diameter 13 km: The Spider crater is situated in a broad and gentle syncline. The central uplift region of Spider displays a very similar arrangement of aligned imbricated fault blocks compared to Upheaval Dome, while the consistency of SSE directed thrusting is even more striking. The thrust slices are oriented bilaterally around the central uplift. In the SSE sector (the proposed down range sector) the slice orientations gradually change towards a NNW-SSE strike. This causes the collision of the two thrust systems along the SSE trending symmetry axis. The thrust sheets are bent and have a concave up range-facing outline, as opposed to the down range-facing outline in Upheaval Dome. Dip of strata within the thrusts range between 20 and 60°. The ramp angles of the thrust slices dip at similar inclinations as the bedding planes. This leads only to a moderate stratigraphic uplift accommodated by the thrusts. The major uplift occurs in the center where a penetrative shock metamorphic overprint exists (shatter cones). A subdivision of the core into two halves could not be found. We suspect that the dominant thrust direction in this crater also reflects a prevailing lateral displacement direction during crater collapse, and thus an oblique impact from NNW as already proposed by [16]. The amount of stratigraphic uplift and the ratio of central uplift radius R_s to the proposed crater radius R are small (0.3?) at Spider relative to Upheaval Dome. However, the outer rim of the structure is poorly defined.

Matt Wilson, NT, Australia, 6.3 x 7.5 km diameter at present level of erosion: Matt Wilson structure is outlined by a ring monocline that delineates an ellipse of 6.3 x 7.5 km with the long axis trending NE-SW. The aspect ratios of the ellipsoid of the crater rim monocline and the ring syncline are both ~1.2. Matt Wilson contains a broad dome-like central uplift of great lateral extent (R_s/R ~0.8). In the center of the dome steeply dipping fault blocks of lower units are exposed. The stratigraphic uplift of the core is ~200 m. Further outwards, fault zones often strike NE-SW. This direction corresponds to the long axis of the ellipsoidal outline and the axis of symmetry. Most of the these faults are strike slip faults and have a transpressive character, often forming positive flower structures. As in Upheaval Dome and Spider, the inner part of the central uplift shows stacked, steeply dipping thrusts. They strike NW-SE (perpendicular to the axis of symmetry) and dip to the NE. Folding of these thrust units along steeply plunging fold axes occur in the innermost part of the structure. We interpret the preferred stacking of thrust sheets both within the central uplift and in the surrounding ring syncline as an up range to downrange transport of rock.

Gosses Bluff, WA, Australia, 24 km diameter at present level of erosion: At Gosses Bluff, SSW directed thrusting is dominant in the central uplift. As in the other craters no up range offset of the central uplift is evident on the basis of geophysical data. In the innermost part of Gosses Bluff, the central uplift is breached in the proposed down range direction.

Discussion and Conclusion: We document remarkably consistent arrangements of imbricate thrust slices in the central uplifts of four complex impact craters. The preferred orientation of these thrusts accommodates shortening in thrust direction. With regard to experimental and numerical studies of oblique impact cratering, we infer that this lateral displacement component reflects a shift in the onset of crater collapse and the migration of the uplifting crater floor down range, i.e. in the impact direction. Thus, this structural arrangement is regarded as a new tool to derive impact trajectories in eroded craters. Validation of the structural method requires craters with other unequivocal attributes for oblique impact craters such as preserved asymmetric ejecta blankets, or elliptical outlines. The elliptical shape of Matt Wilson crater is regarded as an independent proof of our method. As we have found these structural features only in craters with flat lying sedimentary targets this seems to be a prerequisite to form imbricate stacks. Target heterogeneities such as joint sets may influence the specific geometries of the imbricate stacks (convex or concave shapes). A systematic offset of the central uplift with respect to the crater center could not be verified.

Acknowledgement: The project is financed by DFG, grant KE 732/11-1.

References: [1] Gilbert, G. K. (1893) Bull. Philos. Soc. Wash., 241-292. [2] E.M. Shoemaker, 1962, in: Z. Kopal (Ed.), Physics and Astronomy of the Moon, Academic Press, New York, 1962, pp. 283–351. [3] Gault, D. Wedekind, J. A., 1978, Proc. Lunar Planet. Sci. Conf. 9, 3843–3875. [4] Anderson, J.L.B. Schultz, P.H. Heineck, J.T., 2004, MAPS. 39, 303–320. [5] Herrick, R.R. Forsberg-Taylor, N.K., 2003, MAPS, 38, 1551–1578. [6] Scherler, D., Kenkmann, T., Jahn, A., 2006, EPSL 248, 28-38. [7] Shuvalov, V.V. Dypvik, H. 2004, MAPS. 39, 467–479. [8] Elbeshausen, D. et al., 2007, Bridging the Gap II. [9] Schultz, P. H. and Anderson, R. R., 1996, Spec. Pap. Geol. Soc. Am. 302, 397–417. [10] E. Pierazzo, E.., Melosh, H.J., 1999, EPSL. 165, 163–176. [11] Ekholm, A.G. Melosh, H.J. 2001, Geophys. Res. Lett. 28, 623–626. [12] Dahl, J.M. Schultz, P.H., 1998, LPSC 29 #1958. [13] Kenkmann, T., Jahn, A., Scherler, D., Ivanov, B. A., 2005, Spec. Pap. Geol. Soc. Am. 384, 85–115. [14] Kenkmann, T., Poelchau, M., 2008, 39 LPSC. [15] Milton, D.J. Glikson, A.Y. Brett, R., 1996, AGSO J. Aust. Geol. Geophys. 16, 453–486. [16] Shoemaker, E. M., Shoemaker, C. S., 1996, AGSO Australian Journal of Australian Geology & Geophysics, 16, 379-398.

THE REMARKABLE METEORITE IMPACT EVENT ON SEPTEMBER 15, 2007, CARANCAS, PERU: WHAT DID WE LEARN?.

T. Kenkmann[1], N. A. Artemieva[2], K. Wünnemann[1], H. Poelchau[1], D. Elbeshausen [1], H. Nunez del Prado[3], [1]Museum für Naturkunde, Mineralogie, Humboldt-Universität Berlin, Germany, [2] Institute of Geospheres Dynamics, Russian Academy of Sciences, Moscow, Russia, [3]Instituto Geológico Minero y Metalúrgico (INGEMMET), San Borja, Lima, Peru, Peru, thomas.kenkmann@museum.hu-berlin.de

It is a widely accepted view that stony meteorites below a threshold size of ~100 m undergo major disruption and deceleration during their passage through the atmosphere as their strength is less than the aerodynamic stresses that occur in flight. The small fragments that result from break-up rain down at terminal velocity and are not capable of producing impact craters. The Carancas cratering event, however, demonstrates that metre-sized stony meteorites indeed can survive the atmospheric passage under specific circumstances. An H4-5 chondrite [1] struck the Earth south of Lake Titicaca in Peru on September 15, 2007, and formed a crater 14.2 m across. It is the first impact event on Earth of which the impact trajectory as well as the impact itself were witnessed. We present results of a detailed crater survey (Fig. 1) and reconstruct the crater formation. By modelling the atmospheric traverse we demonstrate that a low cosmic velocity (11-14 kms^{-1}), a very shallow entry angle (8-15°), and a low projectile mass (<5 tonnes) are prerequisites for the survival of stony meteoroids with a strength of a few MPa. The Carancas projectile was decelerated to terminal velocity of 200-300 ms^{-1}, insufficient to produce a shock wave with associated deformation features. The impact occurred at a steep angle (70-75°) and transferred an energy of ~62 MJ into the target. Aerodynamic and crater modelling are consistent with field data, microscopic inspection, and observations by witnesses. The probability of such impacts on Earth is about one event every one hundred years.

[1] Meteoritical Bulletin Database, Meteoritical Society: http://tin.er.usgs.gov/meteor/ (2008)

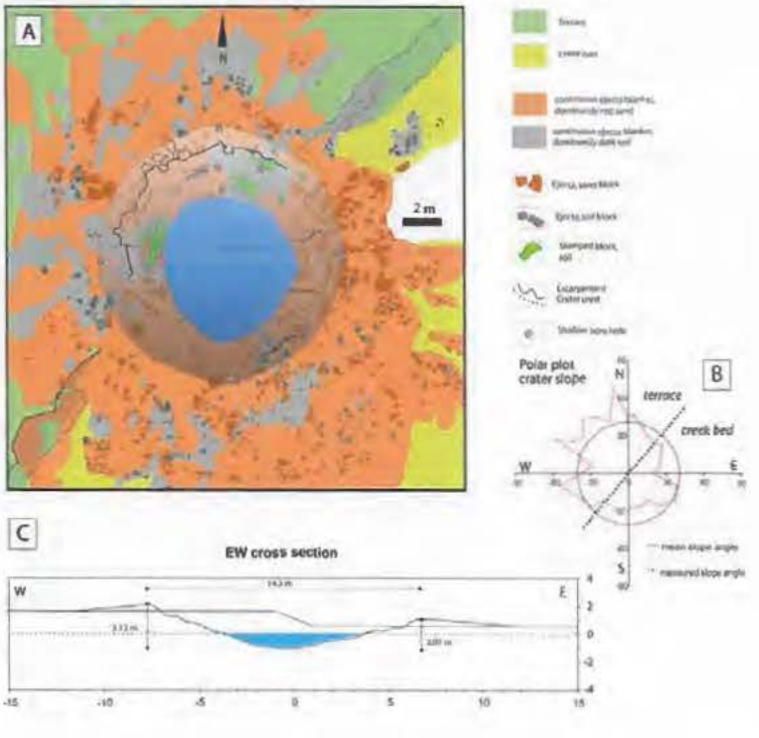

Fig. 1 A, Geological map of the crater. The stippled line delineates the crater crest. Two ejecta lithologies were distinguished: reddish sand and dark soil. Blocks were separately mapped at sizes >0.2 m.. B, Polar plot of the crater slope at the target level showing steep slopes in the NW sector. C, E-W profile through the crater indicates a depth/ diameter ratio of the crater of 0.18 when averaging the altitude differences between the terrace and the creek bed. A parabola fitted to this profile was used to estimate the excavated crater volume, which is about 160 m^3.

REMOTE SENSING AND STRUCTURAL ANALYSIS OF JABAL WAQF AS SUWWAN METEORITE IMPACT.

M. Khirfan[1], T. Kenkmann[2], E. Salameh[1], Y. Omary[1], and W.U. Reimold[1], [1]University of Jordan, jubeiha 11942, Faculty of Science, Jordan (khmaria@hotmail.com); [2]Museum of Natural History (Mineralogy), Humboldt University, Invalidenstrasse 43, 10115 Berlin, Germany.

A large meteorite impact structure has recently been discovered in the Middle East, in Jordan [1], at Jabal Waqf as Suwwan (meaning in Arabic: Mountain of Standing Chert Layers) (Fig. 1). This is the only known impact structure between India and the Mediterranean Sea. Jabal Waqf as Suwwan measures about 6 km in diameter. Its central uplift of ca. 900 m diameter is extremely well exposed and provides a view through the entire stratigraphic sequence. The structure is formed in Lower Cretaceous and early Paleogene strata. Since the original regional mapping of Jordan by the German Mission in the 1960s. the structure had been known as a cryptoexplosion structure. Initial ground-based investigation resulted in findings of many sites with shatter cones in sandstone and limestone, confirming the impact origin. In addition, limited shock metamorphic deformation in quartz has been reported [1,2].

The current study involves thorough investigation of available remote sensing data (Landsat TM 5, aerial photographs) of the area. We will report at the conference lineament and drainage pattern analysis for the impact structure and the region surrounding it. A digital elevation model as well as aspect and slope analyses will be reported.

At present detailed lithological and structural mapping of the entire impact structure, but particularly of the central uplift structure, is carried out, and the results will also feature in our presentation. The discussion of the structural data will focus on the formation mechanisms for central uplift structures of large, complex impact structures, and draw on comparison with Upheaval Dome, formed likes Jabal Waqf as Suwwan entirely in sedimentary target rocks.

References: [1] Salameh E., Khoury H. and Schneider W. 2006. Jebel Waqf as Suwan, Jordan: a possible impact crater- a first approach. Zeitschrift der deutschen Gesellschaft fur Geowissenschaften, 157, 1-8. [2] Salameh, E. et al., Meteoritics and Planetary Science, in press.

Fig.1 Satellite image of the circular Jabal Waqf as Suwwan structure.

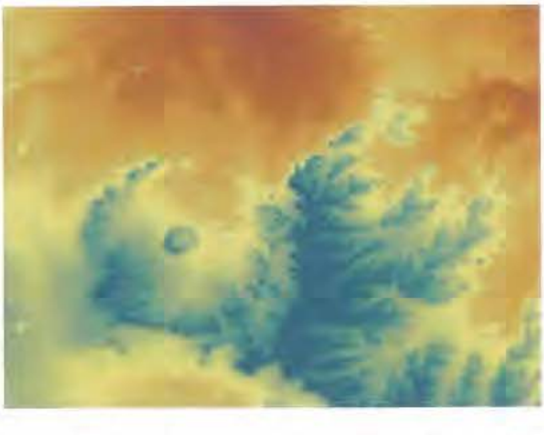

Fig.2 DEM image of the Jabal Waqf as Suwwan structure. The crater structure is about 6 km in diameter.

Fig. 3 Photograph of the southern part of the central uplift. The central uplift consists of tilted and bent blocks of various sizes.

Fig. 4 Shatter Cone within the Upper Cretaceous chert layer. Shatter cones are particularly frequent in the outer region of the central uplift.

COMPARISON OF MARINE-CRATER STRATIGRAPHY: CHESAPEAKE BAY AND WETUMPKA.

D. T. King, Jr.[1], L. W. Petruny[2], R. S. Harris[3], J. Glidewell[1], and R. C. Johnson[1] [1]Geology Office, Auburn University, Auburn, AL 36849 USA [kingdat@auburn.edu], [2]Astra-Terra Research, Auburn, AL 36831-3323 USA [lpetruny@att.net], [3]Dept. Geology, University of Georgia, Athens, GA 30602 [robert_harris@brown.edu].

Introduction: Chesapeake Bay crater, Virginia, is a late Eocene impact structure, which is completely buried beneath the Atlantic Coastal Plain. Chesapeake Bay consists of an inner crater (~ 38 km in diameter) and an outer, annular trough, which gives the structure a diameter of ~ 85 km. Wetumpka impact structure, Alabama, is a Late Cretaceous impact feature, which is moderately eroded and largely exposed near the Gulf Coastal Plain-Piedmont boundary. Wetumpka has an inner crater, which is ~ 5 km in diameter and, on the south and southwest, a ~ 7-km wide surrounding disturbed terrain, which is much like a segment of an annular trough. The shape of Chesapeake Bay crater has been described as an 'inverted sombereo,' and comparably Wetumpka has been called an 'inverted baseball cap.' Both are marine impacts of the continental shelf and the shelf stratigraphy in both instances consisted of a section of unconsolidated clastics underlain by crystalline basement rocks. Post-impact sediments and ejecta are present at Chesapeake Bay, but not at Wetumpka.

Drilling at Chesapeake Bay: Recent drilling at Chesapeake Bay in the inner crater (the Eyreville core), as discussed by [1], revealed a stratigraphy of 444 m of post-impact sediments, which was underlain (in order of penetration) by 652 m of "sediment clast breccia and sediment mega-blocks"[1], 275 m of "granite megablock(s)"[1], 22 m of "sediment with lithic blocks"[1], ~157 m of "suevitic and lithic impact breccia"[1], and "schist and pegmatite, minor impact breccia veins"[1]. This recent drilling ended in the schist and pegmatite unit at a depth of ~ 1,766.3 m.

Drilling at Wetumpka: Drilling during 1998 in the center of Wetumpka's 5-km diameter "inner crater" revealed an upper layer (~ 100 m) of sediment clast breccia and mega-blocks, which was underlain by an upper layer of suevitic and lithic impact breccia (~ 50 m) and a lower breccia layer of varied lithology ranging from sediment clast breccia to crystalline clast breccia (~ 50 m) [2, 3]. The ~ 200 m drill holes ended in the lower breccia layer.

Comparison of drilling results: Because post-impact sediments are likely absent at Wetumpka, the comparison starts at the sediment clast breccia and sediment mega-blocks interval, which is present as the thickest unit in both structures despite the fact that Wetumpka's unit is moderately eroded. Units below the sediment clast breccia and sediment mega-blocks interval are similar in both wells. Schist megablocks compare to granitic blocks in terms of origin.

Drilling penetrated to a point within the fill of the inner central crater in both instances. At Chesapeake Bay, this point was a little over one-half way through the inner basin fill, and at Wetumpka this point was a little under one-half way [3] (Fig. 2).

Comparison of stratigraphy: Chesapeake Bay crater and Wetumpka impact structure have similar inner crater filling stratigraphies, and when proportionately scaled (Fig.1; Wetumpka depths X 1.2), look very similar, especially regarding the relative size of the inner crater and the annular trough zone. If a hole could be drilled to a depth of ~ 1 km at Wetumpka, this would reveal a deeper stratigraphy and basement rock relationships a depths comparable to ~ 5-6 km at Chesapeake Bay.

References: [1] Gohn G. S. et al. (2006) *EOS, 87,* 349, 355. [2] King Jr. D. T. et al. (2002) *EPSL, 202,* 541-549. [3] Johnson R. C. (2007) *MS thesis, Auburn Univ.* [4] Poag C. W. (2004) *Springer Impact Series*.

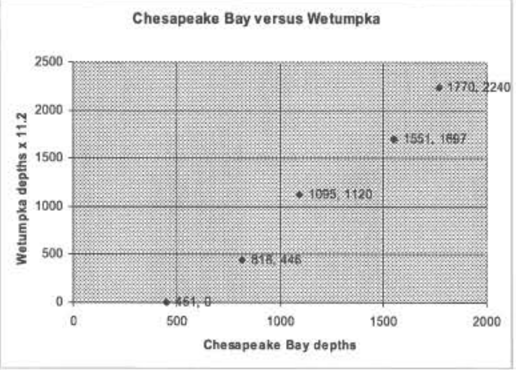

Figure 1. Apparent linear relationship between depths to key levels in the Chesapeake Bay and Wetumpka impact structures in cross-plot. Note that Wetumkpa depths have been multiplied by a factor of 11.2 to account for the scale difference between the two structures. As each point, the numbers are Chesapeake Bay (Eyreville) depth (left), and Wetumpka depth (right). From upper right, the key points plotted are base of cores, top of basement megablocks, top of crystalline megablocks, top of sedimentary slump blocks, and top of impactoclastic sands.

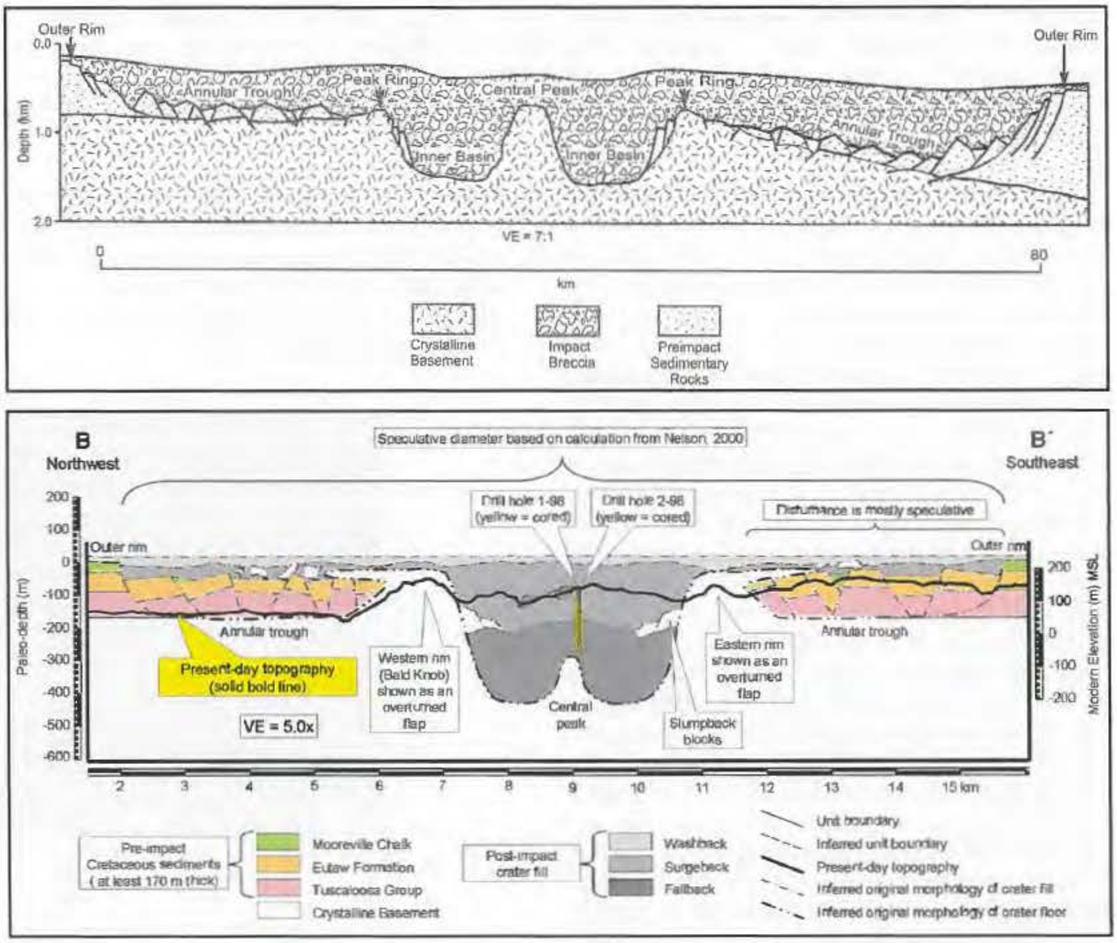

Figure 2. Comparative geologic cross sections of the Chesapeake Bay and Wetumpka impact structures proportionately scaled so that they appear the same size. Cross section at top from [4] and at bottom from [3].

MAGNETIC DETECTION OF LARGE MAGNETIC FIELDS THAT OCCURRED DURING THE VREDEFORT IMPACT, IMPLICATIONS FOR MARS MAGNETIC ANOMALIES .

G. Kletetschka[1,2,3], and T. Adachi[1,2], [1]Catholic University, Physics Department, Washington DC, USA, Kletetschka@nasa.gov, [2]GSFC/NASA, Code 691, Greenbelt, 20771, USA, [3]Institute of Geology, Academy of Sciences of the Czech Republic, Prague, Czech Republic.

Introduction: Margnetic anomalies on Mars generated interest about the impact related magnetization processes. Magnetic studdies on rock specimens from Vredefort crater revealed centimeter scale volumes with intense remanent magnetizations that were randomly oriented in respect to each other [1]. Magnetic grains carrying this magnetic remanence crystallized during the impact [1]. Random orientation causes an absence of large scale magnetic signature over the Vredefort crater and by analogy, may also be responsible for absence of magnetic anomalies on Mars inside the large impact craters opening the possibility for global magntic field on Mars during the formation of large impact craters [1]. We found that portions of these rocks are unusually strongly magnetized, reaching almost saturation level while other portions were virtually demagnetized compared to the magnetization expected from rock forming inside the geomagnetic field during the regular terrestrial rock forming processes. The unusual nature of the magnetization of these rock requires large magnetizing field. We performed magnetic scans over the surfaces of the rock specimens affected by the impact. Magnetic scans over the rock polished surfaces and/or thin sections under different fields gives not only information about the susceptibility distribution over the rock, separation of induced and remanent components of magnetizations, but also can map the magnetization efficency of various rock segments. Even-though the scans were performed with just a vertical component sensor, the nature of magnetization in the samples allows us to determine direction and amplitude of the magnetization volumes within the specimen.

Novel Technique: NASA Goddard Code 691 provided the Magnetic Properties lab previously used for magnetic testing and imaging of the microshutter arrays for James Web Space telescope. Imaging equipment is being used for the described Vredefort rock magnetic imaging.

We take advantage of the close proximity of a Hall sensor probe surface (0.125mm) allowing submilimeter resolution scans with sensitivity resolution better than 10 nT. The Hall sensor is brought into close proximity to the surface and laterally scanned. In order to test the new method we magnetically scan the central portion of the dollar bill (Figure 1). The first scan (A.) shown the natural magnetization and depicts an inverse image indicating original magnetization distribution. After the image was saturated with the field parallel to the positive sensor reading, the image acquired a positive appearance (Figure 1 B). The image resolution appears to be more than an order of magnitude better than similar magnetic scanning using giant magnetoresistance sensors. [2]

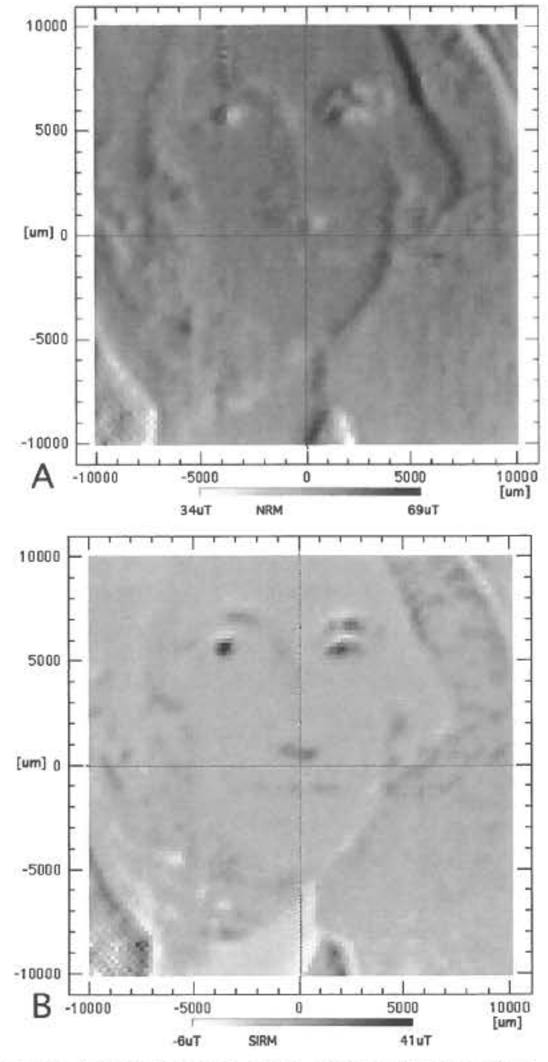

Figure 1: Novel magnetic scans of the central portion of the one dollar bill. Left: The one dollar bill contains natural remanent magnetization (NRM Middle: Magnetic scan image after we applied saturation magnetization (SIRM) to the bill parallel to the ambient field.

Results: Figure 2 shows magnetic scans over the Vredefort granite gneiss sample. The top image is representation of natural remanent magnetization (NRM) while the bottom image shows saturation isothermal remanent magneitzation (SIRM).

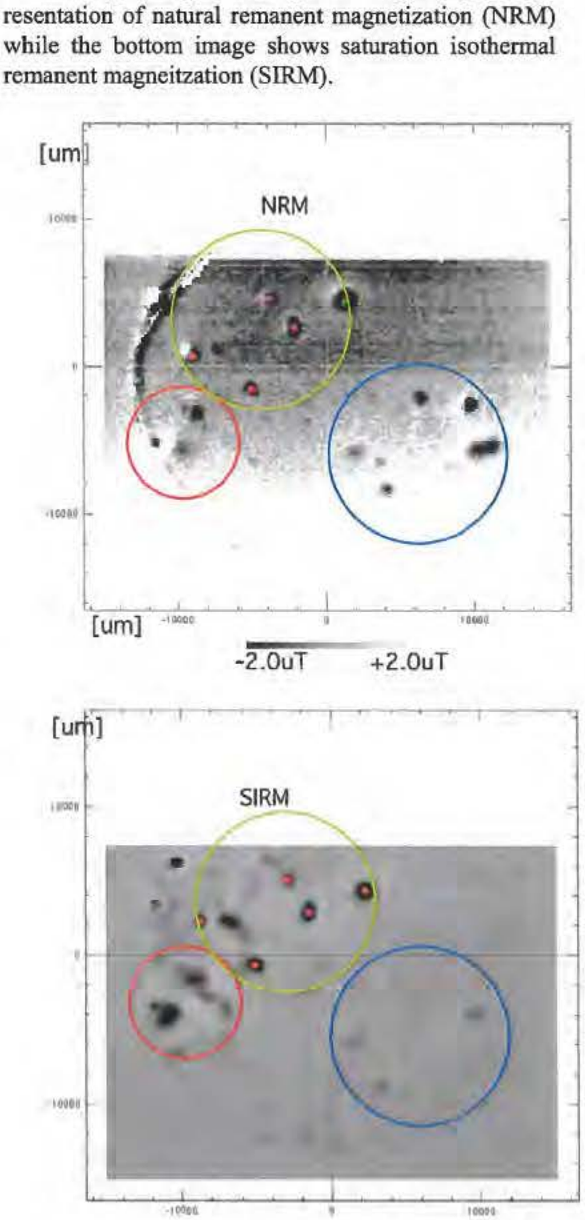

Figure 2: Magnetic scan over (0.2 mm) a flat section of the Vredefort granite gneiss specimen. Top: Vertical component of natural remanent magnetization (NRM), Bottom: Vertical component of saturation isothermal remanent magnetization (SIRM).

Note that the magnetic scale of the NRM scan is adjusted to be 2% of the magnetic scale of the SIRM image. This is because most of the rock that are formed within geomagnetic field acquire ~2% of their saturation remanence [3]. Therefore the similar magnetic intensities (dark color) on both images would correspond to the magnetic grains that formed similarly like magnetic grain in ordinary terrestrial rocks (green circles). However magnetic grains shown in the blue circle indicate that these grains were magnetized more efficiently that regular rocks and therefore may relate to strong magnetic fields that formed during the impact. Finaly the magnetic grain shown by red circles indicate magnetic grains with the original intensity smaller than expected and may represent demagnetization during the impact. The three distinctive regions are apart on cm scale, consistent with observation in [1].

Conclusions:

Novel method allows finding microscopic volumes that were magnetizaed with contrasting magnetic efficiency. The method depicts cm scale volumes of the granite gneiss that were magnetized during the Vredefort impact. Data suggest a presence of large cm-scale magnetic fields during the impact and large cm-scale currents associated with the impact.

Acknowledgement: We thank Robert Hart for providing the rock specimens (granite gneiss) from the outcrops inside the Vredefort crater.

References: [1] Carporzen L., Gilder S. A. and Hart R. G. (2005) *Nature, 435,* 198-201. [2] Uehara M.and Nakamura N. (2007) *Review of Scientific Instruments., 78,* 043708. [3] Kletetschka G. et al. (2003) *Meteoritic & Planetary Science*, 38(3), 399-406.

WHAT CAN BE LEARNED FROM DRILLING INTO IMPACT CRATERS: A REVIEW OF RECENT PROJECTS.

Christian Koeberl[1] [1]Department of Lithospheric Research, University of Vienna, Althanstrasse 14, A-1090 Vienna, Austria. E-mail: christian.koeberl@univie.ac.at.

Introduction: Currently about 170 impact craters are known on Earth; about one third of those structures is not exposed on the surface and can only be studied by geophysics or drilling. The impact origin of geological structures can only be confirmed by petrographic and geochemical studies; thus, it is of crucial importance to obtain samples of subsurface structures. In addition, structures that have surface exposures often require drilling and drill cores, to obtain information of the subsurface structure, to provide groundtruth for geophysical studies, and to obtain samples of rock types not exposed at the surface.

Motivation to Drill (Status): Of the about 175 individual terrestrial impact structures see http://www.unb.ca/passc/ImpactDatabase/ - although the evidence for a few of those listed is not very strong) and other small crater fields currently identified, about half have been drilled in some way or another, although this does not mean that cores were obtained, that drill cores are preserved anywhere for study, or that that the drilling was documented and published. Of those that were drilled, 90% are not exposed on the surface. The initial motivation to drill these structures was either scientific or economic. Drilling was accomplished in order to: (1) confirm the presence of an impact structure and to learn about the physicochemical processes involved through the study of crater geology; and (2) satisfy economic geological interests, such as exploration for hydrocarbons in structural traps. The economic motivation has largely been potential recovery of commercial quantities of hydrocarbons. Indeed, the potential to discover producible quantities of hydrocarbons at terrestrial impact structures is relatively high in sedimentary basins known to contain hydrocarbons, e.g., in North America, approximately 50 % of the known impact structures in hydrocarbon-bearing basins have commercial oil and/or gas fields.

Successful drilling was performed at a number of craters in the form of local, regional, national, or otherwise collaborative projects. Examples are drilling projects in Canada and the former USSR. In many of those cases cores were not documented to the degree that conforms to present-day standards, and/or core are no longer preserved. Other examples of drilling projects include those at the Ries, Manson, Tswaing, Kalkkop, Puchez-Katunki, Morokweng, and Mjolnir craters.

More recently the International Continental Scientific Drilling Program (ICDP) has supported projects to study impact craters. The first ICDP-supported study of an impact structure was the drilling into the 200-km-diameter, K-T boundary age, subsurface Chicxulub impact crater, Mexico, occurred 2001/2, followed by drillings into the Bosumtwi and Chesapeake Bay craters. Soon the El'gygytgyn crater in Siberia will be drilled. For more program details see [1].

Chicxulub: Chicxulub, centered at N 21° 20' and W 89° 30' on the Yucatán Peninsula, México, is the world's third largest known impact structure on Earth. Its formation is widely accepted to have been responsible for the dramatic environmental changes at the Cretaceous-Tertiary (KT) boundary.

The ICDP-financed borehole Yaxcopoil-1 was drilled from December 2001 through March 2002 in the southern sector of the crater. This spot is located about 62 km from the approximate crater center, just off the characteristic high-amplitude magnetic anomalies observed across the central uplift as defined by gravity and seismic data. The Yaxcopoil-1 (Yax-1) borehole was planned to core continuously into the lower part of the post-impact carbonate sequence, the impact breccias, and the displaced Cretaceous rocks. The actual drill site was selected for a variety of logistical reasons. Drilling extended to a depth of 1,510 m. Approximately 795 m of post-impact Tertiary carbonate rocks, 100 m of impactites, and 615 m of pre-impact Cretaceous rocks (megablock) were intercepted. The Tertiary rocks are composed of interlayered carbonaceous siltstones, calcarenite, and rare conglomerate and turbidite. The impactites are composed of suevitic and impact melt breccias that have both undergone significant alteration. These impact breccias have been subdivided into 5 units based on macro- and microscopic observations.

Drill results together with geophysical and borehole database, including new offshore marine seismic data, led to a revised crustal model for the multi-ring Chicxulub structure. The main results were published in two special issues of the journal *Meteoritics and Planetary Science* in June and July 2004. However, given the size of Chicxulub, many questions remain open and additional questions came up as a result of the Yax-1 core results, making Chicxulub an ideal candidate for further drilling studies

Bosumtwi: The 1.07 Ma, 11 km diameter Bosumtwi impact crater in Ghana is one of only four known impact craters associated with a tektite strewn field. It is a well-preserved complex young impact structure, displays a pronounced rim, and is almost completely filled by Lake Bosumtwi, a hydrologically closed basin. Basement rocks are 2.1-2.2 Ga metasediments and metavolcanics of the Birimian Supergroup. Seismic reflection and refraction data defined the position of a 1.9-km-diameter central uplift. An international and multidisciplinary ICDP-led drilling project combined two major scientific interests in this crater: to obtain a complete paleoenvironmental record from the time of crater formation about one million years ago, at a near-equatorial location in Africa, for which very few data are available so far, and to obtain a complete record of impactites at the central uplift and in the crater moat, for ground truthing and comparison with other structures.

The project resulted in retrieval of 16 drillcores within the 8.5-km-diameter Lake Bosumtwi, using the GLAD-800 lake drilling system, from June to October 2004. The 14 sediment cores are being investigated for paleoenvironmental indicators. The two impactite cores, LB-07A and LB-08A were drilled into the deepest section of the annular moat (540 m) and the flank of the central uplift (450 m), respectively. They were the main subject of a special issue of "Meteoritics and Planetary Science" (April/May 2007). Drilling progressed in both cases through the melt rock/impact breccia layer into fractured bedrock. LB-07A comprises lithic (in the uppermost part) and suevitic impact breccias with appreciable amounts of impact melt fragments. Core LB-08A comprises suevitic breccia in the uppermost part, followed with depth by a thick sequence of greywacke dominated metasediment with suevite and a few granitoid dike intercalations. It is assumed that the metasediment package represents bedrock intersected in the flank of the central uplift. I

The results from the Bosumtwi impact crater scientific drilling project are important for comparative studies and re-evaluation of existing data from other terrestrial impact craters, and to understand essential aspects of the impact process.

Chesapeake Bay: This impact structure, 35 Myr old and 85 km in diameter, is one of the largest and best preserved impact structures on Earth. The structure was drilled in the central part at Eyreville in 2005-2006 during an ICDP-USGS drilling project. Three drill cores (Eyreville A, B, and C), intersecting the impact structure to a total depth of 1766 m, were recovered within the central zone of the structure in the deep crater moat. The crater fill comprises post-impact sediments, sediment clast breccias and sedimentary megablocks (the so-called Exmore breccia beds, interpreted as resurge breccias), a large granitic and a small amphibolitic megablock, gravelly sand, suevites and lithic impact breccias (1397-1551 m), and granites/pegmatites and mica schists. In the upper part (above ~1474 m) of the section the suevite is mostly melt rich and contains two intervals (5.5 and 1 m thick) of impact melt rock. In the deeper parts of the section (below 1474 m) mostly suevitic polymict impact breccia alternates with large blocks of cataclastic gneiss. Results of this project are currently being prepared for publication.

Outlook: In 2009 the 18-km-diameter, 3.6 Ma El'gygytgyn impact structure will be drilled in yet another ICDP project, providing again an opportuneity to marry paleoclimate and impact research. This structure is unusual in that the impact occurred into acid volcanic rocks.

However, it is necessary to discuss suggestions towards future drilling projects that are relevant for impact research: what is the importance of studying impact craters and processes, why is it important to drill impact craters or impact crater lakes, which important questions can be answered by drilling, which craters would be good targets and why; is there anything about the impact process, or of impact relevance, that can be learned by drilling outside any craters; what goals should be set for the future; how important is collaboration between different scientific fields collaborating between different science fields? Ipmact cratering studies have much to gain from experience from past drilling projects (ICDP and others), and future scientific drilling of impact structures will provide crucial importance to help us understand the formation of such structures and their geological and biological importance.

References: [1] Koeberl, C., and Milkereit, B. (2007) Continental drilling and the study of impact craters and processes – an ICDP perspective. In: *Continental Scientific Drilling* (eds. Harms, U., Koeberl, C., and Zoback, M.D.), Springer, Heidelberg, p. 95-161.

Acknowledgment: Thanks to W.U. Reimold (HU Berlin), B. Milkereit (Univ. Toronto), G. Gohn (USGS), K. Miller (Rutgers Univ.), J. Brigham-Grette (Univ. Mass.), and M. Melles (Univ. Cologne) and other co-conspirators in the ICDP crater drilling quest, as well as ICDP for funding. Supported by the Austrian Science Foundation FWF, grant P18862-N10 (to C.K.).

IMPACT DEPOSITS AT ROCHECHOUART-CHASSENON-

P. Lambert - Sciences et Applications., Le Lafayette, avenue Kennedy, 33700 Bordeaux-Mérignac, France (lambertbdx@numericable.fr)

Introduction: A fundamental aspect of formation of large meteorite impact is the generation of ejecta deposits. A large effort has recently been expanded towards breccia studies at terrestrial impacts structures (Ries, Bosumtwi, Chixculub, Chesapeake Bay, e.g. [1-4]). They are the only source of ground truth data for proximal impact ejecta studies. Field geology on the Moon, Mars and other planetary bodies of the solar system as well as large-scale experimentation on Earth (explosions) are not realistic. Compared to other terrestrial impact structures, still little is done at Rochechouart-Chassenon. The aim of this paper is to review and update knowledge on its breccia deposits.

Target: The target is constituted of granitic intrusive and metamorphic rocks of Hercynian age, with more mafic formations outcropping locally near the NE corner of the structure (Figure 1).

Impact deposits: Impact melts, suevite and polymict lithic breccias overlie more or less brecciated bedrock of the target. In between, the crater floor is exposed over a ca 12 km central zone (Figure 1). It is flat, gently dipping 6°N, although one can distinguish a faint 4km wide central "rise" up to 70 m above a 4 km wide "annular depression". The breccia deposit is discontinuous. The largest continuous sheet forms a ca 3 km wide circular patch at Chassenon and a 6 km elongated zone in the SW. Suevite always lays above polymict lithic breccias which are only found directly above the target bedrock. The contact is sharp. Its geometry is irregular at the meter scale. The original top of the suevite deposit is displayed in Chassenon, forming a fine stratified layer very similar to ignimbrite. Components, mostly mineral debris, match the lithological composition of the target. The bulk chemical composition matches that of the "average" target, and not that of the underlying suevite (Figure 1). Underlying suevite is stratified. Impact melts form intermittent patches from the "central high" (Babaudus) to the periphery of the deposits (Montoume and Bel Air, see Figure 1). The largest bleb spreads over ca 1 km2 (Valette) but others can be as small as a few meters (Bel Air). The thickness is about 1 meter at Babaudus and Bel Air, a few meters at Valette and about 10 meters at Mountoume where the melt rock displays large vertical joints very similar to cooling joints found in rhyolite lava flows. There is no obvious link between damage in the target and the setting of impact melt. For instance, relatively undisturbed material (shocked < 10 GPa) occurs below the Babaudus melt rock. Unlike Ries deposits, which are fairly homogeneous at the macroscopic scale over the whole structure, those at Rochechouart-Chassenon are highly variable in color and texture, explaining why they are usually referred by locality. Yet the target was more "homogeneous" than at the Ries: petrographic studies show that only fragments of exposed target are found in the various deposits. Despite the granitic composition of the target, macroscopic differences also characterize target rocks (reddish granite and leptynite / dark grey gneiss). These correlate with minor yet significant variations in the Fe-Mg content of the rocks (Figure 1). A similar explanation accounts for the differences between deposits at the various localities. They all plot separately on the Fe-Mg diagram (Fgure 1). The differences correlate with the local setting. Mountoume melt matches the composition of nearby granite and leptynite but not that of the local gneiss. Chassenon suevite matches the composition of local gneiss. Babaudus melt falls in between, suggesting a mixing of nearby leptynite with locally occurring gneiss. The mafic Bel Air melt rock is chemically consistent with the exposures of the mafic rocks in the NW of the target. Scattering of the plots of Rochechouart polymict lithic breccias correlates with the border between two contrasting target formations, gneiss and leptynites (Figure 1).

Discussion: Excavation and readjustment did not mix nor homogenise ejecta at the scale of the crater. This applies to impact melts (already inferred at Ries [1]), but also to suevite and probably to melt free deposits. Melts are unlikely to have ever formed a continuous sheet (no homogenisation of liquids). The integrity of the Chassenon deposit strikingly contrasts with the age (214 +/- 8 MA [9]) and morphology of the structure. It is much less eroded than previously thought, implying a long period of protection from erosion. This places new constraints on the interpretation of the geological evolution of the western part of the Hercynian continent. This also implies that the actual deposits, despite apparent erosion, are representative of the initial crater fill. The full section consists then of about 30 m polymict breccia overlain by up to about 20 m of suevite topped by several meters (?) of ash. Where stratification, bedding and fine debris have already been reported at the top of suevite (exemple at Ries [8]), they always show evidence of reworking associated to water flooding. Here there is no interference with water. The deposit was entirely airborne thus offering a quite unique analogue for KT studies and for plume modelling. The lack of water invasion combined to the proximity with the Mesozoic shore places constraints on the size of the crater and on extension of major faulting in the target. Any readjustment was terminated when the top of the suevite was deposited horizontally. Positioned in the "annular" depression, the Chassenon section places an upper limit on the thickness of the deposits over the whole structure. Melts are then unlikely to have been much thicker than today. Estimates for the total amount of melt in the proximal deposits fall between 0.1<<0.5 km3, including the contribution from suevite.

Conclusions and final remarks: Rochechouart-Chassenon is unique owing to both completeness and accessibility. The crater floor, impact deposits and the target below are readily and simultaneously available for 3D investigation at all scales. Yet knowledge is still rudimentary. Practical means for remediation will be presented while facilitating access to the world scientific community for ground truth data "mining" at Rochechouart-Chassenon (Test Site Initiative) [10].

References: [1] Osinski G.R. (2004), *Earth Planet. Sci. Lett., 226,* 529-543. [2] (2007), *Meteoritcs & Planetary Science*, 42, 481-894. [3] Tuchscherer, M. G. et al. (2005), *Meteoritics & Planetary Science*, 40, 1513-1536. [4] Poag C. W. C. et al. (2004), *Springer-Verlag, Berlin, Heidelberg, New-York,* 522 p. [5] Kraut F. and French B. M. (1971) *J.G.R., 76,* 5407-5413, [6] Lambert P. (1977), *Habilitation Thesis*, Paris-Sud University, 515 p. [7] Lambert P. (1977), *Earth Planet. Sci. Lett., 35,* 258-268. [8] Jankowski B. (1977), *Geologica Bavarica, 75,*155-162. [9] Kelley S.P. and Spray J.G. (1997), *Meteoritics, 32,* 629-636, [10], Lambert P. et al., Companion paper, this volume.

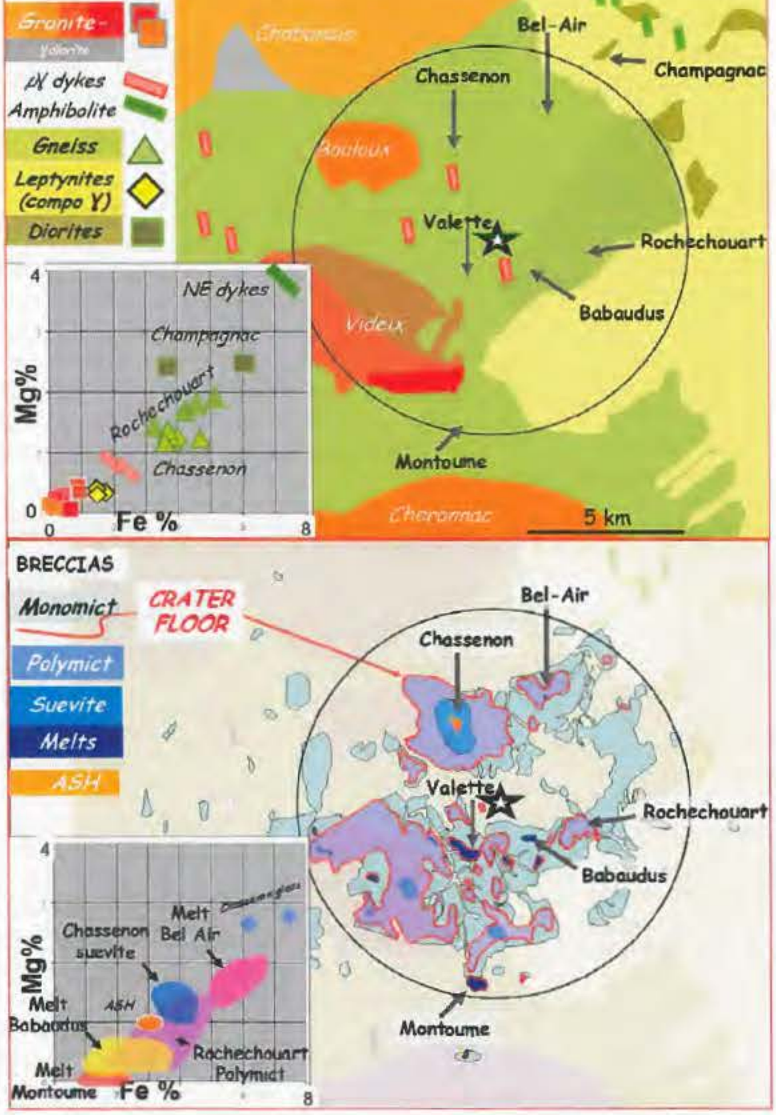

Figure 1: Top- Map of the target formations (impact formations withdrawn); Bottom- Map of the impact formations (target formations withdrawn); Circle: Extent of exposed deposits above the crater floor; Star: Geometric centre of the deposits. Insert on the bottom left of each map: Fe-Mg distribution for the main units (taken from wet analyses/AAS/XRF of samples over ca 250 localities given in [6]. Squares = intrusive bodies, rectangles = dykes, triangles = gneiss, lozenge = leptynite. Color of symbol matches that for each rock type. Compositional variations in gneiss, more mafic near Rochechouart compared to Chassenon, are represented by two nuances of green. Four nuances of red account for variations between the Cheronnac, Bouloux, Chabanais and Videix granites. Videix granite shows compositional gradation with its southern end matching the composition of the Montoume melt rocks. Melt at Montoume stands at one end of a "mafic" trend and Bel air at the other. Chassenon suevite is closer to the mafic pole, whereas Babaudus melt rock is closer to the granite pole.

PHYSICAL MODELING: MULTI-SCALE APPROACH AND ITS APPLICABILITY TO LARGE METEORITE IMPACTS

P. Lambert[1] and H. Trumel[2], [1]Sciences & Applications., Le Lafayette, avenue Kennedy, 33700 Bordeaux Mérignac, France (lambertbdx@numericable.fr), [2]Commissariat à l'Energie Atomique, CEA Le Ripault, BP 16, 37260 MONTS, France (herve.trumel@cea.fr).

Introduction: Simulating large meteorite impacts uses hydrocodes and phenomenological models, generally combining an equation of state and a so-called strength model. Modern equations of state are well suited to describe strong shock effects. In practice, however, this represents a small volume of the affected target. Large and late effects such as readjustment are essentially concerned with materials that are not exposed to shock waves. These effects are generally dealt with using crude strength models (see e.g. [1-2]), although some progress is being made [3].

The rapid evolution of computational capabilities favors the use of more sophisticated elastic-plastic-damage-like strength models available to date (such as [3] or [4]). Nevertheless they suffer a limitation due to the lack of physical link between the model ingredients and material response. The macroscopic (or megascopic for large impact) response of the target is driven by effects and mechanisms occurring at lower scales in the material. To shift from phenomenological to physical modeling thus implies going downscale to identify and quantify the main mechanisms, trans-coding these into a mathematical form, then going back upscale. The aim of this paper is to show that this so-called "multi-scale approach" initiated in the defense community over a decade ago [5-6], and still under development [7-8], can be applied to the study of impact craters.

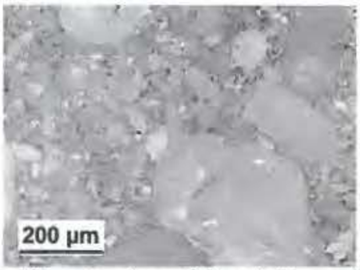

Figure 1: *Microstructure of the pristine material.*

Low-velocity impacts on energetic materials: The defense community is familiar with a vast spectrum of impacts, ranging from very low velocity impact of small projectiles to large impact-like craters produced by shock waves generated by nuclear events. The response of energetic materials to low velocity impacts addresses another limitation of large-scale impact modeling, i.e. what happens in the area where materials are not exposed to a shock wave. As we may see, it also demonstrates some striking similarities with damages encountered at large impact craters, despite the tremendous differences of scale and loading conditions.

The initial microstructure of the studied explosive is similar to that of concrete (Figure 1). Under impacts at velocities below 100 m.s^{-1}, such materials may deflagrate, and safety issues compel one to understand why it does and to build predictive models.

Figure 2: *30 mm wide partial view of a diametral cross section of the recovered target.*

For this purpose, the multi-scale approach starts with the identification of phenomena involved at macro-, meso- and micro-scales, from interpretation of effects recorded at the corresponding scales in samples recovered from a full scale impact experiment (ground truth data supply : Figures 2 and 3). Then a series of well controlled experiments is run on the same material in order to separate and to quantify individual mechanisms, utilizing the same microstructural characterisation approach as applied to the full event (Figures 4-5).

Figure 3: *Detail of Figure 2. Crystallographic phase changes developed along shear localized zones.*

The recovered full-scale target displays a variety of features including: i) localized shear deformation (Figure 2) where solid state phase changes occurs (Figure 3) to be compared to pseudotachylites produced along shear faults, ii) multi-stage plastic deformation similar to kink band and planar features (Figure 4), iii) localized state transition with production of vesicular glass, injected into open fractures (Figure 5 left), or decorating frictional microcracks (Figure 5 right), providing clues for identifying the physical origins of explosions.

Figure 4: *Plastic deformation:-kink bands and planar features (high pressure slow compression experiment)*

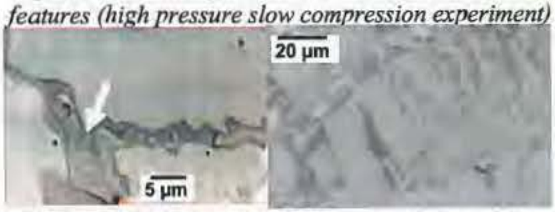

Figure 5: *Vesicular glass in fractures (left) and frictional microcracks (right)(dynamic compression)*

Multi-scale modeling: Multi-scale modeling, or homogenization, has been the subject of a continued effort in mechanics of materials since the 1950s. It has been applied to defense issues for roughly 20 years. An example is given below [8] (Figure 6), aiming at developing a model capable of accounting for frictional microcracks as the physical micromechanism responsible for macroscopic plasticity under predominant shear loading.

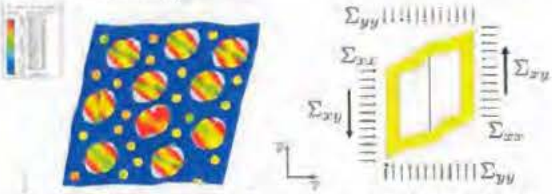

Figure 6: *The material seen as a population of unit cells (left), the idealized unit cell under shear (right).*

A representative volume element is first chosen. It is sized according to the microstructure (1 mm^3 in that case). It is then decomposed into idealized elementary cells (the meso-scale), each of which is composed of a (cracked) grain embedded in an assumed continuous matrix (Figure 6). Then a unit cell model is built, unit cells are assembled, the whole resulting in predictions giving a quite reasonable approximation of the real shear behaviour, including its dependence to pressure.

Application to large impact craters: One of the main purposes of homogenization is to smooth discrete objects (cracks, boundaries) into homogeneous behaviour. Yet limitation comes when softening occurs, favouring strain localization (shears bands, faults). In this case, either new tools [9-10] or a new upscale step are required. At least one or two more intermediate stages could be required for modelling large impact in order to fill the gap between the microscopic effects in rock forming minerals and megascopic effects such as readjusting a multi-kilometer cavity.

Rochechouart-Chassenon "Test-Site": If the solution clearly requires further laboratory scaled experiments, proper access to ground truth data is critical to the whole approach. Those are not accessible to experiments. Terrestrial impact structures can then substitute, especially when erosion gives access to a large portion of the transient crater floor. Although such a case is exceptional, it is met at the ca 25 km Rochechouart-Chassenon astrobleme [11] (Figure 7). Plans will be presented to promote multi-scale modeling research in both the meteorite impact and the defense communities, while facilitating access to this site for ground truth data "mining" ("Test Site Initiative"). Facilities, data and samples will be made available in parallel to the settlement of a Research Center and a Museum in the structure.

Figure 7: *Aerial view of the Rochechouart-Chassenon structure-Red lines : transient crater floor limit.*

Conclusions: Further investigation at terrestrial impact craters is crucial in providing missing information at intermediate scale for multi-scale modeling of large impact. More generally, strong similarities and common interest clearly exists between meteorite impacts and defense studies on multi-scale modeling. The defense community's knowledge and active research in that field are potentially transferable to the impact crater community. The interest for combining efforts is then obvious. The present paper as well as our involvement in developing a permanent research activity at Rochechouart-Chassenon (including the "Test Site Initiative") is a practical attempt in this direction

References: [1] Collins G. (1992) *Ph.D dissertation*, Imperial College of Science, London, UK. [2] Wünnemann K. et al. (2006) *Icarus, 180*, 514-527. [3] Ai H. A. et al. (2006) *Int. J. Impact Engng., 33*, 1–10. [4] Lubliner J. (1989), *Int. J. Solids Struct., 25*, 299-326. [5] Trumel, H. (1996), *Ph.D. dissertation*, Univ. of Poitiers, France. [6] Demol G. et al. (1998), *11th Int. Symp. On Detonation, Snowmass, USA*. [7] Dartois, S. (2008), *Ph.D. dissertation*, Univ. of Poitiers, France. [8] Vivier G. et al. (2007), *17th DYMAT Tech. Meeting*, Cambridge, UK. [9] Aydin A. et al. (2006), *J. Struct. Geology, 1*, 83-98. [10] Crook, T. (2003), *J. Petrol. Sci. Engng., 38*, 17-186. [11] Lambert, P. *Companion paper, this volume.*

STRUCTURAL EVOLUTION OF AN ASYMMETRIC CENTRAL UPLIFT; EFFECTS OF TARGET HETEROGENEITIES OR AN OBLIQUE IMPACT?

C. Lana[1], [1]Department of Geology, University of Stellenbosch, Private Bag X1, Matieland 7620, South Africa; Email: lana@sun.ac.za

Introduction: The 40 km-wide Araguainha impact structure is the largest impact crater in South America. It was excavated in the flat lying sediments of the Parana Basin, in central Brazil [1-4]. Previous studies have has shown that Araguainha preserves a fully exposed central uplift, an annular basin and two main concentric ring features. The central uplift itself is a major structural and morphological feature in the northern parts of the basin [2-4]. Previous studies have identified the central uplift as an asymmetric morphological/structural feature [3, 4]. However, no comprehensive structural analysis has been directed at understanding its geometry. In this contribution, I expand the structural dataset available for Araguainha and present a detailed structural analysis of the impact structure. Thematic Mapper (TM) and Advance Spaceborne Thermal Emission and Reflection Radiometer (ASTER) data are combined with the structural inventory to provide a direct correlation between the morphological and structural features. The objective is to establish the present geometry and understand the nature of strain that led to formation of the central uplift.

The central uplift

The Araguainha central uplift (CU) consists of a 5 km-wide core of crystalline basement core and 4 km-wide collar of upright to slightly overtuned sediments of the Furnas and Ponta Grossa Formations (Parana Group). The contact between the core and collar rocks is partly coreved by fall-back breccia deposits and impact melt rocks [1].

Athough several LandSat images show a symmetric, circular geometry for the central uplift, field-based observations indicate a rather asymmetric distribution of the collar sediments around the granite core. The central uplift displays an off-centered polygonal geometry, with the Furnas Formation being substantially thinner in the northeastern and southeastern sectors. This asymmetric distribution of the sediments relates directly to differential thickening of the strata in each sector of the central uplift. Given the upright orientation of the collar strata and the original thickness of the Furnas sediments (300 meters outside the structure), it is possible to calculate the thinkening of the strata in the collar rock during formation of the CU. We estimate that the Furnas formation was thickened by a factor of 2 in the southeastern sector and a factor of 7 in the northern and northwestern sectors [3, 4].

The inner part of the collar comprises a 500 m-wide complex zone of meter- to hundreds of meter-scale blocks of basal sediments of the Furnas Formation. The blocks were tilted to various degrees, making it difficult to constrain the arrangement of the sediments around the granitic core. Well exposed sections across the collar-core contact indicate that the basal sequence of the Furnas Formation has been duplicated along steep to shallowly dipping reverse fault zones. In a SW-NE section, I observed that m-scale slices of fine grained sandstones of upper Furnas Formation were juxtaposed with basal Furnas conglomerate along a NE-dipping reverse faults. A detailed kinematic analysis of the block movement is difficult because much of the core-collar contact is covered by fall-back breccias. These impact breccias are particularly thick in the NNW sector.

Beyond the 500 m-wide megablock zone, the sediments of the Furnas Formation show more consistent (albeit complex) bedding orientations as a result of a more cohesive deformation. This is particularly true for the upper part of the formation, which is well exposed on several 2-6 km long ridges around the core of the central uplift. Two ridges in the northern, northeastern and northwestern sectors of the collar show a prominent sigmoidal (Z-shape) geometry. The longest ridge spans 6 km from the northern to northeastern sector of the central uplift, but has been segmented by a number of radial to oblique fault zones. The overall orientation of the Furnas bedding is roughly parallel to the NW-SE trend of the ridge. The strata dip steeply NE or are overturned (dipping 40-70 SW) along some segments of the ridge. The bedding has been deformed into hundred-meter scale gentle folds that plunge gently to the NW. These folds are similar in many aspects to radial gentle folds observed in the collar of the Vredefort dome, and are probably associated with buckling and thickening of the Furnas Formation. In addition, several outcrop-scale folds ranging from vertically plunging recumbent to shallowly NW plunging isoclinal indicate that slip movement between the strata contributed for further thickening of the strata. The ridge in the northwestern sector is 2 km long and exposes upright to steeply outward dipping Furnas sandstones. Bedding in the sandstone changes from an east-west trend (tangential to the core-collar contact) to a NNE trend near the contact with the Ponta Grossa Formation. Much of the local variation in bedding orientation relates to fault-related block tilting between fault segments. No visible outcrop-scale folds or extreme variation of bedding have been observed, indicating a less complex deformation pattern in the northwestern sector relative to that of the northern and northeastern sector.

The arrangement of the strata in the southwestern sector follows a similar sigmoidal pattern to that described above. Although there is no prominent ridge in this sector, the sigmoidal (Z-shaped) pattern can be traced along a large number of scattered outcrops from the south to the west along the core-collar contact. The strata change from a NW-SE trend (parallel to the core-collar contact) to a WNW-ESE trend to the south and to the west. Small-scale folding could not be identified, but there is substantial evidence of overturned bedding due to localized block tilting.

Abundant outcrops are found along an east-west trending ridge in the southern sector, which exposes the upper section of the Furnas Formation. The Furnas strata are steeply dipping, with most of the strata dipping south, southeast or southwest. Along the southern face of the ridge, the strata dip 60-80 SW or SE. The slight variation in the overall bedding orientations (from south to southeast or southwest) relates to two main oblique faults that seem to represent conjugate sets of strike slip faults. Large-scale variation in the bedding orientation is also observed, with the beds tilted from subhorizontal to vertical due to large-scale folding of the strata. Local-scale variation also occurs due to outcrop-scale folding. The Furnas Formation has been largely folded into open to tight folds, with most of the folds axes plunging to variable degrees to the south. In addition, I have observed west-verging imbrication features, which together with the fold geometry and the conjugate nature of the faults, suggest an element of E-W compression, consistent with the tangential shortening of the strata during the central uplift formation.

Whilst the ridges from all sectors expose the same upper section of the Furnas sandstones, they display different structural elements and seem to represent independent thrust sheets of the Furnas Formation. Evidence for repetition of the bedding and steep bedding orientations between the ridges in the north and northwest are a clear indication of large-scale imbrication of the km-scale sheets during the central uplift formation. In addition, the change in the strike of the bedding from concentric to oblique/tangential occurs in all individual ridges of the central uplift and may represent zones of convergence between the individual thrust sheets.

Discussion: Thickening of the collar strata was due to progressive deformation, during the lateral movement of the target rocks - from the transient cavity walls to the central part of the crater. We observed that the target rocks followed four main stages of deformation before they finally reached their present upright to overturned orientation in the collar:

- Outcrop-scale folding as a result of differential slip movement between strata. Isoclinal folds have contributed for target thickening in each of the individual ridges (or sheets) of the Furnas Formation. This process might have began much early in the collapse stage, with the inward movement of the target rocks from the transient cavity walls to the central uplift.
- Imbrication of km-scale sheets of Furnas strata: The structural stacking of distinct sheets resulted in the duplication of the stratigraphy in several sectors of the collar of the central uplift. The stacking was also responsible for the present sigmoidal pattern of bedding orientations.
- Lateral constriction of the sediments: The constriction of the sediments led to formation of radially outward plunging gentle folds. Radially plunging folds might have contributed for further thickening of the strata during or shortly after thrust-related imbrication of the large-scale sheets.
- Additional rotation of the bedding due to continuous uplift of the crystalline basement rocks: We believe that additional rotation of the bedding to vertical orientations might have been associated with progressing uplift of the crystalline core to its maximum height.

The asymmetric distribution of the Furnas Formation around the core of the central uplift is either an effect of an oblique impact or pre-impact target heterogeneities. Previous studies have made a strong case that target heterogeneities can generate asymmetries in impact structures [5, 6]. At Araguainha, however, evidence for an oblique impact is not only indicated by a structural thickening north-northwestern sector, but also due to the presence of a thick deposit of fall back breccias the north-northwestern sectors of the central uplift. This could imply that an impact with the downrange direction to the NNW would have caused the structural asymmetry in the central uplift. What remains to be constrained is the internal strain that led to the preferential thickening of the strata in the northwestern sector during the modification phase of the crater formation.

References: [1] Engelhardt et al. (1992) *Meteoritics & Planet. Sci.*, 27, 442–457. [2] Lana et al. (2006) *Geology*, 34, 9-12. [3] Lana et al. (2007) *Geological Society of America Bulletin*, 109, 1135-1146. [4] Lana et al. (2008) *Meteoritics & Planet. Sci.*, 43, in press. [5] Lana et al. *Meteoritics & Planet. Sci.*, 38, 1093-1107. [6] Gulick et al. *Nature Geoscience* 1, 131-135.

Formation of fragment-rich pseudotachylite zones during central uplift formation in the Vredefort Impact Structure, South Africa. D. Lieger[1], U. Riller[2], W. U. Reimold[1], R. L. Gibson[3], [1]Museum for Natural History (Mineralogy), Humboldt University, Invalidenstrasse 43, 10115 Berlin, Germany (daniel.lieger@museum.HU-Berlin.de), [2] School of Geography and Earth Sciences, McMaster University, Hamilton, Canada, [3]Impact Cratering Research Group, School of Geosciences, University of the Witwatersrand, Private Bag 3, P.O. Wits 2050, Johannesburg, South Africa.

Introduction: Target rocks underlying the central portions of large terrestrial impact craters are characterized by the pervasive presence of fragment-rich pseudotachylite bodies. Debates regarding the formation of these bodies include the origin of pseudotachylitic melts, i.e., friction- versus shock-induced melting, melt mobility, causes of target rock fragmentation, as well as timing of fragmentation and melt emplacement with respect to stages of cratering. In order to better understand these processes, we conducted a detailed analysis of pre-impact mineral fabric orientation and pseudotachylite bodies in the core of the Vredefort Dome, the relic of the central upift of the 2.02 Ga Vredefort impact structure.

Results: Our field-based structural analysis focussed on mapping of pre-impact planar mineral fabrics and structural properties of fragment-rich pseudotachylite zones, such as geometry, orientation, brecciation intensity of the zones (Fig. 1). Trajectories of inclined mineral fabrics show that NW-SE striking fabrics prevail in the core centre, whereas circumferential fabric strike is found close to the core-collar boundary. The fabric symmetry is consistent with vertical stretching and uplift of the inner core and outward rotation and dilation in the outer core zone as is predicted by numeric modelling at the erosion level [1].

The geometry of pseudotachylite zone margins and fragments indicates that the zones are essentially fragment- and melt-filled fractures formed by dilation, i.e., volume increase of target rock in the central uplift. This is supported by the fact that strike separation of pre-impact markers at the zone boundaries is generally less than a few centimetres. Thus, the zones formed as tension gashes or hybrid shear faults. Where pseudotachylitic veins overstep each other, their respective tips are curved toward the neighbouring vein, thereby isolating elliptical host rock fragments. This underscores the formation of pseudotachylite zones in terms of fracture mechanics known from brittle deformation.

Fragments in pseudotachylite zones are almost exclusively derived from the immediate host rock, generally display jigsaw geometry, vary greatly in size and are angular to well-rounded. Generally, fragments are more angular and elliptical near zone margins and more rounded and circular in the interior of zones. The traces of pre-impact mineral fabrics on outcrop surfaces suggest that the fragments underwent limited but progressive rotation with increasing distance to zone boundaries. This can be accounted for by rotation of fragments in a viscous medium, such as melt.

Recognition of the pre-impact fit of marker points across pseudotachylitic veins allowed us to determine the components of maximum dilation vectors at a given outcrop surface. Measurement of the component vectors throughout the outer core of the Vredefort Dome indicates either radial or concentric stretching of material, regardless of breccia zone orientation. Pre-impact configuration of fragments in large breccia zones and the paucity of fragments that are exotic with respect to the immediate host rock indicate that generally fragments were not transported distances larger than tens of meters. However, this may not apply for the pseudotachylitic matrix, i.e., former melt.

Interpretation: The well-developed centro-symmetric patterns of distribution, geometry, brecciation intensity (Fig. 1) and maximum dilation directions of pseudotachylite bodies correspond kinematically to the variation in total strain predicted by numerical modelling [1]. Structural properties of the bodies suggest that pseudotachylitic melt is allochthonous and was emplaced at an advanced stage of cratering into tensional fracture zones within the crater floor. Both, concentration of bending strains imparted on target rocks during central uplift formation and thermal stresses induced by the emplacement of allochthonous melt led to fragmentation of target rock. Tensional fracture zones opened in an overall dilational strain field towards the end of cratering and formed low pressure zones, into which melt was likely forcefully drawn. Melt may have been drained from the overlying impact melt sheet or from sites within the crater floor and transported into fragment-rich dilation zones. Our field-based analysis failed to identify the presence of shear faults that could potentially have generated *in situ* frictional melts and fragments. Rather, target rock fragmentation and melt generation that resulted in fragment-rich pseudotachylite bodies are processes separated in space and time during cratering.

References: [1] Ivanov, B. A. (2005) *Sol. Syst. Res., 39,* 381-409.

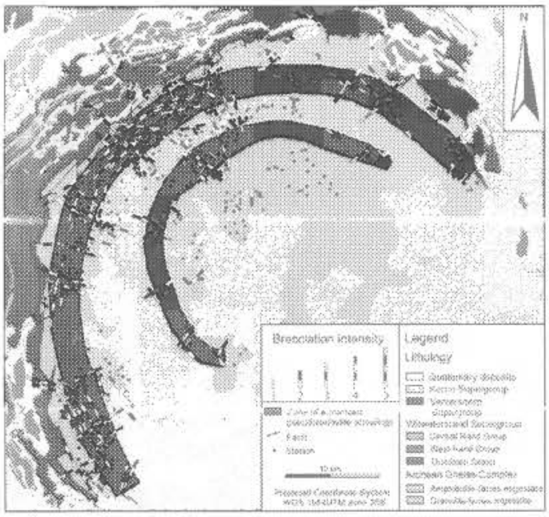

Fig.1: Geological map of Vredefort Dome showing the centro-symmetric distribution and brecciation intensity of fragment-rich pseudotachylite zones.

The Effect of Planet Curvature on the Shock Pressure Field around Martian Impact Basins.

K. L. Louzada[1] and S. T Stewart[1], [1]Department of Earth and Planetary Sciences, Harvard University, 20 Oxford Street, Cambridge MA 02138, U.S.A. (louzada@fas.harvard.edu).

Introduction: The unmagnetized regions (up to 1.4 basin radii), which surround large impact basins on Mars (e.g., Hellas) have been attributed to low pressure (a few GPa) demagnetization in the crust [1, 2]. At shallow depths, where the magnetic minerals are located, pressure estimates are sensitive to the geometry of the interference zone [3]. Impacts can be likened to explosions centered at an equivalent burial depth, *d*, resulting in hemispherical shock wave expansion traveling at the longitudinal wave speed, c_L. Rarefaction waves reflected from the surface travel through the compressed material at a greater sound speed, c_R. In the interference zone, the reflected wave arrives before the direct shock wave has fully compressed the material, effectively reducing the shock pressure.

The depth of the interference zone boundary, *z*, for an impact on a flat plane, has been approximated as:

$$z = \frac{c_L \tau}{2}\left(\frac{4(d^2+s^2)-c_L{}^2\tau^2}{4d^2-c_L{}^2\tau^2}\right)^{1/2}, \qquad (1)$$

where *s* is the distance along the surface from the impact point and τ is the rise time of the shock wave and is approximated by R_{pr}/vi , where R_{pr} is the projectile radius and *vi* is the impact velocity [3].

This approximation, however, is not appropriate for large impacts where the curvature of the planet becomes important and the sound speed increases significantly with depth. It also does not take into account the aforementioned differences between the wave speeds in the compressed and uncompressed material. We performed a simplified ray path numerical calculation to investigate the effects of curvature on the depth of the interference zone and the pressure field around large impact basins.

Calculations: For a Hellas-sized basin forming impact, we assume the impact was vertical at 9 km/s, and that the projectile has a density of 2.9 g/cc and a radius of 230 km [2]. Shock waves were propagated in 2 second time steps radially out from the equivalent explosion point at depth, *d*. This depth is approximated by 0.7**Rpr* (or 161 km) from numerical simulations [4]. In reality the equivalent burial depth may have been shallower; for large projectiles, as the increasing density with depth in the target will inhibit projectile penetration. Below, we build on the foundational work by Melosh [3, 5]. The peak shock pressure inside the isobaric core, P_{ibc} , was determined using the following relations:

$$P_{ibc} = P_0 + (\rho_0 U_s u_p), \qquad (2)$$

$$U_s = C + S u_p, \qquad (3)$$

where P_0 is the initial pressure ($<<P_{ibc}$), and ρ_0 is the uncompressed density of the target (2.9 g/cc), U_s and u_p are the shock and particle velocity respectively, *C* is the bulk sound speed of basalt (3 km/s) and $S = 1.5$ [6]. P_{ibc} was found to be 127 GPa. Outside the isobaric core we assume shock pressure decay follows the simple relationship:

$$P(r) = P_{ibc}(r/d)^{-n}, \qquad (4)$$

where *r* is the distance the wave has travelled and $n \sim 1.2$ [4]. The compressed density was then determined using:

$$\rho = \rho_0 U_s/(U_s - u_p). \qquad (5)$$

and equations 2 and 3.

Mars interior model: A self-consistent thermal structure model for the interior of Mars was obtained from Valencia et al. [7]. The model includes a 50-km thick crust of constant density (2.9 g/cc), which overlies a 2000-km thick mantle. Two phase transitions occur in the mantle which lead to abrupt increases in longitudinal wave speed. The first occurs where olivine transforms to wadsleyite at 1173 km depth. The second occurs just above the core-mantle boundary at 1300 km radius, where rindwoodite transforms to perovskite and magnesiowüstite. The presence of the second transition is sensitive to the chosen mass of the core (15% of the planet in this case).

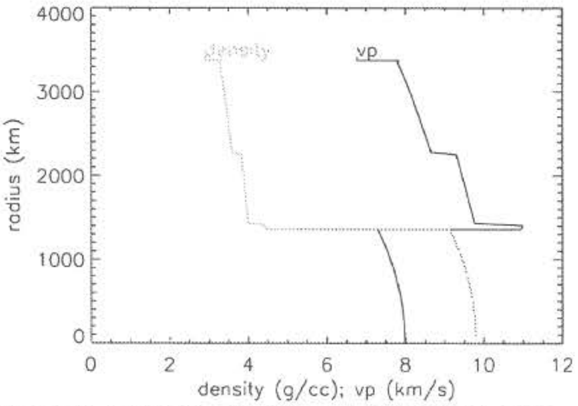

Figure 1: An internal structure model for Mars showing the change in density and longitudinal wave speed with radius. Courtesy of Valencia, et al. [7].

The rarefaction wave speed in the compressed target was determined using $c_R = \sqrt{K(P)/\rho}$ where *K* is the bulk modulus. The crust was modeled as quartz with $K_0 = 38.0$ GPa and $dK/dP = 5.4$; the upper mantle was modeled as forsterite with $K_0 = 136$ GPa and $dK/dP = 3.98$ [8].

Results: The first arrival times of the direct and reflected waves, and their pressures, were binned on a grid spanning the upper mantle and crust (binsize is 36 km by 0.76°). Figure 2a indicates that the rarefaction wave speed is greater than the longitudinal wave speed c_L within approximately 3 isobaric core radii ($\sim 3^*d$). Reflected waves near the impact point shallow in the crust due to the increased rarefaction wave speed, and reflect off the crust-mantle boundary back to the surface before traveling into the mantle. A resultant shadow zone at depth can be seen in figure 2b. Here, blue (orange) colors indicate where the difference in arrival times between the direct and reflected waves is larger (smaller) than the rise time of the shock wave. The boundary of the interference zone is located at the transition between the blue and orange fields. Results from equation 1 are indicated by the dash-dotted line using a constant longitudinal wave speed equal to that of the crust. Deepening of the interference zone near the impact point is due to the relatively high c_R relative to c_L near the impact point. Shallowing of the interference zone boundary further away is a result of the increasing c_L with depth. The effective pressure field (figure 2c) in the interfrence zone for Hellas was calculated using:

$$P_{eff} = P_D + P_R(1 - \Delta t/\tau), \qquad (6)$$

where P_D is the pressure in the direct wave, P_R is the pressure in the reflected wave (<0 tensile) and Δt is the difference in arrival time of the two [1].

Implications: Inferred pressures responsible for the demagnetization of the Martian crust around large impact basins based on equation 1 [1] may have been underestimated. These simple calculations show that the geometry of the interference zone is dependant on the curvature of the planet as well as the chosen layered structure, in particular the presence of the crust. Comparisons with three-dimensional hydrocode shock calculations including self gravity will help to evaluate the validity and robustness of simple ray path calculations.

References: [1] Mohit, P.S. and J. Arkani-Hamed. (2004) *Icarus, 168,* 305-317. [2] Hood, L.L., et al. (2003) *GRL, 30,* 1281-1284. [3] Melosh, H.J. (1984) *Icarus, 59,* 234-260. [4] Pierazzo, E., et al. (1997) *Icarus, 127,* 408-423. [5] Melosh, H.J., *Impact Cratering: A Geologic Process*. 1989, New York: Oxford University Press. 245. [6] Nakazawa, S., et al. (1997) *Planetary and Space Science, 45,* 1489-1492. [7] Valencia, D., et al. (2006) *Icarus, 181,* 545-554. [8] Knittle, E., *Static Compression Measurements of Equations of State (2-6a)*, in *Mineral Physics and Crystallography - A Handbook of Physical Constants*, T.J. Ahrens, Editor. 1995, American Geophysical Union: Washington, DC. p. 98-142.

Acknowledgements: Thanks to D. Valencia and L. Senft (Harvard University), and C. Dalton (Columbia University).

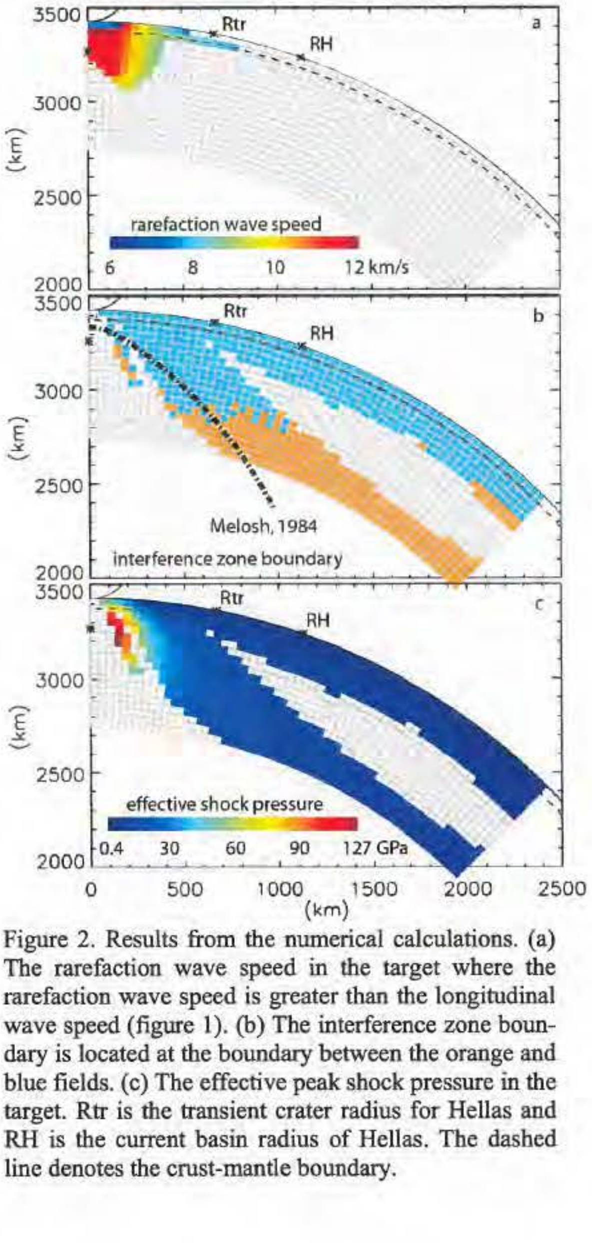

Figure 2. Results from the numerical calculations. (a) The rarefaction wave speed in the target where the rarefaction wave speed is greater than the longitudinal wave speed (figure 1). (b) The interference zone boundary is located at the boundary between the orange and blue fields. (c) The effective peak shock pressure in the target. Rtr is the transient crater radius for Hellas and RH is the current basin radius of Hellas. The dashed line denotes the crust-mantle boundary.

Optical and Scanning Electron Microprobe Study of Shock Veins from the Araguainha Central Uplift, Central Brazil; Evidence for Selective Melting of Rock Forming Minerals and Immiscible Phases in the Impact Melts.

Rogerio Machado[1,2], Cristiano Lana[1], Carlos R. S. Filho[2] and Gary Stevens[1] [1]Department of Geology, Geography and Envi-ronmental Studies, University of Stellenbosch, Private Bag XI, Matieland 7602, Stellebosch, South Africa, [2]Departamento de Geologia e Recursos Naturais, Instituto de Geociencias, State University of Campina (UNICAMP), 13083-970, Brazil.

Introduction: The 40-km-wide Araguainha impact structure is the largest of the six proven impact craters in Brazil. It is located in the northern part of the Parana Basin, in central Brazil (16°47'S e 52°59'W), between Mato Gosso and Goias Federal States. It is also the oldest complex impact crater in the South American continend, dated at 245 Ma [1]. The structure is characterised by an central peak an anular basin and a well preserved rim. The crater rim istelf is defined by radial and concentric faults that juxtapose km-scale blocks of distinct sedimentary strata [2, 3]. The central peak comprises a 5 km-wide core of alkali granites and 3-4 km wide collar of sedimentary rocks including sandstones and siltstones of the Parana Group. The granite and the sandstones are partly corvered by several impact deposits that have been classified by [2] as monomict and polymict breccias and impact melt breccias. Monomict breccias of sandstone are distributed mostly to the southern parts of the central peak. The polymict breccias, mainly distributed in the northern parts of the central peak, comprise a crystalline matrix and angular clasts. The impact melt breccias in southern and central part of the central peak consist predominantly of granitic clasts in crystalline quenched matrix. The melt breccias are underlain by highly fractured alkali granites, which are in turn intruded by shock veins or dikes. Since Engelhardt *et al.* [2] who have provided a detailed description of the impact melts and shock veins in the granitic rocks; there has been little investigation on the origin of these impactites, particularly with regard to the genesis of the melt itself. In this study, we provide results of a detailed optical and scanning electron microprobe study of the shock veins from the core of the Araguainha central peak. The results are used here to understand the processes that let to the generation and crystallization of the impact melts.

Shocks veins: Engelhardt *et al.*, [2] described the shock veins as red dikes because of the high concentration of iron oxide in the melt matrix. These shock veins range from tens to hundreds of centimeters in thickness. The are predominantly hosted in the alkali granitic rocks of the core of the central peak, although a few occurrences have also been observed in the sediments of the collar. The dikes consist of a glassy red matrix that envelops round and angular fragments of the granites. Much of the glass has already been devitrified into a cryptocrystalline groundmass; however, much of the original fluidal texture has been preserved. Individual clasts record several shock metamorphic features, including kink bands in biotite, planar deformation features (PDFs) in quartz and feldsaprs, and isotropisation in plagioclase and K-feldspar. According to Engelhard *et al.* [2] the so called "red dikes" were injected into the granitic rocks due to extensional stresses during the modification stage; most likely during the formation of the central peak.

Sampling and analytical techniques: Samples of the shock veins have been collected along several profiles across central peak of the impact structure. The shock veins analyzed here were relatively narrow (0.5-10 cm-wide) and a few meters long; all hosted in the granitic rocks. Polished thin sections were analyzed at the Department of Geology, University of Stellenbosch. Major element mineral chemistry analyses were performed on a LEO 140VP scanning electron microscope coupled to a Link ISIS energy dispersive spectrometry (EDS) system. The microscope was operated at 20 kV with a beam current of 120 μA and a probe current of 1.50 nA. Acquisition time was set at 50 s and spectra were processed by ZAF corrections and quantified using natural mineral standards. Mineral chemical compositions were recalculated to mineral stoichiometries and the resultant mineral structural formulae were used to evaluate the quality of the analytical data.

Results: Our analysis of the shock veins were focused on the matrix and highly shocked clasts. The matrix displayed a dominantly a criptocrystalline igneous texture, that resulted from either (1) devitrification of a glass and/or (2) fast crystallization of a superheated melt. Although the matrix seems relatively homogenous on handspecmen, optical analysis indicate compositionally heterogeneous texture, with alternating red and brown schlieric domains. In places, these domains seem to form flow lines that surround angular and round clasts of alkali granite in addition to individual quartz grains. EDS analysis (either spot or raster) revealed a predominantly feldspatic composition for the cryptocrystalline groundmass (for both red and brown domains). The flow lines represent alternation between K-feldspar-rich (orthoclase or sanidine) and plagioclase-rich (albite) schlierns. This supported by spectral analysis of compositional maps for Fe, K, Al, Si, Na, Mg that shows the compositional variation of the schlieric domains. The red domains are particularly rich in Na, Mg and Fe whereas the brown domains are richer in K and Si. A distinct type of stretched plagioclase alternate with the schlieric matrix (Fig. 1). This plagioclase isotropic or show radial flamboyant extinctions, clearly distinct from the plagioclase-rich schlieren. It invariably shows internal flow textures and do not contain evidence for cleavage, intragranular cracks or shock-induced fractures. We believe that this plagioclase resulted from shock melting rather than solid-state isotroposation. Electron microprobe analyses indicate that the plagioclase glass is approximately stoichiometric. Submicroscopic grains of hematite and ilmenite are fould disiminated into the plagioclase-rich and K-feldspar-rich schlierens.

Locally, the matrix also preserves submicroscopic igneous textures defined by quenched K-feldspar, plagioclase, hematite and ilmenite. These are minute crystals that grow around the granite clasts and seem to develop radially into the matrix, from the clast rims. In many cases, the rims of clasts are partly digested, and replaced by new feldspar-biotite-hematite rims.

The clast content in the shock veins is highly variable. The clasts composition can range from 10 to 20% of the total volume of the shock veins. They also vary in shape from angular to round fragments, and very often partly corroded by the matrix. The observed clasts in this study are of the order of 0.2 to 5 cm-wide. They comprise either mineral or rock fragments, all of which derived from the alkali granites. The largest fragments consist of K-feldspar, plagioclase, quartz, biotite and muscovite. Nearly all the rock forming minerals record shock metamorphic features. Monomineralic clasts are dominantly quartz, but plagioclase and feldspar may also occur. Quartz occurs as individual grains (nomarly showing PFs or PDFs; Fig. 1). The polygonal grains quartz are also observed. They are often devoid of shock metamorphic features or fractures and seem to result of intense heating derived from the melt matrix. Large K-feldspar megacrystals are found with several sets of PDFs or have been recrystallised into microcrystalline aggregates in the interior of rock fragments. In many places, these aggregates preserve the original morphology of the pre-exiting megacryst. Biotite occurs as several mm-long crystals and commonly displays one or two sets of kink-bands or kink lamellae. When affected by shock fracturing, the biotite crystals breakdown into small (<20 um), acicular hematite grains and/or cubic crystals ilmenite. In many fractures, ilmenite/hematite crystals are surrounded by a cryptocrystalline mesostasis, extremely rich in Al_2O_3 and depleted in SiO_2. This mesostasis is a quenched melt generated due to shock melting of biotite. The quenched melt and the Fe-Ti oxides are also commonly observed along biotite cleave planes, forming elongated pockets near fractures and kink bands. In extreme cases, biotite is completely transformed into Fe-Ti oxide and quenched melt. The later texture explains earlier petrographic observations by Engelhardt *et al* [2] that biotite often occurs surrounded by oxides and in places it is completely opaque.

Discussion: The impact melts studied here occur as injection veinlets or dikes emanating from the fractures in the granitic rocks of the core the Araguainha central uplift. Microscopic observations indicate that the impact melts are present in nearly all the fracture network in the granite, which implies that the shock veins is far more abundant than is suggested in outcrop. Our petrographic observations and mineral chemistry data indicate that these shock veins were derived primarily from the partial melting of K-feldspar, plagioclase and biotite. This concurs with the results from other studies of impact melts, which indicate non-equilibrium fusion of the mechanically weaker ferromagnesian and tetrasilicate minerals in preference to quartz. It is also clear that the Fe-Ti oxides in the veins and impact melt breccia at Araguainha are direct products of biotite breakdown, instead of being fragments derived from brecciation of the target rocks.

Given that the shock veins are hosted in granitic rocks and that they contain dominant a feldspatic matrix, we suggest that the melt itself was derived by partial melting of granitic rocks, with minimum (if any) contribution of the sedimentary rocks. The matrix consists of plagioclase-rich and K-feldspar-rich schlieren, which in many places seem to define flow lines around round and angular clasts. Both plagioclase-rich and K-feldspars-rich schlieren crystallized from distinct immiscible phases in the same impact melt; one phase contained high Na, Fe and Mg and the other was rich in K and Si.

Initial melting temperature of above 1100 °C is indicated by the presence of molten feldpaspar and plagioclase. Evidence from the clasts, suggests that the melt remained hot for sufficient time to convert individual shocked quartz into aggregates of polygonal grains. This is supported by the presence of well crystallized sanidine at the contact between clasts and matrix, which indicate temperature of crystallization between 700-1000°C.

No evidence of shearing or friction melting has been observed along fractures; therefore, the Araguainha shock veins are not bona fide pseudotachylites (e.g., impact melt rocks generated by comminution and frictional melting). The melt behaved a highly mobile fluid that migrated and percolated during the following stages of the cratering event. It seems that a large fraction of this melt accumulated at the crater floor, particularly over the granitic core to form the impact melt breccia.

References: [1]° Hammerschimidt, K. & Engelhardt, W.von. (1995) *Meteoritics, 30:* 227-233. [2]° Engelhardt, W.von *et al.* (1992) *Meteoritics, 27:* 442-457. [3]° Lana *et al.* (2007) *GSA Bulletin, -119:* 1135-1150.

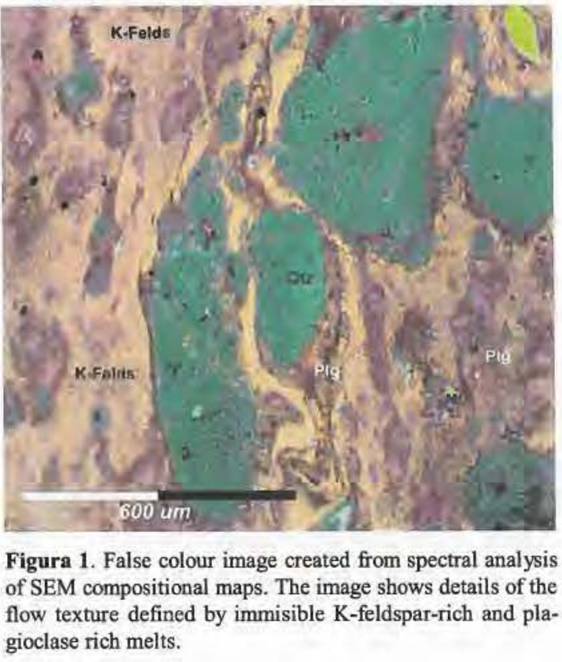

Figura 1. False colour image created from spectral analysis of SEM compositional maps. The image shows details of the flow texture defined by immisible K-feldspar-rich and plagioclase rich melts.

POST-IMPACT THERMAL HISTORY OF THE CHESAPEAKE BAY IMPACT STRUCTURE, BASED ON DOWNHOLE VITRINITE REFLECTANCE, ICDP-USGS EYREVILLE DEEP CORES AND OTHER CORES.

M. L. Malinconico[1], W. S. Sanford[2], and J. W. Horton, Jr.[1] [1]U.S. Geological Survey, MS 926A, Reston, VA 20192, USA, mmalinconico@usgs.gov, [2]U.S. Geological Survey, MS 431, Reston, VA 20192, USA

Introduction: The late Eocene Chesapeake Bay impact structure (CBIS) has been a target of research and water resource drilling for the last two decades, culminating with the 1,766-m deep ICDP-USGS Eyreville corehole in Northampton County, Virginia. This corehole in the deepest part (moat) of the ~38 km diameter central crater [1] provides a long vertical section for sampling to understand post-impact heat transfer processes in a layered, water-sediment-rock target.

Post-impact advective and conductive heating of impact crater-fill materials is common due to residual heat from the impact, melt sheets or segregations, uplifted crustal geotherms, and (or) hydrothermal circulation [2]. This study examines the post-impact thermal history of the CBIS using downhole vitrinite reflectance data from the Eyreville corehole, from the Cape Charles test hole over the central uplift, and previous data from coreholes in and near the outer part of the structure (annular trough) [3].

Results: The Eyreville vitrinite reflectance data show the effects of advective and conductive heating. Thermal maturity of post-impact Coastal Plain sediments (0- 444 m) is typical for the region (0.2- 0.31% R_o) (Figure 1). However, thermal maturity in the underlying sedimentary breccias and sediment megablocks is above background levels; it increases from 444 m to 525 m depth, and then remains constant at ~ 0.44% to the top of a 275-m basement-derived granite body at 1,096 m. This isothermal pattern is typical of vertical advective fluid flow. Below the granite, a short interval of gravelly sand (1371-1397 m) shows an exponential increase in reflectance from 0.47% to 0.59% R_o attributed to conductive heat from an underlying sequence of suevites and clast-rich impact melt rocks (1397-1474 m). Reflectances in the uppermost suevite are 1.2-1.4% R_o. Much higher reflectances (4-8%) of centimeter-scale shale/siltstone clasts, in the suevites and upper sedimentary breccias, are attributed to a pre-impact (Paleozoic?) metamorphic event. Conductive heat from the suevites and impact-melt rocks alone, however, would be insufficient to affect the temperature of sediments more than several tens of meters above the suevite. In numerical calculations of heat flow with kinetic reflectance evolution, modeling the Eyreville suevite as a 385°C cooling "sill" accompanied by compaction-driven vertical fluid flow (0.046 m/year) of fluids from the suevite and deeper basement brines (120°C) through the sediment breccias for 10,000 years closely reproduces the measured reflectance values.

Reflectance values from the Cape Charles borehole over the central uplift (Figure 2) show a similar pattern increasing exponentially with depth from 0.41% to 0.96% in a 90 m contact metamorphic zone above crystalline-clast suevite and crystalline megablocks, and a shallower isoreflectance section (~0.41%) in the upper sediment clast breccia. The thermal aureole is larger at Cape Charles than at the Eyreville site, indicating higher heat flow and (or) thicker heat producing units over the central uplift. Previous data from boreholes in the outer part of the structure (annular trough) [3] reveal no impact-related thermal effects (Figure 3).

Discussion: Thermal maturity measurements and modeling indicate that the crater fill, while heated above background passive-margin gradients, was not as hot as previously hypothesized [3, 4]. Models of CBIS thermal history prior to the Eyreville drilling assumed that deep melt sheets would provide enough heat to produce residual brine from boiling seawater entrapped in the crater fill. However, a large, coherent melt sheet was not found at depths penetrated by the Eyreville core, and modeling of the downhole reflectance data reveals that heat conduction from a deeper heat layer would not reproduce the observations of this study, particularly the isoreflectance interval in the sediment breccias.

Groundwater salinities at and above that of seawater are associated with the crater, and understanding processes that formed the saline ground water was a goal of the scientific drilling [1, 5]. Modeled, moderately heated (120° C) vertical fluid flow from below the drilled section is consistent with patterns of microbe and brine distribution [6, 7]. The results of this study demonstrate the importance of compaction-driven fluid flow in distributing heat in impact craters, particularly marine craters having undercompacted sedimentary fill overlying fractured basement rocks.

References: [1] Gohn G. S. (2006) *EOS, 87,* 349, 355. [2] Naumov M. V. (2005) *Geofluids, 5,* 165-184. [3] Harvey S. V. (2004) unpub. M. S. thesis, Virginia Polytechnical Institute, 35 p. [4] Sanford W. S. (2005) *Geofluids, 5,* 185-201. [5] Sanford W. S. et al. (2004) *EOS, 85,* 369, 377. [6] Cockell et al. (2007) *GSA Abs, 39, 6,* 534. [7] Sanford W. S. et al. (2007) *GSA Abs, 39, 6,* 534.

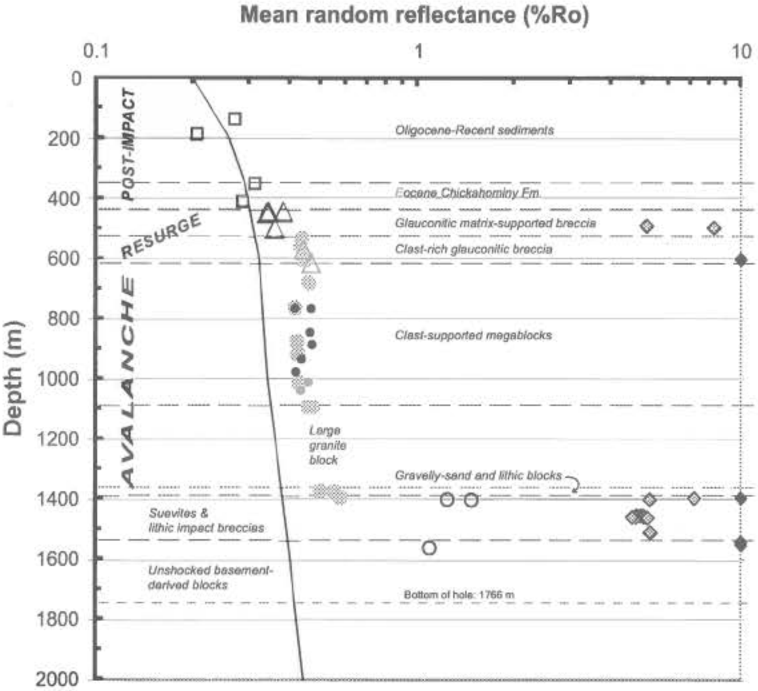

Figure 1: ICDP-USGS Eyreville core (Chesapeake Bay impact crater moat) vitrinite reflectance data, discriminated by lithology.

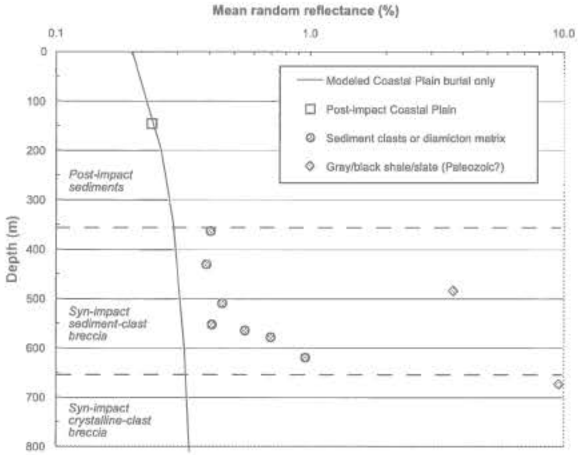

Figure 2 (left): Vitrinite reflectance data from the Cape Charles test hole, central uplift, Chesapeake Bay impact structure.

Figure 3 (below): Interpretive radial cross-section of the Chesapeake Bay impact structure showing general stratigraphy, vitrinite reflectance contours, and relative drill hole locations.

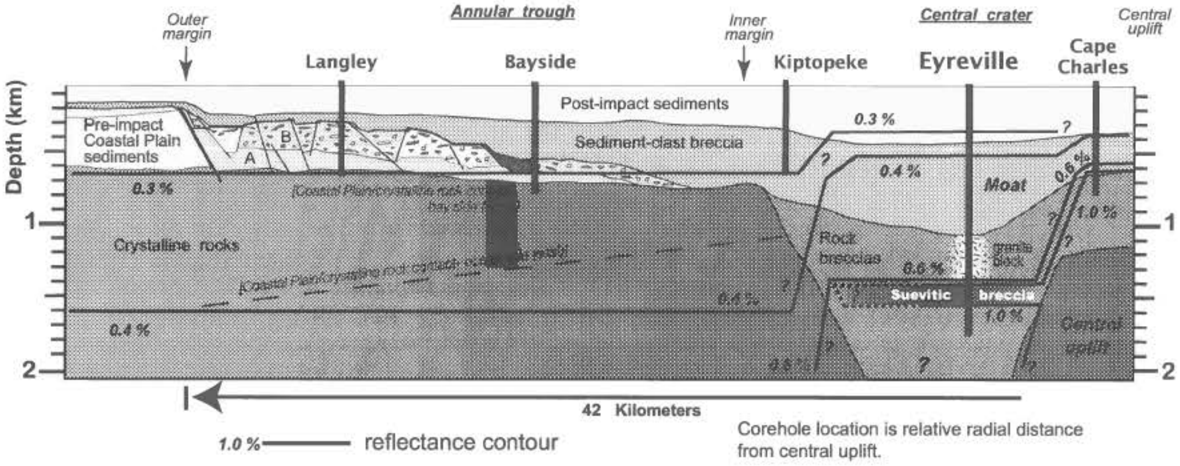

Corehole location is relative radial distance from central uplift.

SPH simulations of planetary-scale impacts. R. A. Marcus[1], S. T. Stewart[2], J. A. Barranco[3], L. Hernquist[1], and D. Sasselov[1], [1]Harvard University Department of Astronomy, 60 Garden St., Cambridge, MA 02138 (rmarcus@cfa.harvard.edu), [2]Harvard University Department of Earth and Planetary Sciences, [3]San Francisco State University Department of Physics and Astronomy

Introduction: Terrestrial planet formation is thought to occur through a multiple stage process that begins with the agglomeration of planetesimals from dust particles and continues through a phase of oligarchic growth that results in a population of roughly 10-50 Moon-to-Mars sized planetary embryos in the terrestrial zone. The final configuration of the planetary system is reached as gravitational interactions between these embryos excite orbital eccentricities and lead to further collisional growth [1].

Planetary-scale impacts remain important in determining the evolution of the terrestrial planets even after the planets are nearly fully formed. A late impact between the proto-Earth and a remaining planetary embryo is widely thought to have formed the Moon [2]. Collisions between the Earth and icy planetary embryos may be the source of Earth's water [3,4]. Similar giant impacts may have occurred in the early histories of Mercury, Venus, and Mars, explaining Mercury's anomalously high density [5], Venus's relatively dry interior [6], and Mars's hemispheric dichotomy [7,8,9].

Our goal here is to investigate various collisional scenarios that may have played a role in the formation of terrestrial planets, both in the Solar System and in extrasolar planetary systems.

Method: We study planetary-scale impacts using the publicly available smoothed particle hydrodynamics (SPH) code GADGET [10]. GADGET employs a novel formulation of SPH with entropy as an independent variable. This formulation manifestly conserves both energy and entropy and has been shown to outperform the standard SPH model, with energy as an independent variable, in a variety of test cases [11]. The code was designed for cosmological simulations of structure formation. The publicly available version of the code performs SPH calculations assuming an ideal gas equation of state. We have modified the code to read tabulated equations of state.

Our modified version of the code has been subjected to multiple test runs. The code yields the expected results both in simulations of planar impacts, for which there is an analytical solution, and for large planetary impacts, for which comparisons to previous numerical work [12] were carried out.

The equations of state for iron and mantle materials were tabulated from the code M-ANEOS [13,14]. A new finely-gridded tabular equation of state is used for H_2O, which includes three solid phases (ices Ih, VI, and VII), liquid, and vapor [15,16]. The EOS of the phases and phase boundaries are based on experimental data [17-20].

Applications: SPH simulations have been used to argue that a major impact event may have played an important role in determining the composition of Mercury, which has twice as high an iron-to-silicate mass ratio as the other terrestrial planets. However, these simulations were carried out using only ~3000 particles, greatly limiting the resolution of the resulting debris cloud and preventing a clear determination of the likelihood of such an impact [5].

A series of recently launched and upcoming missions aim to find transiting Earth-like planets in the habitable zone around their host stars. When planetary transits are detected, the radius of the planet can be determined. Combining this result with the mass of the planet obtained from radial velocity measurements of the star, the mean density of the planet can be calculated. However, there are degeneracies in the mass-radius relationship that make it impossible to uniquely specify the composition of the planet [21]. SPH simulations can be used to not only answer definitively the question of whether a planetary-scale impact occurred early in Mercury's history, but also to help break this degeneracy of the possible compositions of observed transiting extrasolar planets. We aim to carry out a study of the efficiency of collisional mantle stripping across a range of planetary masses ranging from that of Mercury to that of the most massive Super Earths.

While icy planetary embryos have been shown to be a dynamically plausible source of Earth's water [3], the question of how efficiently the Earth can retain the water during these collisions has yet to be answered. As with the problem of collisional mantle stripping, water retention in planetary-scale impacts is a problem that is applicable not only to the Solar System, but also to extrasolar planets. This is also a calculation for which SPH is ideally suited.

We will present example calculations of giant impact events onto rocky and icy bodies using GADGET.

References: [1] Agnor, C. B., Canup, R. M., and Levison H. F. (1999) Icarus 142, 219–237. [2] Canup, R. M. (2004) Icarus 168, 433–456. [3] Morbidelli, A., Chambers, J., Lunine, J. I., Petit, J. M., Robert, F., Valsecchi, G. B., Cyr, K. E. (2000) MAPS 35, 1309–1320. [4] Canup, R. M., Pierazzo, E. (2006) LPS XXXVII, Abstract #2146. [5] Benz, W., Slattery, W. L., Camerson, G. W. (1988) Icarus 74, 516–528. [6] Davies, J. H. (2008) EPSL 268, 376–383. [7] Wilhelms, D. E., Squyres, S. W. (1984) Nature 309, 138–140. [8] Marinova, M. M., Aharonson, O., Asphaug, E. (2007) AGUFM, abstract #P41A-0224 [9] Andrews-Hanna, J. C., Zuber, M. T., Banerdt, W. B. (2008) LPS XXXIX, abstract #1980. [10] Springel, V. (2005) MNRS 364, 1105–1134. [11] Springel, V., Hernquist, L. (2002) MNRS 333, 649–664. [12] Pierazzo, E., Vickery, A. M., Melosh, H. J. (1997) Icarus 127, 408–423. [13] Melosh, H. J. (2000) LPS XXXI, Abstract #1903. [14] Melosh, H. J. (2005) MAPS, submitted. [15] Senft, L. E., Stewart, S. T. MAPS, submitted. [16] Stewart, S. T., Senft, L. E. (2008) LMI IV, abstract. [17] Wagner, W., Pruss, A., (2002) JPCRD 31(2), 387–535. [18] Frank, M. R., Fei, Y. W., Hu, J. Z. (2004) GCA 68(13), 2781–2790. [19] Feistel, R., Wagner, W. (2006) JPCRD 35(2), 1021–1047. [20] Stewart, S. T., Ahrens, T. J. (2005) JGR 110, E03005. [21] Valencia, D., Sasselov, D. D., O'-Connell, R. J. (2007) ApJ 665, 1413–1420.

CRUSTAL CONSEQUENCES OF PLANETARY-SCALE IMPACTS

Margarita M. Marinova[1], Oded Aharonson[1], and Erik Asphaug[2], [1]Caltech, 150-21, Pasadena, CA 91125, mmm@caltech.edu, [2]University of California, Santa Cruz, Earth Sciences Dept., Santa Cruz, CA 95064

Introduction: Planetary-scale impacts, where the resulting crater cavity diameter is a significant fraction of the planet's circumference, are commonly observed in the Solar System: Caloris Basin on Mercury, South Pole-Aitken Basin on the Moon, Hellas Basin and possibly the Northern Lowlands on Mars, Herschel Crater on Mimas, and others. This size regime has not been extensively studied, yet the sphericity of the target and geometry of the gravity field are expected to significantly affect material redistribution, and thus also melt distribution. The change in crater properties with impact angle may be more prominent. For specificity, here we explore a large parameter space for planetary-scale impacts on early Mars, focusing on the resulting melt production and distribution, crustal excavation boundary size and ellipticity, crustal redistribution, depth of impactor penetration, antipodal disruption, escaping and orbiting material, and angular momentum transfer. Subsequent work will focus on impacts into other planetary bodies.

Modeling: We use a 3 dimensional Smoothed Particle Hydrodynamics (SPH) model to simulate the impacts (fig. 1). SPH is a Lagrangian method in which matter is represented by point masses smoothed over a particle radius. Pressure gradients and self-gravitating forces accelerate the particles; there is no material strength. SPH has been extensively used for simulating the Moon-forming impact [1]. In our simulations we nominally use 200,000 particles, giving a resolution (particle diameter) of ~118 km; resolution effect studies show this to be sufficient to resolve the features of interest. The semi-empirical Tillotson Equation of State (EOS) is employed [2].

Figure 1. Simulation timestep (t = 0.58 hrs) for a $1.45x10^{29}$ J, 10 km/s, 45° impact. Color represents internal energy

We simulate impacts with velocities of 6 to 50 km/s (5 km/s is Mars escape velocity, 50 km/s is twice Mars orbital velocity), impact angles of 0° (perpendicular to planet surface), 15°, 30°, 45°, 60°, and 75°, and impact energies of 0.02 – $5.9x10^{29}$ J (nominal 2,300 to 12,000 km craters; [3]).

To allow the accurate evaluation of melt production, a realistic planetary initial internal energy profile was developed. Surface and core-mantle boundary temperatures were set to those of parameterized convection models [4], and an adiabatic compression heating profile with depth was imposed to calculate mantle and core internal energies. The resulting pressure profile and core size are within the expected range [6, 7]. The bulk materials for the mantle and core are taken to be olivine and iron, respectively. An olivine (Fo_{75}) EOS in the Tillotson formulation was developed [5]. A pressure-dependent forsterite melting criterion is used [8].

Results: The simulation results underscore the differences between small (well approximated by explosions in a half-space) and planetary-scale impact processes (where surface curvature and radial gravity are important).

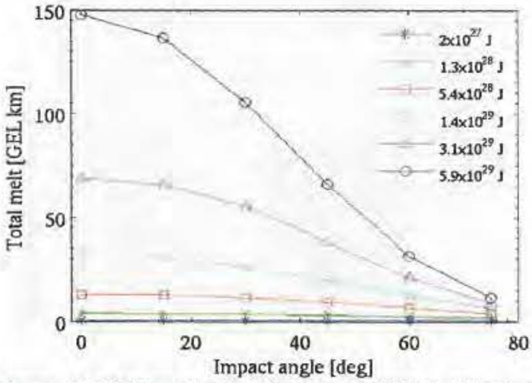

Figure 2. Melt production in terms of Global Equivalent Layer (GEL) depths; velocity averaged for each energy. 1 GEL km = $5.1x10^{20}$ kg.

We find that melt production chiefly scales with impact energy (approximately linearly) and impact angle (inversely), but is also affected by impact velocity. Despite the large representative melt GEL depths that result from the most energetic impacts (fig. 2), the distribution of melt on the surface is highly heterogeneous, with only ~30% of the melt distributed on the surface outside of the crustal excavation boundary. Only for the highest energy, slow and low angle impacts, is more than half of the surface covered by melt, thus possibly resetting the surface and removing all evidence of the impact event.

The impacts are sufficiently energetic to penetrate into the mantle and excavate the overlying crust. The resulting crustal excavation boundary for a given impact energy is generally smaller than is predicted by small (half-space) crater scaling laws. For a given impact energy, increasing both impact velocity and angle significantly reduces the crustal excavation boundary. With increasing impact energy, the elongation resulting by an off-axis impact becomes apparent at smaller angles. For small craters, ellipticity is significant only for highly oblique impacts [9], highlighting the differences in the expression of small, half-space craters and planetary-scale impacts.

Planetary-scale impacts result in ejection distances comparable to the planetary circumference. This, together with the effect of surface curvature, results in the distribution of material over a larger surface area. We find that for impact energies > 10^{29} J and angles < 45°, the ejecta does not lead to annular thickening around the excavation boundary. For highly oblique impacts (> 45°) as well as for lower impact energies, annular crustal thickening is present (fig. 3).

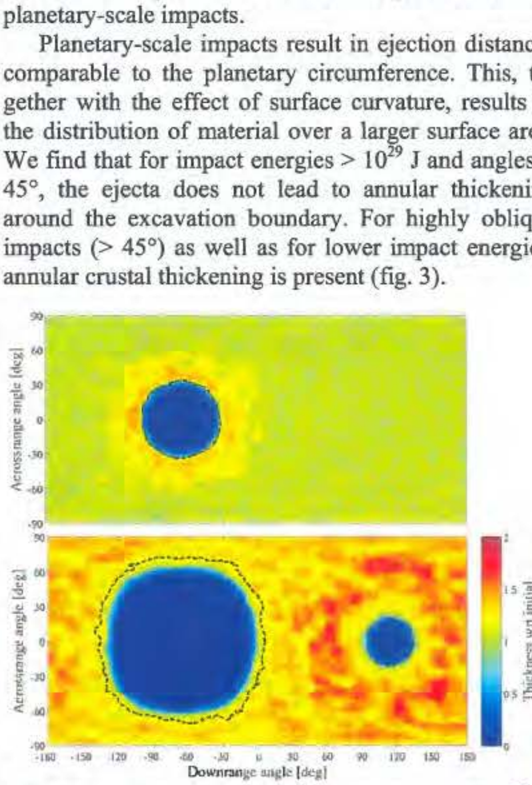

Figure 3. Crustal redistribution for low (5.4×10^{28} J, top) and high (3.1×10^{29} J, bottom) energy impacts. In both cases impact velocity is 10 km/s and angle is 0°. Antipodal disruption is present at the higher energy.

Penetration depth scales approximately linearly with momentum, as expected, and is modulated by impact angle. The highest momentum impacts reach the bottom of the mantle, however, no mixing with core material occurs. High amplitude planetary surface oscillations result from these energetic impacts, and may encourage volcanism due to a weakened lithosphere [10].

Antipodal disruption, including crustal removal and surface melting, is present for all energetic (> 10^{29} J), faster (> 6 km/s), and less oblique impacts (≤ 45°). In the parameter range investigated, the size of the antipodal disruption seen is up to 70° in diameter. For oblique impacts, the center of the disrupted zone is not antipodally aligned with the center of the crustal excavation boundary, with a maximum deviation of 25°.

All impact simulations result in orbiting material, down to the mass (particle) resolution. The highest ejected mass, for a given energy, is by slow (large), highly oblique impacts, yet the amount is only a fraction of the impactor's mass. However, impacts with velocities above ~20 km/s are erosive, a result with relevance to accretion simulations.

The simulations show that planetary-scale impacts can contribute sufficient angular momentum to give a Mars-like planet a rotational period of order a day. The fastest rotation rates result from slow, ~45° impacts . The size of impactors and impact velocities expected at the end of planetary accretion [11], as well as the most likely impact angle [12], are similar to the impact conditions shown by our simulations to produce an about 1 day rotational period on an initially stationary Mars.

The characterization of planetary-scale impacts is especially interesting with respect to understanding the impactors responsible for known impact structures, such as Hellas Basin (2000 km diameter). We have also applied our results to assess whether Mars' Northern Lowlands may be the result of a single large impact [3]. Our simulations show that a ~3×10^{29} J (nominal 10,000 km crater) impact at 6 km/s and at a 45° angle produces features which are consistent with the Northern Lowlands characteristics [5].

The effects of differentiated impactors, as well as impacts into planets with smaller and larger relative core sizes than Mars are currently being investigated.

References:

[1] Canup R.M. and Asphaug E. (2001) *Nature 412*, 708–712. [2] Tillotson J.H. (1962) General Atomic, San Diego, California, Report No. GA-3216, July 18. [3] Wilhelms D.E. and S.W. Squyres (1984) *Nature 309*, 138-140. [4] Hauck S.A. and Phillips R.J. (2002) *JGR 107*, 10.1029/2001JE001801. [5] Marinova M.M., Aharonson O., and Asphaug E. (2008) *Nature*, in press. [6] Bertka C.M. and Fei Y. (1998) *EPSL 157*, 79-88. [7] Yoder C.F. *et al.* (2003) *Science 300*, 299-303. [8] Asimow P.D. (2007) Goldschmidt Conference Abstracts. [9] Gault D.E. and Wedekind J.A. (1978) *EOS (Abstract)59*, 1121. [10] Elkins-Tanton L.T. and Hager B.H. (2005) *EPSL 239*, 219-232. [11] Hartmann W.K. and Davis D.R. (1975) *Icarus 24*, 504-515. [12] Shoemaker E.M. (1962) in *Physics and Astronomy of the Moon.* Academic Press.

MULTIRING BASINS ON ICY SATELLITES: A POST-*GALILEO* VIEW.

William. B. McKinnon[1] and Paul M. Schenk[2], [1]Department of Earth and Planetary Sciences and the McDonnell Center for the Space Sciences, Washington University, Saint Louis, MO 63130 (mckinnon@wustl.edu), [2]Lunar and Planetary Institute, 3600 Bay Area Blvd., Houston, TX 77058 (schenk@lpi.usra.edu).

Introduction: The collapse of large transient impact cavities may lead to the creation of one or more exterior rings [e.g., 1]. The existence and extent of such ring systems depend, at least in part, on the thickness of the mechanical lithosphere at the time and place of impact [2-4]. Icy satellites offer a valuable laboratory to explore this paradigm, in that icy lithospheres can be quite thin and ring systems quite extensive. *Galileo* images and other data have extended our understanding of multiring formation beyond earlier *Voyager*-based views. This is especially true of Europa, which was relatively poorly imaged by *Voyager*, but the focus of an extended campaign by *Galileo*. Post-*Galileo* reviews of cratering on the icy satellites of Jupiter can be found in [5-7]. Here we update and synthesize these works, with a special focus on Europa, because its surface is relatively youthful [5] and its craterforms well preserved.

Europan Multiring Structures: The two largest ring structures on Europa are Tyre (≈160 km across) and Callanish (≈95 km across) [8,9]. Tyre, in particular, was first noted in *Voyager* images as having a bull's-eye-like pattern, which turned out to be compact system of circumferential graben-like troughs, essentially a miniature version of the much larger Valhalla and Asgard/Utgard multiringed structures on Callisto [10], and plausibly related to the hemispherical-scale furrow systems on Ganymede [4,11]. The compact nature of these structures implies a relatively thin icy lithosphere, which is consistent with present-day steep temperature gradients due to strong tidal heating [12]. We can use measurement of trough width (and depth) to constrain heat flows at the time of impact [13].

Heat Flux at Tyre and Callanish: We interpret troughs as graben, and assume that the graben originated or nucleated at the brittle-ductile transition, or BDT (a major mechanical discontinuity) [4,14-16]. To estimate the depth to the BDT (fault intersection), we assume that the graben have a ≈62° sidewall dips (based on the coefficient of friction for water ice [17]). Topographic data for Callanish (Fig. 1) and Tyre [18] indicate trough depths approaching 100 m, which can be used to refine our BDT depth estimates. To first order, fault intersection depths are equal to graben width (within 10%).

Trough widths at Tyre average 1710 ± 610 m (from 57 measurements along several radial transects) and at Callanish 1640 ± 480 m (46 measurements). Graben on the west side of Callanish are generally narrower than those to the east, and there is also a modest trend for troughs to be narrower and shallower (lower strain) with greater distance along specific radial transects (especially for Tyre, where the azimuthal coverage is essentially complete). Our "lithosphere" thickness estimates are comparable to that in [19], $\lesssim 2.5 \pm 0.5$ km (when corrected for numerical error), especially as this estimate refers specifically to the impact site itself.

The depth to the brittle/ductile transition is related to the surface heat flux through the temperature profile in the ice shell and the rheology of water ice. The BDT occurs at a depth and temperature where the differential stress required for ductile flow (here dominated by dislocation creep) at a given strain rate is equal to brittle yield stress. We solve for the surface heat flux as a function of brittle/ductile transition depth for a variety of strain rates potentially appropriate for post-impact graben formation (Fig. 2).

Heat flows are quite high for the BDT depth (graben width) range above, easily exceeding 100 mW m^{-2} for "slow" (i.e., normal) geological strains (10^{-14} s^{-1}),

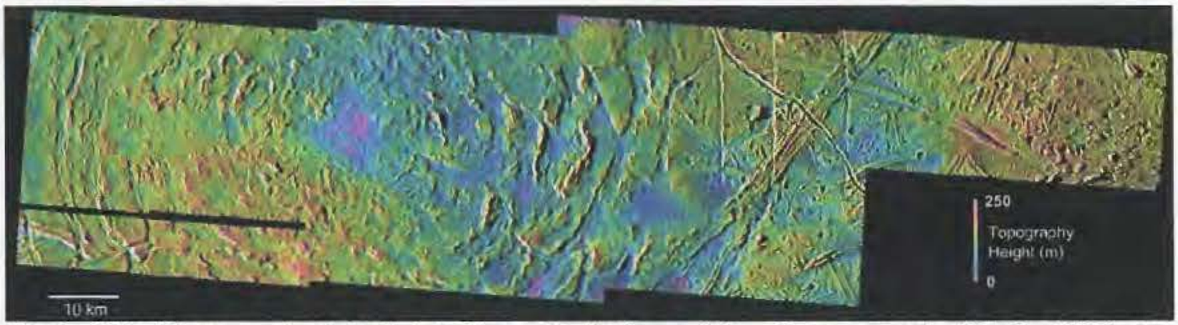

Fig. 1: Callanish topography derived photoclinometrically from and draped over a mosaic of *Galileo* E26 images (45 m/px), with stereo control from overlapping E4 frames. Note central and other depressions; north is up.

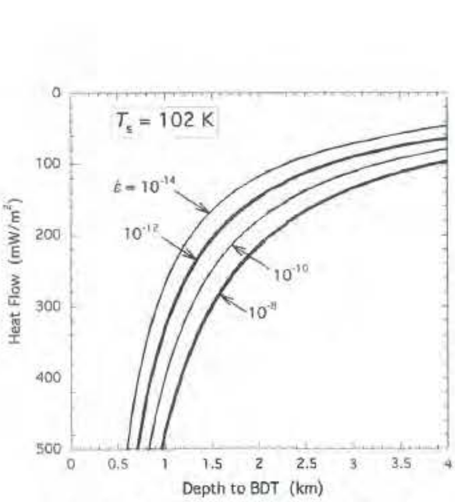

Fig. 2: Surface heat flux as a function of the depth to the brittle/ductile transition for Tyre (surface temperature $T_s \approx 100$ K) or Callanish ($T_s \approx 104$ K) on Europa, for strain rates ranging from the long-term geological ($\sim 10^{-14}$ s^{-1}) to high values more consistent with a post-impact response ($\geq 10^{-8}$ s^{-1}).

and exceeding 200 mW m^{2} for rates more appropriate to post-impact crater collapse or adjustment (e.g., $\geq 10^{-8}$ s^{-1} [1]). Regardless, such heat flows indicate strong and tidal heating at the time of impact (values are similar to or greater than the terrestrial average). More significantly, these heat flows are similar to or much greater than values derived from folding instabilities [20] or flexure [21]. We suspect that fractures in the upper portion of Europa's ice shell reduced the effective thermal conductivity there from the very high values appropriate to cold solid ice.

Ring Mechanics. These results may, alternatively, point towards modification of the original multiring interpretation [1-4]. Conceivably, the viscous flow that extends the overlying ice lithosphere took place on a somewhat longer time scale than that governed by prompt collapse, although some observations of ejecta draping or flooding troughs may contradict this [8]. The Silverpit structure on the North Sea floor may be relevant in this regard. Whatever its origin, there is a central low and circumferential normal faults/graben formed by inward extension of brittle sediments (chalk), on either a collapse or longer time scale [22].

Strain rates for a collapsing transient crater are on the order of the inverse gravitational free-fall time, $\sqrt{g/D} \sim 5 \times 10^{-3}$ s^{-1}, where D is transient crater diameter (~25 km for Tyre) and g is local gravity (1.3 m s^{-2} for Europa). Strain rates decline with a r^{-4} radial dependence [2,15] (or less if the inward flow is channeled), which may explain the larger rift-like features closer to the centers of Tyre and Callanish.

Comparison with Callisto: Although *Galileo* coverage was not sufficient to complete a global inventory as originally hoped [5,11], many regional details at Valhalla, Asgard and elsewhere were revealed. Figure 3 illustrates a digital elevation model (DEM) for a portion of the Asgard radial transect [6]. The irregular, jogging trough is characteristic of "ring graben" in the apparently highly structurally flawed lithosphere of Callisto. We note that an earlier attempt to extract heat flows using the Asgard graben [15] was compromised by use of an incorrect (strong) brittle failure envelope, which led to very low heat flows being obtained. One new structure of note on Callisto is Lofn (Adlinda on *Voyager*-era maps), ~250-km in diameter [6], and surrounded by several low, inward-facing arcuate scarps. Relatively young, Lofn may be stratigraphically and structurally similar to Gilgamesh, the Orientale-class multiring basin on Ganymede [3,5].

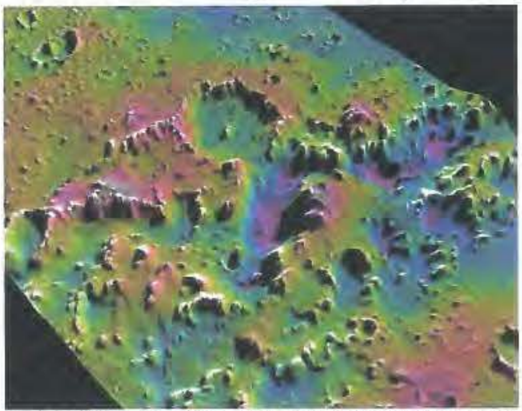

Fig. 3: DEM of portion of Asgard ring graben on Callisto. Swath is 72 km across; graben width ~10 km.

References: [1] Melosh H.J. (1989) *Impact Cratering*, Oxford. [2] Melosh H.J. and McKinnon W.B. (1978) *GRL, 5*, 985–988. [3] McKinnon W.B. and Melosh H.J. (1980) *Icarus, 44*, 454–471. [4] McKinnon W.B. and Parmentier E.M. (1986) in *Satellites*, UA Press, 718–763. [5] Schenk P.M. et al. (2004) in *Jupiter TPSaM*, Cambridge, 427–456. [6] Moore J.F. et al. (2004) in *Jupiter TPSaM*, 397–426. [7] Schenk P.M. and Turtle E.P. (2008) in *Europa*, UA Press, submitted. [8] Moore J.F. (1998) *Icarus, 135*, 127–145. [9] Moore J.F. (2001) *Icarus, 151*, 93–111. [10] McKinnon W.B. (1981) *Multi-Ring Basins, Proc. Lunar Planet. Sci. 12A*, 259–273. [11] Schenk P.M. and McKinnon W.B. (1987) *Icarus, 72*, 209–234. [12] Greeley R.T. et al. (2004) in *Jupiter TPSaM*, 329–362. [13] Lichtenberg K.A. et al. (2006) *LPS XXXVII*, #2399. [14] Golombek M.P. and Banerdt W.B. (1986) *Icarus, 68*, 252-265. [15] Allemend P. and Thomas P.G. (1991) *JGR, 96*, 20,981-20,988. [16] Ruiz J. (2005) *Icarus, 177*, 438-446. [17] Beeman M. et al. (1988) *JGR, 93*, 7625–7633. [18] Schenk P.M. and McKinnon W.B. (2008) *this volume*. [19] Kadel S.D. et al. (2000) *JGR, 105*, 22,657–22,669. [20] Dombard A.J. and McKinnon W.B. (2006) *J. Struct. Geol., 28*, 2259–2269. [21] Nimmo F. et al. (2003) *Geophys. Res. Lett., 30*, no. 5, 1233. [22] Stewart S.A. and Allen P.J. (2005) *GSA Bull., 115*, 354–368.

EQUATIONS OF STATE AND MATERIAL STRENGTH FOR IMPACT CRATERING SIMULATIONS

H. J. Melosh, Lunar and Planetary Lab, University of Arizona, Tucson AZ 85721 USA. jmelosh@lpl.arizona.edu

Introduction: Numerical simulations of impact events rest on three major pillars: Newtonian mechanics, thermodynamics in the form of a relation between pressure, density and internal energy (the equation of state) and the continuum mechanics of material strentth. At the highest pressures and temperatures material strength can be neglected but the equation of state is crucial for adequate representation of the outcome of impact events. This fact was vividly demonstrated by Wada et al. [1] who showed that unless a liquid/vapor transition is corretly incorporated into the equation of state, the giant impact scenario of the moon's formation cannot work.

In contrast, the final stages of crater excavation occur at low pressures where strenth characteristics dominate. In this regime, the observed form of the crater cannot be reproduced without careful attention to the mechanical properties of the surface in which the crater is formed.

Equation of State: The equation of state of materials at high pressure and temperature is so important to the technology of impacts and explosions that many physicist-centuries have been expended in creating plausible equation of state models, and many books on the subject have been written [2, 3, 4]. Nevertheless, most of this effort has focused on materials of technological importance, principally metals.

Over the past several years I have sought to improve this situation and to derive equations of state that describe the solid/liquid/vapor transition in materials of geologic interest. I focused on upgrading a particular equation of state, ANEOS [5], to deal especially with the formation and breakdown of molecular clusters in the vapor phase of complex silicates, SiO_2 in particular [6]. Because most silicates vaporize into diatomic molecules, predominantly metal oxides and oxygen gas at temperatures below about 5,000 K, their vapor is adequately treated as a mixture of diatomic and monatomic species at all temperatures. Even water, a substance of great interest for impacts on the solar systems icy satellites, is reasonably well approximated as a mixture of diatomic species outside of the relatively narrow temperature range from 500 to 1500 K, as illustrated in Figure 1.

The recent modifications of ANEOS also permit introduction of triatomic species in the vapor mixture. Use of this option has permitted a reasonably accurate representation of the equation of state of water in addition to that of silicates such as forsterite, basalt and granite.

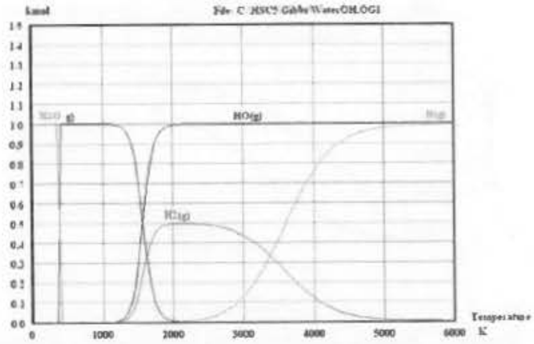

Figure 1. HSC chemistry computation of the molar abundance of species present in water vapor from 300 to 6,000 K at a pressure of 1 bar. Note the predominance of diatomic species, particularly OH, in the vapor at most temperatures.

Many other sophisticated equations of state are presently coming into use, such as PANDA [7] and its derivatives. Although these sophisticated equations tend to run slowly if used simultaneously with a hydrocode, most modern implemtations do the detailed equation of state computations off-line and write out the resulting relations between pressure, density, internal energy and temperature in the form of tables that are accessed from a running hydrocode by interpolation. Although this strategy is computationally efficient, difficulties can nevertheless arise near phase boundaries and work on improving this situation continues.

Porosity: The presence of voids, or porosity, in a material may substantially lower its density and thus increase the amount of PdV heat generated when a shock wave compresses the material to higher density. This results in melting or vaporization at impact velocities normally considered too low to affect these phase changes. Figure 2 illustrates this effect for the mineral Forsterite, described by the ANEOS equation of state. The strength of shock waves in porous material is rapidly damped as mechnical energy is converted to heat. The behavior of porosity in hydrocodes has, to date, usually been modeled using the so-called P-alpha model. This model, however, is highly inefficient for hydrocode computation because it requires a great deal of sub-cycle computations to determine the pressure. A new variation, called the ε-alpha model [8], works directly with variables directly accessible to a hydrocode and permits highly efficient incorporation of porosity into practical computations.

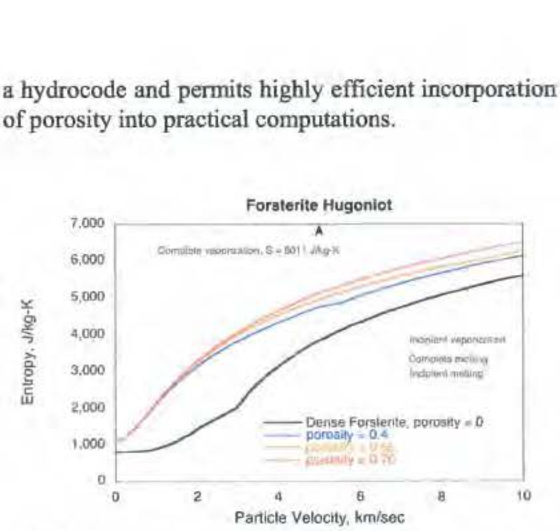

Figure 2. Entropy introduced into Forsterite as a function of impact particle velocity for various initial porosities.

Material Strength Models: As shock pressures in an impact decline, the strength of the rocks surrounding the impact site becomes increasingly important and, eventually, determines the final form of the crater. Whether the crater is simple, complex or ringed by concentric faults depends on the strength and structure of the underlying materials.

Successful models for tensile failure of rock are now well established, most based on the simple Grady-Kipp algorithm [9]. More recently, compressive failure has been modeled by employing a scalar damage criterion in conjunction with classical yield envelope formulations [10]. Such models have resulted in plausible patterns of fracture and strain in the vicinity of impact craters. Even highly complex craters, such as the Chesapeake Bay crater, whose shape was strongly affected by the presence of a weak layer overlying strong basement rocks, has been well modeled using a strength model of this kind [11].

The mere collapse of a transient crater to form a centeral peak or peak ring is predicated upon a substantial weakening of the surrounding target rocks immediately after the impact event itself. The mechanism for this weakening is currently attributed to a change in the rheology of loose rock debris by the presence of strong random vibrations created during the impact [12], although a controversy is currently raging over the possible role of melt formation during sliding of the rocks into the transient crater cavity [13].

Finally, the formation of the great concentric rings observed surrounding large lunar craters and the Chicxulub impact crater in Yucatan have been attributed to the process of "ring tectonics", in which large crustal blocks slide horizontally inward toward the transient cavity, gliding on a weak layer underlying a strong upper crust [14]. Whether this mechanism can operate on the moon depends crucially on the rheology of lunar mantle rocks, probably mostly olivine, at very high stress levels [15]. Recent measurements by S. Karato suggest that at high stresses Peirels forces may drive dislocations in olivine at high enough speeds to produce the necessary low Maxwell time in the mantle of the Earth and moon.

Conclusions: The outcome of high velocity impacts depends crucially on the properties of the materials involved. The thermodynamic equation of state dominates at high temperatures and pressures, whereas constitutive relations govern the final, low pressure expansion of the crater. Other properties, such as porosity, play a role at all stages. More detailed modeling of impact structures in the future hinges on attention to these details and on ever-better measurements of these properties and their incorporation into practical and efficient numerical models.

References:

[1] Wada, K., Kokubo, E. & Makino, J. (2006) *Ap. J.* **638**, 1180. [2] Zharkov, V.N. & Kalinin, V.A. *Equations of State for Solids at High Pressures and Temperatures* 1-257 (Consultants Bureau, New York, 1971). [3] Anderson, O.L. *Equations of State of Solids for Geophysics and Ceramic Science* (Oxford U. Press, New York, Oxford, 1995). [4] Zel'dovich, Y.B. & Raizer, Y.P. *The Physics of Shock Waves and High Temperature Hydrodynamic Phenomena* (Academic, New York, 1967). [5] Thompson, S.L. & Lauson, H.S. *Improvements in the Chart D radiation-hydrodynamic CODE III: Revised analytic equations of state* (Sandia Nat. Lab., Albuquerque, N. M., 1972). [6] Melosh, H.J. (2007) *Meteoritics and Planetary Sciences* **42**, 2079. [7] Kerley, G.I. *User's manual for PANDA II: A computer code for calculating equations of state* (Sandia National Laboratory, Albuquerque, 1991). [8] Wünnemann, K., Collins, G.S. & Melosh, H.J. (2006) *Icarus* **180**, 514. [9] Melosh, H.J., Ryan, E.A. & Asphaug, E. (1992) *J. Geophys. Res.* **97**, 14. [10] Collins, G.C., Melosh, H.J. & Ivanov, B.A. (2004) *Meteoritics and Planet. Sci.* **39**, 217. [11] Kenkmann, T., *et al.* in *GSA Special Paper* (eds. Gohn, G.S.) 2008). [12] Melosh, H.J. & Ivanov, B.A. (1999) *Ann. Rev. Earth Planet. Sci.* **27**, 385. [13] Senft, L.E. & Stewart, S.T. (2008) *LPSC XXXIX* #1391. [14] Melosh, H.J. & McKinnon, W. (1978) *Geophys. Res. Lett.* **5**, 985. [15] Turtle, E.P. *Finite-element modeling of large impact craters: Implications for the size of the Vredefort structure and the formation of multiple ring craters* 1-176 (University of Arizona, Tucson, 1998).

POSSIBLE MECHANISMS OF SUEVITE DEPOSITION IN THE RIES CRATER, GERMANY: ANALYSIS OF OTTING DRILL CORE.

C. Meyer[1], N. Artemieva[2], D. Stöffler[1], W.U. Reimold[1], K. Wünnemann[1] [1]Museum of Natural History, Humboldt University of Berlin, Germany; email: cornelia.meyer@museum.hu-berlin.de, [2]Institute for Dynamics of Geospheres, Russian Academy of Sciences, Moscow, Russia.

Introduction: The Ries ejecta blanket consists of continuous polymict breccia deposits, called Bunte Breccia, derived mainly from sedimentary rocks (with increasing proportion of locally derived materials with increasing distance from the crater) and extending radially to 45 km from the point of impact. On top of this "megabreccia" there are isolated patches of suevite deposits up to a radial distance of ~23 km from the center of the impact structure [1]. The contact between "ground zero" rocks and Bunte Breccia is characterized by substantial mixing caused by ballistic deposition which initiated a ground surge. On the other hand, the contact between suevite and Bunte Breccia is extremely sharp with a transition zone < 10 cm wide [2].

Until recently, the accepted model for the formation of suevite (i.e., the upper section of fallback suevite - ca. 200 m of a total of ca. 270 m - inside the crater cavity and all suevite on the ejecta blanket) has proposed that material was ejected by an upward-rising hemispherical plume comprising a mixture of lithic and mineral fragments of all shock stages, vapor, and molten material. The collapse of the plume eventually resulted in the deposition of the material as a fluidized turbulent mass flow inside the crater basin and in a more patchy distribution outside the inner ring on top of the Bunte Breccia deposited earlier ballistically [3]. This model can explain the sharp Bunte Breccia/suevite boundary. However, preliminary modeling of alleged fallback ejecta in the Bosumtwi crater [4] shows that the amount of fall-back suevite is very small and may create a layer not more than a few meters thick. An alternative interpretation of the suevite deposits inside/outside the crater basin has recently been given by [5], who argued that the suevite components were transported as melt-dominated viscous surface flows outwards from the transient cavity (where they originated), towards, and possibly beyond, the final crater rim.

Methods. The goal of our project is to revisit the suevite problem in an interdisciplinary study by combining geological and petrograhic observations from available outcrops/drill cores with numerical models of crater and ejecta plume formation/deposition.

Petrological methods: In a first step we investigated the drill core (10 cm in diameter) from the "Otting" suevite quarry, which comprises a 9 m thick suevite sequence on top of Bunte breccia. Otting is situated outside the eastern crater rim, 17 km from the impact point. The drill core has been studied by digital stereometric analysis using the "ImageJ" software [6]. Grain sizes of lithic clasts and melt particles were measured every 5 cm on a section of 5 x 10 cm for particles > 1 mm on the plane surface of the half core. The mean orientation of the particles was obtained from stereoplots taken every 10 cm on a section of 10 x 10 cm. The modal content of matrix, clasts, and melt particles was measured every 10 cm on a section of 7.5 x 7.5 cm. In this case the matrix is defined as particles < 1 mm. In order to define the matrix at higher resolution two thin sections were investigated at sampling depths of 131 cm and 870 cm. Grain sizes and content of particles could be measured for sizes > 125 µm. In this case the matrix is defined as particles < 125 µm.

Numerical modeling. The complex behavior of a multiphase gas-flow is modeled with the three-dimensional (3D) hydrocode SOVA [7], which has been successfully used for the modeling of the Ries distal ejecta before [8-9]. What makes this hydrocode particularly suitable for the given application is the implementation of a procedure to describe particle motion in the evolving ejecta-gas plume with momentum-heat transfer between different phases. Turbulent diffusion and viscosity are taken into account in a simplified manner [10].

We modeled a 1.2-km-diameter, 18 km/s asteroid impacting a Ries-like target (600 m of sediments, underlain by crystalline basement) at 45° to the horizon. Sediments were described either by an EOS for dry non-porous calcite or by an EOS for water-saturated 30% porous calcite (assuming pressure-temperature equilibrium between water and calcite). The resulting 12-km-diameter transient cavity has a depth of 5.5 km.

Observations: The mean particle size of the lithic clasts of the Otting core increases gradually with increasing depth, whereas the mean particle size of the melt particles decreases until about 300 cm depth and thereafter increase downward to the bottom. Generally, the lithic particles are always smaller than the melt particles.

On average the melt content of the core is 4 times higher than the content of lithic clasts. This could be confirmed by the analysis of the thin section from 131 cm depth. The abundance of the lihic clasts is constant throughout the length of the core whereas in the macroscopic analysis the melt content seems to decrease over the lowermost meter of the core. The investigation of the thin section from 870 cm depth shows that most of the melt particles in this lowermost section are below the detection limit of 1 mm. With this microscopic analysis we found that the melt content (about 35 %) is as high as in the rest of the drill core. At the macroscopic scale (> 1 mm) the matrix fraction is about 70 % in average and at the microscopic scale (> 125µm) it is about 65 %. The modal composition of the suevite matrix remains to be determined in the ongoing work.

Magmatic and metamorphic lithic clasts could be observed throughout the core. Sedimentary rock clasts were more often found in the lower part of the suevite and most frequently in the last meter above the bottom.

The orientations of the melt particles, which have mostly a strong elliptical shape, are almost horizontal throughout the core, whereas the lithic clasts with their almost isometric shape do not show a preferred orientation.

Deposition of dense ejecta curtains. The numerical modeling yielded the following results: The total amount of ejected material amount to 160 km^3 (with an average sediment/basement proportion of 3:1). The maximum ejection velocity for crystalline rocks does not exceed 1 km/s. Ejecta deposited within a ring with 16-18 km radius (similar to the position of the Otting site) have a deposition velocity of ~350 m/s and consist of a sediment/basement rock mixture.

Using pure ballistics (i.e. motion under gravity but without atmospheric drag) for ejected materials, we receive a reasonable estimate for the total thickness at Otting, i.e. tens of meters of sediments and basement rocks. There are no basement ejecta in the uprange direction. The deposition velocity allows substantial reworking of and mixing with target rocks. The average shock compression of basement rocks is at least 4 times higher than in sediments for any azimuthal angle (16 GPa versus 4 GPa).

Conclusions and discussion. Our modeling results relevant to ballistic deposition do not allow to reproduce the observed ejecta in the suevite layer of Otting: 1) there is just very little melt in the modeled ejecta and 2) separation of sedimentary rocks from basement rocks (i.e. Bunte Breccia and fallout suevite) does not occur. Separation and gradation of two layers (BB and suevite) by atmosphere (fallout) seems improbable as the total ejecta mass per unit area at the Otting site is substantially higher than the mass of the involved atmosphere. Deposition of a suevitic layer as a viscous flow [5] seems also improbable, as viscosity of the flow with solid fragments (i.e. with temperature below the solidus) increases dramatically and prevents spreading to a few km from the transient cavity. We need another mechanism of the ejecta flow "fluidization". One possibility is a gas release (mainly water vapor from sediments) which allows dispersal of the smallest particles and suevite deposition above the ballistically deposited Bunte Breccia (similar to propagation of pyroclastic surge in volcanology) [12].

To verify this assumption by geological investigations we plotted the median grain size of all lithic and melt particles in the suevite against the mean grain size (Fig. 1). In volcanic rocks it is possible to distinguish fallout deposits from pyroclastic flow deposits by dividing such a plot into two areas for the different kind of deposits [11]. Most of our grain size data of the particles would plot in such a figure in the area of pyroclastic flow deposits. One should keep in mind that the grain size distribution of particles in the suevite matrix has not yet been measured in contrast to volcanic deposits. However, plotting the results of our thin section analyses from 131 cm depth (resolution 125 µm) in the diagram the points fall also into the "pyroclastic flow"-field (solid square and circle). But still 65% of the grain size fraction is unclear and should be taken into account, before a final conclusion about the meaning of these data can be reached.

Fig. 1 Distinction between pyroclastic flow and fall out deposits used by [11] for volcanic deposits. Red circles: melt particles; black squares: lithic clasts of the suevite of the Otting drill core

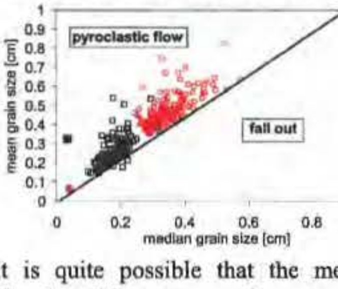

It is quite possible that the mechanism of the suevite deposition was much more complicated: the occurence of density currents with various gas/solid material ratios makes a combination from diluted fallout to a dense basal flow deposition possible.

References:

[1] Stöffler, D. and Ostertag, R. (1983) *Fortschr. Miner.* **61**, 71-116. [2] Wittmann, A. and Kenkmann, T. (2007) *Bridging the Gap II,* abstract #8065. [3] Stöffler, D. (1977) *Geologica Bavarica* **75**, 443-458. [4] Artemieva, N.A. (2008) *LPSC XXXIX,* abstract #1651. [5] Osinski et al. (2004) *Meteoritics Planet. Sci.* **39**, 1655-1683. [6] rsb.info.nih.gov/ij [7] Shuvalov, V.V. (1999) *Shock Waves* **9**, 381-390. [8] Stöffler et al. (2002) *Meteoritics Planet. Sci.* **37**, 1893-1908. [9] Artemieva, N.A. (2006) *LPSC XXXVII,* abstract #1525. [10] Valentine, G.A. and Wohletz, K.H. (1989) *JGR* **94**, 1867-1887. [11] Fisher and Schmincke (1984) *Pyroclastic rocks.* [12] Melosh H.J. (1989) *Impact cratering; a geologic process.*

Assessing different remote sensing techniques for geological mapping in complex impact structures, an example from the Central Rand Group in the Vredefort impact structure. Ch. Mielke[1], U. Riller[2], W.U. Reimold[1], [1]Museum of Natural History, Humboldt-University Berlin, Invalidenstrasse 43, 10115 Berlin, Germany (e-mail: christian.mielke@alice-dsl.de); [2]McMaster University, School of Geography and Earth Sciences, 1280 Main Street West, Hamilton, Ontario, Canada.

Introduction: Remote sensing is a powerful tool for mapping large-scale geological structures such as the Vredefort impact structure. High resolution data sets, such as Advanced Spaceborne Thermal Emission and Reflection Radiometer (ASTER), provide the opportunity to obtain multiple geological and morphological data to assess structure and lithology at various scales. This is demonstrated for a segment of the Central Rand Group from the so-called collar of the Vredefort Dome, the relic of the central uplift of the Vredefort impact structure [Fig. 1].

Fieldwork and remote sensing analysis: For the remote sensing part of our project, we used data from the ASTER sensor, Landsat 7, Shuttle Radar Topography Mission (SRTM), as well as anaglyphs from scanned stereopairs. Lithological and structural information inferred from remote sensing was checked by field geological mapping. Classification of different surface materials revealed that the spectral differences between the lithological units are relatively small in the available data sets. Therefore, it was necessary to also take morphological criteria [1, 2] into account, in order to identify different lithologies with remote sensing techniques.

Geological fieldwork and remote sensing analysis of fault traces revealed a major NW-SE strike trend of first-order faults in the study area [Fig. 2, 3]. However, two second-order trends, i.e., WNW-ESE and NNW-SSE, are also apparent in the data set. Although only few lineament trends deviate from the master trend, a complex fracture system that is perpendicular to the stratification of the collar rocks was identified by field geological mapping. This fracture system is interpreted as an interference pattern of impact-generated and non-impact related fractures.

Based on the definition by [1] and [2], two other lithologic units, the Johannesburg 1 and Turffontein 2 units, were found to be topographically "roughest" in the collar rocks. By contrast, the Johannesburg 2 unit is much smoother than the adjacent Johannesburg 1 and the Turffontein 1 units. Similarly, the Turffontein 2 unit is rougher than the Turffontein 3-5 units. This signal is caused by differences in mineralogical composition. In particular, quartzite beds and sandstones that are more resistant to erosion form topographic ridges, in contrast to argillaceous sandstones and conglomerate reefs that mark topographic depressions and are generally covered by often dense vegetation.

Since all of the exposed rock units are largely made up of quartz, it is almost impossible to distinguish them by spectral analysis. Moreover, various iron oxide crusts are often found within the same unit. Thus, compositionally similar rock units can only be mapped by textural analysis, i.e., occurrence and co-occurrence of filtering. However, following such data manipulation, manual data interpretation is needed to differentiate between different quartzite lithologies.

Conclusions: Our work shows that remote sensing techniques are very useful for geological mapping and structural interpretation in geological terrains, such as complex impact structures. However, different surface conditions, such as vegetation, agricultural activity and weathering crust, collectively, may mask the geological and structural signals. Thus, it is necessary to check the applicability of individual remote sensing tools carefully before interpreting such data in terms of lithology and structure. Finally, the scale of different structures should also be taken into consideration if work is carried out with data sets of variable spatial resolution.

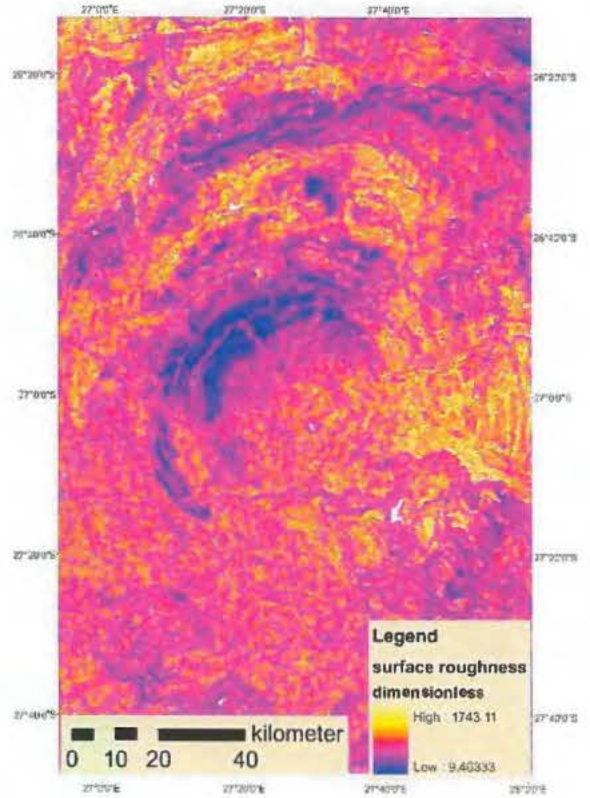

Fig. 1: Image of the Vredefort impact structure showing surface roughness inferred from SRTM data.

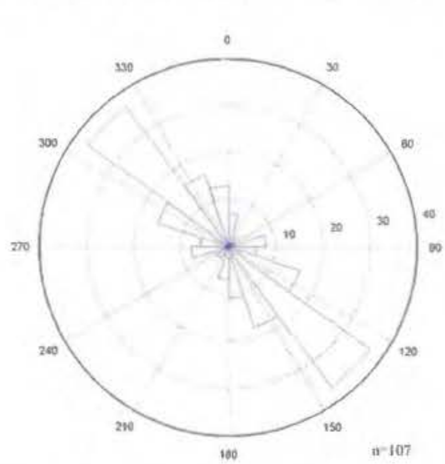

Fig. 2: Diagram showing traces of faults inferred from air photos.

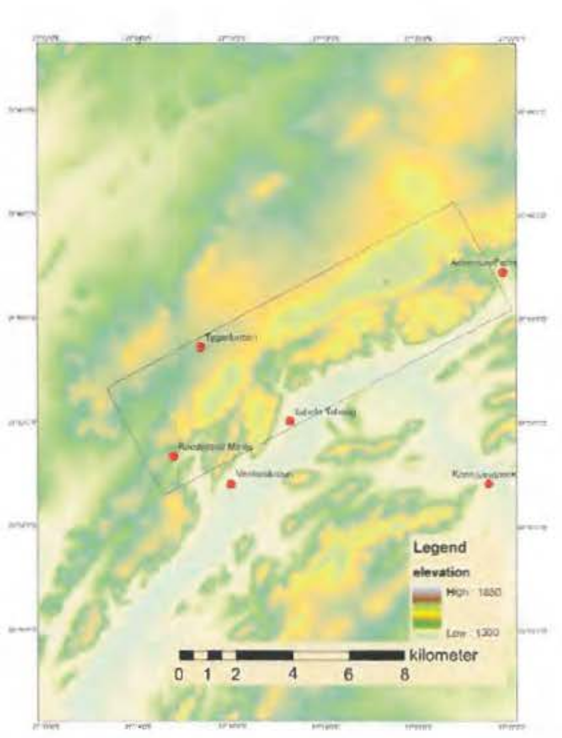

Fig. 3: SRTM relief showing the study area (rectangular box).

References:

[1] Grohmann C. H. et al., 2007, Comp. & Geosci., 33, 10-19; [2] Formento-Trigilio, M.L. and Pazzaglia, F.J., 1998, J. Geol., 106, 433-453.

PETROGENESIS OF CENTRAL PEAK FORMATION ON MARS.

K. A. Milam, Department of Geological Sciences, Ohio University, Athens, OH 45701 (milamk@ohio.edu).

Introduction: Little attention has been paid to the small-scale details recorded in the target rocks within central uplifts of terrestrial impact craters. So it is no wonder that central peaks on other bodies of the inner solar system have been studied even less. Images from the Moon and Venus suggest central uplifts there consist of multiple peaks or discrete blocks concentrated near the crater center. The visible and radar imagery used to study these central uplifts however, suffer from spatial resolutions that are too low to discern the finer-scale fabrics, textures, and structural geology that are being used in the study of terrestrial impacts [1-4].

High-resolution orbital visible imaging instruments that have been flown to Mars however, do provide a means of observing martian central peaks at finer scales and of making comparisons to their terrestrial counterparts. What is emerging is a story very similar to that of central uplifts studied on Earth.

Methods: This study has involved the examination of hundreds of central peaks/uplifts in complex craters across Mars ranging from 15-120 km in diameter using high-resolution imagery from the Mars Orbiter Camera (MOC) on board Mars Global Surveyor (MGS) and the High Resolution Imaging Science Experiment (HiRISE) on board the Mars Reconnaissance Orbiter (MRO). Spatial resolutions of MOC and HiRISE are as low as 1.5 m and 25 cm/pixel respectively. For more information on these instruments see [5-6].

Fifty of these complex craters were selected for detailed study. The majority of studied uplifts are positive topographic features, i.e. actual central peaks. Most of these (80%) however, were poorly exposed due to dust cover, with Dust Cover Index (DCI) values [7] <0.94. A significant portion (36%) of exposed bedrock consists of either low or high albedo material and is massive, limiting observations of textural and structural features. Many (18%) exposed central peaks consist of blocky material that is likely uplifted regolith.

Four (8%) of the studied craters have central uplifts with well-exposed, layered bedrock that displays textures suitable for discerning petrogenetic relationships that have resulted from central peak formation. Observations of actual bedrock and other coarse-grained material is confirmed by high thermal inertia values (313-376 $J\ m^{-2}K^{-1}s^{-1/2}$) [using 8] and DCI values between 0.96-0.99 [7]. All four craters have been imaged by the HiRISE instrument. Two of these also have coverage by MOC narrow angle (MOC-NA) images.

Observations: The exposed layered bedrock reveals that the uplifted crater floors have been extensively faulted, fractured, and folded (Fig. 1). Movement along major faults has resulted in the separation of target rock material into discrete megablocks. Areal exposures of megablocks in the largest crater, Oudemanns (268.2°E, 9.8°S), range from 0.02 to 3.92 km^2. Where measurable, displacements along major faults range from a few meters to > 67 m. Fault breccias (Fig. 2) have been observed along major fault boundaries, similar to terrestrial complex craters. Large displacements suggest that megablock transport during central uplift formation was accomplished along major faults as in terrestrial central peaks [4].

Many megablocks show minimal or no signs of internal deformation at the spatial resolution of the HiRISE or MOC instruments. Some megablocks however, display parallel and sympathetic sets of fractures (Fig. 3) and faults that superficially resemble microfractures and microfaults at the scale of hand specimen viewing. In terrestrial impacts, such fractures and faults have been interpreted to represent rock failure during shock wave passage [4] and initial, minor displacements movement during ascent of crater floor strata. Megablocks are also commonly internally folded. Both fractures and folds truncate along major faults (i.e. megablock boundaries).

Cross-Cutting Relationships: The two best exposed central uplifts (in Martins and Oudemanns craters) show deformation whose cross-cutting relationships are consistent with those in their terrestrial counterparts [4] and the various stages of impact cratering. Fractures and folds are cut and displaced by major faults. Fractures within folded rock show signs of dilation during folding. These observations support initial failure of rock during shock wave passage followed by folding as target rock experienced compression and decompression during uplift. Final movements occurred along major faults and most likely account for the total stratigraphic uplift during central peak formation.

References: [1] Milam et al. (2004) *LPSC XXXV*, Abs. #2073. [2] Milam K. A. and Deane B. (2005) *LPSC XXXVI*, Abs. #2161. [3] Milam K. A. (2006) *LPSC XXXVII*, Abs. #1211. [4] Milam K. A. (2007) *Bridging the Gap II*, Abs. #8053. [5] Malin M.C. and Edgett K. S. (2001) *JGR-Planets, 106*, 23429-23570. [6] McEwen A. S. et al. (2007) *JGR, 112*, doi:10.1029/2005JE002605. [7] Ruff S.W. and Christensen P. R. (2002) *JGR 107*, doi:10.1029/2001JE001580. [8] Putzig N. E. et al (2005), *Icarus, 173*, 325-341.

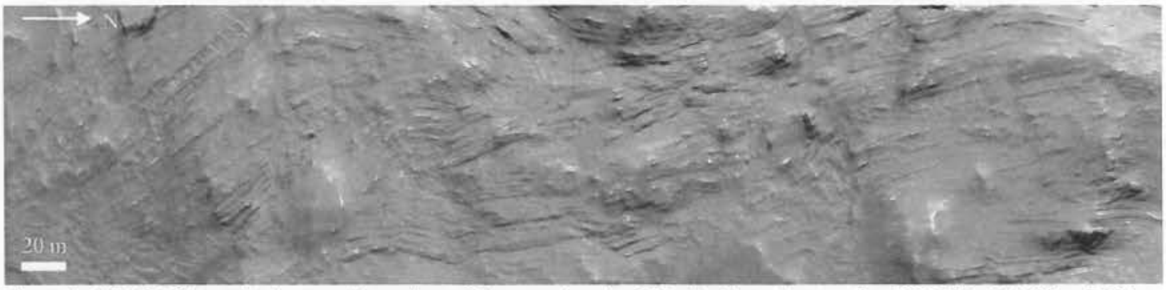

Figure 1. HiRISE false-color image of a portion of the central peak of Martin Crater (centered at 290.72°E, 21.39°S and 62 km diameter). Note the sub-vertically oriented layers, folds, and faults. (NASA/JPL/University of Arizona)

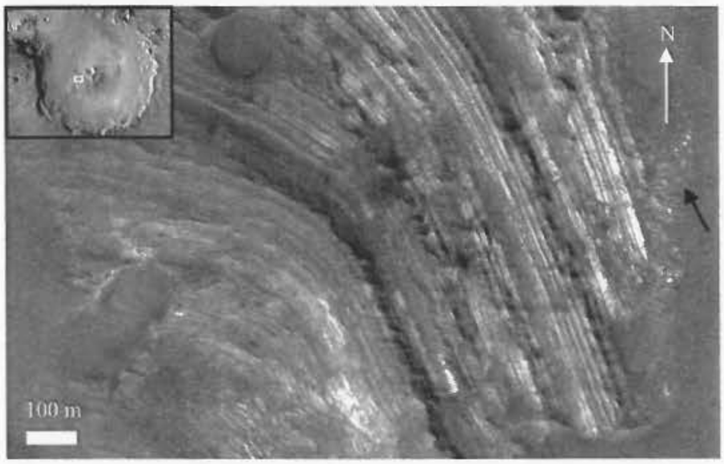

Figure 2. MOC-NA visible image of a single folded megablock along the western flank of the central peak of Oudemanns Crater (centered at 268.2°E, 9.8°S and 120 km diameter). Inset box is a THEMIS daytime surface brightness image mosaic showing the location of MOC-NA image. Black arrow highlights apparent fault breccia along mega-block boundary. (NASA/JPL/University of Arizona)

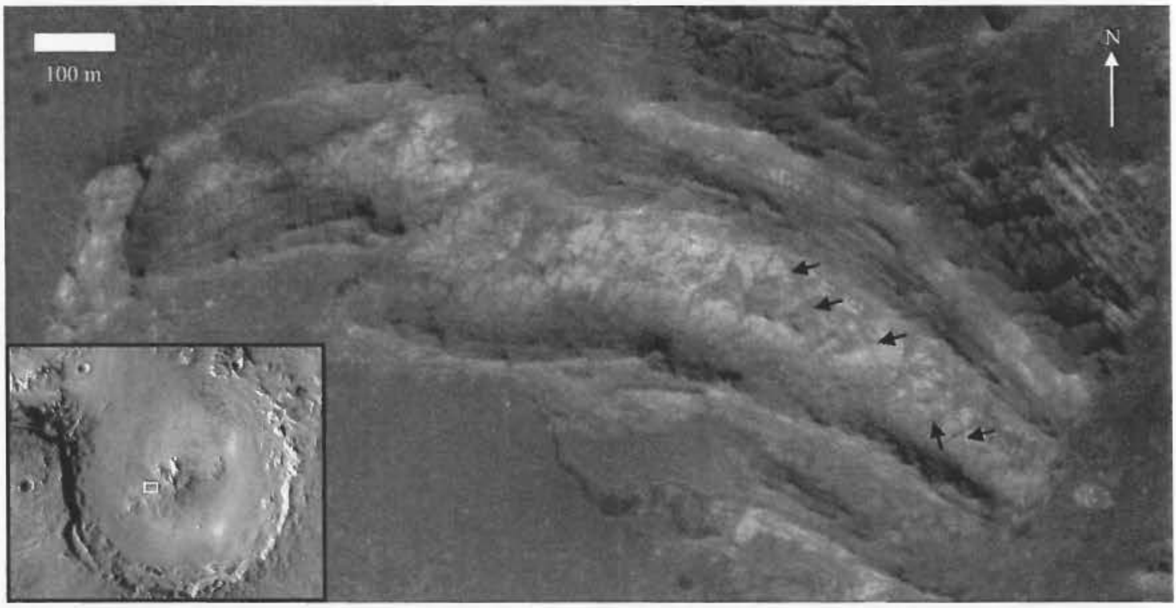

Figure 3. MOC-NA visible image of a single folded megablock within the central peak of Oudemanns Crater (centered at 268.2°E, 9.8°S and 120 km diameter). Inset box is a THEMIS daytime surface brightness image mosaic showing the location of MOC-NA image. Sub-vertically oriented layers are folded and extensively fractured (representative fractures are indicated with arrows). Note that some fractures (example highlighted with double arrows) seem wider to the north, suggesting extension during folding. (NASA/JPL/University of Arizona)

DEFORMATION/MODIFICATION SEQUENCE IN TARGET ROCKS OF COMPLEX CRATERS < 20 KM DIAMETER: IMPLICATIONS FOR IMPACT CRATER IDENTIFICATION.

K. A. Milam[1] and B. Deane[2], [1]Department of Geological Sciences, Ohio University, 316 Clippinger Laboratories, Athens, OH, 45701 (milamk@ohio.edu), [2]Department of Earth and Planetary Sciences, University of Tennessee, 1412 Circle Drive, Knoxville, TN 37996-1410.

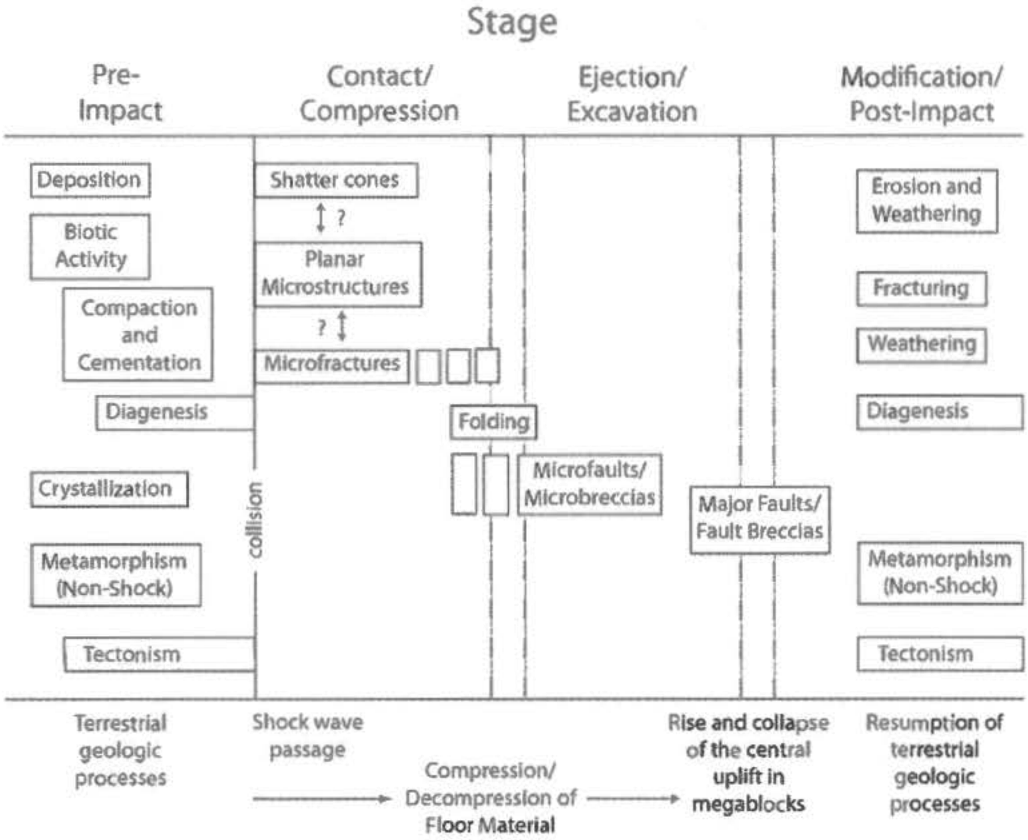

Figure 1. Petrogenetic sequence depicting target rock deformation in central uplifts. This sequence is primarily based on field and petrographic observations of terrestrial complex craters < 20 km diameter.

Previous field work and petrographic observations of central uplift rocks in complex craters [1-4] have led to the identification of fabrics related to deformation of target rocks during impact events. Any of these fabrics may occur as a result non-impact tectonic, mass-wasting, or other processes. However, these features have been associated with known terrestrial impact craters in geologic settings where they are otherwise absent from nearby target rocks. Deformation fabrics increase in density with proximity to the crater center and are most common in areas where unequivocal shock features (shocked phases, high-pressure polymorphs, and shatter cones) have been observed. More importantly, these fabrics occur in a discernible and predictable sequence reflective of the various stages of an impact event (Fig.1).

Regardless of target rock type, primary textures in central uplift rocks are cut by curvilinear shatter cone fractures and parallel sets of microfractures (mfrs) when such deformation fabrics are present. Both shatter cones and mfrs form early during contact/compression and are representative of target rock failure. Their relative order of formation from cross-cutting relationships however, remains inconclusive. Both however, form prior to ejection/excavation as evidenced by their in clasts of crater ejecta/resurge [5, this work]. Rock fracturing begins at relatively low minimum pressures (<2 GPa) and shatter cone formation at higher pressures (~2-30 GPa) when target rock yield strength has been exceeded [6]. This implies that mfr generation may precede shatter cone development, but field verification has so far proven impossible.

Differences in minimum pressures of deformation and fracture style also imply that both fracture types form by differing mechanisms of rock failure.

During compression and the early stages of uplift, rocks are sometimes folded, especially where a lateral transport component is present. This is evidenced by folded layers containing shatter cones and dilated fractures in some central uplifts. Mfrs then develop into microfaults (mfs) as some movement along mfr surfaces occurs. Most mfrs develop into normal mfs, although rare instances (<10%) of reverse mfs do occur. Displacements along individual mfs are minor (typically < 2 cm) and when summed, do not account for the much larger (hundreds of meters) total displacement observed in central uplifts. Concentrations of normal or reverse mfs in various megablocks comprising central uplifts suggest that mf movements are likely during both compression and uplift.

Uplift of the crater center is thought to be accomplished by acoustic fluidization [7] of target rocks. This uplift is accommodated along major faults that bound large (m^3 and km^3 in volume) megablocks of shocked- metamorphosed target rock. Unlike mfs, displacements (tens to hundreds of meters) along major faults can account for the uplift observed in complex craters. Movement along major faults can also generate fault breccias and drag folds, but many major faults superficially resemble and are oriented in a manner similar to that nearby mfs. This suggests that some major faults may develop along pre-existing mfrs and mfs. Some major faults however, do not utilize mfr/mf surfaces, but instead are generated along bedding planes.

There are two primary types of breccias that occur along major fault planes: monomict and polymict. Clasts in monomict breccias are most commonly reflective of adjacent host rock, suggesting local derivation during fault movement. Polymict breccias represent larger displacements along major faults, incorporating a wider variety of lithologies during megablock movement. Some polymict breccias seem to also represent injection of multiple clast and matrix types along fault (and sometimes bedding) planes. Temporal relationships between the two breccia types are still under investigation, but previous investigations [8] have suggested that polymict breccias are first to form.

Recognition of these deformation fabrics and determination that they were formed in the same sequence listed above may prove a useful tool in the initial confirmation of complex craters on Earth and other planets. There are numerous suspected impact structures that have yet to be confirmed because of the lack of definitive or easily identifiable shock features. This may relate to the lack of minerals in target rock that commonly show signs of shock metamorphism (i.e. planar microstructures) or their replacement during diagenesis. Similarly, coarser-grained (i.e. sandstones or plutonic rocks) or highly-weathered rocks may expose only crudely-developed or questionable shatter cone surfaces. Likewise, drill cores from completely buried suspect craters may inadequately sample shocked rocks, making confirmation challenging at best.

The presence of shock deformation fabrics (such as mfrs and mfs) are less dependent on target lithology, are not as affected by post-impact diagenesis, and occur at scales larger than typical shock-metamorphic features (such as PDFs and shatter cones). Thus the identification of these fabrics along with determination of cross-cutting relationships, make this sequence useful for identifying complex craters in the field or under a petrographic microscope. And while these observations primarily apply to smaller (<20 km) complex craters, initial studies [8-9, this work] have suggested that the cross-cutting relationships between some of these fabrics (or their larger-scale equivalents) may apply to larger complex craters as well (such as the 54 km diameter Charlevoix structure). High-resolution visible imagery has likewise suggested that the same fabrics and petrogenetic sequence may apply to central uplifts on Mars [10].

References: [1] Milam et al. (2004) *LPSC XXXV*, Abs. #2073. [2] Milam K. A. and Deane B. (2005) *LPSC XXXVI*, Abs. #2161. [3] Milam K. A. (2006) *LPSC XXXVII*, Abs. #1211. [4] Milam K. A. (2007) *Bridging the Gap II*, Abs. #8053. [5] Osinski G. R. and Spray J. G. (2006) *1st Int. Conf. on Impact Cratering in Solar System*. [6] French B. M. (1998) *Traces of Catastrophe*, LPI, Houston. [7] Melosh, H. J. (1979) *J. Geophys. Res.*,84, 7513-7520. [8] Dressler V.O. and Sharpton V. L. (1997) *Tectonophysics, 275*, 285-311. [9] Martini, J. E. J. (1991) *EPSL, 103*, 285-300. [10] Milam K. A. (2008) *LMI IV*.

GEOPHYSICAL SIGNATURE OF THE FOOTWALL OF LARGE METEORITE IMPACT CRATERS.

B. Milkereit[1], N. Artemieva[2] and H. Ugalde[3], [1]Dept. of Physics University of Toronto (60 St. George Street, Toronto, Ontario M5S 1A7, bm@physics.utoronto.ca), [2]Planetary Science Institute, Tucson, Arizona, [3]McMaster University, Hamilton, Ontario, Canada.

Background and Motivation: Through the integration of remote sensing, potential field and seismic data, exploration drilling and numerical modeling, we can constrain the size, shape and morphology of most terrestrial impact craters. New petrophysical and potential field data from the mid-to small sized Wanapitei, Bosumtwi and Monturaqui structures, as well as seismic data from Chicxulub, Ries, Sudbury and Bosumtwi demonstrate the common geophysical signatures of impacts: pronounced gravity lows, prominent magnetic anomalies and the lack of prominent reflections in the footwall of the craters. Here we investigate strain distribution in the footwall as predicted by impact modeling studies, the cooling history of the footwall and heterogeneities in the footwall as "seen" by seismic and remote sensing data.

Review of Seismic Data: Target rocks are subjected to high pressure and temperature conditions during impact, resulting in fracturing, stress-induced shearing and mixing of materials. There is typically an exponential decay in both porosity and fracture density as radial distance from the crater center increases. Fracture porosity will enhance the first-order gravity low associated with impact structures, and serve to reduce seismic parameters in the second order (velocities and densities) by increasing total porosity out to a limit where impact damage is negligible [1], [2]. In seismic profiles, areas of high brecciation appear transparent; footwall and basement structures in particular show no traceable horizons despite the sometimes large vertical contrasts observed in petrophysical logs. Analysis of physical property logs indicate that these structures have small scale lengths that describe the high degree of mixing and heterogeneity, resulting in only small amounts of seismic scattering. As a consequence of this mixing, pre-impact lithologies are typically disrupted in the vicinity of impact structures, giving rise to characteristic seismic profiles such as those over the Ries, Sudbury and Chicxulub impact structures.

Strain in the Footwall: The 200-km diameter Sudbury crater with its at least 60-km diameter melt pool was formed (compression, excavation, and modification stages) within the first 10 minutes after the impact [5], [6]. All slopes within the final crater (crater rim, peak ring) are usually less than 6-10°. This kind of slopes makes improbable further crater modification by slumping (on a large scale, while small-scale adjustment due to crater cooling and rocks' compaction is still possible). Although "visible" crater is extremely shallow, rocks beneath the floor are severely shocked (up to melting) and brecciated; radial and concentric faults propagate tens of km away from the crater (faults growing downrange are suppressed by lithostatic pressure). Temperatures at the crater floor are close to melting temperature with standard geothermal gradient at the depth of 50 km in the crater center and at the depth of 10 km near the melt pool periphery.

Melt pool differentiation and cooling: Current modeled estimates of shock melting in Sudbury vary in the range from 12, 000 km^3 [6] to 24, 000 km^3 [7] with the melt pool thickness of 3-6 km. This subsequently differentiated into the Sudbury Igneous Complex (SIC). Reconstruction of the original geometry of the structure [8] yields an estimate for the initial melt sheet thickness of at least 2.5 km with a diameter of about 60 km, and total melt volume of $(1–2.5)\times10^4$ km^3. A good correlation between models and observations is partially due to the fact that geologists estimate impact melt, i.e. shock melt plus digested rocks, while modelers estimate shock melt – rocks compressed above given pressure threshold. While part of shock melt is ejected from the crater, some rocks are additionally melted by heat conduction.

According to Zieg and Marsh [9], immediately after the impact, the SIC melt is a viscous polycompositional magma – the result of shock melting of different lithologies within the target down to the mantle. Because of different viscosities, this magma was an emulsion composed of chemically immiscible liquids (as oil and water). For reference, at 1700 °C, granophyre melt is 10-15 times more viscous than norite melt. Within a few years, this emulsion is separated into two layers: denser mafic layer at the bottom (future norite) and lighter felsic layer at the top (future granophyre). Then convection (and hence – quick mixing and cooling) is established within each layer. It ceases when temperature reaches liquidus, i.e. in 10,000 years. After that, slow conductive cooling and solidification continues for at least the next 100,000 years

The new 2D cooling model allows for more accurate definition of temperature evolution in the regions with substantial radial T-gradient (i.e. near the edges of melt pool, near the peak-ring, etc). We started with "artificial" temperature distribution correlated with realistic one, i.e. we had 1) two-layered melt pool at liquidus T; 2) preheated rocks at the central uplift (beneath the melt pool) with standard temperature at a depth of 50 km and 3) strong temperature gradient with standard temperature at the depth of 0-10 km outside the melt pool. We also varied the granophyre/norite thickness ratio from 1:1 through 3:1 to 7:1 keeping the total SIC thickness at 4 km, i.e. norite layer thickness changed from 2 km to 0.5 km – see Fig.1.

Irrespective of the G/N thickness ratio (and similar to 1D model), the hottest part of the SIC is near the crater center at the melt pool bottom and within the footwalls. Although the norite layer solidified prior to the SIC total solidification, its temperature is high enough (above 1000 K) to allow precipitation of sulphides to the footwall.

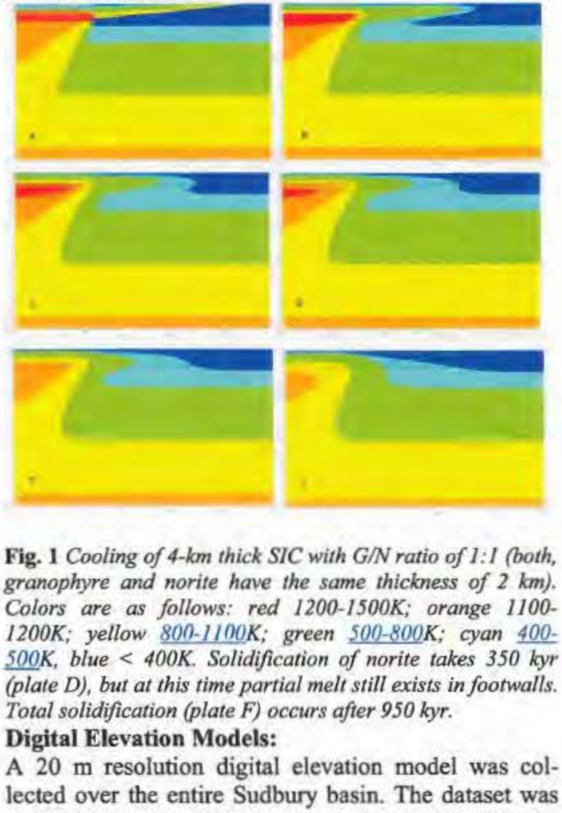

Fig. 1 *Cooling of 4-km thick SIC with G/N ratio of 1:1 (both, granophyre and norite have the same thickness of 2 km). Colors are as follows: red 1200-1500K; orange 1100-1200K; yellow 800-1100K; green 500-800K; cyan 400-500K, blue < 400K. Solidification of norite takes 350 kyr (plate D), but at this time partial melt still exists in footwalls. Total solidification (plate F) occurs after 950 kyr.*

Digital Elevation Models:

A 20 m resolution digital elevation model was collected over the entire Sudbury basin. The dataset was derived from 1;20,000 maps over the province of Ontario, Canada [10]. The data was displayed with different illumination angles to facilitate the discrimination of topographic features.

The data allows the distinction between inside-basin fabric (radial topographic lineaments) to footwall topographic fabric (radial and contact parallel lineaments). This model can be linked to the numerical modeling results on strain distribution and cooling of the SIC.

Conclusions:

For the large Sudbury impact structure cooling and solidification continued up to 1 million years, depending on the total thickness of the melt sheet and norite thickness. For any norite thickness, the hottest part of the SIC is at the melt pool/footwall contact, allowing additional melting of the footwall.

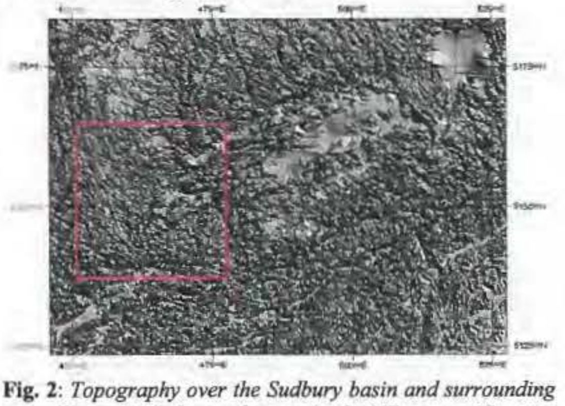

Fig. 2: *Topography over the Sudbury basin and surrounding area. Wanapitei Lake can be seen in the NE corner. The area delimited in red marks the zone of detail in Figure 3.*

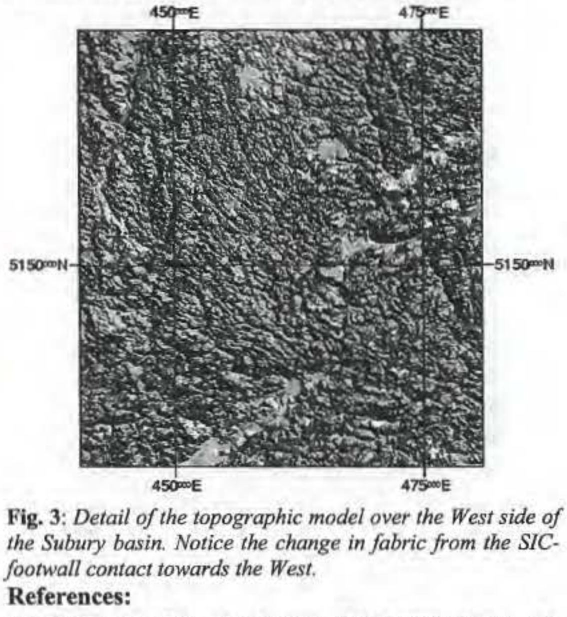

Fig. 3: *Detail of the topographic model over the West side of the Subury basin. Notice the change in fabric from the SIC-footwall contact towards the West.*

References:

[1] Polanskey, C.A. and Ahrens, T.J. (1990) *Icarus, 87*, p.140-155. [2] Xia, K. and Ahrens, T.J. (2001) *Geophys. Res. Letters, 28(18)*, p.3525-3527. [3] Collins G.S., Melosh H.J., and Ivanov B. A. (2004. *M&PS 39*, 217-231. [4] Morgan et al. (2005) *Eos, Transactions American Geophysical Union 86*, 325-328. [5] Ivanov B.A. and Deutsch A. (1999) Sudbury impact event: cratering mechanics and thermal history. In Large Meteorite Impacts and Planetray Evolution II, edited by B.O. Dressler and V.L. Sharpton. GSA Special Paper 339, 223-227. [6] Ivanov B.A. (2005) *Solar System Research 39*, 381-409. [7] Ugalde H. A., Artemieva N., Milkereit B. (2005) *GSA Special Paper, 384*, 25-42. [8] Roest, W.R. and Pilkington, M. (1994) *Geophys. Res. Lett., 21*, 959–962. [9] Zieg M. J. and Marsh B. D. (2005) *GSA Bulletin 117*, 1427-1450. [10] Government of Ontario (2003), Ontario Geospatial Data Exchange (OGDE).

THE ROTER KAMM METEORITE IMPACT CRATER AND ITS EJECTA APRON IN THE SOUTHERN NAMIB DESERT OF SOUTHWESTERN NAMIBIA.

Roy McG. Miller, Consulting Geologist (PO Box 11222, Windhoek, Namibia, rmmiller@mweb.com.na)

Introduction: The almost circular crater [1] is 2.8 km in diameter and is located in an area of vegetated dunes (Fig. 1) punctuated by a few, small, mobile barchan dunes and by shadow dunes on the lee side of the protruding crater rim. The rim is composed entirely of Namaqua gneiss. Its highest point is 140 m above the surrounding plains and 158 m above the deepest point inside the sand-filled crater. Impact glass in an ejecta fragment yielded an ^{40}Ar-^{39}Ar plateau age of 3.7 ± 0.3 Ma [2]. Detail on the crater has been provided in subsequent publications [3-9]. The ejecta apron outside the crater is described in this presentation and by Miller [10].

Pre-impact stratigraphy of the target area: This was as follows:

Sossus Sand Formation (top): Unconsolidated aeolian sands of the present Namib erg; thin but of variable thickness; base about ~4 Ma; still accumulating today. Sporadic outcrops of the underlying stratigraphic units peep through these sands outside the crater;

Rooilepel Sandstone Formation: Red-brown, semi-consolidated aeolianites; equivalent to the aeolian Tsondab Sandstone Formation further north; these aeolianites formed an older, more extensive Namib erg dated between 20 and 5 Ma by an evolutionary sequence of egg shells of ostrich-like birds [11];

Gariep Supergroup: Thin, scattered remnants, often only 2 m thick, of a huge thrust sheet of grey to white limestone with occasional brown jasperoid veins; between 750 and 600 Ma in age; tectonically emplaced onto the underlying gneiss at about 545 Ma;

Namaqua Metamorphic Complex (base): Upper amphibolite facies granitic gneiss; mainly coarse-grained to porphyroblastic, granodioritic biotite gneiss; lesser amounts of coarse-grained leucogneiss; minor short, thin, post-tectonic granitic pegmatites up to 50 cm thick and a few metres long, some zoned with thin, podiform quartz cores; one pair of parallel, post-tectonic quartz veins up to 50 m long and 4 m thick some 1.5 km southwest of the crater; 1200 Ma.

Crater rim: The granodioritic biotite gneiss forms the bulk of the elevated crater rim with the leucogneiss forming the northwestern part. Black and occasionally grey, green or red cataclasite veins (not pseudotachylite) occur in various concentrations around the whole rim. Most have a sub-millimetre thickness but a few are up to 2 cm wide. They occur singly and in clusters and both with and without associated brecciation of the gneiss. A marked radial orientation of the veins occurs along the northwestern and eastern parts of the rim. Many veins in the southern part of the rim are concentrically orientated but have both inward and outward dips. Small patches of brecciated gneiss in the north and east are blackened and soaked by pervasive cataclasite. Radial fractures in a Gariep limestone outcrop just southwest of the crater either contain black cataclasite or are bleached to a mustard colour. Fragments up to 2 cm in size of gneiss and cataclasite veins occur suspended in aeolian sand south of the crater. These vein fragments are commonly 2 mm thick, are unlike any of the veins in the southern part of the rim and are believed to have weathered out of the underlying gneissic basement. A feature of the northwestern, northern and eastern rim are *in situ* patches in the gneiss and associated pegmatites that are variously brecciated and contain blackened feldspar.

Ejecta on the crater rim: Large, disorientated, metre-sized blocks of granodioritic biotite gneiss cover the inner and outer parts of a small portion of the northern rim. A few such blocks occur on the western rim. Other ejecta fragments resting loose on the rim gneisses include, in decreasing order of abundance, reddish vein quartz breccias (the largest >1 m in size and occurring on the eastern and northwestern parts of the rim), fragments of gneiss and pegmatite with blackened feldspar, carbonaceous and graphitic schist, suevite, grey and mustard-coloured limestone, associated brown jasperoid, and rare pink porphyry-like quartz-feldspar rock, sandstone, and metre-size blocks of unbrecciated milky vein quartz (on the northeastern part of the rim). Unusual is a strewn field covering an area of about 1000 m^2 on the inner part of the northwestern rim of blocks of brecciated milky vein quartz up to 30 cm across cut by black veins of almost pure SiO_2 cataclasite between 1 mm and 10 cm wide containing variable amounts of angular milky quartz fragments. The strewn field includes fragments of the cataclasite that separated from the rest of the quartz breccia as well as a few smooth-surfaced, flädle-like fragments of carbonaceous schist breccia. Fragments of gneiss or pegmatite breccia pervaded by black cataclasite and black cataclasite fragments may be weathered out remnants.

Ejecta outside the crater: These are concentrated in an outward-fanning apron north and west of the crater and form a calcretised layer above unconsolidated aeolian sand of the Sossus Sand Formation. A few fragments of brecciated gneiss, black cataclasite and rare suevite, either loose or calcrete cemented, occur on the outer eastern and southern slopes of the rim. Not a single ejecta fragment was found on the Gariep limestone just southwest of the crater. In contrast, ejected fragments of gneiss form an almost continuous blanket between 1 km and 2 km northwest of the crater. Fragments >20 cm in size (Fig. 2) occur in both radial and concentric concentrations relative to the crater rim. The longest such radial arm extends for a distance of 5 km in a northwesterly direction from the northwestern crater rim. The largest fragments of 1m to 1.5 m in size form a concentric swath 1.5 km from the crater rim. Short, black, sub-millimetre cataclasite veins are extremely rare in such fragments. Gneiss fragments with blackened feldspars occur in a few patches and milky quartz fragments identical to those in the strewn field occur in the ejecta apron northwest of the strewn field. The contacts of the leucocratic gneiss to the granodioritic biotite gneiss form fixed points in the crater rim that can be traced into the distribution of the fragments in the ejecta apron but splay outwards away from the crater (Fig. 3). The milky quartz fragments show a similar outward splay.

Projectile trajectory: The limited number of ejecta fragments east and south of the crater, the large concentration of fragments from the north to the west of the crater, the large size of these fragments, the radial and concentric concentrations of the large fragments, the fanning splays of leucogneiss and milky quartz fragments and a slight northwesterly elongation of the crater of about 110 m suggests that the impact projectile followed a northwesterly trajectory.

References: [1] Dietz, R.S. (1965) *Meteoritics, 2,* 311-314. Reproduced 1977 *In*: McCall, G.J.H. (Ed.), Meteorite Craters. *Benchmark Papers in Geology, 36.* Dowden, Hutchinson & Ross, Inc., New York, 364 pp. [2] Hartung, J. et al. (1991) *Meteoritics, 26,* 342-343. [3] Miller, R. McG. and Reimold, W.U. (1987) *Meteoritics, 21,* 456-458. [4] Reimold, W.U. and Miller, R.McG. (1989) *Proc. 19th lunar planetary Sci. Conf., Houston, Lunar and Planetary Inst,* 711-732. [5] Reimold, W.U. et al. *Meteoritics Planet. Sci., 32,* 431-437. [6] Degenhardt, J.J. et al. (1994) *Spec. Pap. Geol. Soc. Am., 293,* 197-208. [7] Degenhardt, J.J. et al. (1996) *Meteoritics Planet. Sci., 31,* 413-415. [8] Grant, J.A. et al. (1997) *JGR, 102,* 16327-16338. [9] Brandt, D. et al. (1998) *Meteoritics Planet. Sci., 33,* 447-453. [10] Miller, R. McG. 2008. *The Geology of Namibia,* Geol. Surv. Namibia, *3,* 26-1 – 26-25. [11] Pickford, M.F.H. et al. (1995) *Geobios., 28,* 85-98.

Figure 1: Oblique aerial view of the 2.8 km diameter Roter Kamm Impact Crater; view westwards across the crater.

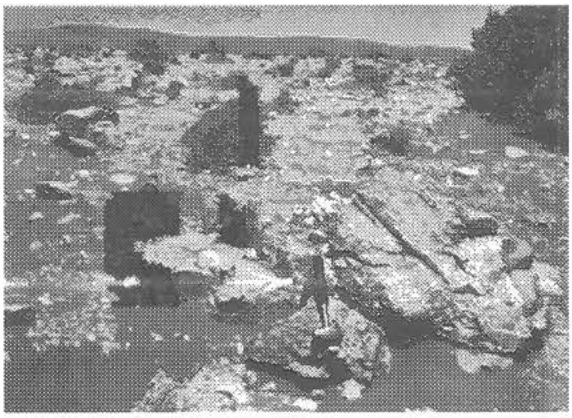

Figure 2: Large ejecta blocks of leucogneiss up to 1.5 km in diameter almost 2 km northwest of the crater; at number 1.5 in Figure 3. Crater rim in background.

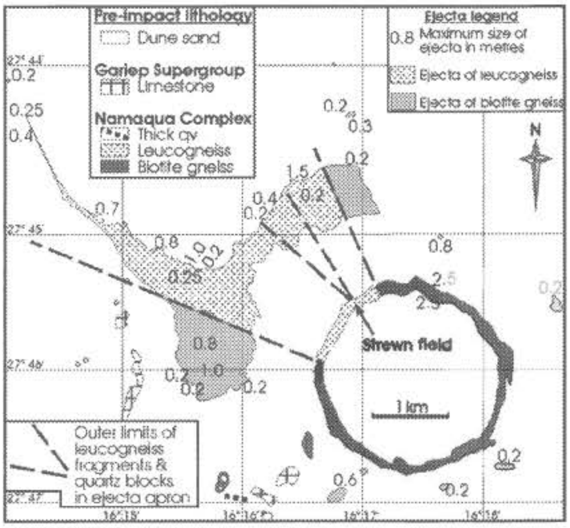

Figure 3: Highly simplified map of the crater showing the ejecta apron to the north and west of the crater and the way in which specific ejecta types fan outwards away from the crater towards the northwest.

PSEUDOTACHYLITIC BRECCIA AND MICROFRACTURE NETWORKS IN ARCHEAN GNEISS OF THE CENTRAL UPLIFT OF THE VREDEFORT DOME, SOUTH AFRICA.

T. Mohr-Westheide[1], W. U. Reimold[1], U. Riller[2], R. L. Gibson[3], [1]Museum for Natural History (Mineralogy), Humboldt University, Invalidenstrasse 43, 10115 Berlin, Germany (Tanja.Mohr@museum.HU-Berlin.de), [2] School of Geography and Earth Sciences, McMaster University, Hamilton, Canada, [3]Impact Cratering Research Group, School of Geosciences, University of the Witwatersrand, Private Bag 3, P.O. Wits 2050, Johannesburg, South Africa.

Objectives: Pseudotachylitic breccias represent the most prominent impact-induced deformation structures in the central uplift of the Vredefort Impact Structure [1, 2]. The Vredefort dome is the type locality for "pseudotachylyte", which can be investigated in detail in a range of different host lithologies. The exact mechanisms by which such melt breccias in impact structures form remains enigmatic (see reviews in Reimold and Gibson 2005): formation of pseudotachylitic breccias has been variously ascribed (e.g., [3, 4]) to impact (shock compression) melting, friction melting, decompression melting, or a combination of these processes. As pseudotachylyte (modern spelling: -ite) is generally considered friction melt formed along fault/shear zones, we prefer the nongenetic term "pseudotachylitic breccias". The genesis of the dome would suggest that such movement zones may occur in abundance, but the enormous volumes observed in the dome seemingly can not be produced along fault/shear zones [5]. And besides, the large displacement zones that such voluminous friction melting might require are not in evidence. While previously some work has focused on orientation and geometry of pseudotachylitic breccia veins, detailed geometric analysis has been hampered by limited outcrop and has not been adequately related to micro-deformation studies of pseudotachylitic breccia bearing rock and associated brittle deformation. This study uses a different by analysis of a polished 3 x 1.5 m granite slab [Fig. 1] from a dimension stone quarry in the core of the Vredefort Dome. The structural analysis of the granite slab was accomplished to add to the statistical outcrop-scale approach of previous work that has focused on the larger veins and dykes and the limited micro-scale work that has suggested that thin veins are shock features. It provides an ideal opportunity to investigate the relation between generation of fractures with and without melt, fracture and breccia intensity, and other geological parameters such as lithology, grain size and mineral fabrics.

Method: Characterization and mapping of microfracture and pseudotachylitic breccia networks with special regard of their orientation, intensity, and 3D geometry forms the basis for this work, on the granite slab and in the field. Hundreds of measurements of the orientations of microfractures and pseudotachylitic breccias were taken in a quarry in the northern part of the Vredefort dome. Also, first investigations of microstructures and pseudotachylitic breccias by optical and scanning electron microscopy will be reported at the conference.

Results: Besides a several dm-wide breccia zone, two types of structures, which mutually cut each other, are macroscopically observed in the granite slab, i.e., generally dark grey to black veinlets of pseudotachylitic breccias and a network of thin, often reddish-brown microfractures. Pseudotachylitic breccias occur as curved or anastomosing veins that commonly include mineral and rock fragments of the host granite gneiss. Five sets of thin. red microfractures are inclined towards each other at angles between 30 and 115°. An observed variation of fracture intensity seems to depend on the mineralogy of the host rock, which is mainly reflected in the variation of plagioclase and K-feldspar modal abundances of the host granite.

Two microfracture systems are apparent in the granite slab. One crosscuts pseudotachylitic breccia matrices and host-rock fragments, the other fracture system is characterized by complex crosscutting relationships to pseudotachylitic breccias: Some pseudotachylitic breccias are cut and displaced by these microfractures, but in larger volumes of massive melt this fracture system is spatially limited to crosscutting only host rock fragments entrained in the breccia matrix. The fracture system limited to fragments in massive melt zones defines the formation of an older microfracture system, which formed prior to fragmentation. Reassembling the rock fragments inside the breccia zone, with respect to an infinite number of paths that the fragments may have taken, allows one to reconstruct their geometric configuration prior to opening of the fracture zone. The investigated breccia zone contains a number of fragments within the melt, which are transected by microfractures of the older fracture system. The microfractures cross the gaps between adjacent fragments but do not transect melt areas.

In the field, a high fracture intensity can, in general, be observed close to large melt-filled fracture zones as well as close to local networks formed by many mm- to cm-wide pseudotachylitic breccia veinlets. With increasing distance from such melt zones, red microfractures display low fracture intensities in the granite gneiss. The structural measurements of thin pseudotachylitic breccia veins and microfractures in stereographic projections from several outcrop sections show that these structures feature characteristic geometric concordance: they mostly occur with similar orientations.

First investigations of microstructures and pseudotachylitic breccias by optical and scanning electron microscopy revealed that the matrix of such melt breccias consists predominantly of silicate phases composed of Si, Al, O, K, Na, Ca and Mg. Additionally, zircon, sphene, magnetite and other iron oxides were recognized within the melt. K-feldspar fragments within the melt are mostly completely recrystallized, unlike quartz or quartz-rich fragments that are only partially annealed. Microstructures of the older fracture system are filled mainly by chlorite. In addition, reflected light microscopy indicates a high content of iron oxide and revealed individual cubiform (probably original magnetite) crystals commonly altered to goethite, which is thought to be responsible for the red coloration. The younger fractures are open micro-joints that are partially filled with carbonate. In some cases, the color of thin pseudotachylitic breccia veinlets changes abruptly from black to red. Black areas contain melt that is rich in Si, Al, O, K, Na, Ca, Mg and Ti. Red areas reflect joint segments, the margins of which are coated with iron oxide. Microscopic evidence for dilation was found at the contacts between breccia veins and host rock. Evidence of melt in cross-cutting microfractures was also recognized on the macroscopic scale [Fig. 2]. Movement (flow) of melt into dilational sites could be detected as various scales (cm to submillimeter) in the form of flow laminations in the matrices of these melt breccias.

Conclusions: The structures apparent in the Vredefort Dome constitute structural deformation-time indicators. This detailed, meter- to centimeter-scale mapping and sampling of breccias and microfractures in the Archean gneiss of the Vredefort Dome has shown that it was affected by 2 microfracture-forming deformation events, one preceding melt emplacement and one following the emplacement of pseudotachylitic melts in dilation zones in the Vredefort dome. Local microfracture intensity seems to be associated with the compositional in the granitic target rock.

The older microfracture system formed prior to melt emplacement but also occurs in cross-cutting relationships to pseudotachylitic breccia veins. We suggest that the cross-cutting relationships between the 2 structures depend on different cooling rates of pseudotachylitic melt, while microfracturing activity continued. Microfractures may well have formed contemporaneous with dilation and fragmentation. The fractures probably opened as the melt was intruded.

Optical microscopic and SEM analysis affirm evidence for movement (flow) of melt into dilational microfractures, which points to a melt flow from large- to small-scale dilational sites; this has also been observed at the macro-scale [Fig. 2]. Microstrucure fillings of the older fracture system contain chlorite, which is likely secondary infill. The filling of secondary carbonate in the younger fracture system indicates that this fracture system was filled in a much cooler environment – likely at a much later stage after impact. Another possibility is a formation of these fractures at times after the impact or due to post-impact reactivation of pre-existing microfractures.

The reconstruction of fragment configuration of the breccia zone investigated on the polished granite gneiss slab has shown that fragments match with each other in a jigsaw fashion, i.e. either no or very little material from the fragments has been "eroded" (melted off, or abraded) away to form melt. The fragmentation of the target rock resulted in volume increase by dilation. This points to mobility of melt but limited movement (rotation) of fragments and suggests that dilation was contemporaneous with melt emplacement.

Unravelling the development of single structural components resulted in a sequence of 4 processes involving both deformation of the target rock and melt emplacement into the deformed host rock. What remains is to unravel the stated problem of how this melt originated in the first place.

References: [1] Dressler, B. O. and Reimold W. U. (2004) Earth-Science Reviews, 67, 1-60. [2] Reimold W. U. and Gibson R. L. (2006) GSA SP 405, 407 pp. [3] Gibson R. L. and Reimold W. U. (2001) The Vredefort impact structure, South Africa, Memoir 92, Council for Geoscience, Pretoria, 110 pp. [4] Gibson R. L. and Reimold W. U. (2005) Shock pressure distribution in the Vredefort impact structure, South Africa. Large Meteorite Impacts III. GSA SP 384, pp. 329-349. [5] Melosh, H.J., 2005. The mechanics of pseudotachylite formation in impact events. In: Impact Tectonics, ed. by Koeberl, C. & Henkel, H.. Impact Studies Series, Springer, Berlin-Heidelberg, 55-80.

Fig. 1: Polished 3 x 1.5 m granite slab from a dimension stone quarry in the Vredefort Dome.

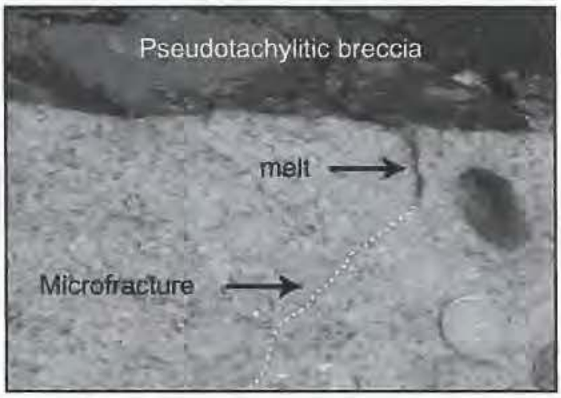

Fig. 2: Photograph of a melt-filled microfracture in the field. Melt has partially (only to the termination of the dark segment) filled an adjacent microfracture. Picture demonstrates melt transport from a large pseudotachylitic breccia zone into a smaller one.

CHICXULUB DISTAL EJECTA: MODELING VERSUS OBSERVATIONS.

J. V. Morgan[1] and N. Artemieva[2,3], Imperial College London, UK, j.morgan@imperial.ac.uk, [2]Institute for Dynamics of Geospheres, 119334 Moscow, Russia, [3] Planetary Science Institute, 85719 Tucson, US, artemeva@psi.edu

Introduction: The K-P boundary is widely recognized as a global ejecta layer formed by a large meteorite impact 65 million years ago. The discovery of an iridium anomaly [1] and shocked quartz grains [2] within the K-P boundary layer provided the strongest confirmation of the impact hypothesis. The thickness and composition of the K-P layer varies with distance from the Chicxulub structure (see [3] for a review). Distal sites (> 4000 km from Chicxulub) are characterized by an ejecta layer of no more than 2-4 mm thick that is enriched in PGEs and contains abundant impact spherules – microkrystites [1,3,4]. The ejecta layer at sites in North America (2000-4000 km from Chicxulub) is 0.5-2.0 cm thick, and has a dual-layer stratigraphy. The upper layer (historically called the fireball layer) is compositionally comparable to the distal ejecta layer. The K-P layer at sites < 2500 km from Chicxulub is quite variable, and appears to depend on whether the site was in the Gulf of Mexico, Caribbean or Atlantic, and whether the site was in shallow or deep water, or was continental [3]. Although we have good constraints on the composition and thickness of the K-P ejecta, we do not have a clear understanding of the mechanism for the transport of these ejecta from the impact site to their final location.

There have been a number of previous attempts to model the ejection/deposition of material from Chicxulub [5-9] with substantial simplifications. Here we attempt to model the entire process, from impact to arrival of the ejecta around the globe.

Numerical model and initial conditions. We model the impactor colliding with the earth and high-velocity impact ejecta motion using the 3D hydrocode SOVA [10] and the ANEOS equations of state for geological materials [11]. All solid/molten ejected materials are disrupted into particles of various sizes. The motion of these fragments in the post-impact plume is described in the frame of two-phase hydrodynamics. We start with standard Chicxulub model: the target consists of 3 km-thick sedimentary cover (calcite), 30-km-thick basement (granite) and mantle (dunite); 14.4-km-diameter asteroid strikes with velocity of of 18 km/s at 45°. Then, we have run a number of other simulations with different impact angles and higher impact velocities (keeping the size of transient cavity equal to 90-100 km), as well as 45°-impact into water-saturated sediments to investigate the effect of changing these parameters on the ejection process.

Distal ejecta. In our standard modeling simulation, we noted a surprising result: basement (both molten and solid) travels at fairly low velocities immediately after ejection and is not subjected to acceleration in the vapor plume. The high-velocity ejecta material in the upper part of the plume is composed exclusively of vaporized projectile and target sediments. Assuming ballistic trajectories, we have used our mass-velocity distribution of ejecta to determine global ejecta thicknesses – see Fig.1. The total amount and estimated thickness of ejecta is comparable with observations, with a few cm at intermediate distances of 1800-2500 km (e.g. in North America), and a few mm thick worldwide (at distances > 4000 km). However, a model of pure ballistic continuation inevitably leads to ejecta thickness decreasing with distance from the crater. Hence, one of the first-order observations – the almost constant 2-3 mm thickness of the global K-P layer, is not replicated in our modeling.

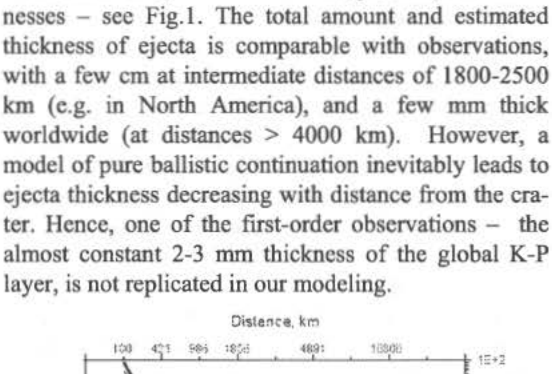

Fig.1 Cumulative mass of ejecta (left axis) versus ejection velocity (bottom axis) is shown by black lines. Ballistic thickness of ejecta (right axis) as a function of distance (top axis) is shown with gray lines. Solid lines are for dry target, dashed ones - for water-saturated sediments. Squares (dry target) and triangles (water saturated sediments) represent worldwide ejecta thickness if high-velocity ejecta are deposited non-ballistically and evenly.

Iridium anomaly. Around 0.14 of the projectile has a velocity between 5 km/s and 11 km/s, and may be distributed worldwide. This is significantly lower than estimates of 0.22 by [1] and 0.5 by [12]. This is an important result as it means that our estimate for the volume of iridium within the global ejecta layer (2.77

x 10^8 kg, assuming Ir in chondrites of 500 ng/g) is similar to the observed volume (2-2.8 x 10^8 kg).

Composition of fireball layer. If projectile and sedimentts with velocities between 5 and 11 km/s (0.14 and 0.35 of the projectile volume, respectively) are distributed around the globe in a similar way, then the distal ejecta would be composed of sediments (72%) and projectile (28%), and the total volume of material is ~770 km^3. This is slightly less the 850 km^3 of K-P spherules world-wide estimated by [3]. Our results suggest that distal spherules are composed from projectile and sediments in a ratio of ~7:3,. If the clay that surrounds the spherules is dominantly locally derived, this would produce a meteoritic content of between 1:4 and 1:6, which is slightly more than observed value of 1:8 [13].

Shocked quartz. The maximum distance reached by the basement rocks traveling on ballistic trajectories is about 700-1000 km. This result does not depend on the impact scenario (angle, velocity) and the distance is only slightly higher if the target is water-saturated. Thus, the model is in contradiction with the observation of shocked-quartz at the K-P boundary.

Proximal glasses. Our estimates of the total melt production from the basement (18,000-28,000 km^3, depending on impact angle and impact velocity) are in a good agreement with simple scaling-based estimates [14,15], geophysical studies [16,17]) and modeling results, which used different hydrocodes [18,19]. The majority of the melt (~80%) lies within or near the crater even at late time moments, and would be a component of melt rocks or melt rich (suevitic) impact breccias. Around ~3% of the total melt produced is ejected from the crater with velocities above 1 km/s and deposited outside the crater rim. The thickness of the melt deposit is about 10 cm – 1m at a distance of 700-1000 km, and this is comparable with the observed volume of Si-rich impact glass deposits.

Non-ballistic transport of distal ejecta. Small particles do not moved ballistically and are suspended in the ejecta plume at high altitudes for a long time. The total amount of this "low-velocity turbulent" ejecta (1-2 km^3) is much lower that would be required to create a worldwide ejecta layer with an average thickness of 2-3 mm, but is enough to produce the total volume of shocked quartz distributed worldwide. These suspended particles (including shocked quartz grains) could be dispersed around the globe by atmospheric flows and slow gravitational settling, similar to volcanic ashes such as in the El Chichon eruption in 1982 [20]. This mechanism was proposed in [21,22] and was modeled by Pope [23] who assumed 10^{16}-10^{17} g of clastic material at stratospheric altitudes near the Chicxulub crater. This variant looks attractive because, such non-ballistic transport of quartz grains at low velocities and low altitudes, would allow PDF to survive upper atmosphere heating during re-entry. If shocked quartz arrived at the same time as the high-velocity ballistic ejecta, the shocked quartz should be annealed [7].

Another possibility is a mechanism termed "floating of impact debris in the atmosphere", suggested in [24]. The principal idea is quite simple: the re-entering of debris heats the atmosphere, which then expands upward and laterally and redistributes the debris around the globe. Unlike for volcanic eruptions, which take several weeks to transport ashes globally, this mechanism can take several hours. If we assume that all high-velocity ejecta (above 4-5 km/s) is distributed non-ballistically and evenly by this way, then the global thickness is roughly equal to 2-3 mm (see square and triangle in Fig. 1). In addition, this transport mechanism would: reduce the total volume of ejecta arriving at North American sites (which is slightly too large in our models), increase the volume of material arriving at distal sites (which is slightly too small in some of our models), as well as enable shocked quartz and zircon to reach distal sites without being annealed. These preliminary results are quite encouraging, as they address all the discrepancies between observational data and purely ballistic models.

References: [1] Alvarez L.W. et al. (1980) *Science 208*, 1095. [2] Bohor B. et al. (1984) *Science 224*, 867-869. [3] Smit J. (1999) *Ann. Rev. Earth Planet. Sci. 27*, 75–113. [4] Hildebrand A.R. (1993) *J. Roy. Astron. Soc. Can. 87*, 77-118. [5] Alvarez W. et al. (1995) *Science 269*, 930–935. [6] Kring D.A., Durda D.D. (2002) *JGR 107(E6)*, 10.1029/2001JE001532. [7] Croskell M. et al. (2002) *Geophys. Res. Lett. 29*, 1940-1944. [8] O'Keefe J. D. et al. (2001) *LPSC 32*, abstr. #2190. [9] Goldin T. and H. J. Melosh (2007) *LPSC 38*, abstr. #2114. [10] Shuvalov V. (1999) *Shock waves 9*, 381-390. [11] Thompson S.L., Lauson H.S. (1972) *SC-RR-61 0714*. Sand. Nat. Lab., Albuquerque, NM, 119 p. [12] Vickery A., Melosh H.J. (1992) *GSA Special Paper 247*, 289–300. [13] Kyte F.T. et al. (1985) *Earth Planet. Sci. Lett. 73*, 183-195.. [14] Kring, D. A. (1995) *JGR 100*, 16979-16986. [15] Pope K. O. et al. (2004) *MAPS* 39, 97-116 [16] Ebbing J. et al. (2001) Planet. Space Sci. 49, 499-509. [17] Morgan et al. (2002) *Tectonophys.* 355, 215–226. [18] Pierazzo E. and Crawford D. (1998) *Lunar Planet. Sci. XXIX*, abstr. 1704. [19] Ivanov B. (2005) *Solar System Res. 39*, 381–409. [20] Rampino M.R., Self S. (1984) *Scientific American 250*, 48–57. [21] Toon O.B. et al. (1997) *Rev. Geophys., 35*, 41–78. [22] Covey C. (1990). *GSA Special Paper 247*, 263–270. [23] Pope K. O. (2002) *Geology 30*, 99-102. [24] Colgate S. A. and A. G. Petschek (1985) *LA-UR-84-3911*, Los Alamos Natl. Lab., NM.

MICROSCOPIC SHOCK-ALTERATION FEATURES IN SHATTER CONES FROM THE SANTA FE IMPACT STRUCTURE, NEW MEXICO, USA.

J. R. Morrow[1], C. Koeberl[2], and W. U. Reimold[3], [1]Dept. of Geological Sciences, San Diego State University, 5500 Campanile Drive, San Diego, California 92182-1020, USA (jmorrow@geology.sdsu.edu), [2]Dept. of Lithospheric Research, University of Vienna, Althanstrasse 14, A-1090 Vienna, Austria (christian.koeberl@univie.ac.at), [3]Museum for Natural History (Mineralogy), Humboldt University, Invalidenstrasse 43, D-10115 Berlin, Germany (uwe.reimold@museum.hu-berlin.de).

Introduction: Field mapping, morphologic analysis, and petrographic examination of recently discovered shatter cones within Paleoproterozoic crystalline rocks exposed over an area >5 km^2, located ~8 km northeast of Santa Fe, New Mexico, USA, give strong diagnostic evidence of a previously unrecognized terrestrial impact structure [1–4]. The shatter cones, which crop out in natural and fresh roadcut exposures (Fig. 1), are composed of nested sub-conical, curviplanar, and flat joint surfaces bearing abundant curved and bifurcating striations that strongly resemble the multiply striated joint surfaces (MSJS) documented from shatter cones in the Vredefort Dome [5, 6]. The cones occur as a penetrative feature in granitoid and supracrustal metamorphic rocks, are large (up to 2 m long and 0.5 m wide at the base), usually display upward-pointing apices, and have subvertical, NE-plunging axes that crosscut regional host-rock fabrics.

The observed shatter cone outcrop area suggests that the minimum final crater diameter of the Santa Fe impact structure was ~6–13 km [4]. Regional exhumation models, together with ongoing work on anomalous breccia units that overlie and crosscut the shatter cone-bearing rocks, indicate that the impact structure is post-Mesoproterozoic [4] and possibly Early Carboniferous or younger in age [2, 3]. A minimum possible age is not known, although the lack of a clearly preserved crater does not favor a geologically recent impact.

Microscopic Shock-Alteration Features: Analysis of petrographic thin sections cut perpendicular to the outer margins of several shatter cones has identified thin rinds or patches, generally <50 μm thick, of cryptocrystalline, dark-green to dark-brown, semi-opaque to rarely isotropic material that coats the shatter cone surfaces (Fig. 2). The dark material also forms apparently discontinuous patches and veinlets that occur parallel to, and sometimes branch from, the coatings on the outer cone surfaces. The majority of the dark material occurs within ~1 mm of the cone margins, although the veinlets, which are probably melt developed along MSJS [5], are generally oriented parallel to subparallel to the cone outer surfaces and occur deeper within the cone interiors. This dark material is consistent with previously documented microscopic glass or melt present along the surfaces of shatter cones from the Vredefort Dome [5, 7] and the Beaverhead [8] and Sudbury [9] structures.

Other alteration present beneath the cone surfaces and directly next to dark veinlets in the cone interiors includes common grain micro-fractures; common fluid micro-inclusions and inclusion patches within mineral grains, which appear in part "toasted"; common sericite replacement within feldspar grains; rare kink bands in mica; rare blocky optical extinction patterns or grain mosaicism; and rare planar microstructures in quartz (Fig. 2). To date, no glassy microspherules, another shock-related feature reported on shatter cone surfaces at Vredefort [7], have been found.

The quartz planar microstructures are present within ~1 mm of the cone surfaces (Figs. 2, 3) and adjacent to dark veinlets in the cone interiors. The planar microstructures, which occur as only one set of parallel lamellae per grain, are highly decorated with fluid micro-inclusions, are ~1–3 μm thick, and are spaced ~2–15 μm apart (Fig. 3). Based on their thickness and spacing, the planar microstructures may represent either planar fractures (PFs) or planar deformation features (PDFs) [10, 11]. Universal stage microscope indexing of 20 planar microstructure-bearing quartz grains showed that 18 of the grains contain sets with a basal (0001) crystallographic orientation (Fig. 3); the other two grains contained PFs with higher index set orientations. Optical mosaicism is also a common property of the planar microstructure-bearing quartz grains.

Summary and Discussion: Together with the large shatter cones, the occurrence of probable melt and basal-oriented quartz planar microstructures near the cone margins give strong evidence of shock metamorphism generated by an extraterrestrial impact event. Consistent with quartz planar microstructures that have been previously documented from other shatter cone localities [e.g., 6, 8, 10, 12], these basal lamellae may represent annealed, micro-inclusion-defined Brazil twins. Based on laboratory single-crystal shock experiments and analyses of naturally shocked crystalline target rocks, the occurrence of basal PDFs in quartz in the absence of higher index plane sets indicates peak shock pressures of ~5–10 GPa [10, 12]. This range is within the broadly constrained pressure regime of ~2–30 GPa for shatter cone formation [11].

Acknowledgments: T. H. McElvain and S. P. Fackelman provided critical field data on the shatter cones. Colleagues at the University of New Mexico and the New Mexico Bureau of Geology and Mineral Resources provided valuable input to our project. Koeberl acknowledges funding by the Austrian Science Foundation FWF, Grant P18862-N10.

References: [1] Fackelman S. P. et al. (2006) *GSA Abstr. with Prog., 38(7)*, 298. [2] McElvain T. H. et al. (2006) *GSA Abstr. with Prog., 38(7)*, 298. [3] Newsom H. E. et al. (2007) *Meteoritics & Planet. Sci., 42*, A117. [4] Fackelman S. P. et al. (2008) *Earth Planet. Sci. Lett.*, in press. [5] Nicolaysen L. O. and Reimold W. U. (1999) *JGR, 104*, 4911–4930. [6] Wieland F. et al. (2006) *Meteoritics & Planet. Sci., 41*, 1737–1759. [7] Gay N. C. et al. (1978) *Earth Planet. Sci. Lett., 41*, 372–380. [8] Hargraves R. B. and White J. C. (1996) *J. Geol., 104*, 233–238. [9] Gibson H. M. and Spray J. G. (1998) *Meteoritics & Planet. Sci., 33*, 329–336. [10] Stöffler D. and Langenhorst F. (1994) *Meteoritics, 29*, 155–181. [11] French B. M. (1998) *LPI Contrib. 954*, 120 pp. [12] Leroux H. et al. (1994) *Tectonophysics, 230*, 223–239.

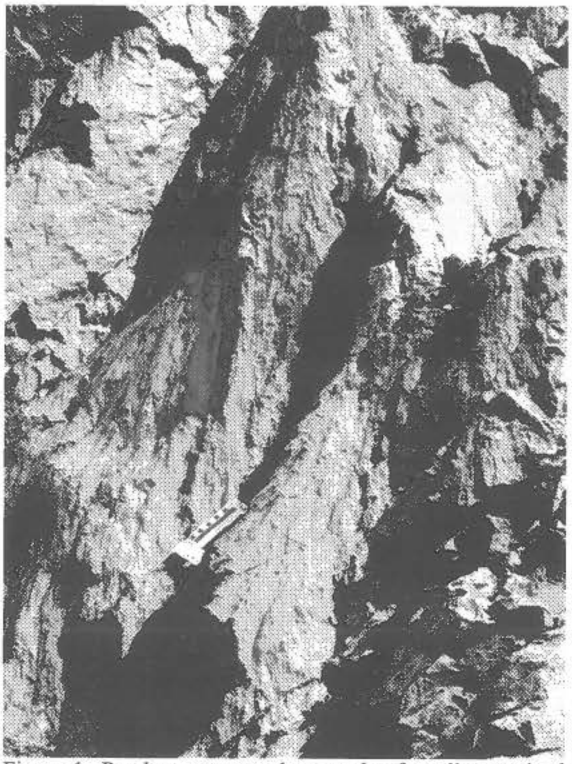

Figure 1. Roadcut outcrop photograph of medium-grained granitoid, showing well-developed, nested, sub-conical to curviplanar shatter cones displaying common multiple sets of striated surfaces with curved, downward-bifurcating striae that form a horsetail-like pattern. Scale is 10 cm long.

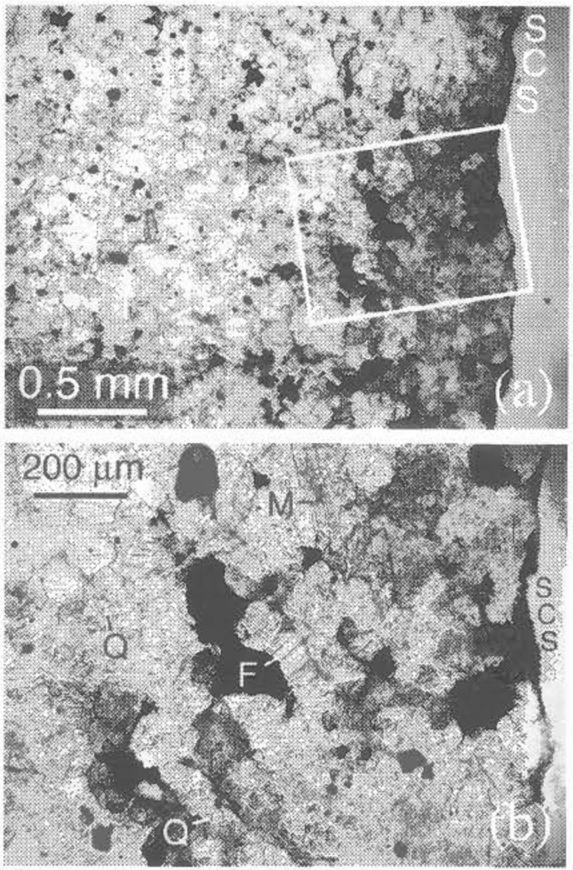

Figure 2. Plane-polarized light, thin section photomicrographs across outer surface of shatter cone in fine-grained quartz schist. (a) Shows steep gradient, over <2 mm, in degree of shock alteration from highly altered cone surface (SCS) to unaltered sample interior to left. (b) Inset view near cone surface, showing thin, semi-opaque to isotropic melt rind on cone surface; micro-fracturing in quartz (Q), feldspar (F), and mica (M) with possible kink bands; fluid micro-inclusions in grains; and planar microstructures in quartz.

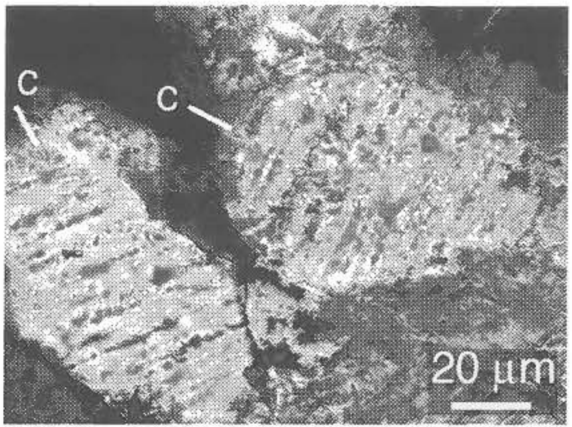

Figure 3. Plane-polarized light, thin-section photomicrograph of quartz with decorated, basal (0001) planar microstructures in grains from shatter cone-bearing, fine-grained quartz schist. Plane spacing is ~5–15 µm, indicating PFs or PDFs.

ALTERATION OF SURFICAL SUEVITES AT THE RIES CRATER, GERMANY: MINERALOGICAL AND STABLE ISOTOPE EVIDENCES.

N. Muttik[1], K. Kirsimäe[2], G. R. Osinski[3], P. Somelar[4] and T. W. Vennemann[5], [1]Department of Geology, University of Tartu, Vanemuise 46, 51014 Tartu, Estonia, nele.muttik@ut.ee, [2]Department of Geology, University of Tartu, Vanemuise 46, 51014 Tartu, Estonia, kalle.kirsimae@ut.ee, [3]Departments of Earth Sciences/Physics and Astronomy, University of Western Ontario, 1151 Richmond Street, London, ON, N6A 5B7, Canada, gosinski@uwo.ca, [4]Department of Geology, University of Tartu, Vanemuise 46, 51014 Tartu, Estonia, peeter.somelar@ut.ee,.[5]Institute of Mineralogy and Geochemistry, University of Lausanne, Building Anthropole, CH-1015 Lausanne, Switzerland, torsten.vennemann@unil.ch.

Introduction: The 24-km diameter Ries impact crater, southern Germany [1] exhibits well-preserved crater fill and surficial suevite deposits that are altered to various extent. It is generally accepted that the alteration of suevites was governed by post-impact hydrothermal fluids reacting with impact-generated glasses and/or fine-grained crystalline basement material [2-4]. The same was assumed for the origin of calcite in the surficial suevites. However, recent studies have suggested that calcite and a substantial proportion of the fine-grained 'clays' in the groundmass of surficial suevites of the Ries represent a combination of primary impact-generated melt phases and high temperature devitrification products [5-6], which are variably altered to smectite type clays. Earlier studies have shown that hydrothermal alteration of the crater-fill suevites (impact melt-bearing breccias) is pervasive and characterized by argillic-type hydrothermal alteration with zeolitization; an early phase of K-metasomatism accompanied by minor albitization and chloritization at temperatures of approximately 200–300 °C [2]. Supposed impact-induced hydrothermal alteration (IHT) within surficial suevites at the Ries crater is limited and typically restricted to montmorillonite and zeolite (mainly phillipsite) deposition within cavities and fractures [2-3].

In this contribution, we discuss the origin of hydrous silicate (clay) phases in surficial suevites that have been previously interpreted as resulting from post-impact hydrothermal processes.

Material and methods: Alteration mineralogy of surficial suevites was studied by means of X-ray diffraction and scanning electron microscopy. The interpretation of phases was checked against the EDS spectra. Stable oxygen isotopic composition was measured in clay separates from the suevite matrix at the Stable Isotope Laboratory, University of Lausanne. Chemical composition of surfical suevite whole-rock samples was analyzed by means of ICP-ES and ICP-MS at the ACME Analytical Laboratories Ltd Vancouver, Canada.

Studied material represents surficial suevites, which were collected from 4 outcrops in the Ries impact structure: Altenbürg, Aumühle, Lehberg, and Oettingen. Altogether 29 samples were studied.

Samples include suevitic material that varies from fresh suevite (with no or limited noticeable alteration) to highly altered suevites.

Results and discussion: The mineral composition of suevite is characterized by an assemblage of montmorillonite-type smectite, plagioclase, quartz and K-feldspar. Both the qualitative and quantitative composition of different suevite types is rather constant and does not show any variation between different locations. However, highly altered suevites contain halloysite in remarkable amounts (up to 81 wt% of crystalline phases). The content of the rest of the minerals are below 5 wt%.

The clay fraction of all samples is characterized by montmorillonite-type smectite, which is indicated by strong 001 reflection at 14-15 Å in air-dried state that expands to 17 Å in ethylene-glycolated states. Structure refinement suggests that montmorillonite is of Al-Fe montmorillonite type. Low-charge octahedrally substituted dioctahedral Al-montmorillonite is a typical low temperature smectite, whereas the high temperature smectite is usually tetrahedrally substituted Al-beidellite [7-8].

The structural composition of smectite does not have any variance regardless to the location within the structure. Moreover, no signs of compositional or structural variation (e.g. illitization) was found between the possible fluid conduits and surrounding rocks that would have been induced by temperature gradients. However, in some samples halloysite along with smectite was identified. Halloysite was found in the same samples where it was identified in whole-rock XRD analysis.

These findings are not consistent with a hydrothermal origin of the suevite clay "alteration" phases with the surfical suevite. Hydrothermal alteration in active endogenic hydrothermal systems is typically characterized by a zonal distribution of alteration and directional distribution of altered minerals that is principally related to mass transfer between minerals and hydrothermal solutions as temperature decreases when the hydrothermal solutions pass through rock [9]. The distribution and morphology of alteration zones are basically influenced by fracture distribution, porosity, and permeability of the rocks. It is expected that conditions such as slow flow rate of solutions, porous rocks, and glassy material, facilitate the growth in size of alteration zones around the fracture [10].

The chemical composition of major oxides in the whole-rock samples agrees with the mineral composition. The composition of material in different types of suevites at a particular location is fairly homogenous, which can be noticed by the generally small variation of major oxides. However, there is substantial systematic variation in contents of major oxides between different locations within the crater.

Freshly broken interior surfaces of a suevite sample have the typical vesicular structure of groundmass and melt phases. The glass phase has frequently a flow-texture and contains irregularly-shaped vesicle inclusions. All samples show the ubiquitous clay coatings and vesicles within the glasses are lined by clay aggregates, which is consistent with the high percentage of clay in the suevite identified by XRD analysis. In addition, other authigenic minerals such as calcite, plagioclase(?), haolloysite(?) and opal-CT were identified by EDS spectra and they have a characteristic morphology when replacing the vitric matrix and glass fragments in studied suevites.

Petrographic relations suggest that the smectite was the first and major mineral to form. The lepispheres of opal-CT that rarely coexist with smectite appear to postdate the major smectite formation.

It is to be noted that the majority of silicate impact glasses and mineral fragments in the suevites are unaltered. The glass appears to have transformed directly to smectite through dissolution of glass to form smectite without forming amorphous precursor or primitive clays. Randomly oriented montmorillonite type smectite flakes fill or coat the walls of existing round cavities and pores that were formed by dissolution of the glass. The observed similarity of the mineral in different parts of the rock and in different localities suggests that the precipitation of smectite has not been controlled by hydrothermal fluids, but rather by percolating meteoritic waters.

Zeolite minerals have been recognized in the groundmass and impact glass clasts of surficial suevites by several authors [3-4; 6], but its abundance is very low and its occurrence is scarce. In this study a trace amount of harmotome type zeolite was identified in only one sample .

The low temperature origin of smectite in surficial suevites at the Ries crater is supported by the $\delta^{18}O$ values of the monomineral smectite fractions. Measurements of $\delta^{18}O$ values vary between 19 to 23‰ VSMOW. According to Vennemann et al. [11] the oxygen isotope compositions of impact glasses at the Ries crater sampled from widely spaced localities are very homogeneous with $\delta^{18}O$ values in the range of 6.7 to 7.4‰. The major modification of the original oxygen values suggests a large water/rock ratio, which also rules out the incipient devitrification of the impact glasses. Moreover, the significant enrichment of ^{18}O implies an alteration at low temperatures. The variation of measured oxygen isotope compositions of smectite in surficial suevites generally agrees with alteration fluids corresponding to the average isotope composition of the (modern) precipitation in the area (-7 to -8‰,) [12] and the mean annual temperature of 9-10 °C.

Conclusions: The mineralogical and isotopic results of this study indicate that the dominant alteration phases are dioctahedral Al-Fe montmorillonite and halloysite, which are typical of low temperature clay minerals. We suggest that the surficial suevites are not altered by hydrothermal processes and that alteration occurred by low temperature subsurface weathering processes. If the surficial suevites were indeed hydrothermally modified during the early stages of the impact cooling, then the alteration was of limited character and is completely masked by later weathering of unstable impactites.

References: [1] Pohl J. et al. (1977) *Impact and Explosion Cratering,* 343-404. [2] Newsom H. E. et al. (1986) *JGR, 91,* 239-251. [3] Osinski G. R. (2005) *Geofluids, 5,* 202-220. [4] Engelhardt W. v. and Graup G. (1984) *Geol. Rundsch., 73,* 447-481. [5] Graup G. (1999) *MAPS 34,* 425-438. [6] Osinski G. R. et al. (2004) *MAPS, 39,* 1655-1683. [7] Meunier A. (2005) *Clays,* 472p. [8] Haymon R. M. and Kastner M. (1986) *GCA, 50,* 1933-1939. [9] Helgeson H. C. (1979) *Am. J. Sci., 267,* 729-804. [10] Inoue A. (1995) *Origin and Mineralogy of Clays,* 268-330. [11] Vennemann T. W. et al. (2001) *GCA, 65,* 1325-1336. [12] Sturm K. et al. (2005) *Hydrol. Process., 19,* 3425-3444.

YAXCOPOIL-1 IMPACT MELT BEARING BRECCIAS: THE CONTROVERSY OVER MULTIPLE COMPOSITION MELTS AND THE ROLE OF HYDROTHERMAL ALTERATION.

H. E. Newsom, M. J. Nelson and M. N. Spilde. University of New Mexico, Institute of Meteoritics, Dept. of Earth and Planetary Sciences, Albuquerque, NM 87131 U.S.A. Email:newsom@unm.edu.

Introduction: The Chicxulub impact crater, Mexico, was formed in a layered target of carbonates and silicates [1, 2]. The Yaxcopoil-1 drill core, in the annular trough of the crater consists of layered impactites with upper "reworked suevite", and lower "impact melt breccia" [3]. Impactites are Mg-, Al-, and K-rich in certain units. Elemental signatures in the impactites cannot be explained by any one unaltered parent lithology. Models that explain the Mg and K signatures can be divided into categories: (1) Formation of Chicxulub impactites from a single silicate melt later altered by aqueous or hydrothermal fluids, or (2) derivation of impactites from at least two Mg-, and/or K-rich primary melt compositions, or (3) some combination of aqueous and hydrothermal alteration and multiple impact melts [4, 5].

Results: Microprobe, SEM, and X-ray diffraction analyses were conducted to determine textural and chemical relationships of melt clasts and matrix, the origin of major element signatures, and to determine if the impactites contain hydrothermal minerals. Quantitative element maps coupled with backscattered electron images were particularly useful for determining the relationships between the chemistry and textures. The results are as follows:

- The matrix is physically distinct from the melt clasts and locally exhibits flow texture around clasts, and alteration to smectite clay.
- The Mg-enrichment is found only in the matrix.
- Calcite is ubiquitous only in matrix material.
- The K-enrichment is present only in the rims of the Si-, Al- rich melt clasts.
- XRD analyses did not detect the presence of chlorite or other hydrothermal minerals.

The lower units at a depth below about 847 m, and presumably deposited first, contain an melt breccia. K-enrichment is seen on puzzle-like angular, silicate melt clast rims in element maps, while the matrix material consists of a separate Mg-rich (20% or greater), lithology with no K-enrichment.

The upper suevite layers above 846 m, and presumably deposited slightly later in time, also contain two lithologies: a Mg- rich matrix lithology containing calcite, and a Si-, Al-, sometimes K- rich lithology. However, these lithologies are represented in both the groundmass and schlieren melts, with evidence for melt immiscibility.

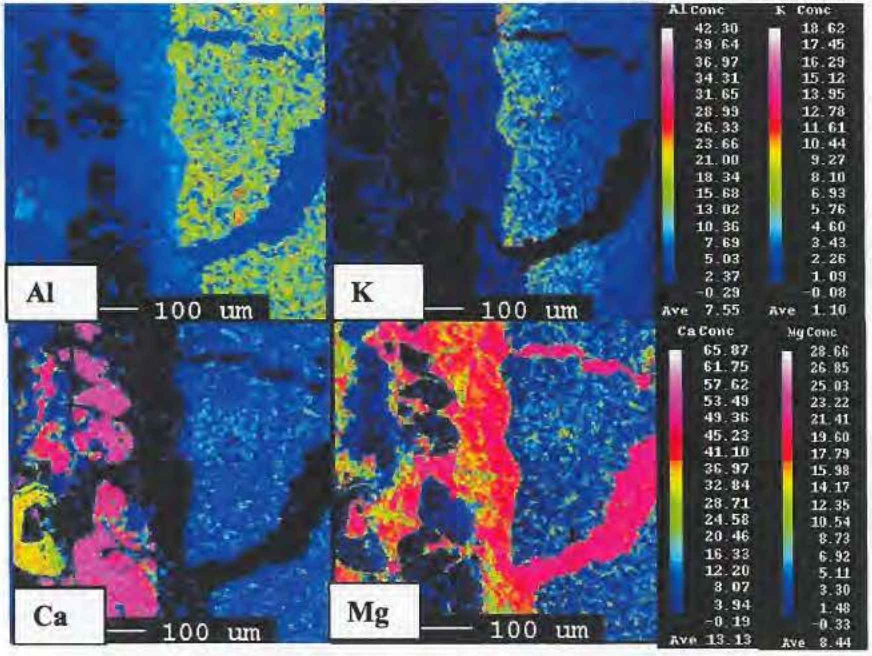

Fig. 1. Quantitative element map with oxides in weight percent of impact melt in Unit 4, sample 641. The data shows an Al-bearing melt clast with puzzle-like fit (upper left) and K-enrichment on edges (upper right). Clasts are crosscut by Mg-rich matrix. Matrix also contains calcite (Highest Ca in lower left).

Discussion: ***Hydrothermal fluids and/or seawater alteration?*** Alteration by hydrothermal fluids has been suggested by several authors [3, 6 – 9]. If the Mg in the matrix material is the result of fine clast material altered by an influx of hydrothermal fluid, then it should have also affected the glass or finely crystalline material of the larger melt clasts. The melt clasts, however, maintain sharp boundaries, with quenched textures at the edges, and no Mg-enrichment. The lack of chlorite or zeolites in the matrix also argues against an extensive hydrothermal regime for the formation of the melt breccia matrix. Ion probe data for Li, Be, B, and Ba by Newsom et al. [10] do not indicate fractionation of these elements, arguing against an extensive hydrothermal system at Yax-1.

If both the Mg and K- enrichments were the result of downwelling seawater [6], then Mg and K would be expected to spatially correlate, and alteration of both matrix and clast glasses would be expected. In addition, studies of both high and low temperature alteration by seawater have found strong preferential enrichment of K, not necessarily Mg [11, 12]. *Therefore, seawater might explain the K enrichment in the melt clasts, but does not appear to be the process responsible for the matrix chemistry. Hydrothermal processes seem to have been of limited importance.*

Origin of Mg-rich matrix as a dolomitic melt? What additional observations constrain the origin of the Mg-rich matrix material? XRD analysis of carefully drilled powders showed that the matrix contains saponite, a Mg-rich clay. Formation of the Mg-rich clay by the fluid alteration of a more Al-rich material, like the melt clasts, is problematic, because Al is not fluid mobile. The least problematic way to explain the Mg-rich matrix is to have Mg-rich starting material in addition to the Si-rich material. Considering the composition of candidate materials including granite, dolomite, basalt, and sedimentary rocks, dolomite is the only natural material of the three that approaches the high Mg concentration of the Yax-1 melt breccia matrix. The complexity of the target source materials for the melt particles has also been noted by Tuchscherer et al. [13]. Zürcher et al. [14] analyzed O , C, and H isotopes, and found a signature they concluded is consistent with the addition of a limestone component, but could very well represent a dolomite component as well.

Dual melts have also been identified at the Ries crater by Graup [15] and Osinski [16], and at the Haughton structure, Canada [17, 18], where evidence suggests that the two components of the matrix resulted from dolomite and silicate melts. In addition, experimental data for shock melting of pure dolomite, and equilibrium melting studies [e.g. 19] suggest that the Mg-Si-rich matrix material could have been produced from a high temperature, impure dolomite melt, while calcite could crystallize out as the other phase in the matrix. *An injected melt derived from dolomite in the target rock is therefore the best explanation for the chemistry and texture of the Mg-rich matrix material.*

Conclusions: These results support the following sequence of events to form the Yax-1 breccias:

(1) Impure dolomite and silicate basement lithologies were melted and ejected during crater formation.

(2) In the lower portion of the ejecta, at a depth associated with lateral surge ejecta dynamics, the silicate melt was quenched, brecciated, and enriched in potassium by seawater, or another K-rich fluid during transport or shortly after deposition. This deposit was slightly later permeated by Mg-rich dolomitic melt, possibly from melt bodies in the ejecta deposit that were not as well mixed as seen in the upper ejecta material. In addition, since other authors [8, 9, 20] have identified carbonate melts, including dolomite clasts in the drill core, this may mean there is actually a larger amount of dolomite melt than previously identified, given the dolomite-rich Cretaceous target.

(3) The dolomite and silicate melt textures in the suevitic upper units appear to be consistent with mixing in the ballistic ejecta down to the millimeter scale during transport. The suevite breccia above 824 m in the sequence consists of schlieren dolomitic and silicate melts containing immiscible melt textures.

References: [1] Alvarez L.W. et al. (1980) *Science, 208,* 1095-1098. [2] Hildebrand A. R. et al. (1991) *Geology, 19,* 867-871. [3] Dressler B.O. et al. (2003). *EOS Transactions, 84,* 125-130 [4] Dressler, B.O. et al. (2004) *MAPS 39,6,* 857-879. [5] Tuchscherer et al. (2004) *MAPS 39,* 955-978. [6] Ames, D.E. et al. (2004) *MAPS 39,* 1145-1168. [7] Zürcher L., and Kring D. A. (2004) *MAPS 39,* 1199-1222. [8] Hecht L., et al. (2004) *MAPS 39,* 1169-1186. [9] Dressler B.O. et al. (2004) *MAPS 39,* 857-878. [10] Newsom et al. (2006) *MAPS 41,* 1929-1945. [11] Staudigal H. and Hart S. (1982) *GCA, 47.* 337-350. [12] Stroncik N.A. and Schmincke H.-U. (2000) *Eos, Transactions*, AGU, *81*, Suppl., pp. 1263. [13] Tuchscherer et al. (2004) *MAPS 41,* 1361-1379. [14] Zürcher L., et al. (2005) *Geological Society of America Spec. Paper 384,* 223-238. [15] Graup, G. (1999) *MAPS 34,* 425-438. [16] Osinski, G.R., et al. (2004) *MAPS 39,* 1655-1683. [17] Osinski, G.R., et al. (2001) *EPSL 194,* 17-29. [18] Osinski, G.R., et al. (2005) *MAPS 40,* 1789-1812. [19] Otto, J.W., and Wyllie, J.P. (1993) *Min. and Pet. 48,* 343-365. [20] Jones, A.P. et al. (2000) *Impacts and the Early Earth* (eds. I. Gilmour and C. Koeberl). pp. 343-361.

Acknowledgements: Yaxcopoil-1 core samples obtained from Chicxulub Scientific Drilling Project team. Research funding provided by NASA Planetary Geology and Geophysics program NNG 05GJ42G (H. Newsom) and NASA Mars Fundamental Research Program. NNG04GE87G (H. Newsom).

THE CONTROL OF TARGET STRUCTURE ON THE CRATER MORPHOLOGY ON THE MOON, MARS, AND VENUS – EVIDENCE AND IMPLICATIONS.

T. Öhman[1,2], M. Aittola[2], V.-P. Kostama[2], J. Korteniemi[2], and J. Raitala[2]. [1]Division of Geology, Department of Geosciences, P.O. Box 3000, FI-90014 University of Oulu, Finland (teemu.ohman@oulu.fi), [2]Division of Astronomy, Department of Physical Sciences, P.O. Box 3000, FI-90014 University of Oulu, Finland.

Introduction: The target topography and especially layering within the target are widely known to cause deviations from the generalized crater-formation mechanisms [1 and references therein]. As a result, the crater morphology changes accordingly. Another, fairly unrecognized source of crater shape variation is the presence of faults, fractures or other similar planes of weakness in the target [e.g. 2, 3]. The resulting polygonal impact crater (PIC) shape can be used as an additional tool in deciphering the tectonic history of a cratered surface [e.g. 4].

Some observations of PICs, both from earlier studies and our on-going research [e.g. 5–7], are not fully explained with the current ideas. Thus, new tentative hypotheses regarding the formation of PICs, as well as the effects of impact basin -induced modification on the surrounding crust are proposed.

A third PIC-formation mechanism? Eppler et al. [3] summarized the two mechanisms known to give rise to a polygonal impact crater. These are the Meteor Crater -type enhanced excavation parallel to target fractures (Model 1, simple craters; straight rim segments at an angle with the fractures), and slumping along the fracture planes (Model 2, complex craters; straight segments parallel to fractures) [3].

When simple and complex PIC rim orientations in the same area (and thus in the same geotectonic environment) are studied, the orientation distributions should differ if simple PICs would form by Model 1 and complex PICs by Model 2. However, at least in the Argyre region, Mars, this is not the case [7]. We were not able to see a statistically significant difference between the simple and complex PIC rim orientations. Thus, perhaps these models are not enough to fully explain the formation of PICs?

Model 2 appears to have a stronger observational and theoretical foundation [7], and Model 1 has only been fully described in one location (Meteor Crater). This leads to the idea that perhaps Model 1 may not be the dominating way to make simple PICs.

Crater rims are formed by the structural uplift of the target material, the injection of breccia dikes, and the ejecta [e.g. 1]. Detailed structural studies of simple and small complex crater rims indicate that thrusts are the dominant structural features there. This provides the rationale for our new hypothesis. We suggest that simple polygonal craters and small, not significantly slumped complex polygonal craters can be formed by thrusting along some pre-existing planes of weakness (Model 3). Such mechanism may be in action with larger complex craters too, but the more substantial collapse of larger craters probably is more dominating factor in the polygonal plan view of large craters.

A "preferred" PIC-formation size? We studied the lunar crater shapes in the near-side of the Moon, mainly in the highlands west and southwest of the Nectaris basin (10°W–40°E, 10°N–50°S). The dataset used was the oblique-illumination photographs of the digital version of the Consolidated Lunar Atlas [9]. We identified 160 named (+7 unnamed) PICs >10 km in diameter. When their size distribution (diameter data taken from the USGS-approved list by McDowell [10]) is compared to that of the 656 non-polygonal named craters in the study area, a clear discrepancy is observed. PICs are relatively fewer in the smallest size range (10–20 km), but from 20 km to 50 km in diameter much more common than could be anticipated from the size distribution of the non-polygonal craters.

Pohn and Offield [8] studied lunar crater morphology as a function of crater diameter. They classified craters in the size range of 16–48 km (which they rounded to 20–45 km) as "polygonal", implying that in the size range of 16–48 km polygonal craters are at least fairly common. Thus, our results match perfectly with the classification by Pohn and Offield [8].

Similar discrepancies in the size distributions of polygonal and non-polygonal craters can be seen on Mars [7] and Venus [6] too. When the crater sizes are normalized by dividing the diameter with the average simple-to-complex transition diameter (D_{tr}, highly variable especially on Mars) on each of the planetary bodies studied, an interesting regularity appears (Fig. 1). It seems that PIC formation is most common in the size range of about 1–5 times the transition diameter, although there is some variation between the different planets. Thus, it appears that the formation of PICs is somehow "preferred" in small to mid-sized complex craters.

Basin-induced conjugate shear fracturing? Impact basins are surrounded by radial and concentric fracture systems. Theoretically post-impact modification of the basins should induce conjugate shear fractures (strike-slip faulting) too [e.g. 11]. These, however, have not been observed, and in the case of the lunar basins it seems that the stress field is not strong enough for actual shear fracturing to take place in significant extent [11]. However, our observations of the PIC rim orientations around Martian basins [7] suggest that perhaps conjugate shear fractures are present there. These inferred possible conjugate sets of fractures surrounding the Argyre and Hellas basins are not readily explained by other tectonism affecting the area and the PICs in it, and their geometry fits the theoretical basin-induced shear fractures. However, more detailed tectonic studies in the vicinity of the Martian (as well as e.g. Mercurian, in the light of the forthcoming Messenger data) impact basins are encouraged to test the validity of this hypothesis. Such studies should involve PICs as well, because it seems apparent that they reflect an old tectonic pattern that may not be manifested by other tectonic features like graben or ridges [7 and references therein].

Discussion and conclusions: Our continuing efforts to describe and understand the formation, occurrence, characteristics, and significance of polygonal impact craters in the Solar System has led to several tentative hypotheses. These can and should be tested. The suggested thrusting mechanism (Model 3, together with Models 1 and 2), for PIC formation could be best tested with impact or explosion experiments in target with controlled or at least carefully measured fractures. The previous studies [e.g. 12, see 7 for other references] have not described the relations between the straight rim segments and the target fractures.

The "preferred" PIC-formation size (small to mid-sized complex craters) hypothesis would be slightly harder to test. Roughly similar size distributions on three planetary bodies require an explanation, even if further studies on other cratered surfaces would yield differing results. The knowledge of the depth and spacing of fractures on different planets would give interesting reference data. 3D-modeling would obviously be desirable for further understanding of all aspects of PIC formation.

To test the highly hypothetical idea of PICs indicative of basin-induced conjugate shear fracturing would require detailed observations of tectonic features surrounding impact basins. New high-resolution datasets of Mars, as well as the forthcoming Messenger imagery of Mercury provide good opportunities for this.

Acknowledgments: Many thanks to Mr. M. Kallo for his substantial input to the lunar PIC research. The Magnus Ehrnrooth Foundation, the Faculty of Science of the University of Oulu, and the North Ostrobothnia Regional Fund of the Finnish Cultural Foundation are thanked for funding the last parts of the research, and Oskar Öflunds Stiftelse for making participation in the LMI IV -conference possible.

References: [1] Melosh H. (1989) *Impact cratering: A geologic process.* Oxford University Press, 245 p. [2] Shoemaker E. (1962) In: Kopal Z. (ed.) *Physics and astronomy of the Moon,* Academic Press, 283–359. [3] Eppler D. et al. (1983) *GSA Bull., 94,* 274–291. [4] Scott D. et al. (1977) *Proc. Lunar Sci. Conf. 9th*, 1119–1130. [5] Öhman T. et. al. (2006) *MAPS, 41,* 1163–1173. [6] Aittola M. et al. (2007) *EMP, 101,* 41–53. [7] Öhman T. et. al. (2008) *MAPS, 43* (accepted). [8] Pohn H. & Offield T. (1970) *USGS Prof. Paper 700-C,* C153–C162. [9] Kuiper G. et al. (1967) *Consolidated Lunar Atlas,* Lunar and Planetary Laboratory, University of Arizona. [10] http://host.planet4589.org/astro/lunar/Craters. [11] Freed A. et al. (2001) *JGR, 106,* 20603–20620. [12] Gault D. et al. (1968) In: French B. & Short N. (eds.) *Shock metamorphism of natural materials,* Mono Book Corp., 87–99.

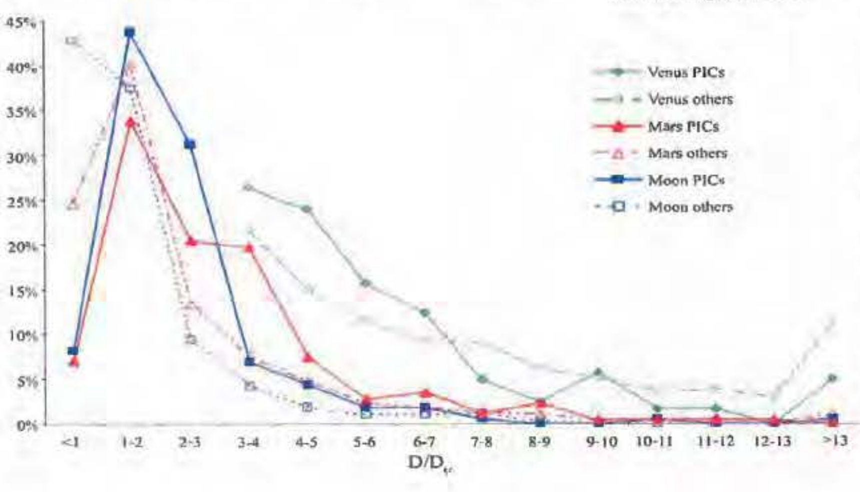

Fig. 1. Size distribution of PICs and non-polygonal ("others") craters on Venus (>12 km) [6], Argyre region of Mars (>5 km) [7], and the Moon (10°W–40°E, 10°N–50°S, >10 km named craters). D_{tr}'s were 4 km, 7 km and 15 km for Venus, Mars and the Moon, respectively. The rapid drop of the number of the smallest Martian PICs and non-polygonal craters is merely an effect of the size selection.

DHALA - A NEW, COMPLEX, PALEOPROTEROZOIC IMPACT STRUCTURE IN CENTRAL INDIA.

J.K. Pati[1], W.U. Reimold[2], C. Koeberl[3], H.K. Singh[1] and P. Pati[1] [1]Department of Earth and Planetary Sciences, Nehru Science Centre, University of Allahabad, Allahabad-211 002, India, E-mail: jkpati@yahoo.co.in, [2]Museum for Natural History (Mineralogy), Humboldt-University in Berlin, Invalidenstrasse 43, 10115 Berlin, Germany; E-mail: uwe.reimold@museum.hu-berlin.de, [3]Department of Geological Sciences, University of Vienna, Althanstasse 14, A-1090, Vienna, Austria; E-mail: Christian.koeberl@univie.ac.at

Introduction: The Dhala structure (N25°17'59.7" and E78°8'3.1") is situated in Shivpuri district, Madhya Pradesh State, India [1,2]. Currently, the diameter of the structure is estimated at 11 km based on field observations. The basement rocks are predominantly composed of granitoids, and in the centralmost part of the structure voluminous melt breccia containing target rock clasts with shock metamorphic features are directly overlain by a post-impact siltstone-shale-sandstone sequence of the Vindhyan Supergroup. Recent geochronological dates suggest that the age of the impact event lies in the range between 1.6 and 2.5 Ga [2,3].

Geology of the Dhala area: The Dhala structure can be easily identified in satellite images with a mesa-shaped central elevated area (CEA; ~2.5 km in diameter), off-center to the mapped outline of the structure, and a weakly defined annular drainage pattern observed on a Survey of India topographic map (54K/3; 1:50,000). The remote sensing study based on Landsat-TM and Indian Remote Sensing (IRS-1D) satellite data ssuggests that the diameter the structure could be as large as 25 km (Fig.1). There are three distinct litho-tectonic domains from north to south. The bedrock lithology mainly includes calc-silicate rocks, granitoids (including rocks of Tonalite-Trondhjemite-Granodiorite affinity), very large quartz veins (GQV) [4], and dolerites, besides a cover sequence comprising shale-siltstone of varying composition and arkosic lenses followed by a shale-sandstone (locally pebbly) unit. There are more than 114 whale-back-like and low-lying monomict granitoid breccia outcrops occurring in the form of a ring of varying clast size. There is a voluminous melt breccia occurring over a length of ~6 km in a semi-circular fashion between E and NE of CEA above and within the monomict granitoid breccia, respectively. The melt breccia lithology has not been observed to the south of the CEA so far.

The cover sediments show distinct sub-horizontal lamination-bedding with syn-sedimentary deformation structures in places. Tectonically, the area shows a strong pervasive and penetrative sub-vertical E-W trending shear (sinistral) fabric in granitoids, which is dissected by GQV (NNE-SSW to NE-SW) and mafic dyke (mostly NW-SE) trends. The shear fabric is observed to swerve with a semi-circular trend to the south of the CEA. The calc-silicate rock is folded on E-W to NW-SE disposed bedding. All rock types show extensive brittle structures (joints and faults) at meso- and macroscopic scales. The faults show both dextral and sinistral displacements and are most conspicuous in GQVs to the SE of the CEA. At least five major inferred faults dissect the CEA. The joints overall show a radial trend, although they are slightly accentuated along E-W, NNE-SSW and NW-SE directions (pre-impact fabric elements).

Evidence of impact: Study of 401 normal and polished thin sections of various rock types has shown the presence of shock metamorphic features in clasts within the melt breccia lithology only. These features include multiple sets of PDFs in quartz and feldspar, ballen texture, checkerboard feldspar, and shock deformed zircons based on Raman spectroscopic study. The geochemical analysis of the melt breccia samples has so far only shown Ir concentrations up to 0.8 ppb that is very close to the detection limit of the INAA instrument [2].

Mineralization: The Geological Survey of India (Central Region) has drilled three boreholes after encountering Cu and Au in parts of Dhala. The Atomic Minerals Division, Government of India has so far drilled 11 boreholes in search of uranium in the Dhala area. The twelve analyzed samples from the Dhala area [2] show Au content between 0.3 and 2.6 ppb. The U content ranges from 1.19 to 7.58 ppb.

Age of the impact: The predominantly granitoid country rocks of 2.5 Ga age are intruded by 2.0-2.15 Ga mafic intrusives. They are overlain by sediments belonging to Vindhyan Supergroup of 1.6 Ga age. Our recent SHRIMP U-Pb single-zircon data [3] further corroborates a 1.6-2.5 Ga age range for the Dhala area.

Conclusion: The present study summarizes the field, petrological, limited geochemical, and geochonological data on the Dhala structure carried out to date. The presence of unequivocal shock metamorphic evidence confirms its impact origin, and at 11 km, it is the largest known impact structure in Southeast Asia. The extensive drilling by government agencies also suggests possible economic mineralization associated with the Dhala structure.

Acknowledgement: JKP thanks the PLANEX Programme, Department of Space, Government of India for funding the study.

References: [1] Pati, J.K. (2005), *MAPS 40* (S): A121. [2] Pati, J.K. et al. (2008) *MAPS* (In Press). [3] Jourdan, F. et al. (2008) *LPSC XXXIX*, Abstract #1244. [4] Pati, J.K. et al. (2007), *Jour. Earth System Sci. 116*, 497-510.

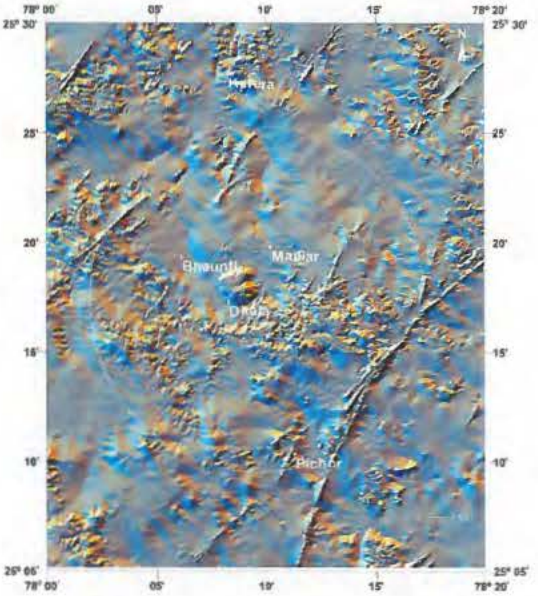

Figure 1. Digital Elevation Model of Dhala impact structure, India based on Survey of India topographic contour data (54K/3, 4, 7 and 8). The estimated diameter (~25 km) based on remote sensing data is shown in dotted line.Linear ridges are quartz veins (GQV).

REMOTE SENSING AND GIS ANALYSES FOR DETERMINING SIZE, MORPHOLOGY AND LITHOLOGICAL MAPPING OF THE VREDEFORT IMPACT STRUCTURE, SOUTH AFRICA

Phillips M.E.[1,2], Townsend C.[1], Bartels K.[1]. [1]Centre for GIS & Remote Sensing, School of Science, University of Greenwich, Chatham Maritime, U.K. [2]Planetary Science Research Group, Environmental Science Department, University of Lancaster, Lancaster, U.K. (email: m.phillips@gre.ac.uk)

Introduction:
The overall geometry and size of the Vredefort Impact Structure are still unresolved. Some workers have used modelling based on cratering processes or geophysics to show that the original diameter could have been at least 250-300km or more [1]. Also, previous studies of the Vredefort Structure have indicated that a number of circular or semi-circular features, at varying radial distances, could be rings related to the original Vredefort event [1-5].

Methods and Results: Landsat TM and ASTER data were used for three interrelated project analyses of the structure over the period 1999-2005, and four fieldwork visits between 1998-2007. Landsat TM uses 6 bands of 30m spatial resolution in the visible and infrared wavelengths, with 1 band of 120m in the thermal infrared [6,7]. ASTER has superior spatial and spectral resolution with 3 visible bands at 15m, 6 infrared bands at 30m and 5 thermal infrared bands at 90m spatial resolutions [8]. These were the first detailed studies of the Vredefort Structure by Remote Sensing methods. Landsat TM was particularly useful for recognising features for the first time, such as radial faults to the north of the Ring Collar (Fig. 1), arcuate drainage patterns and a likely ring feature at a radial distance of 125km, suggesting an overall size =>250km [6,7].

Figure 1. Radial faults in the Foch Thrust Zone (FTZ)

Figure 1 shows the Foch Thrust Zone region north of the Vredefort Ring Collar, with a known thrust fault in yellow, normal faults in white, and a dyke in red. Newly recognised radial faults from these studies [6,7] are shown in black; the large magenta structure in the lower central region is the Losberg Complex. Many of these findings supported work by geophysical methods [1]. Spectral profiling with ASTER data was applied to selected regions where either vegetation cover was low, or where other image processing methods highlighted differences in lithologies, or for impact structure morphologies. An area was investigated at Witkop, matching the spectral library profile of gneiss (Fig. 2) [8].

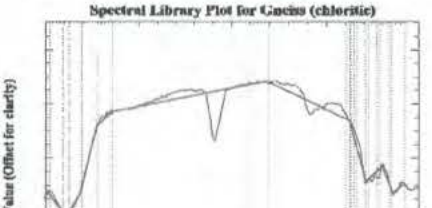

Figure 2. Spectral Profile of gneiss found at Witkop.

In this comparison of observed spectra with library spectra, characteristic absorption features were detected at 0.65µm (band 2, visible green), 2.20µm (band 7, mid-infrared) and 2.35µm (band 9, mid-infrared) [8]. ASTER data was then used successfully for spectral unmixing of specific geological regions and for delineating lithologies [8]. Additionally, Principal Components Analysis (PCA) was used to study Koedoesfontein, a region of quartzites/conglomerates. Two different geological units were observed. The upper half of the sequence belongs to the Turffontein, the lower exposures were discriminated as Johannesburg subgroups of the Central Rand Group, important for gold deposits in the region. Figure 3(a) shows a PCA RGB 123 image of this area. At Dwarsberg, a Dolerite ridge was mapped with PCA, where the ridge was highlighted in strips of magenta and dark blue with a n.east-s.west trend, as displayed in Figure 3(b) [8].

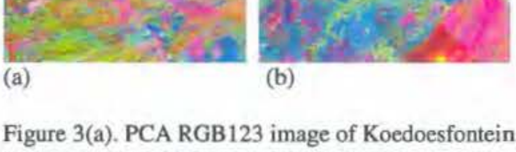

(a) (b)

Figure 3(a). PCA RGB123 image of Koedoesfontein.
(b). PCA RGB123 image of the Dwarsberg area.

GIS and Digital Elevation Model (DEM) mapping was applied to the Vredefort Impact Structure for the first time [9], resulting in more detailed mapping and recognition of other previously unseen and unreported structures. The DEM revealed a previously unreported raised, circular to lobate-like structure in the central Vredefort core, with height ~30m above the local terrain, and diameter ~25km [9]. Estimation of fault and scarp morphologies were visualised in 3D, one example of which is shown in Figure 5.

Figure 5. Perspective view of the FTZ, looking NE [9].

Fig.5 is a perspective view of the Foch Thrust Zone (FTZ), looking along strike towards the NE, with a Landsat TM RGB 641 [6] draped over a 30m DEM, made from digitised contours of 12 x 1:50,000 topographic maps [9]. Vertical exaggeration is x2, area ~10km. A prominent outward-facing scarp morphology is seen, with gentle back slopes and steep faces. This matches the morphology of ring scarps in a multi-ring basin [10]. The DEM was also used to extrapolate radial faults [9] which intersected at the centre of the structure, confirming the radial orientation [8]; and was also applied to an 'inverted cone' model for reconstructing the crater's original size, by extrapolation of the structure at the FTZ and at the Ensels Thrust Zone. This suggests that Vredefort is a multi-ringed structure with at least two rings at diameters 146km and 186km [9]. The model was applied to the third outer ring structure giving a final original structural extent of 281km diameter, in good agreement with other results [3,12]. Figures 6 and 7 show a profile and cross-section covering ~45km out from the Inner Ring Collar.

Conclusion: 3D morphological modelling, combined with recognition of arcuate structures, add to the determination of size, structure and multiple rings at Vredefort. Many of these findings [7,9,11] are in agreement with workers using other multi-disciplinary methods [1-3]. Multi-ring Basins on Earth are difficult to confirm, however, [10,13] and further multi-disciplinary studies integrated with other digital data within a GIS still need to be done.

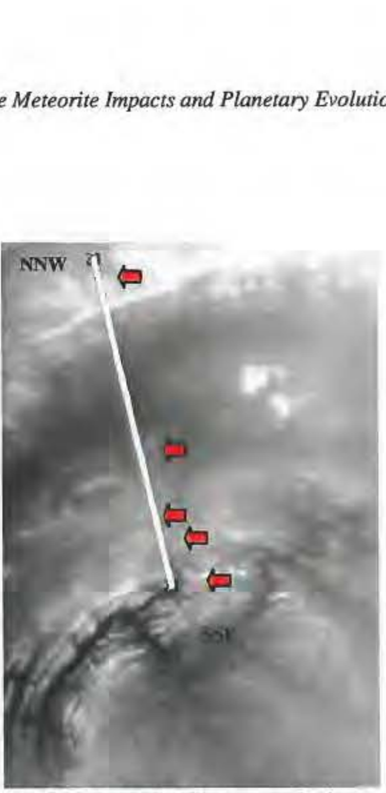

Figure 6. NNW-SSE Profile across the inner rings.

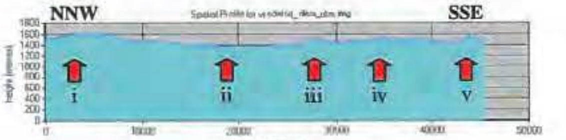

Figure 7. Cross-section of the NNW-SSE Profile highlighting the following features and ring structures:

i. Foch Thrust Fault Zone
ii. Potchefstroom Synclinorium
iii. Ensels Thrust Fault Zone
iv. Outer Limit of Circle 1 Zone
v. Inner Ring Collar (arcuate ring fault)

References: [1] Henkel, H. & Reimold, W.U. 1998. Tectonophysics, 287, 1-20. [2] Andreoli, M.A.G. 1991. Structural Map, Atomic Energy Corporation, Pretoria. [3] Brink, M.C. *et al.* 1997. Tectonophysics, 270, 83-114. [4] Pilkington, M. & Grieve, R.A.F. 1992. Review of Geophysics, 30, 2, 161-181. [5] Rondot, J. 1994. Earth Science Reviews, 35, 331-365. [6] Phillips, M.E. 1999. Unpublished BSc thesis. [7] Phillips, M.E. *et al.* 1999. Abstracts of the 62nd Meteoritical Society Meeting. [8] Bartels, K. 2005. Unpublished BSc Thesis, University of Greenwich, UK. [9] Townsend, C. 2001. Unpublished BSc Thesis, University of Greenwich, UK. [10] Melosh, H.J. 1996. Impact Cratering, A Geologic Process. Oxford Uni. Press. [11] Phillips, M.E. 2001. Norwegian Geographical Membership, GIS Meeting, Bergen, Norway. [12] Grieve, R.A.F. *et al.* 1995. GSA Today, Vol 5 No 10, p 194-197. [13] Thierriault, A. M., *et al.*1997. Meteoritics & Planetary Science, vol. 32, 71-77.

SHORT-TERM EFFECTS OF IMPACT-RELATED HEATING OF THE UPPER ATMOSPHERE.

E. Pierazzo[1] and F. Sassi[2], [1] Planetary Science Inst., 1700 E. Ft. Lowell Rd., Suite 106, Tucson, AZ 85719, USA (betty@psi.edu); [2]National Center for Atmospheric Research, P.O. Box 3000, Boulder, 80307 CO, USA (sassi@ucar.edu).

Introduction. We use WACCM to investigate the effects of a strong, short heating of the upper atmosphere associated with a large impact event, like the one that occurred at the end-Cretaceous (65 Ma). After a large impact, material is ejected ballistically above the atmosphere. As it re-enters the atmosphere at high speed it heats frictionally the upper portion of the atmosphere before reaching terminal velocity. It has been proposed that the resulting infrared radiation from the heated portion of the atmosphere could have been strong enough to ignite surface biomass [1]. Evidence of soot at several K/T boundary sites (see [2], and references therein) suggests that much of the end-Cretaceous biomass was consumed by fire.

Heating from Ejecta Re-entry. Melosh et al [1] estimated the amount of heating released in the upper atmosphere by the re-entry of material ejected from a Chicxulub-size impact. Observations indicate that the Chicxulub distal ejecta layer has a fairly constant thickness around 2-4 mm [3]. Assuming a layer 4 mm thick with an average density of 2500 kg/m^3, Melosh et al. [1] estimated that the layer corresponds to about 10 kg/m^2 of material. To account for a worldwide distribution of ejecta, they assumed that all material was ejected with velocities between 5 and 10 km/s. More recent investigations indicates that even slower ejecta (<5 km/s) could be widely distributed by its interaction with a hot atmosphere [4,5], and material ejected relatively late is probably moving at velocities well below 5 km/s [6]. The total kinetic energy of ejecta moving between 2 and 10 km/s is between 1.5×10^7 and 5×10^8 J/m^2. This energy is released in the upper atmosphere upon ejecta re-entry, and occurs relatively quickly, within a few of hours after impact [1,4,5]. Assuming a 2-hour frame for the re-entry of all impact ejecta, the power released in the upper atmosphere by the Chicxulub impact event is between 2 and 70 kW/m^2. As pointed in [1] and [5] the distribution of ejecta is not globally uniform, and this estimate represents only an average value. Locations at different distances from the impact site will see either much larger or lower energy deposition.

Atmospheric Model. The Whole Atmosphere Community Climate Model (*WACCM*) [7] is a comprehensive numerical model developed to explain the relations and feedbacks between dynamics, chemistry and radiation of the middle and upper atmosphere. The numerical model is based on the National Center for Atmospheric Research (NCAR) Community Atmospheric Model (CAM). The equations of dynamcs and transport are solved by using the explicit flux-form semi-Lagrangian scheme of [8] on a horizontal grid of 2°x2.5° (latitude by longitude). This numerical method calculates explicitely the mass fluxes in and out of a given model volume, thus ensuring mass conservation. Atmospheric dynamics and physics, and the interactive chemistry and physical parameterizations of the upper atmosphere are solved at each time step in a vertical domain that extends from the ground to about 150 km (66 levels). Its standard vertical resolution is variable, from 3.5 km above ~65 km, to 1.1 km in the lower stratosphere (<30 km) and troposphere (with much higher resolution in the planetary boundary layer). The chemistry module of WACCM is based on the 3D chemical transport Model of Ozone And Related Tracers (MOZART) [9,10,11] and includes detailed processes that describe reactions and photolytic processes in the middle and upper atmospheres. MOZART solves for 51 neutral species, including all members of the O_x, NO_x, HO_x, ClO_x, and BrO_x chemical families, along with tropospheric "source species" such as N_2O, H_2O, CH_s, chlorofluorocarbom (CFCs), etc. [12].

We have implemented in WACCM a simple module that reproduces a uniform, strong, short heating in the upper atmosphere. To take into account the initially strong pulse of re-entering material (as suggested by [1]), we use a decreasing exponential function over 2 hours (the time step of the simulation is set to 3 min). The heating is distributed vertically using a Gaussian centered at 75 km and extending from 50 to 100 km. This simplified approach does not yet include important components like variation in heating with distance from impact site, or the presence of a layer of dust in the upper atmosphere that could increase atmospheric opacity and prevent the atmosphere from of radiating part of the heat into space. Nonetheless, the results provide an indication of the magnitude of the perturbation associated with such a large and sudden energy input in the upper atmosphere.

Results. We carried out several short simulations, at most over 16 days, with heatings of 40, 50 and 70 kW/m^2. All simulations start from Jan. 1 initial conditions. Our first goal is to investigate the change in the atmosphere's thermal structure (energy balance) which, in turn, affects the atmosphere's chemical composition and photolysis rates. Figure 1 shows the change (from unperturbed conditions) in long wave (LW) heating at the surface over time for a 50 kW/m^2 heating. Positive values represent LW emission from the surface. The heating in the upper atmosphere produces a strong LW radiation to the surface (negative values means surface is heated from above). The effect appears stronger in the southern hemisphere (especially at high latitudes) where it is summer time. Overall, however, the effect does not extend beyond the first 12-15 hours after injection. The effect on atmospheric chemistry, however, appears to extend well beyond the period of heating. Figure 2 shows the change in zonally averaged ozone column, (total amount of ozone in the atmospheric column overhead) over time for a 50 kW/m^2 heating. It appears that changes of few percents occur over the duration of the simulation, but it is not clear if they will persist beyond that. Reduction of ozone in the upper atmosphere would result in an increase of damaging UV radiation reaching the lower atmosphere. Analogously, we observe a similarly delayed, significant (100%) increase of toxic NO$_s$ in the lower troposphere.

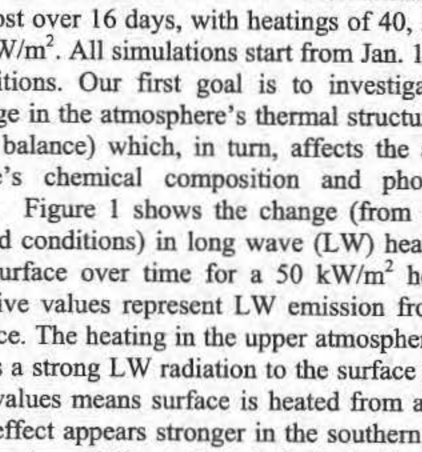

Fig. 1: Zonally averaged surface LW heating (in W/m^2) over the first 5 days after a 50 kW/m^2 heating.

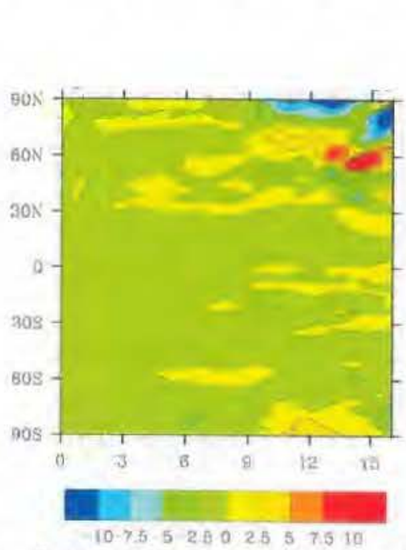

Fig. 2: Zonal average of ozone content in the atmosphere (in Dobson units) over time (days).

Changes in chemistry composition and photolysis rates affect the atmosphere's dynamical structure, with repercussions on the mean meridional circulation, including ozone distribution and production. This effect has never been investigated before and could be extremely important for understanding immediate climatic effects of a large impact.

References: [1] Melosh H..J. et al. (1990) *Nature, 343*, 251-254; [2] Wolbach W.S. et al. (2003) *Astrobiol., 3*, 91-97; [3] Smit J. et al. (1992) *Proc. LPSC, 22*, 87-100; [4] Goldin T.J. Melosh H.J. (2008) *LPSC, 39*, Abs #2469. [5] Artemieva N., Morgan J. (2008) *LPSC, 39*, Abs #1581. [6] Artemieva N. (2008) *LPSC 39*, Abs #1651 [7] Garcia R.R. et al. (2007) *JGR, 112*, D09301, doi:10.1029/2006JD007485; [8] Lin S.-J. (2004) *Mon. Weath. Rev., 132*, 2293-2307; [9] Brasseur G. et al. (1998) JGR, 103, 28265-28283; [10] Hauglustaine D.A. et al (1998) *JGR, 103*, 28291-28335; [11] Horowitz L.W. et al. (2003) *JGR., 108*, 4784, doi: 10.1029/2002JD002853; [12] Kinnison D.E. et al. (2007) *JGR., 112*, D20302, doi:10.1029/2006JD007879.

THE IMPACT HYDROCODE BENCHMARK AND VALIDATION PROJECT. E. Pierazzo[1], N. Artemieva[1,2], E. Asphaug[3], E.C. Baldwin[4], J. Cazamias[5], R. Coker[6], G.S. Collins[7], D.A. Crawford[8], T. Davison[7], D. Elbeshausen[9], K.A. Holsapple[10], K.R. Housen[11], D.G. Korycansky[3], K. Wünnemann[9]. [1]Planetary Science Inst., 1700 E. Ft. Lowell Rd., Suite 106, Tucson, AZ 85719, USA (betty@psi.edu); [2]Inst. Dyn. Geospheres, RAS, Leninsky Pr. 38, 119334 Moscow, Russia; [3]Univ. of Calif. Santa Cruz, S. Cruz, CA 95064, USA; [4]University College London, Gower St., London WC1E 6BT, UK; [5]Univ. of Alabama at Birmingham, Birmingham, AL 35294, USA; [6]Los Alamos Nat. Labs., Los Alamos, NM 87545, USA; [7]Imperial Coll. London, London SW7 2AZ, UK; [8]Sandia Nat. Labs., P.O. Box 5800, Albuquerque, NM 87185, USA; [9]Natural History Museum, Humboldt-Univ., Berlin 10099, Germany; [10]Univ. of Washington, Seattle, WA 98195, USA; [11]The Boeing Company, Seattle, WA 98124, USA.

Introduction: Computer models offer a powerful tool for understanding the mechanics of impact crater formation, but only if properly benchmarked and validated against observations. We present results from the first phase of a project to benchmark and validate shock physics codes used to simulate impact and explosion cratering [1].

The Validation and Benchmarking Project: We have identified a two-part base of standards for comparing and validating hydrocodes. The benchmark component identifies a set of hypothetical explosive and impact events of varying complexity to be run by the impact codes to compare the different numerical and physical models employed in the codes. Simulations are divided into early time, focusing on the early stages of the dynamic explosion process (shock pressure and its decay) and late time, focusing on the crater final morphology (crater collapse and stress/strain fields). The validation component identifies a set of well-documented laboratory and field experiments over a wide range of event sizes, geological materials and problem types to reproduce in code simulations. Laboratory tests are useful because they are conducted under well-known conditions. Field explosion tests provide data over a much larger range of sizes.

The final objective of this study is to provide the test results to the scientific community to help prevent the incorrect and misinformed use of the codes and to provide a set of rules and test cases to follow to properly benchmark and validate hydrocodes to come.

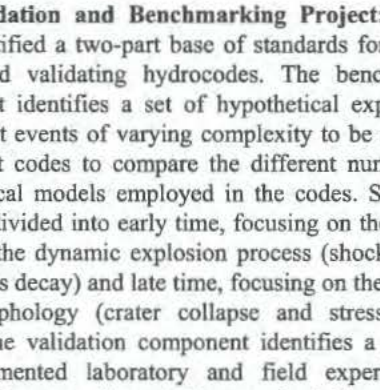

Fig. 1: Shock pressure decay downward from the impact point for a 1-km diameter Al sphere impacting an Al target at 20 km/s.

Impact Hydrocodes: All hydrocodes include the fundamental physics needed to model high-energy impact/explosion events, and can all be used to model general impact/explosion cratering. A variety of 2D and 3D codes were used in this study, from commercial products like AUTODYN [2], to codes developed within the scientific community like SOVA [3], SPH [4], ZEUS-MP [5], iSALE/iSALE3D [6,7], and codes developed at National Laboratories like ALE3D [8], CTH [9], SAGE/RAGE [10]. Each code has been extensively tested individually, but no collective benchmarking/validation has ever been carried out.

Benchmarks: Our first benchmark tests consist of an Al sphere 1km in diameter impacting an Al target at 5 and 20 km/s perpendicularly and at 45° from the surface. Aluminum is a simple material with a well-known and well-modeled equation of state. Different equations of state models are used in the test runs, such as Tillotson, ANEOS tables, SESAME and LEOS tables. To test potential effects of mesh resolution, each code was run at given resolutions, ranging from 5 to 40 cells-per-projectile-radius (cppr) or adaptive mesh refinement (AMR). For the test in question this corresponds to a cell size of 100m down to 12.5m or smaller for AMR.

Figure 1 shows shock pressure decay in the target (early-time stage) for a 20 km/s vertical impact. Overall, shock pressure variability from code to code is within 10 to 15% for the 20 km/s impact simulations. The simulations with lower impact velocities show slightly larger variability. We found that significant variability occurs due to code setup. It is thus important for users to understand the effects of internal code setup such as temporal and spatial stability parameters (Courant number or artificial viscosity).

The Validation Testing: The first validation tests chosen for this project include relatively simple materials like water and aluminum.

Water test: Simulations of impacts and explosions in water do not need a strength model and gravity only needs to be included to model the late stages of crater growth. We modeled the Boeing quarter space laboratory experiment of a glass sphere, 2 mm in diameter, impacting water at 4.64 km/s [11]. This experiment used a rectangular box made from 1.25 cm thick Al, 76cm×38cm×23cm in size (a thick plexiglass window was inserted close to the impact point for viewing purposes). Ambient chamber pressure was around 3400 Pa (above the vapor pressure). Diagnostics measured during the experiment were crater profile at given times (up to 83 msec), and ejection velocities of a few small glass beads floating on the surface.

Aluminum test: We modeled the laboratory experiments of an Al sphere, 6.35 mm in diameter, impacting at 7 km/s Al alloy cylinders (few tens of millimeters in thickness and diameter) of varying strength [12]. For this test we chose two alloys, 1100-O, which has a strain rate dependent strength, and 6061-T6, whose strength is insensitive to strain rate. The diagnostics of the experiment were crater radius and depth over time.

Validation Results: In the simulations projectile size, impact velocity/angle, shape and material (glass or Al), and target material (water or Al) are fixed input conditions. Technical details, material models and relative parameters for the materials were chosen by individual modelers. This is an important difference from benchmark tests that focus on comparing code performances given well-constrained simple tests. One important component of validation testing consists in testing the modelers identification and use of the proper material models. One of our goals in this context is to verify how modelers' choices can affect the output results.

Water Test: In the early stages of the water impact all the codes appear to follow the experimental data quite closely (Fig. 2). The early evolution (<3.5 ms) of crater radius and depth with time shows variability in the model results compared to the experiments of less than 15%. The full coverage of the validation test is available for three codes: ALE3D, CTH, and ZEUS-MP2, with iSALE covering about half of the experiment duration. Only one time step is available for AUTODYN (not enough for an assessment of its performance). Generally, the codes tend to underestimate the experimental crater diameter and depth. Simulations with ALE-3D, CTH, iSALE, RAGE and SOVA appear to follow the experimental data quite closely. Simulations with ZEUSMP2 (heavily modified to model impact cratering) seem to develop instabilities beyond 2 msec (Fig. 2). Possible reasons for the instabilities are problems with boundary conditions, problems at free surfaces and material interfaces.

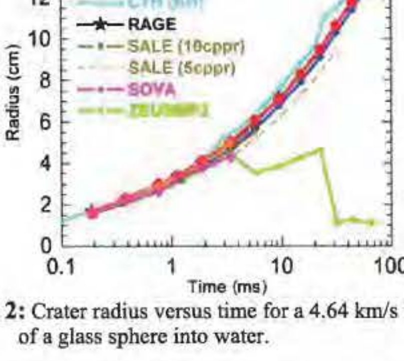

Fig. 2: Crater radius versus time for a 4.64 km/s impact of a glass sphere into water.

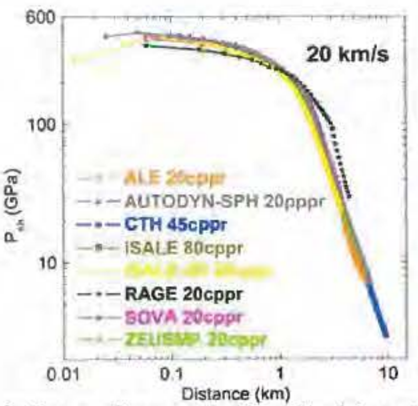

Fig. 3: Crater radius over time for a 7 km/s impact of an Al sphere into Al 6061-T6.

Aluminum Test: Four code results are available for Al 6061-T6 and Al 1100-O targets. Simulation were carried out with different resolutions (from AMR to 10 cppr) and varying strength model (Johnson-Cook in CTH, Von Mises in iSALE, Steinburg-Guinan in AUTODYN and RAGE). Overall, the code results are in relatively good agreement with the experimental data. For the impacts into Al 6061-T6 targets the numerical codes tend to slightly underestimate the crater radius (Fig. 3) and overestimate the crater depth. For impacts into an Al 1100-O target code results are closer to experimental values.

This work is supported by NASA Grant NNX06AD65G.

References: [1] Pierazzo E. et al. (2008) *MAPS, Submitted.* [2] Century Dyn., Inc. (2003) *AUTODYN Theory Manual 4.3.* [3] Shuvalov V.V. (1999) *Shock Waves, 9,* 381. [4] Benz W., Asphaug E. (1994) *Icarus, 107,* 98. [5] Hayes et al. (2006) Astroph. J. Supp., 165, 188. [6] Wünnemann K. et al. (2006) *Icarus, 180,* 514. [7] Elbeshausen D. et al. (2007) LPSC, 38, Abst. #1952. [8] Sharp R. (2004) *UCRL-MA-152204 Rev.1.* [9] McGlaun J.M. et al. (1990) *Int. J. Impact Eng., 10,* 351. [10] Gittings M.L. (1992) *Def. Nucl. Agency Num. Meth. Symp., 28-30 April 1992.* [11] Schmidt R.M., Housen K.R. (1987) *Int. J. Imp. Eng., 5,* 543. [12] Prater R. (1970) Tech Rep. AD0718461.

STRUCTURAL ASPECTS OF METEOR CRATER AND THEIR EFFECT ON CRATERING.

M. H. Poelchau[1], T. Kenkmann[1], D. A. Kring[2], [1]Museum für Naturkunde, Invalidenstr. 43, 10115 Berlin, Germany, [2]Center for Advanced Space Studies, LPI, Houston, Texas. (michael.poelchau@museum.hu-berlin.de)

Introduction: Meteor Crater, located in Arizona, USA, shows obvious morphological deviations from a circular crater shape. Its square shape has been interpreted to be a consequence of a regional joint system that runs diagonally to the square [1,2; Fig. 1a].

Meteor Crater was structurally examined to investigate the effects of target anisotropies and obliquity on the cratering process. Here we present structural data and first qualitative models are shown to explain the phenomena observed in the field. In particular, detailed measurements of bedding strike and dip were collected around the entire crater rim together with GPS data.

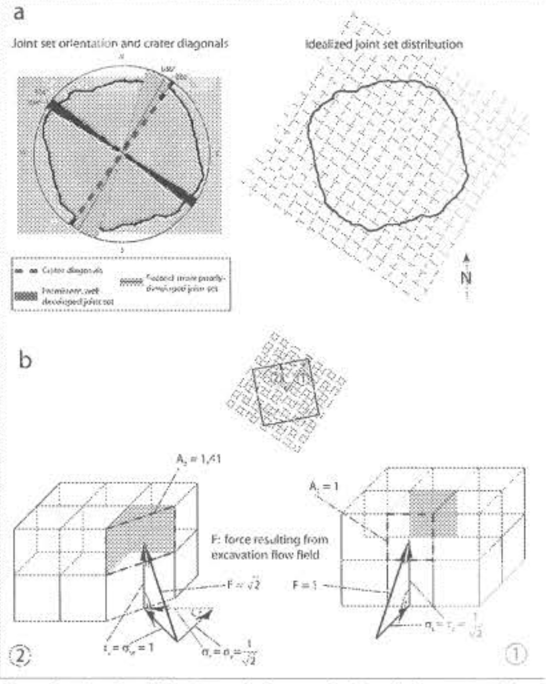

Fig. 1: A simplified model correlating joint sets (data from [2]) and bedding planes with crater formation.

Joints: Field data from [2] shows a striking correlation between crater diagonals and the orientation of joint sets. These joints have a spacing ranging between 0.5-10 m and have subdivided the target into small, square-shaped units (Fig. 1a).

Tear faults: Joint sets form structurally weak zones along which tear faults have propagated during crater formation. The major tear faults are oriented subparallel to these joints. Tear faults are localized expressions of differential movement between blocks that occurred during rim uplift. The main component of movement is vertical, along with a rotational component or "scissors type of displacement" [1] that tips the blocks outwards. The highest uplift of strata (e.g. ~45 m displacement in the SE) occurs along these faults. This has led to an asymmetric structure of the crater rim in which the entire S and N sides of the rim appear as lower, down-faulted blocks relative to the corners, as shown in the bedding data.

Bedding data: For the display in a stereo plot (Fig. 2) the bedding dataset was split into crater corners and sides. The data shows four clusters of poles reflecting the four sides of the crater wall. The N and S sides have more concentrated poles, compared to the more scattered E and W sides. This indicates rotation in the E and W sides. The S side dips more gently on average than the E and W sides, while the N side has the steepest dip. The SE and SW corners show strong scattering and rotation. The data is more complex than a simple, square-shaped deviation. The factors that we believe control this complex, non-radial behavior are discussed below.

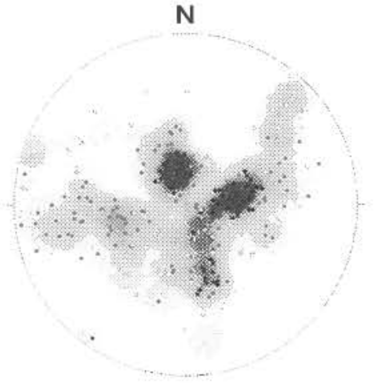

Fig. 2: Stereo plot of 298 bedding points. White: corners; black: sides of crater wall.

Uplift: The elevation of both the lower Coconino-Kaibab (CK) contact and the Kaibab-Moenkopi (KM) contact were measured for a better control of differential uplift in the crater wall. Based on geological and topographical maps, average height of the CK contact is ~1645 m within and 1590 m outside the crater. Maximum elevation of the CK contact is higher in the corners of the crater (>1670 m) than along the sides (~1640 m), resulting in an uplift from pre-impact CK elevation of ~50 m on the sides to a maximum of 80 m in the corners (the contact is not exposed in the NW corner). This differential uplift between corners and sides is a result of major tear faults located in all four corners of the crater.

GPS data of the KM contact situated in the upper crater rim principally correspond to the CK contact and reveal a correlation between the distance of beds from the crater center and their elevation. Although the correlation is rough, there is a definite trend for the KM contact to be in a higher position the further away it is from the crater center, that is the more they are located in the corners of the quadrangular crater. Undulations in the height of the KM contact are caused by injections of coherent fault blocks into the upper crater wall, which we denote as "thrust wedges".

Thrust wedges: In addition to the two directions of weakness caused by joint sets and used by tear faults, a third zone of weakness can be found in the horizontal layering of rock beds. Thrust wedges use this zone of weakness and can be found in several areas of the crater wall [1]. These wedges have an effect on uplift. Where they occur, the top Kaibab and Moenkopi units are arched up and form anticlinal features (Fig. 3b).

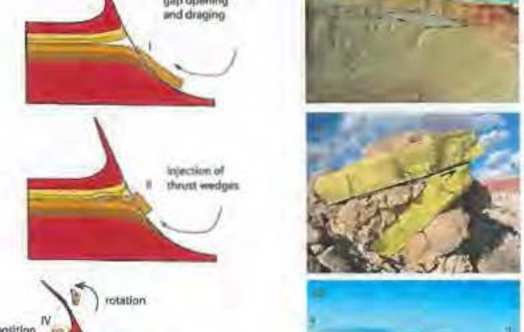

Fig. 3: Field observations and a model for the formation of "thrust wedges".

Model 1: Based on field observations (Fig. 3b-d) we propose a model for the formation of thrust wedges. We assume that during crater excavation, outward and upward directed excavation flow opens small gaps along horizontal areas of weakness in upper stratigraphic units (Fig. 3a-I), which are used by the tips of incipient thrust wedges (II). Further thrusting of these wedges into the gaps creates additional uplift, raising overlying units to a higher elevation than neighboring beds. In the ejecta, meter sized units of Kaibab were found with obliquely terminating bedding planes (Fig. 3c,d). We interpret these as thrust ramps from the initial phase of thrust wedge formation, which were then excavated (III) and deposited as ejecta (IV).

Model 2: In an attempt to understand the mechanical aspects behind the formation of the square shape of Meteor Crater, we suggest a simplified, qualitative model that compares surface stress to the excavation force exerted on rock units (Fig. 1). In this model we divide the target rock into discrete cubes, based on the two joint sets plus horizontal layering planes. During cratering, the excavation flow field that ejects rock is directed outward and upward in the upper part of the crater. For simplification, we assume the flow field is oriented radially from the crater center and upwards at 45° (Fig. 1b). We can observe two situations in this model, one where the flow field is directed parallel to one of the joint sets (Fig. 1b-1), and one which is directed at a 45° angle to both joint sets (Fig 1b-2). The flow field exerts a force on the cube, which is proportional to the exposed surface of the cube, thus resulting in a force that is $\sqrt{2}$ times stronger in 2. This force can be split into horizontal and vertical components that correspond to normal stress (σ_x, σ_y) and shear stress (τ_z), respectively. Vector addition (Fig. 1b) shows that the ratio of normal stress to shear stress in situation 1 is $\sigma_y : \tau_z = 1$. In situation 2 the ratio is $(\sigma_x + \sigma_y) : \tau_z = \sqrt{2}$, due to the larger surface area exposed to the flow field and the circumstance that shear stress is exerted on two surfaces of the cube (marked in gray in Fig 1b), as opposed to one surface in situation 1. As less shear stress is resolved in situation 1 excavation should progress faster and further, and the initial circular crater shape should start getting corners, resulting in the final square shape seen in Meteor Crater. It should be noted that target anisotropies such as joints become important mainly in the final stages of crater excavation, when the stresses induced by the excavation flow are in the order of the strength of the target material.

Conclusions: This model provides a basic understanding of how joint sets and weaknesses in bedding planes affect the late stages of the cratering process. Questions remain on how the more detailed, complex structures in the crater rim were formed. Certain aspects, like the somewhat counterintuitive correlation between radial distance and uplift in Meteor Crater still need to be contemplated.

Acknowledgements: We would like to thank the DFG for funding this project (KE 732-11/1).

References: [1] Shoemaker E. M. (1960) *Structure of the Earth's Crust and Deformation of Rocks. Rept. 18*, 418-434. [2] Roddy D. J. (1978) *Proc. Lunar Planet. Sci. Conf.* 9^{th}, 3891-3930.

RIES CRATER, GERMANY: THE ENKINGEN MAGNETIC ANOMALY AND ASSOCIATED DRILL CORE SUBO 18.

Jean Pohl[1], Klaus Poschlod[2], Uwe Reimold[3], Claudia Crasselt[3], [1]Department of Earth and Environmental Sciences, University of Munich, Theresienstrasse 41, 80333 Munich, Germany, pohl@geophysik.uni-muenchen.de [2]Geological Service, Bavarian Environment Agency, Heßstrasse 128, 80797 Munich, Germany, [3]Museum for Natural History (Mineralogy), Humboldt-Universität, Invalidenstrasse 43, 10115 Berlin, Germany.

Introduction - The suevite in the Ries impact crater is characterized by an often strong, reverse remanent magnetization [e.g. 1, 2]. This results in negative magnetic anomalies showing the distribution of the suevite in the crater. Fig. 1 shows the ground magnetic anomalies of the total intensity. The main mass of the suevite (so-called crater suevite) is located within the inner crystalline ring of the crater and covered by post-impact lake sediments. The inner line corresponds to the 150 m isopach of the lake sediments after Ernstson (1974). The extension of the crater is indicated by the outer line showing the structural rim.

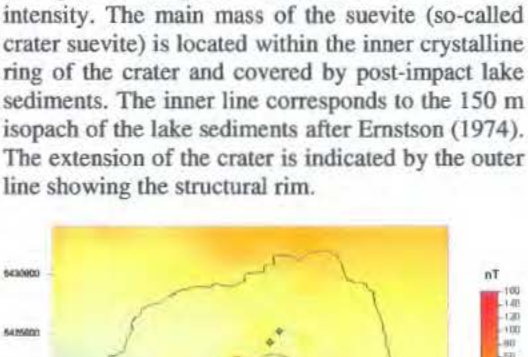

Fig. 1 Total magnetic intensity map for the Ries crater. Width of the area shown is 33 km. N is up.

Ejected suevite is found between the inner ring and the structural rim, and outside of the structural rim, with a thickness of ca. 10 to 20 m. A local magnetic anomaly (Wö) indicates the location of an 80 m thick suevite occurrence below 20 m of lake sediments drilled in 1965 (drill core Wörnitzostheim).

The Enkingen magnetic anomaly - Another local anomaly is located near the village Enkingen situated on the inner ring. A preliminary ground survey of this anomaly was done in 1970 [4]. A more detailed survey was carried out in 2006/2007. Fig. 2 shows the Enkingen total intensity anomaly. Village houses and other human constructions limited the survey to a certain extent. Also a thick gas pipeline produced a series of strong anomalies trending roughly N-S. In spite of these limitations the anomaly is well defined. The maximum amplitude is comparable to that of the Wörnitzostheim magnetic anomaly.

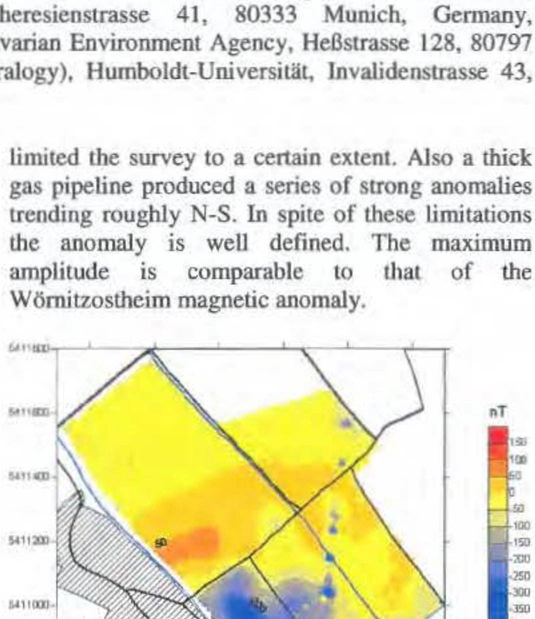

Fig. 2 Detailed map of the Enkingen magnetic anomaly and location of the SUBO 18 Enkingen borehole (star symbol). N is up.

The Enkingen drill core SUBO 18 - A drilling program of the Geological Service of Bavaria offered the opportunity to drill a 100 m deep cored hole in the area of the anomaly from November 29 to December 8 2006 with a core diameter of 10 cm. Core recovery was mostly close to 100 %, but limited parts of the cores disintegrated on recovery. The location of the drill hole is shown in Fig. 2.

The core stratigraphy involves: 0 to 4.5 m - fluviatile Quaternary deposits, clay and gravel; 4.5 to 21 m - Paleogene clays of the Ries crater lake; from 21 to 100 m suevite and impact melt rocks. The drill hole unfortunately did not penetrate into the expected crystalline basement rocks of the inner ring, but modelling of the magnetic source body indicates that the bottom of the hole was not far from the basement rocks. Granitic basement was detected in a shallow bore hole south of Enkingen at a depth of 38 m [5]. The Enkingen suevite and melt body is located on the inner flank of the inner ring.

The suevite and impact melt rock section is highly diverse in terms of suevite types (by groundmass composition, particle size, induration, alteration state, carbonate presence or absence, clast population, clast grain size variations, and maximum clast contents). For example, melt fragment content varies from <10 to >60 %. Transition from suevite to massive impact melt rock is gradational. The bottommost 13 meters of massive impact melt rock are also very heterogeneous, both with regard to texture and clast content. Whereas crystalline rock derived clasts are the dominant clast species throughout the impact breccias, the lowermost part contains significant amounts of sedimentary clasts as well (estimated at 1-3 %, maximum). Detailed petrographic analysis of the core and first chemical studies are in progress.

Magnetic properties of the suevite core - Magnetic susceptibility along the core was measured with a portable kappameter (KT-5, Geofyzika Brno). For petrological investigations and remanence measurements, all coherent core sections were cut along their axis and inch cores were drilled for magnetic measurements where possible. Results of these measurements are shown in Fig. 3. The suevite has high, strongly varying negative magnetic remanence and magnetic susceptibility and very high Koenigsberger ratios (remanent magnetization versus induced magnetization). The amplitudes of the magnetic anomaly can easily be explained by the magnetization of the suevite. A remarkable fact is that the impact melt rocks at the lower end of the drill core have relatively low remanent magnetizations and higher magnetic susceptibilities.

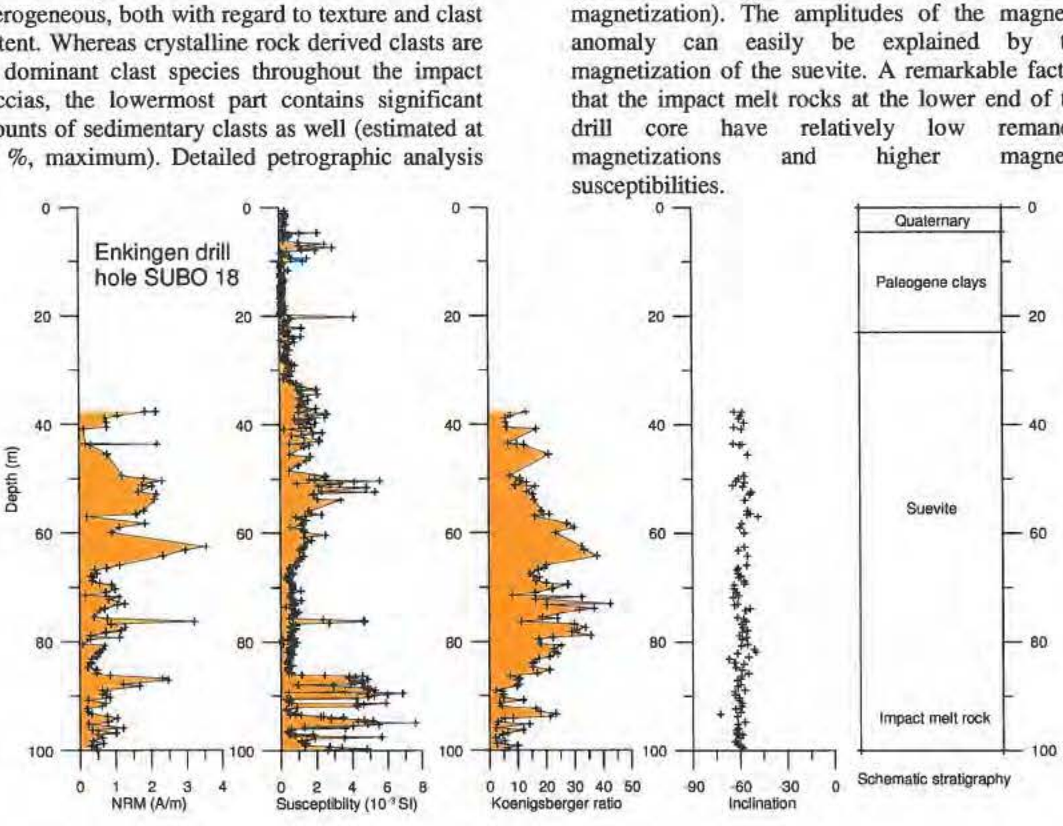

Fig. 3 Preliminary magnetic properties of the Enkingen SUBO 18 drill core. The Koenigsberger ratio is the ratio of the natural remanent magnetization (NRM) to the locally induced magnetization.

We will present a detailed discussion of the magnetic record and petrographic characteristics of the SUBO 18 core at the Large Meteorite Impacts conference.

References: [1] Pohl, J. 1965, Neues Jahrbuch für Mineralogie, Monatshefte 1965, 268-276. [2] Pohl et al. 1977 in: Impact and Explosion Cratering (Roddy et al., Eds.), 343-404. [3] Ernstson, K. 1974, J. of Geophysics 40, 639-659. [4] Engelhard L. 1971, Z. für Geophysik 37, 667-678. [5] Deffner, C. and Fraas, O. 1877, Begleitworte zur geognostischen Specialkarte von Württemberg, Bopfingen und Ellenberg, 36 p.

GEOPHYSICS AND DEEP COREHOLES REVEAL ANATOMY AND COMPLEX INFILLING OF THE CENTRAL CRATER, CHESAPEAKE BAY IMPACT STRUCTURE, U.S.A.

D.S. Powars[1], R.D. Catchings[2], G.S. Gohn[1], J.W. Horton, Jr.[1], L.E. Edwards[1], D.L. Daniels[1], [1]U.S. Geological Survey, MS 926A, Reston, VA 20192, USA, dspowars@usgs.gov, [2] U.S. Geological Survey, 345 Middlefield Rd., MS 977, Menlo Park, CA 94857.

Introduction: The Chesapeake Bay impact structure (CBIS) is the largest known impact crater in the United States. It formed at 35.5 Ma when a ~3-km-diameter asteroid or comet crashed into the Atlantic Ocean ~160 km offshore from Virginia's late Eocene paleo-coastline (located west of the present Fall Line) [1]. The multi-layered wet-target consisted of an eastward dipping crystalline basement overlain by a wedge of eastward thickening (450- to 1220-m) unconsolidated sediments and an eastward deepening (90- to >300-m) ocean. The eastern part of the target had significantly deeper basement rocks, deeper and thicker sediment cover, and deeper water than the western part. This asymmetry significantly affected the complex infilling of the central crater.

The elevation of the suevite in the moat of the central crater appears to be at about the same depth as the top of the crystalline basement at its deepest part. The basement elevation would affect the possibility of spillover. Similarly, the elevations of the top of the impact-related sediment-clast breccias and the top of preimpact sediment layers on the eastern side are approximately the same and may be causally related.

The upper crater fill is interpreted as deposits formed by multi-directional, multiple resurge-wave reverberations (termed here oscillation resurge waves) and represent thoroughly remixed impact debris.

Recent USGS Focus On the Central Crater:
Since 2004, the USGS has focused on mapping the structure, stratigraphy, and water quality of the central crater. A partially cored, 823-m-deep test hole was drilled at the town of Cape Charles over the central uplift, and the continuously cored ICDP-USGS 1.76-km-deep Eyreville corehole (EC) was drilled into the moat. A variety of geophysical data were gathered in the 85 to 90-km-diameter CBIS. A 30-km long, low-fold seismic reflection and refraction survey, and a parallel detailed gravity survey were acquired along a radial transect from the crater's center to nearly half-way across the annular trough. Several 1- to 2-km long high-resolution seismic profiles (5-m source and geophone spacing) were also acquired at various points along the transect, including two 1.4-km-long profiles that crisscross over the deep EC [2,3]. These images provide semi-3D, detailed views of the stratigraphy and structure of the upper 1.0 km of the central part of the moat [4,5].

Overview of the Central Crater:
On the basis of our seismic, gravity, and corehole data, we interpret a 35- to 38-km-diameter, asymmetrical central crater with a 10-km-wide (short axis, SW-NE), flat-topped, crystalline central uplift. This central uplift corresponds to a gravity high (up to -22.5 mGal) and is overlain by (in ascending order): ~350 m of polymict, suevitic crystalline-clast breccia, ~300-m of sediment-clast breccia, and ~355-m of post-impact sediments (largely based on Cape Charles test hole) [6,7]. Seismic, gravity, and corehole data show that the ~13-km-wide elliptical moat surrounds the central uplift and contains ~215 m of basement-derive schist and granite pegmatite with impact breccia dikes and veins; ~150 m of suevite and lithic impact breccias; ~925 m of low-velocity and low-density, mixed sediment breccia and crystalline-rock megablocks, including a 275 m granitic megablock(s); ~650 m of sediment clast/block breccia; and ~444 m of postimpact sediments [8]. The low-fold seismic reflection images suggest the moat may extend to as deep as 3.5 km. A complex multi-layered sequence of high- and low-velocity materials in the lowest ~km of the moat likely consists of crystalline-rock breccias, as well as possible sedimentary breccias (some stratified), and/or metamorphic or cataclastic remnants of the transient cavity wall, or possibly a melt sheet [9]. The central uplift is highly fractured and has collapsed onto the top of the lowest (2.25-km-depth) low-velocity layer of the moat, suggesting that the central uplift was elevated prior to the time all or most of the collapse debris from the transient cavity wall reached the inner moat. Relatively steep gravity (19.5 mGal to 25.0 mGal), resistivity, and seismic-velocity gradients, and inward-dipping reflections, mark the collapsed central crater's margin and raised rim. The moat is ~13-km-wide, irregularly shaped, and locally includes several gravity highs that suggest local pockets of melt and basement-derived megablocks, uplifted fault blocks, or irregularities in the inner basin's margin due to differences in target rock properties.

The upper 652 m of sediment clast/block breccia penetrated by the EC have been subdivided into four lithostratigraphic units, here interpreted in descending order as: (1) a matrix-supported, sediment- and crystalline-clast oscillation-resurge breccia with boulders (83 m); (2) a 50:50 matrix:clast, sediment-and crystalline-clast oscillation-resurge breccia with boulders and blocks (91 m); (3) a boulder- and block-supported, sediment-clast resurge breccia 249 m); and (4) a block-supported, sediment avalanche deposit (229 m) [10,11].

High-Resolution Seismic and Eyreville Core Correlation: Preliminary data processing and analysis indicate excellent correlation of the seismic images with the EC, including individual block and impact-debris patterns in the upper 300 to 400 m of the impactites that reveal a multidirectional emplacement. Reflection patterns are consistent with variations in conditions and processes within the central crater during impact and suggest deposition by resurge and oscillation-resurge wave interactions for these upper impactites.

Postimpact sediments. Strong, mostly continuous, subhorizontal reflections typical of marine strata represent the postimpact sediment units (upper Eocene to upper Miocene) identified in the EC from 444 to 60 m depth. Continuous reflections, including reflections that dip into a paleochannel, characterize the top 60 m of the core and correlate with Pliocene to late Pleistocene shallow-marine to marginal marine sands and basal gravels. On the 30-km-long, low-fold seismic profile, the postimpact strata dip toward, and thicken above, the center of the moat with relatively minor disruption. Reflection patterns reveal both differential compaction and faulting.

Synimpact breccias. In contrast to the postimpact reflectors, the upper ~80 to 90 m of synimpact deposits are represented by subhorizontal, overlapping-to-shingled reflections that dip and pinch out in various directions. These reflections correlate with EC where there are multiple fining-upward sequences in matrix-supported breccia. The upper sequence grades into to stratified sand and laminated clay-silt. This section is dominated by a muddy glauconite-quartz sand matrix containing mixed-age microfossils, Cretaceous sediment clasts, and locally abundant ejected crystalline clasts (some shocked, some melt fragments, most <1m) [12]. These shingled fining-upward sequences are interpreted as oscillation resurge waves.

Seismic signatures vary laterally in the underlying ~100 to 125 m-thick section of the moat, and the reflections are highly disrupted. This interval has discontinuous, chaotic reflections that bound relatively continuous lenses. These lenses truncate, overlap, and pinch out in multiple directions and correlate with the 618 to 527 m depth in the EC, where matrix-supported breccias have about a 50:50 mixture of matrix and boulder and blocks. The majority these clasts are oxidized clay-silt clasts. Crystalline clasts are locally common. A few fining-upward sequences are also present. This section is here interpreted as oscillation-resurge deposits that bulldozed and deposited large piles of blocky debris. This unit is underlain by ~250 m of relatively continuous reflections that pinch out in various directions and by chaotic, discontinuous reflections, some of which show imbrication. This interval correlates with clast-supported, sediment-clast breccias assigned to the lower resurge section in the EC (867 to 618 m depth), and it is dominated by Lower Cretaceous clasts of sand and oxidized clay-silts (1-30 m intersected diameter). The mixed-age resurge matrix is absent from a 142 m interval above the basal 13 m, but is sporadically present as layers and/or injections in the immediately overlying 106.5 m interval. Many of the clasts have relict bedding that is highly contorted at various scales. Clast margins are highly deformed; and within-clast shearing and brecciation are evident. Some preimpact stratigraphy appears to be preserved. This interval is interpreted as a chaotic combination of ocean-resurge deposits and reworking of the underlying Lower Cretaceous sediment debris-avalanche deposits (1,096 to 867 m depth). The seismic data show an overall decrease in the size of the blocks from the top of the suevite upward and that there is considerable lateral variability throughout the impactite section.

High-Resolution and Low-Fold Seismic Correlation: Correlation of the high-resolution seismic images with the 30-km-long low-fold seismic profile [8] shows that four strong reflections correlate with the upper 652 m of impactites. These reflections represent, in descending order: (1) the lower 65 m of the shingled, matrix-supported, sediment- and crystalline-clast oscillation-resurge unit; (2) the upper 60 m of the more chaotic boulder- and block-supported, sediment-clast resurge unit; (3) 55 m of liquefied sand in the lower half of this boulder- and block-supported, sediment-clast resurge unit; (4) and the lower 100 m of the clast-supported, sediment-clast breccia unit interpreted as sediment avalanche from collapse of the upper part of the transient crater-wall. Across the inner part of the moat the upper three strong reflectors dip away from the central uplift into the central part of the moat, suggesting either an anti-resurge or postdepositional compaction of these units away from the central uplift. The lowest reflector dips from the opposite direction inward from the central-crater rim to the central part of the moat and is consistent with a transient crater-wall avalanche interpretation.

Collectively, the seismic images suggest that the upper impactites in the central crater are highly variable laterally, with lithologically similar units at different depths deposited from multiple directions at multiple times.

References: [1] Horton J.W. Jr. et al. (2005) in Horton et al., *USGS Professional Paper 1688*, A1-A24. [2] Catchings, R.D. et al. (2007) *GSA Abstracts 39(6)*, 450. [3] Powars, D.S. et al. (2007) *GSA Abstracts 39(6)*, 533. [4] Powars, D.S. et al. (2007) *EOS 88(52)*, Fall Meet. Suppl., Abstract U21E-07. [5] Catchings R. D. et al., (2007) *EOS, 88(52)*, Fall Meet. Suppl., Abstract U21E-06. [6] Sanford et al. (2004) *EOS 85(39), 369.* [7] Gohn, G.S. et al. *USGS OFR* 2007-1094. [8] Gohn G.S. et al. *EOS 87(35), 349.* [9] Catchings et al., JGR, (in press). [10] Gohn, G.S. et al. (2007) *GSA Abstracts, 39(6), 532.* [11] Powars, D.S. et al. (2007) *GSA Abstracts, 39(6), 314.* [12] Morrow J.R. (2007) *GSA Abstracts 39(6), 451.*

Tectosilicate oikocrysts in impact melt-hosted mafic xenoliths, contact sublayer of the Sudbury Igneous Complex, Canada.

Stephen A. Prevec, Barbara K. Kuhn and Steffen H. Büttner, Dept. of Geology, Rhodes University, P.O. Box 94, Grahamstown, South Africa. s.prevec@ru.ac.za, b.kuhn@ru.ac.za and s.buettner@ru.ac.za.

Introduction: Contact metamorphic temperatures associated with the margins of the Sudbury Igneous Complex (SIC) have previously been identified at around ≥ 600°C based on orthopyroxene-bearing granitoids consistent with pyroxene hornfels facies conditions [1]. Footwall temperatures in excess of 900°C have been implied on the premise that pre-existing shock minerals (specifically diaplectic plagioclase) have been obliterated by thermal recrystallisation adjacent to the SIC margins [1]. More recently, thermal modelling has been used to propose marginal temperatures locally higher still, in excess of the basalt liquidus [2]. In this study, an "ultramafic" xenolith from the Whistle sublayer embayment has been found to display oikocrystic alkali feldspar, not previously described from within the impact melt sheet. The only textural precedent is oikocrystic quartz described from granitoid gneissic footwall in Trill Township [1].

Geological Setting: The contact sublayer to the SIC is the basal component of what is thought to be an impact melt sheet, where it interacts with footwall rocks (predominantly basalts and granitoid gneisses). The contact sublayer is fundamentally a breccia itself, hosting a variety of footwall-derived and autobrecciated fragments, frequently along with mineralised sulphides. Samples of ultramafic and mafic xenoliths were extracted from the Whistle mine open pit in the northeasterm corner of the SIC. Sample SPS-96-02 is a sulphide-bearing hornblende-plagioclase biotite rock (a biotite amphibolite), and is interpreted as a meta-melanorite. Sm-Nd mineral isochron isotopic evidence [3] supports the interpretation of juvenile origin, and therefore of an autobrecciated xenolith. It is also characterised by the occurrence of a high proportion of oikocrystic tectosilicates (e.g., Fig. 1), hosting stubby, often euhedral laths of plagioclase feldspar, and also (less typically) orthopyroxenes, amphiboles and biotite.

Oikocryst Characterisation: Two distinct types of oikocrystic tectosilicate are present in this sample. Perhaps slightly more abundant are those dominated by typically coarse-grained quartz of isometric or irregular shape, exhibiting straight or coarsely serrated grain boundaries. These crystals may host relatively coarse-grained inclusions of sericitised plagioclase, biotite and amphibole, and may be intergrown with adjacent grains of plagioclase or occasionally microcline. Inclusions and intergrowth boundaries are characterised by linear (often euhedral) boundaries, reminiscent of a graphic texture. The more classically-symplectic granophyric texture, rare in this rock, is characteristic of SIC melt rocks in general, and these coarse quartz grains are therefore classified as igneous oikocrysts.

More distinctively, the rock contains coarse-grained anhedral (presumably) spherical poikiloblasts of untwinned tectosilicate ophitically hosting subhedral plagioclase laths. These oikocrysts are optically biaxial negative with a moderate 2V, and are revealed by electron probe microanalyses (EMPA) to have a composition of an alkali feldspar with minimal An content and Or contents ranging from Or_{60} to Or_{69}, averaging Or_{63}, compositionally consistent with sanidine. More sodic outliers (at Or_{49} and Or_{18}) are attributed to the presence of albite-rich feldspar as or in a very thin reaction zone at the contact between oikocryst and plagioclase chadocryst. This very localised sodic enrichment is also evident in backscattered electron imaging, but was not consistently detectable by EMPA.

Figure 1. Oikocrystic alkali feldspar (about 5 mm across), encompassing pre-existing feldspar and pyroxene grains.

Plagioclase feldspars displaying typical lamellar twinning were analysed both from clusters of decussate-textured subhedral plagioclase which is not obviously associated with oikocrysts, and from laths included within the sanidine oikocrysts. The plagioclase composition ranges between An_{39} and An_{55}, averaging An_{43} (andesine). This is rather more sodic than is typical of plagioclase in unaltered sublayer norite xenoliths from the same location [4], and is consistent with secondary amphibolitisation of the xenolith.

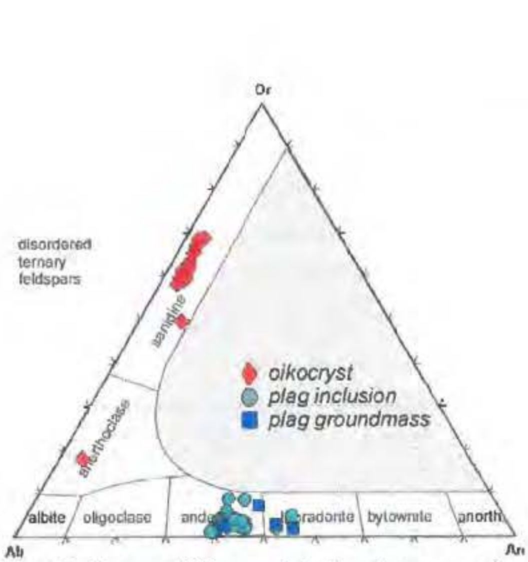

Figure 2. Ternary feldspar plot, showing compositions of oikocrysts in contrast to those of plagioclase chadocrysts and groundmass laths.

Implications: Alkali feldspar compositions of *ca.* Or_{60} require hypersolvus temperatures, in excess of about 650°C (the top of the solvus, which is relatively pressure-insensitive). Application of a two-feldspar geothermometer [5] based on average Ab-An-Or compositions of the coexisting plagioclase and alkali feldspar in the sample indicate an equilibrium temperature of about 900°C. The occurrence of hypersolvus alkali feldspar as anhedral oikocrysts is consistent with secondary metamorphic growth at the highest grades of contact metamorphism (*vis.* sanidinite facies); the textures of the sanidine and coarse-grained quartz, along with other complementary evidence of resorption of phases such as plagioclase and biotite, support a "secondary magmatic" (i.e., new melting) origin for the oikocrystic tectosilicates. This paragenesis is strongly favoured by circumstances involving superheated impact melt and an active magmatic system, while not necessarily precluding a more conventional magmatic derivation.

Acknowledgements

Peter Lightfoot and Reid Keays are acknowledged for engaging the senior author's interest in Sudbury.

References:

[1] Dressler, B.O. (1984) in *The Geology and Ore Deposits of the Sudbury Structure*, Ont. Geol. Surv. Spec. Pub. 1, 97–136.

[2] Prevec, S.A. & Cawthorn, R.G. (2002) JGR 107, 2176, 10.1029/2001JB000525.

[3] Prevec, S.A., Lightfoot, P.C. & Keays, R.R. (2000) Lithos 51, 271-292.

[4] Prevec, S.A. (2000) Min. Pet. 68, 141-157.

[5] Wen, S. & Nekvasil, H. (1994) Comp. Geosci. 20, 1025-1040.

STRUCTURE AND MORPHOLOGY OF THE MULTIRING LUNAR BASINS.

S. G. Pugacheva, V.V. Shevchenko, V. I. Chikmachev, Sternberg State Astronomical Institute, Moscow University, Russia, Universitetsky avenue, 13, pugach@sai.msu.ru.

Introduction: The morphological features of the multiring lunar basins are considered. The common characteristics of the multiring basins and South Pole –Aitken basin were researched. The nature and origin of a unique formation, which is still conditionally called the South Pole--Aitken basin, remain one of the most important problems in recent studies of the Moon. The basin, which apparently belongs to the pre-Imbrian Period, is the largest ring formation not only on the lunar surface, but also in the entire Solar System. Not only the basin dimensions on an absolute scale but also the fact that the basin diameter almost coincides with the lunar diameter are of interest. A similar relationship is not observed on other silicate or icy bodies in the Solar System.

Morphology of the multiring lunar basins. The morphology of the multiring structures discover the some general laws. The study of the morphological features of the ring structures showed that the ring structures more than 300 km in diameter have outer and inner rings. The relation of diameter of the outer and inner concentric rings in structures close to 2 of independent from a site and age of structure. The correlation of the excavation depth (H) on the depression diameter (D) from the data in Wieczorek and Phillips [1] may be written in the general form

$$H=0.078*D+11.833,$$

for the ring structures 200-500 km in diameter. The surface of the inner ring structure is a little differ from a typical lunar highlands. The bottom of many circular structures is filled in full or in part the substance of the dark lava. Multiring formations are typical structures of the shock origin for the surface of the planets of the terrestrial type and satellites. Table shows some multiring structures with diameter of the outer rings more than 300.

Multiring structure of the South Pole-Aitken Basin. A comparison of the considered characteristics on the absolute scale of magnitudes quite definitively indicates that the South Pole-Aitken basin structure is unique. A uniquely small depth-diameter ratio for the SPA basin is confirmed by comparing it to similar characteristics of the largest ring formations on the Moon. Wieczorek and Phillips indicated that the depth-diameter ratio for the SPA basin is an order of magnitude as small as the value determined by extrapolating a similar dependence for ring structures large than 200 km.

To analyse propreties of the concentric system we have compiled a variety altitude data sets to construct general hypsographic map of the lunar far side included the ring basin structure: Clementine laser altimetry results [2], Zond catalog of the absolute heights [3], catalog of the lunar limb heights [4].

Based on the analysis of the hypsometric data were constructed ellipses corresponding to the boundary height (Fig.1). Using the Monte-Carlo method were determined the height boundaries and were distinguished four height ring. It was established that the height zones have the shape of ellipses. Circular scattering was observed for a small area (H less than –5 km). The major semiaxis of the elliptic ring is given in the table.

Outmost ring size of the basin. General size of the SPA basin is defined by outermost ring of the structure that has been extensively modified by post-SPA impact events. According to [5] multiple craters are superposed on the SPA basin. This process brings forward extensive destruction of the initial form of the outmost basin ring. So, we generalized structure of the SPA basin we conclude that can observe a relic relief in this area now. It's reason of the large range of estimations of initial SPA basin size.

We tried to trace relic features of the possible initial outermost basin rim. Fig. 2 shows 3-D model of relief corresponding outmost basin ring. This model shares out relief, which has height more than 0 km. As usually, this level is in agreement with lunar sphere of radius equal 1738.0 km. However, the model shown in Fig. 2 is "flat", i.e. it is constructed on the plain without considering spherical effect.

On the basis of our ring reconstruction we concluded that original size of the SPA basin (outermost ring diameter) is approximately 3300 km. Then we find the basin outermost ring center at roughly 180° and 40°S.

Name of the multiring Lunar Basin	Coordinates of the center outer ring ($\lambda^{\circ}/\varphi^{\circ}$)	Diameter of the rings, km (outer / inner rings)
Poincare	+163.6/-56.7	140/319
Schrodinger	+133.7/-75.6	140/324
Korolev	-157.4/-4.4	215/453
Mare Nectaris	+35.0/-15.0	413/729
Mare Orientale	-95.0/-20.0	300/480/642/961
Mare Imbrium	-15.0/+35.0	610/1104
South Pole-Aitken Basin (SPA)	180.0/-40.0	210/640/970/3500
	(the major semiaxis of the elliptic ring)	

Inner structure of the South Pole-Aitken basin. As following from Fig. 1 the border of the depression with values of heights $H < 0$ km has form of the near right ellipse. Dimensions of the oval formation are approximately 2200 km x 1800 km. Center of the ellipse displaces from center of the outermost rim to the south on ~ 300 km. The next depression has oval form too (Fig. 3). The elevation level of the its border is $H < -4$ km. The transversal is about 1400 km, and ratio of the axes is equal to 1,2. Center of the depression displaces from center of the outermost ring to the south-east on ~ 500 km. The deepest inner depression has nearly circular form with diameter of 600 km. Its height level is $H < -6$ km. Its center displaces from the basin center to the south-east on more than 700 km. This sketch-map of the ring structure is shown in Fig. 3.

Conclusions. On the basis of our study of the generalized structure of the SPA basin we conclude that giant impact which formed this basin unit was oblique or trajectory of the impactor was tangent to the surface of the lunar sphere. Because of very small value of ratio "deep – diameter" (~ 0.004) and small possibility of the long-term viscous relaxation [6, 7] we propose that impactor had a small density of its matter. The impactor was not a planetesimal or large asteroid because direction of its supposed traectory was nearly perpendicular to the ecliptic plane. In the case we can assume it was a giant hyperbolic or long-period comet body.

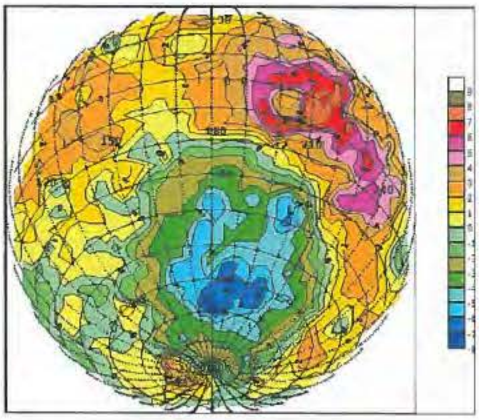

Figure 1. The hypsometric map of the lunar hemisphere including the Spa basin. The map was constructed in the perspective azimuthal orthographic projection. The initial data and construction method are described in the text.

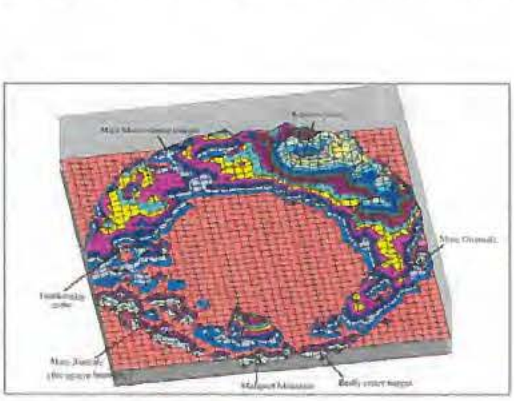

Figure 2. The structure of the SPA basin outer ring (the 3D projection). The relief is shown relative to the daturence surface corresponding to a sphere with a radius of 1738 km. The contour lines are drawn at an interval of 0.5 km. The vertical scale is increased compared to the liner scale. The hypsometric structure of the SPA inner depression is not indicated.

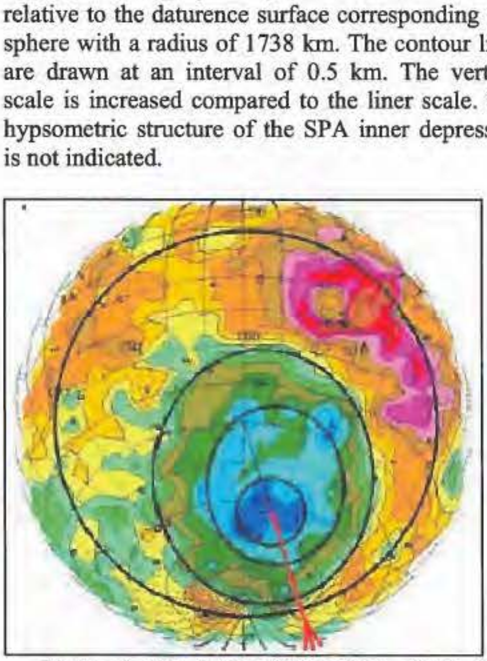

Figure 3 The distinguished rings of the lunar South-Pole Aitken basin structure is marked.

References. [1] Wieczorek M.A. and Phillips R.J. (1999) *Icarus, 139*, 246-259. [2] Spudis P.D., Reisse R.A., Gillis J.J. (1994) *Science,* 266, 1848-1851. [3] Chikmachev V.I. and Shevchenko V.V. (1999) *Atron. Vestn., 33*, 2, 18-28. [4] Nefed'ef A.A. (1958) *Izvestia of Kazan' Univ. Astronom. observ.* No. 30. [5] Hiesinger H., Head J.W. III (2003) *Mi-crosymposium 38, Moscow,* Abstract # MS107. [6] Shevchenko V.V., Chikmachev V.I., Pugacheva S.G., (2007) *Atron. Vestn.,41*, 6, 483-499. [7] Chikmachev V.I., Pugacheva S.G., Shevchenko V.V. (2005) *LPS XXXVI,* Abstract # 1078.

PETROPHYSICAL AND PALAEOMAGNETIC STUDIES OF THE KEURUSSELKÄ IMPACT STRUCTURE, CENTRAL FINLAND.

S. Raiskila[1] , T. Elbra[1] , T. Öhman[2] and L. J. Pesonen[1], [1]Department of Physics, P.O. Box 64, FIN-00014 University of Helsinki, Finland, E-mail: selen.raiskila@helsinki.fi, [2]Department of Geology, P.O. Box 3000, FIN-90014, University of Oulu, Finland

Introduction: Keurusselkä impact structure was found in 2004 [1], [2]. It is located in central Finland (62°08'N, 24°37'E) in crystalline basement (Central Finland Granitoid Complex) of Paleoproterozoic age (1.88Ga). The structure diameter, as based on shatter cone findings, is about 14 km. This indicates that shatter cone area could represent a central uplift of a middle sized complex crater. Due to strong erosion only the lowest bottom of the original crater is preserved. Presumably the age of the structure is thereby less than 1.0Ga. Despite the remarkable shatter cone findings no other impact evident such as PDF's or impact melt has been found yet. SEM analysis has revealed so far only weak shock features.

Sampling and measurements: The sampling at Keurusselkä started in 2007. Samples were collected from shatter cone outcrops [3] (Fig 1) and along a profile in order to study the petrophysical properties as a function of the radial distance from the proposed central uplift. Altogether, 131 hand samples from 29 outcrops were collected and prepared as a standard cylinders with 390 specimens. Specimens were investigated with mineralogical, palaeomagnetis and petrophysical methods in order to identify shock features. Petrophysical properties (susceptibility, density, NRM and Q-value) and thermomagnetic as well as hysteresis properties were measured at Solid Earth Geophysics labratory in University of Helsinki. SEM analysis were performed in collaboration with the Geological Survey of Finland in order to define the magnetic carriers.

Results: The susceptibility and density of the rocks in Jylhänniemi area is higher compared to the values from surroundings sites. Thermomagnetic measurements, hysteresis measurements and SEM analysis revealed that the carrier for remanence is magnetite, which was observed between 570 and 580 °C. Most of the samples behaved erratically on AF demagnetization, which made the component separation difficult. More detailed results are presented in the poster.

Fig 1. Jylhänniemi site with remarkable shatter cones in crystalline basement.

References:

[1] Hietala S. and Moilanen J. (2004) *LPS XXXVI*, Abstract #1619 . [2] Pesonen L.J. et al. (2004) *Meteoritics & Planet. Sci., 39,* Abstract #5068. [3] Hietala S. and Moilanen J. (2007) *LPS XXXVIII,* Abstarct #1762.

DEBATE ABOUT IMPACTITE NOMENCLATURE – RECENT PROBLEMS. W. U. Reimold[1], J. W. Horton Jr.[2], and R.T. Schmitt[1], [1]Museum for Natural History (Mineralogy), Humboldt-University in Berlin, Invalidenstrasse 43, 10115 Berlin, Germany (e-mail uwe.reimold@museum.hu-berlin.de); [2]U.S. Geological Survey, 926A National Center, Reston, VA 20192, USA.

Introduction: Following several years of discussion of an informally proposed impactite nomenclature [1], Stöffler and Grieve (2007) [2] published the long awaited and immediately widely recognized proposal on impactite nomenclature on behalf of the IUGS Subcommission on the Systematics of Metamorphic Rocks. In the authors' own words, this proposed nomenclature represents "provisional results" of the subcommission's work. The classification comprises systematics of lithologic types generated in *single* as well as *multiple impacts*, with a particular subdivision for *proximal* and *distal impactites*. Already, the proposed terminology is being widely applied within the impact-cratering community, although with varied degrees of rigidity/flexibility. However, recent studies bring up specific problems that suggest that parts of the classification need revisiting.

Suevites: Significant debate has ensued as a consequence of two publications [3,4] promoting the idea that suevite from the Ries crater, for 50 years considered a melt-fragment-bearing impactite with an essentially clastic matrix ("particulate matrix" according to [2]), should rather be considered impact melt rock with a melt groundmass. This idea questions the validity of the term "suevite" (and by implication) the entire polymict-impact-breccia nomenclature of the IUGS subcommission.

Further suevite issues have arisen from the detailed studies of cores from two ICDP drilling projects in impact structures. First, drill cores LB-07A and LB-8A from the interior of the Bosumwti impact structure in Ghana [5,6] brought a series of impactites to the fore that seemingly comprises both suevite (with melt fragments) and lithic impact breccia (devoid of melt fragments). Melt-bearing and melt-free breccias were classified from thin section studies that imply that these two breccia types occur intimately intercalated – or that sampling for thin section production sometimes intersected a few small melt particles, sometimes not. This raises the question whether there should be a set minimum limit of melt abundance, such as 1 vol%, in order to distinguish bona fide suevite from polymict lithic impact breccias that do not have a melt fragment component at all.

Scale of classification: A related issue is how the nomenclature applies at scales larger than a meter for units on geologic maps, columns, and cross sections. This question arose from current efforts to prepare a geologic column for impactites drilled by ICDP/USGS in the moat of the Chesapeake Bay impact structure [7]. The general lithostratigraphic classification of units (>1 m) in parts of a ca. 154 m interval of impactites [8], based on macroscopic core examination and petrographic data from dozens of thin sections, locally differs from the classification of selected specific samples within these units based on detailed petrographic analysis. An issue was whether entire units in the lower part of this impactite interval (between 1,551 and 1,474 m depth) should be called "melt-poor suevite" where macroscopic melt particles are either absent or unconfirmed and only a small fraction of many samples studied in thin section contain rare microscopic melt particles and, thus, are suevite. The general term "polymict impact breccia" is being used for these geologic units [8], while individual samples are more specifically classified as lithic impact breccia or suevite, depending on the presence or absence of melt particles. "Polymict impact breccia" in Stöffler and Grieve's (2007) glossary and "polymict breccia" in their Table 2 are interchangeable variations of the same term, which their Table 2 shows to be a general category that encompasses both suevite (with cogenetic melt particles) and lithic impact breccia (without melt particles). Thus, if part of a large polymict impact breccia unit is suevite, this does not require all of it to be suevite.

Marine impactites: The Chesapeake Bay drill core also contains a thick sequence described as "sediment-clast breccia and sediment megablocks" [7], including the informally named Exmore beds or Exmore breccia [9, 10]. This sequence is interpreted to be related to avalanching and ocean resurge processes in the immediate period following the deposition of coherent impactite [10]. However, parts of this sequence contain shocked mineral grains, impact metamorphosed lithic clasts, and rare impact melt clasts; the latter could locally preclude the term "sediment-clast breccia" for melt-bearing zones and favor calling them "suevite." This entire sequence could well be considered a form of "impactite" [10], and parts are essentially a mixture of reworked shock-affected and impact-melted particles derived from within the transient impact crater with much larger volumes of unshocked resurge sediment from a wider region. This form of "secondary impactite" (formation or modification of impact breccias by or as an immediate consequence of marine impact, in general) is not considered by the proposed IUGS nomenclature of impactites.

Transitional lithology: Studies of Chesapeake Bay impact breccias and also of impactites recently procured in the SUBO 18 Enkingen borehole in the southern Ries crater [11] have indicated another serious issue: Like the suevites and lithic impact breccias from Bosumtwi and the lower part of the Chesapeake Bay impactite sequence, which seemingly are intercalated with locally gradational boundaries, there are 75 m of *suevites and impact melt rocks* in the Enkingen borehole that show a complex gradation from massive melt-matrix-dominated breccia to particulate, typical suevite with individual and well separated melt fragments (at vastly different proportions (<20% to >65%). In addition, there occurs a series of transitional types of melt-rich breccia, including a prominent "ignimbrite-like" assemblage of macroscopically welded melt fragments that are separated only by millimeter-wide seams of "suevitic" particulate groundmass. This transitional lithology between impact melt rock and suevite is clearly not recognized by the IUGS proposal. This obviously leads to the question whether [3,4] may have studied such melt-dominated material forming a pod or lens within regular suevite with a lithic/mineral clast-dominated, although melt-fragment-bearing groundmass.

Pseudotachylitic breccias: Finally, the proposed IUGS nomenclature for *impactites* also contributes to the "pseudotachylite" issue [12,13]. It refers to (ibid) "Shock veins and vein networks (previously termed "pseudotachylites") are formed during the compression stage, since they often occur as clasts within later formed breccia dykes" [2]. In Table 2 of this classification, this group of rocks falls into the compartment "Dykes, veins and vein networks," – which in the text is further subdivided to include impact breccia and shock vein occurrences. The cited definition clearly does away with the "pseudotachylite controversy" by reducing this term to only one meaning: shock melt veins produced during shock compression. Unfortunately, the glossary term attached to the IUGS nomenclature "Impact pseudotachylite (*Pseudotachylite* produced by *impact metamorphism*, Dyke-like breccia formed from frictional melting in the basement of impact craters, resulting often in irregular vein-like networks. Typically, it contains unshocked and shocked mineral and lithic clasts in a fine-grained aphanitic matrix, see also *melt vein*)" reopens the controversy by adding frictional genesis to the earlier shock melting genesis. The term "melt vein" is said to be synonymous to "shock vein".

Checking the IUGS nomenclature of *fault rock* terms [14], one finds ("fig. 2.3.1.") that pseudotachylite is classified under "cohesive fault rock". The IUGS nomenclature for *contact metamorphic rocks* [15] defines pseudotachylite as produced by "*frictional heating in fault zones*" (p. 9). The now quite old pseudotachylite problem is alive and well (see also various abstracts to this conference). Vredefort pseudotachylitic breccias are debated to be the result of shock melting, friction melting, or decompression melting, or whether they could represent influx of impact melt rock from the level of the crater floor.

Conclusion: This review of selected problems is likely not an exhaustive account of impactite nomenclature issues. However, it may suffice to demonstrate the importance of this subject, and the confusion that in all likelihood affects every impact worker. It is proposed to use the Large Meteorite Impacts IV conference for detailed discussion of these problems, and to attempt to prepare recommendations for consideration upon revision and finalization of the IUGS nomenclature of impactites.

References: [1] Stöffler, D. & Grieve, R.A.F., 1994, LPS XXV, 1347-1348; [2] http://www.bgs.ac.uk/SCMR/docs/papers/paper_11.pdf & http://www.bgs.ac.uk/SCMR/glossary2.html; [3] Osinski, G.R., 2003, MAPS 38, 1641-1668; [4] Osinski, G.R., 2004, EPSL 226, 529-543; [5] Coney, L. et al., 2006, MAPS 42, 569-589; [6] Ferrière, L. et al., 2006, MAPS 42, 611-633; [7] Gohn, G. et al., 2006, EOS 87, No. 35, 29 August 2006, 3pp.; [8] Horton, J.W. Jr. et al., this volume; [9] Poag, W. et al., 2004, The Chesapeake Bay Crater, Springer, Berlin-Heidelberg, 522pp.; [10] Horton, J.W. Jr. et al., 2008, GSA SP 437; [11] Phl, J. et al., this volume; [12] Reimold, W.U. & Gibson, R.L., 2005, Impact Tectonics, Springer, Berlin-Heidelberg, pp. 1-53; [13] Reimold, W.U. & Gibson, R.L., Chemie der Erde 66, 1-35; [14] http://www.bgs.ac.uk/SCMR/docs/papers/paper_3.pdf;[15] http://www.bgs.ac.uk/SCMR/docs/papers/paper_10.pdf

GEOLOGICAL EVIDENCE FOR ACOUSTIC FLUIDIZATION IN LARGE IMPACT STRUCTURES.

U. Riller[1] and D. Lieger[2], [1]School of Geography and Earth Sciences, McMaster University, Hamilton, Canada (rilleru@mcmaster.ca), [2]Museum of Natural History (Mineralogy), Humboldt University, Invalidenstrasse 43, 10115 Berlin, Germany.

Introduction: Acoustic fluidization of target rock has been invoked as mechanism accomplishing high deformation rates during transformation of transient craters into final craters with flat floors, notably of large impact structures [1, 2]. The modified concept of acoustic fluidization, known as the block oscillation model [2], predicts fragmentation of target rocks on the decameter to hundred meter scale. Apparently, such discontinuous deformation along with pressure fluctuations transiently lowers overall rock cohesion and allows target rock to behave mechanically as a fluid during cratering. However, geological evidence for fluid-like behavior of target rocks and its immediate regain in mechanical strength at the end of cratering does not seem to have been recognized in large terrestrial impact structures.

Although generally not attributed to acoustic fluidization, target rocks in the central portions of large terrestrial impact structures such as Sudbury, Canada, and Vredefort, South Africa, are characterized by the pervasive presence of fragment-rich pseudotachylite bodies. Debates regarding the formation of these bodies include the origin of melts, i.e., friction- versus shock-induced melting, their mobility, cause of target rock fragmentation and timing of breccia body formation with respect to cratering stages. Structural observations from Sudbury and Vredefort suggest that fragment-rich pseudotachylite zones may well be important agents of acoustic fluidization.

Results: The size of fragment-rich pseudotachylite bodies at both impact structures ranges from mm- to cm-wide veins, dm- to m-scale dikes, to up to hundreds of meters wide, irregular or pocket-like bodies. Despite pervasive fragmentation, target rocks of both impact structures are characterized by a remarkable structural continuity of pre-impact geological units and mineral fabrics on the decameter scale and larger. This continuity indicates that overall target rocks behaved mechanically as a continuum during crater formation and that slip on proposed, apparently kilometer-scale, impact-induced discontinuities is likely of minor importance during the crater modification, at least at the exposed crustal levels of both impact structures.

The geometry of pseudotachylite zone margins and fragments indicates that the zones are essentially fragment- and melt-filled fractures formed by dilation, i.e., volume increase of target rock. This is supported by strike separations of pre-impact markers at the zone boundaries, which are generally less than a few centimeters. Thus, the zones formed as tension gashes or hybrid shear faults. We failed to identify impact-induced shear faults that could potentially have generated friction melts and fragments. Where pseudotachylitic veins overstep each other, their respective tips are curved toward the neighboring vein, thereby isolating elliptical host rock fragments. This underscores the formation of pseudotachylite zones by discontinuous deformation on the outcrop scale.

Recognition of the pre-impact fit of marker points across pseudotachylitic veins and dikes allowed us to determine the components of maximum dilation vectors at a given outcrop surface at Vredefort. Measurement of the component vectors throughout the outer core of the Vredefort Dome indicates either radial or concentric stretching of material, regardless of breccia zone orientation. This is in agreement with strain accumulation predicted from numerical modeling [3] and suggests that pseudotachylite zones formed at an advanced stage of cratering, likely during formation and collapse of the central uplift.

Pre-impact configuration of fragments in large breccia zones and the paucity of fragments that are exotic with respect to the immediate host rock indicate that fragments were not transported distances larger than tens of meters. However, this may not apply for the pseudotachylitic matrix, i.e., former melt. Collectively, (1) overall dilation and volume increase during target rock fracturing, (2) incipient fragmentation and jigsaw geometry of fragments, (3) en-echelon vein geometry, (4) evidence for thermal corrosion of fragments and (5) apparent lack of bona fide shear faults point to an allochthonous origin of the melt.

Interpretation: Popular models of pseudotachylite formation assume that fragmentation and melt generation occur during a single process, either driven by gravitationally-induced shearing or slip on prominent discontinuities, or by the interaction of the shock wave with target rock. Our structural observations suggest that fracturing and melt generation are processes that are separated in space and time during cratering. Specifically, fracturing and fragmentation is related to dilation of target rock, which accomplished large-scale bending of the uplifted rocks during late stages of cratering [3]. Thereby, tensional fracture zones led to shape change of the crater floor, whereby differential displacement parallel to the zone walls is minimal, generally on the order of centimeters or less for pseudotachylite veins. This agrees with the observed structural continuity and overall mechanical coherence of target rocks during late-stage cratering. During this deformation, dilatational fracture zones formed likely low pressure zones into which melt, possibly drained from the overlying impact melt sheet, was drawn forcefully.

Based on our observations, fragment-rich pseudotachylite zones formed during crater modification, the cratering stage at which acoustic fluidization is believed to be active [2]. Thus, pseudotachylite zones may well constitute the discontinuities accomplishing acoustic fluidization. Other important characteristics of the block oscillation model of acoustic fluidization are the speed of sound, apparently much lower in the matrix between the blocks than in the blocks, and the immediate regain in mechanical strength of target rocks at the end of cratering [2]. Pseudotachylitic melt separating blocks and enveloping fragments during overall target rock fluidization and rapid solidification of the melt at the end of crater formation are in agreement respectively with these characteristics of the block oscillation model. We regard fragment-rich pseudotachylite bodies as viable candidates for accomplishing acoustic fluidization in large impact structures.

References: [1] Melosh, J. H. (1979) *JGR, 84,* 7513-7520. [2] Melosh, J. H., and Ivanov, B. A. (1999) *Annu. Rev. Earth Planet. Sci. 27*, 385-415. [3] Ivanov, B. A. (2005) *Sol. Syst. Res., 39*, 381-409.

FIRST LARGE METEORITE IMPACT STRUCTURE DISCOVERED IN THE MIDDLE EAST: JEBEL WAQF AS SUWWAN, JORDAN

Elias Salameh[1], Hani Khoury[1], Wolf Uwe Reimold[2], Werner Schneider[3], and Thomas Kenkmann[3]
[1]University of Jordan, Faculty of Science, Amman 11492, Jordan (salameli@ju.edu.jo; khouryhn@ju.edu.jo)
[2]Museum for Natural History, Humboldt University, Invalidenstrasse 43, 10115 Berlin, Germany (uwe.reimold@museum.hu-berlin.de)
[3]Im Ziegenförth 15, 38108 Braunschweig, Germany.

Corresponding author: W.U. Reimold (uwe. reimold@museum.hu-berlin.de)

Abstract

A 5.5 km diameter, complex, circular structure was discovered in the central eastern region of the Kingdom of Jordan. Initial groundtruthing revealed complex geological structures including a prominent outer rim rising up to 60 m above the surrounding plain, an intermediate ring of 20 m elevation within a ring syncline, and a central zone of stratigraphically uplifted sedimentary strata characterized by intense macroscopic (folding and faulting, widespread cataclasis) and locally intense mesoscopic (cataclasis) deformation. Not less than 10 sites with shatter cone development in fine-grained sandstone or limestone have been mapped to date. This confirms that the Jebel Waqf as Suwwan structure was formed as the result of the impact of an extraterrestrial projectile. Search for impact-diagnostic micro-deformation has been rather unsuccessful: only 1 quartz grain with both planar deformation features and planar fractures has been detected so far. Most of the ca. 70 samples returned for micropetrographic analysis consist of extremely fine-grained chert, siltstone, or marly limestone. Cataclasis is widespread in chert and limestone, also on the micro-scale. Considering the severely limited amount of characteristic impact micro deformation, and the stratigraphic situation within the central uplift, one tends to blame exhumation of a relatively deep level of the central uplift, besides the generally limited development of characteristic shock micro deformation in porous sedimentary rocks, in comparison to shock overprint on crystalline target rock.

Recrystallization of micro-crypto crystalline chert could be an indication for impact-diagnostic micro-deformation. New field data would be presented during the conference.

A GALLERY OF MULTIRING BASINS ON EUROPA, GANYMEDE, AND CALLISTO.

Paul M. Schenk[1] and William. B. McKinnon[2], [1]Lunar and Planetary Institute, 3600 Bay Area Blvd., Houston, TX 77058 (schenk@lpi.usra.edu), [2]Department of Earth and Planetary Sciences and the McDonnell Center for the Space Sciences, Washington University, Saint Louis, MO 63130 (mckinnon@wustl.edu).

Introduction: The largest craters on Earth, the other terrestrial planets, and major icy satellites (of Jupiter) possess one or more exterior rings. The formation of these rings is thought to be linked to the scale of the impact and lithosphere thickness at the time of impact [e.g., 1]. Yet this influence of "mechanical stratigraphy" on final crater morphology remains a hypothesis, albeit one increasingly subject to theoretical, numerical, laboratory analogue, and field testing. In the present context, field work means imagery and topography, in contrast to in situ studies such as at Vredefort. Here we present a variety of multiring forms as observed on large icy satellites by NASA's *Galileo* (and in some cases, *Voyager*) missions. Further discussion can be found in [2].

Tyre (Europa): The largest multiring structure on Europa is Tyre (≈160 km across) [3]. A type example of the Valhalla class, it is defined by an extensive zone of circumferential graben and normal faults. Both the modest scale of the structure and narrowness of the ring graben indicate a very high heat flow (which is in turn a function of ongoing tidal heating [5]), and illustrates that formation multiringed structures of this type was not restricted to ancient Solar System epochs.

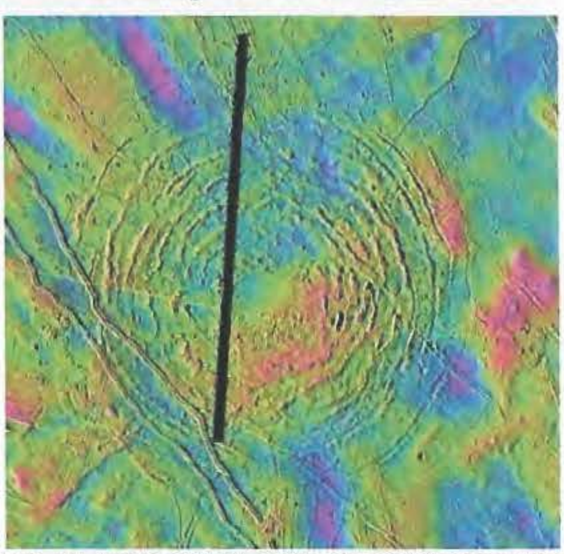

Fig. 1: Image of Tyre, with color-coded topography based on photoclinometry (purple, low; red, high; range ~750 m). Many domed and depressed features are real, but the general reliability of long-wavelength information (including the rise in the central southeast portion of the structure) is uncertain [from 4].

Asgard (Callisto): The second largest multiringed system on Callisto (~1600 km across), *Galileo* images confirmed an outer zone of graben and an inner zone of inward-facing normal faults. The width and spacing of the graben confirm that even at ~4 GYA Callisto's

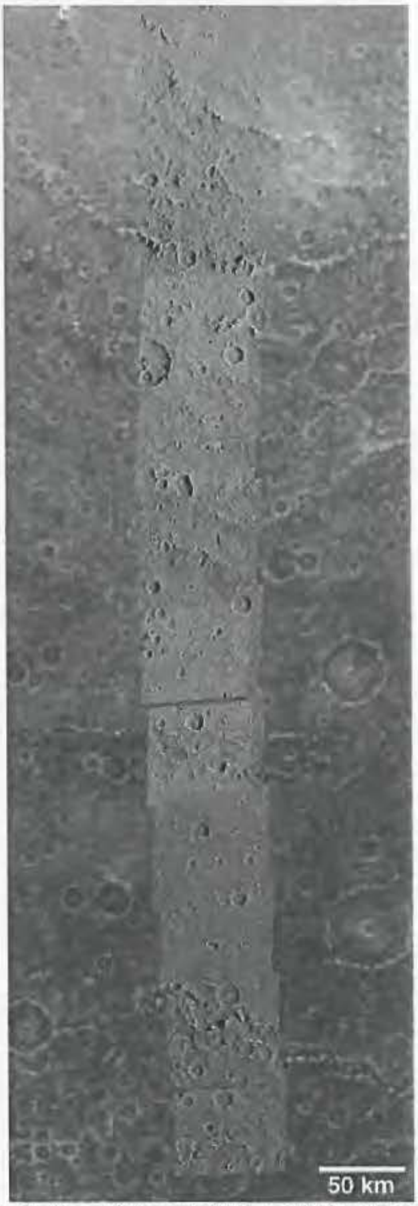

Fig. 2: Portion of Asgard high-resolution transect [6]. Irregular graben at bottom is seen overlaid on photoclinometrically-derived topography in Fig. 3 in [2].

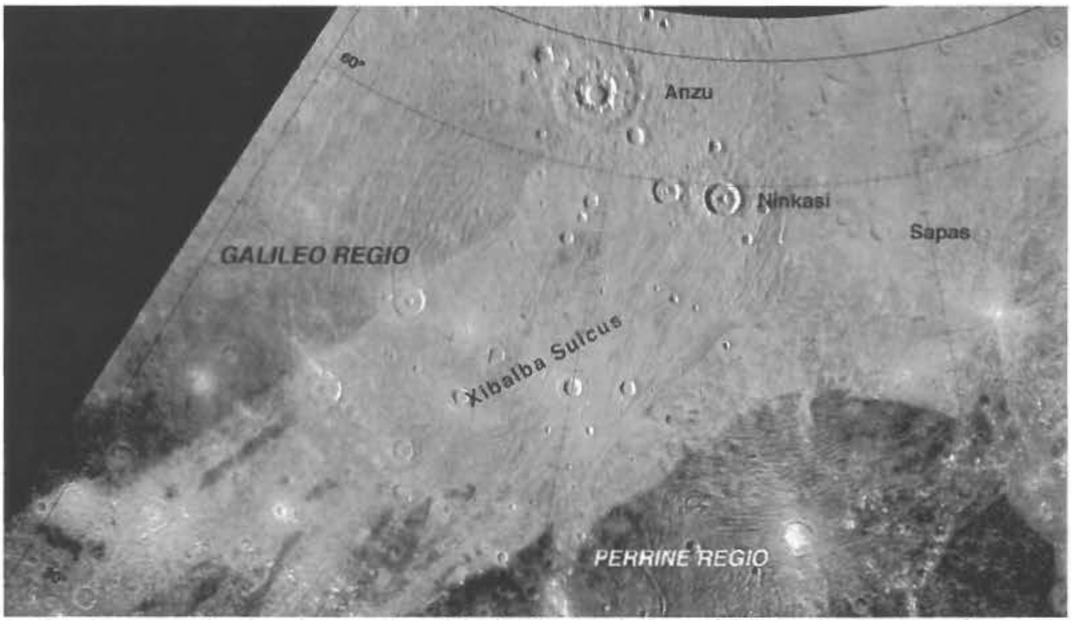

Fig. 3: Equal-area mosaic of northern section of the leading hemisphere of Ganymede. Portions of two ~1000-km sized, Valhalla-class multiring systems are seen, one in eastern Galileo Regio and one in northern Perrine Regio.

heat flow was many times less than that of Europa today. Unfortunately, much of Valhalla, Asgard, as well as the superposed Utgard multiringed system [7], was poorly or not imaged by *Galileo*.

Perrine and eastern Galileo Regio (Ganymede): An enormous, hemispherical scale, Valhalla-like furrow system lies at the stratigraphic base of two major regions of ancient, dark terrain, Galileo and Marius Regiones [8]. A smaller system was identified in Perrine Regio, and though better imaging of this system was not obtained, *Galileo* did discover a portion of a similar system in eastern Galileo Regio. These may represent two independent impacts (similar to Asgard and Utgard), but being similar in size may also be surviving fragments of a *single* multiringed system. If the latter, offsets of their respective centers of curvature imply substantial spreading as part of bright terrain formation (one of the mechanisms discussed in [9]).

"Lofn" (Callisto): The youngest basin on Ganymede, Gilgamesh, has a much more modest set of inward facing scarps, and is closer to Orientale in structure. It indicates a decline in heat flow and an increase in lithosphere thickness during Ganymede's geological history [10]. It also raises the question of transitional structures, in scale or time, on Europa [4] and Callisto. For Callisto at least, that structure may be Lofn (Adlinda in *Voyager*-era maps). Inward facing scarps can be identified at up to 225 km from the center of an ~120-km wide central floor. In this, Lofn resembles Gilgamesh, but at 4/5 scale, and also implies secular cooling and thickening of Callisto's lithosphere.

References: [1] Melosh H.J. (1989) *Impact Cratering*, Oxford. [2] McKinnon W.B. and Schenk P.M. (2008) *this volume*. [3] Moore J.F. (2001) *Icarus, 151*, 93–111. [4] Schenk P.M. and Turtle E.P. (2008) in *Europa*, UA Press, submitted. [5] Greeley R.T. et al. (2004) in *Jupiter TPSaM*, Cambridge, 329–362. [6] Moore J.F. et al. (2004) in *Jupiter TPSaM*, 397–426. [7] McKinnon W.B. (1981) *Multi-Ring Basins, Proc. Lunar Planet. Sci. 12A*, 259–273. [8] Schenk P.M. and McKinnon W.B. (1987) *Icarus, 72*, 209–234. [9] Pappalardo R.T. et al. (2004) in *Jupiter TPSaM*, 363–396. [10] McKinnon W.B. and Melosh H.J. (1980) *Icarus, 44*, 454–471.

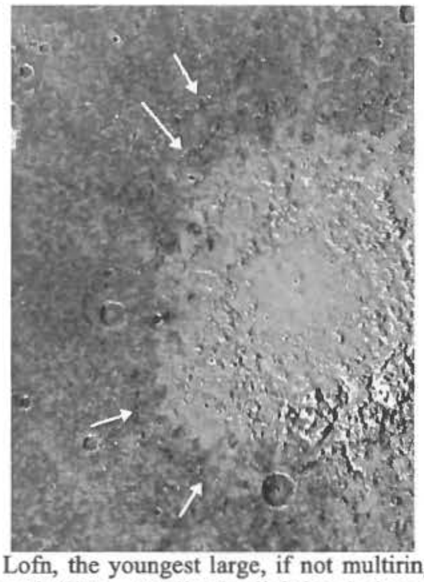

Fig. 4: Lofn, the youngest large, if not multiringed, impact on Callisto. While the lighting is less than ideal, inward-facing scarps can be identified (arrows).

CAN IMPACT EJECTA SURVIVE FLUVIAL REWORKING? M. Schmieder[1] and E. Buchner, Institut für Planetologie, Universität Stuttgart, Herdweg 51, D-70174 Stuttgart, Germany; [1]martin.schmieder@geologie.uni-stuttgart.de.

Impact ejecta reworked by various sedimentary processes have been reported from a number of impact structures on Earth [1]. Tsunami-reworked layers of impact glass/spherules and shocked mineral grains at K/T boundary sections associated with the Chicxulub impact structure, Mexico, were described by [2] and [3]. At marine impact structures, such as Lockne, Sweden, impact ejecta are commonly reworked within submarine turbiditic 'resurge breccia' deposits [4]. At impact structures degraded by glacial erosion, e.g., the <1.9 Ga Paasselkä impact structure, Finland, glacial float may contain proximal ejecta material [5]. In contrast to the marine and glacial processes mentioned above, impact ejecta reworked by fluvial processes are sparsely mentioned in the literature, which suggests that shocked mineral grains and impact glasses are unstable when eroded and transported in fluvial systems.

Here we report impact ejecta that show sedimentological evidence for at least three steps of high-level fluvial reworking. Well-rounded Ries ejecta material (suevite-derived shocked quartz grains, diaplectic quartz/feldspar glass, and lithic clasts of Bunte Breccia and suevite within multi-generation sandstone pebbles) is distributed within post-impact fluvial sandstones locally known as the 'Monheimer Höhensande' [6] (Figs. 1-3); the latter were carried and deposited within a water distribution network that incised into the eastern part of the Ries ejecta blanket soon after the impact event. Our findings document, for the first time, that intensely shocked quartz grains and diaplectic glass can survive short-range multiple fluvial reworking.

References: [1] Simonson B. M. and Glass B. P. (2004) *Ann. Rev. Earth Pla. Sci., 32,* 329-361. [2] Smit J. (1999) *Ann. Rev. Earth Pla. Sci., 27,* 75-113. [3] Maurrasse F. J.-M. R. and Sen G. (1991) *Science, 252,* 1690-1693. [4] Sturkell E. F. F. (1998) *Geol Rdsch., 87,* 253-267. [5] Schmieder M. et al. (2008) *Meteoritics and Planetary Science* (in press). [6] Schmidt-Kaler H. (1974) *Geol. Blätter NO-Bayern, 24,* 101-105.

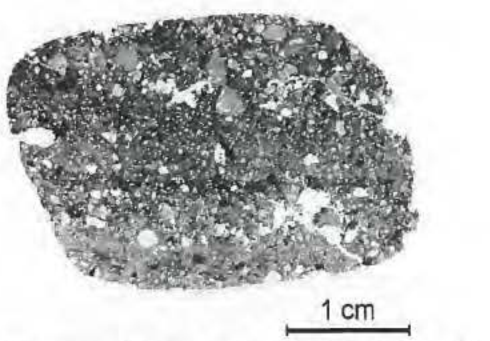

Fig. 1: Well-rounded, layered, and graded sandstone pebble (Monheimer Höhensande) that contains multiply reworked Ries ejecta material.

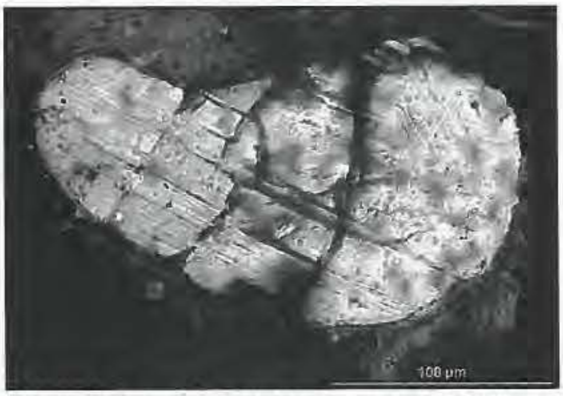

Fig. 2: Well-rounded shocked quartz grain with PDFs and planar fractures in sandstone pebble from the Monheimer Höhensande.

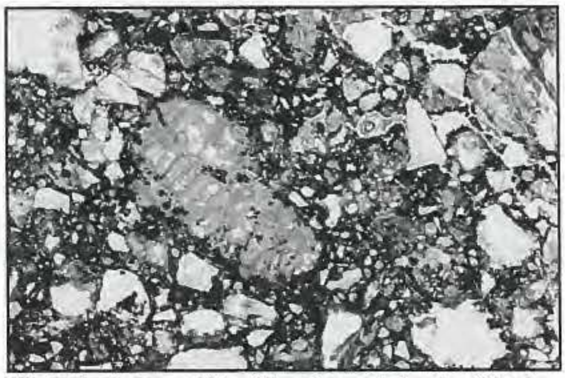

Fig. 3: Sandstone pebble with well-rounded grain of diaplectic quartz glass (kidney-shaped grain near centre) from the Monheimer Höhensande. Image width ~1.5 mm.

PALEOENVIRONMENTAL CHARTS FOR TERRESTRIAL IMPACT STRUCTURES - A SIMPLE TOOL TO TEST IMPACT AGES AND MARINE/CONTINENTAL IMPACT CONDITIONS.

M. Schmieder[1] and E. Buchner, Institut für Planetologie, Universität Stuttgart, Herdweg 51, D-70174 Stuttgart, Germany; [1]martin.schmieder@geologie.uni-stuttgart.de

Introduction and Background: Most of the ~175 impact structures currently known on Earth are still insufficiently dated [1-2]. At buried or deeply eroded impact structures that lack material suitable for isotopic dating, stratigraphic methods provide the only con-straints for the timing of crater formation; in many cases, only the maximum age (the actual age of the shocked target rock) is given in the literature and in terrestrial impact crater listings [3]. In addition to isotopic and stratigraphic dating, paleogeographic considerations may help to test and refine poor and/or equivocal impact ages as recently done for Puchezh-Katunki (Russia) and Obolon (Ukraine) [4].

Paleogeographic studies are, furthermore, an essential tool to discriminate between impact structures that formed in continental or marine environments. Only a small number (~25) of marine terrestrial impact structures have been reported so far [5]. Structural and sedimentological investigations (e.g., the recognition of submarine resurge breccia deposits) helped to reveal some additional marine impact structures, such as Obolon (Ukraine) [6]. However, further efforts need to focus on the recognition of marine impact structures on Earth.

Data: Combining recent paleogeographic maps of North America (provided by Ron Blakey, Northern Arizona University [7]) with impact ages available in the literature [3; 8-14], we present a preliminary set of paleoenvironmental charts for some selected North American impact structures (USA: Ames, Oklahoma; Avak, Alaska; Crooked Creek, Missouri; Newporte, North Dakota; Sierra Madera, Texas; Upheaval Dome, Utah; Wells Creek, Tennessee; Canada: Carswell, Saskatchewan; Charlevoix, Québec; Pilot, Northwest Territories; Steen River, Alberta; Fig. 1).

Interpretation and Results: In accordance with [7], given that both the paleogeographic maps and impact ages can include uncertainties, the paleoenvironmental charts suggest that Newporte (~500 Ma [8]) and Steen River (91 ± 7 Ma [9]) formed under marine conditions and that Ames (>470 Ma [10]), Avak (~93-88 Ma [11]), Charlevoix (~450-480 Ma [12]), and Carswell (115±10 Ma [13]) are probably marine impact structures. The Pilot (445±2 Ma [13]) event was obviously a continental impact scenario, as most likely was the Wells Creek (200±100 Ma [14]) impact. Charts exhibit transitions in environmental conditions for Crooked Creek (320±80 Ma [14]), Upheaval Dome (<170 Ma [3]), and Sierra Madera (<100 Ma [14]). New field studies and the detection of structural and sedimentological features diagnostic for marine or continental impact, respectively, might strongly narrow the age windows for these structures.

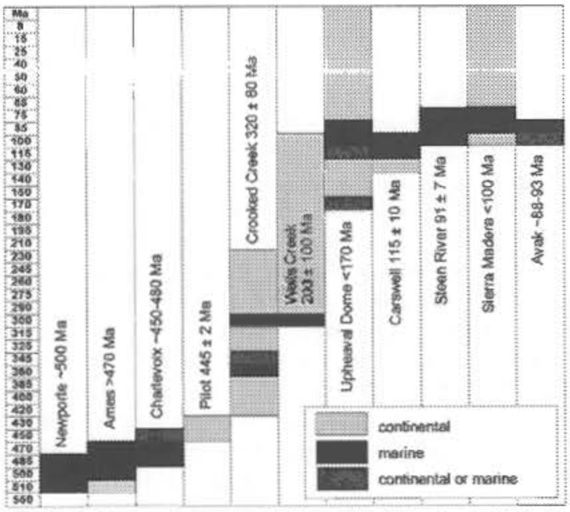

Fig.1: Paleoenvironmental charts for 11 selected North American impact structures (according to [7]).

References: [1] Reimold W. U. (2007) *Meteoritics & Planet. Sci.*, 42, 1467-1472. [2] Renne P. R. et al. (2007) *Geochim. Cosmochim. Acta*, 71, A833. [3] Earth Impact Database, available online at http://www.unb.ca/passc/ImpactDatabase (accessed May 09, 2008). [4] Schmieder M. and Buchner E. (2008) *Geol. Mag.*, 145 (in press). [5] Dypvik H. and Jansa L. F. (2003) *Sed. Geol.*, 161, 309-337. [6] Valter A. A. (2002) *Proc. 8th ESF-IMPACT*, 66. [7] Blakey R. C. (2006) North American Paleogeographic Maps, available online at http://jan.ucc.nau.edu/~rcb7/nam.html (accessed May 09, 2008). [8] Koeberl C. and Reimold W. U. (1995) *Geochim. Cosmochim. Acta*, 59, 4747-4767. [9] Grieve R. A. F. (2006) *Impact Structures in Canada*. Geol. Assoc. Canada, GEOtext, 5, 210 pp. [10] Koeberl C. et al. (2001) *Meteoritics & Planet. Sci.*, 36, 651-669. [11] Banet A. C. and Fenton J. P. G. (2007) *GSA Spec. Pap.*, 437, 139-145. [12] Whitehead J. et al. (2003) *LMI III*, Abstract #4084. [13] Bottomley R. J. et al. (1990) *Proc. LPSC*, 20, 421-431. [14] Grieve R. A. F. (1991) *Meteoritics*, 26, 175-194.

ON THE DISTRIBUTION OF IMPACT MELT AND BASEMENT CLASTS IN THE CHICXULUB EJECTA BLANKET.

F. Schönian, D. Stöffler and T. Kenkmann, Museum für Naturkunde, Humboldt-Universität zu Berlin, Invalidenstrasse 43, D-10115 Berlin, frank.schoenian@museum.hu-berlin.de.

Introduction: The ejecta blanket of the Chicxulub impact crater (Ø 180 km, 65 Ma) was discovered in several wells close to the crater (UNAM 5, 6, and 7 [1]) and mapped over a large area on the southern Yucatán Peninsula, where it covers a preexisting Upper Cretaceous Karst topography [2, 3]. A rough estimate of its content in impact melt, usually altered to clay, was used to calculate melt production during the impact event [4]. However, since the ejecta blanket eroded karst lithologies [5] it was doubted that clay particles generally represent altered melt and assumed that they are at least in part derived from the subsurface by impact-induced erosion. Consequently estimates of the actual amount and the distribution of melt particles as well as crystalline basement clasts are crucial for the understanding of the impact event and the processes of ejecta emplacement.

The proximal ejecta blanket: The drill cores UNAM 5 (U5, 105 km S' of impact center) and UNAM 7 (U7, 126 km SE' of impact center) were described in detail and the amount of melt and basement clast macroscopically determined [6]. The impactites comprise a lower dolomitic megabreccia with large anhydrite megablocks (at 678.1 to 348.8 m in U7) and an upper unit of melt-rich suevites (503.9 to 332 m in U5 and 348.8 to 220.8 m in U7). The breccias can be subdivided into 6 units at U5 and U7 [6].

UNAM 5 suevites (1.17 crater radii – cr). The lower unit of U5 (U5-6) contains abundant impact melt derived from sedimentary rocks (25-40%) and a variable amount of melt derived from crystalline lithologies (5-20%) as well as basement clasts (5-20%). The "sedimentary melt" is absent in units U5-4 and -3 but "crystalline melt" varies between 10 and 30% and crystalline clasts between 0 and 20%. Both, melt and basement clasts, are slightly higher in U5-3 (10-35% and 5-30%). Melt remains high in the fallback suevite of U5-2 (15-40%) but crystalline fragments diminish to 2-10%. The redeposited suevite of U5-1 contains 10-15% of basement clasts and 15-20% of melt.

UNAM 7 megabreccia and contact (1.4 cr). The thick megabreccia sequence (unit U7-6) does not contain any crystalline basement clasts but has a small amount of black or bottle-green melt fragments of 1-3% within the breccia matrix. The contact with the suevites is transitional. In unit U7-5 the first larger melt clasts >3 cm occur well below the base of the lower suevite. The upper part of this unit is an alternating succession of melt-rich, irregular suevitic lenses and the dolomitic, sedimentary breccia. Large melt clasts are present in the lowermost suevites, but dolomitic portions do occur up to 327 m and karstified anhydrite clasts up to m 318 m. The contact should be placed at 348.8 m [6].

UNAM 7 suevites. The lower suevite of U7-4 has a variable but rather high content of green to greenish grey melt clasts (20-40%) but contains only 5-10% of highly shocked crystalline fragments. "Sedimentary melt" is very rare (3-10%). The latter rises in U7-3 to about 15-25%, while "crystalline melt" remains rather constant at 25-30% and basement clasts low at 3-8%. The middle suevite (U7-2) is very heterogeneous and has a high content of dispersed greenish melt particles (35-50%) and contains a slightly higher amount of shocked crystalline fragments (10-15%). Rarely large clasts of "sedimentary melt" are present. In the upper suevite (U7-1) the amount of greenish melt diminishes significantly to 10-20%, but "sedimentary melt" rises slightly to 10-20%. The content of basement clasts is variable, but low (5-10%).

The intermediate ejecta blanket: Outcrops of the ejecta blanket on the central Yucatán Peninsula are rare. The closest unequivocal exposure of the Chicxulub ejecta is a quarry near the village of Ukum in Campeche at 220.5 km from the impact center. Other important outcrops can be found at distances between 283.5 km (Paraiso roadcut) and 298.5 km (Sandoval quarry). Exposures usually display the lower ejecta blanket, since upper parts are removed by erosion.

Ukum quarry (2.45 cr). In the Ukum quarry a thick evaporitic succession (mainly anhydrite) of the Upper Cretaceous Icaiche Formation is overlain by an oligomict breccia of allochthonous limestone and dolomite clasts within a relatively well consolidated dolomitic matrix. Because clasts often display abrasion features such as polish and striations, the breccia could be related to the ejecta blanket [7]. Clasts are probably derived from Upper Cretaceous dolomite and limestone exposures nearby. No crystalline lithologies and no altered melt fragments could be found at this locality.

Paraiso roadcut (3.15 cr). At the outcrop of Paraiso an alternate layering of marls, clays and recrystallized limestones of the Morocoy Formation is overlain by a polymict breccia, composed largely of the underlying lithologies. However, allochthonous dolomite boulders with matrix-coatings are also present. Clay particles are dispersed throughout the matrix, but they resemble the underlaying laminated clays and can not be interpreted as altered impact melt. No basement clasts could be found.

Sandoval quarry (3.32 cr). Sandoval is a medium sized quarry where a polymict breccia composed of limestone and dolomite clasts within a poorly consolidated carbonate-rich matrix are exposed. The variable clasts display different source areas and do rarely show abrasion features. A shocked quartz grain from the insoluble residue of the matrix confirms the impact origin of this breccia. Clay clasts that probably can be interpreted as altered impact melt occur with amounts of 1-2% within the matrix. Again, no crystalline basement clasts are present.

The distal ejecta blanket: Beyond 300 km distance from the impact center (3.33 cr) the Chicxulub ejecta blanket is widely distributed and easily accessible across the southern Yucatán Peninsula. The best known examples are the outcrops in the Rio-Hondo-area along the border between Mexico and Belize.

Sarabia quarry (3.6). At Sarabia, a large quarry in the Chetumal area, clay particles are dispersed at an amount of ~5% throughout the matrix of the ejecta blanket and can at least in part be interpreted as altered impact melt. Large melt fragments were found as well as shocked crystalline clasts. Both occur close to the base of the ejecta rather than at its top. They are not enriched in any layer, but mixed with the bulk ejecta material composed of dolomite clasts floting in a well consolidated dolomitic matrix. The basal contact with the Upper Cretaceous Barton Creek dolomites is heavily sheared and no basal ejecta layer is present.

Ramonal roadcut (3.73 cr). At the Ramonal roadcut a lower layer rich in spheroids and vesiculated clay particles is filling a karst depression (Ramonal N) and overlying heavily karstified bedrock of the Barton Creek formation (Ramonal S) [2, 3]. Here clay clasts form 10 to 15% of the bulk material and can be interpreted as altered melt. Small vesiculated glass shards are present within the ejecta matrix. Larger melt clasts are very rare, but shocked crystalline fragments could be recovered from this basal layer.

Rio Hondo region (3.7-3.86 cr). Farther south the ejecta blanket is highly heterogeneous and does contain a variable amount of clay particles (5-20%, in local pockets to 40-50%). However, these clays can not unequivocally be interpreted as altered melt. The basal layer of Ramonal is not present, but crystalline basement clasts could be found at two localities. Again, these clasts are mixed within the bulk ejecta material and occur close to the base of the ejecta blanket.

Southcentral Yucatán Peninsula (3.3-3.8 cr). The Chicxulub ejecta blanket is widely distributed on the southcentral Yucatán Peninsula, but yet poorly studied. At many localities clay particles, that in part can be interpreted as altered melt, are distributed to various amounts within the ejecta matrix. Shocked quartz was found in the insoluble residue of the matrix at at least one locality. However, crystalline basement clasts where not found at any of these localities. Their occurence seem to be restricted to the Rio Hondo region.

Discussion and conclusions: Due to the uncertainties in interpreting clay particles either as altered impact melt or as clasts derived from subsurface erosion it appears to be difficult to estimate the amount of melt distributed within the ejecta at the present state of knowledge. Nevertheless, several important observations could be made:

1. Melt particles do rarely occur within the Bunte-Breccia-like unit (megabreccia) of U7.

2. The transition from the megabreccia to the suevites of U7 with breccia-in-breccia textures and intact large melt fragments indicates a turbulent mixing between vapor plume and ejecta curtain material.

3. The absence of crystalline basement clasts and the scarcity of (possible) melt fragments at intermediate distances from the crater indicates ejecta curtain material, also if the breccias are largely composed of locally eroded materials.

4. The occurrence of basement and melt clasts at low levels within the ejecta blanket beyond 3.5 cr indicates an 'inverse stratigraphy' compared to the sequence of the U7 drill core.

5. The absence of such crystalline lithologies and large melt clasts at localities on the southcentral Peninsula might bear information on the impact angle.

The observed 'inverse stratigraphy' and the mixing with the bulk ejecta material implies that impact melt and basement clasts arrived first at the distal localities and were subsequently eroded by the evolving secondary ejecta flow that followed ballistic emplacement [3]. At few localities (e.g. Ramonal N) this primary ejecta is still preserved in paleodepressions of the Upper Cretaceous topography. The primary ejecta flow might be driven by atmospheric turbulences (ring vortices) that mixed curtain and plume material close to the crater and overran the ballistic ejecta [cf.8].

References: [1] Urrutia-Fucugauchi J. et al. (1996) *Geophys. Res. Let. 23(13)*, 1565-1568. [2] Pope K. O. et al. (2005) *GSA Spec. Pap. 384,* 171–190. [3] Kenkmann T. and Schönian F. (2006) *Meteoritics & Planet. Sci. 41(10),* 1587-1603. [4] Pope K.O. et al. (2004) *Meteoritics & Planet. Sci. 39(1)*, 97-116. [5] Schönian F. et al. (2003) *3rd Int. Conf. Large Met. Impacts*, Abstract #4128. [6] Schönian F. et al. (2006) *LPS XXXVII*, Abstract #2229. [7] Schönian F. et al. (2005) *LPS XXXVI*, Abstract #2389. [8] Barnouin-Jha O. et al. (2005) *JGR 110*, E04010, 1-22.

FRICTIONAL MELT FORMATION AROUND LARGE CRATERS.

L. E. Senft[1] and S. T. Stewart[1], [1]Dept. of Earth & Planetary Sciences, Harvard University, 20 Oxford St., Cambridge, MA 02138 (lsenft@fas.harvard.edu).

Introduction: Frictional melts (pseudotachylites) are observed around many large impact craters and may play a role in aiding crater collapse. Here we use numerical modeling to predict where frictional melts should form and compare results to field observations.

Background: Lab and field measurements have demonstrated that there is a significant reduction in friction along a fault at high slip rates (~1 m/s) and long displacements (>1 m) [1-6]. This reduction occurs in two stages (with a strengthening regime in between): (1) flash heating along asperities (melting occurs along a small surface area of the fault), and (2) generation of a continuous melt layer along the fault. The friction during stage (2) is determined by a balance between melt production, melt loss, and melt viscosity [2,7]. Lab measurements of low friction are in agreement with field estimates of co-seismic friction [3], suggesting that frictional melting plays an important role in determining the strength along some faults.

Cratering Simulations: Crater formation is simulated using a quasi-static strength-damage model for rocks with dynamic strength reduction due to frictional melting. The quasi-static strength-damage model of Collins et al. [8] is implemented in the CTH shock physics code [9]. In this model, the shear yield strength is degraded from an intact strength to a damaged strength, which is controlled by motion along fractures. The damaged strength follows a friction law, $Y_d = Y_c + \mu P$ (Y_d is the damaged strength, Y_c is the cohesion, μ is the coefficient of friction, and P is the pressure), where μ is 0.85 for low pressures and 0.6 for higher pressure and Y_c is 0 [10]. Tensile strength is a function of damage, and void is added when a cell is failing in tension to simulate tensile crack formation. As an approximation of frictional melting effects, when (1) the shear strain rate (in terms of the square root of the second invariant of the deviatoric strain rate tensor, $II'_{\dot{\epsilon}}$), (2) the damage, and (3) the integrated plastic shear strain times the projectile diameter are above certain cutoff values ($\dot{\epsilon}_{cut}$, d_{cut}, and ϵ_{cut}), then the coefficient of friction is reduced to a new value (μ'). μ' is some complex function involving a number of factors, including velocity, rock type, fault geometry, and slip distance, but we approximate it by a single value for exploratory purposes. We choose $\dot{\epsilon}_{cut} = 0.01\ \mathrm{s}^{-1}$ and $\mu' = 0.2$ based on lab data of frictional melting. To restrict frictional melting to fractured material, we choose $d_{cut} = 0.9$. An integrated strain cutoff is necessary because even if strain rates are high, a threshold amount of slip must occur to generate enough energy for melting. Note that the slip must be scaled by some length parameter (otherwise frictional melting will occur at craters of all sizes, because the strains are similar even though the displacements are not). This parameter should be the fault length, however this is impossible to ascertain during the simulation. Instead we scale by the projectile diameter, based on the assumption that longer faults are produced around larger craters. We experimented with a range of choices for ϵ_{cut} and chose a value (1 m) that precluded frictional melting around small, simple craters (where fault displacements are too small for frictional melting), while allowing it around larger craters. This value is consistent with lab measurements of the slip needed to generate melting (>1 m) in rocks.

Results: Figure 1 shows the results for the impact of a 10-km in diameter impactor hitting the Earth's surface at 17 km/s (Chicxulub-size; a geotherm and lithostatic pressure are included). The target and projectile are basaltic. The target is well resolved: 125 meters per cell (80 cells across the projectile). A-D show areas (red) where frictional melting is occurring and E-H show integrated plastic shear strain.

During shock wave expansion and crater excavation (E) conical (concave down) shear localizations (which we interpret as fractures or fracture networks) are formed behind the shock wave. The strain rates and displacements are high enough during their formation to generate frictional melts (A). Note that spontaneous localization of deformation is seen in all calculations whether or not frictional melting effects are accounted for; however, it is the additional decrement of the friction due to these effects that allows the fractures to grow. Because the fracture zones are weak, slip occurs preferentially along them; this causes stress to concentrate at the tip of the fractures until failure and extension occur. After passage of the shock wave, the strain rates decay and frictional melting temporarily ceases. The stresses created by the transient crater's gravitationally unstable shape build up until new fractures are generated with strain rates high enough to undergo frictional melting. Vertical fractures under the floor (labeled 1 in B) aid floor uplift and shallow listric fractures in the wall (labeled 2 in B) aid wall collapse. At later times, slip transfers from the vertically oriented fractures under the floor to a set of steeply dipping concentric fractures under the crater (labeled 3 in C), which shallow as the crater collapses (labeled 4 in D). The frictional melting that appears to be occurring along the x=0 boundary in C and D is an artifact resulting from the centerline boundary condition. The width, spacing, and number of fractures is resolution dependent; however, their basic presence and orientation is not. Note also that the actual fractures will be thinner than the calculation; artificial viscosity and the eulerian meshing spreads the deformation across multiple cells.

Comparison with Field Observations: The model predictions for where frictional melting should occur are broadly consistent with the location and orientation of pseudotachylites around terrestrial craters. The most extensively studied impact related pseudotachylites are around Vredefort Dome (>250 km diameter), South Africa and the Sudbury Structure (>200 km diameter), Canada. Note that the term "pseudotachylite" indicates a melted zone but does imply a genetic origin; pseudotachylites at impact craters may be shock induced and/or friction induced melts [11]. Pseudotachylites around Sudbury are concentrated into three large rings (with randomly oriented smaller networks in between); the first ring encircles the central uplift and the second two appear to be related to wall and terrace collapse [12]. Our model shows a zone of frictional melting surrounding the central uplift (features labeled 1 in B, 3 in C and 4 in D), and a zone of shallowly dipping listric faults undergoing frictional melting at and beyond the rim area (features labeled 2 in B). This is consistent with the zones observed at Sudbury. The floor directly under the central uplift is not observable at Sudbury; however this area is well exposed at Vredefort. Pseudotachylites are abundant in the crater floor at Vredefort, and while they do not show any preferred orientation, most have steep to vertical dips [13]. It is possible that the observed pseudotachylites were formed during shock wave expansion (A) and/or as vertical faults during floor collapse (features labeled 1 in B).

Simulations of smaller complex craters (10's km in diameter) with frictional melting mainly display movement along deep seated concentric faults, such as those seen in C and D.

Summary: We performed cratering simulations with a simple proxy for frictional melting, with parameters constrained by lab results. The simulations predict the location and timing for frictional melt formation, and the results are in good agreement with field observations. Frictional melting may play a significant role during crater collapse. Finally, we note that the occurrence of frictional melting will depend on rock type; this abstract discussed only crystalline targets, but future work will consider sedimentary targets.

References: [1] A. Tsutsumi and T. Shimamoto (1997) GRL 6, 699. [2] T. Hirose and T. Shimamoto (2005) JGR 110, 2004JB003207. [3] G. DiToro et. al. (2006) Science 311, 647. [4] K. Mizoguchi et. al. (2007) GRL 34, 2006GL027931. [5] D. L. Goldsby and T.E. Tullis (2002) GRL 29(17), 2002GL015240. [6] G. DiToro, D.L. Goldsby, and T.E. Tullis (2004) Nature 427, 436. [7] H.J. Melosh (2005) in Impact Sudies, vol 6; eds C. Koeberl and H. Henkel [8] G.S. Collins and H.J. Melosh (2004) MAPS 39, 217. [9] L.E. Senft and S.T. Stewart (2007) JGR 112, 2007JE002894. [10] J. Byerlee (1978) Pure App. Geophys. 116, 615. [11] W.U. Reimold (1995) Earth Sci. Rev. 39, 247. [12] J.G. Spray, H.R. Butler, and L.M. Thompson (2004) MAPS 39, 287. [13] B.O. Dressler and W.U. Reimold (2004) Earth Sci. Rev. 67, 1.

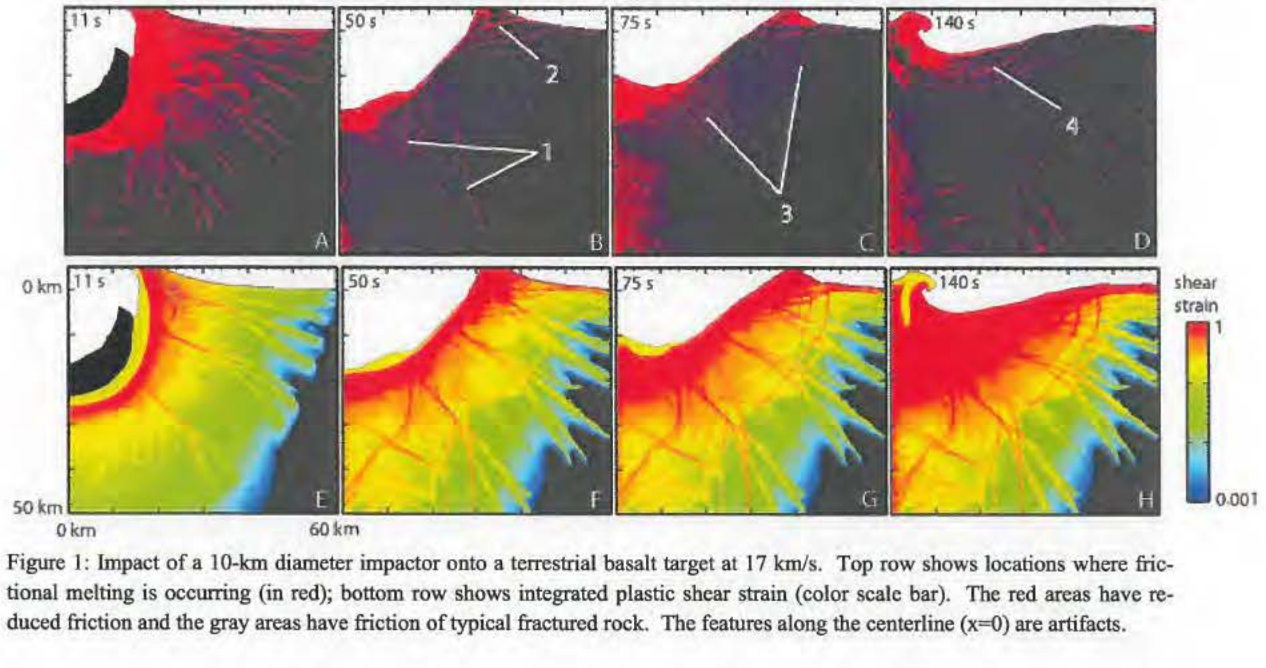

Figure 1: Impact of a 10-km diameter impactor onto a terrestrial basalt target at 17 km/s. Top row shows locations where frictional melting is occurring (in red); bottom row shows integrated plastic shear strain (color scale bar). The red areas have reduced friction and the gray areas have friction of typical fractured rock. The features along the centerline (x=0) are artifacts.

ADVANCES IN MODELING COLLISIONS ON ICY BODIES.

S. T. Stewart and L. E. Senft. Dept. of Earth & Planetary Sciences, Harvard University, 20 Oxford St., Cambridge, MA 02138, U.S.A. (sstewart@eps.harvard.edu).

Introduction: Impact cratering is one of the major geologic processes on the icy planets and satellites in the solar system. Impact cratering calculations have been used to suggest the presence of transient liquid water [1-4] and to infer the thickness of brittle crusts [5]. These studies rely heavily on the accuracy of (1) the model equation of state of H_2O to infer the post-impact temperature field and the occurrence of phase changes and (2) the constitutive model to describe the quasi-static and dynamic strength of the material. Here, we present recent advances in the quality of equation of state and constitutive models for H_2O and implications for collisional processes on icy bodies.

Equation of State Model: Because of the complexity of the H_2O phase diagram, most equation of state (EOS) models used in hydrocode calculations have been tailored to specific phases with little or no ability to extend calculations to broad regions of the phase diagram. In general the phase diagram has been simplified, with one solid phase, liquid, and vapor, such as the ANEOS model described in [5]. Recent development includes an ANEOS-derived tabular multiphase EOS that includes all of the stable solid phases, liquid, and vapor [6].

We have developed a new tabular EOS for H_2O [7]. The table includes three solid phases (ices Ih, VI, and VII), liquid, and vapor. The EOS of the phases and phase boundaries are experimentally determined. The liquid and vapor are described by the International Association for the Properties of Water and Steam (IAPWS) [8]. The EOS of ice Ih is given by [9]. The EOS of ices VI and VII are taken from [10], and the phase boundaries are given by [8, 11]. The model shock Hugoniots starting as liquid and ice Ih are in excellent agreement with experimental data.

A crucial experimental data set that has been lacking for EOS model validation is shock temperature measurements starting in the ice phase (shock temperatures in liquid water have been measured by [12, 13]). In the Shock Compression Laboratory at Harvard, we have new peak-shock and post-shock temperature measurements in ~150 K polycrystalline ice Ih in the peak shock pressure range of 8.2 to 13.6 GPa [14]. Peak shock temperatures range from 666 to 1044 K and post-shock temperatures are 380 to 495 K. The new tabular EOS is a great improvement over previous EOS models in this pressure range (Fig. 1).

The post-shock temperature provides direct information about the onset and kinetics of shock-induced phase changes. The shock states at these modest pressures are all supercritical (critical point: 647 K, 22 MPa). Under most impact conditions, the isentropic release path intersects the saturation vapor curve. In the μs time scale of the experiments, the observed post-shock temperatures fall on the saturation vapor curve. Further decompression requires the formation of vapor, and the necessary volume expansion is inhibited by the geometry and time scale of the experiment. Transiently hot and pressurized liquid water may lead to interesting dynamic phenomena during crater formation.

The post-shock temperature measurement on the saturation vapor curve defines the entropy in the shock state. Hence, we derive the critical shock pressure required for incipient vaporization to be 8 GPa (3.6 GPa) for release to 1 bar (6 mbar) ambient pressure. The critical shock pressure required for complete vaporization is derived from the new EOS table to be 53 GPa (65 GPa) for release to 1 bar (6 mbar), in excellent agreement with calculations in [10]. Accurate EOS are required to define the initial shock pressure field from the impact and the volumes of shock-induced vapor and melt. Shock-induced vaporization and melting steepen the shock wave decay profile. For ice on ice impacts at 5 km/s and peak pressures around 12 GPa, the power law decay exponent is -1.9 at distances between 2 and 8 projectile diameters. The decay exponent steepens to -3.4 for impacts at 20 km/s and peak pressures of 150 GPa.

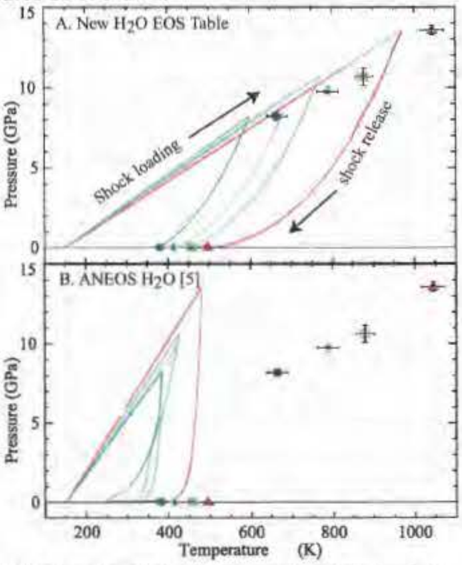

Fig. 1. Peak and post-shock temperature data (paired points, [14]) compared with calculated shock loading and release

paths from two different model equations of state (lines).

Strength Model: A typical strength model describes the quasi-static response of a material to deviatoric stresses, with weakening due to fracturing (described by a dimensionless damage variable). For crater formation, dynamic weakening processes must also be considered (e.g., acoustic fluidization or frictional melting).

We implemented the quasi-static strength-damage model developed by [15] in the CTH shock physics code [16] and fitted parameters for H_2O based on laboratory data. In this model, shear strength is linearly degraded from an intact strength value (strength controlled by the creation of new fractures) to a fragmented (strength controlled by friction) value. A dimensionless scalar variable called damage is introduced to track this degradation; completely intact rock has a damage of zero, and completely fragmented rock has a damage of one. Thus, shear strength is a function of damage, temperature, and pressure, and tensile strength is a function of damage.

Strength parameters are chosen by fitting to quasi-static laboratory test data [17-20]. The shear strength data of intact (non-damaged) ice [20] (circles) and the shear strength data of fragmented (damaged) ice [18] (triangles) are compared to the quasi-static strength-damage model in Fig. 2. Note that the strength of ice has a strong temperature dependence. We fit a temperature degradation function to uniaxial compression data from [17] and use this to calculate the strengths at other temperatures. For example, the 210 K intact and damaged shear strength curves are shown in Fig. 2.

Measurements of fresh complex craters on the icy satellites show that these craters are generally much shallower than their lunar counterparts [21, 22], which is expected as a result of the very low coefficient of friction of ice (~0.2 for cold ice, 77 K) as compared to rock (~0.6). Cratering simulations using the quasi-static strength model have shown that craters in pure ice surfaces or rocky surfaces with icy layers have shallow depth to diameter ratios [7, 22].

Furthermore, crater collapse may be aided by frictional melting processes [23, 24]. Frictional melting is observed in laboratory experiments on ice [25] under conditions that should be pervasive during impact events. The dynamic reduction in friction is significant: at a temperature of -10° C, the coefficient of friction of ice approaches 0.001 as the sliding velocity along a fault approaches 1 m/s [25]. Thus, frictional melting effects need to be considered when modeling impacts on icy bodies.

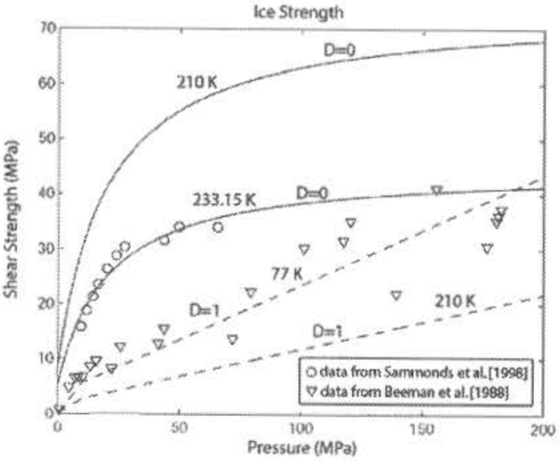

Fig. 2. Shear strength (in terms of the square root of the second invariant of the deviatoric stress tensor, $\sqrt{J_2}$) for fragmented ice (i.e. ice-on-ice friction; dashed lines) and intact ice (solid lines). Also shown are strength curves at 210 K, appropriate for models of cratering on Mars.

Summary: We have developed a new multi-phase equation of state for H_2O and a strength model for ice that are appropriate for the wide range of impact conditions in the solar system. With these advances, we are able to model collisions onto icy bodies with much better accuracy.

References: [1] Artemieva, N. and J.I. Lunine (2005) *Icarus* **175**, 522. [2] Artemieva, N. and J. Lunine (2003) *Icarus* **164**, 47. [3] Pierazzo, E., N.A. Artemieva, and B.A. Ivanov (2005) *GSA* **384**, 443. [4] Stewart, S.T., J.D. O'Keefe, and T.J. Ahrens (2004) *Shock Comp. Cond. Mat. - 2003*, 1484. [5] Turtle, E.P. and E. Pierazzo (2001) *Science* **294**, 1326. [6] Ivanov, B.A. (2005) *LPSC* **36**, Abs. 1232. [7] Senft, L.E. and S.T. Stewart (submitted) *MAPS*. [8] Wagner, W. and A. Pruss (2002) *JPCRA* **31**, 387. [9] Feistel, R. and W. Wagner (2006) *JPCRA* **35**, 1021. [10] Stewart, S.T. and T.J. Ahrens (2005) *JGR* **110**, E03005. [11] Frank, M.R., Y.W. Fei, and J.Z. Hu (2004) *Geo. Cos. Acta* **68**, 2781. [12] Kormer, S.B. (1968) *Soviet Physics USPEKHI* **11**, 229. [13] Lyzenga, G.A., et al. (1982) *Jour. Chem. Phys.* **76**, 6282. [14] Stewart, S.T., A. Seifter, and A.W. Obst (2008) *LPSC* **39**, Abs. 2301. [15] Collins, G.S., H.J. Melosh, and B.A. Ivanov (2004) *MAPS* **39**, 217. [16] Senft, L.E. and S.T. Stewart (2007) *JGR* **112**, E11002. [17] Arakawa, M. and N. Maeno (1997) *Cold Reg. Sci. Tech.* **26**, 215. [18] Beeman, M., W.B. Durham, and S.H. Kirby (1988) *JGR* **93**, 7625. [19] Lange, M.A. and T.J. Ahrens (1983) *JGR* **88**, 1197. [20] Sammonds, P.R., S.A.F. Murrell, and M.A. Rist (1998) *JGR* **103**, 21,795. [21] Schenk, P.M. (2002) *Nature* **417**, 419. [22] Bray, V.J., et al. (submitted) *MAPS*. [23] Senft, L.E. and S.T. Stewart (2008) *LPSC* **39**, Abs. 1417. [24] Senft, L.E. and S.T. Stewart (2008) *LMI IV*, Abs. 3077. [25] Maeno, N., et al. (2003) *Can. Journ. Phys.* **81**, 241.

DEVELOPMENT OF GEOTOURISM IN THE NATIONAL GEOPARK RIES, SOUTHERN GERMANY

D. Stöffler[1], G. Pösges[2],and R. Barfeld[3]. [1]Natural History Museum, Humboldt-University, D- 10115 Berlin, Germany, dieter.stoeffler@museum.hu-berlin.de; [2]Ries Crater Museum, Eugene-Shoemaker-Platz 1, D-86720 Nördlingen, Bavaria, Germany; ZERIN (Centre for Ries Crater and Impact Research Nördlingen), Vordere Gerbergasse 3, D-86720 Nördlingen, poesges.gisela@noerdlingen.de; [3]Ing.- Büro Barfeld, Hutergasse 1, D-86720 Noerdlingen, Bavaria, Germany, ibbarfeld@t-online.de

Introduction. The Geopark Ries in Southern Germany represents a unique natural and cultural landscape that has its origin in a cosmic event. The Geopark covers an area of 1800 km^2 comprising 5 different counties with a total of 53 communities. Therefore, the Ries is the most densely populated impact crater on Earth. Because of its unique characteristics the "Ries of Nördlingen" has been certified as a National Geopark in May 2006. It is the first Geopark in Bavaria [1, 2, 3].

The Ries crater: The „Ries of Nördlingen", a 25 km sized circular basin, and its satellite crater – the 3.8 km sized Steinheim basin – were formed 14.5 million years ago by the impact of a large asteroid (~ 1.2 km in diameter) which was orbited by a small satellite (~ 200 m in diameter) [4, 5]. The Ries crater is the only so-called complex impact crater worldwide where the crater structure and a large part of the ejecta blanket are well preserved and morphologically still visible. The double crater – Ries and Steinheim - represents a singularity in the natural heritage of Europe as it offers an extraordinary example of an interaction between a special type of landscape and its cultural development. In contrast to all other types of natural environments on Earth impact craters such as the Ries crater are formed as an extreme short and highly dynamic process. The Ries impact during which a transient, ~ 5 km deep and 12 km wide crater collapsed into a flat, 600 m deep crater with a central ring structure and a 25 km wide crater rim, took place within a time frame of only about one minute. During this short crater-forming process several "new" rock types such as "Suevite" and "Bunte Breccia" were formed [6, 7] (Figs. 1 and 2).

Fig. 1: Suevite on top of Bunte Breccia, Aumühle, Ries

In fact, The Ries is the type locality of suevite, an impact breccia named after the Latin word "suevia" (German = Schwaben) and used now for this type of rock worldwide [7]. After the impact the crater contained a lake for about 2 millions years in which post-impact freshwater limestone was formed. These different types of rocks have been used as building stones and also as source products for the cement production located in the Ries. The cathedral of Nördlingen and even relics of Roman buildings consist of suevite.

Goals of the Geopark: The park is aimed to highlight this unique region for laymen visitors as well as geological experts by demonstrating its origin and history from its cosmic roots to its terrestrial after-effects. Besides geological outcrops and quarries, there are other attractive sightseeing sites which include relics of the first stone-age settlements (some 40,000 years old) to be found in karst caves, as well as relics of the Celtic, Roman and Alemannic settlements [e.g., 8]. The Geopark is extremely rich in the testimony of Middle age architecture as documented by cities, castles, monasteries and churches.

Project planning and implemetation: As part of the development of the National Geopark Ries a systematic assessment of a total of about 350 geotopes is currently undertaken [3]. The mapping effort and the archiving of relevant data include also deep drilling sites which help to get information about the deep structure and lithological character of the Ries impact crater. Five geotopes within the area of the Geopark Ries belong to the list of "Bavarias most beautiful geotopes" which is an intiative of the Bavarian State Office for Environmental Protection. As a next step after completion of the archiving effort touristically attractive geotopes will be selected and combined into a network of sightseeing tours for Geopark tourists. At this time 16 different sightseeing tours have been defined. They include tours to be made by car (or bus), bicycle and by walking and are planned for short and long duration visits of the Geopark (1-5 days). It is planned to implement about 10 of these tours.

Although the project planning for the Geopark Ries, and its implementation are not yet completed, the park offers already several attractive elements: (1) A professionally made "Information Center" in the heart of the middle age city of Nördlingen, (2) a first visitor tour through the crater, the so-called "Schäferweg" ("Shepherd Trail") (3) the Ries Crater Museum at Nördlingen established in 1990 [9] and devoted not only to the Ries but also to impact processes in the Solar System in general, (4) the "Trail of Planets" starting at the cathedral of Nördlingen (Sun) and ending at the crater rim which represents the orbit of Pluto, and (5) the ZERIN (Center for Ries and impact crater research) which archives drill cores and other samples from the Ries and offers facilities for visiting scientists.

References. [1] Pösges G., Barfeld R. and Stöffler D. (2008) *Schriftenreihe der Deutschen Geologischen Gesellschaft, Heft 56, 22-25,* Hannover. [2] Stöffler D., Pösges G., Arp G., Kenkmann T., Reimold U. and Wünnemann K. (2008) *3rd International UNESCO Conference on Geoparks, 22.06.–26.06. 2008, Osnabrück.* [3] Barfeld R., Pösges G. and Stöffler D. (2008) *Schriftenreihe der Deutschen Geologischen Gesellschaft, Heft 56, 22-25,* Hannover. [4] Stöffler D. et al. (2002) Meteoritics & Planet. Sci. 37, 1893-1907. [5] Wünnemann K. et al. (2004) in Kenkmann T. et al. (eds.) Large meteorite impacts III, Geological Society of America Special Paper 384, 67-83. [6] Stöffler D. (1966) *Contr. Mineral. and Petrol. 12, 15-24.* [7] Stöffler, D. and Grieve, R. A. F. *(2007)* in Fettes D. and Desmons J. (eds.) *Metamorphic Rocks: A Classification and Glossary of Terms, Recommendations of the IUGS, 111-125, 126-242,* Cambridge Univ. Press, Cambrige, [8] Krause R. (2004) *Arch. Inf. Baden-Württemberg 47,* Stuttgart. [9] Pösges G. and Schieber M. (1997) *Academy Bulletin Nr. 253, Bavarian Academy for Teacher Training,* Dillingen , Pfeil-Verlag, München.

Fig. 2: Formation of the Ries impact crater; yellow = Tertiary, blue = Malmian, brown = Triassic, pink = crystalline rocks; projectile diameter = 1.2 km;

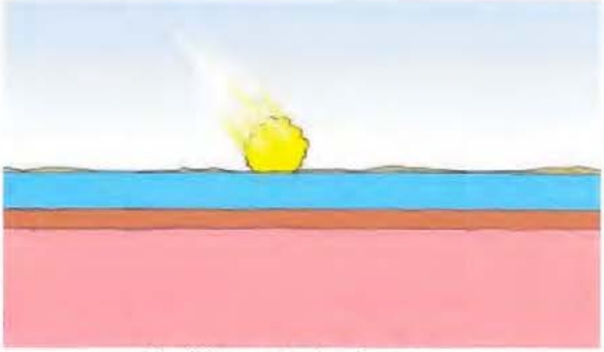

10 milliseconds after impact

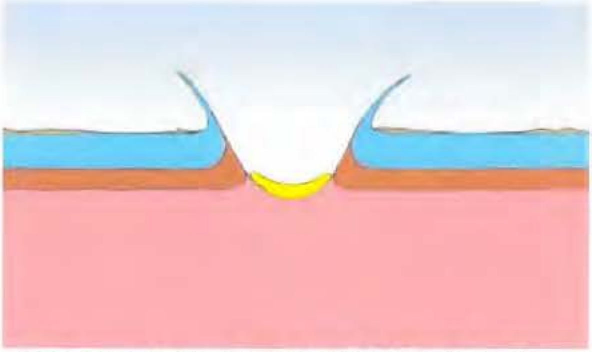

Beginning of crater formation after 60 milliseconds

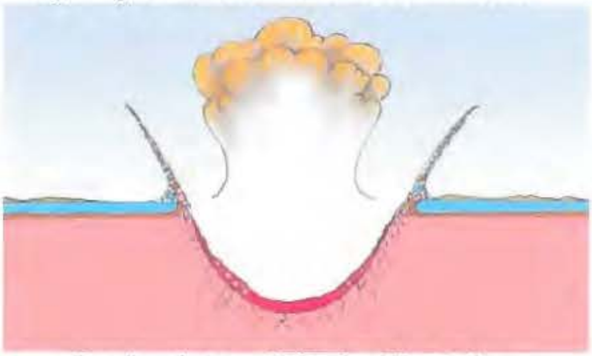

Deep "transient crater" after about 10 seconds

Collapse of the "transient crater" and deposition of ejected rock masses after 1 minute

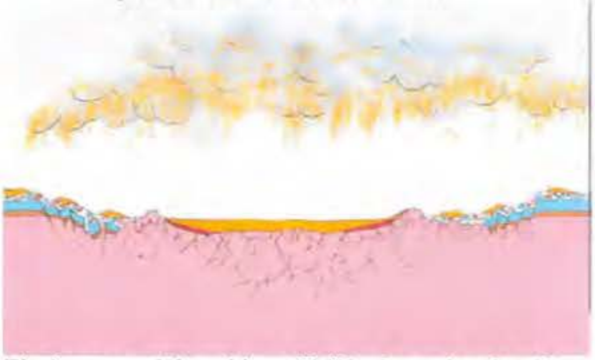

Final crater and deposition of fall back suevite after 10 minutes; orange = suevite, red = impact melt rock

BRECCIAS AND GEOLOGICAL SETTING OF THE SANTA FE, NEW MEXICO USA IMPACT STRUCTURE.

E. L. Tegtmeier[1], H. E. Newsom[1], W. E. Elston[1], and T. H. McElvain[2], [1] Department of Earth and Planetary Sciences, University of New Mexico, MSC03- 2050 Albuquerque 87131, teggy@unm.edu, newsom@unm.edu, [2]111 Lovato Lane, Santa Fe, NM 87505.

Introduction: The discovery of shatter cones [1] in Proterozoic crystalline rocks in the western foothills of the southern Sangre De Cristo Mountains [2], a branch of the southern Rocky Mountains near Santa Fe New Mexico, USA, has prompted a study of widespread pervasive brecciation. Current reconnaisance is concentrated on a belt 6 km west of the shatter cones The emphasis is on field work and petrography. A search for additional impact criteria of impact is in progress.

Shatter cones crop out over a distance of 1.6 km along NM State Highway 475, beginning ~8 km east of the Santa Fe city limits (Fig. 1). Due to mountainous topography, their north-south extent has not yet been determined but is estimated to be < 1 km on either side of the road. The shatter cones locality is not brecciated significantly; pervasive brecciation increases towards the west. Breccias have been found 10 km ESE but their full extent in the intervening area not known. The problem of their distribution is complicated by multiple tectonic events before, after, and possibly coincident with the inferred impact event. The structure of the region is one of the most controversial topics in New Mexico geology: major Phanerozoic faults with lateral displacement > 100 km have been proposed [3]. One major fault terminates the shatter cone locality to the east.

Geologic Setting: The southern Sangre de Cristo range is a block of biotite schist and granite gneiss with metamorphic age 1.65 Ga, invaded by pegmatites and other granitoid rocks at 1.4 Ga. In the western foothills, Pennsylvanian (Upper Carboniferous) carbonates rest on Proterozoic rocks with depositional contact. Major disturbances associated with the 1.65 and 1.4 Ga Proterozoic episodes antedate shatter cone formation and pervasive brecciation. Later tectonic events include the rise of the Pennsylvanian to Permian Ancestral Rockies, Cretaceous to Paleocene Laramide orogeny and a sequence of late Cenozoic events culminating in vertical movement of several km (uplift of the present north-trending mountains and subsidence of the Rio Grande Rift to the west).

Shatter cones and pervasive brecciation occur in all types of Proterozoic rocks. Pennsylvanian and younger rocks are locally brecciated where cut by faults related to Phanerozoic tectonic events. The timing of inferred impact is probably constrained between emplacement of granitoids and Pennsylvanian deposition. However, within 2 m of the Pennsylvanian-Proterzoic contact, Pennsylvanian and Proterozoic clasts are locally intermingled. (Fig. 2) This probably reflects mass wasting during uplift of the Ancestral Rockies. However, impact during or after an early stage of Ancestral Rocky tectonism cannot be ruled out.

Regional Brecciation: West from the shatter cone outcrops, three major gradational transitions of brecciation intensity can be recognized:

Within 1 km, the crystalline rocks are broken by numerous faults with m-range displacements in random orientations. The rocks appear to be jostled without significant displacement. Type of brecciation depends on rock type. The granite gneiss breaks into blocks up to m size with varying degrees of fractal internal brecciation whereas biotite schists are broken into decimeter to meter size blocks. (Fig. 3)

Within 2.5 km, the rocks are still jostled by numerous faults. The maximum size of angular granite gneiss clasts has decreased to ~ 10 cm set in a fractal matrix of similar material. In general, the fracturing appears to haved occured in-situ with little displacements of clasts. Biotite schist is internally fractured, sheared, and boudinaged along contacts with granite gneiss (Fig. 4). From this locality to the west internal brecciation decreases to the edge of the range.

Pods of Granite Gneiss Breccia: Numerous breccia pods, (horizontal dimensions ≤ 10x15 m, vertical exent unknown) form conspicuous walls aligned NNW. They are confined to the zone of most pervasive brecciation. Within the pods, granite gneisss clasts range from cm to m, supported by a fractal matrix of the same material heavily impregnated with hematite. Horizontal zoning suggests that the pods were emplaced by vertical movement. Within 1 m of breccia pod contacts with wall-rock, clasts tend to be subrounded, whereas internally they are angular. Where breccia pods were emplaced in biotite schist, clasts of schist ≤ 1 m occur within 1 m of the contact. They are enclosed by rinds, cm's wide, made up of accreted mm-cm size granite gneiss fragments (Fig. 5).

Timing of Brecciation: In Pennsylvanian rocks brecciation is confined to the vicinity of Phanerozoic structures. Complications arise because of possible reactivation of Proterozoic structures. However, brecciation is much more widespread in the Proterozoic rocks. The evidence suggests that brecciation occurred well before the onset of Pennsylvanian deposition.

Interpretations: Shatter cones are the only definitive evidence for impact. Because outcrops are limited to one mountain range of controversial structure, the geometry and erosion level of the inferred impact structure remain uncertain.

Speculatively, the zone of pervasive breccias suggests passage of an impact-induced shock wave which fractured rocks to the limit of microscopic resolution, but only caused m-scale displacements. The breccia pods may have been emplaced from above into zones of subcrater dilation, along pre-existing fractures.

References: [1] Fackelman, S.P. et al. (2006) *Geol. Soc. America Abstr. W. Programs,* v. 38, No. 7, p. 298. [2] Read, A. S. et al. (2003), *Open File Map GM 32,* N.M. Bur. Geology & Mineral Resources, 1:24,000 [3] Cather, S. M. et al. (2006) *Geol. Soc. America Geosphere* v. 2, p. 299-323.

Acknowledgements: Partial funding from NASA P.G. &G. program (H. Newsom).

Figures: Distances are in km (miles), along NM State 475, from shatter cone outcrops.

Figure 1. Shatter cones in granite gneiss. 9 km (5.7 mi) from intersection of NM State 475 and NM state 590

Figure 2. Clast of Proterozoic granite gneiss in brecciated Pennsylvanian Limestone. Little Tesuque Canyon, 4 km west of location of figure 3.

Figure 3: Interlayered granite gneiss and biotite schist offset by randomly oriented m-scale faults. Granite gneiss is broken to decimeter to m size clasts. Biotite schist is sheared and broken to similar scale. Height of photo ~3 m. 2.5 km (1.5 mi).

Figure 4: Pennsylvanian limestone on blocks of intensely brecciated granite gneiss and biotite schist. Height is 3 m. 2.6 km (1.55mi).

Figure 5: Clast of biotite schist with accretionary envelope near contact of breccia pod. 200 m from figure 3.

MORPHOLOGICAL INVESTIGATION OF VREDEFORT USING REMOTE SENSING, GIS AND 3D MODELLING

C. L. Townsend[1], M.E. Phillips[1,2], [1]Centre for GIS & Remote Sensing, School of Science, University of Greenwich, Chatham Maritime, U.K. [2]Planetary Science Research Group, Environmental Science Department, University of Lancaster, Lancaster, U.K. (email: Carl Townsend, skymapper639@impactcraters.info)

Introduction: Vredefort is an old (2.2Ga), highly eroded remnant meteorite impact structure. The original size, morphology and exact type of impact structure at Vredefort has been the subject of some considerable research and debate, [1-5] and a number of methods have been used to determine this, including Geophysics [1], Structural Geology [2,3], and Remote Sensing [6]. To this end, several 3D Digital Elevation Models (DEMs) of Vredefort were created, and together with with existing Landsat Thematic Mapper (TM), geological and digitized vector data, were integrated into a GIS for analysis [7].

Methodology: 12, 1:50,000 topographic maps, covering an area of approximately 4700km^2 of the Vredefort area were used to create the 3 DEMs in 100, 30 and 10 metre resolutions (Fig.1).

Figure 1. 30m DEM of Vredefort, approx. 53km x 90km

Crucially, various Landsat TM image band combinations from a previous study of Vredefort [6] were also integrated and draped over the DEM. to assist in the recognition, identification and confirmation of structural features previously identified by RS [6,8] (Fig. 2). These features were also investigated by means of a series of 2D topographic profiles generated from the DEM.

Figure 2. False Colour Landsat RGB 457 draped over the DEM showing the Inner Ring Collar and Vaal River (red). View looking North.

Drainage features from these maps were also captured into a GIS, along with faults/fractures around the Inner Ring Collar from a 1:250,000 geological map (Fig.3)

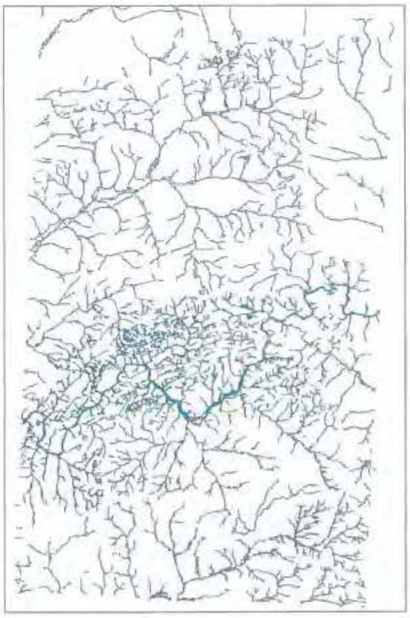

Figure 3. Drainage patterns at Vredefort.

Results: Integrating the DEM with the Landsat imagery and drainage patterns confirmed the existence of a number of previously reported [6,8] radial features at intervals along the Foch Thrust Zone and perpendicular to it, which when extrapolated intersect at the centre of the Vredefort Structure. These radial features were also observed along the Ensels Thrust Zone and the Inner Ring Collar [6-8]. By using the DEM and topographical profiling, geological thrust fault angle data from the Foch and Ensels Thrust zones, and estimates for the amount of vertical erosion, an Inverted Cone Model was developed in order to produce an 'upwards and outwards' extrapolation of Vredefort, in an effort to determine the original size of the structure [7]. The model applied found that Vredefort would have had at least two ring structures at diameters of 146km and 186km, identified as the Ensels and Foch Thrust Zones respectively The model was then applied to the Rietfontein fault and Rand Anticline (outside of the DEM area) to give a final diameter of 281km. Finally, the DEM revealed the existence of a previously unreported, circular to lobate structure with a diameter of approximately 18km and a relief of about 60m within the very central core of Vredefort itself (Figures 4 and 5).

Figure 4. DEM of the central core structure approx 40km x 40km

Figure 5. Field photo of part of the central core structure, looking Northeast (Photo by author)

Conclusions: Vredefort is very likely a multi-ring structure, with at least two, probably three ring structures, in agreement with previous workers [1-3,9]. However, while multi-ring structures are apparently common on other bodies in the Solar System, they appear to be quite rare on Earth [10,11]. Improved satellite imagery, and the creation of high resolution DEMs of large areas together with the integration of vector data, geological, geophysical and structural data into a GIS and 3D environment, can be a useful and powerful technique in determining the exact types and morphologies of other large impact structures on Earth.

References: [1] Henkel, H. & Reimold, W.U. 1998. Tectonophysics, 287, 1-20. [2] Andreoli, M.A.G. 1991. Structural Map, Atomic Energy Corporation, Pretoria. [3] Brink, M.C. *et al.* 1997. Tectonophysics, 270, 83-114. [4] Pilkington, M. & Grieve, R.A.F. 1992. Review of Geophysics, 30, 2, 161-181. [5] Rondot, J. 1994. Earth Science Reviews, 35, 331-365. [6] Phillips, M.E. 1999. Unpublished BSc thesis. [7] Townsend, C. 2001. Unpublished BSc Thesis, University of Greenwich, UK. [8] Phillips, M.E. *et al.* 1999. Abstracts of the 62nd Meteoritical Society Meeting. [9] Grieve, R.A.F. *et al.* 1995. GSA Today, Vol 5 No 10, p 194-197. [10] Melosh, H.J. 1996. Impact Cratering, A Geologic Process. Oxford Uni. Press. [11] Thierriault, A. M., *et al.*1997. Meteoritics & Planetary Science, vol. 32, 71-77.

PGE ENRICHMENT AT THE KTB: IS IT A SIGN OF CAUSE OR A SIGN OF EFFECT?

M. Tredoux, Dept of Geology, University of the Free State, PO Box 339, Bloemfontein 9300, South Africa; mtredoux.sci@ufs.ac.za.

Introduction: The status of the Chicxulub impact event as the sole destroyer of the dinosaurs, and all the other species which became extinct at the end of the Cretaceous Era, has by now become entrenched in the broader scientific literature. The associated idea that the presence of platinum-group elements (PGE) in the boundary sediments is strong, perhaps even the strongest, evidence for this impact is equally strongly held. However, there is no *de facto* evidence that the PGE found at the KTB is either primary, or unique.

Features with the PGE signature at the KTB: If the siderophile geochemistry of the KTB is a primary, essentially undisturbed fall-out layer, one would expect that (i) it is present at all well-preserved KTB sections, and (ii) interelement ratios are preserved and that they are close to those of some known meteorite type. At closer inspection of the global KTB geochemistry it becomes clear that neither of these conditions hold true. Verhagen et al. [1] were just one of many sets of workers who reported finding no anomalous chemical signature at a KTB in the Kwazulu-Natal province of South Africa, despite evidence from nano- and micro-fossils and O and C stable isotope anomalies, that the boundary was well preserved and stratigraphically complete. As far as the second citerion above goes, Tredoux et al. [2] pointed out that the PGE chemistry differed between the northern and southern hemispheres and that neither the inter-PGE ratios, nor ratios of the base metals, were chondritic; these authors ascribed the differences to formation of the anomalies in the boundary layer sediments subsequent to deposition. The global variability of the PGE was also investigated by Evans et el. [3], who attributed it to preferential oxidation of Ru relative to Ir in an ejecta cloud.

Is the geochemical signature of the KTB unique?: Coal measures, and other reduced sedimentary rocks, often have elevated concentrations of siderophile elements [2]; these enhanced levels are almost certainly not of a primary nature, but accummulated from circulating groundwater in response to changing redox conditions. A case can be made that the PGE anomaly often recorded in the KTB, a horizon marking a mass extinction, after all, with high levels anoxia in many cases, may also have been altered, or even formed entirely, by such secondary processes. It is interesting in this regards to note that that the mineralogy at the South African KTB site, where no elemental anomaly was found [1], is oxidized (carbonate) and contains no visible reduced components.

Source(s) of the geochemical signature of the KTB: The global variablity of the inter-PGE ratios may be a result of fractionation in the ejecta cloud [3], but Occam's razor compells one to also consider the much simpler option, *scilicet* that there were more than one contributing factor to the atmospheric and marine chemistry at the KTB time. The recent work of, for example, Courtillot and Renne [4] and Chenet et el. [5] on the Deccan Traps has shown conclusively that not only was the amount of toxic chemistry added to the atmosphere by the trap volcanoes extremely large, but also that it was added in a very short time (three events in <10000 years). These authors believe that the scenario they have uncovered can easily account for the mass extinction event, with the impact at Chicxulub being the 'final nail in the coffin' (my quotation marks). A mixture of geochemical signatures derived from two end-members, the one being the aerosols from basalt volcanism (mainly in the southern hemisphere) and the other an ejecta cloud (mainly in the northern hemisphere) would account exactly for the geochemical variability seen in the KTB sediments worldwide [2].

As a final comment, I think that it is interesting to bear in mind that, despite extremely intensive field work and research over the last two decades, a convincing siderophile anomaly has been found at only one (the KTB) of the five great Phanerozoic mass extinction event. On the other hand, of the five major continental flood events in the Phanerozoic, all but one (the Karoo-Ferrar) are exactly coincident with a major mass extinction.

References: [1] Verhagen B. Th.et al. (1990) *Chem. Geol., 80,* 1319-325. [2] Tredoux et al. (1989) *J. Geol., 97,* 585-605. [3] Evans N.J. (1995) *EPS, 134,* 141-153. [4] Courtillot V. and Renne P. (2003) *C.R. Acad. Sci. Paris, 335,* 113-140. [5] Chenet et al. (submitted to JGR).

MORPHOLOGICAL DIFFERENCES BETWEEN IRGHIZITES AND SPLASH-FORM GLASSES FROM LONAR CRATER – EVIDENCE OF DIFFERENT CONDITIONS OF ORIGIN OF THOSE GLASSES.

Ivan Vetvicka[1,2], Jan Frank[3], Jan Drtina[4], [1]CTU Prague, Faculty of Nuclear Sciences, [2] Observatory of Prague, corresponding address: Prevoznicka 14, 143 00 Praha 12 – Modrany, Czech republic, nunatak@centrum.cz, [3]Tesarik a Frank – Surveying Services, Ltd., U Stadionu 467, 271 11 Neratovice, CZ, honza.frank@seznam.cz, [4]Zakladani staveb, a.s., jdrtina@email.cz

Introduction: Zhamanshin impact crater is located in Kazakhstan (48° 21.6′ N, 60° 59.1′ E), the outer diameter of the crater being 13 km [1]. Zhamanshin is world famous by its unique association of impact glasses which are usually divided into two groups: irghizites and zhamanshinites [1,2,3,4]. Zhamanshinites are up to 50 cm big glassy or recrystalized bodies, some of them looking volcanic bombs [1,2]. Irghizites often look like volcanic lapilli usually not bigger than 3 cm [1,2]. Irghizites have a fibered structure. Small spherules of glass are stuck on their surface [1]. This paper accepts classification of glasses from Zhamanshin into three gropups [5]: Together with irghizites and zhamanshinites another group of glasses is recognized: akmurynites which are usually described as dull (mat) or corroded irghizites [6]. Akmurynites have no fibered structure, there are no glassy spheurules on their surface, and their chemical composition differs from irghizites.

The Lonar meteorite crater lies in India (19° 58′ N, 76° 31′ E). The crater diameter is 1830 m and it attracts researchers, because it is the only known impact crater in basalts on the Earth. Therefore it is possible to compare this structure with impact craters on the Moon [7] and some regions of Mars [8]. In the Lonar crater, there were also found impact glasses, the detailed description is in [8]. This paper is focused especially on splash-form glasses which hardly ever exceed 1 cm in size, resemble irghizites and are probably similar to the "a" type in [8]. In our research massive glasses from Lonar which can be compared with zhamanshinites, were not classified in detail.

Three weeks in 2002, the authors of this paper were collecting impact glasses in the Zhamanshin impact crater. In 2006, Jan Frank collected glasses in the Lonar crater (locality Glass Pit 120 m SE from the crater rim, described in [9]. The paper is introducing results of morphological research of those glasses carried out by naked eye.

Results and conclusion: Irghizites originated by accretion of plastic fibres and small spherules of glass. The enclosed photos (a-i) can prove, that this genesis is not typical only of clues of glass described by [1], but fibres and spehurles could create compact samples as well to give rise to splash form shapes. Surprising is the big volume of small glassy spherules in forming of bigger samples.

However, irghizites from Zhamanshin are not the only known impact glasses in the world on whose surface there are small spherules or fibres of glass. Similar objects were also found on the surface of splash-form glasses from the Lonar crater (photos g and i). Nevertheless, the surface spherules of Lonar splash-form glasses are much less abundant and are smaller compared to surphace spherules on the irghizites. Only one glass fibre was found on the Lonar splash-form glass surface. In this case, the accretion of spherules and fibres was almost total, or this process was not their main forming mechanism and the accretion appears marginal compared to irghizites. Even in their case, it is not clear, if accretion of fibres and spherules was the only irghizite-forming mechanism.

Both, irghizites and splash-form glasses from Lonar were ejected into the atmosphere during the impact process. The surface of irghizites is mostly smooth and lustrous. Therefore it is evident that the plastic glass matter of irghizites had sufficient time to be smoothened by the surface forces in liquid glass. Moreover, those forces formed spheric shapes of pieces of glass smaller 1 mm. On the opposite, in the Lonar splash-form glasses the smooth lustrous samples are very rare. Most splash-form glasses from Lonar have a dull (matt) and rough surface. The smoothening proces could be blocked by high glass viscosity, or by permanent collisions with other particles. The impact glasses from Lonar were ejected together with ash and other impact ejecta [10]. It is assumed that it is the numerous collisions with particles of impact ash and dust that prevented the splash-form Lonar glasses form forming the smooth lustrous surface. Only the trajectories of rare lustrous samples ejected them out of the cloud of ash and dust, whereas most of the irghizites were flying for some time out of the cloud of ash and dust.

Fig. 1 a-i: a: Irghizite originated by accretion of fibres, b,c: Irghizite originated by accretion of fibres and spherules, d: Bizzare irghizite originated by accretion of droplets and spheres, e: unusual irghizite created only by acretion of spheres (Some spheres can be seen deeply engaged in the main body), f: Splash-form irghizite with glass fibre stuck on its surface, g: Splash-form glass from Lonar crater with the glass fibre on its surface, h: Typical splash-form irghizite with spheres stuck on its surface, i: Splash-form glass from Lonar with spherules of glass stuck on its surface. a-i: Scale in mm, photo Ivan Vetvicka (2007).

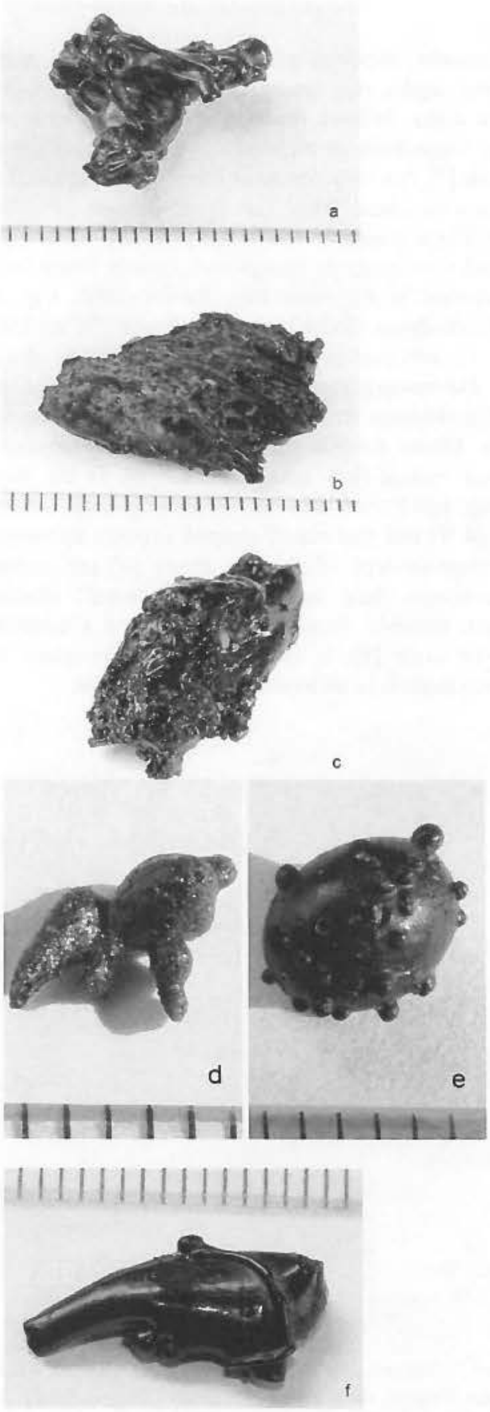

References: [1] Florenskij P.V., Dabiza A.I. (1980) Meteoritnyj krater Zhamanshin, 1-128. [2] Masaitis V.L. (1999) *Meteoritics & Planet. Sci.,* 34, 691-711. [3] Koeberl Ch., Frederiksson K. (1986) *Meteoritics & Planet. Sci.,* 78, 80-88. [4] Feldman V., Sazonova L. (1993) *Petrology,* 1, 6, 596-614 [5] Vetvicka I., Frank J., Drtina J. (2004) *Sklar a keramik,* 54, 199-200 [6] Bouska V., Borovec Z., Čimbalnikova A., Kraus I., Lajcakova A., Pacesova A. (1987) Prirodni skla 1-264. [7] Frederiksson K., Dube A., Milton D.J., Balasundaram M.S. (1973) *Science,* 180, 862-864. [8] Osae S., Misra S., Koeberl Ch., Sengupta D., Ghosh S. (2005) *Meteoritics & Planet. Sci.,*40, 1473-1492. [9] Maloof A.C., Louzada K.L., Stewart S.T., Weiss B.P. (2005) Role of Volatilies and Atmosphere on Martian Impact Craters, Abstract # 3046. [10] Louzada K.I., Maloof A.C., Newsom H.E., Weiss B.P., Wright S.P. (2005) Role of Volatilies and Atmosphere on Martian Impact Craters, Abstract # 3045.

PROCESSES AND PRODUCTS OF THE MARINE ALAMO IMPACT EVENT, CENTRAL GREAT BASIN, WESTERN USA. J. E. Warme[1], J. R. Morrow[2], and J. A. Pinto[3], [1]Dept. of Geology and Geological Engineering, Colorado School of Mines, Golden, Colorado 80401, USA (jwarme@mines.edu), [2]Dept. of Geological Sciences, San Diego State University, 5500 Campanile Drive, San Diego, California 92182-1020, USA (jmorrow@geology.sdsu.edu), [3]INTEVEP-PDVSA, Building South 1, Floor 2, Office 202, 1201, Los Teques, Venezuela.

Introduction: Recent work has partitioned the distribution of the Alamo Breccia in southeastern Nevada and western Utah, western USA, into six genetic Realms (Fig. 1) that provide a working model for the early Late Devonian (~382 Ma), marine Alamo Impact Event [1]. Each Realm exhibits discrete impact processes and stratigraphic products (Table 1), which preserve an exceptionally well-exposed record of both proximal and distal marine impact phenomena. The first five Realms (Rim, Ring, Runup, Seismite, and Runoff) form roughly concentric semicircular bands onshore across the Devonian shallow-water carbonate platform. The sixth, the Runout/Resurge Realm, consists of offshore channels of thick, off-platform Alamo Breccia and large, crater-proximal olistoliths.

Processes and Products: *(1) Shock Waves*: Widespread evidence of the passing impact shock waves, including potentially the superimposed effects of Love, Rayleigh, and rarefaction components, is recorded in the platform Realms by large, tabular carbonate megaclasts and fluidized bedding and clasts. Other seismic-related features include (a) in the Ring Realm, a monomict, fluidized detachment surface defining the base of the Alamo Breccia (Unit D of past work); (b) in the Rim, Runout/Resurge, and Runup Realms, liquefied clastic injection dikes and sills; and (c) in the Runup and Seismite Realms, chaotic, strata-bound sequences. Because the pre-Alamo Event sedimentary-target sequence was dominated by early-cemented carbonates, fracturing, folding, and acoustic fluidization dominated over liquefaction, an important process recorded at other marine, sedimentary-target impact sites, e.g., Wetumpka [2] and Chesapeake Bay [3]. *(2) Other Shock Deformation*: These features include macroscopic, autochthonous to parautochthonous shatter cone-like structures documented in the Rim Realm [1] and widespread planar microstructure-bearing shocked quartz recovered from the Alamo Breccia in all Realms except the Seismite [e.g., 4, 5, 6]. *(3) Shock Melt*: Probable evidence for melt occurs as unusual, plastically deformed clasts and microscopic carbonate quench fabrics within interpreted fallback breccias (Units 3 and 4) in the Rim Realm at Tempiute Mountain (TEM, TMS, Fig. 1) [1], and as small, globular silicate grains disseminated within Alamo Breccia matrix [6]. *(4) Ejecta*: A wide variety of proximal and distal ejecta are preserved, including weak iridium enrichment, shocked quartz grains, carbonate accretionary lapilli, rare accretionary "bombs", target-rock lithic clasts, fallback breccias in the Rim Realm, and large megaclasts or olistoliths in the Runout/Resurge Realm [7] that may represent transported fragments of a crater-proximal "flap" [cf. 8]. *(5) Crater Modification*: These products, which are probably more widespread than currently recognized, include listric faults interpreted in the outer Ring Realm (DEL, Fig. 1), probable slump blocks in the Rim Realm (TEM, TMS, Fig. 1), and possibly the olistoliths described above. *(6) Marine-target Effects*: Offshore effects in the Runout/Resurge Realm consist of seafloor erosion and thick Alamo Breccia channel fill probably deposited during resurge flow into the crater [6]. In the Ring, Runup, and Runoff Realms, normally graded tsunamiites [4, 5] and thin runoff channel deposits containing continent-sourced siliciclastic grains [6] are present. Microscopic fluid inclusion-rich "toasted" shocked quartz, possibly forming in response to a saturated marine target [9], is also widespread throughout the Alamo Breccia in all Realms but the Seismite.

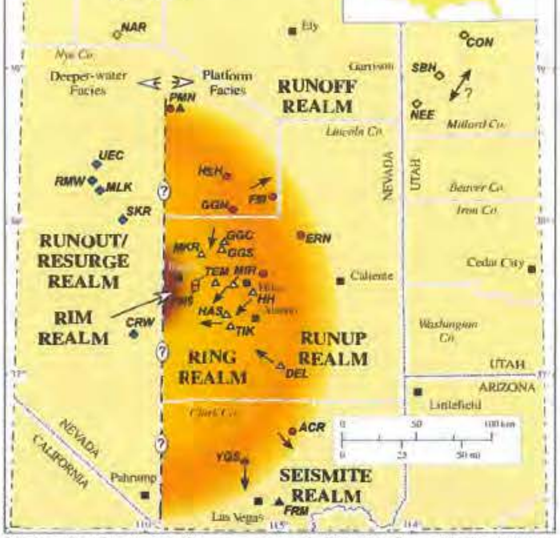

Figure 1. Tectonically unrestored distribution of six Alamo Breccia Realms, showing key localities (abbreviations). Arrows show paleocurrent directions. Modified from [1].

Acknowledgments: C. A. Sandberg, A. C. Chamberlain, H.-C. Kuehner, and F. G. Poole are recognized for their contributions to the Alamo project. Morrow acknowledges support from NSF Grant #0518166.

References: [1] Pinto J. A. and Warme J. E. (2008) *GSA Spec. Pap. 437*, 99–137. [2] King D. T., Jr., et al. (2006) *Meteoritics & Planet. Sci., 41,* 1625–1631. [3] Horton J. W., Jr., et al. (2008) *GSA Spec. Pap. 437*, 73–97. [4] Warme J. E. and Sandberg C. A. (1995) *CFS, 188*, 31–57. [5] Warme J. E. and Kuehner H.-C. (1998) *Int. Geol. Rev., 40*, 189–216. [6] Morrow J. R. et al. (2005) *GSA Spec. Pap. 384*, 259–280. [7] Sandberg C. A. et al. (2006) *Conf. on Imp. Craters as Indicat. Planet. Environ. Evol. and Astrobiol.*, Östersund, CD-ROM. [8] Lindström M. et al. (2005) *Impact Tectonics*, 357–388. [9] Whitehead J. et al. (2002) *Geology, 30*, 431–434.

Process	Product	Realm [1] (Fig. 1)	Representative Localities (Fig. 1)
1) Surface Shock Waves (Love, Rayleigh, rarefaction)			
Proximal:	Tabular mega-clasts; fluidized bedding and clasts	Rim; Ring	TEM, TMS; DEL, HAS, HH, MIR, TIK
	Liquified clastic injection sills and dikes	Rim; Runout/ Resurge; Runup	TEM, TMS; UEC; PMN
Distal:	Seismites	Seismite	FRM
	Fluidized bedding	Runoff; Seismite	DVG, SBH; FRM
2) Shock Deformation			
Megascopic: (autochthonous)	Shatter cone-like structures	Rim	TEM, TMS
Microscopic: (allochthonous)	Planar fractures and planar deformation features in quartz	All except Seismite	CON, DVG, FM, HAS, HH, MLK, PMN, TEM, TMS
3) Shock Melt			
Carbonate:	Fallback breccias, Units 3 and 4, Tempiute Mountain	Rim	TEM, TMS
Silicate:	Amorphous and isotropic globular particles in Alamo Breccia matrix	Rim; Ring; Runoff; Runout/Resurge	TEM, TMS; HAS, MIR, TIK; CON; MLK
4) Ejecta			
Proximal:	Lapilli and lapillistone	Rim; Ring	TEM; HAS, MIR, HH, TIK
	"Bombs"	Ring; Runout/Resurge	HH; MLK
	Target-rock clasts	Rim; Ring; Runout/Resurge; Runup	TEM, TMS; HAS, TIK; MLK, SKR; FM, PMN
	Fallback breccias, Units 3 and 4, Tempiute Mountain	Rim	TEM, TMS
	Olistoliths or "flap" remnants(?)	Runout/Resurge	MLK
Proximal and distal:	Shocked quartz grains	All except Seismite	DVG, FM, HAS, HH, MLK, NAR, PMN, TEM, TMS
	Weak iridium anomaly	Ring; Runoff	MKR; CON, DVG
5) Crater Modification			
	Listric faults	Ring	DEL
	Rim-proximal slump blocks, Unit 3 fallback breccia, Tempiute Mountain	Rim	TEM, TMS
	Olistoliths or "flap" remnants(?)	Runout/Resurg e	MLK
6) Marine-target Effects			
	Seafloor erosion	Runout/Resurge	MLK, SKR
	Tsunamiites	Ring; Runup; Runoff(?)	HAS, HH, MIR; ERN, FM; CON, DVG
	Resurge channel deposits	Runout/Resurge	MLK, SKR, UEC
	Onshore runoff channel deposits	Runoff	CON, DVG, SBH
	"Toasted" shocked quartz grains	All except Seismite	DVG, FM, HAS, HH, MIR, MLK, PMN, TEM, TIK

Table 1. Impact processes, resulting products, and positions within genetic Realms of the Alamo Impact Event.

DOES CHICXULUB POSSESS A DIFFERENTIATED MELT SHEET? M. R. Warner[1], J. V. Morgan[1], R. A. F. Grieve[1,2], P. J. Barton[3], G. L. Christeson[4], S. P. S. Gulick[4], A. T. Surendra[3], [1] Earth Science and Engineering, Imperial College London, London SW7 2AZ, UK, j.morgan@imperial.ac.uk, [2]Earth Science Sector, NRCan, Ottawa, Canada K1A OE4, [3]Department of Earth Sciences, University of Cambridge, Cambridge CB3 0EZ, UK, [4]Institute of Geophysics, Jackson School of Geosciences, University of Texas at Austin, TX 78759, USA.

Introduction: The Chicxulub crater is approximately the same size as Sudbury [1] and thus may also possess a differentiated melt sheet. Sparse core from two drill holes (C-1 and S-1) that penetrated the top 400-500 m of impactites in the central basin at Chicxulub suggest that the uppermost units may have a similar stratigraphy to the SIC at Sudbury [2]. Allogenic clast-and melt-rich impact breccias, of a similar description to the Onaping formation, were found to overlie clast-poor impact melts. However, the sampling is too sparse and shallow to tell us whether the melt sheet is differentiated at Chicxulub.

New seismic data, acquired in 2005, has provided us with high-resolution reflection images and refraction velocities within the central basin, across the expected location of the Chicxulub melt sheet [3]. Here we present these seismic data and make comparisons with observational data from Sudbury, to provide some insight into the nature of the impactite sequence at Chicxulub.

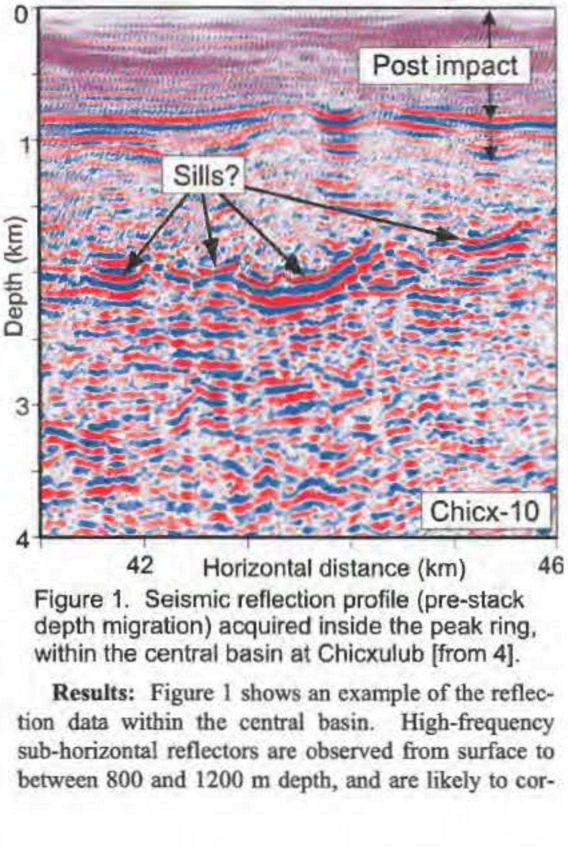

Figure 1. Seismic reflection profile (pre-stack depth migration) acquired inside the peak ring, within the central basin at Chicxulub [from 4].

Results: Figure 1 shows an example of the reflection data within the central basin. High-frequency sub-horizontal reflectors are observed from surface to between 800 and 1200 m depth, and are likely to correspond to the post-impact sediments. There is an interval of chaotic reflectivity underlain by bright, low-frequency reflectors between 1500 and 2300 m depth. These reflectors are typically saucer-shaped [4], and are comparable in shape and size, to intrusive sills that have been observed in 3D marine seismic data around the UK [5].

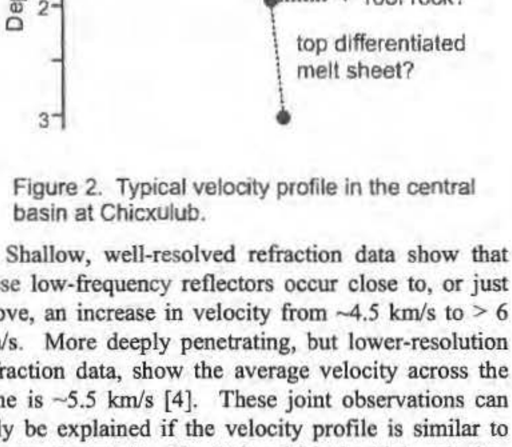

Figure 2. Typical velocity profile in the central basin at Chicxulub.

Shallow, well-resolved refraction data show that these low-frequency reflectors occur close to, or just above, an increase in velocity from ~4.5 km/s to > 6 km/s. More deeply penetrating, but lower-resolution refraction data, show the average velocity across the zone is ~5.5 km/s [4]. These joint observations can only be explained if the velocity profile is similar to the one depicted in Fig. 2, in which the high-velocity-layer at ~1.6-2 km depth is sufficiently thin to not significantly dominate the average velocity in this region.

Discussion: The impact melt sheet and Onaping formation at Sudbury are exposed at surface, and distinct changes in lithology are observed (Fig. 3a [6]). The granophyre and norite are interpreted as the upper and lower layers of a differentiated melt sheet [7], and the Onaping largely as various types of fall-back breccia [6]. P-wave velocity measurements (Fig. 3b) show that the average velocity increases from the Dowling member to the granophyre, and is highest in the norite [8]. There is, however, a slight increase in velocity at the base of the Onaping, in the Sandcherry member (Fig. 3b), and then the velocity decreases in the granophyre below [8].

If we assume that the velocity changes at Chicxulub reflect the same features as at Sudbury, then one possible interpretation of the Chicxulub seismic data is that the section between the post-impact sediments and high-velocity-layer is equivalent to the Dowling member of the Onaping formation, and that the thin high velocity zone is equivalent to the Sandcherry member. At Chicxulub, these sections are ~600-1000 m and 200-300 m thick respectively, slightly less than observed at Sudbury, where they are around 1000 and 400 m thick [6, 7]. An alternative interpretation for the high-velocity-layer is that it represents intrusive sills. A more detailed analysis of the positioning of the high velocity layer in the refraction data (Fig. 2) and the sills in the reflection profiles (Fig. 1) may help us distinguish between these two possibilities. Dykes and sills have also been identified within the Onaping, and are interpreted as originating from the impact melts below [6].

Impact melt sheets typically have a chilled clast-rich roof rock – formed from the uppermost melts that have cooled and solidified first [9]. The aphanitic vitric clasts within the Sandcherry member have a composition that is close to the felsic norite [6]. One explanation for this is that the Sandcherry was part of the uppermost melt sheet that solidified first (i.e. a roof rock), and was subsequently heavily disrupted by both the differentiation of the melt pool and explosive hydrothermal processes. At both Chicxulub and Sudbury, the velocity decreases beneath the high-velocity-layer (Fig. 2 and 3b). This might mean that the rocks below 2 km depth at Chicxulub are the upper layer of a differentiated melt sheet – as is the granophyre at Sudbury. Hence, these seismic data offer some support for the idea that Chicxulub does possess a differentiated impact melt sheet. Future ICDP drilling within the central basin would resolve this issue.

References:

[1] Grieve R. A. F. and Therriault A. (2000) *Ann. Rev. Earth Planet. Sci., 28,* 305-338. [2] Sharpton V. et al. (1996) GSA Spec. vol. *307,* 55-74. [3] Gulick et al. (2008), Nature Geosci. 1, 131-135. [4] Surendra, A. T. (2007) PhD Thesis, Univ Cambridge. [5] Hansen D. and Cartwright J. A. (2006) J. Geol Soc. London *163,* 509-523. [6] Ames D. E. et al. (2002) Econ. Geol., *97,* 1541-1562. [7] Grieve R.A.F. et al. (1991) JGR, *96,* 22753-22764. [8] Salisbury et al. (1994) GRL, *21,* 923-927. [9] Grieve et al. (1977) IEC, 791-814.

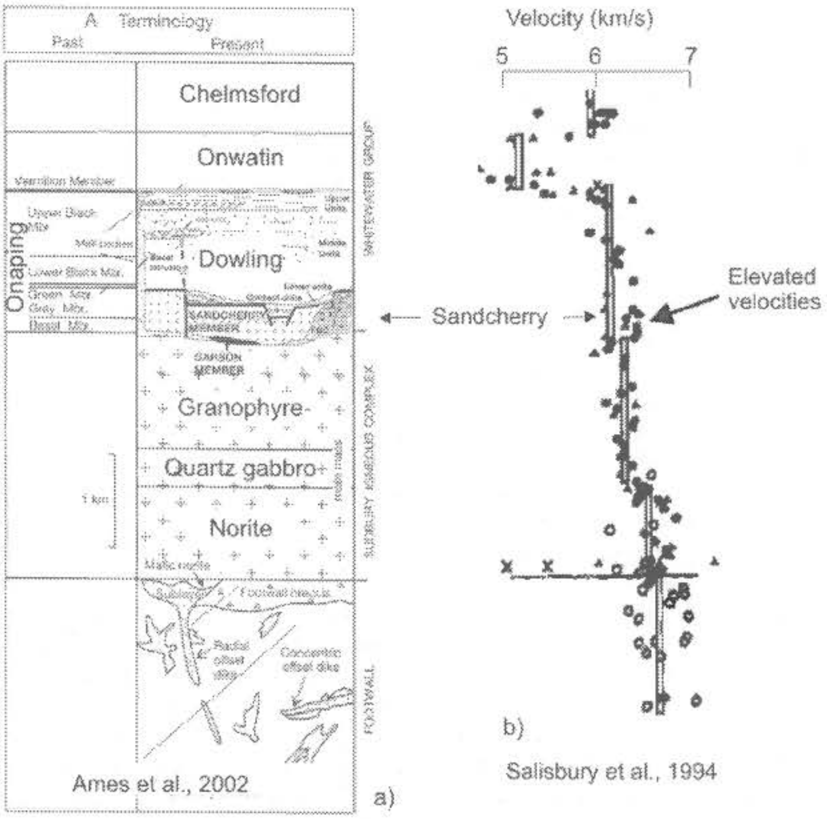

Figure 3 a) Simplified stratigraphy for the Sudbury structure [6] and b) P wave velocity measurements [8].

THE VOLUME OF IMPACT MELT IN THE CHESAPEAKE BAY CRATER.

A. Wittmann[1], W. U. Reimold[2]
[1]Lunar and Planetary Institute, Houston, TX 77058, USA, wittmann@lpi.usra.edu, [2]Museum of Natural History (Mineralogy), Humboldt-University, Invalidenstr. 43, 10115 Berlin, Germany, uwe.reimold@museum.hu-berlin.de.

Introduction: The late Eocene Chesapeake Bay impact structure formed as a ~40 km diameter complex crater on the continental margin of Virginia that collapsed to a ~85 km diameter final structure [1]. The target was composed of ~1500 m of water and siliciclastic sediments on top of a crystalline basement [2]. An ICDP-USGS drilling through the annular moat of the crater recently recovered a 154 m thick section of impact breccias and melt rocks below 1397 m of resurge debris and post-impact sediments [3]. These ground-zero deposits recorded the earliest cratering processes and potentially contain information about the effect of volatiles on the formation of impactite deposits in a large terrestrial impact structure.

Samples and Methods: Impact melts were characterized microscopically in 69 drill core samples from the continuous section of impact breccias and melt rocks. A continuous set of digital photographs of core boxes courtesy of David S. Powars, USGS, was then used to determine the amount of melt within the section. These observations were confirmed at the USGS drill core repository.

Results: The main mass of impact melt in drill core Eyreville-B is concentrated in two 5.5 and 1 m thick bodies of clast-rich impact melt rock. In addition, many small-scale occurrences of pods and particles of impact melt occur within suevites. Their distribution is limited to the upper part of the pre-resurge section (Fig. 1) and add to a cummulative maximum amount of ~17 m. The Chesapeake Bay crater has no continous melt sheet. Throughout the resurge deposits, a melt component <0.3 vol. % occurs that locally accounts for up to 63 vol% in thin sections with melt shards [4].

Discussion: Extrapolating the amount of melt to a circular area of a 28 km diameter transient cavity gives an estimate for a total mass of melt that was retained within the crater of at most 10.5 km^3. This agrees with findings of a test drilling into the central uplift, which recovered a ~114 m thick, largely suevitic impact breccia deposit [3]. Moreover, gravity and magnetic survey data modeling predicted the presence of impact melt bodies with an approximate volume of 0.4 - 7 km^3 [5] that surround the central peak. The approximate amount of ~10 km^3 is less than 0.5 % of the ~230 km^3 of impact melt that are predicted from scaling relationships of [6] for terrestrial impact structures in crystalline basement targets. Taking scaling relationships at face value, a melt sheet with an average thickness of ~ 370 m could have formed from the amount of melt produced from an impact event the size of Chesapeake Bay. Possible causes for the low melt volume in the Chesapeake Bay crater are:

Removal / reworking of melt by the resurge flow. At the site of the drilling, a continuous melt sheet should have been preserved if it had formed. Typically, melt sheets in complex craters in this structural position are overlain by slump and fallback suevites [7]. Such rocks are present in the upper 35 m of the sequence (sub-units S3-SU). Blocks or boulders of impact melt rock of a thicker, reworked melt sheet were never described from the resurge deposits and melt fragments and shocked tectosilicates are a minor component therein [2, 4].

A strongly oblique (<30°) and / or a slow impact. This would cause a lower amount of impact melt and a shallower transient cavity floor with a decreased shock metamorphic overprint [8]. A low angle of impact is expected to produce a depressed crater rim, which could have better accommodated resurge of a shallow ocean [9]. Geophysical data for Chesapeake Bay suggest an asymmetrical geometry of the limits of the central crater [2]. Geogphysical modelling reveals an ovoid central peak with a central magnetic anomaly that is offset from the center of the structure [5]. These authors suggest a likely effect of target geometry on this feature but also discuss the possibility of a highly oblique impact with a NW-SE trajectory to produce this feature. The distribution of tektites in the North American strewn field to the SE of the impact site may be another indicator for such an oblique impact trajectory [10]. However, impact parameters that influence the amount of melt produced, e.g. velocity of the projectile and its size, are hard to constrain.

Stacking of slumped breccia layers in the moat. A buried melt sheet below allogenic breccias was not resolved in a seismic experiment across the drill site [11]. Nor is such a scenario indicated by magnetic and gravimentric data [5]. Commonly, the basic stratigraphy of the transient cavity is retained in complex craters with a continuous melt sheet on top of polymict breccias and the autochthonous, shocked basement [7]. These authors also suggested that excavation efficiency decreases with increasing transient cavity size as a consequence of greater velocity attenuation in the melt. Therefore, the pre-resurge section in the Eyreville drilling appears typical for a crater filling sequence of a small complex crater with a disrupted or missing melt sheet. The amount of impact melt encountered within the transient cavity is deficient with regard to observational scaling relationships from craters that dominantly formed in crystalline basement.

Increased excavation efficiency from sediments. Craters that form dominantly in sedimentary targets excavate more efficiently due to excessive release of volatiles [12]. These authors predicted that the proportions of recognizable impact melt rocks at craters in largely sedimentary targets is two orders of magnitude less than at similar size craters in crystalline targets. Similar low abundances of impact melt are retained at the Ries Crater, Germany, the Haughton crater, Canada, Bosumtwi,, Ghana, and the Logoisk crater in Belarus [6, 13].

Following [14], the discrepancy between the amount of melt retained in a crater could relate to the proportion of the sedimentary target at depth of excavation and melting. At Chesapeake Bay, a thickness of sediments and water column of ~1200-1500 m at the center of the structure can be assumed, which translates to a relative proportion of 40-50 % of the excavation depth [15] and ~25 % of the maximal depth of melting [6]. This relationship may account for the melt deficient central crater at Chesapeake Bay and the dispersal of melt to form the North American tektite strewn field and microtektites that are known from ODP sites across the world.

Conclusions: The ICDP-USGS Eyreville B drilling revealed the presence of ~17 m of impact melt in a 154 m thick continuous sequence of pre-resurge impact breccias and melt rocks. No continous melt sheet formed at Chesapeake Bay. A high sedimentary target component led to a dispersal of melt to form the North American tektite strewn field and microtektites.

References: [1] Collins G. S. & Wünnemann K. (2005) *Geology, 33*, 925-928. [2] Horton J. W., Jr. et al. (2005) *USGS Prof. Pap. 1688*, 464 pp. [3] Horton J. W., Jr. et al. (2008) *GSA Sp. Pap. 437*, 73-97. [4] Reimold W. U. et al. (in prep.) *GSA Sp. Pap.* [5] Shah, A. K. et al. (2005) *Geology, 33*, 417-420. [6] Grieve, R. A. F. & Cintala, M. J. (1992) *Meteoritics 27*, 526-538. [7] Grieve, R. A. F. et al. (1977) in *Impact and Explosion Cratering, Roddy, D. J., Pepin, R. O., Merrill, R. B. (eds.)*, Pergamon Press, 791-814. [8] Pierazzo, E. et al. (1997) *Icarus 127*, 408-423. [9] Herrick, R. R. & Forsberg-Taylor, N. K. (2003) *MAPS 38*, 1551-1578. [10] Stöffler, D. et al. (2002) *MAPS 37*, 1893-1907. [11] Catchings R. D. et al. (in press) *JGR*. [12] Kieffer S. W. & Simonds S. H. (1980) *Rev. Geophy. Space Ph. 18*, 143-181. [13] Artemieva N. A. (2007) *MAPS 42*, 883-894. [14] Kring, D. A. (2005) *Geochem. 65*, 1-46. [14] Melosh, H. J. M. (1989) *Impact cratering*, Oxford U. Press, 245 pp.

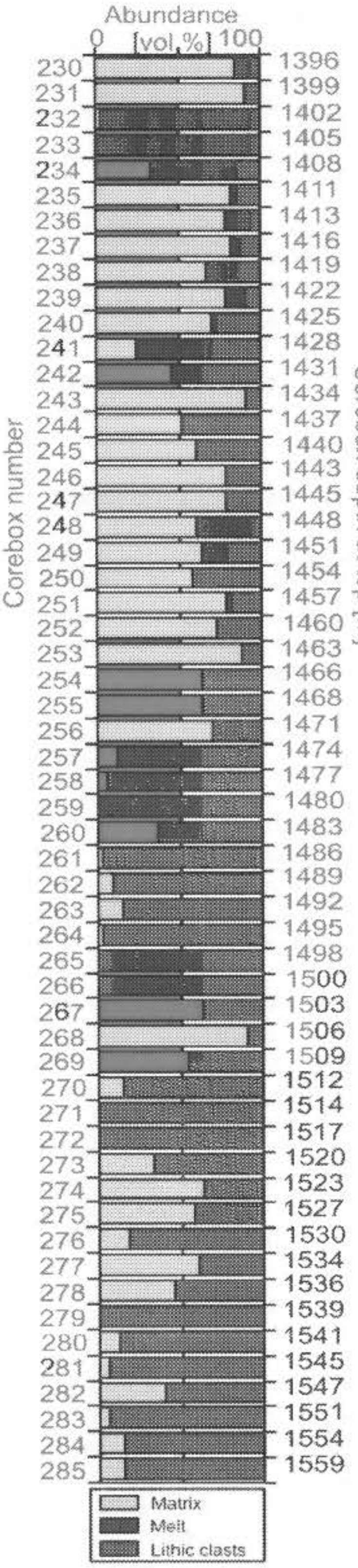

Fig. 1 Melt pods and lithic clasts >4,8 cm in impact breccia section of drill core Eyreville-B.

PRELIMINARY AGE OF IMPACT MELTS FROM THE CHESAPEAKE BAY IMPACT STRUCTURE.

A. Wittmann[1,3], V. A. Fernandes[2], P. R. Renne[2], R. T. Schmitt[3], W. U. Reimold[3], L. Hecht[3], H. Povenmire[4], [1]Lunar and Planetary Institute, Houston TX 77058, USA, wittmann@lpi.usra.edu; [2]Berkeley Geochronology Center, 2455 Ridge Road, Berkeley, CA 94709, U.S.A., [3]Museum of Natural History, Mineralogy, Humboldt-University Berlin, 10115 Berlin, Germany, [4]H. Povenmire, Florida Institute of Technology, Melbourne, FL 32901, USA.

Introduction: The late Eocene Chesapeake Bay impact structure formed as a ~40 km diameter complex crater and collapsed to a ~85 km diameter structure on the continental margin of Virginia. The target was composed of ~1500 m of water and siliciclastic sediments on top of a crystalline basement [1]. The age of the Chesapeake Bay impact appears fairly well constrained:

1. Paleontogical studies of post-impact transitional sediments within the impact structrue suggest an age of 35.7 - 35.8 Ma [2];
2. Correlations with ejecta deposits in ocean drilling project sites indicate an age of 35.2 - 35.5 Ma [3].
3. Correlation of assumed sedimentation rates with magnetochrons and microfossil biozones yield an age of 35.78 Ma for the event [4].
4. Georgiaite and Bediasite tektites of the North American Strewn Field give weighted-mean total-fusion $^{40}Ar/^{39}Ar$ ages of 35.4 +/- 0.6 Ma [5] and 35.3 ± 0.1 Ma ($\pm 1\sigma$) [3]; similar K-Ar ages of 35.2 +/- 0.7 Ma were found for Georgiaite tektites [6].
5. The oldest fission track ages of 35 Ma for Georgiaite tektites coincide with those of Bediasite tektites [7].

Especially the link of distal ejecta with the Chesapeake Bay event is problematic because four other impact structures are known with a late Eocene age that potentially produced impact ejecta: Popigai, Siberia, 100 km Ø, 35.7 ± 2 Ma [8], and in Canada Mistastin, 28 km Ø, 36.4 ± 4 Ma, Haughton, 20.5 km Ø, ~ 39 Ma, and Wanapitei, 7.5 km Ø, 37.2 ± 1.2 Ma [9, and references therein]. The ICDP-USGS Eyreville-B drilling, located through the annular moat, 9 km from the center of the Chesapeake Bay crater recently recovered a 154 m thick section of impact breccias and melt rocks [10,11]. These melt rocks provide a first opportunity to directly date the Chesapeake Bay impact.

Samples and Methods: Two samples of pristine impact melt rock were chosen for analysis. One represents a hypocrystalline, clast-rich melt rock that contains domains of glassy melt in-between orthopyroxene and spinel phenocrysts (Figs. 1 A-B). The other is a holocrystalline variety that cooled more slowly and is composed of orthopyroxene – spinel – plagioclase – sanidine – cordierite – quartz (tridymite, cristobalite ?) - biotite microphenocrysts (Figs. 1 C-D). Moreover, one Bediasite and one Georgiaite tektite were analyzed. Defocussed-beam electron microprobe analysis (EMPA) was carried out to determine the major and minor element compositions of the samples. IR-laser probe step-heating was performed on irradiated, hand-picked fragments of melt that were produced from ~ 5 mm thick sample slabs of each impact melt sample. Locations and states of preservation of the samples were checked microscopically on thin sections from the opposite faces of the sample slabs. Details on the analytical methods employed is given by [12].

Results: EMPA determined ~ 3 wt.% K_2O in the glassy, hypocrystalline melt [11] and ~8 wt.%. K_2O in the matrix of the holocrystalline melt. The glassy melt retained volatile contents of ~5 vol.%, which is indicated by consistent 95 wt.% totals. The Bediasite and Georgiaite tektites exhibit typical compositions within the compositional ranges reported in the literature (e.g., [13], [14]). Preliminary, mean $^{40}Ar/^{39}Ar$ total fusion ages for ten fragments of a georgiaite and of a bediasite are 34.64 ± 0.51 Ma and 34.58 ± 0.34 Ma, respectively. These ages are similar to ages reported previously [3-6], but display excess scatter (MSWD>6) suggestive of subtle. variable alteration. $^{40}Ar/^{39}Ar$ analyses on the holocrystalline melt are characterized by large MSWD (>>1) and a wide range of ages. Some hypocrystalline melt fragments show MSWD of ~1 and ages between ~44.8 and ~48.1 Ma.

Discussion: Radioisotopic dating of impact melts has been recognized as a potentially problematic endeavor [15]. Several complicating factors may prohibit the inference of meaningful ages such as the existence of inherited Ar, which cannot be thermally resolved from radiogenic Ar by incremental heating. In the case of the samples analyzed in this study, the hypocrystalline melt indicates strong disequilibrium. It preserved glassy melt and abundant incorporated tectosilicate clasts that indicate variable states of assimilation. Therefore, inherited radiogenic argon from variable sources poses an analytical challenge. The holocrystalline sample also contains incorporated tectosilicate clasts but the thorough crystallization suggests better equilibration.

Other potential problems could be alteration features. Although microscopic control was exerted on the samples for dating, alteration features like spherulitic devitrification due to hydration of glass, alteration to chlorite-smectites and mineralization of zeolites in vugs could potentially be a problem. However, if this were the case, younger ages would be expected. Such a trend was not observed in the melts but has to be considered for the analyzed tektites, which gave an age slightly younger than those previously reported [3,5-7].

Vugs in the melt rocks could potentially have served as traps for volatiles. Microscopic control did not indicate the presence of such vugs in the sampled domains, nor did it indicate the presence of fluid inclusions in glassy melt that could have trapped inherited argon.

Summary: The initial Ar-Ar results obtained by step heating of impact melt rocks from the Chesapeake Bay impact structure suggest that this material contains different ^{40}Ar components that are not straight forward to distinguish ^{40}Ar/^{39}Ar results for fragments of one bediasite and one georgiaite are slightly younger than, but within error of, ages previously reported [3-6]. Possible disturbances of the argon systematics in these samples will be studied by step-heating analysis. Further investigation of the impact melt data will be undertaken to determine, if different ^{40}Ar components (i.e. radiogenic vs. inherited) can be resolved.

Acknowledgments: K. Ross, T. Becker, T. Teague, P. Czaja and H. R. Knoefler for sample preparation and assistance with microprobe and Ar-analyses.

References: [1] Collins & Wünnemann (2005) *Geology, 33*, 925-928. [2] Horton et al. (2005) *USGS Professional Paper #1688*, 464 pp. [3] Poag & Aubry (1995) *Palaios 10*, 16-43. [4] Poag et al. (2004) *The Chesapeake Bay Crater*, Springer, Berlin, 522 pp. (1997) *JGR, 90*, 1151–1154. [5] Glass et al. (1986) *Chem. Geol. 59*, 181-186. [6] Albin (1997) *PhD thesis*, UGA, Athens, 302 pp. [7] Storzer et al. 1973) *JGR 78*, 4915-4919. [8] Bottomley et al. (1997) *Nature, 388*, 365-368. [9] Sherlock et al. (2005), *MAPS 40*, 17777-1778. [10] Wittmann et al. (2008); *LPS XXXIX*, Abstract # 2435. [11] Fernandes et al. (2008); *LPS XXXIX*, Abstract # 2483. [12] Jourdan et al. (2008), *EPSL 265*, 438-449. [13] Koeberl (1988) *Meteoritics 23*, 161-165. [14] Albin et al. (2000) *MAPS 35*, 795-806. [15] Jourdan et al. (2007) GCA 71, 1214-1231.

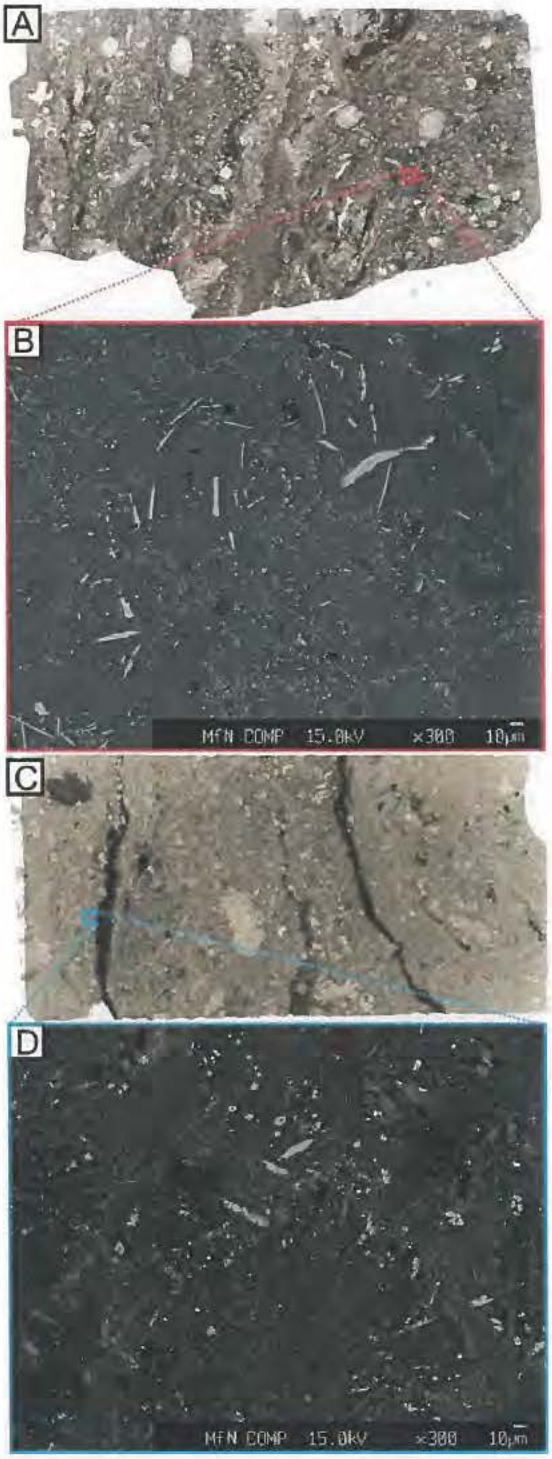

Fig.1 Melt rock samples, width ~4 cm (A and C).
A – Thin section scan of hypocrystalline melt rock;
B – SEM-BSE image of glassy melt, bright Opx laths, spherulitic Pl, dispersed Spl and assimilated quartz clast.
C - Thin section scan of holocrystalline melt rock;
D – SEM-BSE image of crystallized melt with radial Pl-spherulites, few bright Opx, dispersed, bright Spl, some euhedral zoned sanidine and cordierite.

EJECTA FACIES AT LONAR CRATER, INDIA: INVENTORY OF EXPECTED IMPACTITES, THERMAL INFRARED SPECTROSCOPY, AND IMPLICATIONS FOR MARS

Shawn Wright, School of Earth and Space Exploration, Arizona State University, Tempe, AZ 85287-6305, **Shawn.P.Wright@asu.edu**

Introduction: While a common goal of the study of terrestrial impact sites and their impactites is for insight into the impact process, another goal is the application of these data and lessons learned to the understanding of the surfaces of other planetary bodies. Here, the ejecta structure of one unique terrestrial ejecta blanket is described in detail along with descriptions of impactite sample analyses and how these data can be applied current and future rovers of Mars and perhaps the Moon.

Lonar Crater ejecta structure: Whereas field data of any preserved terrestrial ejecta blanket is relevant to understanding the impact process and products, studies of Lonar Crater, India have implications for Mars [1-4]. The target Deccan basalt provides an opportunity to examine terrestrial shocked basalt similar to shergottites from Mars [4-5]. Further, Deccan basalt has been labeled as an excellent analog for Surface Type 1, a thermal infrared spectral type identified from orbital and Rover observations [6]. Field geology at Lonar Crater (diameter = 1.8 km) reveals a DLE structure with two distinct layers of ejecta [1,7] (**Figure 1**). The lower unit is lithic breccia extending to the limits of the continuous ejecta blanket (CEB), or 1.4 km (~1 ½ crater radii) from the crater rim and measuring ~8 m at maximum thickness. The clasts in the lithic breccia are angular, highly fractured, and either unshocked (mineralogically) or Class 1 shocked basalt (0-20 GPa) [1], which consists of fractured grains but no melting or mineral phase changes [1]. As shock pressures are typically 1-2 GPa near the crater rim, no intense shock metamorphism has occurred. From comparisons to basalt flows exposed in the crater walls, the clasts originated from both the oldest flows that have more secondary mineralization of groundmass and from the youngest flows that lack this feature. This is attributed to the level of the pre-impact water table of the ~65 Ma Deccan basalts [7]. The matrix consists of finely pulverized basalt. In theory, this unit grades into what would be overturned or inverted strata near the crater rim, but the crater has degraded since its initial diameter (1.7 km, based on gravity surveys [2]), meaning that ~50 m of the original crater rim has eroded to contribute to the post-crater fill. The upper ejecta unit is a suevite breccia containing clasts shocked to all degrees of shock pressure from unshocked up to Class 5 (> 80 GPa) of Kieffer *et al.* [1]. The suevite layer measures ~1 m in thickness and extends to ~0.5 km (~½ crater radii) from the rim. The matrix is finely pulverized basalt but with the addition of local glass spherules, beads, and dumbbells [1,2] reportedly not found in the lithic breccia unit.

This DLE structure described for Lonar Crater is similar, if not identical, to the "throw out" and "fall out" layers observed at Meteor Crater [8] or the Bunte Breccia and Suevite at Ries Crater [9], and suggests that two processes are responsible [10,11] for the ballistic emplacement of the lithic breccia moments before the "falling out" of the fall-out suevite layer. Shoemaker [8] identified a suevite layer within Meteor Crater, then later surmised that this unit likely used to be thicker in near-rim regions of the CEB, but has eroded, as the fine matrix of this unit is easily transported by the SW winds of the Colorado Plateau to leave behind the clasts of the suevite layer as a lag [8].

Whereas the lower, more weathered basalt flows have not been identified as protoliths for Classes 2 through 5 in the suevite breccia, heavily fractured basalt corresponding to these basalt flows is observed that are either unshocked or Class 1, implying that these deeper strata are incorporated into the suevite layer. At Meteor Crater, the Coconino Sandstone serves as a lithologic tracer, as highly shocked lechatlerite is distributed in the Meteor Crater fall-out layer [8], suggesting material deep in the target sequence is incorporated into this unit. This provides data to "ground truth" modeling of Lonar Crater, Meteor Crater, and similar small (1-2 km diameter) craters [12].

Table 1. Inventory of Lonar ejecta layers and materials

Airfall fines?
(not found at Lonar or Meteor Crater but theorized based on nuclear tests)

Suevite breccia
clasts: target rock subjected to all degrees of shock metamorphism, including Class 2 through Class 5

matrix: pulverized fines + melt spherules, beads

melts: clasts of Class 5 plus spherules, beads in matrix

Lithic Breccia:
clasts: unshocked + some Class 1 target rock subjected to low (<< 10 GPa) pressures

matrix: pulverized fines

melts: none

Figure 1 (right). Structure of the Lonar Crater, India ejecta blanket. The figure represent a stratigraphic cross section viewed as a slice through the Lonar ejecta. The number on the clasts represents the class of shocked basalt [1], and thus the shock level, with "un" representing unshocked basalt.

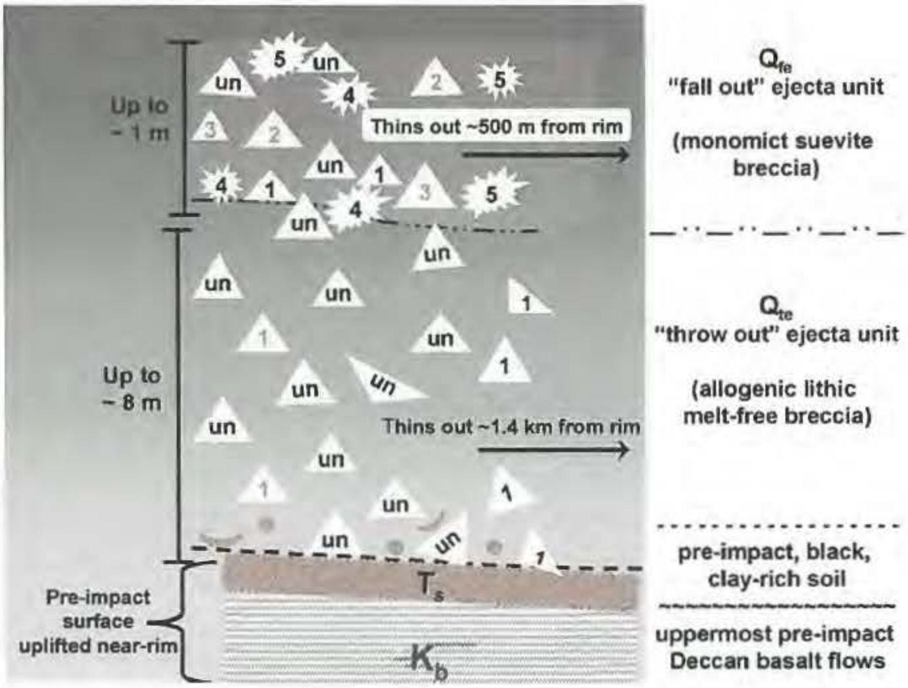

Spectroscopy: The uniqueness of the Lonar target rocks provides ideal samples to acquire the TIR spectra of various degrees of shocked basalt. Due to detection limit (~10%) of TIR spectroscopy and the overall scarcity of materials shocked to intermediate (~20 GPa) to high pressures (~1%) [13], these data are better applied to current and future rover (field) data of individual rocks rather than the large pixels associated with orbital TIR remote sensing. However, regardless of remote sensing, the amount of impactites found in the martian soil (either by sample return or in-situ analysis) has implications for the impact and geologic history of that regolith. TIR spectroscopy for each member of the list of impactites (Table 1) is shown as Figure 2. The more predominant type of impactite is pulverized basalt fines that make up the bulk of both ejecta units. Details on the spectroscopy of Class 2 (20-40 GPa) [14] and Class 5 impact melts [4] are described in previous conference proceedings. SEM and petrographic data will be shown.

Acknowledgements: H.E. Newsom is thanked for discussions. P.R. Christensen provided financial support and guidance for early Lonar efforts. The Barringer Family Fund provided funding for a future trip to Lonar for more sample collection. A. Dube, K. Louzada, A.C. Maloof, J.R. Michalski, S. Misra, S.T. Stewart-Mukhopadhyay, and B.P. Weiss are thanked for field discussions at Lonar.

References: [1] Kieffer *et al.* (1976) *Lun. Plan Sci. Conf. VII*, 1391-1412 [2] Fudali *et al.* (1980) *Moon & Planets 23*, 493-515 [3] Stewart *et al.* (2005) *Rol. Vol. Atm. Martian Impact Crater.*, #3045 [4] Wright *et al.* (2006) *LPSC XXXVII*, #1786 [5] Wright (2007) *7th Int. Conf. Mars*, #3399 [6] Bandfield *et al.* (2000) *Science 287*, 1626-1630 [7] Wright and Newsom (2008) *GRL*, submitted [8] Shoemaker (1963) *Moon, Meteorites, & Comets 4*, 301-335 [9] Hörz *et al.* (1983) *Rev. Geophys. Space Phys. 21*, 1667-1725 [10] Barlow *et al.* (2000) *J. Geophys. Res. 105*, 26733-26738 [11] Komatsu *et al.* (2007) *J. Geophys. Res. 112*, 10.1029/2006JE002787 [12] Wright (2007), *Bridg. Gap. II*, #8061 [13] French (1998) *Traces of Catastrophe* [14] Wright (2008) *LPSC XXXIX*, #2330

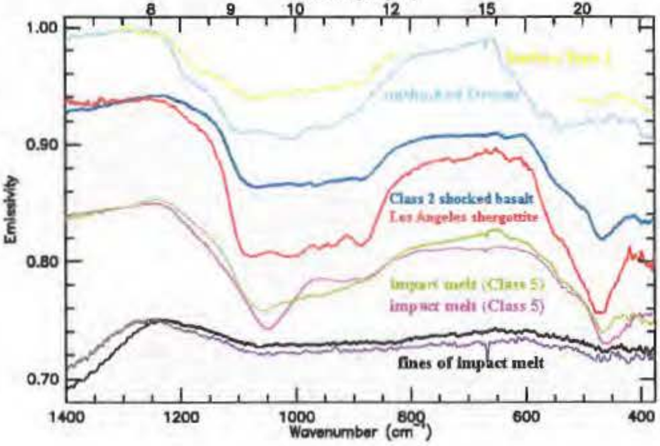

Figure 3 (above). TIR spectra of various Lonar impactites Surface Type 1, an orbital TIR end-member and the laboratory spectrum of the Los Angeles shergottite are shown for comparison. Spectra are offset for clarity.

LIMITATIONS OF POINTS-SOURCE ANALOGY FOR METEORITE IMPACT AND IMPLICATIONS TO CRATER-SCALING

K. Wünnemann[1], G. S. Collins[2], D. Elbeshausen[1] [1]Humboldt-Universität zu Berlin, Museum für Naturkunde, D-10099 Berlin, Germany [2]Impacts and Astromaterials Research Centre, Department of Earth Science and Engineering, Imperial College London, London SW7 2AZ, UK (Contact: kai.wuennemann@museum.hu-berlin.de).

Introduction: The dimensions of meteorite impact craters provide an important measure of the energy that was released by an impact event. To evaluate the consequences accompanying the strike of a meteorite, therefore, it is of particular importance to find a relationship between crater size and impact energy. Deducing the original size of the impactor from a given crater size is impossible because velocity, impact angle and material properties are usually unknown. The inverse question, however, of how large a crater will be produced by an impact of given size, mass, velocity, and angle of incidence has been investigated in many experimental [1,2] and numerical modeling studies [3], which have resulted in the development of so-called scaling laws.

A fundamental assumption underlying cratering scaling laws is that an impact event may be approximated as a stationary point source of energy and momentum buried at a certain depth in the target, analogous to the detonation center of an explosive source [4,5,6,7]. If this assumption holds true for any hypervelocity impact, the kinetic energy (and momentum) of the impactor that is effectively available as an energy (and momentum) point source is defined, according to the theory, by the so-called coupling parameter. It is assumed that the coupling parameter combines the properties of the impactor (velocity U, diameter L, density δ) into one scalar parameter: $C=LU^{\mu}\delta^{\nu}$ [6]. In two theoretical end-member cases, the coupling parameter is exactly proportional to the kinetic energy (where $\nu=1/3$, $\mu=2/3$) or the momentum ($\nu=1/3$, $\mu=1/3$) of the impactor, respectively. However, experimental evidence suggests that the coupling parameter is somewhere between these limits; in other words, it is proportional to some combination of kinetic energy and momentum ($\nu=1/3$; $1/3<\mu<2/3$) [6]. The exact form of the coupling parameter appears to depend on target properties. In addition, impact angle plays an important role [8] and has not yet been successfully incorporated into scaling laws.

We conducted numerous numerical impact experiments (hydrocode models) of crater formation to investigate crater dimensions as a function of projectile properties (impact velocity, size, density, angle of incidence) and target characteristics (density, coefficient of friction, cohesion, porosity, gravity). Here we present the available data base in comparison to experimental data and discuss the implications of our results for impact crater scaling.

Pi-group scaling: The primary purpose of scaling laws is to meaningfully extrapolate the results of small scale laboratory impact experiments so that they may be applied to large scale natural craters. To achieve this, dimensionless ratios are used to estimate the relative importance of different physical processes during crater formation. Dimensionless measures of the properties of impactor and target can be related to scaled crater dimensions implying that the relative crater size is independent of the real size of an impact event.

The most successful approach in dimensional analysis of impact crater scaling is the so-called Pi-group scaling [4]. Instead of defining for instance the crater volume V as function of six (or more) target and projectile properties (e.g., $V=\mathrm{F}(U,\rho,\delta,Y,g,m)$, where U is impact velocity ρ is target density, δ is projectile density, Y is strength, g is gravity, and m is projectile mass) the use of dimensionless ratios reduces the number of independent variables to three: $\pi_V=\mathrm{F}(\pi_2,\pi_3,\pi_4)$, where the so-called crater efficiency $\pi_V = \rho V/m$, the gravity-scaled size of an impact event $\pi_2=1.61gL/U^2$, and the strength-scaled size $\pi_3= Y/(\delta U^2)$, and the density ratio $\pi_4=\rho/\delta$. Note that the angle of impact θ is yet not considered in this concept (compare [9]).

The assumption that an impact can be represented as a stationary point-source has been shown to imply that many impact-related phenomena are related to the dimensionless ratios π_2, π_3 and π_4 by power laws. For instance, if gravity is the dominant influence on crater growth, crater efficiency π_V can be expressed as a power-law of π_2 and π_4: $\pi_V=C_V\,\pi_4^{\alpha}\,\pi_2^{\beta}$, where the exponents α, β are related to the exponent in the coupling parameter: $\beta=-3\mu/(2+\mu)$, and $\alpha=(2+\mu-6\nu)/(2+\mu)$ [4]. A large number of impact experiments in sand and water [1,2] have demonstrated the utility of this, and other power law relationships, over the parameter range that can be realized in impact experiments (Fig.1). Note, that the dashed lines were fitted to data from cratering experiments for $\pi_2<10^{-5}$ [1].

Comparison between experimental and modeling data: We conducted a series of numerical experiments of crater formation with the well-known hydrocode iSALE [10,11]. First, we kept the impact velocity constant at $U=6.5$ km/s, comparable to velocities in laboratory experiments, and varied projectile size and gravity to investigate how crater efficiency changes with π_2. In general, we found a good agreement between numerical models and experimental data for purely hydrodynamic targets (water) and dry sand (Fig. 1). For the latter, appropriate values for the coefficient of friction and porosity were required to match the experimental data.

For an oblique angle of incidence the models show that crater efficiency decreases with decreasing angle of incidence (Fig. 2) [8]. The data can still be approximated by a power-law for low impact velocities ($U=6.5$ kms), a density ratio between projectile and target $\pi_4=1$, and impact angles

θ>30°. All available data (for vertical and oblique impacts and same friction coefficient) plot approximately on the same line if the velocity U is replaced by the vertical velocity component $u_v=\sin\theta\ U$ in the definition of the gravity-scaled sized of an event π_2: $\pi_V=C_V\,\pi_4^{\alpha}\,\pi_2^{\beta}\,\sin^{-2\beta}\theta$ [8,9].

Limitations of point-source: The fact that cratering efficiency (and a number of other measures of an impact) is related to π_2 by a power-law is indirect support for the validity of the point-source approximation. However, the finite size of the impactor implies that close to the impact site the point source approximation must break down. In other words, the point source approximation can only be strictly valid at sufficient distances from the impact (and, accordingly, a certain time after impact). Thus, we can define the "coupling zone" to be the near-field region within which the point-source approximation does not hold. Processes that occur in the coupling zone may still follow a power-law behavior but in such cases the power-law exponent may not be proportional to the velocity exponent μ, which it should be if the point-source approximation applies.

Experiments that imaged the evolution of crater growth in both vertical and oblique impacts [12] provide compelling evidence that the stationary point source concept may not hold for oblique impacts, or strong contrasts in density between projectile and target for instance due to porosity (dissipative targets, compare [4,5]). However, little numerical work has been done to constrain the dimensions of the coupling zone (and how this is affected by impactor and target properties), or to examine whether the size of the coupling zone is different for the various impact related phenomena for which scaling laws exist (e.g. ejection velocities, crater growth rate, shock pressure decay). Our goal here is to quantify the size of the coupling zone as a function of impactor and target properties and, thus, to put constraints on the applicability of the point source solution and Pi-group scaling for processes related to crater formation such as crater dimensions, ejection of material, and shock wave propagation.

Impact crater scaling laws might be expected to break down when the volume of the coupling zone is comparable to or larger than the crater volume. [6] suggested that the coupling zone might have a radius of ~2 impactor radii; in this case, the point-source approximation would be invalid for cratering efficiencies π_V less than ~8. For typical impact scenarios on Earth (coefficient of friction=0.7, g=9.81, U=18 km/s), cratering efficiencies of 10 or lower equate to an impactor size of L>100 km ($\pi_2 > 5\times10^{-3}$) for a vertical impact and L>20 km ($\pi_2 > 1\times10^{-3}$) for oblique (30°). This would suggest that impact cratering scaling laws are applicable over almost the entire range of interest in planetary cratering. However, preliminary results of our numerical models indicate that the coupling zone is larger than two projectile radii, particularly in oblique impacts and impacts with large projectile-to-target density or porosity ratios.

Acknowledgements: This work was funded by DFG- Wu 355/5-1 and NERC grant NE/B501871/1

References: [1] Schmidt, R. M. and Housen, K. R. (1987) IJIE, 5, 543-560; [2] Gault, D. E., Sonett (1982), GSA Special Paper 190, 69-92; [3] O'Keefe J.D., Ahrens T.J. (1993), JGR, 17,011-17,028; [4] Holsapple K.A., Schmidt R.M. (1987) JGR, 6350-6376; [5] Holsapple K.A. (1987), Int. J. Impact. Engng., 343-355; [6] Holsapple K.A. (1993), Annu. Rev. Planet. Sci. 12:333-73; [7] Housen K.R., Holsapple K.A. (2003), Icarus, 102-119; [8] Elbeshausen D., Wünnemann K., Collins G.S. (2008), LPSC XXXIX, 1795; [9] Chapman, C. R. and McKinnon, W. B. (1986), Satellites, Univ. of Arizona Press, 492-580; [10] Wünnemann K., Collins G.S., Melosh H.J. (2006), Icarus, 514-527; [11] Elbeshausen D., Wünnemann K., Collins G.S. (2007), LPSC XXXVIII, 1952; [12] Anderson J.L.B., Schultz P.H. (2006) Int. J. Impact. Engng., 33:35-44.

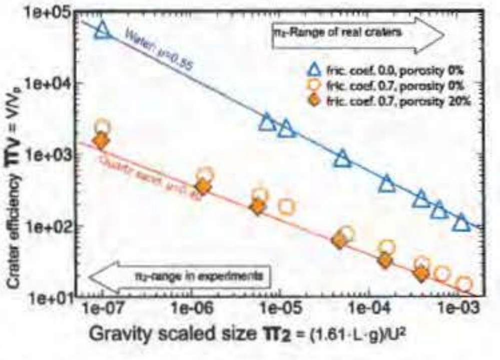

Fig. 1: *Gravity-scaled size π_2 versus crater efficiency π_V for vertical impacts. Triangles, diamonds and circles represent numerical modeling results. The impact velocity was 6.5 km/s in all models. Solid lines are based on impact crater experiments [Schmidt87].*

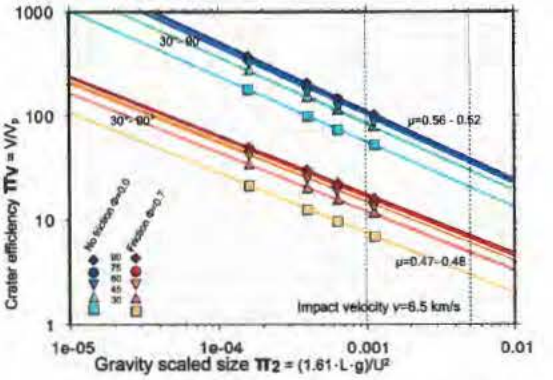

Fig. 2: *Gravity-scaled size π_2 versus crater efficiency π_V for oblique impacts (θ=30°-90°) and different friction coefficients ϕ. Blue lines correspond to a ϕ =0.0, yellow-red lines correspond to ϕ=0.7. The impact velocity was 6.5 km/s in all models.*

MAGNETIC FABRICS OF ARAGUAINHA IMPACT STRUCTURE (CENTRAL BRAZIL): IMPACT PRODUCTS AND COLLAPSE HISTORY IN THE CENTRAL PEAK-RING.

[1]E. Yokoyama; [1]R. I. F. Trindade; [2]C. C. Lana; [1]Y.R.Marangoni; [3]E.Tohver; [1](Instituto de Astronomia Geofisica e Ciencias Atmosfericas - USP, Rua do Matao 1226, Sao Paulo, SP 05508-090, Brazil ; elder@iag.usp.br), [2](Department of Geology - University of Stellenbosch, Private Bag X1-Matieland, Stellenbosch, WC 7620, South Africa ; lana@sun.ac.za), [3](School of Earth and Geographical Sciences Perth-University of Western Australia, 35 Stirling Highway, Crawley, WA 6009, Australia ; etohver@cyllene.uwa.edu.au).

Introduction: A meteorite impact hit central Brazil ca. 250 Ma ago, just prior to the Permo-Triassic boundary, leaving a 40 km wide complex impact structure (the largest impact structure identified in South America)[1,2]. It is a well-preserved and shallowly eroded crater, that provides unparalleled opportunity to study the kinematics of peak-ring crater formation.

Results: This crater developed on sediments of the intracratonic Paraná basin. The impact has excavated more than 2 km of the original sedimentary pile, bringing to the surface granites and host metamorphic rocks of the basement after collapse. It comprises a central peak ring, annular basin, two main ring features and deformed rims. Field observations and petrographic studies in impact-related materials inside the central peak ring allow recognition of four lithofacies (metamorphic basement, cataclastic porphyritic-granite, impact melts and polymitic breccias) that record different magnetic fabrics. Cataclastic porphyritic granite record the crater collapse fabric orientation, whereas the other rocks record a process after crater collapse, comprising molten rocks covered by breccias.

Conclusion: The comparison of available models of collapse of craters complex with these observations show, for the first time, that the crystalline embasament may have acquired hydrodynamic behavior during the process of collapse.

References: [1] Engelhardt et al. (1995), Meterotics and Planetary Science. [2] Lana et al. (2007), GSA Bulletin.